SHEDDING LIGHT ON THE NERVOUS SYSTEM: PROGRESS IN NEUROPHOTONICS RESEARCH

EDITED BY: Jean-Claude Béïque, Yves De Koninck and Edward S. Ruthazer

PUBLISHED IN: Frontiers in Neural Circuits

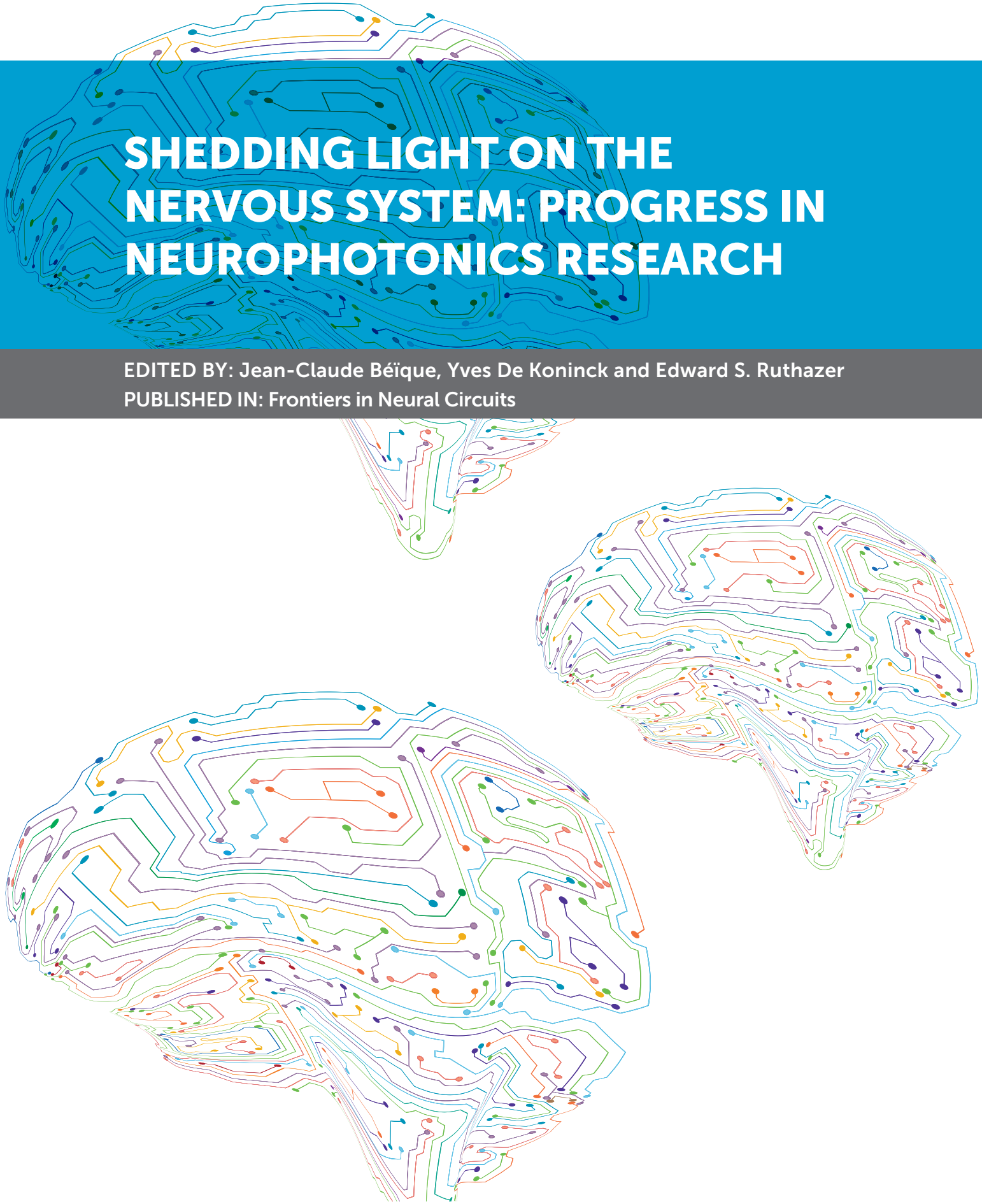

frontiers Research Topics

ISSN 1664-8714
ISBN 978-2-88976-481-5
DOI 10.3389/978-2-88976-481-5

About Frontiers

Frontiers is more than just an open-access publisher of scholarly articles: it is a pioneering approach to the world of academia, radically improving the way scholarly research is managed. The grand vision of Frontiers is a world where all people have an equal opportunity to seek, share and generate knowledge. Frontiers provides immediate and permanent online open access to all its publications, but this alone is not enough to realize our grand goals.

Frontiers Journal Series

The Frontiers Journal Series is a multi-tier and interdisciplinary set of open-access, online journals, promising a paradigm shift from the current review, selection and dissemination processes in academic publishing. All Frontiers journals are driven by researchers for researchers; therefore, they constitute a service to the scholarly community. At the same time, the Frontiers Journal Series operates on a revolutionary invention, the tiered publishing system, initially addressing specific communities of scholars, and gradually climbing up to broader public understanding, thus serving the interests of the lay society, too.

Dedication to Quality

Each Frontiers article is a landmark of the highest quality, thanks to genuinely collaborative interactions between authors and review editors, who include some of the world's best academicians. Research must be certified by peers before entering a stream of knowledge that may eventually reach the public - and shape society; therefore, Frontiers only applies the most rigorous and unbiased reviews.
Frontiers revolutionizes research publishing by freely delivering the most outstanding research, evaluated with no bias from both the academic and social point of view. By applying the most advanced information technologies, Frontiers is catapulting scholarly publishing into a new generation.

What are Frontiers Research Topics?

Frontiers Research Topics are very popular trademarks of the Frontiers Journals Series: they are collections of at least ten articles, all centered on a particular subject. With their unique mix of varied contributions from Original Research to Review Articles, Frontiers Research Topics unify the most influential researchers, the latest key findings and historical advances in a hot research area! Find out more on how to host your own Frontiers Research Topic or contribute to one as an author by contacting the Frontiers Editorial Office: frontiersin.org/about/contact

SHEDDING LIGHT ON THE NERVOUS SYSTEM: PROGRESS IN NEUROPHOTONICS RESEARCH

Topic Editors:
Jean-Claude Béïque, University of Ottawa, Canada
Yves De Koninck, Laval University, Canada
Edward S. Ruthazer, McGill University, Canada

Citation: Béïque, J.-C., De Koninck, Y., Ruthazer, E. S., eds. (2022). Shedding Light on the Nervous System: Progress in Neurophotonics Research. Lausanne: Frontiers Media SA. doi: 10.3389/978-2-88976-481-5

Table of Contents

frontiers | Frontiers in Neural Circuits

EDITORIAL
published: 17 May 2022
doi: 10.3389/fncir.2022.901376

Editorial: Shedding Light on the Nervous System: Progress in Neurophotonics Research

Edward S. Ruthazer[1], Jean-Claude Béïque[2] and Yves De Koninck[3]*

[1] Department of Neurology and Neurosurgery, Montreal Neurological Institute-Hospital, McGill University, Montreal, QC, Canada, [2] Brain and Mind Research Institute, University of Ottawa, Ottawa, ON, Canada, [3] Department of Psychiatry and Neuroscience, Institut Universitaire en santé mentale de Québec, Université Laval, Quebec City, QC, Canada

Keywords: optogenetics, calcium imaging, fluorescence, microscopy, methods, review

Editorial on the Research Topic

Shedding Light on the Nervous System: Progress in Neurophotonics Research

The goal of understanding the brain is more than just a scientific endeavor. It is an existential aspect of human nature to want to understand what underlies our own consciousness and thought processes. But the awesome complexity and interconnectivity of the brain pose many challenges to our traditional reductionist approaches to understanding biological phenomena. While nobody actually believes that individual neurons have ideas or that synapses have memories, our best hope for understanding the mechanisms that endow this remarkable organ with the ability to write novels and cure diseases is to study the behavior and interactions of those unitary elements from which the brain is assembled. Addressing this task with the required spatial and temporal scale poses a formidable experimental challenge. True scientific progress and opportunities often occur when distinct fields of study collide; the merging of traditional neuroscience approaches with the ability to control light in space and time certainly provides an explicit and spectacular example. Still in its infancy, the expanding field of neurophotonics has already singularly propelled brain research forward. Broadly defined, neurophotonics is the use of light to measure or manipulate the form and function of individual or ensembles of brain cells, from neurons to glia, even extending to neurovascular coupling. It is in this ability to individually and non-invasively read and control the activity and signaling of multiple brain cells and even synapses, where the neurophotonic revolution has truly shone.

Arguably it was the timely convergence of few key optical and genetic breakthroughs in the past quarter-century that helped reveal the awesome potential of optical approaches to studying the brain. The original cloning, optimization and expression of Enhanced Green Fluorescent Protein (EGFP) derived from bioluminescent *Aequoria victoria* jellyfish opened the door to a broad palette of genetically-encoded fluorescent proteins with diverse spectral and optical properties (Tsien, 1998; Shaner et al., 2005). In addition to a seemingly limitless number of fusion proteins used to study subcellular protein distribution and interactions, perhaps the most functionally significant application of EGFP derivatives has been the development of genetically-encoded calcium indicators (GECIs), like GCaMP and R-GECO, that permit single cell calcium transients to be monitored throughout a neuronal network (Chen et al., 2013; Enterina et al., 2015). The ability to simultaneously detect neuronal and glial activation in hundreds or even thousands of cells non-invasively has been a game-changer for understanding how networks of brain cells function and dynamically interact both *in vitro* and *in vivo*.

This approach, monitoring activity across cells in the brain, was further enhanced by the discovery that the light-gated ion channel called channelrhodopsin-2, derived from the phototactic

Edited and reviewed by:
Petr Tvrdik,
University of Virginia, United States

****Correspondence:***
Edward S. Ruthazer
edward.ruthazer@mcgill.ca

Received: *21 March 2022*
Accepted: *28 April 2022*
Published: *17 May 2022*

Citation:
Ruthazer ES, Béïque J-C and De Koninck Y (2022) Editorial: Shedding Light on the Nervous System: Progress in Neurophotonics Research. Front. Neural Circuits 16:901376. doi: 10.3389/fncir.2022.901376

green alga *Chlamydomonas reinhardtii*, could be used to optically drive action potential firing when expressed in neurons (Nagel et al., 2003; Boyden et al., 2005). A bevy of additional light-gated channels and transporters were identified and engineered to permit precise activation and suppression of neural activity using light in genetically defined populations of brain cells (Kim et al., 2017). Thus, with the emergence of these families of genetically-encoded tools to monitor and to alter neural activity, the field of optogenetics was born. The neuroscientist's optical armamentarium was no longer restricted to observing neural activity, but now squarely included the ability to perturb it with unprecedented ease and precision.

The last element that has truly brought the applications for these powerful tools into clear focus is the microscope itself. While there is no doubt that optogenetics has been exploited brilliantly using conventional microscopy of cultured cells, as well as fiber fluorimetry and wearable 1p fluorescence miniature microscopes *in vivo*, it was the contemporary development of non-linear optical fluorescence microscopy, especially two-photon laser-scanning microscopy (2PLSM), that permitted the full potential of EGFP and GECIs to be applied in the mammalian brain. By restricting fluorescence excitation exclusively to a focal plane, 2PLSM allows deep tissue single-plane imaging as well as full 3D imaging of labeled cells without the severe image degradation caused by out-of-focus fluorescence excitation that plagues conventional microscopy in scattering tissue like brain (Svoboda and Yasuda, 2006). An alternative approach to solving the problem of image haze in more optically accessible translucent organisms like zebrafish larvae (or optically cleared fixed tissue samples) is selective plane illumination microscopy (SPIM), sometimes called light-sheet microscopy, that allows the entire volume of a zebrafish brain to be imaged by repeatedly scanning a thin plane of excitation light up and down through the fish at high speed while acquiring diffraction-limited images with a sensitive digital camera (Huisken and Stainier, 2009). The growing array of sensors, into neurotransmitter and enzymatic sensors, and emergent means to target them to specific cell compartments, coupled with fiber-optic probes to deliver and collect light deep in the brain, open unprecedent capabilities to link intricate cell signaling to behavior, ranging from single-cell photometry to measurements from large ensembles. At the other extreme of imaging approaches, is superresolution nanoscopy, which includes single-molecule localization techniques like direct stochastic optical reconstruction microscopy (dSTORM) and stimulated emission depletion (STED) microscopy (Willig et al., 2006; Klein et al., 2014). Nanoscopy utilizes clever computational and optical strategies to surpass the diffraction limit of image resolution, approaching molecular scale discrimination of objects.

The articles submitted to this Research Topic fall into three overlapping categories: General reviews of optogenetics for the study of synaptic or circuit plasticity, methodological reports of novel experimental tools and algorithms using neurophotonic data, applications of optogenetics to understanding neurological disorders and basic brain circuit function.

A comprehensive and provocative review by Lee et al. covers the diverse optogenetic tools that have been applied to the art of "circuit-bashing" (i.e., functional and anatomical dissection of local and long-range connectivity) with a focus on experiments exploiting cell-type specific expression of optogenetic actuators and inhibitors. This article also discusses numerous important caveats and limitations of optogenetic methods. Other reviews in the Research Topic instead focus more sharply on applications of neurophotonics techniques in specific circuits, in particular the spinal cord (Harding et al.) and the visual system (Rangel Olguin et al.), including in depth discussions of calcium imaging and viral-based methods to study neuronal connectivity. Morales et al. examine memory encoding analyzed with optogenetic tools, while the use of optophysiology to reveal mechanisms underlying synaptic plasticity, and in particular the functional matching of pre- and postsynaptic efficacy, a question that lends itself particularly well to the subcellular resolution offered by optical approaches, is presented in a thought-provoking review by Sanderson et al.

One important objective of the CNP is the development and dissemination of useful optogenetic tools for neuroscience research. This Research Topic introduces a number of technological advances, ranging from CREMSCLE (Cre-Mediated Single Cell Labeling by Electroporation), a simple trick for labeling single neurons using easy-to-implement bulk electroporation methods (Schohl et al.) all the way to a full protocol for building and using an acousto-optic deflector-based random access 2-photon microscope together with software to facilitate high-frequency (3 Hz) functional imaging across hundreds of synaptic sites on a complex 3D dendritic arbor (Sakaki et al.).

The implantation of GRIN lenses and subsequent calcium signal acquisition via a head-mounted portable miniature microscope (a.k.a, "miniscope") provides a powerful means for studying the brain of awake behaving animals engaged in more naturalistic tasks. While this powerful method holds great promise for understanding the relationship of behaviors to complex neuronal responses, like place cell activity in the deep hippocampus for example, one of the challenges of 1P calcium imaging *in vivo* is the proper segmentation of unfocused images as well as the conversion of fluorescence signals to electrophysiologically meaningful data. To this end, Tran et al. discuss the benefits of applying machine learning algorithms to single-cell region-of-interest identification. This work is complemented by an innovative approach developed by Etter et al. for predicting animal behaviors from neuronal calcium signals, surprisingly by entirely foregoing the temptation to try to infer spiking events and frequencies and instead using a naïve Bayesian classifier to generate a probability function to directly relate behaviors to complex calcium signals.

Despite the appeal of functional imaging from hundreds of neurons, sometimes the temporal resolution of electrode recording offers the best approach to understanding circuit function. Mocanu and Shmuel provide a detailed protocol and evaluation of the use of relatively low-resolution intrinsic signal optical imaging to target recording electrode penetrations or virus injection.

Original research reports presented in this Research Topic are similarly broad in scope, starting with two superresolution

nanoscopy papers, one using STED and the other using dSTORM. The STED study cleverly applies machine learning approaches to generalize, based on measurements made across vast populations of synapses in culture, about the relative distances between specific pre and postsynaptic proteins under baseline conditions and following chemical induction of synaptic plasticity, thus providing novel insights into how the pre and postsynaptic terminals reorganize at the molecular level (Wiesner et al.). The dSTORM study instead examines the known phenomenon of cyclical pulsatile release of growth hormone (GH) driven by GH releasing hormone (GHRH) neurons in the hypothalamus (Bednarz et al.). Using superresolution imaging to identify excitatory and inhibitory synapses in GHRH neurons based on proximity of vglut2-PSD95 pairs and vgat-gephyrin pairs respectively, they made the remarkable finding that while inhibitory synapse number was relatively stable over the 3 h cycle of waxing and waning GH release, excitatory synapses dynamically formed and disassembled over the same period, presumably mediating the cyclical GH release.

Naturally, several papers based on optogenetic reagents for activation and inhibition of signaling featured as well. An innovative paper by Luyben et al. presents a new transgenic mouse line expressing a photoactivatable adenylyl cyclase (PAC) protein. Combining PAC activation with electrophysiology and voltage sensitive dye measurements, the authors demonstrated that a robust synaptic long-term potentiation in hippocampus could be induced by optogenetically elevating postsynaptic cAMP. The study by Lafferty and Britt offers more of a cautionary tale. They examined the consequences of optogenetic silencing of inputs to nucleus accumbens (NAc) using illumination of the light-driven proton pump ArchT on feeding behavior in mice. Remarkably, they found that fiber optic-mediated inhibition in the NAc of the axon terminals of basolateral amygdala and paraventricular thalamus inputs had dramatically different effects on feeding behavior than did direct somatic silencing of these input nuclei. The researchers provided a possible explanation for this difference by showing that the frequency of spontaneous excitatory postsynaptic currents onto NAc was unexpectedly elevated by axon terminal ArchT illumination, probably owing to local changes in pH. This meticulous study should serve as a valuable cautionary note to be aware of potential off-target effects whenever using optogenetic approaches.

Sitting at the other end of the imaging scale is an original research paper using mesoscopic imaging of the entire visual cortex in GCaMP6s transgenic mice (Laliberté et al.). The investigators sought to observe changes in stimulus selectivity over a week of presentation of conditioning stimuli favoring a specific stimulus orientation. They found that specifically under conditions of cholinergic enhancement, significant levels of stimulus conditioning took place. This series of studies from subsynaptic resolution molecular analysis of plasticity up to mesoscopic calcium imaging of the entire visual cortex reveal the impressive scope offered by neurophotonic approaches to explore plasticity mechanisms in the brain.

Finally, the most impactful promise of neurophotonics technology lies in its potential for helping us understand neurological disease and eventually to offer cures. For example, one of the very first proposals for the application of optogenetics was to treat blindness (Bi et al., 2006). Epilepsy is one of the most important neurological conditions for which basic neuroscience research has been able to yield invaluable pharmacological and surgical interventions. Animal models of seizure have been critical to advancing our understanding the etiology of this devastating condition. Neurophotonics can shed light here too. Cela and Sjöström report on their optogenetic kindling model which offers some of traditional hallmarks of electrical kindling models, but without the accompanying confound of physical damage and astrogliosis and with the possibility of cell-type specificity for a much deeper mechanistic understanding of the contributions of different cellular players in seizure.

In their forward-looking perspective article, Shen et al. discuss the promise and challenges of using optogenetics therapeutically to treat human neurological disease. In addition to its original application to treating blindness, the possibility of all-optical deep brain stimulation for treating movement disorders and optogenetic silencing as a way to target brain areas associated with devastating chronic pain are discussed, with a very pragmatic consideration of what improvements are needed for optogenetic constructs, such as red-shifting activation wavelengths to permit transcranial illumination and improving viral vectors for more targeted delivery with minimal antigenicity.

The rapidity and extent with which optogenetics has assumed a prominent place in basic and translational neuroscience research, going from a figurative to literal spark in someone's eye in just a few years, is awe inspiring and an explicit testament of its truly revolutionary nature. New reporters and activators are emerging constantly, with considerable excitement over the newest generation of genetically-encoded voltage indicators (Abdelfattah et al., 2019). With new opportunity also comes new challenges. Just finding efficient ways to store the vast quantities of data generated from long streams of volumetric fluorescence recordings, not to mention the increasing open science demands for sharing raw data online, poses a challenge that will require major international standardization initiatives, such as the Neurodata Without Borders project (Teeters et al., 2015). Fortunately, the neuroscience community has already proven itself eager to collaborate on these and other issues, and there is no shortage of innovators, as this Research Topic nicely confirms. The future of neurophotonics is bright.

AUTHOR CONTRIBUTIONS

The manuscript was written by ER and edited by J-CB and YD. All authors contributed to the article and approved the submitted version.

FUNDING

This project was made possible by the Canadian Neurophotonics Platform (CNP), which has evolved into the Canadian Optogenetics and Vectorology Foundry, established in 2015

with generous funding from the Brain Canada Foundation, through the Canada Brain Research Fund, with the financial support of Health Canada and partners. The platform supports neuroscience research and training throughout Canada and internationally by promoting the development and dissemination of key reagents and tools for optogenetics, fiber photometry, and light microscopy-based research (RRID:SCR_016477).

REFERENCES

Abdelfattah, A. S., Kawashima, T., Singh, A., Novak, O., Liu, H., Shuai, Y., et al. (2019). Bright and photostable chemigenetic indicators for extended in vivo voltage imaging. *Science (New York, N.Y.)*. 365, 699–704. doi: 10.1126/science.aav6416

Bi, A., Cui, J., Ma, Y. P., Olshevskaya, E., Pu, M., Dizhoor, A. M., et al. (2006). Ectopic expression of a microbial-type rhodopsin restores visual responses in mice with photoreceptor degeneration. *Neuron*. 50, 23–33. doi: 10.1016/j.neuron.2006.02.026

Boyden, E. S., Zhang, F., Bamberg, E., Nagel, G., and Deisseroth, K. (2005). Millisecond-timescale, genetically targeted optical control of neural activity. *Nature Neurosci.* 8, 1263–1268. doi: 10.1038/nn1525

Chen, T. W., Wardill, T. J., Sun, Y., Pulver, S. R., Renninger, S. L., Baohan, A., et al. (2013). Ultrasensitive fluorescent proteins for imaging neuronal activity. *Nature*. 499, 295–300. doi: 10.1038/nature12354

Enterina, J. R., Wu, L., and Campbell, R. E. (2015). Emerging fluorescent protein technologies. *Curr. Opin. Chem. Biol.* 27, 10–17. doi: 10.1016/j.cbpa.2015.05.001

Huisken, J., and Stainier, D. Y. (2009). Selective plane illumination microscopy techniques in developmental biology. *Development (Cambridge, England)*. 136, 1963–1975. doi: 10.1242/dev.022426

Kim, C. K., Adhikari, A., and Deisseroth, K. (2017). Integration of optogenetics with complementary methodologies in systems neuroscience. *Nature Rev. Neurosci.* 18, 222–235. doi: 10.1038/nrn.2017.15

Klein, T., Proppert, S., and Sauer, M. (2014). Eight years of single-molecule localization microscopy. *Histochem. Cell Biol.* 141, 561–575. doi: 10.1007/s00418-014-1184-3

Nagel, G., Szellas, T., Huhn, W., Kateriya, S., Adeishvili, N., Berthold, P., et al. (2003). Channelrhodopsin-2, a directly light-gated cation-selective membrane channel. *Proc. Natl. Acad. Sci. U.S.A.* 100, 13940–13945. doi: 10.1073/pnas.1936192100

Shaner, N. C., Steinbach, P. A., and Tsien, R. Y. (2005). A guide to choosing fluorescent proteins. *Nature Methods*. 2, 905–909. doi: 10.1038/nmeth819

Svoboda, K., and Yasuda, R. (2006). Principles of two-photon excitation microscopy and its applications to neuroscience. *Neuron*. 50, 823–839. doi: 10.1016/j.neuron.2006.05.019

Teeters, J. L., Godfrey, K., Young, R., Dang, C., Friedsam, C., Wark, B., et al. (2015). Neurodata without borders: creating a common data format for neurophysiology. *Neuron*. 88, 629–634. doi: 10.1016/j.neuron.2015.10.025

Tsien, R. Y. (1998). The green fluorescent protein. *Annu. Rev. Biochem.* 67, 509–544. doi: 10.1146/annurev.biochem.67.1.509

Willig, K. I., Kellner, R. R., Medda, R., Hein, B., Jakobs, S., and Hell, S. W. (2006). Nanoscale resolution in GFP-based microscopy. *Nature Methods*. 3, 721–723. doi: 10.1038/nmeth922

Conflict of Interest: The authors declare that the research was conducted in the absence of any commercial or financial relationships that could be construed as a potential conflict of interest.

Publisher's Note: All claims expressed in this article are solely those of the authors and do not necessarily represent those of their affiliated organizations, or those of the publisher, the editors and the reviewers. Any product that may be evaluated in this article, or claim that may be made by its manufacturer, is not guaranteed or endorsed by the publisher.

frontiers in Neural Circuits

METHODS
published: 29 January 2020
doi: 10.3389/fncir.2020.00003

A Step-by-Step Protocol for Optogenetic Kindling

Elvis Cela[1,2] *and P. Jesper Sjöström*[1]*

[1] Brain Repair and Integrative Neuroscience Program, Centre for Research in Neuroscience, Department of Medicine, Department of Neurology and Neurosurgery, Montreal General Hospital, The Research Institute of the McGill University Health Centre, Montreal, QC, Canada, [2] Integrated Program in Neuroscience, McGill University, Montreal, QC, Canada

Electrical kindling, repeated brain stimulation eventually resulting in seizures, is widely used as an animal model of epileptogenesis and epilepsy. However, the stimulation electrode used for electric kindling targets unknown neuronal populations and may introduce tissue damage and inflammation. Optogenetics can be used to circumvent these shortcomings by permitting millisecond control of activity in genetically defined neurons without gross injury or inflammation. Here we describe an easy step-by-step protocol for optogenetic kindling – optokindling – by which seizures are eventually elicited in initially healthy mice through repeated light stimulation of neurons expressing Channelrhodopsin-2 (ChR2). Chronic EEG recordings may be performed over large time scales to monitor activity while video camera monitoring may be used to assess the behavioral severity of seizures. In conclusion, with optokindling, neuroscientists can elucidate the circuit changes that underpin epilepsy while minimizing the contribution of confounding factors such as brain damage and inflammation.

Keywords: epilepsy, optogenetics, seizure, animal model, kindling, protocol, Channelrhodopsin

OPEN ACCESS

Edited by:
Yves De Koninck,
Laval University, Canada

Reviewed by:
Heiko J. Luhmann,
Johannes Gutenberg University Mainz, Germany
Aleksey V. Zaitsev,
Sechenov Institute of Evolutionary Physiology and Biochemistry (RAS), Russia

***Correspondence:**
P. Jesper Sjöström
jesper.sjostrom@mcgill.ca

Received: *25 October 2019*
Accepted: *10 January 2020*
Published: *29 January 2020*

Citation:
Cela E and Sjöström PJ (2020) A Step-by-Step Protocol for Optogenetic Kindling. Front. Neural Circuits 14:3. doi: 10.3389/fncir.2020.00003

INTRODUCTION

Epilepsy is the fourth most common neurological disorder with over 3 million people affected in the United States alone (Hirtz et al., 2007). It is characterized by recurring seizures, or aberrant neuronal firing, and epileptogenesis is the process by which the healthy brain becomes epileptic (Chang and Lowenstein, 2003). The steps that underpin epileptogenesis remain unclear and they require animal models for their elucidation (Löscher, 2002). Animal models of induced seizures such as electrical kindling have been particularly helpful as they can transform a healthy animal into an epileptic one gradually over time while parameters such as seizure severity and duration are monitored (Goddard, 1967). However, with electrical kindling, it is not possible to target specific neuronal types during stimulation. Furthermore, the stimulating electrode introduces marked tissue damage, making it hard to tease apart the contribution of aberrant activity to epileptogenesis from that of brain damage and inflammation. This lack of experimental control has hampered progress toward a complete understanding of epileptogenesis at the neuronal level.

By using optogenetics, it is possible to circumvent these drawbacks by allowing genetic labeling and activity control of specific subsets of neurons. Indeed, optogenetics has been used in several studies to halt, as well as elicit seizures (Cela and Sjöström, 2019). Recently, we developed an

optogenetic variant of classical electrical kindling (optokindling) based on repeated laser-light stimulation of pyramidal cells (PCs) in motor cortex (M1) (Cela et al., 2019). Our optokindling model mimicked classical electrical kindling in several ways: increased seizure severity and increased seizure duration over stimulating sessions, decreased seizure threshold and long-term retention of seizure susceptibility (Cela et al., 2019). Since we fluorescently tagged opsin-expressing PCs, we could identify the neurons that were directly stimulated. Furthermore, astrogliosis and gross neuronal damage were undetectable in our model, because the fiberoptic patch cable used for laser-light delivery did not penetrate the brain but was implanted above it. Our optokindling protocol resulted in 9 out of 12 animals developing seizures within 13 sessions of stimulation (Cela et al., 2019).

Here, we describe in detail and in simple terms the necessary steps to carry out optokindling in initially healthy wild-type mice. The present optokindling protocol can easily be adapted for use with other cells types.

SURVIVAL SURGERY

Virus Handling and Storage

The below steps outline how to obtain, prepare, and use the virus for opsin delivery.

Note 1: Plasmids for custom viral constructs can be ordered from Addgene. The choice of promoter will determine efficiency and timecourse of expression, as well as the cell specificity.

Note 2: Adeno-associated virus (AAV) vectors can be ordered from university virus cores (e.g., Pennsylvania or North Carolina). Several different serotypes of virus have been used to express ChR2, from AAV2 to AAV9. In our study, we decided to use AAV5 after trying AAV2 and AAV8 with mixed success. The choice of virus serotype is not always straightforward, as outcome may depend on many factors, such as cell type, tissue, species, animal age, etc. In particular, different serotypes preferentially infect different tissue, a concept known as tropism (Naso et al., 2017). Viral injection can also result in an immune response, such that subsequent injections with the same serotype may be considerably less efficacious; this problem can be alleviated by switching serotype (Mendoza et al., 2017). Previous discussion of genetic targeting techniques for opsins should guide decision making with regard to serotype (Sjulson et al., 2016; Cela and Sjöström, 2019). Ultimately, the choice of serotype is, however, largely a matter of trial and error.

(1) To aliquot the virus, ensure proper protection is worn in accordance with the chosen biosafety level of the virus to be used.
(2) Thaw viral stock on ice outside of biosafety cabinet and aliquot 5 μL into small Eppendorf tubes for use on surgery day.
(3) Discard waste into 10% bleach solution.
(4) Label and store aliquots at −80°C.

Stereotaxic Surgery for Viral Expression of ChR2 and Ferrule Implantation

The protocol presented here outlines how to use optokindling to gradually induce seizures in initially healthy animals.

Note: Prior to survival surgery, all surgical tools should have been autoclaved and ferrules for implantation prepared (Preparation stage, **Figure 1**). It may be important to use only male mice to avoid hormonal contributions to seizure outcome, unless this is what is studied (Curry, 1974). We furthermore recommend using animals in the P30-45 age range – younger animals have critical periods that may affect epileptogenesis, while older animals are not ideal should, e.g., acute slice experiments subsequently be required. We recommend using control animals where AAV-EYFP is injected instead of AAV-ChR2, to test for effects of the surgical procedure itself. Another type of control is to inject the AAV-ChR2 virus but ommit the optokindling.

Preparation: Confirm that you will have the right number of animals required for surgery.

(1) Make sure fiber-optic ferrules have been prepared according to standard procedures (Zhang et al., 2010). The length of fiber protruding from the ferrule should be sufficient to target the brain area of interest.
(2) Using a micropipette puller (e.g., Sutter P-1000, Narishige PC-10, or Zeitz DMZ), pull glass micropipettes with ∼100 μm or smaller tip size for viral injection. Alternatively, small-gauge Hamilton syringes (e.g., Neuros series) can be used.
(3) Prepare working concentrations of Meloxicam (20 mg/kg) and Buprenorphine (0.1 mg/kg).
(4) Prepare EEG recording screws by soldering copper wire to stainless steel screws (e.g., McMaster Carr, 000–120 × 1/8).

Day 1

Note: Keep the surgeries as short as possible (e.g., under 3 h). Lengthy surgeries typically result in lower success rates. Follow standard analgesia/anesthesia practises according to your local Standard Operating Procedure (SOP). The volume of AAV injected depends on serotype and desired volume of brain area to target. We used 1.2 μl per hemisphere of the original titer provided by the UNC virus core, which was $1 - 8 \times 10^{12}$ viral genomes per milliliter. We recommend starting with the full concentration of virus and performing serial dilutions in 10× increments until the desired volume of transfection is reached after imaging. We induced anesthesia using an isoflurane/oxygen mix (4%) while the animal is placed in a scavenger cage (e.g., Harvard Apparatus, 75-0239). After the animal is non-responsive to tail-pinch, quickly remove the animal from the cage and connect to the nose hole of the stereotaxic holder (e.g., Stoelting Just for Mouse). This ensures that the animal is sufficiently anesthetized.

(1) Once in the stereotax, affix the ear bars and position the head securely so that the head does not move when lightly prodded. Keep an eye on animal breathing rate throughout

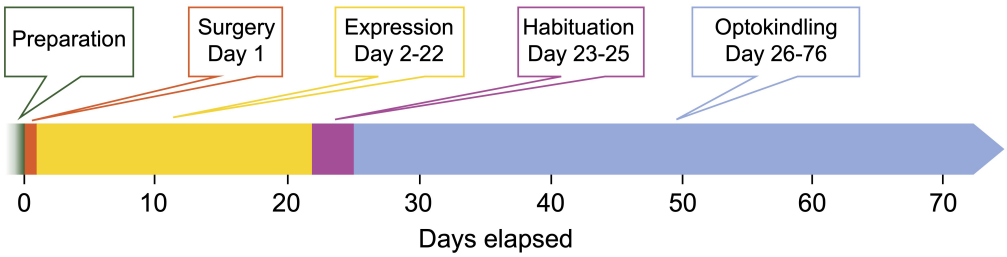

FIGURE 1 | Timeline of the optokindling protocol. This timeline indicates the number of days elapsed from start as well as the duration of each step. *Preparation:* All materials for surgery and optoelectronic components are prepared. *Surgery (1 day):* Animals are injected with AAVs and implanted with fiberoptic ferrules and EEG electrodes. This important step sets the foundation for the rest of the experiments. *Expression (21 days):* This waiting period is required to reach sufficiently high ChR2 expression levels. *Habituation (3 days):* To ensure that animals are not stressed by experimenter handling during the subsequent optokindling period, animals are habituated. *Optokindling (50 days):* While optokindling, animal behavior is monitored, and outcomes such as seizure duration and severity are quantified. The time required for optokindling is 50 days provided the 25 stimulation sessions are spaced ∼48 h apart. It is likely possible to stimulate more often, e.g., every 24 h.

the surgery, to make sure that rate of respiration does not depress severely.

(2) Shave the hairs on the head using a trimmer (e.g., Harvard Apparatus, 729063) and apply iodine solution to the head over the head. Make a midline incision on the head using a scalpel so that the skull is visible. Wipe off any blood with cotton swabs and then peel back any fatty tissue obstructing the full view of the skull.

(3) Mark the skull locations undergoing injection using a surgical marker over the *X* and *Y* stereotaxic coordinates obtained from the Mouse Atlas (e.g., Paxinos and Franklin AP). Open a 1-mm craniotomy over the left target brain using a 9-mm dental drill (e.g., Ram Products, TECH2000). Hydrogen peroxide wash may help stop blood emanating from the skull prior to craniotomy.

(4) Using a programmable pump (e.g., Harvard Apparatus PHD series), inject 1.2 μL AAV-ChR2 bilaterally into brain area under investigation. Aim for 100 μl/min allowing for an additional 5 min for the injection needle to stay in place to help the virus diffuse.

(5) If performing bilateral injections, follow the same procedure outlined in (4) on the other hemisphere.

(6) Dry the skull thoroughly (e.g., Puritan cotton-tipped applicators) whilst making sure to keep the craniotomy area moist with saline solution.

(7) Using the stereotax, place the ferrule with optic fiber attached that was made in Preparation day to the desired brain depth (pia if stimulating cortex). Begin making a mound around the ferrule using dental cement (e.g., Patterson Dental Ortho-Jet). If more stability is required, warmed agar can be used as well, although make sure it has cooled to 37°C before placing it down.

(8) If performing bilateral stimulation, follow the same steps as in (7) with the other ferrule.

(9) Using the dental drill, make holes that are just to the depth of the pia but no further – this is where the electrode screws will be affixed to the skull. The recording screws should lie as close as possible to the stimulation site. The ground reference screws can be placed close to the cerebellum, one on each hemisphere for bilateral recording.

(10) After the recording and reference screws have been affixed to the skull, continue building up the dental cement mound that was started in step (6).

(11) Remove the animal from the stereotax and allow recovery on a heating pad.

(12) Rinse the glass micropipette with 10% bleach and discard in a sharps container.

(13) Discard excess virus in 10% bleach and disinfect all surfaces and instruments that may have come in contact with the virus. Re-freeze unused virus at −80°C.

(14) When the animal has awakened, place it back in the animal rack cage.

Day 2

(1) Refer to your university SOPs for pain assessment and management. Inject analgesics such as Meloxicam according to the SOP.

(2) Check on the animals at least once a day for the next week to make sure they recover from surgery properly.

Optokindling Procedure

Note: Waiting 21 days is recommended for most AAVs to sufficiently drive expression of ChR2 (**Figure 1**). Depending on the vector you use, you may have to wait a different length of time.

Day 23

(1) Habituate the animals for the next three days by connecting them to optic fibers (e.g., Thorlabs FT200EMT), allowing ∼20 min inside the recording cage once a day.

(2) Check light responses by stimulating with two pulses of light 10 ms in duration while monitoring the amplified EEG signal (e.g., AM Systems Extracellular Amplifier). Responses in the EEG may vary from hundreds of microvolts to several millivolts depending on extent of viral expression and light stimulation intensity, as well as ChR2 variant used.

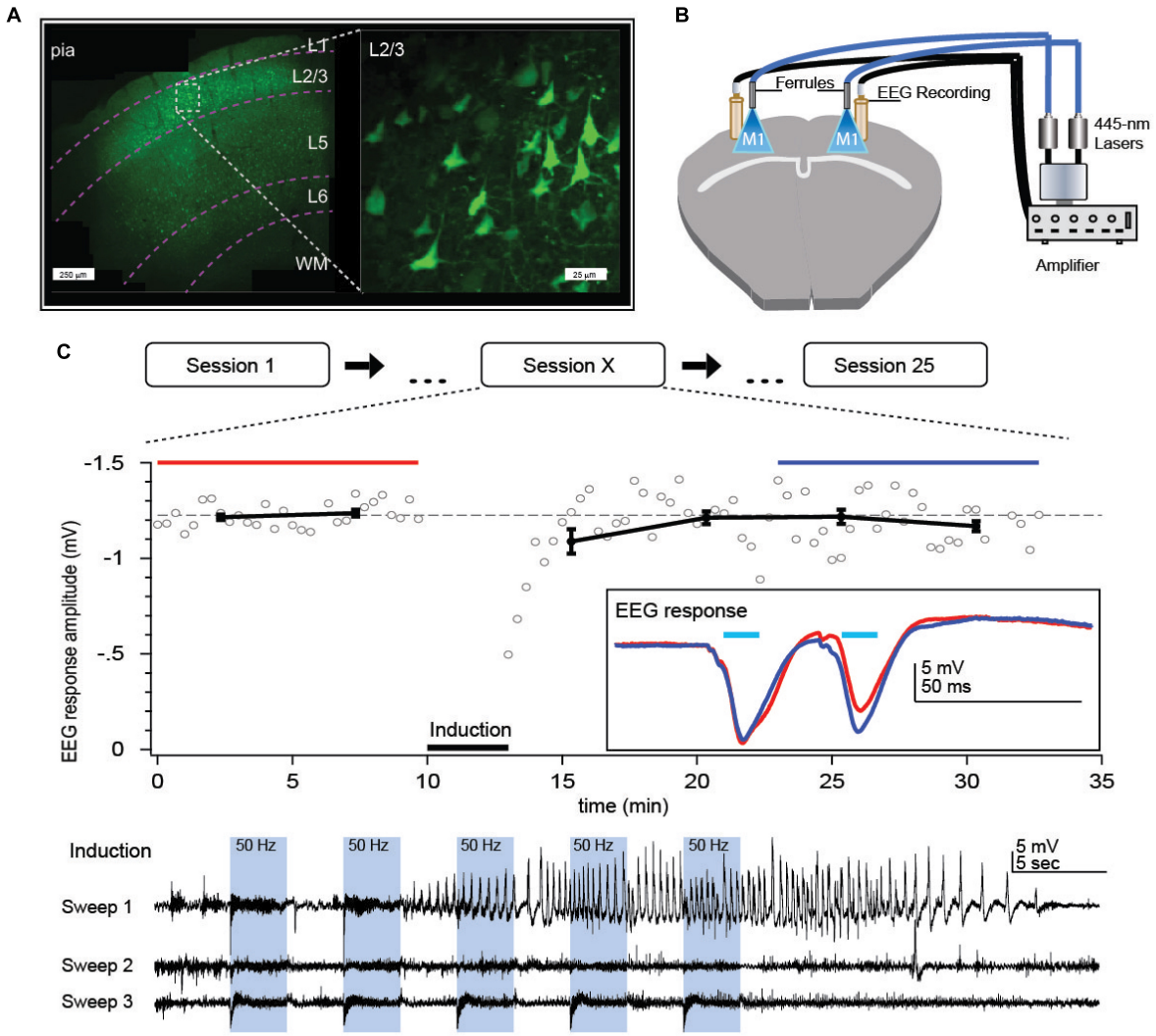

FIGURE 2 | Optokindling protocol for gradual increase of seizure susceptibility *in vivo*. **(A)** Coronal M1 section indicating ChR2 expression primarily in L2/3. Inset shows close-up of L2/3 ChR2-expressing PCs. **(B)** Bilateral implantation of recording screws allows EEG recording whilst fiber-optic ferrule implantation above pia facilitate ChR2 activation without damaging the brain. Fiber optic cables were air-coupled to 445-nm lasers. EEG signals were amplified and then digitized by a computer (not shown). **(C)** During each stimulation session, M1 was repeatedly exposed to 445-nm laser light ("Induction"), delivered as 15 bouts of 3-s-long 50-Hz bursts of 5-ms pulses, divided into three sweeps delivered once a minute. Sessions were repeated every 2 days, 25 times or more. In this example, a prominent seizure was evoked in the first induction sweep of session $X = 15$. We measured EEG responses to 30-Hz paired-pulse laser stimuli for 10 min before and 20 min after the optokindling induction to look for long-term changes in circuit plasticity. *Inset:* Paired-pulse EEG responses before (red) and after (blue) indicated a change in EEG dynamics but not amplitude. Reproduced from Cela et al. (2019).

Day 26

(1) Run stimulation protocol consisting of two pulses at 10 ms repeated every 20 s for 10 min, then 50-Hz bouts for three times, followed by two pulses at 10 ms repeated every 20 s for 20 min again (Cela et al., 2019). The total stimulation time will be ∼33 min.

(2) At the start of the EEG recording, also start video recording to capture behavioral severity of seizures (e.g., Logitech C525 webcam). Later, the video will be used to assign a Racine score to behaviorally quantify seizures.

(3) Return the animal to its original cage after unhooking ferrule and EEG attachments.

(4) Repeat these stimulation sessions every 48 h until at least session 25 has been reached (**Figure 2**).

Note: Try using two cameras, one above and one to the side of the animal for improved capture of behavior (**Figure 3**). Relying on two or more people to score seizure behavior helps to eliminate scoring bias, resulting in more reliable results.

MATERIALS AND REAGENTS

Hardware

Computer (SuperLogics, SL-DK-H61MX-1D).

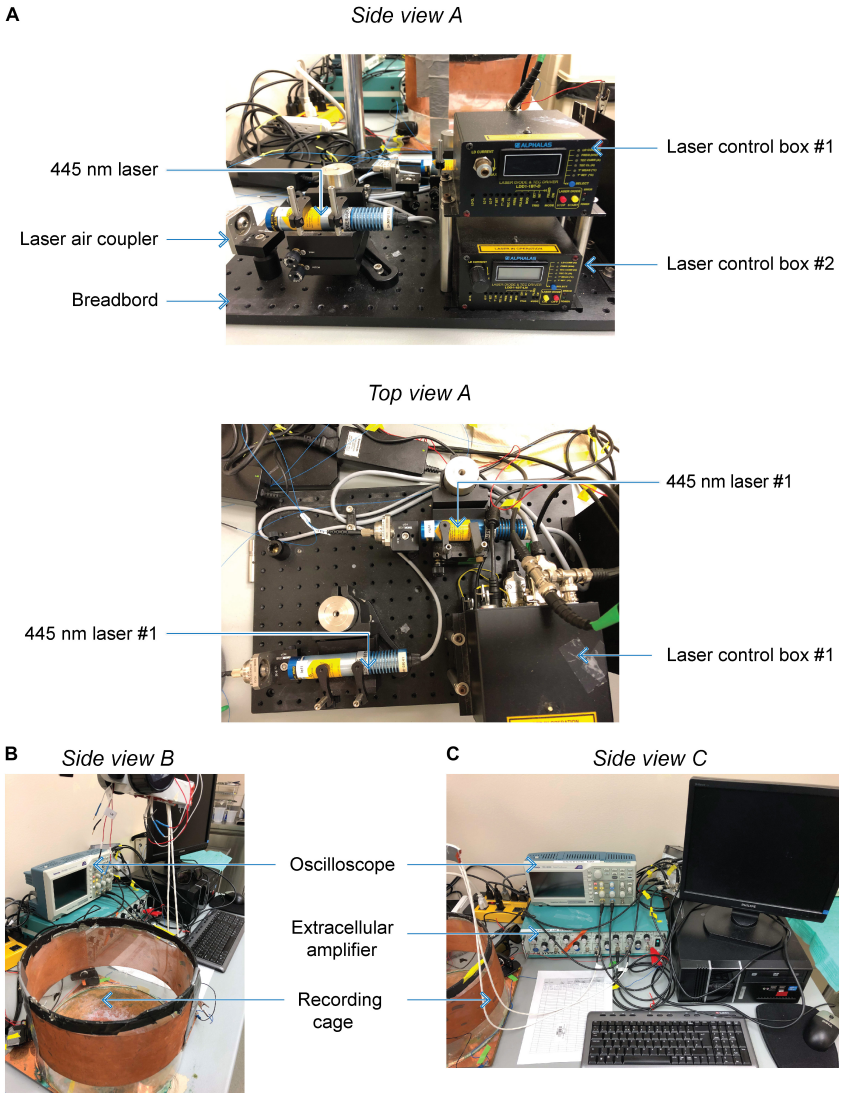

FIGURE 3 | Custom optokindling platform for simultaneous ChR2 excitation and EEG recording. **(A)** Side view A shows both laser control boxes with one 445-nm laser mounted to a breadboard. The laser air coupler collects the laser beam into an FC-PC fiber optic cable using a fiber port collimator. Top view A shows both 445-nm lasers mounted on the breadboard. **(B)** Side view B shows the Faraday cage where EEG recordings are performed as well as the extracellular amplifier used during recordings. **(C)** Side view C shows the oscilloscope used to display EEG signals during acquisition as they are digitized by the data acquisition board and stored on the computer.

Data acquisition board (e.g., NI PCI-6221 or newer PCIe DAQ).
BNC cables (Newark).
Data acquisition software (Igor Pro, Wavemetrics Inc.).
Glass pipette puller (Sutter P1000).
Copper sheet (McMaster Carr, 89675K31).
Extracellular amplifier (AM Systems, Model 1700).
Recording camera (Logitech, C525).
Recording software (ISpy).

Optics

ChR2 excitation laser (e.g., inexpensive eBay laser, or Alphalas GmbH, Monopower-455-150-MM-TEC).
FC-PC patch cable (Thorlabs, M83L01).
FC-PC fiber port collimator (Thorlabs PAF2P-18A).
Breadboard (e.g., Thorlabs, MBH1224).
V-clamp (e.g., Thorlabs, C1513/M).
Ceramic ferrules (Thorlabs, CFLC230-10).
Fiber stripping tool (Thorlabs, T10S13).
Three-hole fiber stripper (Thorlabs, FTS4).
Fiber polishing film (Thorlabs, LF1D, LF3D, LF6D).
Fiber polishing disk (Thorlabs, D50-FC).

Surgery

Channelrhodopsin-2 Adeno-associated virus (e.g., UNC Virus Core).

Dental cement powder (Patterson Dental, 459-8371).
Dental cement liquid (Patterson Dental, 459-3869).
Bulldog clamps (Fine Science Tools, 18050-28).
Silicone mixing cup (Henry Schein, 5100062).
Betadine solution (Purdue Pharma, 40889).
Absorption sponges (Fine Science Tools, 18105-03).
Cauterizer (Fine Science Tools, 18010-00).
Skin marker (Fine Science Tools, 18000-30).
Extra fine Forceps (Fine Science Tools, 11152-10).
Bonn scissors (Fine Science Tools, 14084-08).
Dumont forceps (Fine Science Tools, 11251-35).
Straight forceps (Fine Science Tools, 11000-12).
Scalpel handle (Fine Science Tools, 10003-12).
Scalpel blades (Fine Science Tools, 10010-00).
Suture needles (Fine Science Tools, 12050-01).
Microdrill burrs (Fine Science Tools, 19008-14).
Cordless hair clipper (Harvard Apparatus, 729063).
Stereotax (e.g., Just for Mouse Stoelting Co., 51730).
Mouse mask (Harvard Apparatus, 72-6044).
Syringe pump (Harvard Apparatus, 70-4507).
Anesthesia system (Harvard Apparatus, 75-0239).
Heating pad (Kent Scientific, DCT-15).
Microdrill (Ram Products, TECH2000ON/OFF).
Lubricant eye ointment (AKORN, Artificial Tears).
Mouse atlas (Paxinos and Franklin, Academic Press).
Stereomicroscope (Leica A60).
Meloxicam (Metacam, 5 mg/ml).
Buprenorphine (Vetergesic, 0.3 mg/ml).
EEG recording screws 000–120 × 1/8 (McMaster-Carr, 90910A600).
Gold-plated jacks (Warner Instruments, 64-132).

SUMMARY AND FUTURE DIRECTIONS

Optokindling shares several hallmark features with electrical kindling (Goddard, 1983), including the gradual development of a lowered seizure threshold and longer seizure duration, as well as an increase in behavioral severity of seizures over time (Cela et al., 2019). This increased propensity for more severe seizures of longer duration is retained in the long term even in the absence of ongoing stimulation, which as in Goddard's original model (Goddard, 1967) is in keeping with a form of long-term memory, in further agreement with classic electric kindling.

By relying on gradual development of seizures based on cell-type specific activation, the optokindling model opens up new avenues for exploring the microcircuit plasticity that underlies epileptogenesis (Cela and Sjöström, 2019). This sets the optokindling model apart from other optogenetic models of epilepsy that rely on directly driving the seizures already in naïve animals (Khoshkhoo et al., 2017). In our hands, optokindling did not result in any detectable spontaneous seizures, as has been previously shown with electrical kindling (e.g., Michael et al., 1998). This is arguably both a pro and a con: it provides improved experimental control, but it comes at the cost of reduced biological realism, since epilepsy by definition involves spontaneous seizures. Additionally, we have highlighted typical setbacks associated with the protocol and how to circumvent them (**Table 1**).

Optokindling could also be improved upon. For example, optokindling may be combined with other readouts, such as calcium imaging, to take advantage of the genetic specificity

TABLE 1 | Troubleshooting – list of common pitfalls and how to circumvent them.

Problem	Potential cause	Solution
No EEG response during habituation	Virus leakage during injection or wrong serotype/promoter for cells of interest	(1) Slice brain of animal and visualize under microscope to see if virus is expressed to sufficient levels (2) Confirm placement of screws and electrical continuity
Cap falls off between stimulation sessions	Insufficient drying time between dental cement applications	Ensure that dental acrylic is put on in layers and allow drying between them
Animal is visibly uncomfortable during stimulation sessions	Animal is not sufficiently habituated to new housing or recording setup	(1) Make sure mouse is habituated properly and has had time to settle for 72 h if it is being shipped from elsewhere (2) Make sure mouse is habituated to recording setup for 3 days
Ferrule comes off between sessions	Animal is moving excessively during connection or insufficient levels of dental cement applied	(1) Using Dremel, slightly buff the bottom part of the ferrule that is being placed in the brain for better acrylic adherence (2) Make sure that only about half of ferrule is embedded to allow enough surface area for the sleeve mated to the optic fiber to hold on to
Insufficient power reaches end of ferrule	Ferrule is damaged during connection or laser is underpowered	(1) Make sure that FC-PC coupler has correct NA so that laser light is collected (2) Check for light leaks and/or breaks in the fiber ferrule
Mouse is gasping or wet cough during surgery	Surgery is >3 h	(1) Atropine can help loosen up airways (2) Try repositioning mouse in stereotax to open up trachea

(Khoshkhoo et al., 2017). While motor cortex was targeted in our original study (Cela and Sjöström, 2019), other brain areas such as hippocampus or amygdala are likely more susecptible (Goddard et al., 1969), allowing for more rapid optokindling. Indeed, a recent study shows that optogenetic kindling works well in the hippocampus (Klorig et al., 2019).

Using optokindling, seizures can be elicited by avoiding gross brain damage and targeting other cell populations of interest such as interneurons. The optokindling model may thus provide novel therapeutic insights not only for treatment of the symptoms of epilepsy, i.e., the seizures, but also for the actual process of epileptogenesis, which is causally related to chronic epilepsy (Cela and Sjöström, 2019).

DATA AVAILABILITY STATEMENT

The raw data supporting the conclusions of this article will be made available by the authors, without undue reservation, to any qualified researcher.

ETHICS STATEMENT

The animal study was reviewed and approved by the Montreal General Hospital Facility Animal Care Committee (The MGH FACC), and adhered to the guidelines of the Canadian Council on Animal Care (CCAC).

AUTHOR CONTRIBUTIONS

All authors listed have made a substantial, direct and intellectual contribution to the work, and approved it for publication.

FUNDING

This work was supported by a Savoy Foundation Research Grant (PS), EU FP7 FET-Open grant 243914 (PS), CFI LOF 28331 (PS), CIHR OG 126137 (PS), CIHR PG 389378 (PS), CIHR NIA 288936 (PS), FRQS CB Sr 254033 (PS), NSERC DG 418546-2 (PS), NSERC DG 2017-04730 (PS), and NSERC DAS 2017-507818 (PS). The funders had no role in study design, data collection and interpretation, or the decision to submit the work for publication.

ACKNOWLEDGMENTS

We thank Alanna Watt, Amanda McFarlan, Airi Watanabe, Hovy Wong, and Libin Zhou for useful discussions.

REFERENCES

Cela, E., McFarlan, A. R., Chung, A. J., Wang, T., Chierzi, S., Murai, K. K., et al. (2019). An optogenetic kindling model of neocortical epilepsy. *Sci. Rep.* 9:5236. doi: 10.1038/s41598-019-41533-2

Cela, E., and Sjöström, P. J. (2019). Novel optogenetic approaches in epilepsy research. *Front. Neurosci.* 13:947. doi: 10.3389/fnins.2019.00947

Chang, B. S., and Lowenstein, D. H. (2003). Epilepsy. *N. Engl. J. Med.* 349, 1257–1266.

Curry, J. J. (1974). Prepyriform seizure thresholds during the estrous cycle in female rats. *Exp. Neurol.* 42, 300–306. doi: 10.1016/0014-4886(74)90027-2

Goddard, G. V. (1967). Development of epileptic seizures through brain stimulation at low intensity. *Nature* 214, 1020–1021. doi: 10.1038/2141020a0

Goddard, G. V. (1983). The kindling model of epilepsy. *Trends Neurosci.* 6, 275–279.

Goddard, G. V., Mcintyre, D. C., and Leech, C. K. (1969). A permanent change in brain function resulting from daily electrical stimulation. *Exp. Neurol.* 25, 295–330. doi: 10.1016/0014-4886(69)90128-9

Hirtz, D., Thurman, D. J., Gwinn-Hardy, K., Mohamed, M., Chaudhuri, A. R., and Zalutsky, R. (2007). How common are the "common" neurologic disorders? *Neurology* 68, 326–337. doi: 10.1212/01.wnl.0000252807.38124.a3

Khoshkhoo, S., Vogt, D., and Sohal, V. S. (2017). Dynamic, cell-type-specific roles for GABAergic interneurons in a mouse model of optogenetically inducible seizures. *Neuron* 93, 291–298. doi: 10.1016/j.neuron.2016.11.043

Klorig, D. C., Alberto, G. E., Smith, T., and Godwin, D. W. (2019). Optogenetically-induced population discharge threshold as a sensitive measure of network excitability. *eNeuro* 6:ENEURO.0229-18.2019. doi: 10.1523/ENEURO.0229-18.2019

Löscher, W. (2002). Animal models of epilepsy for the development of antiepileptogenic and disease-modifying drugs. A comparison of the pharmacology of kindling and post-status epilepticus models of temporal lobe epilepsy. *Epilepsy Res.* 50, 105–123. doi: 10.1016/s0920-1211(02)00073-6

Mendoza, S. D., El-Shamayleh, Y., and Horwitz, G. D. (2017). AAV-mediated delivery of optogenetic constructs to the macaque brain triggers humoral immune responses. *J. Neurophysiol.* 117, 2004–2013. doi: 10.1152/jn.00780.2016

Michael, M., Holsinger, D., Ikeda-Douglas, C., Cammisuli, S., Ferbinteanu, J., Desouza, C., et al. (1998). Development of spontaneous seizures over extended electrical kindling: I. Electrographic, behavioral, and transfer kindling correlates. *Brain Res.* 793, 197–211.

Naso, M. F., Tomkowicz, B., Perry, W. L. III, and Strohl, W. R. (2017). Adeno-Associated Virus (AAV) as a vector for gene therapy. *BioDrugs* 31, 317–334. doi: 10.1007/s40259-017-0234-5

Sjulson, L., Cassataro, D., Dasgupta, S., and Miesenböck, G. (2016). Cell-specific targeting of genetically encoded tools for neuroscience. *Annu. Rev. Genet.* 50, 571–594. doi: 10.1146/annurev-genet-120215-035011

Zhang, F., Gradinaru, V., Adamantidis, A. R., Durand, R., Airan, R. D., De Lecea, L., et al. (2010). Optogenetic interrogation of neural circuits: technology for probing mammalian brain structures. *Nat. Protoc.* 5, 439–456. doi: 10.1038/nprot.2009.226

Conflict of Interest: The authors declare that the research was conducted in the absence of any commercial or financial relationships that could be construed as a potential conflict of interest.

frontiers in Neural Circuits

BRIEF RESEARCH REPORT
published: 25 March 2020
doi: 10.3389/fncir.2020.00010

Off-Target Influences of Arch-Mediated Axon Terminal Inhibition on Network Activity and Behavior

Christopher K. Lafferty[1,2] *and Jonathan P. Britt*[1,2]*

[1]*Department of Psychology, McGill University, Montreal, QC, Canada,* [2]*Center for Studies in Behavioral Neurobiology, Concordia University, Montreal, QC, Canada*

Archaerhodopsin (ArchT)-mediated photoinhibition of axon terminals is commonly used to test the involvement of specific long-range neural projections in behavior. Although sustained activation of this opsin in axon terminals has the unintended consequence of enhancing spontaneous vesicle release, it is unclear whether this desynchronized signaling is consequential for ArchT's behavioral effects. Here, we compare axon terminal and cell body photoinhibition of nucleus accumbens (NAc) afferents to test the utility of these approaches for uncovering pathway-specific contributions of neural circuits to behavior. First, in brain slice recordings we confirmed that ArchT photoinhibition of glutamatergic axons reduces evoked synaptic currents and increases spontaneous transmitter release. A further consequence was increased interneuron activity, which served to broadly suppress glutamate input *via* presynaptic $GABA_B$ receptors. *In vivo*, axon terminal photoinhibition increased feeding and reward-seeking behavior irrespective of the afferent pathway targeted. These behavioral effects are comparable to those obtained with broad inhibition of NAc neurons. In contrast, cell body inhibition of excitatory NAc afferents revealed a pathway-specific contribution of thalamic input to feeding behavior and amygdala input to reward-seeking under extinction conditions. These findings underscore the off-target behavioral consequences of ArchT-mediated axon terminal inhibition while highlighting cell body inhibition as a valuable alternative for pathway-specific optogenetic silencing.

Keywords: optogenetics, ArchT, nucleus accumbens, photoinhibition, reward-seeking

OPEN ACCESS

Edited by:
Yves De Koninck,
Laval University, Canada

Reviewed by:
Naofumi Uesaka,
The University of Tokyo, Japan
Catherine J. C. Weisz,
National Institutes of Health (NIH), United States

***Correspondence:**
Jonathan P. Britt
jonathan.britt@mcgill.ca

Received: *30 December 2019*
Accepted: *09 March 2020*
Published: *25 March 2020*

Citation:
Lafferty CK and Britt JP (2020) Off-Target Influences of Arch-Mediated Axon Terminal Inhibition on Network Activity and Behavior. Front. Neural Circuits 14:10. doi: 10.3389/fncir.2020.00010

INTRODUCTION

The nucleus accumbens (NAc) is a forebrain structure that regulates the vigor of reward-seeking. Its excitatory inputs likely encode motivational states and the presence of reward-associated cues (Mannella et al., 2013). For example, paraventricular thalamic (PVT) input regulates food-seeking behavior under conditions of hunger and threat (Labouèbe et al., 2016; Choi and McNally, 2017; Do-Monte et al., 2017; Cheng et al., 2018; Choi et al., 2019), while basolateral amygdala (BLA) input encodes the motivational value of reward-associated cues (Ambroggi et al., 2008; Stuber et al., 2011; Esber and Holland, 2014).

Few studies, however, have directly compared the behavioral consequences of pathway-specific manipulations, so it remains unclear how each input distinctly contributes to effective reward-seeking. Maladaptive alterations in the strength of NAc inputs are thought to underlie discrete aspects of psychopathologies, including the aversive symptoms of drug withdrawal (Neumann et al., 2016; Zhu et al., 2016) and stress susceptibility in animal models of depression (Bagot et al., 2015). Thus, pathway-specific inactivation of these inputs is critical to gaining insight into how this circuitry contributes to healthy and unhealthy behavior alike.

Archaerhodopsin (ArchT)-mediated photoinhibition of axon terminals is commonly used to test the involvement of specific long-range neural projections in behavior. Sustained activation of this outward proton pump in axon terminals effectively decreases evoked transmitter release but alkalizes affected axon terminals, which has the unintended consequence of increasing spontaneous vesicle release (El-Gaby et al., 2016; Mahn et al., 2016). It is unclear whether ArchT's off-target effects undermine the interpretation of its behavioral effects or still permit assessment of pathway-specific function. If the aberrant spontaneous vesicle release recruits local circuit feedforward inhibition, as previously suggested (Mahn et al., 2016), the intended pathway-specific nature of the manipulation may be compromised.

The shortcomings of ArchT terminal inhibition have been well characterized in acute slice preparations (El-Gaby et al., 2016; Mahn et al., 2016), but *in vivo* applications of this technique are still widely used to study the circuit-level basis of specific behaviors (Herrera et al., 2016; Yamamoto and Tonegawa, 2017; Mangieri et al., 2018), particularly concerning NAc inputs (Stefanik et al., 2016; Zhu et al., 2016; Reed et al., 2018; Trouche et al., 2019). Thus, there remains a need to validate the pathway-specific nature of this manipulation in behaving animals.

Here, we compare photoinhibition targeted to the axon terminals or cell bodies of NAc inputs. We test the efficacy of these two approaches for uncovering pathway-specific contributions of the PVT-NAc and BLA-NAc pathways to behavior. We first demonstrate in brain slice recordings that ArchT photoinhibition of glutamatergic fibers effectively reduced evoked excitatory synaptic currents. We also report that it increased asynchronous transmitter release and consequently interneuron spiking, which broadly suppressed glutamate release *via* presynaptic $GABA_B$ receptors. *In vivo*, excitatory axon terminal photoinhibition increased feeding and effortful reward-seeking irrespective of the pathway targeted. These effects are comparable to those obtained with broad inhibition (O'Connor et al., 2015) or lesions (Bowman and Brown, 1998) of NAc projection neurons. In contrast, cell body inhibition of NAc afferents from the PVT and BLA revealed pathway-specific contributions to distinct aspects of reward-seeking when food was available and during extinction, respectively. These data underscore the off-target behavioral consequences of ArchT-mediated terminal inhibition while highlighting cell body inhibition as a valuable alternative for pathway-specific optogenetic silencing.

MATERIALS AND METHODS

Experimental Model and Subject Details

Adult wild-type and transgenic C57BL/6J mice were used, including tdTomato Cre-reporter mice (JAX#007914) and parvalbumin-Cre mice (JAX#008069, Jackson Laboratory, Sacramento, CA, USA). All animals were bred in-house and kept on a reverse light cycle with a 12 h photoperiod. Animals underwent surgery at approximately 3 months of age (25–30 g). Six weeks later they were placed on a restricted feeding schedule and maintained at 85–90% of their pre-surgery body weight. The number of male and female mice were balanced within groups. All experiments were conducted following the Canadian Council of Animal Care and the McGill Animal Care Committee.

Method Details

Viral Constructs and Surgery

Before surgery, animals were anesthetized using a ketamine (Ventoquinol, 100 mg/kg) and xylazine (Bayer, 10 mg/kg) cocktail. The skull of the animal was then secured to a stereotaxic frame (Kopf Instruments) and prepared for intracranial virus injections according to the standard stereotaxic procedure. Seven-hundred nanoliter of virus (5.0×10^{12} GC/ml) was injected bilaterally over 10 min using a Nanoject II Injector with an oil-filled glass micropipette pulled to a tip diameter of 10 μm (Drummond Scientific, 3-000-203-G/X).

For axonal photoinhibition experiments, rAAV5-CaMKIIα-eArchT3.0-eYFP (UNC Vector Core) was delivered into the BLA (AP −1.8 mm, ML ±2.8 mm, DV −5.15 mm) and PVT (AP −1.1 mm, ML ±0.35 mm, DV −3.3 mm) of different cohorts of wildtype mice. Optical fibers with a 200 μm core were implanted in the NAc 10 min later (10° angle, AP 1.5 mm, ML ±1.35 mm, DV −4.6 mm). Animals used for brain slice electrophysiology experiments included PV reporter mice and were prepared in the same manner, but optical fibers were not implanted.

For afferent-specific cell body photoinhibition experiments, retroAAV2-CAG-ArchT-GFP (Neurophotonics Centre at Université Laval) was delivered to the NAc (AP 1.5 mm, ML ±0.62 mm, DV −4.7 to −4.2) and an optical fiber was placed above the BLA (AP −2.06 mm, ML ±3 mm, DV −4.02 mm) or PVT (10° angle, AP −1.20 or −0.95 mm, ML ±0.56 mm, DV −2.82 mm) of different cohorts of wildtype mice.

Behavioral Testing

Mice were trained in sound-attenuating chambers (Med Associates), in which levers were extended on either side of a centrally located food receptacle. A house light and speaker were located on the opposite side of the chamber. All behavioral data were collected using the Med Associates software.

Food-restricted mice were tethered to optical fiber and placed in these operant chambers daily for 40-min sessions. One lever was randomly designated the active lever. Initially, each press on this lever was reinforced with the delivery of 30 μl of a 15% sucrose solution (m/v) to the food receptacle and a tone

presentation (4.8 kHz, 80 dB, 5 s duration). After mice earned 40 rewards in a single session, we switched them to a variable ratio (VR3) reinforcement schedule. The number of active lever presses required for reward delivery and tone presentation then varied randomly between 1 and 5. Inactive lever presses were always inconsequential. Both levers remained extended throughout each session.

Photoinhibition experiments were carried out after animals consistently attained 20 rewards per daily session. Photoinhibition involved bilateral intracranial light delivery (532 nm, 10 mW) for two 8-min periods within the 40-min session. The timing of the photoinhibition periods was counterbalanced across 2 days of testing. Animals subsequently experienced two sessions under extinction conditions, in which presses on the active lever were no longer reinforced. Both extinction sessions were preceded by three daily sessions on the VR3 reinforcement schedule.

Brain Slice Electrophysiology

Mice were anesthetized and perfused with a modified artificial cerebrospinal fluid that contained, in mM, 92 NMDG, 20 HEPES, 25 glucose, 30 $NaHCO_3$, 1.25 NaH_2PO_4, 2.5 KCL, 5 sodium ascorbate, 3 sodium pyruvate, 2 thiourea, 10 $MgSO_4$, 0.5 $CaCl_2$ (pH 7.35). Two-hundred micrometer thick coronal slices containing the NAc were prepared using a VT-1200 vibratome (Leica) and held at 34°C for 10 min in this same solution. Slices were then transferred to a "holding ACSF" at room temperature, which was identical except that NaCl (92 mM) was included instead of NMDG and the $MgSO_4$ and $CaCl_2$ concentrations were 1 and 2 mM, respectively. The ACSF used on the patch rig was maintained at 31°C and contained, in mM, 119 NaCl, 2.5 KCL, 1.25 NaH_2PO_4, 2 $MgSO_4$, 2 $CaCl_2$, 24 $NaHCO_3$, and 12.5 glucose. All ACSF preparations were saturated with 95% O_2 and 5% CO_2. Cells were visualized on an upright microscope with infrared differential interference contrast and fluorescence microscopy. Whole-cell patch-clamp recordings were made using a MultiClamp 700B amplifier using 2 kHz lowpass Bessel filter and 10 kHz digitization with pClamp 11 software (Molecular Devices). Recordings were made using glass pipets with resistance 4.0–6.0 MΩ, filled with an internal solution containing, in mM, 117 cesium methanesulfonate, 20 HEPES, 0.4 EGTA, 2.8 NaCl, 5 TEA-Cl, 4 Mg-ATP and 0.4 Na-GTP (pH 7.3). Projection neurons identified by morphology, membrane resistance, and hyperpolarized resting membrane potential were patched in the NAc shell in areas with bright eYFP fluorescence. Patched cells were held at −70 mV to record evoked and spontaneous EPSCs or at 0 mV to record spontaneous IPSCs. sEPSCs were recorded over 10 min (5 min per condition). sIPSCs were recorded over 30 min. EPSCs were evoked in pairs (50 ms interval) once per minute for 30 min with a single stimulating electrode positioned 100–200 mm dorsal to the recorded neuron. Recordings that included photoinhibition and CGP55984 lasted 15 min (5 min per condition). Series resistance (10–25 MΩ) remained stable throughout data collection. To record interneuron spiking, cell-attached recordings were carried out on $tdTomato^+$ neurons of PV-reporter mice in the NAc shell in areas with bright eYFP fluorescence. Recordings of spiking activity took place over 10 min (5 min per condition). Opsin activation was achieved with 590 nm light (2 mw, ThorLabs, DC4104) directed through the microscope objective.

Histology

At the end of each behavioral experiment, animals were anesthetized with 270 mg/kg Euthansol (Merck) and transcardially perfused with 4% paraformaldehyde (PFA, Sigma-Aldrich). Brains were removed, post-fixed in PFA for 24 h, and then transferred to PBS for 48 h. Tissue was then sliced into 60 μm sections on a vibratome (Leica VT1000s) and mounted on microscope slides with a MOWIOL plus DAPI (Sigma-Adrich, St. Louis, MO, USA) solution.

Quantification and Statistical Analysis

For electrophysiological recordings, all data were normalized to the last 3 min of the baseline condition of a given recording. The frequency of sEPSCs, sIPSCs, and spiking was calculated by counting the number of events that occurred in 1-min bins across each recording. Once normalized, these data were used for all time-course graphs. For summary graphs, the mean normalized frequency was calculated for each experimental condition.

Two-tailed paired *t*-tests and two-way ANOVAs were used for statistical comparisons of behavior across photoinhibition conditions and across pathways.

Sidak's multiple comparisons tests were conducted for all ANOVA *post hoc* tests. The significance of all statistical tests was determined using $\alpha = 0.05$. All data are reported as the mean ± SEM.

RESULTS

ArchT-Mediated Axonal Inhibition of NAc Afferents Increases Reward-Seeking Behavior

The PVT-NAc pathway is thought to integrate hunger signals (Kelley et al., 2005; Kirouac, 2015; Labouèbe et al., 2016; Meffre et al., 2019) while the BLA-NAc pathway processes reward-predictive stimuli (Ambroggi et al., 2008; Esber and Holland, 2014; Beyeler et al., 2018), so we hypothesized that inhibition of these pathways would differentially influence the vigor of food-seeking and responsivity to reward-associated cues, respectively. We used an axon terminal photoinhibition strategy to test this idea, bilaterally targeting light to the NAc of mice expressing ArchT in their PVT or BLA (**Figure 1A**). We trained the mice to lever press for food reward on a variable ratio schedule of reinforcement (VR3) and compared their lever press and food port responses within behavioral sessions, across periods with and without intracranial light delivery. We also assessed the behavioral impact of photoinhibition during interspersed extinction sessions when lever presses were not reinforced.

Photoinhibition of PVT and BLA axons in the NAc increased the frequency of active lever pressing (**Figures 1B,C**), whereas intracranial light delivery in GFP-only control mice did not affect reward-seeking behavior. Photoinhibition of PVT and BLA axons also increased inactive lever responding during extinction

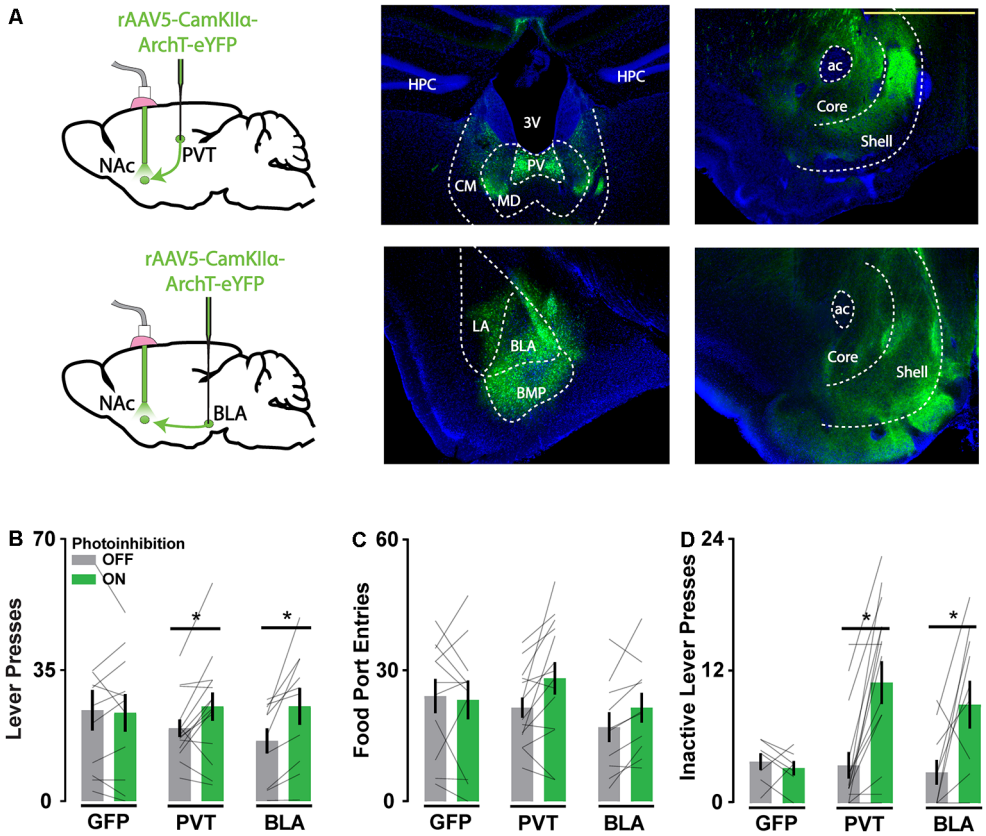

FIGURE 1 | Archaerhodopsin (ArchT)-mediated axon terminal inhibition of glutamate afferents in the Nucleus accumbens (NAc) increases reward-seeking behavior. **(A)** Schematic of viral injections and optic probe placements (*left*). Representative coronal brain slices showing ArchT-eYFP expression in PVT and BLA neurons (*middle*) and their associated axons in the NAc (right). Scale bar, 500 μm. **(B,C)** Photoinhibition of PVT and BLA axons increased active lever responses (n_{GFP} = 11; n_{PVT} = 14; n_{BLA} = 10; $F_{(2,32)}$ = 3.96, $p < 0.05$; for significant *post hoc* tests $t_{(32)} > 2.63$) but not food port entries when reward was available ($F_{(2,32)}$ = 2.52, p = 0.10). **(D)** During extinction, photoinhibition of PVT and BLA axons increased inactive lever responses (n_{GFP} = 7; n_{PVT} = 15; n_{BLA} = 10; $F_{(2,29)}$ = 4.70, $p < 0.05$; for significant *post hoc* tests $t_{(29)} > 3.31$). Error bars represent SEM. *Signifies $p < 0.05$. 3V, third ventricle; ac, anterior commissure; BLA, basolateral amygdala; BMP, posterior basomedial amygdaloid nucleus; CM, central medial thalamic nucleus; HPC, hippocampus; LA, lateral amygdaloid nucleus; MD, mediodorsal thalamic nucleus; PV, paraventricular thalamic nucleus.

sessions (**Figure 1D**), consistent with general disinhibition of behavior. These behavioral effects are comparable to those obtained with direct NAc neuron photoinhibition (O'Connor et al., 2015) and NAc lesions (Bowman and Brown, 1998), which suggests that any inhibitory influence on NAc physiology may similarly disinhibit reward-seeking. Alternatively, given the known off-target effects of ArchT-mediated axonal inhibition, this approach to inhibiting specific pathways may generate broad, unintended disturbances in NAc physiology.

Axon Terminal Inhibition of Excitatory NAc Afferents Increases Local Inhibitory Signaling

We examined the off-target consequences of the ArchT photoinhibition of PVT and BLA axons in NAc neuron brain slice recordings (**Figure 2A**). We first confirmed that opsin activation in PVT and BLA axons reduced the amplitude of electrically-evoked excitatory postsynaptic currents (eEPSCs) in NAc neurons (**Figures 2B,C**), consistent with the intended purpose of the manipulation. We next monitored the frequency of spontaneous EPSCs (sEPSCs) and found it to be elevated during periods of ArchT activation (**Figures 2D–F**), consistent with previous results (Mahn et al., 2016). There was no change in the amplitude or decay time of spontaneous synaptic currents in response to photoinhibition (**Supplementary Figures S1A–D**), nor was there any effect of light on eEPSCs or sEPSCs in recordings from wildtype animals (**Supplementary Figures S2A,B**).

Possibly the asynchronous glutamate release may not directly alter the firing rate of NAc projection neurons, since they have a resting membrane potential close to −80 mV and are thought to fire action potentials upon concerted excitatory input (Goto and Grace, 2008). However, certain interneuron populations in the NAc are highly excitable and may be responsive to small changes in excitatory signaling. To evaluate whether interneuron activity is affected by ArchT-mediated increases in asynchronous glutamate release, we monitored spontaneous

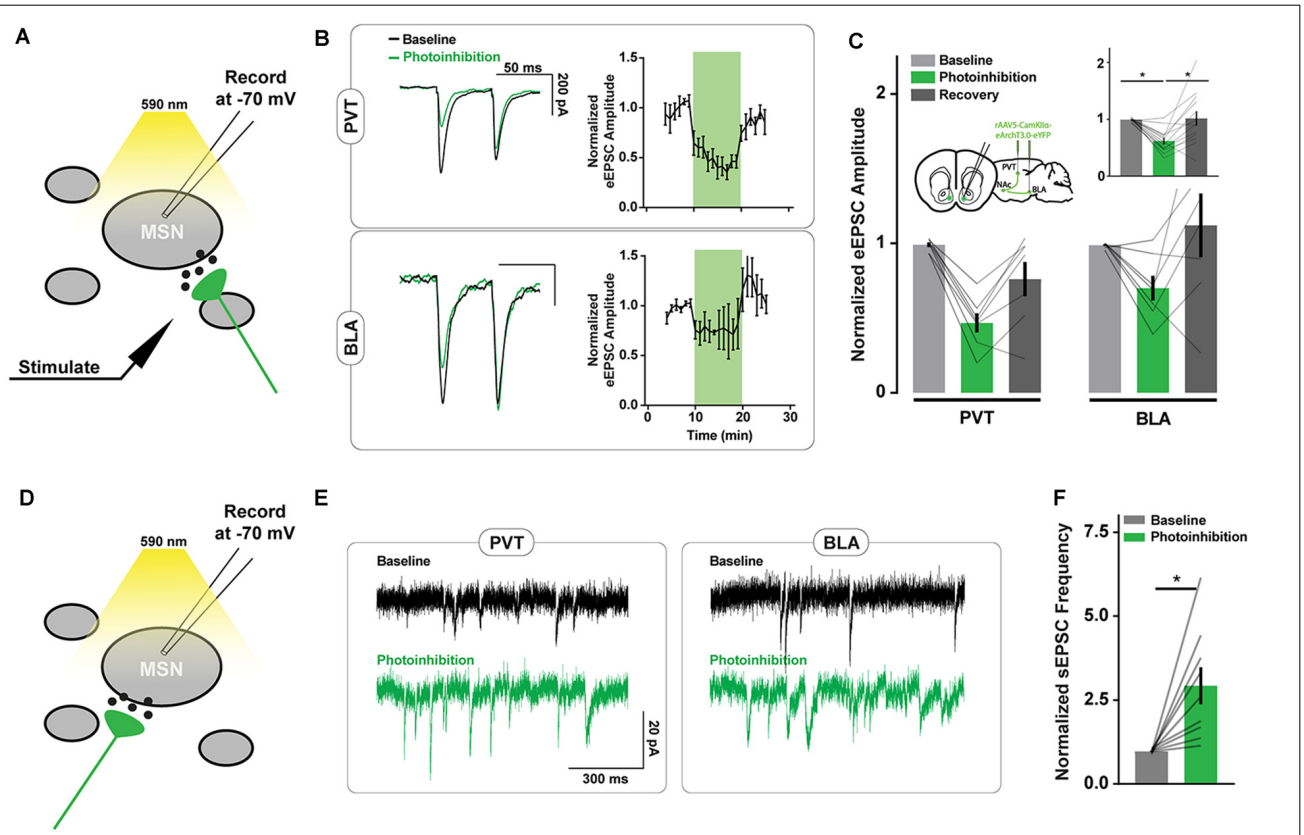

FIGURE 2 | ArchT-mediated inhibition of excitatory axons in the NAc increases spontaneous excitatory postsynaptic currents (sEPSC) frequency. **(A)** Schematic of brain slice recording conditions where electrically-evoked-EPSCs were recorded from NAc spiny neurons before, during, and after Arch-mediated photoinhibition of excitatory axon terminals. **(B)** Example recordings from NAc neurons showing changes in the amplitude of electrically-evoked EPSCs during photoinhibition of PVT (*top left*) and BLA (*bottom left*) axons in the NAc. Summary of relative change in EPSC amplitudes (*right*) over time in response to photoinhibition during minutes 10–20. **(C)** Summary of effect of photoinhibition on EPSC amplitudes. Inset shows data collapsed across pathways, highlighting main effect of photoinhibition [n_{PVT} = 7(3 animals); n_{BLA} = 7(3); $F_{(2,24)}$ = 10.40, $p < 0.001$; $t_{baseline\ vs.\ inhibition\ (24)}$ = 4.18*; $t_{baseline\ vs.\ inhibition\ (24)}$ = 3.68*]. **(D)** Schematic of brain slice recording conditions where spontaneous EPSCs were recorded from NAc spiny neurons during the Arch-mediated photoinhibition of excitatory axon terminals. **(E)** Example NAc neuron recordings highlighting the increase in spontaneous EPSCs that accompanied Arch-mediated inhibition of PVT and BLA axons. **(F)** Summary of effect of photoinhibition on normalized sEPSC frequency [n = 9(3); $t_{(8)}$ = 3.48, $p < 0.0$]. Error bars represent SEM. *Signifies $p < 0.01$. MSN, the medium spiny neuron.

inhibitory postsynaptic currents (sIPSCs) in NAc neurons. The frequency but not the amplitude of sIPSCs was elevated during PVT and BLA axon photoinhibition (**Figures 3A–C**, **Supplementary Figure S1B**), consistent with the hypothesis that local inhibitory signaling is upregulated by unintended glutamate release from ArchT-expressing fibers.

To more directly evaluate this hypothesis, we recorded the spiking activity of parvalbumin-positive (PV) interneurons in the NAc of PV-tdTomato mice in response to ArchT photoinhibition of PVT and BLA axons (**Figure 3D**). We found a sharp increase in PV interneuron spiking following opsin activation, irrespective of its localization to PVT or BLA axons (**Figures 3E,F**). While it is unclear if this increase in spiking is a direct consequence of asynchronous glutamate release, it suggests that activation of ArchT in any collection of excitatory axons in the NAc may cause common disruptions in NAc physiology.

While excess PV interneuron activity directly inhibits NAc projection neurons, it may also broadly suppress glutamate release *via* presynaptic $GABA_B$ receptors located on excitatory afferents (Kupferschmidt and Lovinger, 2015). Indeed, bath application of the $GABA_B$ receptor antagonist CGP55984 at 2 μM partially reversed the effects of axonal ArchT activation on eEPSC amplitude and pulse paired ratios (**Figures 3G–J**) without affecting baseline measures of eEPSC amplitude or sEPSC frequency (**Supplementary Figure S3**). This result raises further doubt about the pathway-specificity of the axonal inhibition approach.

Cell Body Inhibition of NAc Afferents Reveals Pathway-Specific Contributions of PVT and BLA Inputs to Reward-Seeking

To re-evaluate the validity of the behavioral findings we obtained with axonal ArchT activation, we repeated the experiments described above using an alternative approach to disrupting pathway function. Capitalizing on the efficient axon terminal-infecting virus retroAAV, we drove ArchT expression in all NAc-projecting neurons and targeted light to the PVT or BLA

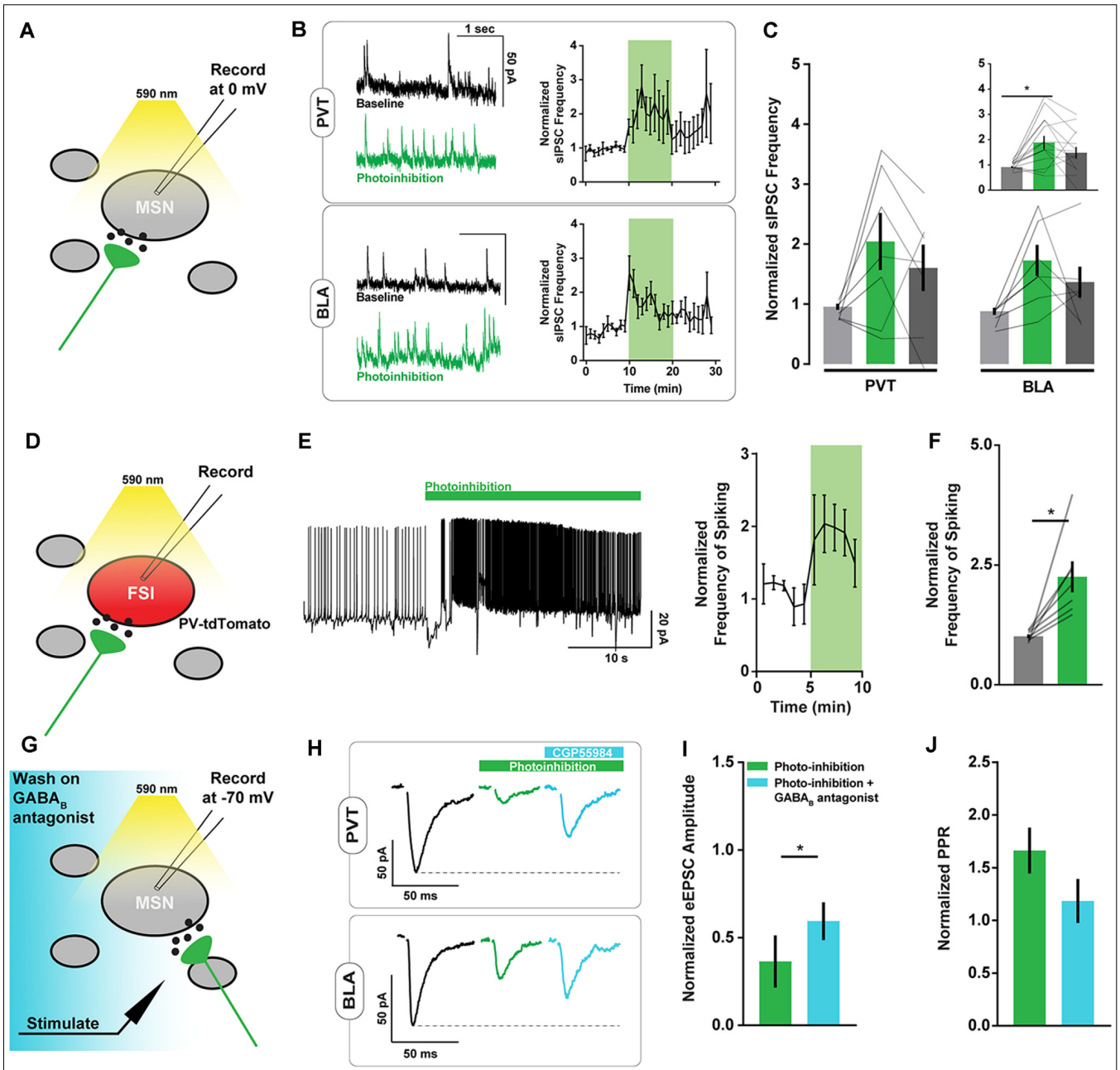

FIGURE 3 | ArchT-mediated inhibition of excitatory axons in the NAc increases spiny neuron spontaneous inhibitory postsynaptic currents (sIPSC) frequency and PV+ interneuron spiking. **(A)** Schematic of brain slice recording conditions where spontaneous IPSCs were recorded from NAc spiny neurons before, during, and after Arch-mediated photoinhibition of excitatory axon terminals. **(B)** Example NAc neuron recordings showing changes in sIPSC frequency during photoinhibition of PVT (*top left*) and BLA (*bottom left*) axons in the NAc. Summary of relative change in sIPSC frequency over time in response to photoinhibition (*right*). **(C)** Summary of effect of photoinhibition on sIPSC frequency. Inset shows data collapsed across pathways, highlighting main effect of photoinhibition [n_{PVT} = 7(3 animals); n_{BLA} = 7(3); $F_{(2,24)}$ = 7.26, $p < 0.01$; $t_{baseline\ vs.\ inhibition\ (24)}$ = 3.79*]. **(D)** Schematic of brain slice recording conditions where spiking activity was recorded in tdTomato-labeled PV+ fast-spiking interneurons (FSIs) during Arch-mediated photoinhibition of excitatory afferent inputs. **(E)** Example recording from a PV+ interneuron in the NAc showing elevated spiking activity coincident with Arch-mediated axon terminal photoinhibition (*left*). Summary of relative change in FSI spiking frequency over time in response to photoinhibition (*right*). **(F)** Summary of effect of photoinhibition on normalized interneuron spiking [n = 7(2); $t_{(6)}$ = 3.64, $p < 0.05$]. **(G)** Schematic of brain slice recording conditions, where electrically-evoked EPSCs were recorded from NAc spiny neurons during Arch-mediated photoinhibition of excitatory axon terminals in the presence of a $GABA_B$ antagonist (CGP55984). **(H)** Example NAc neuron recordings showing the effects of a $GABA_B$ antagonist on evoked EPSC amplitudes during photoinhibition of PVT (*top*) and BLA axons (*bottom*). **(I,J)** Summary of effect of $GABA_B$ antagonist on evoked EPSC amplitude [n = 3(2); $t_{(2)}$ = 5.51, $p < 0.05$] and normalized pulse-paired ratio (PPR; $t_{(2)}$ = 2.90, p = 0.10) during photoinhibition of excitatory axon terminals. Baseline data not shown. Error bars represent SEM. *Signifies $p < 0.05$. FSI, fast-spiking interneuron; MSN, the medium spiny neuron.

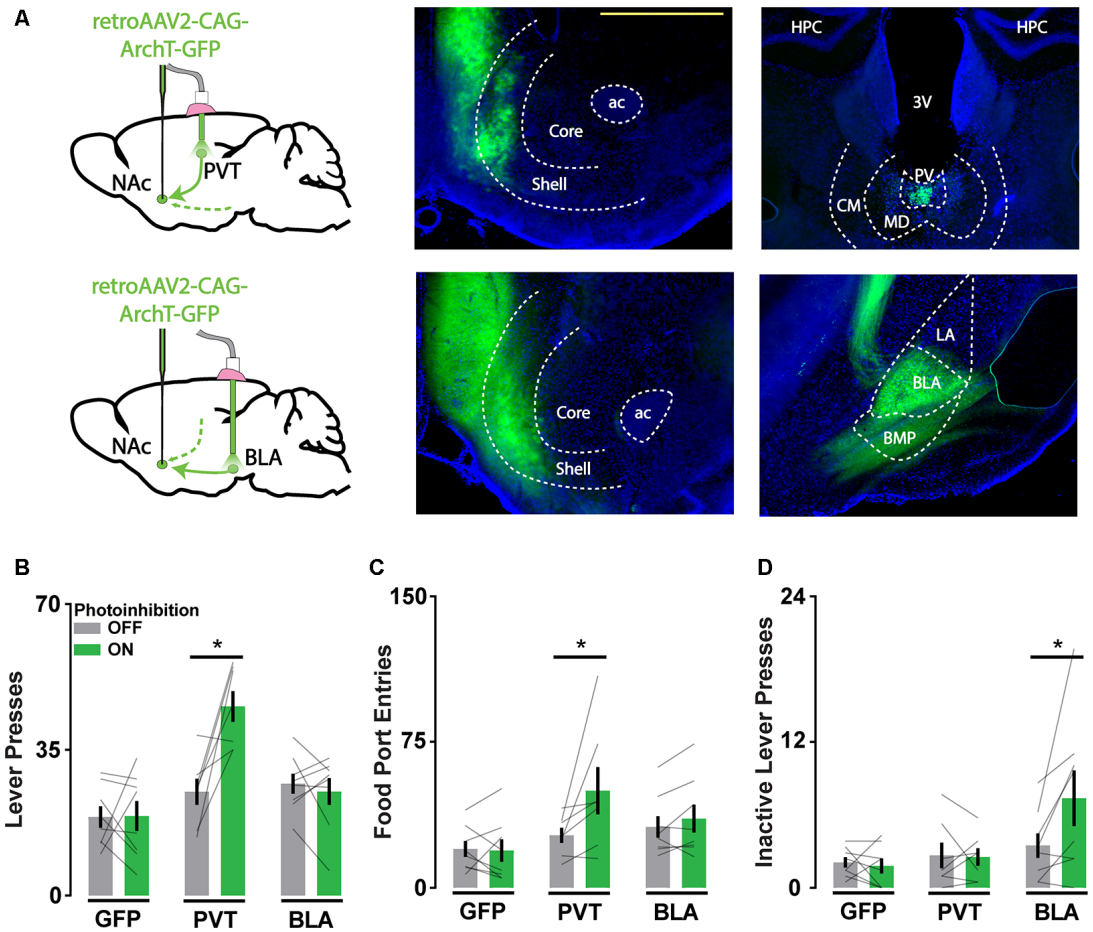

FIGURE 4 | Cell body inhibition of NAc afferents reveals pathway-specific contributions of PVT and BLA inputs to reward-seeking. **(A)** Schematic of viral injections and optic probe placements (*left*). Representative coronal brain slices showing ArchT-GFP expression in axon terminals in the NAc (*middle*) and in soma that project to the NAc in the PVT and BLA (*right*). Scale bar, 500 μm. **(B,C)** Photoinhibition of NAc-projecting PVT neurons increases active lever responses (n_{GFP} = 8; n_{PVT} = 7; n_{BLA} = 8; $F_{(2,20)}$ = 8.31, $p < 0.01$, $t_{PVT(20)}$ = 4.68*) and food port entries ($F_{(2,20)}$ = 3.76, $p < 0.05$; $t_{PVT(20)}$ = 3.47*). **(D)** During extinction, photoinhibition of NAc-projecting BLA neurons increases inactive lever responses ($F_{(2,20)}$ = 4.32, $p < 0.05$; $t_{BLA(20)}$ = 3.44*). Error bars represent SEM. *Signifies $p < 0.05$. 3V, third ventricle; ac, anterior commissure; BLA, basolateral amygdala; BMP, posterior basomedial amygdaloid nucleus; CM, central medial thalamic nucleus; HPC, hippocampus; LA, lateral amygdaloid nucleus; MD, mediodorsal thalamic nucleus; PV, paraventricular thalamic nucleus.

(**Figure 4A**). This method provided pathway specificity, but the manipulation occurred upstream of the NAc. These animals were trained and tested in the same manner as before, and we evaluated the differential influence of PVT and BLA pathways on operant reward-seeking behavior.

With light directed to the PVT and BLA in different cohorts of mice, we found that photoinhibition of the PVT-NAc pathway but not the BLA-NAc pathway increased lever press and food port responding when food was available (**Figures 4B,C**). This result was consistent with previous findings that implicate PVT input in the integration of hunger signals that regulate the vigor of food-seeking. In contrast, photoinhibition of the BLA-NAc pathway but not the PVT-NAc pathway increased inactive lever responding during extinction when food was not available (**Figure 4D**). This finding is consistent with the role of BLA input in regulating cue-reward associations. Together, these results suggest that soma-targeted photoinhibition is a valuable alternative to axon-targeted photoinhibition for assessing pathway-specific contributions to behavior, as only the former revealed dissociable influences of PVT and BLA afferents to the NAc on reward-seeking.

DISCUSSION

In trying to identify dissociable influences of PVT and BLA input to the NAc on reward-seeking behavior, we compared axon-targeted and soma-targeted photoinhibition strategies using the outward proton pump ArchT. We found that axon terminal inhibition increased reward-seeking behavior similarly when targeted to either pathway, whereas pathway-specific inhibition of upstream cell bodies produced dissociable behavioral effects that were consistent with previous literature. NAc neuron brain slice recordings confirmed that activation of

ArchT in excitatory axon terminals reduces eEPSCs yet increases sEPSCs. The pathway-specific nature of this manipulation was undermined by a concomitant increase in GABAergic interneuron activity, which was associated with a broad $GABA_B$ receptor-dependent reduction in eEPSC amplitudes. These results suggest that the ArchT photoinhibition of excitatory axons has off-target consequences that generally disrupt NAc physiology, which may explain why similar changes in behavior result from the inhibition of distinct axonal inputs. Soma-targeted photoinhibition appears to be a valuable alternative for pathway-specific optogenetic silencing.

The NAc integrates excitatory input from several limbic structures (Mannella et al., 2013) and is a convergent site of dysregulation in many psychiatric disorders (Ahmari et al., 2013; Bagot et al., 2015; Francis et al., 2015; Creed et al., 2016; Neumann et al., 2016). Identifying the distinct behavioral contributions of these excitatory inputs is challenging because they similarly engage NAc physiology (Britt et al., 2012) and originate in regions that are themselves highly interconnected (Pitkänen et al., 2000; Li and Kirouac, 2008; Do-Monte et al., 2015). The study of these circuit elements thus heavily relies on our ability to selectively disrupt pathway-specific function. Unfortunately, many of the optogenetic tools commonly used to silence long-range neural projections have unclear limitations *in vivo*, and their off-target effects may mask pathway-specific differences, particularly in highly integrative structures such as the NAc. Accordingly, there is considerable value in comparing different pathway-specific inhibition strategies for manipulating multiple, parallel long-range projections.

Alternatives to Targeting ArchT Photoinhibition to Axon Terminals

Optogenetic approaches for silencing neural activity have repeatedly been found to produce off-target effects and unpredictable changes in network activity that preclude straightforward interpretations of experimental outcomes. For example, tissue heating in response to prolonged light delivery is sufficient to alter potassium conductance in striatal neurons (Owen et al., 2019). Additionally, ion transporters such as ArchT and halorhodopsin can dramatically alter the intracellular ionic environment affecting the pH level and chloride reversal potential, respectively (Raimondo et al., 2012; Mahn et al., 2016). These disruptions are most pronounced in axons on account of their relatively small intracellular volume. A separate issue is the rebound excitation that often follows any acute hyperpolarization (Arrenberg et al., 2009).

Fortunately, new tools and experimental approaches have mitigated some of these unintended effects. The development of highly effective retrograde viral vectors (Tervo et al., 2016) has facilitated projection-specific cell body photoinhibition strategies, as demonstrated here. This approach benefits from the capacity of the soma to buffer against significant changes in pH and ionic composition (Wiegert et al., 2017). Opsin expression can be further restricted with intersectional strategies involving recombinase proteins such as Cre or FLP and retrograde viral vectors. This approach may be necessary when targeting specific pathways within reciprocally connected brain regions.

Anion-conducting channelrhodopsins (ACRs) may be the best option currently available for photoinhibition experiments. Since their conductance is dependent on the membrane potential, their activation can shunt voltage fluctuations of the cell without inducing strong hyperpolarization or significantly altering the ionic environment (Berndt et al., 2016). The light-driven chloride channels that have been engineered (eACRs; Berndt et al., 2014) or found in nature (GtACRs; Govorunova et al., 2015) are also more light-sensitive than any presently used ion transporter opsins. Unfortunately, chloride channels appear to be excitatory in many axons, due to locally elevated chloride concentrations (Khirug et al., 2008; Malyshev et al., 2017). Soma-restricted GtACR variants have been developed to circumvent this issue, but their expression level has to be optimized to minimize their excitatory influence in the axon hillock (Mahn et al., 2018).

These new tools have fewer drawbacks than their predecessors, but it remains difficult to interpret the effects of inhibiting specific projections that are embedded in recurrent circuitry (Spellman et al., 2015; Do-Monte et al., 2017). It is unclear how silencing a pathway will ultimately affect downstream neurons, let alone the network as a whole. Limiting the duration of photoinhibition may mitigate some concerns, but the organization of the affected circuitry and behavioral state of the animal should be carefully considered.

PVT and BLA Inputs to the NAc Influence Discrete Aspects of Reward-Seeking

PVT and BLA projections to the NAc have been found to promote and discourage reward-seeking in different contexts (Stuber et al., 2011; Millan et al., 2015; Zhu et al., 2016; Do-Monte et al., 2017; Bercovici et al., 2018; Reed et al., 2018; Shen et al., 2019). For instance, photostimulation of PVT input to the NAc can reduce or increase sucrose-seeking behavior (Labouèbe et al., 2016; Do-Monte et al., 2017; Cheng et al., 2018), while photostimulation of different fibers in the BLA-NAc pathway can generate place preference or aversion (Shen et al., 2019). These mixed effects likely reflect the heterogeneity of the PVT and BLA. By studying coarse disruptions of pathway activity alongside manipulations of genetically and spatially defined subpopulations in varied contexts (Labouèbe et al., 2016; Shen et al., 2019), we can begin to understand the net contributions of these pathways to behavior.

Here, we identified a unique role of PVT inputs in modulating the vigor of food-seeking behavior, which is consistent with a wealth of literature implicating this structure in integrating hunger signals and regulating feeding (Kelley et al., 2005; Stratford and Wirtshafter, 2013; Kirouac, 2015; Labouèbe et al., 2016; Choi and McNally, 2017; Do-Monte et al., 2017; Cheng et al., 2018; Meffre et al., 2019). While stimulation of a smaller glucose-sensing subset of PVT-NAc projectors can promote consumptive behavior (Labouèbe et al., 2016), we find that the net effect of bulk PVT-NAc inhibition is an increase in food-seeking, consistent with the net reductions in PVT-NAc pathway activity that have been observed in the rostral NAc during feeding (Reed et al., 2018). Gross excitatory drive from this input may, therefore, gate food-seeking

behaviors by downregulating NAc activity overall, while smaller, genetically defined populations—like those that sense low levels of interstitial glucose (Labouèbe et al., 2016)—may target relatively circumscribed areas of the NAc which have opposing influences on feeding behavior.

Our soma-targeted photoinhibition of the BLA-NAc pathway did not affect lever-pressing behavior when food was available but increased it under extinction conditions, consistent with the role of this pathway in regulating operant responding following changes in outcome (Shiflett and Balleine, 2010). BLA-NAc activity may thus have a pronounced role in behavioral suppression under varied conditions. Overall, the use of increasingly refined tools to inhibit projection-specific activity will aid efforts to dissect neural circuit function concerning behavior.

DATA AVAILABILITY STATEMENT

The datasets generated for this study are available on request to the corresponding author.

ETHICS STATEMENT

The animal study was reviewed and approved by Canadian Council of Animal Care and the McGill Animal Care Committee.

AUTHOR CONTRIBUTIONS

CL and JB conceived the study, designed the experiments, and wrote the manuscript. CL conducted the experiments. JB supervised the research.

FUNDING

This work was supported by the Natural Sciences and Engineering Research Council (05069-2014 to JB and CGSD3-534197-2019 to CL), the Canadian Institutes of Health Research (PT-74038 to JB), and McGill's Healthy Brains for Healthy Lives CFREF (to CL).

SUPPLEMENTARY MATERIAL

The Supplementary Material for this article can be found online at: https://www.frontiersin.org/articles/10.3389/fncir.2020.00010/full#supplementary-material.

FIGURE S1 | ArchT-mediated photoinhibition of excitatory axons in the NAc does not affect the amplitude or the decay rate of spontaneous synaptic currents. Related to **Figures 2**, **3**. Summary of effect of ArchT axon terminal inhibition on **(A)** the amplitude of spontaneous EPSCs [n = 9(3 animals); $t_{(8)} = 0.13$, $p = 0.90$], **(B)** the decay rate of spontaneous EPSCs (n = 8(3); $t_{(7)} = 1.61$, $p = 0.15$], **(C)** the amplitude of spontaneous IPSCs [n = 14(6); $t_{(13)} = 1.22$, $p = 0.25$], and **(D)** the decay rate of spontaneous IPSCs [n = 14(6); $t_{(13)} = 0.46$, $p = 0.65$].

FIGURE S2 | Light alone does not affect the amplitude of eEPSCs or the frequency of sEPSCs in NAc cell recordings from wildtype animals. Related to **Figure 2**. Summary of the effect of light on **(A)** the amplitude of evoked EPSCs [n = 8(3 animals); $t_{(7)} = 2.11$, $p = 0.07$] and **(B)** the frequency of spontaneous EPSCs ($t_{(7)} = 0.63$, $p = 0.55$).

FIGURE S3 | In the absence of photoinhibition, a GABAB antagonist does not affect the amplitude of eEPSCs or the frequency of sEPSCs recorded from NAc neurons of wildtype animals. Related to **Figure 3**. Summary of the effect of light on **(A)** the amplitude of evoked EPSCs [n = 5(3 animals); $t_{(4)} = 0.80$, $p = 0.47$] and **(B)** the frequency of spontaneous EPSCs ($t_{(4)} = 0.08$, $p = 0.94$).

REFERENCES

Ahmari, S. E., Spellman, T., Douglass, N. L., Kheirbek, M. A., Simpson, H. B., Deisseroth, K., et al. (2013). Repeated cortico-striatal stimulation generates persistent OCD-like behavior. *Science* 340, 1234–1239. doi: 10.1126/science.1234733

Ambroggi, F., Ishikawa, A., Fields, H. L., and Nicola, S. M. (2008). Basolateral amygdala neurons facilitate reward-seeking behavior by exciting nucleus accumbens neurons. *Neuron* 59, 648–661. doi: 10.1016/j.neuron.2008.07.004

Arrenberg, A. B., Del Bene, F., and Baier, H. (2009). Optical control of zebrafish behavior with halorhodopsin. *Proc. Natl. Acad. Sci. U S A* 106, 17968–17973. doi: 10.1073/pnas.0906252106

Bagot, R. C., Parise, E. M., Pena, C. J., Zhang, H. X., Maze, I., Chaudhury, D., et al. (2015). Ventral hippocampal afferents to the nucleus accumbens regulate susceptibility to depression. *Nat. Commun.* 6:7062. doi: 10.1038/ncomms8062

Bercovici, D. A., Princz-Lebel, O., Tse, M. T., Moorman, D. E., and Floresco, S. B. (2018). Optogenetic dissection of temporal dynamics of amygdala-striatal interplay during risk/reward decision making. *eNeuro* 5:ENEURO.0422-18.2018. doi: 10.1523/ENEURO.0422-18.2018

Berndt, A., Lee, S. Y., Ramakrishnan, C., and Deisseroth, K. (2014). Structure-guided transformation of channelrhodopsin into a light-activated chloride channel. *Science* 344, 420–424. doi: 10.1126/science.1252367

Berndt, A., Lee, S. Y., Wietek, J., Ramakrishnan, C., Steinberg, E. E., Rashid, A. J., et al. (2016). Structural foundations of optogenetics: determinants of channelrhodopsin ion selectivity. *Proc. Natl. Acad. Sci. U S A* 113, 822–829. doi: 10.1073/pnas.1523341113

Beyeler, A., Chang, C. J., Silvestre, M., Leveque, C., Namburi, P., Wildes, C. P., et al. (2018). Organization of valence-encoding and projection-defined neurons in the basolateral amygdala. *Cell Rep.* 22, 905–918. doi: 10.1016/j.celrep.2017.12.097

Bowman, E. M., and Brown, V. J. (1998). Effects of excitotoxic lesions of the rat ventral striatum on the perception of reward cost. *Exp. Brain Res.* 123, 439–448. doi: 10.1007/s002210050588

Britt, J. P., Benaliouad, F., McDevitt, R. A., Stuber, G. D., Wise, R. A., and Bonci, A. (2012). Synaptic and behavioral profile of multiple glutamatergic inputs to the nucleus accumbens. *Neuron* 76, 790–803. doi: 10.1016/j.neuron.2012.09.040

Cheng, J., Wang, J., Ma, X., Ullah, R., Shen, Y., and Zhou, Y. D. (2018). Anterior paraventricular thalamus to nucleus accumbens projection is involved in feeding behavior in a novel environment. *Front. Mol. Neurosci.* 11:202. doi: 10.3389/fnmol.2018.00202

Choi, E. A., Jean-Richard-Dit-Bressel, P., Clifford, C. W. G., and Mcnally, G. P. (2019). Paraventricular thalamus controls behavior during motivational conflict. *J. Neurosci.* 39, 4945–4958. doi: 10.1523/JNEUROSCI.2480-18.2019

Choi, E. A., and McNally, G. P. (2017). Paraventricular thalamus balances danger and reward. *J. Neurosci.* 37, 3018–3029. doi: 10.1523/JNEUROSCI.3320-16.2017

Creed, M., Ntamati, N. R., Chandra, R., Lobo, M. K., and Luscher, C. (2016). Convergence of reinforcing and anhedonic cocaine effects in the ventral pallidum. *Neuron* 92, 214–226. doi: 10.1016/j.neuron.2016.09.001

Do-Monte, F. H., Minier-Toribio, A., Quinones-Laracuente, K., Medina-Colon, E. M., and Quirk, G. J. (2017). Thalamic regulation of sucrose seeking during unexpected reward omission. *Neuron* 94, 388.e4–400.e4. doi: 10.1016/j.neuron.2017.03.036

Do-Monte, F. H., Quiñones-Laracuente, K., and Quirk, G. J. (2015). A temporal shift in the circuits mediating retrieval of fear memory. *Nature* 519, 460–463. doi: 10.1038/nature14030

El-Gaby, M., Zhang, Y., Wolf, K., Schwiening, C. J., Paulsen, O., and Shipton, O. A. (2016). Archaerhodopsin selectively and reversibly silences synaptic transmission through altered pH. *Cell Rep.* 16, 2259–2268. doi: 10.1016/j.celrep.2016.07.057

Esber, G. R., and Holland, P. C. (2014). The basolateral amygdala is necessary for negative prediction errors to enhance cue salience, but not to produce conditioned inhibition. *Eur. J. Neurosci.* 40, 3328–3337. doi: 10.1111/ejn.12695

Francis, T. C., Chandra, R., Friend, D. M., Finkel, E., Dayrit, G., Miranda, J., et al. (2015). Nucleus accumbens medium spiny neuron subtypes mediate depression-related outcomes to social defeat stress. *Biol. Psychiatry* 77, 212–222. doi: 10.1016/j.biopsych.2014.07.021

Goto, Y., and Grace, A. A. (2008). Limbic and cortical information processing in the nucleus accumbens. *Trends Neurosci.* 31, 552–558. doi: 10.1016/j.tins.2008.08.002

Govorunova, E. G., Sineshchekov, O. A., Janz, R., Liu, X., and Spudich, J. L. (2015). Natural light-gated anion channels: a family of microbial rhodopsins for advanced optogenetics. *Science* 349, 647–650. doi: 10.1126/science.aaa7484

Herrera, C. G., Cadavieco, M. C., Jego, S., Ponomarenko, A., Korotkova, T., and Adamantidis, A. (2016). Hypothalamic feedforward inhibition of thalamocortical network controls arousal and consciousness. *Nat. Neurosci.* 19, 290–298. doi: 10.1038/nn.4209

Kelley, A. E., Baldo, B. A., and Pratt, W. E. (2005). A proposed hypothalamic-thalamic-striatal axis for the integration of energy balance, arousal and food reward. *J. Comp. Neurol.* 493, 72–85. doi: 10.1002/cne.20769

Khirug, S., Yamada, J., Afzalov, R., Voipio, J., Khiroug, L., and Kaila, K. (2008). GABAergic depolarization of the axon initial segment in cortical principal neurons is caused by the Na-K-2Cl cotransporter NKCC1. *J. Neurosci.* 28, 4635–4639. doi: 10.1523/JNEUROSCI.0908-08.2008

Kirouac, G. J. (2015). Placing the paraventricular nucleus of the thalamus within the brain circuits that control behavior. *Neurosci. Biobehav. Rev.* 56, 315–329. doi: 10.1016/j.neubiorev.2015.08.005

Kupferschmidt, D. A., and Lovinger, D. M. (2015). Inhibition of presynaptic calcium transients in cortical inputs to the dorsolateral striatum by metabotropic $GABA_B$ and mGlu2/3 receptors. *J. Physiol.* 593, 2295–2310. doi: 10.1113/JP270045

Labouèbe, G., Boutrel, B., Tarussio, D., and Thorens, B. (2016). Glucose-responsive neurons of the paraventricular thalamus control sucrose-seeking behavior. *Nat. Neurosci.* 19, 999–1002. doi: 10.1038/nn.4331

Li, S., and Kirouac, G. J. (2008). Projections from the paraventricular nucleus of the thalamus to the forebrain, with special emphasis on the extended amygdala. *J. Comp. Neurol.* 506, 263–287. doi: 10.1002/cne.21502

Mahn, M., Gibor, L., Patil, P., Cohen-Kashi Malina, K., Oring, S., Printz, Y., et al. (2018). High-efficiency optogenetic silencing with soma-targeted anion-conducting channelrhodopsins. *Nat. Commun.* 9:4125. doi: 10.1038/s41467-018-06511-8

Mahn, M., Prigge, M., Ron, S., Levy, R., and Yizhar, O. (2016). Biophysical constraints of optogenetic inhibition at presynaptic terminals. *Nat. Neurosci.* 19, 554–556. doi: 10.1038/nn.4266

Malyshev, A. Y., Roshchin, M. V., Smirnova, G. R., Dolgikh, D. A., Balaban, P. M., and Ostrovsky, M. A. (2017). Chloride conducting light activated channel GtACR2 can produce both cessation of firing and generation of action potentials in cortical neurons in response to light. *Neurosci. Lett.* 640, 76–80. doi: 10.1016/j.neulet.2017.01.026

Mangieri, L. R., Lu, Y., Xu, Y., Cassidy, R. M., Xu, Y., Arenkiel, B. R., et al. (2018). A neural basis for antagonistic control of feeding and compulsive behaviors. *Nat. Commun.* 9:52. doi: 10.1038/s41467-017-02534-9

Mannella, F., Gurney, K., and Baldassarre, G. (2013). The nucleus accumbens as a nexus between values and goals in goal-directed behavior: a review and a new hypothesis. *Front. Behav. Neurosci.* 7:135. doi: 10.3389/fnbeh.2013.00135

Meffre, J., Sicre, M., Diarra, M., Marchessaux, F., Paleressompoulle, D., and Ambroggi, F. (2019). Orexin in the posterior paraventricular thalamus mediates hunger-related signals in the nucleus accumbens core. *Curr. Biol.* 29, 3298.e4–3306.e4. doi: 10.1016/j.cub.2019.07.069

Millan, E. Z., Reese, R. M., Grossman, C. D., Chaudhri, N., and Janak, P. H. (2015). Nucleus accumbens and posterior amygdala mediate cue-triggered alcohol seeking and suppress behavior during the omission of alcohol-predictive cues. *Neuropsychopharmacology* 40, 2555–2565. doi: 10.1038/npp.2015.102

Neumann, P. A., Wang, Y., Yan, Y., Wang, Y., Ishikawa, M., Cui, R., et al. (2016). Cocaine-induced synaptic alterations in thalamus to nucleus accumbens projection. *Neuropsychopharmacology* 41, 2399–2410. doi: 10.1038/npp.2016.52

O'Connor, E. C., Kremer, Y., Lefort, S., Harada, M., Pascoli, V., Rohner, C., et al. (2015). Accumbal D1R neurons projecting to lateral hypothalamus authorize feeding. *Neuron* 88, 553–564. doi: 10.1016/j.neuron.2015.09.038

Owen, S. F., Liu, M. H., and Kreitzer, A. C. (2019). Thermal constraints on *in vivo* optogenetic manipulations. *Nat. Neurosci.* 22, 1061–1065. doi: 10.1038/s41593-019-0422-3

Pitkänen, A., Pikkarainen, M., Nurminen, N., and Ylinen, A. (2000). Reciprocal connections between the amygdala and the hippocampal formation, perirhinal cortex and postrhinal cortex in rat. A review. *Ann. N Y Acad. Sci.* 911, 369–391. doi: 10.1111/j.1749-6632.2000.tb06738.x

Raimondo, J. V., Kay, L., Ellender, T. J., and Akerman, C. J. (2012). Optogenetic silencing strategies differ in their effects on inhibitory synaptic transmission. *Nat. Neurosci.* 15, 1102–1104. doi: 10.1038/nn.3143

Reed, S. J., Lafferty, C. K., Mendoza, J. A., Yang, A. K., Davidson, T. J., Grosenick, L., et al. (2018). Coordinated reductions in excitatory input to the nucleus accumbens underlie food consumption. *Neuron* 99, 1260.e4–1273.e4. doi: 10.1016/j.neuron.2018.07.051

Shen, C. J., Zheng, D., Li, K. X., Yang, J. M., Pan, H. Q., Yu, X. D., et al. (2019). Cannabinoid CB_1 receptors in the amygdalar cholecystokinin glutamatergic afferents to nucleus accumbens modulate depressive-like behavior. *Nat. Med.* 25:350. doi: 10.1038/s41591-019-0372-z

Shiflett, M. W., and Balleine, B. W. (2010). At the limbic-motor interface: disconnection of basolateral amygdala from nucleus accumbens core and shell reveals dissociable components of incentive motivation. *Eur. J. Neurosci.* 32, 1735–1743. doi: 10.1111/j.1460-9568.2010.07439.x

Spellman, T., Rigotti, M., Ahmari, S. E., Fusi, S., Gogos, J. A., and Gordon, J. A. (2015). Hippocampal-prefrontal input supports spatial encoding in working memory. *Nature* 522, 309–314. doi: 10.1038/nature14445

Stefanik, M. T., Kupchik, Y. M., and Kalivas, P. W. (2016). Optogenetic inhibition of cortical afferents in the nucleus accumbens simultaneously prevents cue-induced transient synaptic potentiation and cocaine-seeking behavior. *Brain Struct. Funct.* 221, 1681–1689. doi: 10.1007/s00429-015-0997-8

Stratford, T. R., and Wirtshafter, D. (2013). Injections of muscimol into the paraventricular thalamic nucleus, but not mediodorsal thalamic nuclei, induce feeding in rats. *Brain Res.* 1490, 128–133. doi: 10.1016/j.brainres.2012.10.043

Stuber, G. D., Sparta, D. R., Stamatakis, A. M., Van Leeuwen, W. A., Hardjoprajitno, J. E., Cho, S., et al. (2011). Excitatory transmission from the amygdala to nucleus accumbens facilitates reward seeking. *Nature* 475, 377–380. doi: 10.1038/nature10194

Tervo, D. G., Hwang, B. Y., Viswanathan, S., Gaj, T., Lavzin, M., Ritola, K. D., et al. (2016). A designer AAV variant permits efficient retrograde access to projection neurons. *Neuron* 92, 372–382. doi: 10.1016/j.neuron.2016.09.021

Trouche, S., Koren, V., Doig, N. M., Ellender, T. J., El-Gaby, M., Lopes-Dos-Santos, V., et al. (2019). A hippocampus-accumbens tripartite neuronal motif guides appetitive memory in space. *Cell* 176, 1393.e16–1406.e16. doi: 10.1016/j.cell.2018.12.037

Wiegert, J. S., Mahn, M., Prigge, M., Printz, Y., and Yizhar, O. (2017). Silencing neurons: tools, applications and experimental constraints. *Neuron* 95, 504–529. doi: 10.1016/j.neuron.2017.06.050

Yamamoto, J., and Tonegawa, S. (2017). Direct medial entorhinal cortex input to hippocampal CA1 is crucial for extended quiet awake replay. *Neuron* 96, 217.e4–227.e4. doi: 10.1016/j.neuron.2017.09.017

Zhu, Y., Wienecke, C. F., Nachtrab, G., and Chen, X. (2016). A thalamic input to the nucleus accumbens mediates opiate dependence. *Nature* 530, 219–222. doi: 10.1038/nature16954

Conflict of Interest: The authors declare that the research was conducted in the absence of any commercial or financial relationships that could be construed as a potential conflict of interest.

frontiers in Neural Circuits

REVIEW
published: 02 April 2020
doi: 10.3389/fncir.2020.00009

Illuminating Relationships Between the Pre- and Post-synapse

*Thomas M. Sanderson[1], John Georgiou[1] and Graham L. Collingridge[1,2,3]**

[1] Lunenfeld-Tanenbaum Research Institute, Toronto, ON, Canada, [2] Tanz Centre for Research in Neurodegenerative Diseases, Department of Physiology, University of Toronto, Toronto, ON, Canada, [3] Glutamate Research Group, School of Physiology, Pharmacology and Neuroscience, University of Bristol, Bristol, United Kingdom

Excitatory synapses in the mammalian cortex are highly diverse, both in terms of their structure and function. However, relationships between synaptic features indicate they are highly coordinated entities. Imaging techniques, that enable physiology at the resolution of individual synapses to be investigated, have allowed the presynaptic activity level of the synapse to be related to postsynaptic function. This approach has revealed that neuronal activity induces the pre- and post-synapse to be functionally correlated and that subsets of synapses are more susceptible to certain forms of synaptic plasticity. As presynaptic function is often examined in isolation from postsynaptic properties, the effect it has on the post-synapse is not fully understood. However, since postsynaptic receptors at excitatory synapses respond to release of glutamate, it follows that they may be differentially regulated depending on the frequency of its release. Therefore, examining postsynaptic properties in the context of presynaptic function may be a useful way to approach a broad range of questions on synaptic physiology. In this review, we focus on how optophysiology tools have been utilized to study relationships between the pre- and the post-synapse. Multiple imaging techniques have revealed correlations in synaptic properties from the submicron to the dendritic level. Optical tools together with advanced imaging techniques are ideally suited to illuminate this area further, due to the spatial resolution and control they allow.

Keywords: probability of neurotransmitter release, AMPA receptor, mGluRs, presynapse, postsynapse, styryl dyes, imaging, synaptic function

OPEN ACCESS

Edited by:
Jean-Claude Béïque, University of Ottawa, Canada

Reviewed by:
Aleksey V. Zaitsev, Institute of Evolutionary Physiology and Biochemistry (RAS), Russia
Roberto Araya, Université de Montréal, Canada

***Correspondence:**
Graham L. Collingridge
collingridge@lunenfeld.ca

Received: *31 October 2019*
Accepted: *06 March 2020*
Published: *02 April 2020*

Citation:
Sanderson TM, Georgiou J and Collingridge GL (2020) Illuminating Relationships Between the Pre- and Post-synapse. Front. Neural Circuits 14:9. doi: 10.3389/fncir.2020.00009

INTRODUCTION

Synapses in the brain are diverse, plastic structures with distinct morphologies (Walmsley et al., 1998; Rollenhagen and Lubke, 2006). Even within one type of synapse, the excitatory cortical synapse, a large degree of structural and functional heterogeneity is observed, which is likely of relevance to the information processing that contributes to memory and cognition (Harris and Stevens, 1989; Schikorski and Stevens, 1999; Matsuzaki et al., 2004; Noguchi et al., 2005; Harvey et al., 2008; Tanaka et al., 2008; Araya et al., 2014). Many experimental techniques have been utilized to understand synaptic physiology (Glasgow et al., 2019); however, light-based imaging techniques are particularly powerful for studying this area.

Ultrastructural studies help illustrate the extent of synaptic variability. They have revealed that spine head volume in the hippocampus can vary by ∼180 fold, postsynaptic density (PSD) area by ∼70 fold, spine length by ∼10 fold, and synaptic vesicle number by ∼500 fold (Harris and Stevens, 1989). The richness in synaptic form is likely a consequence of molecular composition.

For example, overexpression of postsynaptic proteins such as PSD-95 (El-Husseini et al., 2000), Shank (Sala et al., 2001), and GluA2 (Passafaro et al., 2003) can drive the morphological enlargement of spines. Conversely, the specific morphologies may act to influence the molecular composition. For example, mushroom spines with smaller heads and long spine necks slow the diffusion of AMPA receptors (AMPARs) (Ashby et al., 2006), which may make the AMPAR complement in the spine head more stable.

The functionality of synapses is related to their structure and molecular composition. For example, one highly reproduced finding that mirrors the presynaptic structural diversity of synapses is that the probability of neurotransmitter release [P(r)] at central synapses is highly variable. The diversity of P(r) has been measured using a variety of methods including the progressive block by the use-dependent NMDA receptor (NMDAR) antagonist MK-801 (Hessler et al., 1993; Rosenmund et al., 1993), the activity-dependent uptake of styryl dye (Murthy et al., 1997; Sanderson et al., 2018), high affinity calcium indicators like Oregon Green BAPTA-1 (Emptage et al., 1999, 2003; Ward et al., 2006; Enoki et al., 2009; Padamsey et al., 2017, 2019) or the glutamate sensor SF-iGluSnFR (Jensen et al., 2019; Soares et al., 2019). P(r) correlates with structural features of synapses such as the active zone area (Schikorski and Stevens, 1997; Holderith et al., 2012) and also with the readily releasable pool size (Dobrunz and Stevens, 1997) which is thought to consist of those vesicles docked at the active zone (Schikorski and Stevens, 1997; Murthy et al., 2001). These findings suggest P(r) is powerfully influenced by presynaptic structural attributes.

When the post-synapse is studied, a similar correspondence between structure and function is observed. A precise relationship exists between the molecular complement of spines and their geometry. For example, the PSD length and basal AMPAR expression are positively correlated, with functional AMPARs expressed at a similar density across different spines (Takumi et al., 1999; Tanaka et al., 2005). In addition, probing synaptic function by focally uncaging caged glutamate at synapses using two-photon stimulation (Mitchell et al., 2019), has revealed that expression of glutamate receptors is correlated with spine volume (Noguchi et al., 2005) and that long-term potentiation (LTP)-associated changes in volume correlate with changes in conductance (Matsuzaki et al., 2004).

Many factors influence the relationship between postsynaptic structure and function. For example when specific proteins such as PSD-95 are knocked out, there is a resultant increase in silent synapses on mature spines (Beique et al., 2006). Additional contributions, such as astrocytes, play important roles in synapse development and function; however, a more detailed description of how they influence the pre- and post-synapse is beyond the scope of this review. The role of astrocytes in synapse physiology is described in several recent reviews (Allen and Eroglu, 2017; Rose et al., 2017; Dallerac et al., 2018). Here, we summarize some of the findings that suggest both pre- and post-synaptic activity is highly coordinated and discuss functional imaging studies that suggest multiple mechanisms are involved in ensuring the pre- and post-synaptic compartments are functionally aligned.

POSTSYNAPTIC MANIPULATIONS INFLUENCE THE PRESYNAPSE

Ultrastructural studies suggest that numerous features of the pre- and post-synapse are correlated. These include relationships between the PSD size and the active zone size, and between the postsynaptic spine head volume and the number of vesicles in the presynaptic varicosity (**Figures 1A,B**) (Harris and Stevens, 1989; Schikorski and Stevens, 1997, 1999). These interrelations in structural composition indicate there are mechanisms to ensure that as synapses are modified, for example, over development or due to synaptic plasticity, the pre- and post-synapse remain proportional to one another. In addition to driving an increase in spine size as mentioned above, overexpressing postsynaptic proteins results in enhanced miniature excitatory postsynaptic current (mEPSC) frequency, often interpreted as reflecting an increase in P(r), as well as a range of other measures of presynaptic function (El-Husseini et al., 2000; Sala et al., 2001). The presynaptic effect is indicative of a functional increase in synaptic activity that may be in proportion to the increase in postsynaptic spine size. Due to the similar density of functional AMPAR expression (Takumi et al., 1999; Tanaka et al., 2005), this would also be proportional to postsynaptic function.

Conversely, knocking down AMPARs reduces presynaptic functionality, suggested by reduced mEPSC frequency and reduced uptake of antibody directed against the vesicular protein synaptotagmin. When other measures of presynaptic activity were examined, by measuring paired pulse facilitation and MK-801 block, there was no difference detected. This led the authors to conclude that a subset of synapses had become inactive, leaving the remaining synapses with unaltered P(r) (Tracy et al., 2011). Two types of release have been identified, one responsible for mEPSCs, which does not require presynaptic action potentials, the other involved in evoked release, which does (Kavalali, 2015). Presynaptic NMDARs regulate these two forms of release differentially, for example, they may act to regulate mEPSC release via c-Jun N terminal Kinase, whereas they may regulate evoked release via Rab3-interacting molecule (RIM) 1 (Abrahamsson et al., 2017). A possible alternative interpretation of the constellation of presynaptic changes that accompany postsynaptic AMPAR knockdown (Tracy et al., 2011) is that they indicate a deficit in neurotransmitter release that does not require presynaptic action potentials.

PRE- AND POST-SYNAPTIC PROTEINS ARE ALIGNED AT THE SUBMICRON LEVEL

The ability to image synaptic proteins using super resolution imaging has resulted in the discovery of subsynaptic domains. These are ∼70–80 nm domains enriched with PSD-95, Homer, and AMPARs at the post-synapse of excitatory synapses (Fukata et al., 2013; MacGillavry et al., 2013; Nair et al., 2013; Tang et al., 2016; Hruska et al., 2018). These domains are of uniform size and

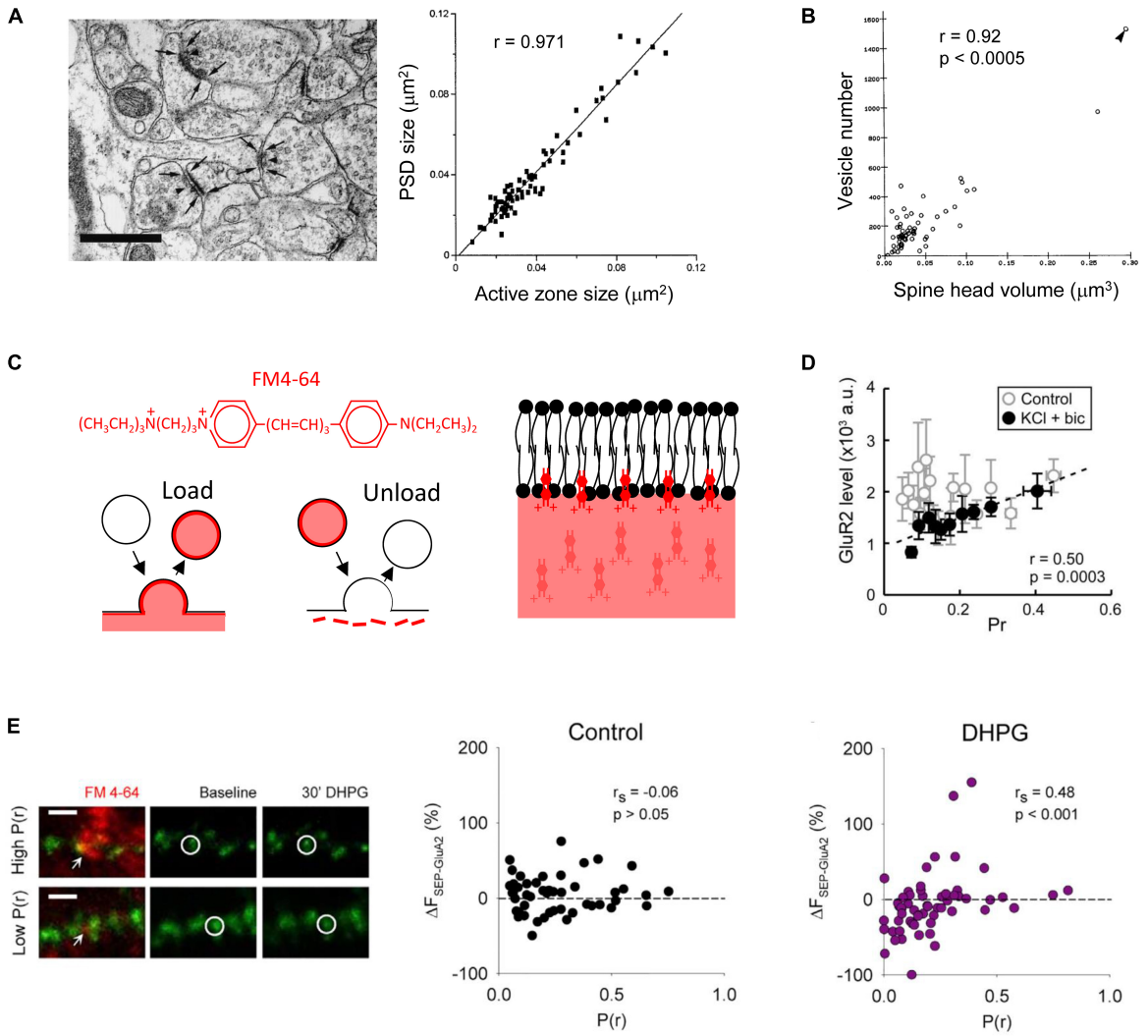

FIGURE 1 | Multiple pre- and post-synaptic features are correlated. Analysis of electron micrographs indicates that **(A)** the postsynaptic density (PSD) size correlates with the presynaptic active zone size, scale bar in image on left is 0.5 μm [Schikorski and Stevens, 1997, copyright (1997) Society for Neuroscience]; and **(B)** the postsynaptic spine head volume correlates with the number of vesicles in the presynaptic varicosity [Harris and Stevens, 1989, copyright (1989) Society for Neuroscience]. **(C)** FM4-64 is a red styryl dye that allows simultaneous imaging with green fluorescent proteins. It is an amphipathic molecule that is taken into lipid membranes due to a lipophilic portion but does not fully cross due to a polar head. It can be loaded and unloaded in an activity-dependent way. Scheme based on that in Betz et al., 1992 [copyright (1992) Society for Neuroscience]. **(D)** In dissociated cultured neurons, no functional relationship is observed in control conditions when P(r) is measured using loading of FM dye and postsynaptic strength by immunofluorescence imaging against GluA2. However, if activity is elevated by application of potassium chloride and bicuculline, a correlation is observed due to the down regulation of surface GluA2 at low P(r) synapses [Tokuoka and Goda, 2008, copyright (2008) National Academy of Sciences]. **(E)** Application of the group I mGluR agonist DHPG results in downregulation of AMPARs at low P(r) synapses. P(r) estimated by FM4-64 loading (red) and postsynaptic strength indicated by SEP-GluA2 fluorescence (green). Example of FM4-64 loading and SEP-GluA2 fluorescence in images on left, scale bar represents 2 μm. Arrows indicate FM4-64 puncta used to estimate P(r). Circles indicate a SEP-GluA2 punctum at the synapse opposed to the FM4-64 labeling. Reproduced from Sanderson et al. (2018) under CC BY-NC-ND license.

are regulated by palmitoylation and by interactions with stargazin (Fukata et al., 2013; Nair et al., 2013).

Examining synapses using 3D stochastic optical reconstruction microscopy (3D-STORM) (Huang et al., 2008) has revealed that the subsynaptic domains at the post-synapse are related to the presynapse in trans-synaptic nanocolumns. These consist of enriched areas of PSD-95 and AMPARs that are located directly opposite the presynaptic release machinery characterized as containing RIM (Tang et al., 2016). Presynaptic vesicle fusion was detected preferentially at areas of RIM enrichment, suggesting that this nanoscale architecture is relevant for synaptic function. That the presynaptic release machinery relates so precisely to the postsynaptic receptors that detect release is predicted to affect the efficiency of synaptic transmission (Nair et al., 2013). For example, this organization is estimated to enhance synaptic strength by 20 % compared to if pre- and post-synaptic proteins were organized uniformly (Tang et al., 2016).

Stimulated emission depletion (STED) microscopy (Willig et al., 2006) has revealed that since trans-synaptic nanocolumns are of remarkably similar size, this means that large synapses that contain more synaptic proteins do not have larger trans-synaptic nanocolumns, but have a greater number of similarly sized domains. When structural plasticity is induced, the modular addition of new trans-synaptic nanocolumns is particularly apparent at later time points (>2 h after induction). The pre- and post-synaptic elements of trans-synaptic nanocolumns remain aligned even though they are mobile when undergoing structural plasticity (Hruska et al., 2018).

MEASUREMENT OF P(r) USING FM DYES

In order to study pre-synapse function, imaging techniques have proved invaluable. Styryl dyes such as FM1-43 or FM4-64 have proved useful as they offer the benefits of being amenable to measuring P(r) of evoked neurotransmission directly, and can be used in semi-intact (e.g., slice) preparations. FM dyes were used originally to study vesicle recycling at the frog neuromuscular junction (Betz and Bewick, 1992; Betz et al., 1992) and the hippocampus (Ryan et al., 1993), enabling multiple presynaptic boutons to be studied simultaneously in response to direct electrical stimulation.

These amphipathic dyes are incorporated into biological lipid membranes due to their short hydrophobic tail, but do not pass all the way through the membrane due to the highly charged hydrophilic group at the opposite end of the molecule (**Figure 1C**) (Betz et al., 1992). When applied to biological preparations these dyes therefore stain all external membranes. Following release of neurotransmitter through fusion of a vesicle with the presynaptic membrane, the vesicular membrane and associated proteins are recycled via clathrin-dependent endocytosis (Brodin et al., 2000; Watanabe et al., 2013). If external membranes have been stained with FM dye, this recycling process results in newly recycled vesicles that are also stained with dye. Dye in external membranes can then be washed out, leaving only those internalized vesicles that can be visualized as puncta by confocal or multiphoton microscopy and when photo converted can be visualized in synaptic vesicles by electron microscopy (Harata et al., 2001; Branco et al., 2008). The development of agents that reduce background FM staining (Kay et al., 1999; Pyle et al., 1999) have enabled the use of this technique in brain slice preparations (Johnstone and Raymond, 2013; Sanderson et al., 2018) as well as facilitating their use in dissociated culture (Tokuoka and Goda, 2008).

FM dye uptake has been used in two ways to assess presynaptic activity. The first involves loading FM dye into presynaptic vesicles using a low number of electrical stimulations, a protocol that results in individual peaks in the fluorescence intensity frequency histogram that likely represent the fluorescence from individual vesicles (Murthy et al., 1997). With reference to the number of stimulations used to load the presynaptic boutons with dye, and the fluorescence value ascribed to a single vesicle, this staining procedure allows the P(r) to be estimated (Murthy et al., 1997; Tokuoka and Goda, 2008; Sanderson et al., 2018). When loaded in a hippocampal slice using a stimulating electrode the dye reveals very sparse labeling. If care is taken to ensure that the stimulation strength is similar to that used in slice electrophysiology experiments, the labeled synapses can be related to those studied using electrophysiology (Sanderson et al., 2018). In addition, FM dyes can be loaded into dissociated cultured neurons using a high concentration of potassium. This depolarizes the cells causing release followed by loading of the entire recycling pool of vesicles. Since the size of the recycling pool is correlated with P(r) (Rosenmund and Stevens, 1996; Dobrunz and Stevens, 1997; Murthy et al., 1997), this method has also been used to assess presynaptic activity levels (Kay et al., 2011).

THE DEVELOPMENT OF FUNCTIONALLY CORRELATED PRE- AND POST-SYNAPTIC COMPARTMENTS

A functional correlation between pre- and post-synaptic activity has been observed under a variety of conditions. An initial connection was observed by relating the intensity of GluA1 immunofluorescence staining in dissociated culture to the uptake of antibody directed against the vesicular protein synaptotagmin (Thiagarajan et al., 2005). However, using FM dyes it was found that this functional correlation is only seen if the neuronal network exhibits sufficient activity. In dissociated cultured neurons, using loading of FM1-43 to measure P(r), and an antibody against the AMPAR subunit GluA2 as a measure of postsynaptic strength, a functional correlation emerged when neuronal activity was elevated pharmacologically (**Figure 1D**) (Tokuoka and Goda, 2008). Furthermore, where postsynaptic function has been assessed using focal uncaging of caged glutamate, a correlation between P(r) emerged over development, in a manner that depended on neuronal activity (Kay et al., 2011). These observations have revealed that an activity-dependent correlation between pre- and post-synaptic function emerges during development. This leads to the question as to the underlying mechanisms?

SEP-TAGGED RECEPTORS REVEAL AMPAR TRAFFICKING IS INFLUENCED BY P(r)

Live cell imaging aimed at understanding the AMPAR trafficking that contributes to the expression of hippocampal synaptic plasticity has helped shed light on the activity-dependent mechanisms that may underlie the correspondence between pre- and post-synaptic properties. One imaging method involves using super ecliptic pHluorin (SEP), a pH-sensitive variant of Green Fluorescent Protein that yields greater fluorescence at neutral pH compared to acidic pH. SEP expression allows the preferential imaging of GluA2 at the cell surface where pH is ∼7, rather than in the endocytic pathway where pH is ∼5. Versions of this fluorophore were initially developed, and have been used

extensively, to study presynaptic secretion (Miesenbock et al., 1998; Sankaranarayanan et al., 2000; Voglmaier et al., 2006; Lindskog et al., 2010; Henry et al., 2012). This methodology was then adopted for the study of postsynaptic receptor trafficking, where AMPARs were shown to rapidly internalize in response to activation of NMDARs (Ashby et al., 2004). This approach has since been used extensively to study various aspects of AMPAR receptor trafficking (Ashby et al., 2004, 2006; Kopec et al., 2006, 2007; Lin and Huganir, 2007; Yudowski et al., 2007; Heine et al., 2008; Lin et al., 2009; Araki et al., 2010, 2015; Patterson et al., 2010; Thorsen et al., 2010; Makino and Malinow, 2011; Sanderson et al., 2011, 2018; Zhang et al., 2011, 2015).

We have recently combined the use of SEP-GluA2 and FM4-64 to investigate the relationship between postsynaptic AMPAR trafficking and P(r) at individual hippocampal synapses (Sanderson et al., 2018). In particular, we studied a form of synaptic plasticity that is induced by a brief application of the group 1 mGluR agonist dihydroxyphenylglycine (DHPG), termed DHPG-long term depression (DHPG-LTD) (Palmer et al., 1997). The dual probes validated the notion that AMPAR trafficking contributes to the expression of DHPG-LTD (Snyder et al., 2001; Moult et al., 2006; Casimiro et al., 2011) and may occur only at a subset of synapses (Xiao et al., 2001; Sanderson et al., 2011). More interestingly, the optical approach also revealed that the DHPG-induced SEP-GluA2 trafficking is correlated with P(r), such that reductions in AMPARs occur predominantly at low P(r) synapses (**Figure 1E**).

Where manipulations have been performed that modulate P(r), for example, changing the calcium to magnesium ratio, the magnitude of DHPG-LTD and the extent of AMPAR trafficking is altered in a way that is consistent with this mechanism. For example, increasing the calcium to magnesium ratio results in higher P(r) and DHPG-LTD and SEP-GluA2 trafficking are both reduced; if the ratio is decreased to lower P(r) then LTD and GluA2 trafficking are both increased (Oliet et al., 1997; Watabe et al., 2002; Sanderson et al., 2018).

MECHANISMS OF P(r)-DEPENDENT mGluR ACTIVATION

Why does DHPG-induced AMPAR trafficking occur predominantly at low P(r) synapses? DHPG-LTD can be triggered by either mGluR1 or mGluR5 (Gladding et al., 2009b; Sanderson et al., 2016). The trigger for DHPG-LTD in organotypic slices is mGluR1 (Nadif Kasri et al., 2011; Sanderson et al., 2018) and using a similar imaging approach mGluR1 was tagged with SEP in order to compare its expression and trafficking with P(r). The approach revealed that specifically at *high* P(r) synapses theta burst stimulation (TBS) induces downregulation of mGluR1 resulting in lower basal mGluR1 levels (**Figure 2A**) (Sanderson et al., 2018). Therefore, DHPG-induced AMPAR trafficking occurs predominantly at *low* P(r) synapses because this is where the trigger, mGluR1, is expressed most highly. As theta burst activity develops over the course of development (Charlesworth et al., 2015; Kim et al., 2016), this mechanism may contribute to the emergence of a correlation between P(r) and postsynaptic function at later developmental stages (Kay et al., 2011).

Inhibition of excitatory amino acid transporters (EAATs) was found to enhance the trafficking of SEP-mGluR1 suggesting that the selective effect of theta bursts at high P(r) synapses is likely because the greater frequency of glutamate release at these synapses results in more spillover of glutamate to peri-synaptic areas where mGluRs are expressed (Sanderson et al., 2018). Consistent with this hypothesis, STED imaging has revealed that LTP causes the withdrawal of astroglial processes from synapses, and in so doing facilitates the spillover of glutamate (Henneberger et al., 2018). Consequently, released glutamate would gain access to peri-synaptically expressed receptors such as mGluR1 and so may be necessary for the theta burst-induced mGluR1 trafficking detailed above. Whether this modulation of astroglia occurs more readily at high P(r) synapses remains to be investigated.

POSSIBLE FUNCTIONAL CONSEQUENCES OF P(r) INFLUENCED AMPAR TRAFFICKING

What are the possible functional consequences of a relationship between P(r) and AMPAR trafficking? Here we put forward a few suggestions.

Theta-Burst Stimulation (TBS)

We found that TBS induces SEP-GluA2 trafficking in synapses of intermediate P(r) via a mechanism that requires mGluR1 activation (**Figure 2B**) (Sanderson et al., 2018). That theta bursts have this effect may indicate that mGluR-induced AMPAR trafficking can sculpt neuronal networks in an input specific way. The recruitment of this mechanism only at synapses of intermediate P(r) is likely because a balance exists between mGluR1 expression levels and sufficient release of glutamate to activate them. High P(r) synapses may be protected from the effects of mGluR1 activation due to their downregulation, and mGluRs at low P(r) synapses may not be appropriately activated due to insufficient release of glutamate. According to this hypothesis, intermediate P(r) synapses are in a "Goldilocks zone" in which the glutamate released by theta burst stimulation is sufficient to activate mGluRs to induce AMPAR trafficking, but not enough to cause the internalization of mGluRs themselves.

Synaptic Down-Scaling

An additional potential mechanism involves mGluR activation via non glutamatergic signaling and the immediate early gene (IEG) Homer 1a (**Figure 2C**) (Brakeman et al., 1997; Ango et al., 2001). An increase in excitability as a result of *in vitro* application of a $GABA_A$ antagonist such as bicuculline results in decreased synaptic transmission due to the cell wide downregulation of surface AMPARs, a form of homeostatic plasticity termed synaptic scaling-down (Turrigiano, 2008). The expression of Homer 1a is also driven by increases in neuronal excitability, and when expressed it activates group I mGluRs in an agonist-independent way by disrupting crosslinking of constitutively

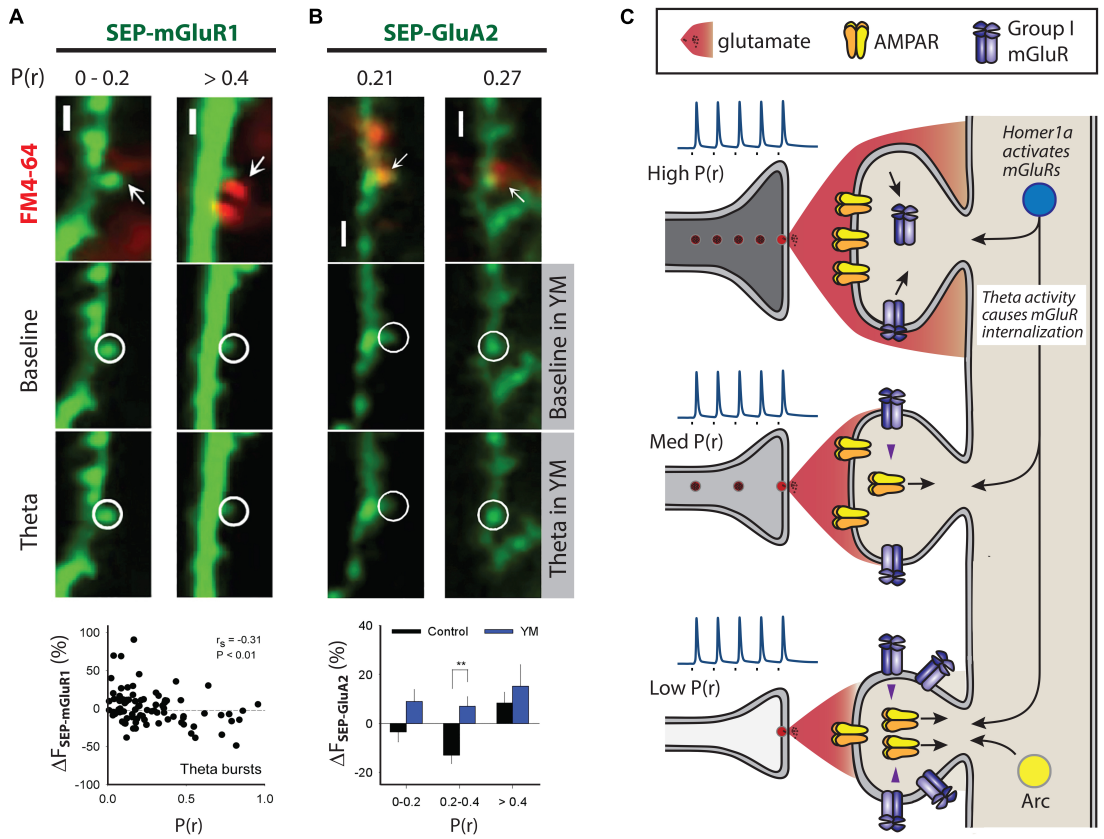

FIGURE 2 | Mechanisms that may contribute to differential AMPAR trafficking. Multiphoton images in **(A)** and **(B)** show examples of SEP fluorescence (green) and FM4-64 staining (red) to estimate P(r), scale 2 μm. **(A)** Theta burst activity induces trafficking of SEP-mGluR1 in organotypic slices such that decreases are seen at high P(r) synapses. P(r) estimated by loading of FM4-64. **(B)** Theta burst activity engages mGluR1 at intermediate P(r) synapses, defined as $0.2 < P(r) < 0.4$, to induce SEP-GluA2 trafficking (lower left images). P(r) estimated by loading of FM4-64, YM indicates the mGluR1 specific antagonist YM 298198 at 2 μm (lower right images). ** indicates $p < 0.01$. **(A)** and **(B)** reproduced from Sanderson et al. (2018) under CC BY-NC-ND license. **(C)** Scheme compares physiological responses to presynaptic activity at three synapses that are of low, medium and high P(r). Inset spikes are action potentials generated upon nerve stimulation (square) with relative amount of glutamate neurotransmitter released from vesicles. Pre- and post-synaptic structural features are correlated, as are functional measures, such as AMPAR expression and P(r). High P(r) synapses express fewer mGluR group I receptors due to the action of theta burst activity. Theta burst activity is also able to induce AMPAR trafficking at a subset of medium P(r) synapses (Sanderson et al., 2018). Arc is expressed at less active synapses where its expression correlates with AMPAR removal, and thus could contribute to a mechanism that would ensure lower levels of AMPARs at these synapses (Okuno et al., 2012). Homer1a is able to induce AMPAR trafficking by triggering group I mGluRs in an agonist-independent way (Hu et al., 2010). Homer1a may therefore be an effective trigger for group I mGluRs at less active synapses.

expressed versions of Homer (Brakeman et al., 1997; Ango et al., 2001; Hu et al., 2010). Homer 1a-mGluR signaling is the trigger for the AMPAR trafficking in synaptic scaling-down and overexpression of Homer 1a is able to drive AMPAR trafficking in an mGluR1/5-dependent way (**Figure 2C**) (Hu et al., 2010). As mGluR1 is enriched at low P(r) synapses (Sanderson et al., 2018), it is possible that AMPAR trafficking induced by Homer1a-mGluR1 signaling would be more likely to occur at low P(r) synapses. Therefore, synaptic scaling-down may also act to ensure functional registration between the pre- and post-synapse via this mechanism. Where it was found that elevated neuronal activity is needed for a correlation in pre- and post-synaptic function to emerge, a very similar protocol to that which induces synaptic scaling-down was used and the alterations in AMPAR expression were exclusively at low P(r) synapses (**Figure 1D**) (Tokuoka and Goda, 2008). Putting these results together presents a plausible case for mGluR-triggered AMPAR trafficking that is engaged by elevated neuronal activity and that acts at low P(r) synapses to ensure a functional correlation between the pre- and post-synapse.

As direct pharmacological activation of group I mGluRs using DHPG also results in AMPAR downregulation primarily at low P(r) synapses (Sanderson et al., 2018), it could be that synaptic scaling-down and mGluR-LTD are two manifestations of the similar underlying mechanisms? Indeed, there are other points of similarity between these forms of plasticity. For example, in some conditions, glutamate release is enhanced in mGluR-LTD (Xu et al., 2013), the AMPAR trafficking in synaptic scaling-down occludes that induced by DHPG (Hu et al., 2010) and some molecular mechanisms are utilized in both forms of plasticity, notably tyrosine dephosphorylation (Moult et al., 2006; Hu

et al., 2010). However, it is worth noting that not all molecular mechanisms are necessarily shared. For example, no role for Homer 1a has been found in mGluR-LTD (Hu et al., 2010). Also, other forms of synaptic scaling alter the induction of synaptic plasticity by altering the properties of neurotransmitter release (Soares et al., 2017) demonstrating that links between different forms of plasticity may be complex. In summary, it is perhaps reasonable to conclude that some but not all mechanisms may be shared between mGluR-LTD and synaptic scaling-down.

Of significant interest is whether the mechanisms revealed by making these experimental manipulations are engaged in endogenous physiological processes. One exciting possibility is that Homer 1a-induced synaptic scaling-down is engaged during sleep. Synaptic Homer1a is upregulated during sleep where it orchestrates synaptic downregulation as a result of group I mGluR-induced AMPAR trafficking and dephosphorylation (Diering et al., 2017). These findings are consistent with the synapse homeostasis hypothesis that suggests that information is encoded during waking hours via LTP-induced increases in synapse strength, followed by synapse weakening during sleep (Tononi and Cirelli, 2014). Ultrastructural studies suggest that large synapses are spared when synapses undergo weakening during sleep (de Vivo et al., 2017). As structural features of synapses are correlated with their function, e.g., PSD size is correlated with active zone size, which correlates with the number of docked vesicles and P(r) (Dobrunz and Stevens, 1997; Schikorski and Stevens, 1997; Murthy et al., 2001; Holderith et al., 2012), the identity of the stable synapses that are resistant to weakening during sleep may correspond to high P(r) synapses that exhibit lower levels of mGluR1 due to theta burst activity (Sanderson et al., 2018). If so, this would be consistent with Homer1a-mGluR signaling during sleep selectively downregulating low P(r) synapses that express higher levels of mGluR1. In the context of the sleep–wake cycle, the access Homer1a has to the synapse may be gated by noradrenergic and adenosine signaling (Diering et al., 2017), and so these additional regulatory mechanisms will also determine the extent of mGluR activation and consequent weakening of synapses.

Heterosynaptic Plasticity

An additional potential mechanism by which mGluRs could be activated in a way that depends on P(r) is an input non-specific way through heterosynaptic signaling. If LTP is induced at a cluster of synapses, as has been observed to occur *in vivo* in response to sensory experience (Makino and Malinow, 2011), neighboring non-conditioned synapses become downregulated due to mGluR activity (Oh et al., 2015; Winnubst et al., 2015). This downregulation involves removal of AMPARs from synapses, suggested by SEP-GluA2 imaging, and also spine shrinkage. The location of the mGluR trigger for the heterosynaptic signaling has not been defined and may be at the conditioned synapses, and a diffusible signaling molecule may diffuse to neighboring non-conditioned synapses. Alternatively, the group I mGluR may be located at the non-conditioned synapse and be activated via non-glutamatergic signaling, for example, the IEG Homer 1a. The second scenario is consistent with low P(r) synapses that express higher levels of group I mGluRs but that are activated less often, being more susceptible to downregulation via heterosynaptic signaling.

Interestingly, using inducible presynaptic expression of tetanus toxin light chain to suppress transmitter release, the IEG Arc was found to be trafficked specifically to synapses with reduced activity, in a process termed inverse synaptic tagging (Okuno et al., 2012). The trafficking occurred via an interaction with CAMKIIβ and the extent of the Arc enrichment correlated with AMPAR removal occurring at those synapses. As Arc is also involved in mGluR-LTD (Waung et al., 2008), it raises the possibility that low activity synapses are specialized for downregulation via mGluR-dependent signaling of the kind that is recruited in mGluR-LTD. To test this hypothesis, the expression levels and activation of other signaling molecules involved in mGluR-LTD (Gladding et al., 2009b; Sanderson et al., 2016) could be investigated with respect to synaptic activity levels.

ROLE OF RETROGRADE MESSENGERS IN COORDINATING THE PRE- AND POST-SYNAPSE

In addition to the mechanisms detailed above, signals that involve retrograde messengers may coordinate the pre- and post-synapse. For example, these may be of relevance to the increase in presynaptic activity induced by overexpression of postsynaptic scaffolding proteins (El-Husseini et al., 2000; Sala et al., 2001). In particular, the role of retrograde messengers in coordinating the pre- and post-synapse has been studied with reference to the increase in synaptic strength that can be induced by pharmacological blockade of post-synapse function, a manipulation that may be of relevance to sensory impairment or neural damage for example as a result of stroke (Thiagarajan et al., 2005). These studies have found that brain derived neurotrophic factor (BDNF) may act as a retrograde messenger, synthesized at the post-synapse in response to phospholipase D and mammalian target of rapamycin complex 1 (mTORC1) signaling (Jakawich et al., 2010; Lindskog et al., 2010; Henry et al., 2012, 2018) (**Figure 3A**). These presynaptic changes occur simultaneously with increases in postsynaptic AMPAR number via mTORC-independent protein synthesis.

The adaptations in response to postsynaptic receptor blockade typically occur over the time frame of hours (Thiagarajan et al., 2005; Jakawich et al., 2010; Lindskog et al., 2010; Henry et al., 2012). However, molecular alterations that could underlie the functional correlation between the pre- and post-synapse occur much more rapidly. Retrograde messengers were first proposed as a means by which LTP, thought to be triggered by the activation of postsynaptic NMDARs, may result in a persistent increase in neurotransmitter release. NO is thought to act as a retrograde messenger in LTP (Zhuo et al., 1993) and its fast diffusion time may allow activity-dependent increases in function at the pre- and the post-synapse to

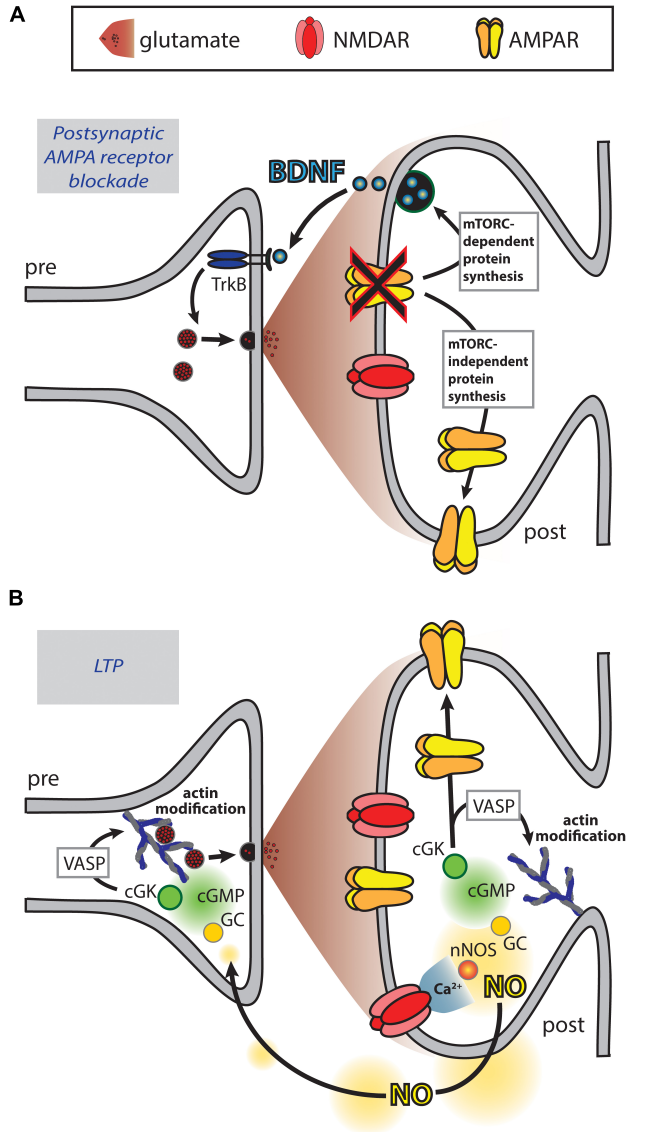

FIGURE 3 | Retrograde messengers may coordinate pre- and post-synaptic function. **(A)** Blockade of postsynaptic AMPARs results in mTORC-dependent protein translation of BDNF that acts as a retrograde messenger to enhance presynaptic release. Additionally, mTORC-independent protein translation results in increased postsynaptic AMPAR expression (Thiagarajan et al., 2005; Jakawich et al., 2010; Lindskog et al., 2010; Henry et al., 2012, 2018). **(B)** During LTP induction, calcium influx through NMDARs activates neuronal nitric oxide synthase (nNOS), which catalyzes the production of nitric oxide (NO). NO diffuses to the pre- and post-synaptic compartments where it activates the guanylate cyclase (GC), cGMP, cGMP-dependent protein kinase (cGK) signaling cascade, resulting in enhanced presynaptic synaptophysin puncta and postsynaptic AMPAR puncta (Antonova et al., 2001; Wang et al., 2005). At both the pre- and post-synapse cGK activates VASP, a protein that plays a role in actin modification. Additionally, cGK phosphorylates the AMPAR subunit GluA1 driving enhanced surface expression (Serulle et al., 2007).

be coordinated. For example, immunofluorescence imaging has revealed that NMDAR-dependent chemical LTP induces NO signaling that results in increased expression of synaptic markers simultaneously at both the pre- and the post-synapse leading to increased levels of co-localization between them (Antonova et al., 2001; Wang et al., 2005). These effects were found to be mediated via the guanosine 3′,5′ cyclic monophosphate (cGMP)-dependent signaling pathway leading to phosphorylation of the actin regulator VASP. As these and other cGMP-dependent effects are observed at both the pre- and post-synapse (Wang et al., 2005; Sanderson and Sher, 2013), NO-induced cGMP signaling could occur in both compartments to bring about coordinated changes (**Figure 3B**). Actin-dependent modification of spine structure may undergo bidirectional modulation via cAMP and cGMP signals (see review by Borovac et al., 2018) and so possibly these mechanisms could contribute to modifying spine structure, as well as modifying the expression of synaptic proteins, to ensure that the pre- and post-synapse are matched. Numerous other signaling molecules and potentially even ions such as potassium act as retrograde messengers in LTP (Bliss and Collingridge, 1993; Regehr et al., 2009) and may therefore also coordinate changes in pre- and post-synaptic function.

There is evidence that mGluR-LTD is expressed via both pre- and post-synaptic changes (Fitzjohn et al., 2001; Snyder et al., 2001; Xiao et al., 2001; Rouach and Nicoll, 2003; Tan et al., 2003; Huang et al., 2004; Moult et al., 2006; Gladding et al., 2009a; Casimiro et al., 2011; Sanderson et al., 2011, 2018; Eales et al., 2014), with pre-synaptic changes triggered via activation of post-synaptically expressed mGluRs and release of retrograde messengers such as 12-lipoxygenase metabolites of arachidonic acid (Watabe et al., 2002; Feinmark et al., 2003). In this form of plasticity, it is possible that pre- and post-synaptic changes may be coordinated which may result in the two compartments remaining functionally matched. mGluRs also induce structural changes at spines (Kamikubo et al., 2006; Shinoda et al., 2010; Hasegawa et al., 2015) possibly by regulating the actin cytoskeleton via a mechanism that involves an interaction between GluA2 and N-cadherin leading to the actin regulator cofilin (Zhou et al., 2011). Therefore, mGluR function may also be involved in triggering changes to the structure of synapses as well as their molecular composition, and so may play a role in ensuring these two aspects of synapse physiology are in step.

In addition to diffusible signaling molecules, precise co-ordination between the pre- and post-synapse occurs via direct physical interactions. The matching of AMPARs with the presynaptic release machinery in trans-synaptic molecular "nanocolumns" (Tang et al., 2016) depends on the C-terminal region of Neuroligin-1 and if its function is perturbed, then synaptic transmission is diminished (Haas et al., 2018). This is proposed to be due to Neuroligin-1 performing a linking role between presynaptic neurexins, which it binds via its extracellular N-terminal region, and PSD-95-anchored AMPAR nanodomains, which it binds via its intracellular C-terminal domain.

In summary, there appear to be multiple signaling mechanisms and dedicated molecular machinery that could

result in coordination between changes at the pre- and post-synapse.

PATTERNING OF SYNAPTIC CONNECTIONS

Above we have summarized data indicating that the pre- and the post-synapse are structurally and functionally correlated, that multiple mechanisms may bring this about including mGluR signaling, and that the expression of mGluRs may play a role in patterning the modulation of synapse strength in several physiological situations. It is not clear how synapses with certain physiological characteristics, including P(r), are arranged on the dendritic trees of excitatory neurons. Are dendrites structured such that synapses with certain properties are located in specific locations? A range of studies have addressed this question and found that synapses diminish in size toward the ends of basal and apical oblique dendrites (Katz et al., 2009; Grillo et al., 2018), while increasing along the somato apical-dendritic axis (Magee and Cook, 2000). The arrangement of synaptic properties may have implications for the integration of synaptic inputs at proximal and distal locations. For example, at proximal locations inputs require strict temporal coincidence in order to sum linearly, whereas at distal locations inputs are amplified more strongly without the need for precise coincidence (Branco and Hausser, 2011). This could lead to proximal and distal dendrites processing different streams of information: Temporally coded information at proximal dendrites and rate based information at distal dendrites (Branco and Hausser, 2011). These synaptic integration properties may be influenced by differential calcium responses at different dendritic locations (Walker et al., 2017).

The properties of neighboring synapses have been examined using similar imaging techniques to those used to investigate intra-synaptic properties. For example, measurement of P(r) using FM dyes has been used to reveal that neighboring synapses on the same dendritic branch have very similar P(r) and that the P(r) is set by the local activity level (Branco et al., 2008). This results in a negative correlation between the density of synaptic contacts and their P(r) and that directly modulating dendritic depolarization can influence P(r), both locally and globally. Neighboring synaptic inputs have been observed to exhibit correlated activity over a range of developmental time points when examined both *in vitro* and *in vivo* (Kleindienst et al., 2011; Takahashi et al., 2012; Winnubst et al., 2015; Wilson et al., 2016; Iacaruso et al., 2017; Scholl et al., 2017). It is therefore plausible that similar P(r) at neighboring synapses may be induced by similar endogenous activity at neighboring co-active synapses.

At the post-synapse, mechanisms also exist that may result in neighboring synapses having similar characteristics. One such mechanism may be calcium-induced calcium release, as in developing synapses this can result in enhanced potentiation at coincidentally active neighboring spines, resulting in clustered synapse maturation (Lee et al., 2016). Conversely, synapses that neighbor a group of co-active synapses, but that are not coincidentally active themselves, are weakened (Oh et al., 2015; Winnubst et al., 2015). Mechanisms such as these may contribute to the clustered postsynaptic enhancement of synapses *in vivo* that occurs in response to sensory experience (Makino and Malinow, 2011).

Astrocytes may also play a role in regulating synaptic P(r), since when astrocytic function is perturbed the P(r) of heterosynaptic inputs become less divergent, implying that astrocytes play a role in maintaining heterogeneity of P(r) over the entire cell (Letellier et al., 2016). The investigation on the role of astrocytes on P(r) utilized two heterosynaptic inputs, which would be unlikely to make synapses that neighbor each other. Therefore presumably the role astrocytes play in maintaining heterogeneity of P(r) is not "local" and is therefore distinct from the mechanisms that ensures similarity of P(r) of neighboring synapses (Branco et al., 2008).

FUTURE DIRECTIONS AND PROSPECTS

A major area of neuroscience research is aimed at understanding the processes involved in synaptic plasticity, the most extensively studied of which is NMDAR-dependent LTP (Bliss and Collingridge, 1993). Although it is well established that this form of LTP involves both pre- and post-synaptic alterations, including changes in P(r) as well as AMPAR number and properties (Bliss and Collingridge, 2013), these pre- and post-synaptic processes are usually studied in isolation. Our recent finding that P(r) can affect the re-distribution of AMPARs adds an extra layer of complexity to the understanding of plastic events at the level of the single synapse. The induction of LTP by TBS triggers an initial short-term potentiation (STP) component that is mediated by an increase in P(r). It would be predicted that this would result in an internalization of some of the mGluR1 that may be present at the synapse and thereby protect the synapse from postsynaptic weakening mediated by this receptor. This is turn would help stabilize AMPARs that are inserted during LTP. In contrast, in the absence of STP the AMPARs that are inserted during LTP could be more labile since they would be more susceptible to mGluR1-mediated synaptic weakening. At CA3–CA1 principal synapses, mGluR1 is expressed predominantly early in development where it may contribute the refinement of hippocampal synaptic connectivity. Indeed, early in development at these synapses, LTP is predominantly mediated by an increase in P(r) (Palmer et al., 2004), though this changes to a postsynaptically dominated LTP mechanism via a switch triggered by presynaptic kainate receptors (Lauri et al., 2006).

At certain other synapses, such as the parallel synapses between granule cells and Purkinje cells, mGluR1 is the trigger for LTD in adult tissue (Aiba et al., 1994; Conquet et al., 1994) and postsynaptic mechanisms appear to dominate

(Wang and Linden, 2000). Whether similar mechanisms to rapidly coordinate pre- and post-synaptic functionality operate at these cerebellar synapses and elsewhere in the CNS remains to be determined.

In summary, rapidly coordinated changes in pre- and post-synaptic activity, mediated by the actions of the neurotransmitter itself, are likely to impact on many facets of synaptic transmission and plasticity in health and disease. These are areas ripe for future investigation.

AUTHOR CONTRIBUTIONS

The review was written by TS and edited by JG and GC.

FUNDING

We are grateful for the support of a Canadian Institutes of Health Research (CIHR) Foundation grant (154276) to GC.

REFERENCES

Abrahamsson, T., Chou, C. Y. C., Li, S. Y., Mancino, A., Costa, R. P., Brock, J. A., et al. (2017). Differential regulation of evoked and spontaneous release by presynaptic NMDA Receptors. *Neuron* 96, 839-855 e835.

Aiba, A., Chen, C., Herrup, K., Rosenmund, C., Stevens, C. F., and Tonegawa, S. (1994). Reduced hippocampal long-term potentiation and context-specific deficit in associative learning in mGluR1 mutant mice. *Cell* 79, 365–375. doi: 10.1016/0092-8674(94)90204-6

Allen, N. J., and Eroglu, C. (2017). Cell biology of astrocyte-synapse interactions. *Neuron* 96, 697–708. doi: 10.1016/j.neuron.2017.09.056

Ango, F., Prezeau, L., Muller, T., Tu, J. C., Xiao, B., Worley, P. F., et al. (2001). Agonist-independent activation of metabotropic glutamate receptors by the intracellular protein Homer. *Nature* 411, 962–965. doi: 10.1038/35082096

Antonova, I., Arancio, O., Trillat, A. C., Wang, H. G., Zablow, L., Udo, H., et al. (2001). Rapid increase in clusters of presynaptic proteins at onset of long-lasting potentiation. *Science* 294, 1547–1550. doi: 10.1126/science.1066273

Araki, Y., Lin, D. T., and Huganir, R. L. (2010). Plasma membrane insertion of the AMPA receptor GluA2 subunit is regulated by NSF binding and Q/R editing of the ion pore. *Proc. Natl. Acad. Sci. U.S.A.* 107, 11080–11085. doi: 10.1073/pnas.1006584107

Araki, Y., Zeng, M., Zhang, M., and Huganir, R. L. (2015). Rapid dispersion of SynGAP from synaptic spines triggers AMPA receptor insertion and spine enlargement during LTP. *Neuron* 85, 173–189. doi: 10.1016/j.neuron.2014.12.023

Araya, R., Vogels, T. P., and Yuste, R. (2014). Activity-dependent dendritic spine neck changes are correlated with synaptic strength. *Proc. Natl. Acad. Sci. U.S.A.* 111, E2895–E2904. doi: 10.1073/pnas.1321869111

Ashby, M. C., De La Rue, S. A., Ralph, G. S., Uney, J., Collingridge, G. L., and Henley, J. M. (2004). Removal of AMPA receptors (AMPARs) from synapses is preceded by transient endocytosis of extrasynaptic AMPARs. *J. Neurosci.* 24, 5172–5176. doi: 10.1523/jneurosci.1042-04.2004

Ashby, M. C., Maier, S. R., Nishimune, A., and Henley, J. M. (2006). Lateral diffusion drives constitutive exchange of AMPA receptors at dendritic spines and is regulated by spine morphology. *J. Neurosci.* 26, 7046–7055. doi: 10.1523/jneurosci.1235-06.2006

Beique, J. C., Lin, D. T., Kang, M. G., Aizawa, H., Takamiya, K., and Huganir, R. L. (2006). Synapse-specific regulation of AMPA receptor function by PSD-95. *Proc. Natl. Acad. Sci. U.S.A.* 103, 19535–19540. doi: 10.1073/pnas.0608492103

Betz, W. J., and Bewick, G. S. (1992). Optical analysis of synaptic vesicle recycling at the frog neuromuscular junction. *Science* 255, 200–203. doi: 10.1126/science.1553547

Betz, W. J., Mao, F., and Bewick, G. S. (1992). Activity-dependent fluorescent staining and destaining of living vertebrate motor nerve terminals. *J. Neurosci.* 12, 363–375. doi: 10.1523/jneurosci.12-02-00363.1992

Bliss, T. V., and Collingridge, G. L. (1993). A synaptic model of memory: long-term potentiation in the hippocampus. *Nature* 361, 31–39. doi: 10.1038/361031a0

Bliss, T. V., and Collingridge, G. L. (2013). Expression of NMDA receptor-dependent LTP in the hippocampus: bridging the divide. *Mol Brain* 6:5. doi: 10.1186/1756-6606-6-5

Borovac, J., Bosch, M., and Okamoto, K. (2018). Regulation of actin dynamics during structural plasticity of dendritic spines: signaling messengers and actin-binding proteins. *Mol. Cell Neurosci.* 91, 122–130. doi: 10.1016/j.mcn.2018.07.001

Brakeman, P. R., Lanahan, A. A., O'Brien, R., Roche, K., Barnes, C. A., Huganir, R. L., et al. (1997). Homer: a protein that selectively binds metabotropic glutamate receptors. *Nature* 386, 284–288. doi: 10.1038/386284a0

Branco, T., and Hausser, M. (2011). Synaptic integration gradients in single cortical pyramidal cell dendrites. *Neuron* 69, 885–892. doi: 10.1016/j.neuron.2011.02.006

Branco, T., Staras, K., Darcy, K. J., and Goda, Y. (2008). Local dendritic activity sets release probability at hippocampal synapses. *Neuron* 59, 475–485. doi: 10.1016/j.neuron.2008.07.006

Brodin, L., Low, P., and Shupliakov, O. (2000). Sequential steps in clathrin-mediated synaptic vesicle endocytosis. *Curr. Opin. Neurobiol.* 10, 312–320. doi: 10.1016/s0959-4388(00)00097-0

Casimiro, T. M., Sossa, K. G., Uzunova, G., Beattie, J. B., Marsden, K. C., and Carroll, R. C. (2011). mGluR and NMDAR activation internalize distinct populations of AMPARs. *Mol. Cell. Neurosci.* 48, 161–170. doi: 10.1016/j.mcn.2011.07.007

Charlesworth, P., Cotterill, E., Morton, A., Grant, S. G., and Eglen, S. J. (2015). Quantitative differences in developmental profiles of spontaneous activity in cortical and hippocampal cultures. *Neural Dev.* 10:1. doi: 10.1186/s13064-014-0028-0

Conquet, F., Bashir, Z. I., Davies, C. H., Daniel, H., Ferraguti, F., Bordi, F., et al. (1994). Motor deficit and impairment of synaptic plasticity in mice lacking mGluR1. *Nature* 372, 237–243. doi: 10.1038/372237a0

Dallerac, G., Zapata, J., and Rouach, N. (2018). Versatile control of synaptic circuits by astrocytes: where, when and how? *Nat. Rev. Neurosci.* 19, 729–743. doi: 10.1038/s41583-018-0080-6

de Vivo, L., Bellesi, M., Marshall, W., Bushong, E. A., Ellisman, M. H., Tononi, G., et al. (2017). Ultrastructural evidence for synaptic scaling across the wake/sleep cycle. *Science* 355, 507–510. doi: 10.1126/science.aah5982

Diering, G. H., Nirujogi, R. S., Roth, R. H., Worley, P. F., Pandey, A., and Huganir, R. L. (2017). Homer1a drives homeostatic scaling-down of excitatory synapses during sleep. *Science* 355, 511–515. doi: 10.1126/science.aai8355

Dobrunz, L. E., and Stevens, C. F. (1997). Heterogeneity of release probability, facilitation, and depletion at central synapses. *Neuron* 18, 995–1008. doi: 10.1016/s0896-6273(00)80338-4

Eales, K. L., Palygin, O., O'Loughlin, T., Rasooli-Nejad, S., Gaestel, M., Muller, J., et al. (2014). The MK2/3 cascade regulates AMPAR trafficking and cognitive flexibility. *Nat. Commun.* 5:4701. doi: 10.1038/ncomms5701

El-Husseini, A. E., Schnell, E., Chetkovich, D. M., Nicoll, R. A., and Bredt, D. S. (2000). PSD-95 involvement in maturation of excitatory synapses. *Science* 290, 1364–1368.

Emptage, N., Bliss, T. V., and Fine, A. (1999). Single synaptic events evoke NMDA receptor-mediated release of calcium from internal stores in hippocampal dendritic spines. *Neuron* 22, 115–124. doi: 10.1016/s0896-6273(00)80683-2

Emptage, N. J., Reid, C. A., Fine, A., and Bliss, T. V. (2003). Optical quantal analysis reveals a presynaptic component of LTP at hippocampal Schaffer-associational synapses. *Neuron* 38, 797–804. doi: 10.1016/s0896-6273(03)00325-8

Enoki, R., Hu, Y. L., Hamilton, D., and Fine, A. (2009). Expression of long-term plasticity at individual synapses in hippocampus is graded, bidirectional, and mainly presynaptic: optical quantal analysis. *Neuron* 62, 242–253. doi: 10.1016/j.neuron.2009.02.026

Feinmark, S. J., Begum, R., Tsvetkov, E., Goussakov, I., Funk, C. D., Siegelbaum, S. A., et al. (2003). 12-lipoxygenase metabolites of arachidonic acid mediate metabotropic glutamate receptor-dependent long-term depression at

hippocampal CA3-CA1 synapses. *J. Neurosci.* 23, 11427–11435. doi: 10.1523/jneurosci.23-36-11427.2003

Fitzjohn, S. M., Palmer, M. J., May, J. E., Neeson, A., Morris, S. A., and Collingridge, G. L. (2001). A characterisation of long-term depression induced by metabotropic glutamate receptor activation in the rat hippocampus in vitro. *J. Physiol.* 537, 421–430. doi: 10.1111/j.1469-7793.2001.00421.x

Fukata, Y., Dimitrov, A., Boncompain, G., Vielemeyer, O., Perez, F., and Fukata, M. (2013). Local palmitoylation cycles define activity-regulated postsynaptic subdomains. *J. Cell Biol.* 202, 145–161. doi: 10.1083/jcb.201302071

Gladding, C. M., Collett, V. J., Jia, Z., Bashir, Z. I., Collingridge, G. L., and Molnar, E. (2009a). Tyrosine dephosphorylation regulates AMPAR internalisation in mGluR-LTD. *Mol. Cell. Neurosci.* 40, 267–279. doi: 10.1016/j.mcn.2008.10.014

Gladding, C. M., Fitzjohn, S. M., and Molnar, E. (2009b). Metabotropic glutamate receptor-mediated long-term depression: molecular mechanisms. *Pharmacol. Rev.* 61, 395–412. doi: 10.1124/pr.109.001735

Glasgow, S. D., McPhedrain, R., Madranges, J. F., Kennedy, T. E., and Ruthazer, E. S. (2019). Approaches and limitations in the investigation of synaptic transmission and plasticity. *Front. Synaptic Neurosci.* 11:20. doi: 10.3389/fnsyn.2019.00020

Grillo, F. W., Neves, G., Walker, A., Vizcay-Barrena, G., Fleck, R. A., Branco, T., et al. (2018). A distance-dependent distribution of presynaptic boutons tunes frequency-dependent dendritic integration. *Neuron* 99, 275-282 e273. doi: 10.1016/j.neuron.2018.06.015

Haas, K. T., Compans, B., Letellier, M., Bartol, T. M., Grillo-Bosch, D., Sejnowski, T. J., et al. (2018). Pre-post synaptic alignment through neuroligin-1 tunes synaptic transmission efficiency. *eLife* 7:e31755

Harata, N., Ryan, T. A., Smith, S. J., Buchanan, J., and Tsien, R. W. (2001). Visualizing recycling synaptic vesicles in hippocampal neurons by FM 1-43 photoconversion. *Proc. Natl. Acad. Sci. U.S.A.* 98, 12748–12753. doi: 10.1073/pnas.171442798

Harris, K. M., and Stevens, J. K. (1989). Dendritic spines of CA 1 pyramidal cells in the rat hippocampus: serial electron microscopy with reference to their biophysical characteristics. *J. Neurosci.* 9, 2982–2997. doi: 10.1523/jneurosci.09-08-02982.1989

Harvey, C. D., Yasuda, R., Zhong, H., and Svoboda, K. (2008). The spread of Ras activity triggered by activation of a single dendritic spine. *Science* 321, 136–140. doi: 10.1126/science.1159675

Hasegawa, S., Sakuragi, S., Tominaga-Yoshino, K., and Ogura, A. (2015). Dendritic spine dynamics leading to spine elimination after repeated inductions of LTD. *Sci. Rep.* 5:7707. doi: 10.1038/srep07707

Heine, M., Groc, L., Frischknecht, R., Beique, J. C., Lounis, B., Rumbaugh, G., et al. (2008). Surface mobility of postsynaptic AMPARs tunes synaptic transmission. *Science* 320, 201–205. doi: 10.1126/science.1152089

Henneberger, C., Bard, L., Panatier, A., Reynolds, J. P., Medvedev, N. I., Minge, D., et al. (2018). LTP induction drives remodeling of astroglia to boost glutamate escape from synapses. *BioRxiv [Preprint]*

Henry, F. E., McCartney, A. J., Neely, R., Perez, A. S., Carruthers, C. J., Stuenkel, E. L., et al. (2012). Retrograde changes in presynaptic function driven by dendritic mTORC1. *J. Neurosci.* 32, 17128–17142. doi: 10.1523/JNEUROSCI.2149-12.2012

Henry, F. E., Wang, X., Serrano, D., Perez, A. S., Carruthers, C. J. L., Stuenkel, E. L., et al. (2018). A Unique Homeostatic Signaling Pathway Links Synaptic Inactivity to Postsynaptic mTORC1. *J. Neurosci.* 38, 2207–2225. doi: 10.1523/JNEUROSCI.1843-17.2017

Hessler, N. A., Shirke, A. M., and Malinow, R. (1993). The probability of transmitter release at a mammalian central synapse. *Nature* 366, 569–572. doi: 10.1038/366569a0

Holderith, N., Lorincz, A., Katona, G., Rozsa, B., Kulik, A., Watanabe, M., et al. (2012). Release probability of hippocampal glutamatergic terminals scales with the size of the active zone. *Nat. Neurosci.* 15, 988–997. doi: 10.1038/nn.3137

Hruska, M., Henderson, N., Le Marchand, S. J., Jafri, H., and Dalva, M. B. (2018). Synaptic nanomodules underlie the organization and plasticity of spine synapses. *Nat. Neurosci.* 21, 671–682. doi: 10.1038/s41593-018-0138-9

Hu, J. H., Park, J. M., Park, S., Xiao, B., Dehoff, M. H., Kim, S., et al. (2010). Homeostatic scaling requires group I mGluR activation mediated by Homer1a. *Neuron* 68, 1128–1142. doi: 10.1016/j.neuron.2010.11.008

Huang, B., Wang, W., Bates, M., and Zhuang, X. (2008). Three-dimensional super-resolution imaging by stochastic optical reconstruction microscopy. *Science* 319, 810–813. doi: 10.1126/science.1153529

Huang, C. C., You, J. L., Wu, M. Y., and Hsu, K. S. (2004). Rap1-induced p38 mitogen-activated protein kinase activation facilitates AMPA receptor trafficking via the GDI.Rab5 complex. Potential role in (S)-3,5-dihydroxyphenylglycene-induced long term depression. *J. Biol. Chem.* 279, 12286–12292. doi: 10.1074/jbc.m312868200

Iacaruso, M. F., Gasler, I. T., and Hofer, S. B. (2017). Synaptic organization of visual space in primary visual cortex. *Nature* 547, 449–452. doi: 10.1038/nature23019

Jakawich, S. K., Nasser, H. B., Strong, M. J., McCartney, A. J., Perez, A. S., Rakesh, N., et al. (2010). Local presynaptic activity gates homeostatic changes in presynaptic function driven by dendritic BDNF synthesis. *Neuron* 68, 1143–1158. doi: 10.1016/j.neuron.2010.11.034

Jensen, T. P., Zheng, K., Cole, N., Marvin, J. S., Looger, L. L., and Rusakov, D. A. (2019). Multiplex imaging relates quantal glutamate release to presynaptic Ca(2+) homeostasis at multiple synapses in situ. *Nat. Commun.* 10:1414. doi: 10.1038/s41467-019-09216-8

Johnstone, V. P., and Raymond, C. R. (2013). Postsynaptic protein synthesis is required for presynaptic enhancement in persistent forms of long-term potentiation. *Front. Synaptic Neurosci.* 5:1. doi: 10.3389/fnsyn.2013.00001

Kamikubo, Y., Egashira, Y., Tanaka, T., Shinoda, Y., Tominaga-Yoshino, K., and Ogura, A. (2006). Long-lasting synaptic loss after repeated induction of LTD: independence to the means of LTD induction. *Eur. J. Neurosci.* 24, 1606–1616. doi: 10.1111/j.1460-9568.2006.05032.x

Katz, Y., Menon, V., Nicholson, D. A., Geinisman, Y., Kath, W. L., and Spruston, N. (2009). Synapse distribution suggests a two-stage model of dendritic integration in CA1 pyramidal neurons. *Neuron* 63, 171–177. doi: 10.1016/j.neuron.2009.06.023

Kavalali, E. T. (2015). The mechanisms and functions of spontaneous neurotransmitter release. *Nat. Rev. Neurosci.* 16, 5–16. doi: 10.1038/nrn3875

Kay, A. R., Alfonso, A., Alford, S., Cline, H. T., Holgado, A. M., Sakmann, B., et al. (1999). Imaging synaptic activity in intact brain and slices with FM1-43 in *C. elegans*, lamprey, and rat. *Neuron* 24, 809–817. doi: 10.1016/s0896-6273(00)81029-6

Kay, L., Humphreys, L., Eickholt, B. J., and Burrone, J. (2011). Neuronal activity drives matching of pre- and postsynaptic function during synapse maturation. *Nat. Neurosci.* 14, 688–690. doi: 10.1038/nn.2826

Kim, J., Goldsberry, M. E., Harmon, T. C., and Freeman, J. H. (2016). Developmental changes in hippocampal ca1 single neuron firing and theta activity during associative learning. *PLoS One* 11:e0164781. doi: 10.1371/journal.pone.0164781

Kleindienst, T., Winnubst, J., Roth-Alpermann, C., Bonhoeffer, T., and Lohmann, C. (2011). Activity-dependent clustering of functional synaptic inputs on developing hippocampal dendrites. *Neuron* 72, 1012–1024. doi: 10.1016/j.neuron.2011.10.015

Kopec, C. D., Li, B., Wei, W., Boehm, J., and Malinow, R. (2006). Glutamate receptor exocytosis and spine enlargement during chemically induced long-term potentiation. *J. Neurosci.* 26, 2000–2009. doi: 10.1523/jneurosci.3918-05.2006

Kopec, C. D., Real, E., Kessels, H. W., and Malinow, R. (2007). GluR1 links structural and functional plasticity at excitatory synapses. *J. Neurosci.* 27, 13706–13718. doi: 10.1523/jneurosci.3503-07.2007

Lauri, S. E., Vesikansa, A., Segerstrale, M., Collingridge, G. L., Isaac, J. T., and Taira, T. (2006). Functional maturation of CA1 synapses involves activity-dependent loss of tonic kainate receptor-mediated inhibition of glutamate release. *Neuron* 50, 415–429. doi: 10.1016/j.neuron.2006.03.020

Lee, K. F., Soares, C., Thivierge, J. P., and Beique, J. C. (2016). Correlated synaptic inputs drive dendritic calcium amplification and cooperative plasticity during clustered synapse development. *Neuron* 89, 784–799. doi: 10.1016/j.neuron.2016.01.012

Letellier, M., Park, Y. K., Chater, T. E., Chipman, P. H., Gautam, S. G., Oshima-Takago, T., et al. (2016). Astrocytes regulate heterogeneity of presynaptic strengths in hippocampal networks. *Proc. Natl. Acad. Sci. U.S.A.* 113, E2685–E2694. doi: 10.1073/pnas.1523717113

Lin, D. T., and Huganir, R. L. (2007). PICK1 and phosphorylation of the glutamate receptor 2 (GluR2) AMPA receptor subunit regulates GluR2 recycling after

NMDA receptor-induced internalization. *J. Neurosci.* 27, 13903–13908. doi: 10.1523/jneurosci.1750-07.2007

Lin, D. T., Makino, Y., Sharma, K., Hayashi, T., Neve, R., Takamiya, K., et al. (2009). Regulation of AMPA receptor extrasynaptic insertion by 4.1N, *phosphorylation and palmitoylation*. *Nat Neurosci* 12, 879–887. doi: 10.1038/nn.2351

Lindskog, M., Li, L., Groth, R. D., Poburko, D., Thiagarajan, T. C., Han, X., et al. (2010). Postsynaptic GluA1 enables acute retrograde enhancement of presynaptic function to coordinate adaptation to synaptic inactivity. *Proc. Natl. Acad. Sci. U.S.A.* 107, 21806–21811. doi: 10.1073/pnas.1016399107

MacGillavry, H. D., Song, Y., Raghavachari, S., and Blanpied, T. A. (2013). Nanoscale scaffolding domains within the postsynaptic density concentrate synaptic AMPA receptors. *Neuron* 78, 615–622. doi: 10.1016/j.neuron.2013.03.009

Magee, J. C., and Cook, E. P. (2000). Somatic EPSP amplitude is independent of synapse location in hippocampal pyramidal neurons. *Nat. Neurosci.* 3, 895–903. doi: 10.1038/78800

Makino, H., and Malinow, R. (2011). Compartmentalized versus global synaptic plasticity on dendrites controlled by experience. *Neuron* 72, 1001–1011. doi: 10.1016/j.neuron.2011.09.036

Matsuzaki, M., Honkura, N., Ellis-Davies, G. C., and Kasai, H. (2004). Structural basis of long-term potentiation in single dendritic spines. *Nature* 429, 761–766. doi: 10.1038/nature02617

Miesenbock, G., De Angelis, D. A., and Rothman, J. E. (1998). Visualizing secretion and synaptic transmission with pH-sensitive green fluorescent proteins. *Nature* 394, 192–195. doi: 10.1038/28190

Mitchell, D. E., Martineau, E., Tazerart, S., and Araya, R. (2019). Probing single synapses via the photolytic release of neurotransmitters. *Front. Synaptic Neurosci.* 11:19. doi: 10.3389/fnsyn.2019.00019

Moult, P. R., Gladding, C. M., Sanderson, T. M., Fitzjohn, S. M., Bashir, Z. I., Molnar, E., et al. (2006). Tyrosine phosphatases regulate AMPA receptor trafficking during metabotropic glutamate receptor-mediated long-term depression. *J. Neurosci.* 26, 2544–2554. doi: 10.1523/jneurosci.4322-05.2006

Murthy, V. N., Schikorski, T., Stevens, C. F., and Zhu, Y. (2001). Inactivity produces increases in neurotransmitter release and synapse size. *Neuron* 32, 673–682. doi: 10.1016/s0896-6273(01)00500-1

Murthy, V. N., Sejnowski, T. J., and Stevens, C. F. (1997). Heterogeneous release properties of visualized individual hippocampal synapses. *Neuron* 18, 599–612. doi: 10.1016/s0896-6273(00)80301-3

Nadif Kasri, N., Nakano-Kobayashi, A., and Van Aelst, L. (2011). Rapid synthesis of the X-linked mental retardation protein OPHN1 mediates mGluR-dependent LTD through interaction with the endocytic machinery. *Neuron* 72, 300–315. doi: 10.1016/j.neuron.2011.09.001

Nair, D., Hosy, E., Petersen, J. D., Constals, A., Giannone, G., Choquet, D., et al. (2013). Super-resolution imaging reveals that AMPA receptors inside synapses are dynamically organized in nanodomains regulated by PSD95. *J. Neurosci.* 33, 13204–13224. doi: 10.1523/JNEUROSCI.2381-12.2013

Noguchi, J., Matsuzaki, M., Ellis-Davies, G. C., and Kasai, H. (2005). Spine-neck geometry determines NMDA receptor-dependent Ca2+ signaling in dendrites. *Neuron* 46, 609–622. doi: 10.1016/j.neuron.2005.03.015

Oh, W. C., Parajuli, L. K., and Zito, K. (2015). Heterosynaptic structural plasticity on local dendritic segments of hippocampal CA1 neurons. *Cell Rep.* 10, 162–169. doi: 10.1016/j.celrep.2014.12.016

Okuno, H., Akashi, K., Ishii, Y., Yagishita-Kyo, N., Suzuki, K., Nonaka, M., et al. (2012). Inverse synaptic tagging of inactive synapses via dynamic interaction of Arc/Arg3.1 with CaMKIIbeta. *Cell* 149, 886–898. doi: 10.1016/j.cell.2012.02.062

Oliet, S. H., Malenka, R. C., and Nicoll, R. A. (1997). Two distinct forms of long-term depression coexist in CA1 hippocampal pyramidal cells. *Neuron* 18, 969–982. doi: 10.1016/s0896-6273(00)80336-0

Padamsey, Z., Tong, R., and Emptage, N. (2017). Glutamate is required for depression but not potentiation of long-term presynaptic function. *eLife* 6:e29688. doi: 10.7554/eLife.29688

Padamsey, Z., Tong, R., and Emptage, N. (2019). Optical quantal analysis using Ca(2+) indicators: a robust method for assessing transmitter release probability at excitatory synapses by imaging single glutamate release events. *Front. Synaptic Neurosci.* 11:5. doi: 10.3389/fnsyn.2019.00005

Palmer, M. J., Irving, A. J., Seabrook, G. R., Jane, D. E., and Collingridge, G. L. (1997). The group I mGlu receptor agonist DHPG induces a novel form of LTD in the CA1 region of the hippocampus. *Neuropharmacology* 36, 1517–1532. doi: 10.1016/s0028-3908(97)00181-0

Palmer, M. J., Isaac, J. T., and Collingridge, G. L. (2004). Multiple, developmentally regulated expression mechanisms of long-term potentiation at CA1 synapses. *J. Neurosci.* 24, 4903–4911. doi: 10.1523/jneurosci.0170-04.2004

Passafaro, M., Nakagawa, T., Sala, C., and Sheng, M. (2003). Induction of dendritic spines by an extracellular domain of AMPA receptor subunit GluR2. *Nature* 424, 677–681. doi: 10.1038/nature01781

Patterson, M. A., Szatmari, E. M., and Yasuda, R. (2010). AMPA receptors are exocytosed in stimulated spines and adjacent dendrites in a Ras-ERK-dependent manner during long-term potentiation. *Proc. Natl. Acad. Sci. U.S.A.* 107, 15951–15956. doi: 10.1073/pnas.0913875107

Pyle, J. L., Kavalali, E. T., Choi, S., and Tsien, R. W. (1999). Visualization of synaptic activity in hippocampal slices with FM1-43 enabled by fluorescence quenching. *Neuron* 24, 803–808. doi: 10.1016/s0896-6273(00)81028-4

Regehr, W. G., Carey, M. R., and Best, A. R. (2009). Activity-dependent regulation of synapses by retrograde messengers. *Neuron* 63, 154–170. doi: 10.1016/j.neuron.2009.06.021

Rollenhagen, A., and Lubke, J. H. (2006). The morphology of excitatory central synapses: from structure to function. *Cell Tissue Res.* 326, 221–237. doi: 10.1007/s00441-006-0288-z

Rose, C. R., Felix, L., Zeug, A., Dietrich, D., Reiner, A., and Henneberger, C. (2017). Astroglial glutamate signaling and uptake in the hippocampus. *Front. Mol. Neurosci.* 10:451. doi: 10.3389/fnmol.2017.00451

Rosenmund, C., Clements, J. D., and Westbrook, G. L. (1993). Nonuniform probability of glutamate release at a hippocampal synapse. *Science* 262, 754–757. doi: 10.1126/science.7901909

Rosenmund, C., and Stevens, C. F. (1996). Definition of the readily releasable pool of vesicles at hippocampal synapses. *Neuron* 16, 1197–1207. doi: 10.1016/s0896-6273(00)80146-4

Rouach, N., and Nicoll, R. A. (2003). Endocannabinoids contribute to short-term but not long-term mGluR-induced depression in the hippocampus. *Eur. J. Neurosci.* 18, 1017–1020. doi: 10.1046/j.1460-9568.2003.02823.x

Ryan, T. A., Reuter, H., Wendland, B., Schweizer, F. E., Tsien, R. W., and Smith, S. J. (1993). The kinetics of synaptic vesicle recycling measured at single presynaptic boutons. *Neuron* 11, 713–724. doi: 10.1016/0896-6273(93)90081-2

Sala, C., Piech, V., Wilson, N. R., Passafaro, M., Liu, G., and Sheng, M. (2001). Regulation of dendritic spine morphology and synaptic function by Shank and Homer. *Neuron* 31, 115–130. doi: 10.1016/s0896-6273(01)00339-7

Sanderson, T. M., Bradley, C. A., Georgiou, J., Hong, Y. H., Ng, A. N., Lee, Y., et al. (2018). The probability of neurotransmitter release governs AMPA receptor trafficking via activity-dependent regulation of mGluR1 surface expression. *Cell Rep* 25, 3631-3646 e3633. doi: 10.1016/j.celrep.2018.12.010

Sanderson, T. M., Collingridge, G. L., and Fitzjohn, S. M. (2011). Differential trafficking of AMPA receptors following activation of NMDA receptors and mGluRs. *Mol. Brain* 4:30. doi: 10.1186/1756-6606-4-30

Sanderson, T. M., Hogg, E. L., Collingridge, G. L., and Correa, S. A. (2016). Hippocampal metabotropic glutamate receptor long-term depression in health and disease: focus on mitogen-activated protein kinase pathways. *J. Neurochem.* 139(Suppl. 2), 200–214. doi: 10.1111/jnc.13592

Sanderson, T. M., and Sher, E. (2013). The role of phosphodiesterases in hippocampal synaptic plasticity. *Neuropharmacology* 74, 86–95. doi: 10.1016/j.neuropharm.2013.01.011

Sankaranarayanan, S., De Angelis, D., Rothman, J. E., and Ryan, T. A. (2000). The use of pHluorins for optical measurements of presynaptic activity. *Biophys. J.* 79, 2199–2208. doi: 10.1016/s0006-3495(00)76468-x

Schikorski, T., and Stevens, C. F. (1997). Quantitative ultrastructural analysis of hippocampal excitatory synapses. *J. Neurosci.* 17, 5858–5867. doi: 10.1523/jneurosci.17-15-05858.1997

Schikorski, T., and Stevens, C. F. (1999). Quantitative fine-structural analysis of olfactory cortical synapses. *Proc. Natl. Acad. Sci. U.S.A.* 96, 4107–4112. doi: 10.1073/pnas.96.7.4107

Scholl, B., Wilson, D. E., and Fitzpatrick, D. (2017). Local order within global disorder: synaptic architecture of visual space. *Neuron* 96:e1124. doi: 10.1016/j.neuron.2017.10.017

Serulle, Y., Zhang, S., Ninan, I., Puzzo, D., McCarthy, M., Khatri, L., et al. (2007). A GluR1-cGKII interaction regulates AMPA receptor trafficking. *Neuron* 56, 670–688. doi: 10.1016/j.neuron.2007.09.016

Shinoda, Y., Tanaka, T., Tominaga-Yoshino, K., and Ogura, A. (2010). Persistent synapse loss induced by repetitive LTD in developing rat hippocampal neurons. *PLoS One* 5:e10390. doi: 10.1371/journal.pone.0010390

Snyder, E. M., Philpot, B. D., Huber, K. M., Dong, X., Fallon, J. R., and Bear, M. F. (2001). Internalization of ionotropic glutamate receptors in response to mGluR activation. *Nat. Neurosci.* 4, 1079–1085. doi: 10.1038/nn746

Soares, C., Lee, K. F. H., and Beique, J. C. (2017). Metaplasticity at CA1 synapses by homeostatic control of presynaptic release dynamics. *Cell Rep.* 21, 1293–1303. doi: 10.1016/j.celrep.2017.10.025

Soares, C., Trotter, D., Longtin, A., Beique, J. C., and Naud, R. (2019). Parsing out the variability of transmission at central synapses using optical quantal analysis. *Front. Synaptic Neurosci.* 11:22. doi: 10.3389/fnsyn.2019.00022

Takahashi, N., Kitamura, K., Matsuo, N., Mayford, M., Kano, M., Matsuki, N., et al. (2012). Locally synchronized synaptic inputs. *Science* 335, 353–356. doi: 10.1126/science.1210362

Takumi, Y., Ramirez-Leon, V., Laake, P., Rinvik, E., and Ottersen, O. P. (1999). Different modes of expression of AMPA and NMDA receptors in hippocampal synapses. *Nat. Neurosci.* 2, 618–624. doi: 10.1038/10172

Tan, Y., Hori, N., and Carpenter, D. O. (2003). The mechanism of presynaptic long-term depression mediated by group I metabotropic glutamate receptors. *Cell Mol. Neurobiol.* 23, 187–203.

Tanaka, J., Horiike, Y., Matsuzaki, M., Miyazaki, T., Ellis-Davies, G. C., and Kasai, H. (2008). Protein synthesis and neurotrophin-dependent structural plasticity of single dendritic spines. *Science* 319, 1683–1687. doi: 10.1126/science.1152864

Tanaka, J., Matsuzaki, M., Tarusawa, E., Momiyama, A., Molnar, E., Kasai, H., et al. (2005). Number and density of AMPA receptors in single synapses in immature cerebellum. *J. Neurosci.* 25, 799–807. doi: 10.1523/jneurosci.4256-04.2005

Tang, A. H., Chen, H., Li, T. P., Metzbower, S. R., MacGillavry, H. D., and Blanpied, T. A. (2016). A trans-synaptic nanocolumn aligns neurotransmitter release to receptors. *Nature* 536, 210–214. doi: 10.1038/nature19058

Thiagarajan, T. C., Lindskog, M., and Tsien, R. W. (2005). Adaptation to synaptic inactivity in hippocampal neurons. *Neuron* 47, 725–737. doi: 10.1016/j.neuron.2005.06.037

Thorsen, T. S., Madsen, K. L., Rebola, N., Rathje, M., Anggono, V., Bach, A., et al. (2010). Identification of a small-molecule inhibitor of the PICK1 PDZ domain that inhibits hippocampal LTP and LTD. *Proc. Natl. Acad. Sci. U.S.A.* 107, 413–418. doi: 10.1073/pnas.0902225107

Tokuoka, H., and Goda, Y. (2008). Activity-dependent coordination of presynaptic release probability and postsynaptic GluR2 abundance at single synapses. *Proc. Natl. Acad. Sci. U.S.A.* 105, 14656–14661. doi: 10.1073/pnas.0805705105

Tononi, G., and Cirelli, C. (2014). Sleep and the price of plasticity: from synaptic and cellular homeostasis to memory consolidation and integration. *Neuron* 81, 12–34. doi: 10.1016/j.neuron.2013.12.025

Tracy, T. E., Yan, J. J., and Chen, L. (2011). Acute knockdown of AMPA receptors reveals a trans-synaptic signal for presynaptic maturation. *EMBO J.* 30, 1577–1592. doi: 10.1038/emboj.2011.59

Turrigiano, G. G. (2008). The self-tuning neuron: synaptic scaling of excitatory synapses. *Cell* 135, 422–435. doi: 10.1016/j.cell.2008.10.008

Voglmaier, S. M., Kam, K., Yang, H., Fortin, D. L., Hua, Z., Nicoll, R. A., et al. (2006). Distinct endocytic pathways control the rate and extent of synaptic vesicle protein recycling. *Neuron* 51, 71–84. doi: 10.1016/j.neuron.2006.05.027

Walker, A. S., Neves, G., Grillo, F., Jackson, R. E., Rigby, M., O'Donnell, C., et al. (2017). Distance-dependent gradient in NMDAR-driven spine calcium signals along tapering dendrites. *Proc. Natl. Acad. Sci. U.S.A.* 114, E1986–E1995. doi: 10.1073/pnas.1607462114

Walmsley, B., Alvarez, F. J., and Fyffe, R. E. (1998). Diversity of structure and function at mammalian central synapses. *Trends Neurosci.* 21, 81–88. doi: 10.1016/s0166-2236(97)01170-3

Wang, H. G., Lu, F. M., Jin, I., Udo, H., Kandel, E. R., de Vente, J., et al. (2005). Presynaptic and postsynaptic roles of NO, cGK, and RhoA in long-lasting potentiation and aggregation of synaptic proteins. *Neuron* 45, 389–403. doi: 10.1016/j.neuron.2005.01.011

Wang, Y. T., and Linden, D. J. (2000). Expression of cerebellar long-term depression requires postsynaptic clathrin-mediated endocytosis. *Neuron* 25, 635–647. doi: 10.1016/s0896-6273(00)81066-1

Ward, B., McGuinness, L., Akerman, C. J., Fine, A., Bliss, T. V., and Emptage, N. J. (2006). State-dependent mechanisms of LTP expression revealed by optical quantal analysis. *Neuron* 52, 649–661. doi: 10.1016/j.neuron.2006.10.007

Watabe, A. M., Carlisle, H. J., and O'Dell, T. J. (2002). Postsynaptic induction and presynaptic expression of group 1 mGluR-dependent LTD in the hippocampal CA1 region. *J. Neurophysiol.* 87, 1395–1403. doi: 10.1152/jn.00723.2001

Watanabe, S., Rost, B. R., Camacho-Perez, M., Davis, M. W., Sohl-Kielczynski, B., Rosenmund, C., et al. (2013). Ultrafast endocytosis at mouse hippocampal synapses. *Nature* 504, 242–247. doi: 10.1038/nature12809

Waung, M. W., Pfeiffer, B. E., Nosyreva, E. D., Ronesi, J. A., and Huber, K. M. (2008). Rapid translation of Arc/Arg3.1 selectively mediates mGluR-dependent LTD through persistent increases in AMPAR endocytosis rate. *Neuron* 59, 84–97. doi: 10.1016/j.neuron.2008.05.014

Willig, K. I., Kellner, R. R., Medda, R., Hein, B., Jakobs, S., and Hell, S. W. (2006). Nanoscale resolution in GFP-based microscopy. *Nat. Methods* 3, 721–723. doi: 10.1038/nmeth922

Wilson, D. E., Whitney, D. E., Scholl, B., and Fitzpatrick, D. (2016). Orientation selectivity and the functional clustering of synaptic inputs in primary visual cortex. *Nat. Neurosci.* 19, 1003–1009. doi: 10.1038/nn.4323

Winnubst, J., Cheyne, J. E., Niculescu, D., and Lohmann, C. (2015). Spontaneous activity drives local synaptic plasticity in vivo. *Neuron* 87, 399–410. doi: 10.1016/j.neuron.2015.06.029

Xiao, M. Y., Zhou, Q., and Nicoll, R. A. (2001). Metabotropic glutamate receptor activation causes a rapid redistribution of AMPA receptors. *Neuropharmacology* 41, 664–671. doi: 10.1016/s0028-3908(01)00134-4

Xu, W., Tse, Y. C., Dobie, F. A., Baudry, M., Craig, A. M., Wong, T. P., et al. (2013). Simultaneous monitoring of presynaptic transmitter release and postsynaptic receptor trafficking reveals an enhancement of presynaptic activity in metabotropic glutamate receptor-mediated long-term depression. *J. Neurosci.* 33, 5867–5877. doi: 10.1523/JNEUROSCI.1508-12.2013

Yudowski, G. A., Puthenveedu, M. A., Leonoudakis, D., Panicker, S., Thorn, K. S., Beattie, E. C., et al. (2007). Real-time imaging of discrete exocytic events mediating surface delivery of AMPA receptors. *J. Neurosci.* 27, 11112–11121. doi: 10.1523/jneurosci.2465-07.2007

Zhang, J., Wang, Y., Chi, Z., Keuss, M. J., Pai, Y. M., Kang, H. C., et al. (2011). The AAA+ ATPase Thorase regulates AMPA receptor-dependent synaptic plasticity and behavior. *Cell* 145, 284–299. doi: 10.1016/j.cell.2011.03.016

Zhang, Y., Cudmore, R. H., Lin, D. T., Linden, D. J., and Huganir, R. L. (2015). Visualization of NMDA receptor-dependent AMPA receptor synaptic plasticity in vivo. *Nat. Neurosci.* 18, 402–407. doi: 10.1038/nn.3936

Zhou, Z., Hu, J., Passafaro, M., Xie, W., and Jia, Z. (2011). GluA2 (GluR2) regulates metabotropic glutamate receptor-dependent long-term depression through N-cadherin-dependent and cofilin-mediated actin reorganization. *J. Neurosci.* 31, 819–833. doi: 10.1523/JNEUROSCI.3869-10.2011

Zhuo, M., Small, S. A., Kandel, E. R., and Hawkins, R. D. (1993). Nitric oxide and carbon monoxide produce activity-dependent long-term synaptic enhancement in hippocampus. *Science* 260, 1946–1950. doi: 10.1126/science.8100368

Conflict of Interest: The authors declare that the research was conducted in the absence of any commercial or financial relationships that could be construed as a potential conflict of interest.

frontiers in Neural Circuits

REVIEW
published: 24 April 2020
doi: 10.3389/fncir.2020.00018

Light Up the Brain: The Application of Optogenetics in Cell-Type Specific Dissection of Mouse Brain Circuits

Candice Lee[1], Andreanne Lavoie[2,3], Jiashu Liu[2,3], Simon X. Chen[1,4,5] and Bao-hua Liu[2,3]**

[1] Department of Cellular and Molecular Medicine, University of Ottawa, Ottawa, ON, Canada, [2] Department of Biology, University of Toronto Mississauga, Mississauga, ON, Canada, [3] Department of Cell and Systems Biology, University of Toronto, Toronto, ON, Canada, [4] Brain and Mind Research Institute, University of Ottawa, Ottawa, ON, Canada, [5] Center for Neural Dynamics, University of Ottawa, Ottawa, ON, Canada

The exquisite intricacies of neural circuits are fundamental to an animal's diverse and complex repertoire of sensory and motor functions. The ability to precisely map neural circuits and to selectively manipulate neural activity is critical to understanding brain function and has, therefore been a long-standing goal for neuroscientists. The recent development of optogenetic tools, combined with transgenic mouse lines, has endowed us with unprecedented spatiotemporal precision in circuit analysis. These advances greatly expand the scope of tractable experimental investigations. Here, in the first half of the review, we will present applications of optogenetics in identifying connectivity between different local neuronal cell types and of long-range projections with both *in vitro* and *in vivo* methods. We will then discuss how these tools can be used to reveal the functional roles of these cell-type specific connections in governing sensory information processing, and learning and memory in the visual cortex, somatosensory cortex, and motor cortex. Finally, we will discuss the prospect of new optogenetic tools and how their application can further advance modern neuroscience. In summary, this review serves as a primer to exemplify how optogenetics can be used in sophisticated modern circuit analyses at the levels of synapses, cells, network connectivity and behaviors.

Keywords: optogenetics, neural connectivity, GABAergic neurons, neural circuit function, neural circuits and behavior

OPEN ACCESS

Edited by:
Edward S. Ruthazer, McGill University, Canada

Reviewed by:
Jonathan T. Ting, Allen Institute for Brain Science, United States
Antoine Adamantidis, University of Bern, Switzerland

****Correspondence:***
Simon X. Chen
schen2@uottawa.ca;
schen84@gmail.com
Bao-hua Liu
baohua.liu@utoronto.ca

Received: *30 December 2019*
Accepted: *31 March 2020*
Published: *24 April 2020*

Citation:
Lee C, Lavoie A, Liu J, Chen SX and Liu B-H (2020) Light Up the Brain: The Application of Optogenetics in Cell-Type Specific Dissection of Mouse Brain Circuits. Front. Neural Circuits 14:18. doi: 10.3389/fncir.2020.00018

INTRODUCTION

In the past decades, numerous newly developed techniques have greatly assisted in dissecting connectivity and function of the brain. However, only a handful of them have influenced and advanced modern neuroscience as heavily as optogenetics. This state-of-the-art technique utilizes light-sensitive channels or pumps, known as opsins, to manipulate the activity of neurons. In addition, when it is combined with the Cre-*Lox* recombinase system, it provides a spatiotemporally precise method to reversibly turn on and off the activity of genetically defined or projection-specific groups of neurons. In this review, we will first highlight the use of optogenetics in the investigation of neural connectivity, both within and between brain regions, and then its applications in identifying the functional roles of specific neural circuit components in behavior and physiology. Finally, we will discuss some of the limitations and future directions of optogenetics. Although most of the examples in this review come from studies of sensory and motor systems, their diverse experimental designs and underlying principles are potentially useful for advancing our understanding of the structure and function of other brain circuits.

Opsins used in optogenetics were first discovered in microbes (Soliman and Trüper, 1982; Mukohata et al., 1988) and later cloned and introduced into neurons (Boyden et al., 2005). These microbial opsins can be divided into excitatory opsins and inhibitory opsins. The most commonly used excitatory opsin is channelrhodopsin (ChR2), a cation channel that opens in the presence of blue light (∼470 nm) to depolarize neurons (Nagel et al., 2003). In contrast, inhibitory opsins, such as the chloride pump halorhodopsin (eNpHR) and the proton pump Archaerhodospin (Arch), mediate hyperpolarizing currents which impede action potentials upon yellow light illumination (∼580 nm) (Zhang et al., 2007; Chow et al., 2010). In this review, we will primarily focus on the applications of commonly used opsins, rather than covering all the different variants. However, we will introduce a few recently developed opsins in order to illustrate the diverse properties of optogenetics and its unique applications.

CONNECTIVITY

Neural circuits consist of heterogeneous cell-types receiving distinct inputs from both local and long-range sources. Dissecting the intricate connections of these neural circuits has been a long-standing challenge for neuroscientists, largely due to technical limitations in identifying and targeting specific neuronal cell-types. Although traditional methods of circuit analysis have been useful in gaining a gross understanding of macroscale and mesoscale features of brain connectivity, these techniques are limited. For example, anatomical circuit tracing with anterograde or retrograde reagents can only suggest potential innervations, without confirming the presence of functional synaptic contacts (Zeng, 2018); electron microscopy, despite its capability of identifying synapses, is labor and time intensive and cannot reveal the type or function of the synapse (Burette et al., 2015); electrical stimulation of axonal tracts, which is used to reveal functional connectivity, indiscriminately activates all fibers passing the stimulation site (Klauer et al., 1990); pairwise whole-cell recording, a gold standard for establishing connectivity, is technically challenging and time consuming and suffers from a small yield (Xue et al., 2014). Mitigating all the above issues, optogenetics, combined with the Cre-*Lox* recombinase system, provides a cell-type specific and high-throughput method for dissecting circuit connectivity.

Local Connectivity

Neural circuits are characterized by entangled connections between various types of neurons within the network, making detailed dissection of local circuit connectivity extremely difficult. Optogenetics has simplified experimental designs for analysis of local connectivity and has greatly boosted the efficiency of data collection. For example, by selectively expressing ChR2 in a specific population of neurons, one can study the connectivity from those ChR2-expressing neurons onto other non-ChR2 expressing neurons with ease and speed (Adesnik and Scanziani, 2010; Adesnik et al., 2012). In this experimental design, optogenetic stimulation replaces the electrical stimulation in paired whole-cell clamp recordings and greatly increases the yield and the chance of detecting connectivity, since multiple presynaptic neurons can be activated simultaneously by the light-evoked current (Seeman et al., 2018) and the spatiotemporal pattern of optogenetic stimulation can be flexibly readjusted (Adesnik and Scanziani, 2010; Adesnik et al., 2012). Notably, when this optogenetic method of local circuit analysis was compared to traditional pairwise patch clamp methods, both gave rise to similar connection probabilities, validating the utility of optogenetics in the study of local circuit connectivity (Seeman et al., 2018).

When combined with cell-type specific Cre mouse lines, optogenetics can also be used to study the connectivity of genetically-defined populations within local circuits. For instance, in the visual cortex, Pfeffer et al. (2013) examined the pattern of connectivity between three major subtypes of GABAergic inhibitory interneurons, parvalbumin (Pvalb), somatostatin (Sst), and vasoactive intestinal peptide (VIP) expressing interneurons (**Figure 1A**). Until recently, these different GABAergic subtypes were poorly characterized, as they are intermingled in the cerebral cortex and could not be specifically targeted with electrical or pharmacological manipulations. By expressing ChR2 in one population at a time and recording from different interneuron subtypes identified by single-cell reverse-transcription PCR, the authors were able to elucidate microcircuit motifs. They found that Pvalb interneurons preferentially inhibit pyramidal neurons and other Pvalb interneurons; Sst interneurons preferentially inhibit pyramidal neurons and all other interneuron types except themselves; and VIP interneurons preferentially inhibit Sst interneurons (Pfeffer et al., 2013). The sample sizes required to deduce connection probabilities and circuit motifs are difficult to achieve using paired recordings. But with a high-throughput optogenetic design, as the above experiment, cell-type specific connectivity analysis becomes surmountable.

Local connectivity can also be investigated between layers of the cortex. For instance, Bortone et al. (2014) used optogenetics to investigate how layer 6 (L6) excitatory neurons can regulate the strength of cortical responses throughout cortical depth. With the help of the L6 specific Cre mouse line, neurotensin receptor 1 (*NTSR1*)-Cre, they optogenetically stimulated L6 neurons and identified the recruitment of unique L6 fast-spiking interneurons with massive translaminar axons whose activation suppresses neurons across laminar layers.

Projection-Specific Connectivity

Prior to the development of optogenetics, it was practically impossible to activate only a specific group of axonal projections. Electrical stimulation of axon tracts indiscriminately activates all fibers that pass through the stimulated area, including axons originating from different brain structures and ones projecting to different areas (Schwarz et al., 2015). Therefore, electrical stimulation will activate several pathways in parallel, which complicates data interpretation. These off-target effects can now be mitigated through the use of optogenetics. Optogenetics enables specificity at several levels: the injection location of the opsin-expressing virus provides a degree of spatial specificity for

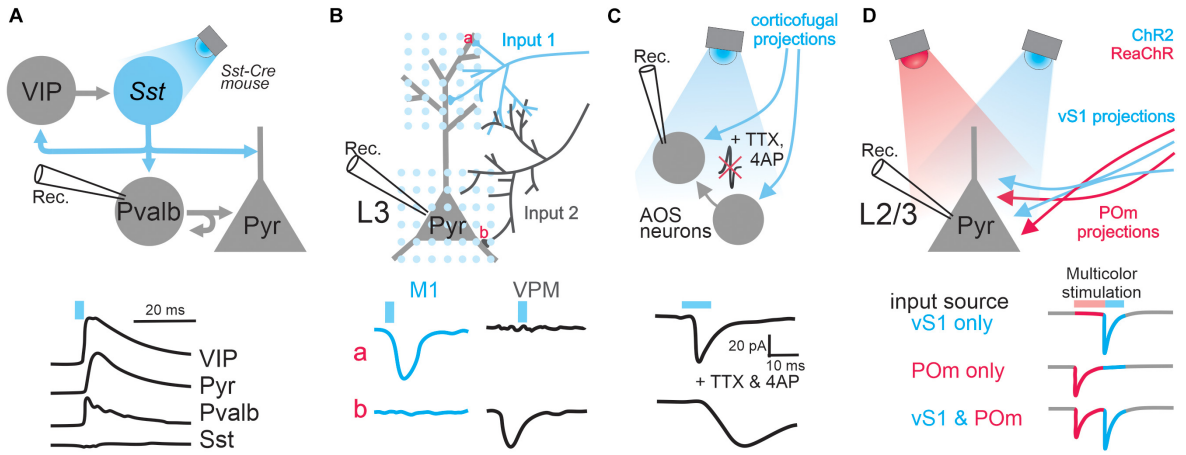

FIGURE 1 | Applications of optogenetics in the analysis of circuit connectivity. **(A)** The examination of the connection from Sst positive GABAergic interneurons to excitatory pyramidal neurons and various types of GABAergic interneurons by photo-stimulating Sst neurons expressing ChR2. Top, schematic of experimental design; bottom traces, example IPSCs received by different types of cells upon Sst activation. **(B)** Subcellular ChR2-assisted circuit mapping (sCRACM) to reveal subcellular organization of two different long-range inputs impinged onto L3 pyramidal neurons. Bottom traces, example EPSCs when stimulating M1 or VPM inputs at particular domains (a, the tuft branches; b, basal dendrites). **(C)** The examination of corticofugal innervation onto brainstem AOS neurons by pharmacologically blocking action potentials. Bottom traces: example EPSCs before and after blocking action potentials. **(D)** Dual-channel mapping to resolve two different inputs received by L2/3 pyramidal neurons. ChR2 and ReaChR are expressed in axons coming from vS1 and POm, respectively. Bottom traces, the colored segments represent the EPSC components mediated by activating POm input or vS1 input. The blue or pink bars above traces represent light stimulation.

presynaptic source; the use of the Cre-*lox* system enables cell-type specificity; and the range of the light illumination provides a final level of specificity. For example, this method was successfully applied to explore the differential connectivity of thalamocortical and corticothalamic pathways that are entwined with each other (Cruikshank et al., 2010). This approach was also applied to dissect specific basolateral amygdala projections to the central nucleus of the amygdala (Tye et al., 2011).

The power of optogenetic-based projection analysis is exemplified by a study that dissected the laminar organization of long-range callosal projections linking the barrel cortices of the two hemispheres in slice preparation (Petreanu et al., 2007). Layer 2/3 of the barrel cortex receives input from several structures such as the thalamus, other cortical areas including the contralateral barrel cortex, and local circuits (Lubke and Feldmeyer, 2007). Since the axons of these inputs are intermingled in the barrel cortex, it is impossible to electrically stimulate only axons coming from the contralateral barrel cortex, namely the callosal axons, in order to investigate the laminar organization of their innervations. Therefore to address this question, Petreanu et al. (2007) unilaterally expressed ChR2 in layer 2/3 of the barrel cortex contralateral to the recording sites (**Figure 1B**). Because ChR2 was expressed throughout the neurons, including their axons projecting to the recording site of the barrel cortex, blue light illumination over the recording sites activated ChR2-expressing axons directly and thus stimulated only callosal input. Using this so-called ChR2-assisted circuit mapping (CRACM), the authors (Petreanu et al., 2007) systematically examined the strength of long-range callosal innervation received by neurons in individual layers of the barrel cortex and found that laminar specificity of this long-range cortical innervation is identical to local innervation (Petreanu et al., 2007). This study demonstrated that the CRACM method can reliably drive projection-specific inputs without the need to preserve their tracts in slices. However, one should be cautious of some limitations of this technique: its validation requires knowledge of the anatomy and cell types of the circuits under investigation; and severed axons in slice preparation have a limited supply of synaptic vesicles, which can be quickly depleted if one uses prolonged or particularly strong stimulation (Hass and Glickfeld, 2016).

Optogenetics can also be used to locate the synaptic innervation of long-range projections tagged by the expression of ChR2. In a subsequent study, Petreanu et al. (2009) slightly modified their CRACM protocol (**Figure 1B**): a blue laser beam was restricted to a small spot and raster scanned the area containing the dendritic tree of a cortical pyramidal neuron; direct activation of presynaptic terminals was achieved by pharmacologically blocking the propagation of optogenetically evoked action potentials. By recording from a postsynaptic neuron while systematically photostimulating its inputs at different locations, one can generate a 2D map of the long-range connections, a method named subcellular ChR2-assisted circuit mapping (sCRACM). With this elegant design, Petreanu et al. examined the spatial distribution of synaptic inputs onto the dendritic arborization of layer 3 and layer 5 pyramidal neurons in the barrel cortex (Petreanu et al., 2009). They found that different inputs target different apical or basal domains of those neurons.

Establishing Polysynaptic vs. Monosynaptic Connections

Optogenetic stimulation of long-range projections can induce responses in recorded neurons via direct synaptic contacts (monosynaptic input) and/or indirectly via recurrent

connections from other neurons in the network (polysynaptic input). To establish monosynaptic connectivity, one can pair ChR2 assisted optogenetic stimulation with pharmacology. By blocking voltage-gated sodium channels with tetrodotoxin (TTX) and potassium channels with 4-Aminopyridine (4AP), action potentials and thereby polysynaptic inputs will be prevented. Consequently, any remaining light-evoked response in recorded neurons must come directly from the activation of axon terminals that express ChR2. For instance, the long-range connectivity between the visual cortex and the brainstem accessory optic nuclei (AOS) was investigated by Liu et al. (2016; **Figure 1C**). The authors expressed ChR2 in the visual cortex and then photostimulated terminals of corticofugal axons while performing whole-cell recordings from AOS neurons. By suppressing action potentials with two different cocktails of drugs, they definitively confirmed the presence of monosynaptic connections from the visual cortex to the AOS. Without optogenetics, this experiment would not be possible, as the corticofugal axons from the visual cortex to AOS do not form a single nerve bundle, which is required for effective electrical stimulation, but instead intermingle with axons of other types of inputs. A similar design was also used to examine monosynaptic connectivity from burst-firing neurons in the subiculum to the neurons in the entorhinal cortex (Wozny et al., 2018). ChR2 was selectively expressed in burst-firing neurons by injecting the Cre-dependent *ChR2* virus into the subiculum of *VGLUT2-ires-Cre* mice, where Cre exists only in burst-firing neurons. In the presence of TTX, the authors elucidated monosynaptic connections from the axons of those burst-firing subiculum neurons with slice electrophysiology.

Characterization of the Synapse

Beyond the identification of connectivity, when combined with pharmacology, optogenetics can be used to probe the properties of synapses. It was thought that dopaminergic projections might co-release glutamate and dopamine (Stuber et al., 2010). However, evidence supporting this idea came from studies where electrical stimulation was used to activate dopaminergic neurons, which could activate glutamatergic neurons in the neighborhood (Hnasko et al., 2010). The non-specific activation makes it difficult to discern whether the release of glutamate and dopamine indeed occur from the same terminal or two different termimals (Gu, 2010). To solve this issue, Tritsch et al. (2012) expressed ChR2, using the *Slc6a3-IRES-Cre* mouse line, in dopaminergic neurons to specifically activate dopaminergic neurons in the substantia nigra pars compacta (SNc) and pharmacologically isolated currents mediated by different neurostransmitters. Surprisingly, when they activated these neurons in the SNc and recorded from neurons in the dorsal striatum, they found both glutamatergic excitatory post-synaptic current and GABAergic inhibitory post-synaptic current, as well as amperometric dopamine transients. By combining cell-type specific optogenetics with pharmacology, they were able to definitively identify co-release of dopamine, glutamate and GABA (Tritsch et al., 2012). A similar method was also used to identify the co-release of both glutamate and dopamine by dopaminergic axonal terminals coming from the ventral tagmental area (VTA) to the prefrontal cortex (Perez-Lopez et al., 2018).

The ability to selectively activate specific projections using optogenetics also enables the characterization of synapses of local versus long-range neuronal populations. The VTA receives long-range inhibitory input from GABAergic neurons in the rostromedial tegmental area. Using ChR2, Polter et al. (2018) activated this inhitibitory input and observed that glycine receptor blocker, strychnine, significantly reduced the amplitude of inhibitory postsynaptic currents (IPSCs) in VTA neurons. They then added bicuculline, a $GABA_A$ receptor blocker, along with strychnine and all residual IPSCs were abolished, suggesting this inhibitory projection co-releases GABA and glycine. They also performed the same recording with ChR2 expressed in VTA GABAergic interneurons to stimulate local inhibition, but did not find co-release of glycine (Polter et al., 2018). They proceeded to perform further characterization of these two inhibitory inputs received by VTA neurons. For example, they utilized light stimulation to compare paired-pulse ratios of those two types of inhibitory synapses, demonstrating how optogenetics can be used to characterize synaptic properties of distinct neuronal populations.

Dual-Channel Mapping

A single neuron might receive multiple inputs coming from different regions, representing multiplexed streams of information transmission (Petreanu et al., 2009; Oh et al., 2014). Understanding this input convergence is a fundamental but difficult task since it requires the technical capability of individually manipulating different types of inputs. This independent control of different inputs is impossible with electrical stimulation when the axons of those inputs are intermingled. This technical challenge was solved through the use of dual-color optogenetics when Hooks et al. studied the convergence of two different intermingled inputs in the primary motor cortex (Hooks et al., 2015; **Figure 1D**). In order to achieve this, they chose two opsin variants that prefer different wavelengths of light: blue light sensitive ChR2 was used to excite axons originating from the barrel cortex and ReaChR, an opsin activated by orange light (Lin et al., 2013), to perturb input from the posterior medial thalamic nucleus. Despite the distinct optimal excitation wavelengths of the two opsins, blue light can in fact excite ReaChR as well as ChR2. Therefore, when illuminated by blue light, both pathways will be stimulated, complicating data interpretation. To solve this complication, the authors created a clever protocol that reversibly inactivates ReaChR prior to activating ChR2 (Hooks et al., 2015), allowing complete separation of the two inputs. Indeed, with whole-cell recording they found that the input from the somatosensory cortex and that from the thalamus converge on the same layer 2/3 neurons in the motor cortex. Since this optogenetic dual-channel stimulation does not require the spatial segregation of axons of different inputs – a condition demanded by electrical stimulation – this mapping method can in principle be generalized on any convergent circuit system and is especially indispensable in the case where axons of distinct origins intermingle.

In vitro slice electrophysiology is a gold standard to determine connectivity between pairs of neurons. Although care is taken to preserve the integrity of the circuit during slice preparation and to maintain similar physiological conditions to live animals during recording, some damage and cell death is inevitable, and impedes faithful quantification of neuronal connectivity. To address this issue, efforts had been made to examine connectivity in a physiologically pristine environment with the help of optogenetics. For example, Pala and Petersen (2015) performed *in vivo* whole-cell recordings from GABAergic interneurons in L2/3 of the barrel cortex to examine the connection from excitatory pyramidal neurons. To precisely measure unitary excitatory postsynaptic potentials (uEPSPs) in GABAergic interneurons, these researchers introduced plasmid DNA encoding ChR2 into a single L2/3 pyramidal cell with electroporation and elicited one action potential per stimulus with very brief light pulses. In particular, they compared the uEPSPs response between Pvalb and Sst inhibitory neurons, finding that each inhibitory population differed in the probability, time course, strength, reliability, and short-term synaptic plasticity of their response to excitatory stimulation. This finding largely agrees with previous *in vitro* results (Pala and Petersen, 2015).

FUNCTIONAL DISSECTION

Thus far, we have discussed how optogenetic strategies can aid the dissection of circuit connectivity. Beyond characterizing connectivity, optogenetics is also an extremely powerful tool when investigating the functional roles of specific neural circuits in animal behavior and physiology. *In vivo* investigations present a unique set of demands and limitations. For many years, researchers have relied on extracellular recordings to investigate neural activity *in vivo*. Although this method allows monitoring activity from large populations of neurons, the type of neuron recorded cannot be identified in most cases, limiting its applications in the study of cell-type specific functions. Optogenetic tagging provides a feasible solution to this problem. For example, Lima et al. (2009) restricted the expression of ChR2 to Pvalb interneurons in the auditory cortex and inserted a recording electrode into this cortical area. When they illuminated this area with brief pulses of blue light, short latency spikes that are precisely synchronized with the light pulse were reliably elicited in a population of neurons, distinguishing them as Pvalb interneurons expressing ChR2. These authors also used this approach to identify auditory cortical neurons projecting to the contralateral hemisphere, namely callosal projection neurons, for which a retrograde herpes simplex virus-1 (HSV-1) encoding ChR2 injected to the auditory cortex in one hemisphere was used to tag callosal projection neurons in the other hemisphere (Lima et al., 2009). These two examples demonstrate the utility of this optogenetic tagging technique for both cell-type and projection-type specific functional circuit analyses.

In addition to identifying neuron type *in vivo*, optogenetics can also be used to manipulate neuronal activity during behavior. The canonical experiment to define a neural correlate of a behavior is to activate or silence the putative correlate *in vivo* and assess whether and how the behavior is altered. For decades, the field had relied on electrical stimulation/lesions and pharmacological activation/silencing, however, these techniques of circuit manipulation have intrinsic problems. They offer little to no temporal precision, nor cell-type specificity; furthermore, lesions are permanent and can result in unpredicted plasticity and compensatory mechanisms that confound results (Whishaw, 2000; Murphy and Corbett, 2009). The advent of optogenetics enables immediately reversible manipulation and allows trial-by-trial and within-animal comparisons in a single session. The remainder of the review will examine how the use of optogenetics has enabled cell-type and projection-specific circuit dissection of visual, somatosensory and motor function *in vivo*.

Visual Cortex

Since Hubel and Weisel first discovered the fundamentals of visual processing in the primary visual cortex (Hubel and Wiesel, 1959, 1963, 1968), numerous studies have extensively examined and characterized visual processing in different model systems. These studies revealed that stimulus features such as orientation and direction are encoded in the mammalian visual cortex through tuned neural responses at both the level of single neurons and cortical columns. However, due to the prevalence of pyramidal neurons over GABAergic inhibitory neurons in the cortex, the "blind" electrophysiological recording methods used in these studies primarily characterized pyramidal neurons and could not clearly elucidate how other cell-types might contribute to this neural code.

A long-standing question in the field has been to understand how orientation selectivity emerges in the visual cortex. For many years it had been speculated that inhibition from GABAergic interneurons may shape tuning of pyramidal neurons (Sillito et al., 1980; Sato et al., 1996; Ringach et al., 2003; Liu et al., 2011), although findings have been inconclusive until recently since this hypothesis could not be directly examined before the invention of optogenetics and inhibitory neuron-specific mouse lines. Using high-speed calcium imaging or *in vivo* cell-attached recordings paired with subtype-specific optogenetic activation, Wilson et al. (2012) demonstrated that different subtypes of GABAergic interneurons indeed have distinct roles in shaping pyramidal neuron responses to visual stimuli. The authors expressed ChR2 in either Pvalb or Sst interneurons in the primary visual cortex in order to activate each subtype independently while showing the mouse oriented drifting gratings (**Figure 2A**). They also used simultaneous calcium imaging or cell-attached recordings to characterize the orientation tuning of pyramidal neurons. By comparing pyramidal neuron tuning curves with and without optogenetic activation of Sst or Pvalb interneurons, they found that Pvalb and Sst populations exert distinct computational control on the responses of pyramidal neurons. Sst interneuron activation resulted in uniform subtractive inhibition in pyramidal neurons across all directions of drifting gratings. Pvalb interneuron activation, on the other hand, led to divisive inhibition in pyramidal cells, where the effects of inhibition were strongest when the grating was at the neuron's preferred orientation. In this way, Sst interneurons sharpen

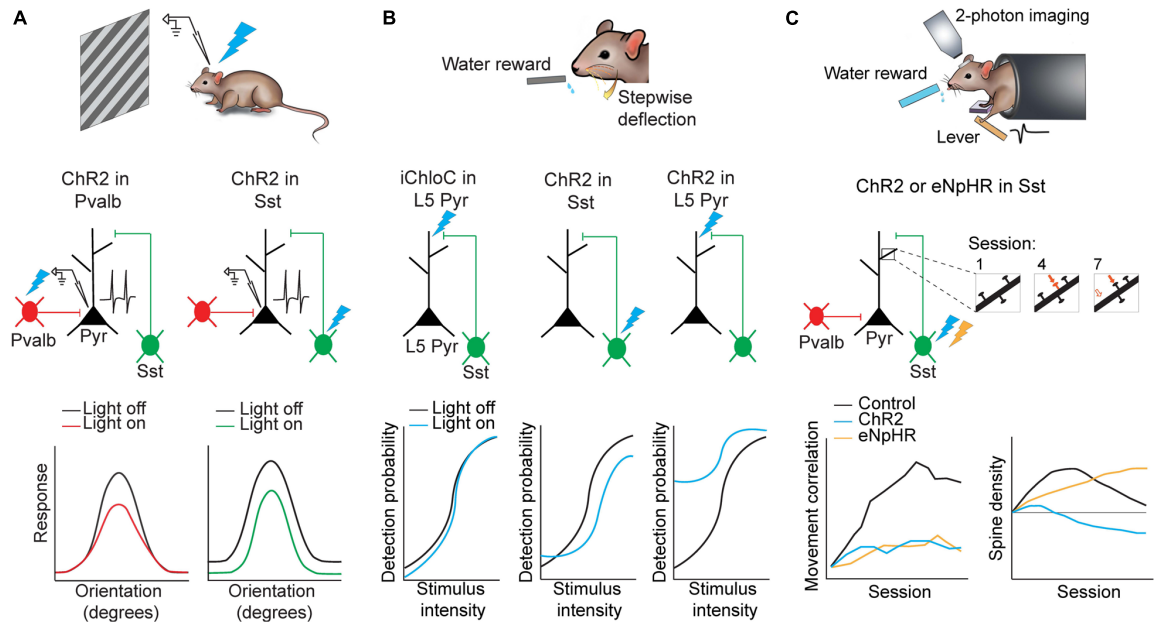

FIGURE 2 | Applications of optogenetics in the analysis of circuit functions. **(A)** Mice were presented with oriented drifting gratings while *in vivo* cell-attached recordings of putative pyramidal neurons in the visual cortex were performed. Either Pvalb or Sst interneurons were photoactivated using ChR2. Pvalb interneuron photoactivation (left) resulted in divisive inhibition of pyramidal neurons where suppression was stronger at orientations where pyramidal neuron responses were also stronger. Sst interneuron photoactivation (right) resulted in subtractive inhibition where suppression was uniform along all orientations. Adapted from Wilson et al. (2012). **(B)** Mice were trained to lick for a water reward in response to whisker stimulation of varying intensities. Perceptual detection as a function of stimulus intensity formed a sigmoid curve. When L5 pyramidal neuron apical dendrites were photoinhibited (iChloC) or when Sst interneurons were photoactivated (ChR2), the curve shifted to lower detection probabilities. When L5 pyramidal neuron apical dendrites were photoactivated (ChR2), the curve shifted to higher detection probabilities. Adapted from Takahashi et al. (2016). **(C)** Mice were trained to press a lever following an auditory cue to obtain a water reward. Two-photon imaging was performed in M1 throughout learning to track dendritic spine dynamics in pyramidal neurons. Control animals developed a stereotyped lever-press movement with learning but this was impaired if Sst interneurons were photoactivated (ChR2) or photoinhibited (eNpHR) (bottom left). Furthermore Sst interneuron photoinhibition resulted in increased stabilization of dendritic spines while photoactivation resulted in increased elimination. (bottom right). Adapted from Chen et al. (2015).

stimulus selectivity in the visual cortex, while Pvalb interneurons modulate response gain but preserve stimulus selectivity (Wilson et al., 2012). Moreover, bidirectional manipulation of Pvalb interneurons in another study using ChR2 or Arch to activate or silence Pvalb interneurons respectively, further supports the role of Pvalb interneurons in modulating the gain of pyramidal neuron responses without strongly altering tuning properties (Atallah et al., 2012). Importantly, without this cell-type specific optogenetics, it would be impossible to target or manipulate different types of neurons.

In addition to its applications in local microcircuitry, optogenetics has also been used to investigate the role of long-range inputs in visual processing. To parse the role of specific inputs to the visual cortex, Zhang et al. (2014) used a virus to express ChR2 in the cingulate cortex and then shone blue light on the visual cortex, thus exciting only the axons projecting from the cingulate cortex to the visual cortex. Activation of this top-down projection sharpened tuning of pyramidal neurons in the visual cortex and improved behavioral performance in a visual discrimination task (Zhang et al., 2014). The authors further examined which cell-types in the visual cortex might be receiving this input from the cingulate cortex. Tracing experiments revealed that Pvalb, Sst and VIP interneurons in the visual cortex all receive long-range top-down input from the cingulate cortex. Hence, to delineate subtype-specific roles in this projection, the authors again, expressed ChR2 in the cingulate cortex, but they additionally expressed the inhibitory opsin, eNpHR, in either Pvalb, Sst or VIP interneurons in the visual cortex. By patching pyramidal neurons in the visual cortex and either (i) silencing one subtype of local inhibitory neurons, (ii) activating cingulate axons, or (iii) doing both simultaneously, the effect of cingulate cortex projections on the different inhibitory populations was dissected. By taking advantage of projection-based and cell-type based optogenetics, the researchers were able to demonstrate that cingulate cortex input activates all three types of inhibitory neurons. However, Sst and Pvalb interneuron activation inhibited a broad cortical area, while VIP interneuron activation selectively enhances responses in the center region. Therefore, VIP interneurons may have a unique role of disinhibiting the center, while Sst interneurons inhibit the surround, thus explaining a facilitatory center and a suppressive surround of top-down modulation during visual processing.

Somatosensory Cortex

Optogenetics has also been employed in the somatosensory cortex to dissect the function of specific projections during perception of sensory stimuli. By expressing the inhibitory opsin Arch in the secondary motor cortex (M2), Manita et al. (2015)

used amber light in the primary somatosensory cortex (S1) to inactivate projections from M2 to S1, while simultaneously recording from S1 with either multi-unit electrodes or patch-clamp electrode. Using this preparation, the authors compared the neural response in S1 following hindpaw stimulation with and without perturbation of M2 innervation. They found that silencing M2 projections did not alter fast, putative bottom-up responses to sensory stimuli but did lead to a significant reduction in the slower second wave of top-down activity, suggesting M2 provides significant top-down modulation on S1 activity following sensory stimuli. Furthermore, using a miniature wireless LED device that can be implanted onto a freely moving, behaving mouse, they found that silencing M2 projections to S1 impaired tactile discrimination, revealing that M2 projections to S1 contribute to this type of sensory processing (Manita et al., 2015). This study demonstrates the importance of *in vivo* optogenetic approaches, since large scale network activity in response to sensory stimuli cannot be studied *in vitro*.

Another study used optogenetics in S1 to reveal the importance of dendritic activity in layer 5 (L5) pyramidal neurons in sensory perception (Takahashi et al., 2016). The authors first trained mice to lick for a reward following whisker deflection until an 80% success rate was achieved. They then constructed a psychometric curve by varying the intensity of the whisker deflection to uncover the intensity threshold for perceptual detection (**Figure 2B**). A multi-pronged approach was then employed to dissect the neural correlate of sensory perception in S1. Remarkably, using three distinct optogenetic approaches, the animal's detection probability curve was shifted bidirectionally. First, the authors used iChloC, an inhibitory chloride-conducting channelrhodopsin (Wietek et al., 2015), expressed in L5 pyramidal neurons to silence apical dendrites of L5 pyramidal neurons in behaving mice, which was achieved by calibrating light intensity *ex vivo* to target superficial layers of S1 without affecting activity at the soma of L5 pyramidal neurons located deeper in the cortex. Silencing the L5 pyramidal neuron dendrites shifted the detection probability curve to higher intensity values when compared to light-off trials, implying mice had impaired detection ability. Second, to further understand the local microcircuit, the authors expressed ChR2 in Sst interneurons, which preferentially inhibit apical dendrites of pyramidal neurons. Activating Sst interneurons also significantly shifted the detection probability to higher intensities. Finally, activation of ChR2 expressed in L5 pyramidal neurons shifted the detection probability to significantly lower detection probabilities and caused a substantial increase in false detection rates. The use of optogenetics enables a reversible approach for within animal and within session comparisons between light on and light off trials.

Motor Cortex

The motor cortex is unique among primary cortical areas in that its primary function is to activate muscles and execute movements. Inactivation techniques such as pharmacological inactivation or lesions lack the temporal resolution needed to dissect circuit contributions to specific aspects or components of a movement, such as an arm movement versus digit movement in a reaching task. Additionally, motor cortex lesions impair movement but do not result in the complete loss of movement (Castro, 1972; Alaverdashvili and Whishaw, 2008) due to compensatory mechanisms that change motor function over time (Whishaw, 2000), further obscuring motor cortex functions under normal conditions.

The ultra-fine temporal precision of optogenetics makes it an ideal tool for addressing these open questions regarding the motor cortex. In recent years, the use of optogenetics in the motor cortex has elicited a range of results, some of which do not support previous findings in lesion studies, further demonstrating how lesion and pharmacological studies can be limiting when probing complex systems conveying multiplexed information. To test the role of the motor cortex in learned behaviors, Guo et al. (2015) used a transgenic mouse line expressing ChR2 in all GABAergic neurons and trained head-fixed mice on a forelimb pellet reaching task until the mice achieved expert level. Following training, they used optogenetic activation of GABAergic inhibitory neurons to silence the central forelimb area of the motor cortex. Remarkably, they demonstrated that silencing the motor cortex before movement blocked the initiation of reaching, while silencing the same area following movement initiation caused the mouse to pause with its limb protracted. The other limbs and any untrained movements such as grooming were unaffected. In fact, turning off the motor cortex and then releasing the inhibition was sufficient to initiate reaching movement outside of trials when there was no task-related cue or food reward present, indicating that the release of inhibition could trigger the full activation sequence for the trained reach movement. Previous lesion studies have demonstrated impairments in behaviors but failed to reveal such a robust effect (Castro, 1972; Alaverdashvili and Whishaw, 2008). This can perhaps be explained by compensatory mechanisms that can contribute to recovery of movement when the motor cortex malfunctions for long periods of time (Murphy and Corbett, 2009), demonstrating the advantage of fast and reversible optogenetics.

Furthermore, learning a new movement has been shown to be associated with the emergence of a reproducible neuronal activation pattern in the motor cortex that is specific to the learned movement (Peters et al., 2014). Subcellularly, motor learning also induces the addition and selective elimination of dendritic spines on pyramidal neurons to reorganize synaptic connections in the motor cortex (Xu et al., 2009; Peters et al., 2014; Chen et al., 2015). However, until recently, the role of GABAergic interneurons in motor learning was not clear. Using a combination of two-photon imaging and optogenetics, Chen et al. (2015) demonstrated that Pvalb and Sst interneurons have distinct roles in motor learning (**Figure 2C**). The authors trained mice on a cued forelimb lever press task. Mice demonstrated increased success rate and highly correlated, stereotyped press movements over the course of training, hallmarks of learning. The authors then used ChR2 or eNpHR to activate or inhibit Sst interneurons respectively during each session throughout learning, while assessing learning-induced spine reorganization in pyramidal neurons in the motor cortex. Activation of Sst interneurons during motor learning led to increased elimination

of newly-formed spines, thus abolishing learning-induced spine reorganization. In contrast, inhibiting Sst interneurons led to decreased elimination of newly-formed spines and hyper-stabilized the spines, thus disrupting the reorganization process. Both optogenetic activation or inhibition of Sst interneurons impaired learning and impaired the ability to form stereotyped press movements across trials. Lastly, when Sst interneurons were manipulated during the task in mice that had already been trained, the movement was unaffected, indicating that the activity of Sst interneurons may be involved in regulating structural remodeling in pyramidal neurons only during motor learning and is, therefore, most critical for the acquisition of motor memories but not the execution of previously learned movements (Chen et al., 2015).

The contribution of long-range input to motor function has also been examined using optogenetics. To understand the role of thalamus and the anterior motor lateral area (ALM), two main sources of inputs to the primary motor cortex, in movement, Guo et al. (2017), utilized potent circuit silencing strategies that activate GABAergic inhibitory neurons innervating those two brain regions. The authors used ChR2 to optogenetically stimulate GABAergic axonal terminals coming from the thalamic reticular nucleus to remove the contribution from thalamic input or, they optogenetically activated inhibitory interneurons in ALM to examine the contribution from ALM. Along with silencing either thalamic activity or ALM activity, they also conducted simultaneous multi-unit recordings in ALM or thalamus while mice performed a lick – no lick task. The task made use of a delay period between the go cue and the movement, which allowed for the assessment of preparatory activity in these regions preceding movement. Intriguingly, they found that silencing thalamus during the delay period almost entirely abolished ALM spiking. Similarly, silencing ALM strongly reduced thalamic spiking. This suggests that ALM and thalamus are connected in a recurrent loop resulting in persistent spiking. Lastly, silencing either area significantly impaired the mice's performance in the task when contralateral movements were required but ipsilateral movements were unaffected (Guo et al., 2017), demonstrating that this loop is critical for movement preparation. Optogenetics is essential when dissecting movements that operate on millisecond to second timescales, as this type of detailed movement deconstruction and delineation is not possible with slower approaches such as pharmacology or DREADDs.

Optogenetic activation of GABAergic inhibitory neurons in the visual cortex or in the thalamic reticular nucleus has also been used to shut down local recurrent excitation or long-range thalamocortical excitation respectively, in order to elucidate their contribution to cortical visual processing (Li et al., 2013; Lien and Scanziani, 2013; Reinhold et al., 2015).

OPTOGENETICS IN DIVERSE ANIMAL MODELS

This review has primarily focused on the use of optogenetics in mice because of the extensive availability of transgenic mouse lines that permit cell-type specific circuit dissection. However, it is important to note that optogenetics can also be used in other animal models. In particular, rats present a desirable animal model, because they can learn more complex tasks, and because their larger size, relative to mice, enables them to tolerate implants more easily. Recently, more and more transgenic rat lines have become available, which makes the aforementioned cell-type specific experimental designs feasible for this animal model. For example, Witten et al. (2011) used *Tyrosine hydroxylase (Th):Cre* transgenic rats to drive the expression of the Cre recombinase under the dopaminergic specific *Th* promoter. By injecting Cre-dependent *ChR2* virus in the VTA, the expression of ChR2 was restricted to dopaminergic neurons in the VTA. With this model, they investigated cell-type specific circuitry driving positive reinforcement during intracranial self-stimulation (ICSS). During a freely moving ICSS task, optogenetic stimulation of dopaminergic neurons in the VTA occurred when rats nosepoked one of the two identical ports, but not when they poked the other one. This simple optogenetic activation of dopaminergic system during behavior strongly biased rats to the port associated with optogenetic stimulation, but not the other port, thus demonstrating that activation of dopaminergic cells in the VTA is sufficient to drive ICSS.

Optogenetics has also been used in rats to investigate projection-specific contributions to motivation. For instance, Warden et al. (2012) targeted medial prefrontal cortex (mPFC) neurons that project to the dorsal raphe nucleus (DRN) by virally expressing ChR2 in mPFC neurons and photostimulating their axons in the DRN. The authors used a protocol of alternating 2 min light-on epochs followed by 2 min light-off epochs for five cycles during the forced swim test, allowing multiple within session comparisons. They observed a robust increase in kick frequency during light-on epochs relative to light-off epochs. In contrast, when they activated the mPFC-lateral habenula pathway in the same way, kick frequency during light-on epochs was robustly decreased. These projection-specific, opposing behavioral phenomena were not seen when all mPFC neurons were non-selectively photostimulated. These results demonstrate that optogenetic activation of projection-specific pathways arising from the same brain area can result in opposite behavioral effects and further corroborate the need for circuit specific perturbation in behavioral studies.

Optogenetics has also been used in higher mammals, such as Rhesus monkeys, enabling the causal study of circuits involved in complex behaviors and neurological diseases (Han et al., 2009; Jazayeri et al., 2012; Shewcraft et al., 2020). In the first study that validated the use of optogenetics in non-human primates, Han et al. used lentivirus to express ChR2 in the frontal cortex of macaques, and established that viral expression of opsins is safe and can support long-term experiments (Han et al., 2009). Even though there is a lack of genetically modified Cre-expressing monkey lines, cell-type specific promoters can be used to target unique neuronal populations. For instance, Stauffer et al. (2016) used virus with a dopaminergic cell-specific *Th* promoter to express Cre recombinase alongside a cre-dependent *ChR2* virus, thus restricting ChR2 expression to

dopaminergic neurons in the midbrain. They then demonstrated that the activation of this dopaminergic population promotes reward-related learning at both cellular and behavioral levels. Similarly, the Purkinje cell specific promotor *L7/Pcp2* has been used to selectively drive ChR2 expression in Purkinje cells in the cerebellum occulomotor vermis (El-Shamayleh et al., 2017), and the *CaMKII* promotor has been used to express ChR2 in pyramidal neurons in the frontal cortex (Han et al., 2009). In addition to cell-type specificity, projection-specific optogenetics has also been achieved in Macaque monkeys. Galvan et al. expressed ChR2 in the primary motor cortex of macaque monkeys and optogenetically activated the terminals of the corticothalamic projection from the motor cortex, revealing that this projection pathway plays a modulatory role in the thalamus (Galvan et al., 2016). These studies in non-human primates demonstrate the wider applicability of optogenetics for circuit and behavior analysis with both projection (Inoue et al., 2015; Galvan et al., 2016) and cell-type specificity (Han et al., 2009; Jazayeri et al., 2012; Klein et al., 2016; Nakamichi et al., 2019).

FUTURE DIRECTIONS

New Variants of Opsins

Over the past decade, several newly developed variants of opsins have enabled the use of optogenetics in investigations that were not technically possible with earlier variants. Although this review is not intended to provide a comprehensive overview of different opsins, this section will highlight some experimental designs that leveraged unique properties of engineered opsin variants.

When first introduced into neurons, ChR2 was demonstrated to drive spike trains ranging from 5 to 30 Hz (Boyden et al., 2005). However many neurons are capable of firing far beyond 30 Hz (O'Connor et al., 2010). High-speed opsins are indispensable to investigate fast spiking neuron types such as Pvalb interneurons (Chrobak and Buzsaki, 1998; Hajos et al., 2004); hence, oChIEF was developed in 2009 (Lin et al., 2009), ChETA developed in 2010 (Gunaydin et al., 2010), and Chronos developed in 2014 (Klapoetke et al., 2014). These ChR2 variants can reliably evoke ultra fast spiking in neurons, up to 100 Hz.

One advantage of these ultra fast opsins was demonstrated when studying the importance of long-term potentiation (LTP) for memory formation (Bliss and Lomo, 1973). Although this hypothesis had existed for many years, it was difficult to test it directly *in vivo*, because of the lack of tools to induce LTP in live animals. A classical LTP protocol for slice preperation involves high-frequency tetanic electrical stimulation (a train of brief pulses at 50–100 Hz) of the tract of presynaptic axons, which is not feasible for *in vivo* experiments. However, the ultra fast opsins which support reliable optogentic stimulation up to 100 Hz provide an opportunity. Nabavi et al. (2014) used AAV to express oChIEF in the medial geniculate nucleus and the auditory cortex of rats and implanted a cannula in the lateral amygdala to deliver light to the oChIEF expressing axon terminals originating from the medial geniculate nucleus and auditory cortex. The authors then delivered five trains of brief light pulses at 100 Hz and used *in vivo* field recordings to confirm the induction of LTP. When this optical stimulus used to induce LTP, was paired with a foot shock in a cued fear conditioning paradigm, the rats performed the conditioned fear response. In contrast, when the optical stimulus and the shock were unpaired, the rats did not perform the conditioned fear response, suggesting they had not formed the cued-fear memory. In this experiment, the reliable high frequency optogenetic stimulation of axon terminals depends on several desirable properties of oChIEF, such as fast opening and closing rates, high light sensitivity and the low channel inactivation (Lin, 2011; Hass and Glickfeld, 2016).

In addition to ChR2 variants with faster kinetics, step function opsin (SFO) (Berndt et al., 2009) and stabilized step function opsin (SSFO) (Yizhar et al., 2011) have been engineered to produce very slow kinetics, which confer a unique set of experimental advantages. These opsins have mutations at the C128 position in ChR2 that substantially extend the period of activation. They are also capable of bistable switching, in which they can be activated with blue light to produce prolonged depolarization that can be rapidly terminated with amber light. While SFO can support stable depolarization for minutes (Berndt et al., 2009), SSFO mediated depolarization is stable over the 30 min time scale (Yizhar et al., 2011). This unique property makes SSFO useful for *in vivo* investigations since complex animal behaviors typically occur on the timescale of minutes. In addition, SSFO can also be useful when optogenetics is paired with two-photon calcium imaging, since it solves the issue of visible light from optogentic stimulation interferring with GCaMP based calcium imaging. For example, Makino and Komiyama (2015) used a virus carrying a Cre-dependent *SSFO* gene to conditionally express SSFO in Sst inhibitory neurons of *Sst-Cre* mice, and expressed GCaMP6f in pyramidal neurons. With this design, the researchers optogenetically turned Sst interneuron activity on (using blue light) and off (using amber light), while performing calcium imaging of mostly pyramidal neurons. The use of SSFO in this study enabled cell-type specific optogenetic manipulation throughout the entire course of a complex behavioral task with simultaneous calcium imaging. This study also exemplifies the flexibility of optogenetics, enabling within animal and within session controls.

The level of control achieved through optogenetics can be extended even further using the opto-XR family of opsins. This family of opsins was engineered by replacing the intracellular loops of rhodopsin with those from specific G-protein coupled receptors, allowing photoactivation with light to initiate intracellular signaling pathways (Airan et al., 2009). One example is opto-α1-adrenergic receptor (AR), which when photostimulated, led to a significant increase in IP_3 signaling in HEK cells. When this chimeric opsin-receptor was expressed in the nucleus accumbens of mice and photoactivated during a place preference task, mice spent significantly more time in the conditioned area in the subsequent session than control mice without the optical stimulation, indicating that opto-α1-AR can alter cell signaling *in vivo* and affect animal behavior (Airan et al., 2009). This experiment demonstrates the applicability of

optogenetics, beyond ionic manipulations, to study effects of metabotropic cell signaling on behavior.

Single Cell Optogenetics

Neurons in the cortex, even of the same cell type, fire at different times, and this asynchronous firing across space and time is essential for information coding (Goard and Dan, 2009). However, so far, most of the optogenetic applications took reductionist approaches in which all opsin-expressing neurons or axonal projections were activated or inhibited at the same time by uniform light illumination. Because these approaches cannot recapitulate the natural firing patterns of groups of neurons, they limit the understanding of the physiology of neural circuits. Moreover, the dependence of cell-type specific optogenetics on Cre mouse lines limits the freedom of experimental designs. To solve these issues, new techniques which enable selective manipulation of arbitrarily defined neuronal ensembles at a single-cell spatial resolution and at a sub-millisecond temporal resolution are required. In recent years, advances in two directions have been improving fine spatiotemporal optogenetic control: single-cell photostimulation and new opsins of fast kinetics, high conductance, and subcellularly restricted expression. In an early attempt to achieve photostimulation at a single-cell resolution, a small, focal laser spot of blue light was used to raster scan brain tissue in which some neurons expressed ChR2. (Wang et al., 2007). However, this one-photon excitation method suffers from low penetration depth, lack of optical sectioning, and degraded lateral resolution due to light scattering, resulting in unwanted activation of the axons of passage and out of focus somata. To mitigate those issues, the non-linearity of two-photon excitation was used (Rickgauer and Tank, 2009; Prakash et al., 2012). However, traditional two-photon excitation methods are limited by poor temporal precision, as a focused infrared laser must raster scan the surface of opsin-expressing somata to induce enough photocurrent. To surmount the limitation of slow scanning, two parallel illumination methods were invented – computer generated holography (CGH) (Begue et al., 2013; Dal Maschio et al., 2017; Forster et al., 2017; Ronzitti et al., 2017) and generalized phase contrast (GPC) (Papagiakoumou et al., 2010). These techniques rely on phase modulation to make a pattern of infrared illumination precisely matching the three-dimensional profiles of neurons of interest, therefore allowing simultaneous two-photon activation of multiple neuronal targets at once (Gerchberg and Saxton, 1972; Sinclair et al., 2004). When combined with temporal focusing, these parallel illumination methods can reach micrometer resolution even at a depth of hundreds of micrometers in scattering brain tissues. Advances in these state-of-the-art approaches provides a new avenue to systematically map the connectivity of neuronal networks at a cellular resolution.

In addition to the development of single-cell photostimulation, the engineering of new opsins also contributes to single-cell optogenetics. For example, neurons in most of the brain areas are surrounded by numerous neurites of nearby cells, and most methods for expressing opsins will lead to opsin expression in neighboring neurites as well. As a consequence, even with single-cell photostimulation methods mentioned above, the stimulation light will inevitably stimulate dendrites and axons which pass by the targeted neurons. To address this issue, a high-performance somatic opsin, soCoChR, was generated (Shemesh et al., 2017). The expression of the high-photocurrent channelrhodopsin (CoChR) was restricted primarily to the cell bodies of cortical neurons by fusing a short amino-terminal segment of the kainate receptor KA2 subunit to this opsin. With the help of two-photon CGH, soCoChR allows the activation of individual neurons at cellular resolution with sub-millisecond temporal precision. Future work employing both single-cell stimulation and soCoChR will enable more reliable mapping of neuronal connectivity in intact brain circuits.

Moreover, sub-millisecond optogenetics can also be helpful for exploring the connectivity of fast-spiking neurons, such as interneurons (Hajos et al., 2004). Chronos is a fast opsin that can be combined with two-photon parallel illumination to drive spiking up to 100 Hz with sub-millisecond onset precision and cellular resolution. The high spatiotemporal resolution and high rate of optogenetic stimulation exemplified in the above will be essential for faithfully replicating the asynchronous activity in neuronal networks *in vivo*.

LIMITATIONS AND ALTERNATIVE STRATEGIES

Optogenetics is, however, not without limitations. In fact, in some circumstances, it can result in paradoxical and undesirable effects. Inhibitory chloride pumps such as eNpHR can lead to a change in inhibitory signaling that outlasts the photostimulation (Raimondo et al., 2012; Mahn et al., 2016). Long duration photoinhibition through chloride pumps can alter the chloride ion gradient and therefore change $GABA_A$ receptor reversal potential, resulting in synaptically evoked spiking following photoinhibition (Raimondo et al., 2012). A similar phenomenon can be seen when using light-driven outward proton pumps such as Arch. Prolonged eNpHR activation overwhelms the neuron's mechanisms for chloride homeostasis (Raimondo et al., 2012), while prolonged Arch activation can overwhelm the cell's mechanisms for pH regulation (Mahn et al., 2016). These effects can be mitigated through the use of a pulsing or sinusoidal light stimulus instead of a constant stimulus, by minimizing the intensity and duration of photoinhibition (Raimondo et al., 2012) and by using ramp termination of photostimulation instead of step termination (Mahn et al., 2016).

Another option for photoinhibition is to use ChR2 to activate GABAergic inhibitory neurons. Although this method is more effective than direct photoinhibition by the proton pumps Arch and Jaws (Chuong et al., 2014; Li et al., 2019), it also has its own limitations. For instance, optogenetically activating all GABAergic inhibitory neurons in the cortex will drastically shut down the activity of all principal cells, including various types of cortical projection neurons (e.g., corticocortico, corticothalamic, and corticofugal projections) (Babl et al., 2019). This non-specifical circuit manipulation introduces a confounding factor: we cannot determine if experimental effects result from the direct suppression of the specific pathway of interest or the

concurrent suppression of multiple output pathways (Babl et al., 2019). Furthermore, another confounding factor is the rebound activity caused by abruptly terminating the photostimulation of inhibitory neurons. Those synchronized spiking events cross a large number of neurons and can last several seconds, disrupting the functionality of cortical circuits. Therefore, caution should be used when choosing an opsin and when designing a photostimulation method (Liu et al., 2016; Guo et al., 2017).

Moreover, the methods of expression should also be carefully considered. Transgenic lines result in global opsin expression, which leads to at least two complications: first, photostimulation may activate neurons that are located outside of the target region but have axons passing through this region; second, one-photon photostimulation, which has poor spatial resolution, may activate opsin expressing neurons which neighbor the target region. While the use of virus can resolve the issues associated with transgenenic lines by spatially confining opsin expression, some caveats associated with this expression method should also be considered. First, Jackman et al. (2014) reported artificial synaptic depression in hippocampal neurons when ChR2 was expressed using specific AAV virus serotypes, including AAV1, AAV5, and AAV8. But this artifact did not occur when ChR2 was expressed transgenically or with AVV9. Second, some types of viral expression systems are cytotoxic. For instance, the expression of target genes mediated by rabies virus leads to rapid cell death starting 1 week after viral injection (Wickersham et al., 2007), preventing its use for long-term functional experiments. Third, virus-based expression can also be limited by viral tropism in certain brain regions. For example, canine adenovirus and herpes simplex virus 1, two retrograde viruses, labeled largely non-overlapping populations of the basolateral amygdala that project into the prefrontal cortex (Senn et al., 2014). Therefore, one should carefully design experiments, considering the trade-off between transgenic lines and viral methods.

Furthermore, *in vivo* optogenetics is heavily limited by the level of invasiveness. Implementing optogenetics *in vivo* requires either a cranial window for superficial brain areas or an optical fiber implant to deliver light. For deep brain regions, implants also require aspiration of tissue superficial to the target site. Chemogenetics is therefore an appealing alternative as it is effective, minimally invasive, reversible and highly specific. Chemogenetic approaches include Pharmacologically Selective Actuator Modules (PSAMs) and their corresponding Pharmacologically Selective Effector Modules (PSEMs) (Magnus et al., 2011). PSAMs are a toolbox of engineered chimeric ligand-gated ion channels that selectively bind the corresponding, engineered PSEM. For example, combining a pharmacologically selective ion binding domain with the serotonin 3a receptor or with glycine receptors, results in a chimeric channel that selectively binds PSEM and gates depolarizing cation current or hyperpolarizing chloride current respectively. These channels can be expressed *in vivo* and PSEM can be delivered through an intraperitoneal (i.p.) injection (Magnus et al., 2011). Designer Receptors Exclusively Activated by Designer Drugs (DREADDs) are another common chemogenetic toolbox that utilize engineered G-protein coupled receptors to regulate neuronal activity. Two of the most commonly used DREADDs are hM3Dq, an engineered Gq-coupled receptor and hM4di, an engineered Gi-coupled receptor (Armbruster et al., 2007). hM3Dq and hM4Di, which effectively mediate neuronal activation or silencing, respectively, when exposed to their pharmacologically inert ligand, clozapine-N-oxide (CNO) (Armbruster et al., 2007; Alexander et al., 2009; Zhu et al., 2014). For *in vivo* experiments, CNO can be delivered via an i.p. injection to perturb the activity of all neurons which express DREADDs. Alternatively, when DREADDs are expressed in specific populations of projection neurons and CNO is be locally infused in a post-synaptic region, projection-specific activation (Vazey and Aston-Jones, 2014) or silencing (Mahler et al., 2014; Stachniak et al., 2014; Zhu et al., 2016) of axon terminals can be achieved. However, it is worth noting that CNO has dose-dependent side effects: excessive CNO is converted to clozapine and could alter animal behavior independent of DREADDs (Manvich et al., 2018). These side effects can be reduced by using an appropriate dosage of CNO. Overall, chemogenetics offers many of the same advantages as optogenetics but has the additional advantage of being minimally-invasive, making it an ideal technique for targeting deep brain structures. When combined with an intersectional approach, chemogenetics can also be used for cell-type and projection-specific dissection. Chemogenetics however, lacks the fast kinetics of optogenetics, therefore limiting its applications in reversible circuit manipulation.

Other less prevalent solutions to the invasiveness of optogenetics also exist. Transcranial near-infrared optogenetics utilizes synthesized Lanthanide-doped upconversion nanoparticles (UCNPs), which convert near infrared photons into high energy visible light sufficient to activate opsins (Chen et al., 2018). For example, the authors expressed ChR2 in the VTA, and injected UCNPs into the VTA. Afterward, they delivered near infrared light outside of the skull, which was sufficient to evoke firing in ChR2 expressing neurons in the VTA (Chen et al., 2018). Additionally, magnetic manipulation of neural activity, dubbed Magneto2.0 (Wheeler et al., 2016), also offers a non-invasive solution; however, it remains unclear whether this approach can reliably manipulate neuronal circuits in various brain structures, as conventional optogenetic methods have (Meister, 2016; Kole et al., 2019; Wang et al., 2019; Xu et al., 2019). In conclusion, experimentalists now have numerous techniques at their finger tips for flexible manipulations of neuron activity both *in vitro* and *in vivo*. Among these techniques optogenetics provides numerous powerful advantages for modern circuit dissection.

AUTHOR CONTRIBUTIONS

All authors contributed to writing the review.

FUNDING

This work was supported by grants from Natural Sciences and Engineering Research Council of Canada (NSERC).

REFERENCES

Adesnik, H., Bruns, W., Taniguchi, H., Huang, Z. J., and Scanziani, M. (2012). A neural circuit for spatial summation in visual cortex. *Nature* 490, 226–231. doi: 10.1038/nature11526

Adesnik, H., and Scanziani, M. (2010). Lateral competition for cortical space by layer-specific horizontal circuits. *Nature* 464, 1155–1160. doi: 10.1038/nature08935

Airan, R. D., Thompson, K. R., Fenno, L. E., Bernstein, H., and Deisseroth, K. (2009). Temporally precise in vivo control of intracellular signalling. *Nature* 458, 1025–1029. doi: 10.1038/nature07926

Alaverdashvili, M., and Whishaw, I. Q. (2008). Motor cortex stroke impairs individual digit movement in skilled reaching by the rat. *Eur. J. Neurosci.* 28, 311–322. doi: 10.1111/j.1460-9568.2008.06315.x

Alexander, G. M., Rogan, S. C., Abbas, A. I., Armbruster, B. N., Pei, Y., Allen, J. A., et al. (2009). Remote control of neuronal activity in transgenic mice expressing evolved G protein-coupled receptors. *Neuron* 63, 27–39. doi: 10.1016/j.neuron.2009.06.014

Armbruster, B. N., Li, X., Pausch, M. H., Herlitze, S., and Roth, B. L. (2007). Evolving the lock to fit the key to create a family of G protein-coupled receptors potently activated by an inert ligand. *Proc. Natl. Acad. Sci. U.S.A.* 104, 5163–5168. doi: 10.1073/pnas.0700293104

Atallah, B. V., Bruns, W., Carandini, M., and Scanziani, M. (2012). Parvalbumin-expressing interneurons linearly transform cortical responses to visual stimuli. *Neuron* 73, 159–170. doi: 10.1016/j.neuron.2011.12.013

Babl, S. S., Rummell, B. P., and Sigurdsson, T. (2019). The spatial extent of optogenetic silencing in transgenic mice expressing channelrhodopsin in inhibitory interneurons. *Cell Rep.* 29, 1381–1384.e4. doi: 10.1016/j.celrep.2019.09.049

Begue, A., Papagiakoumou, E., Leshem, B., Conti, R., Enke, L., Oron, D., et al. (2013). Two-photon excitation in scattering media by spatiotemporally shaped beams and their application in optogenetic stimulation. *Biomed. Opt. Exp.* 4, 2869–2879. doi: 10.1364/BOE.4.002869

Berndt, A., Yizhar, O., Gunaydin, L. A., Hegemann, P., and Deisseroth, K. (2009). Bi-stable neural state switches. *Nat. Neurosci.* 12, 229–234. doi: 10.1038/nn.2247

Bliss, T. V., and Lomo, T. (1973). Long-lasting potentiation of synaptic transmission in the dentate area of the anaesthetized rabbit following stimulation of the perforant path. *J. Physiol.* 232, 331–356. doi: 10.1113/jphysiol.1973.sp010273

Bortone, D. S., Olsen, S. R., and Scanziani, M. (2014). Translaminar inhibitory cells recruited by layer 6 corticothalamic neurons suppress visual cortex. *Neuron* 82, 474–485. doi: 10.1016/j.neuron.2014.02.021

Boyden, E. S., Zhang, F., Bamberg, E., Nagel, G., and Deisseroth, K. (2005). Millisecond-timescale, genetically targeted optical control of neural activity. *Nat. Neurosci.* 8, 1263–1268. doi: 10.1038/nn1525

Burette, A., Collman, F., Micheva, K. D., Smith, S. J., and Weinberg, R. J. (2015). Knowing a synapse when you see one. *Front. Neuroanat.* 9:100. doi: 10.3389/fnana.2015.00100

Castro, A. J. (1972). The effects of cortical ablations on tongue usage in the rat. *Brain Res.* 45, 251–253. doi: 10.1016/0006-8993(72)90233-8

Chen, S., Weitemier, A. Z., Zeng, X., He, L., Wang, X., Tao, Y., et al. (2018). Near-infrared deep brain stimulation via upconversion nanoparticle-mediated optogenetics. *Science* 359, 679–684. doi: 10.1126/science.aaq1144

Chen, S. X., Kim, A. N., Peters, A. J., and Komiyama, T. (2015). Subtype-specific plasticity of inhibitory circuits in motor cortex during motor learning. *Nat. Neurosci.* 18, 1109–1115. doi: 10.1038/nn.4049

Chow, B. Y., Han, X., Dobry, A. S., Qian, X., Chuong, A. S., Li, M., et al. (2010). High-performance genetically targetable optical neural silencing by light-driven proton pumps. *Nature* 463, 98–102. doi: 10.1038/nature08652

Chrobak, J. J., and Buzsaki, G. (1998). Gamma oscillations in the entorhinal cortex of the freely behaving rat. *J. Neurosci.* 18, 388–398. doi: 10.1523/jneurosci.18-01-00388.1998

Chuong, A. S., Miri, M. L., Busskamp, V., Matthews, G. A., Acker, L. C., Sorensen, A. T., et al. (2014). Noninvasive optical inhibition with a red-shifted microbial rhodopsin. *Nat. Neurosci.* 17, 1123–1129. doi: 10.1038/nn.3752

Cruikshank, S. J., Urabe, H., Nurmikko, A. V., and Connors, B. W. (2010). Pathway-specific feedforward circuits between thalamus and neocortex revealed by selective optical stimulation of axons. *Neuron* 65, 230–245. doi: 10.1016/j.neuron.2009.12.025

Dal Maschio, M., Donovan, J. C., Helmbrecht, T. O., and Baier, H. (2017). Linking neurons to network function and behavior by two-photon holographic optogenetics and volumetric imaging. *Neuron* 94, 774–789.e5. doi: 10.1016/j.neuron.2017.04.034

El-Shamayleh, Y., Kojima, Y., Soetedjo, R., and Horwitz, G. D. (2017). Selective optogenetic control of purkinje cells in monkey cerebellum. *Neuron* 95, 51–62.e4. doi: 10.1016/j.neuron.2017.06.002

Forster, D., Dal Maschio, M., Laurell, E., and Baier, H. (2017). An optogenetic toolbox for unbiased discovery of functionally connected cells in neural circuits. *Nat. Commun.* 8:116. doi: 10.1038/s41467-017-00160-z

Galvan, A., Hu, X., Smith, Y., and Wichmann, T. (2016). Effects of optogenetic activation of corticothalamic terminals in the motor thalamus of awake monkeys. *J. Neurosci.* 36, 3519–3530. doi: 10.1523/JNEUROSCI.4363-15.2016

Gerchberg, R., and Saxton, W. (1972). A practical algorithm for the determination of phase from image and diffraction plane pictures. *Optik* 35, 237–246.

Goard, M., and Dan, Y. (2009). Basal forebrain activation enhances cortical coding of natural scenes. *Nat. Neurosci.* 12, 1444–1449. doi: 10.1038/nn.2402

Gu, X. L. (2010). Deciphering the corelease of glutamate from dopaminergic terminals derived from the ventral tegmental area. *J. Neurosci.* 30, 13549–13551. doi: 10.1523/JNEUROSCI.3802-10.2010

Gunaydin, L. A., Yizhar, O., Berndt, A., Sohal, V. S., Deisseroth, K., and Hegemann, P. (2010). Ultrafast optogenetic control. *Nat. Neurosci.* 13, 387–392. doi: 10.1038/nn.2495

Guo, J. Z., Graves, A. R., Guo, W. W., Zheng, J., Lee, A., Rodríguez-González, J., et al. (2015). Cortex commands the performance of skilled movement. *Elife* 4:e10774.

Guo, Z. V., Inagaki, H. K., Daie, K., Druckmann, S., Gerfen, C. R., and Svoboda, K. (2017). Maintenance of persistent activity in a frontal thalamocortical loop. *Nature* 545, 181–186. doi: 10.1038/nature22324

Hajos, N., Palhalmi, J., Mann, E. O., Nemeth, B., Paulsen, O., and Freund, T. F. (2004). Spike timing of distinct types of GABAergic interneuron during hippocampal gamma oscillations in vitro. *J. Neurosci.* 24, 9127–9137. doi: 10.1523/JNEUROSCI.2113-04.2004

Han, X., Qian, X., Bernstein, J. G., Zhou, H. H., Franzesi, G. T., Stern, P., et al. (2009). Millisecond-timescale optical control of neural dynamics in the nonhuman primate brain. *Neuron* 62, 191–198. doi: 10.1016/j.neuron.2009.03.011

Hass, C. A., and Glickfeld, L. L. (2016). High-fidelity optical excitation of cortico-cortical projections at physiological frequencies. *J. Neurophysiol.* 116, 2056–2066. doi: 10.1152/jn.00456.2016

Hnasko, T. S., Chuhma, N., Zhang, H., Goh, G. Y., Sulzer, D., Palmiter, R. D., et al. (2010). Vesicular glutamate transport promotes dopamine storage and glutamate corelease in vivo. *Neuron* 65, 643–656. doi: 10.1016/j.neuron.2010.02.012

Hooks, B. M., Lin, J. Y., Guo, C., and Svoboda, K. (2015). Dual-channel circuit mapping reveals sensorimotor convergence in the primary motor cortex. *J. Neurosci.* 35, 4418–4426. doi: 10.1523/JNEUROSCI.3741-14.2015

Hubel, D. H., and Wiesel, T. N. (1959). Receptive fields of single neurones in the cat's striate cortex. *J. Physiol.* 148, 574–591. doi: 10.1113/jphysiol.1959.sp006308

Hubel, D. H., and Wiesel, T. N. (1963). Shape and arrangement of columns in cat's striate cortex. *J. Physiol.* 165, 559–568. doi: 10.1113/jphysiol.1963.sp007079

Hubel, D. H., and Wiesel, T. N. (1968). Receptive fields and functional architecture of monkey striate cortex. *J. Physiol.* 195, 215–243. doi: 10.1113/jphysiol.1968.sp008455

Inoue, K. I., Takada, M., and Matsumoto, M. (2015). Neuronal and behavioural modulations by pathway-selective optogenetic stimulation of the primate oculomotor system. *Nat. Commun.* 6:8378. doi: 10.1038/ncomms9378

Jackman, S. L., Beneduce, B. M., Drew, I. R., and Regehr, W. G. (2014). Achieving high-frequency optical control of synaptic transmission. *J. Neurosci.* 34, 7704–7714. doi: 10.1523/JNEUROSCI.4694-13.2014

Jazayeri, M., Lindbloom-Brown, Z., and Horwitz, G. D. (2012). Saccadic eye movements evoked by optogenetic activation of primate V1. *Nat. Neurosci.* 15, 1368–1370. doi: 10.1038/nn.3210

Klapoetke, N. C., Murata, Y., Kim, S. S., Pulver, S. R., Birdsey-Benson, A., Cho, Y. K., et al. (2014). Independent optical excitation of distinct neural populations. *Nat. Methods* 11, 338–346. doi: 10.1038/nmeth.2836

Klauer, S., Sengpiel, F., and Hoffmann, K. P. (1990). Visual response properties and afferents of nucleus of the optic tract in the ferret. *Exp. Brain Res.* 83, 178–189. doi: 10.1007/bf00232207

Klein, C., Evrard, H. C., Shapcott, K. A., Haverkamp, S., Logothetis, N. K., and Schmid, M. C. (2016). Cell-targeted optogenetics and electrical microstimulation reveal the primate koniocellular projection to supra-granular visual cortex. *Neuron* 90, 143–151. doi: 10.1016/j.neuron.2016.02.036

Kole, K., Zhang, Y., Jansen, E. J. R., Brouns, T., Bijlsma, A., Calcini, N., et al. (2019). Assessing the utility of Magneto to control neuronal excitability in the somatosensory cortex. *Nat. Neurosci.* doi: 10.1038/s41593-019-0474-4

Li, N., Chen, S., Guo, Z. V., Chen, H., Huo, Y., Inagaki, H. K., et al. (2019). Spatiotemporal constraints on optogenetic inactivation in cortical circuits. *Elife* 8. doi: 10.7554/eLife.48622

Li, Y. T., Ibrahim, L. A., Liu, B. H., Zhang, L. I., and Tao, H. W. (2013). Linear transformation of thalamocortical input by intracortical excitation. *Nat. Neurosci.* 16, 1324–1330. doi: 10.1038/nn.3494

Lien, A. D., and Scanziani, M. (2013). Tuned thalamic excitation is amplified by visual cortical circuits. *Nat. Neurosci.* 16, 1315–1323. doi: 10.1038/nn.3488

Lima, S. Q., Hromadka, T., Znamenskiy, P., and Zador, A. M. (2009). PINP: a new method of tagging neuronal populations for identification during in vivo electrophysiological recording. *PLoS ONE* 4:e6099. doi: 10.1371/journal.pone.0006099

Lin, J. Y. (2011). A user's guide to channelrhodopsin variants: features, limitations and future developments. *Exp. Physiol.* 96, 19–25. doi: 10.1113/expphysiol.2009.051961

Lin, J. Y., Knutsen, P. M., Muller, A., Kleinfeld, D., and Tsien, R. Y. (2013). ReaChR: a red-shifted variant of channelrhodopsin enables deep transcranial optogenetic excitation. *Nat. Neurosci.* 16, 1499–1508. doi: 10.1038/nn.3502

Lin, J. Y., Lin, M. Z., Steinbach, P., and Tsien, R. Y. (2009). Characterization of engineered channelrhodopsin variants with improved properties and kinetics. *Biophys. J.* 96, 1803–1814. doi: 10.1016/j.bpj.2008.11.034

Liu, B. H., Huberman, A. D., and Scanziani, M. (2016). Cortico-fugal output from visual cortex promotes plasticity of innate motor behaviour. *Nature* 538, 383–387. doi: 10.1038/nature19818

Liu, B. H., Li, Y. T., Ma, W. P., Pan, C. J., Zhang, L. I., and Tao, H. W. (2011). Broad inhibition sharpens orientation selectivity by expanding input dynamic range in mouse simple cells. *Neuron* 71, 542–554. doi: 10.1016/j.neuron.2011.06.017

Lubke, J., and Feldmeyer, D. (2007). Excitatory signal flow and connectivity in a cortical column: focus on barrel cortex. *Brain Struct. Funct.* 212, 3–17. doi: 10.1007/s00429-007-0144-2

Magnus, C. J., Lee, P. H., Atasoy, D., Su, H. H., Looger, L. L., and Sternson, S. M. (2011). Chemical and genetic engineering of selective ion channel-ligand interactions. *Science* 333, 1292–1296. doi: 10.1126/science.1206606

Mahler, S. V., Vazey, E. M., Beckley, J. T., Keistler, C. R., McGlinchey, E. M., Kaufling, J., et al. (2014). Designer receptors show role for ventral pallidum input to ventral tegmental area in cocaine seeking. *Nat. Neurosci.* 17, 577–585. doi: 10.1038/nn.3664

Mahn, M., Prigge, M., Ron, S., Levy, R., and Yizhar, O. (2016). Biophysical constraints of optogenetic inhibition at presynaptic terminals. *Nat. Neurosci.* 19, 554–556. doi: 10.1038/nn.4266

Makino, H., and Komiyama, T. (2015). Learning enhances the relative impact of top-down processing in the visual cortex. *Nat. Neurosci.* 18, 1116–1122. doi: 10.1038/nn.4061

Manita, S., Suzuki, T., Homma, C., Matsumoto, T., Odagawa, M., Yamada, K., et al. (2015). A top-down cortical circuit for accurate sensory perception. *Neuron* 86, 1304–1316. doi: 10.1016/j.neuron.2015.05.006

Manvich, D. F., Webster, K. A., Foster, S. L., Farrell, M. S., Ritchie, J. C., Porter, J. H., et al. (2018). The DREADD agonist clozapine N-oxide (CNO) is reverse-metabolized to clozapine and produces clozapine-like interoceptive stimulus effects in rats and mice. *Sci. Rep.* 8:3840. doi: 10.1038/s41598-018-22116-z

Meister, M. (2016). Physical limits to magnetogenetics. *Elife* 5. doi: 10.7554/eLife.17210

Mukohata, Y., Sugiyama, Y., Ihara, K., and Yoshida, M. (1988). An Australian halobacterium contains a novel proton pump retinal protein: archaerhodopsin. *Biochem. Biophys. Res. Commun.* 151, 1339–1345. doi: 10.1016/s0006-291x(88)80509-6

Murphy, T. H., and Corbett, D. (2009). Plasticity during stroke recovery: from synapse to behaviour. *Nat. Rev. Neurosci.* 10, 861–872. doi: 10.1038/nrn2735

Nabavi, S., Fox, R., Proulx, C. D., Lin, J. Y., Tsien, R. Y., and Malinow, R. (2014). Engineering a memory with LTD and LTP. *Nature* 511, 348–352. doi: 10.1038/nature13294

Nagel, G., Szellas, T., Huhn, W., Kateriya, S., Adeishvili, N., Berthold, P., et al. (2003). Channelrhodopsin-2, a directly light-gated cation-selective membrane channel. *Proc. Natl. Acad. Sci. U.S.A.* 100, 13940–13945. doi: 10.1073/pnas.1936192100

Nakamichi, Y., Okubo, K., Sato, T., Hashimoto, M., and Tanifuji, M. (2019). Optical intrinsic signal imaging with optogenetics reveals functional cortico-cortical connectivity at the columnar level in living macaques. *Sci. Rep.* 9:6466. doi: 10.1038/s41598-019-42923-2

O'Connor, D. H., Peron, S. P., Huber, D., and Svoboda, K. (2010). Neural activity in barrel cortex underlying vibrissa-based object localization in mice. *Neuron* 67, 1048–1061. doi: 10.1016/j.neuron.2010.08.026

Oh, S. W., Harris, J. A., Ng, L., Winslow, B., Cain, N., Mihalas, S., et al. (2014). A mesoscale connectome of the mouse brain. *Nature* 508, 207–214. doi: 10.1038/nature13186

Pala, A., and Petersen, C. C. H. (2015). In vivo measurement of cell-type-specific synaptic connectivity and synaptic transmission in layer 2/3 mouse barrel cortex. *Neuron* 85, 68–75. doi: 10.1016/j.neuron.2014.11.025

Papagiakoumou, E., Anselmi, F., Begue, A., de Sars, V., Gluckstad, J., Isacoff, E. Y., et al. (2010). Scanless two-photon excitation of channelrhodopsin-2. *Nat. Methods* 7, 848–854. doi: 10.1038/nmeth.1505

Perez-Lopez, J. L., Contreras-Lopez, R., Ramirez-Jarquin, J. O., and Tecuapetla, F. (2018). Direct glutamatergic signaling from midbrain dopaminergic neurons onto pyramidal prefrontal cortex neurons. *Front. Neural Circ.* 12:70. doi: 10.3389/fncir.2018.00070

Peters, A. J., Chen, S. X., and Komiyama, T. (2014). Emergence of reproducible spatiotemporal activity during motor learning. *Nature* 510, 263–267. doi: 10.1038/nature13235

Petreanu, L., Huber, D., Sobczyk, A., and Svoboda, K. (2007). Channelrhodopsin-2-assisted circuit mapping of long-range callosal projections. *Nat. Neurosci.* 10, 663–668. doi: 10.1038/nn1891

Petreanu, L., Mao, T., Sternson, S. M., and Svoboda, K. (2009). The subcellular organization of neocortical excitatory connections. *Nature* 457, 1142–1145. doi: 10.1038/nature07709

Pfeffer, C. K., Xue, M., He, M., Huang, Z. J., and Scanziani, M. (2013). Inhibition of inhibition in visual cortex: the logic of connections between molecularly distinct interneurons. *Nat. Neurosci.* 16, 1068–1076. doi: 10.1038/nn.3446

Polter, A. M., Barcomb, K., Tsuda, A. C., and Kauer, J. A. (2018). Synaptic function and plasticity in identified inhibitory inputs onto VTA dopamine neurons. *Eur. J. Neurosci.* 47, 1208–1218. doi: 10.1111/ejn.13879

Prakash, R., Yizhar, O., Grewe, B., Ramakrishnan, C., Wang, N., Goshen, I., et al. (2012). Two-photon optogenetic toolbox for fast inhibition, excitation and bistable modulation. *Nat. Methods* 9, 1171–1179. doi: 10.1038/nmeth.2215

Raimondo, J. V., Kay, L., Ellender, T. J., and Akerman, C. J. (2012). Optogenetic silencing strategies differ in their effects on inhibitory synaptic transmission. *Nat. Neurosci.* 15, 1102–1104. doi: 10.1038/nn.3143

Reinhold, K., Lien, A. D., and Scanziani, M. (2015). Distinct recurrent versus afferent dynamics in cortical visual processing. *Nat. Neurosci.* 18, 1789–1797. doi: 10.1038/nn.4153

Rickgauer, J. P., and Tank, D. W. (2009). Two-photon excitation of channelrhodopsin-2 at saturation. *Proc. Natl. Acad. Sci. U.S.A.* 106, 15025–15030. doi: 10.1073/pnas.0907084106

Ringach, D. L., Hawken, M. J., and Shapley, R. (2003). Dynamics of orientation tuning in macaque V1: the role of global and tuned suppression. *J. Neurophysiol.* 90, 342–352. doi: 10.1152/jn.01018.2002

Ronzitti, E., Conti, R., Zampini, V., Tanese, D., Foust, A. J., Klapoetke, N., et al. (2017). Submillisecond optogenetic control of neuronal firing with two-photon holographic photoactivation of chronos. *J. Neurosci.* 37, 10679–10689. doi: 10.1523/JNEUROSCI.1246-17.2017

Sato, H., Katsuyama, N., Tamura, H., Hata, Y., and Tsumoto, T. (1996). Mechanisms underlying orientation selectivity of neurons in the primary visual

cortex of the macaque. *J. Physiol.* 494(Pt 3), 757–771. doi: 10.1113/jphysiol.1996.sp021530

Schwarz, L. A., Miyamichi, K., Gao, X. J., Beier, K. T., Weissbourd, B., DeLoach, K. E., et al. (2015). Viral-genetic tracing of the input-output organization of a central noradrenaline circuit. *Nature* 524, 88–92. doi: 10.1038/nature14600

Seeman, S. C., Campagnola, L., Davoudian, P. A., Hoggarth, A., Hage, T. A., Bosma-Moody, A., et al. (2018). Sparse recurrent excitatory connectivity in the microcircuit of the adult mouse and human cortex. *Elife* 7. doi: 10.7554/eLife.37349

Senn, V., Wolff, S. B., Herry, C., Grenier, F., Ehrlich, I., Grundemann, J., et al. (2014). Long-range connectivity defines behavioral specificity of amygdala neurons. *Neuron* 81, 428–437. doi: 10.1016/j.neuron.2013.11.006

Shemesh, O. A., Tanese, D., Zampini, V., Linghu, C., Piatkevich, K., Ronzitti, E., et al. (2017). Temporally precise single-cell-resolution optogenetics. *Nat. Neurosci.* 20, 1796–1806. doi: 10.1038/s41593-017-0018-8

Shewcraft, R. A., Dean, H. L., Fabiszak, M. M., Hagan, M. A., Wong, Y. T., and Pesaran, B. (2020). Excitatory/inhibitory responses shape coherent neuronal dynamics driven by optogenetic stimulation in the primate brain. *J. Neurosci.* 40, 2056–2068. doi: 10.1523/JNEUROSCI.1949-19.2020

Sillito, A. M., Kemp, J. A., and Patel, H. (1980). Inhibitory interactions contributing to the ocular dominance of monocularly dominated cells in the normal cat striate cortex. *Exp. Brain Res.* 41, 1–10. doi: 10.1007/bf00236673

Sinclair, G., Leach, J., Jordan, P., Gibson, G., Yao, E., Laczik, Z., et al. (2004). Interactive application in holographic optical tweezers of a multi-plane Gerchberg-Saxton algorithm for three-dimensional light shaping. *Opt. Exp.* 12, 1665–1670. doi: 10.1364/opex.12.001665

Soliman, G. S., and Trüper, H. G. (1982). Halobacterium pharaonis sp. nov., a new, extremely haloalkaliphilic archaebacterium with low magnesium requirement. *Zentralblatt Bakteriol. Mikrobiol. Hygiene: I Abt Originale C: Allgem. Angew. Ökol. Mikrobiol.* 3, 318–329. doi: 10.1016/s0721-9571(82)80045-8

Stachniak, T. J., Ghosh, A., and Sternson, S. M. (2014). Chemogenetic synaptic silencing of neural circuits localizes a hypothalamus–>midbrain pathway for feeding behavior. *Neuron* 82, 797–808. doi: 10.1016/j.neuron.2014.04.008

Stauffer, W. R., Lak, A., Yang, A., Borel, M., Paulsen, O., Boyden, E. S., et al. (2016). Dopamine neuron-specific optogenetic stimulation in rhesus macaques. *Cell* 166, 1564–1571.e6. doi: 10.1016/j.cell.2016.08.024

Stuber, G. D., Hnasko, T. S., Britt, J. P., Edwards, R. H., and Bonci, A. (2010). Dopaminergic terminals in the nucleus accumbens but not the dorsal striatum corelease glutamate. *J. Neurosci.* 30, 8229–8233. doi: 10.1523/JNEUROSCI.1754-10.2010

Takahashi, N., Oertner, T. G., Hegemann, P., and Larkum, M. E. (2016). Active cortical dendrites modulate perception. *Science* 354, 1587–1590. doi: 10.1126/science.aah6066

Tritsch, N. X., Ding, J. B., and Sabatini, B. L. (2012). Dopaminergic neurons inhibit striatal output through non-canonical release of GABA. *Nature* 490, 262–266. doi: 10.1038/nature11466

Tye, K. M., Prakash, R., Kim, S. Y., Fenno, L. E., Grosenick, L., Zarabi, H., et al. (2011). Amygdala circuitry mediating reversible and bidirectional control of anxiety. *Nature* 471, 358–362. doi: 10.1038/nature09820

Vazey, E. M., and Aston-Jones, G. (2014). Designer receptor manipulations reveal a role of the locus coeruleus noradrenergic system in isoflurane general anesthesia. *Proc. Natl. Acad. Sci. U.S.A.* 111, 3859–3864. doi: 10.1073/pnas.1310025111

Wang, G., Zhang, P., Mendu, S. K., Wang, Y., Zhang, Y., Kang, X., et al. (2019). Revaluation of magnetic properties of Magneto. *Nat Neurosci.* doi: 10.1038/s41593-019-0473-5

Wang, H., Peca, J., Matsuzaki, M., Matsuzaki, K., Noguchi, J., Qiu, L., et al. (2007). High-speed mapping of synaptic connectivity using photostimulation in Channelrhodopsin-2 transgenic mice. *Proc. Natl. Acad. Sci. U.S.A.* 104, 8143–8148. doi: 10.1073/pnas.0700384104

Warden, M. R., Selimbeyoglu, A., Mirzabekov, J. J., Lo, M., Thompson, K. R., Kim, S. Y., et al. (2012). A prefrontal cortex-brainstem neuronal projection that controls response to behavioural challenge. *Nature* 492, 428–432. doi: 10.1038/nature11617

Wheeler, M. A., Smith, C. J., Ottolini, M., Barker, B. S., Purohit, A. M., Grippo, R. M., et al. (2016). Genetically targeted magnetic control of the nervous system. *Nat. Neurosci.* 19, 756–761. doi: 10.1038/nn.4265

Whishaw, I. Q. (2000). Loss of the innate cortical engram for action patterns used in skilled reaching and the development of behavioral compensation following motor cortex lesions in the rat. *Neuropharmacology* 39, 788–805. doi: 10.1016/s0028-3908(99)00259-2

Wickersham, I. R., Lyon, D. C., Barnard, R. J., Mori, T., Finke, S., Conzelmann, K. K., et al. (2007). Monosynaptic restriction of transsynaptic tracing from single, genetically targeted neurons. *Neuron* 53, 639–647. doi: 10.1016/j.neuron.2007.01.033

Wietek, J., Beltramo, R., Scanziani, M., Hegemann, P., Oertner, T. G., and Wiegert, J. S. (2015). An improved chloride-conducting channelrhodopsin for light-induced inhibition of neuronal activity in vivo. *Sci. Rep.* 5:14807. doi: 10.1038/srep14807

Wilson, N. R., Runyan, C. A., Wang, F. L., and Sur, M. (2012). Division and subtraction by distinct cortical inhibitory networks in vivo. *Nature* 488, 343–348. doi: 10.1038/nature11347

Witten, I. B., Steinberg, E. E., Lee, S. Y., Davidson, T. J., Zalocusky, K. A., Brodsky, M., et al. (2011). Recombinase-driver rat lines: tools, techniques, and optogenetic application to dopamine-mediated reinforcement. *Neuron* 72, 721–733. doi: 10.1016/j.neuron.2011.10.028

Wozny, C., Beed, P., Nitzan, N., Possnecker, Y., Rost, B. R., and Schmitz, D. (2018). VGLUT2 functions as a differential marker for hippocampal output neurons. *Front. Cell Neurosci.* 12:337. doi: 10.3389/fncel.2018.00337

Xu, F. X., Zhou, L., Wang, X. T., Jia, F., Ma, K. Y., Wang, N., et al. (2019). Magneto is ineffective in controlling electrical properties of cerebellar Purkinje cells. *Nat Neurosci.* doi: 10.1038/s41593-019-0475-3

Xu, T., Yu, X., Perlik, A. J., Tobin, W. F., Zweig, J. A., Tennant, K., et al. (2009). Rapid formation and selective stabilization of synapses for enduring motor memories. *Nature* 462, 915–919. doi: 10.1038/nature08389

Xue, M., Atallah, B. V., and Scanziani, M. (2014). Equalizing excitation-inhibition ratios across visual cortical neurons. *Nature* 511, 596–600. doi: 10.1038/nature13321

Yizhar, O., Fenno, L. E., Prigge, M., Schneider, F., Davidson, T. J., O'Shea, D. J., et al. (2011). Neocortical excitation/inhibition balance in information processing and social dysfunction. *Nature* 477, 171–178. doi: 10.1038/nature10360

Zeng, H. (2018). Mesoscale connectomics. *Curr. Opin. Neurobiol.* 50, 154–162. doi: 10.1016/j.conb.2018.03.003

Zhang, F., Wang, L. P., Brauner, M., Liewald, J. F., Kay, K., Watzke, N., et al. (2007). Multimodal fast optical interrogation of neural circuitry. *Nature* 446, 633–639. doi: 10.1038/nature05744

Zhang, S., Xu, M., Kamigaki, T., Hoang, Do, J. P., Chang, W. C., et al. (2014). Selective attention, Long-range and local circuits for top-down modulation of visual cortex processing. *Science* 345, 660–665. doi: 10.1126/science.1254126

Zhu, H., Pleil, K. E., Urban, D. J., Moy, S. S., Kash, T. L., and Roth, B. L. (2014). Chemogenetic inactivation of ventral hippocampal glutamatergic neurons disrupts consolidation of contextual fear memory. *Neuropsychopharmacology* 39, 1880–1892. doi: 10.1038/npp.2014.35

Zhu, Y., Wienecke, C. F., Nachtrab, G., and Chen, X. (2016). A thalamic input to the nucleus accumbens mediates opiate dependence. *Nature* 530, 219–222. doi: 10.1038/nature16954

Conflict of Interest: The authors declare that the research was conducted in the absence of any commercial or financial relationships that could be construed as a potential conflict of interest.

frontiers in Neural Circuits

METHODS
published: 15 May 2020
doi: 10.3389/fncir.2020.00019

A Probabilistic Framework for Decoding Behavior From *in vivo* Calcium Imaging Data

Guillaume Etter, Frederic Manseau and Sylvain Williams**

Douglas Mental Health University Institute, McGill University, Montreal, QC, Canada

Understanding the role of neuronal activity in cognition and behavior is a key question in neuroscience. Previously, *in vivo* studies have typically inferred behavior from electrophysiological data using probabilistic approaches including Bayesian decoding. While providing useful information on the role of neuronal subcircuits, electrophysiological approaches are often limited in the maximum number of recorded neurons as well as their ability to reliably identify neurons over time. This can be particularly problematic when trying to decode behaviors that rely on large neuronal assemblies or rely on temporal mechanisms, such as a learning task over the course of several days. Calcium imaging of genetically encoded calcium indicators has overcome these two issues. Unfortunately, because calcium transients only indirectly reflect spiking activity and calcium imaging is often performed at lower sampling frequencies, this approach suffers from uncertainty in exact spike timing and thus activity frequency, making rate-based decoding approaches used in electrophysiological recordings difficult to apply to calcium imaging data. Here we describe a probabilistic framework that can be used to robustly infer behavior from calcium imaging recordings and relies on a simplified implementation of a naive Baysian classifier. Our method discriminates between periods of activity and periods of inactivity to compute probability density functions (likelihood and posterior), significance and confidence interval, as well as mutual information. We next devise a simple method to decode behavior using these probability density functions and propose metrics to quantify decoding accuracy. Finally, we show that neuronal activity can be predicted from behavior, and that the accuracy of such reconstructions can guide the understanding of relationships that may exist between behavioral states and neuronal activity.

Keywords: calcium imaging, decoding, bayesian inference, hippocampus, spatial coding

OPEN ACCESS

Edited by:
Jean-Claude Béïque,
University of Ottawa, Canada

Reviewed by:
Daniel W. Wesson,
University of Florida, United States
Richard Naud,
University of Ottawa, Canada

****Correspondence:***
Guillaume Etter
etterguillaume@gmail.com
Sylvain Williams
sylvain.williams@mcgill.ca

Received: *31 October 2019*
Accepted: *06 April 2020*
Published: *15 May 2020*

Citation:
Etter G, Manseau F and Williams S (2020) A Probabilistic Framework for Decoding Behavior From in vivo Calcium Imaging Data. Front. Neural Circuits 14:19. doi: 10.3389/fncir.2020.00019

INTRODUCTION

Early *in vivo* studies have established relationships between external variables and neuronal activity, including (but not restricted to) auditory information in the auditory cortex (Katsuki et al., 1956), visual stimuli in the visual cortex (Hubel and Wiesel, 1962), and spatial information in the hippocampus (O'Keefe and Dostrovsky, 1971). Based on the widely influential information theory (Shannon, 1948), it has previously been proposed that neurons can act as 'communication channels' between physiological variables (input) and spike trains (output) (Richmond and Optican, 1990;

Richmond et al., 1990; Skaggs et al., 1993). In addition to providing metrics to quantify the extent to which external variables can be encoded in neurons, these studies laid the first foundations in establishing computational tools to predict animal behavior merely using neuronal activity. This process, termed decoding, is essential in understanding the role of neuronal activity in behavior, and the success rate of predictions can be used as a metric of understanding of a given system. Among techniques that have been described in this context, Bayesian decoding in particular has been relatively popular and widely used (Brown et al., 1998; Zhang et al., 1998; Gerwinn, 2009; Quian Quiroga and Panzeri, 2009; Koyama et al., 2010).

While the literature on *in vivo* neuronal physiology has been largely dominated by electrophysiological studies, calcium imaging methods have recently gained popularity. Originally performed at the single cell level with the aid of calcium sensors (Grynkiewicz et al., 1985; Persechini et al., 1997), calcium imaging can now be performed *in vivo,* in large neuronal assemblies, and over very long periods of time (Ziv et al., 2013; Sheintuch et al., 2017; Gonzalez et al., 2019). These major improvements coincided with the development of genetically encoded calcium indicators (GECI), including the popular GCaMP (Nakai et al., 2001; Tian et al., 2009; Ohkura et al., 2012; Chen et al., 2013). In recent years, calcium imaging methods have seen the development of various computational tools that solve the problem of signal extraction from raw calcium imaging video recordings. In particular, several groups have proposed open-source software codes to perform fast, recursive motion correction (Pnevmatikakis and Giovannucci, 2017), offline (Pnevmatikakis et al., 2016; Zhou et al., 2018) and online (Giovannucci et al., 2017) extraction of neuronal spatial footprints and their associated calcium activity, temporal registration of neurons across days (Sheintuch et al., 2017), and complete analysis pipelines have been made available (Giovannucci et al., 2018). The aforementioned open source codes have significantly facilitated the analysis of calcium imaging datasets. Most often, one of the objectives when using such a tool is to understand the neural basis of behavior. Unfortunately, there are only a few open source analysis toolboxes that can relate calcium imaging data to behavior to this day (Tegtmeier et al., 2018[1]). While these useful analytical tools allow the exploration of relationships between calcium signals and behavior, they are mostly restricted to visualization and correlation. Previous studies have made use of naive Bayesian classifiers to infer rodent behavior from calcium imaging data recorded in the motor cortex (Huber et al., 2012; Kondo et al., 2018), hippocampus (Ziv et al., 2013; Mau et al., 2018; Gonzalez et al., 2019), or amygdala (Grewe et al., 2017). While these analyses usually result in accurate predictions of behaviors, there is no consensus on the methodology, and in particular the input signal to the classifier, or other preprocessing steps (e.g. smoothing of neuronal tuning curves used by the classifier).

While calcium imaging does not allow the determination of exact spike timing, some methods have been proposed to approximate spiking activity from calcium imaging data by deconvolving calcium transients (Deneux et al., 2016; Pachitariu et al., 2018; Rahmati et al., 2018). Consequently, one strategy that can be employed is to first estimate deconvolution parameters from ground truth data (e.g. *in vitro* unit recording in brain slices combined with calcium imaging) to then apply them to recordings performed *in vivo*. However, one major caveat with this approach is that physiological responses can differ greatly between *in vivo* and *in vitro* conditions (Belle et al., 2018) leading to erroneous parameter estimation. Another obstacle to using deconvolved signals and estimated spikes to decode calcium activity is that the very nature of calcium imaging does not allow to determine exact spike timing. While unit recordings are typically done at sampling rates exceeding 10 KHz, 1-photon microendoscopes used in freely moving animals usually sample images at 30 frames per second or less, and spike trains will generally be associated with large calcium transients of varying size and duration. Consequently, one could for example correctly estimate that a neuron fires 10 action potentials based on the observation of a single calcium transient, however, the exact timing of each spike would remain unknown, and could happen anywhere within a ∼33 ms window (for calcium imaging performed at 30 Hz).

Importantly, another issue encountered when performing calcium imaging with GCaMP is photobleaching, which leads to a progressive loss of signal due to the destruction of fluorescent proteins that report calcium influx. Unlike electrophysiological unit recordings that can be performed for several hours, calcium imaging is thus typically performed for shorter durations. While it is possible to follow GCaMP-positive cell assemblies over months (Ziv et al., 2013; Sheintuch et al., 2017), each recording session has to be limited in duration to avoid photobleaching. This results in low sampling that can be problematic when trying to associate neuronal activity with a certain behavior: some behavioral states can be over- or underrepresented and concurrently, calcium activity can be too sparse to establish tuning curves of neuronal activity.

Here, we propose simple analytical methods to relate calcium activity to behavior by (1) extracting periods of activity in calcium imaging data without approximating spike timing and subjecting actual data to null hypothesis testing in order to solve the problem of low sampling, (2) decoding behavior by using previously computed probability density functions in a naive Bayesian classifier, and (3) reconstructing neuronal activity from behavior and assessing the quality of neuronal coding.

RESULTS

Establishment of Probabilistic Neural Tuning Curves

To demonstrate the usefulness of our method, we performed calcium imaging in a well characterized system: CA1 pyramidal cells of the dorsal hippocampus (**Figure 1A**). These neurons are known to display spatial tuning and are commonly referred to as place cells (O'Keefe and Dostrovsky, 1971). We trained a mouse to run back and forth on a 100 cm long linear track by providing sucrose water rewards at each end of the track

[1]www.miniscope.org

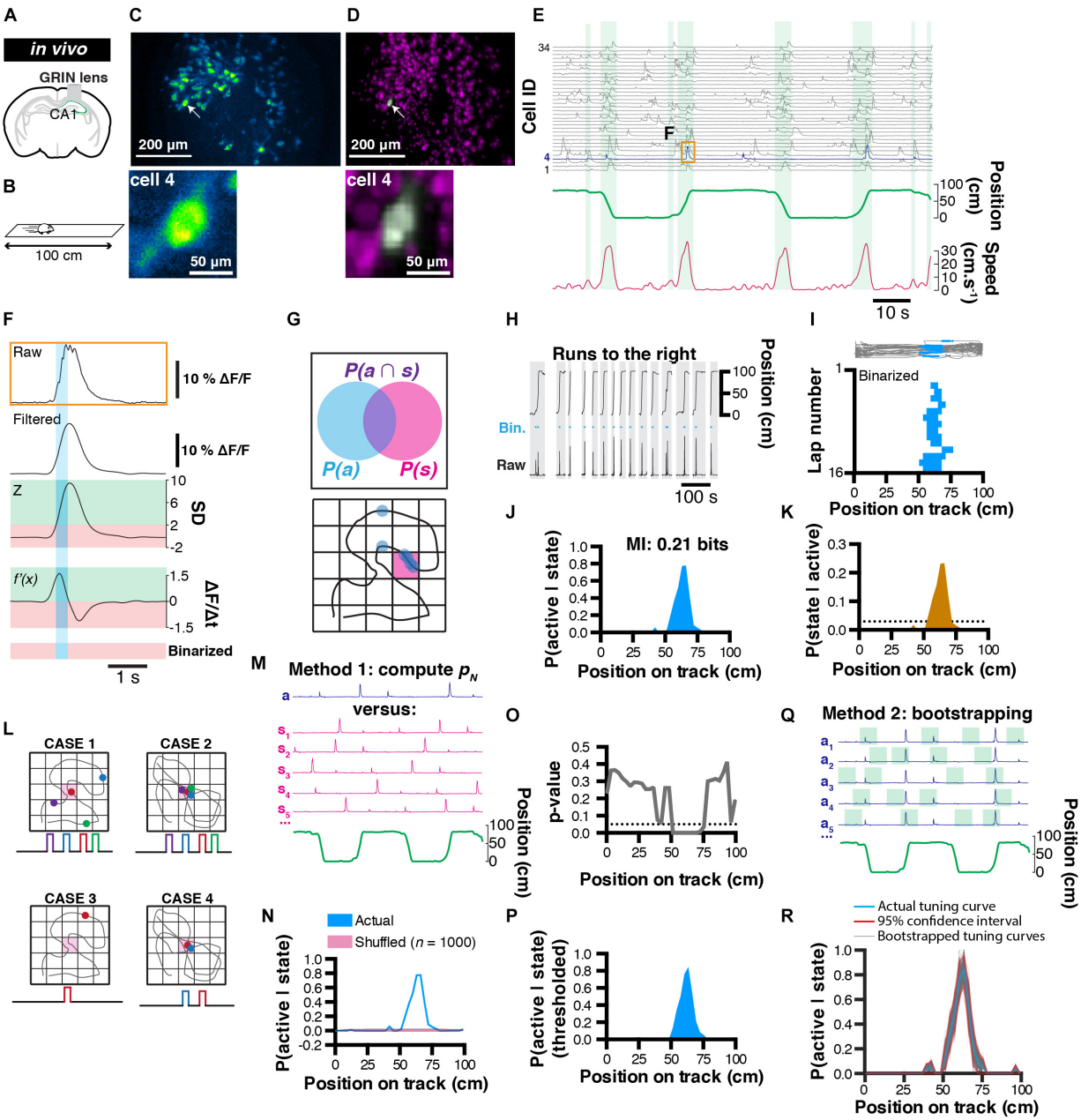

FIGURE 1 | Rationale for extracting spatial coding characteristics of CA1 pyramidal cells. **(A)** Diagram of GRIN lens implanted over CA1 pyramidal cells of the dorsal hippocampus. **(B)** Calcium imaging was performed as a mouse was running in alternating directions on a linear track. **(C)** Maximum projection of the corresponding field of view. **(D)** Corresponding extracted spatial footprints using CNMFe. **(E)** Example traces from a subset of extracted cells aligned with position on a linear track and locomotor speed. Running epochs are indicated with green stripes. **(F)** Example raw transient (top) from one cell and corresponding filtered, z-scored, first-derivative, and binarized signals. **(G)** Rationale used to extract unconditional and joint probabilities from binarized data that can be later used to compute conditional probabilities. **(H)** Mouse location on the linear track with corresponding raw calcium activity and derived binary trace (blue). Only runs to the right are considered here. **(I)** (Top) mouse trajectory on the linear track (gray) with corresponding locations where one cell's binarized activity was detected (blue dots), and (bottom) location of binarized activity on the linear track for each run (n = 16 runs). **(J)** Probability P(active| state) of cell #4 to be active given the location on the linear track, and corresponding mutual information (MI, top). **(K)** Derived posterior probability of the mouse being in a location given cell activity P(state| active) (ocher) compared to uniformity (dotted line). **(L)** Example cases of poor variable coding (case 1), superior variable coding (case 2), poor variable coding with sparse information (case 3), and superior variable coding with sparse information (case 4). **(M)** Method for computing a p-value: actual (a) calcium trace, corresponding circular permutations (s_n), and corresponding location (green). **(N)** Probability P(active| state) of cell #4 being active given location (blue) and corresponding average shuffled distribution from n = 1000 surrogates (the thickness of the line represents the SEM). **(O)** p-Value computed using actual data and shuffled surrogates for each location of the linear track. **(P)** Thresholded place field retaining only significant P(active| state) values. **(Q)** Method for computing 95% confidence interval from bootstrap samples. **(R)** Actual tuning curve P(active| state) (blue) and corresponding 95% confidence interval (red) computed from bootstrap samples (gray; n = 1000).

and scheduling homecage access to water every day (**Figure 1B**). We recorded ∼400 neurons in these conditions (**Figure 1C**). After extracting neuronal spatial footprints (**Figure 1D**), we visualized corresponding calcium activity along with the position and locomotor speed of the animal (**Figure 1E**). Previous studies have shown that immobility periods are associated with replay of experience (Foster and Wilson, 2006; Diba and Buzsáki, 2007; Davidson et al., 2009). In order to focus on the spatial tuning curves of CA1 neurons, we therefore excluded periods of immobility (<5 cm.s^{-1}) that could potentially contain periods of neuronal activity that reflect tuning to internal, rather than external variables.

In order to compute probabilities that will be used in later analyses of tuning curves, we sought to discriminate periods of activity versus inactivity. To this end, we devised a simple binarizing method where raw calcium signals are first filtered (to remove high frequency fluctuations that could erroneously be detected as transient rise periods), and we considered periods of activity as following the two criteria: (1) the signal amplitude of a normalized trace has to be above 2 standard-deviations, and (2) the first order derivative has to be positive (thus corresponding to a transient rise period; **Figure 1F**).

Extracting Probability Values in a Bayesian Context

Following the binarization of raw calcium traces, we propose a probabilistic framework to describe how the activity of a neuron encodes a certain behavior or state (**Figure 1G**). To this end, we can first compute the probability of a neuron to be active *P(A)* using the following formula:

$$P\ (A)\ = \frac{time\ active}{total\ time} \tag{1}$$

P(A) only informs on the activity rate of a neuron over the course of a recording session and corresponds to the marginal likelihood in a Bayesian context. We can also compute the probability of spending time in a given behavioral state *i*:

$$P\ (S_i)\ = \frac{time\ in\ state\ i}{total\ time} \tag{2}$$

P(S) can be informative on whether the distribution of behavioral states is homogeneous or inhomogeneous, which can potentially lead to biases in further analyzes. In a Bayesian context, *P(S)* corresponds to the prior. Additionally, the joint probability $P\ (S_i \cap\ A)$ of a given neuron to be both active and in a given state *i* will be later used to compute information metrics:

$$P\ (S_i \cap\ A)\ = \frac{time\ active\ while\ in\ state\ i}{total\ time} \tag{3}$$

We can then compute the probability that a cell is active given the animal is in a state *i*:

$$P\ (A|S_i)\ = \frac{time\ active\ while\ in\ state\ i}{time\ in\ state} \tag{4}$$

$P\ (A|S)$ is more informative and can be interpreted as a tuning curve. In a Bayesian framework, this probability is also known as the likelihood. For example, a probability value of 0.8 means that a cell is active 80 % of the time when the animal is in a given behavioral state.

In our example, we isolated running periods when the mouse was running toward the right hand side of the linear track (**Figure 1H**), and divided the track in 3 cm bins. Each bin thus represents a discrete state, and while visualizing the activity of neuron #4 for each run, it is apparent that this cell displays some spatial tuning (**Figure 1I**). We thus computed $P\ (S_i|A)$ for that cell and found a peak likelihood of 0.78 at ∼64.5 cm from the left hand side of the track (**Figure 1J**). Finally, using classical Bayesian inference, we can infer the probability that the animal is in a state S_i given neuronal activity A:

$$P\ (S_i|A)\ = \frac{P\ (A|S_i)\ \times \mathrm{P}\ (\mathrm{S}_i)}{P\ (A)} \tag{5}$$

$P\ (S|A)$ is the posterior probability distribution of states given neuronal activity and will be used later on to decode behavior.

Testing Significance of Tuning Curves

One current issue with calcium imaging is photobleaching, which prevents extended recordings and thus restricts the sampling of both neuronal activity and behavioral data. Experimenters can thus be frequently faced with one of four cases: first, sampling of both behavior and neuronal activity are sufficient, and there is no apparent relationship between these two variables (**Figure 1L**, case 1). Secondly, sampling is sufficient and there is a very clear relationship between behavior and neuronal activity (**Figure 1L**, case 2). Thirdly, sampling is too low to observe a clear phenomenon (not enough coverage of behavioral states, sparse neuronal activity; **Figure 1L**, case 3). Lastly, behavioral sampling is sufficient, but neuronal activity is sparse and while there is an apparent relationship between behavior and neuronal activity, there is no absolute confidence that this could indeed be the case (**Figure 1L**, case 4). In every case, we will want to test whether the tuning curves that have been derived are significantly different from chance.

Deriving p-values from shuffled distributions

One solution we propose to this problem is to confront the actual data to a null hypothesis that there is no relationship between behavior and neuronal activity. To this end, we generated a distribution of tuning curves that are computed from the actual calcium trace, but that has been shifted in time so that any potential relationship to behavior is lost. Circular permutations can be used to remove the temporal relationship that exists between neuronal activity and behavior; **Figure 1M**). We recommend this shuffling method because it preserves the temporal structure of calcium transients and leads to more conservative results, as opposed to a complete randomization of every data point which often gives rise to non-physiological data, and thus inflates the significance value of results. The choice of a null hypothesis should, however, be determined carefully depending on the nature of the question asked. In our example, we performed $n = 1000$ random circular permutations, computed the mean as well as standard error of the mean (SEM), and compared it to our actual tuning curve (**Figure 1N**). Because the shuffled data points cannot be assumed to be distributed

normally, transforming the actual data into a *z*-score cannot be used to derive a measure of significance. Instead, one can compute a *p*-value that corresponds to the number of data points from the shuffled distribution that are greater than the actual data, divided by the number of permutations (Cohen, 2014). Note that using this method, the *p*-value can take null values in the event where all data points from the shuffled distribution fall under the actual data. After computing a *p*-value value from our actual data and shuffled distribution (**Figure 1O**), a threshold (typically of 0.05 or 0.01) can be used to display only significant data points (we used a 0.05 threshold in our example; **Figure 1P**).

Deriving confidence intervals using bootstrap samples

Another challenge associated with sparse sampling of behavior and/or neuronal activity is estimating the reliability of tuning curves. One method to circumvent this problem is to derive statistics (mean and confidence interval) from bootstrapped samples (Kass et al., 2014). To this end, we can measure several times (e.g. n = 1000 samples) our likelihood P(A|S) on a portion of the data (e.g. 50% randomly chosen data points) and with replacement (the same data points can be used in different bootstrap samples; **Figure 1Q**). Using these parameters (n = 1000 bootstrap samples using 50% of the data), we display every bootstrap tuning curve along with the corresponding 95% confidence interval (**Figure 1R**).

Information Metrics

Numerous studies have applied metrics derived from information theory (Shannon, 1948) to neuronal data (Skaggs et al., 1993; see Dimitrov et al., 2011 for review). While the information held within a single spike is difficult to approximate with calcium imaging, mutual information (MI) can be used to describe the amount of information about one variable through observation of another variable (neuron activity and behavioral state in our example) using unconditional and joint probabilities:

$$MI = \sum_{i=1}^{M} \sum_{j=1}^{2} P(S_i \cap A_j) \times \log_2\left(\frac{P(S_i \cap A_j)}{P(S_i) \times P(A_j)}\right)$$

where M is the total number of possible behavioral states, $P(S_i \cap A_j)$is the joint probability of behavioral state i to be observed concurrently with activity level j. Note that in our case we consider only two levels of activity j (active versus inactive). The MI index is a practical way of sorting neurons by the amount of information they encode (**Supplementary Figure 1**), and it was previously found that although related, MI is more reliable and scalable than other spatial information metrics (Souza et al., 2018). In our example, cell #4 displays 0.21 bits of information while considering only trajectories to the right (**Figure 1J**). On the other hand, it is possible to assess the significance of MI values by using the same techniques described in section "Information Metrics." An example of MI values compared to shuffled surrogate can be found in **Supplementary Figure 1a**.

Decoding of Behavior From Calcium Imaging Data

Extracting tuning curves for each individual neuron can shed light about their activity pattern but does not fully explain a particular behavior. Importantly, the temporal coordination of large neuronal assemblies is likely to provide more information about the specificity of generated behaviors. In our example, we would like to understand the relationship between location (without discriminating left/right trajectories at first) and the activity patterns of a large (∼400) cell assembly. When a given neuron is active, the posterior probability density function (Eq. 5) computed earlier gives an estimate of the likely position of the mouse on the linear track. The most likely position of the mouse given that a neuron can be estimated as the location corresponding to the maximum value of the posterior probability density function. *P(S)* can be measured directly (in our case, it is the general likelihood of finding the mouse in any given location; **Figure 2A**, teal line in the bottom panel) or kept uniform. In the latter case, we make no prior assumption about the potential location of the mouse on the linear track and attribute equal probability for each location (**Figure 2A**, orange line in the bottom panel).

Decoding Behavior Using Activity From Multiple Neurons

To predict the mouse state using the activity from multiple neurons, it is more efficient to take the product (rather than the sum) of *a posteriori* probabilities, because null values translate into an absolute certainty that the mouse cannot be in a given state considering the activity of a given neuron. Importantly, this can only be done under the assumption that every neuron is independent from each other, which is unlikely to be the case in practice because of neuroanatomical connectivity or other reasons: for example on a linear track the same sequence of neuronal activity is expected to be observed for each trajectory. In the case of interdependent neurons, posterior probabilities would have to be computed for each dependent neuronal ensemble, and the reconstructions would be expected to be more accurate at the expense of requiring significantly larger training datasets. Therefore, assuming that recorded neurons are independent trades off decoding accuracy for computing time. We can then rewrite our equation to include tuning curves from multiple neurons:

$$P\ (S|A) = \prod_{k=1}^{N} \frac{P\ (A_k|S)\ \times P\ (S)}{P\ (A_k)} \tag{6}$$

where $P\ (S|A)$is a vector of *a posteriori* behavioral states and N corresponds to the number of neurons used. In our example, we can measure the activity of every neuron k at a given time point (**Figure 2B**), derive the associated tuning curves (**Figure 2C**, top panel), and corresponding posterior location probability (**Figure 2C**, bottom panel). Importantly, while equation (7) is fundamentally correct, the repeated product of small values (such as probability values that are between 0 and 1) will lead to numerical underflow when computed on most softwares available currently. Although this is not a problem when decoding activity

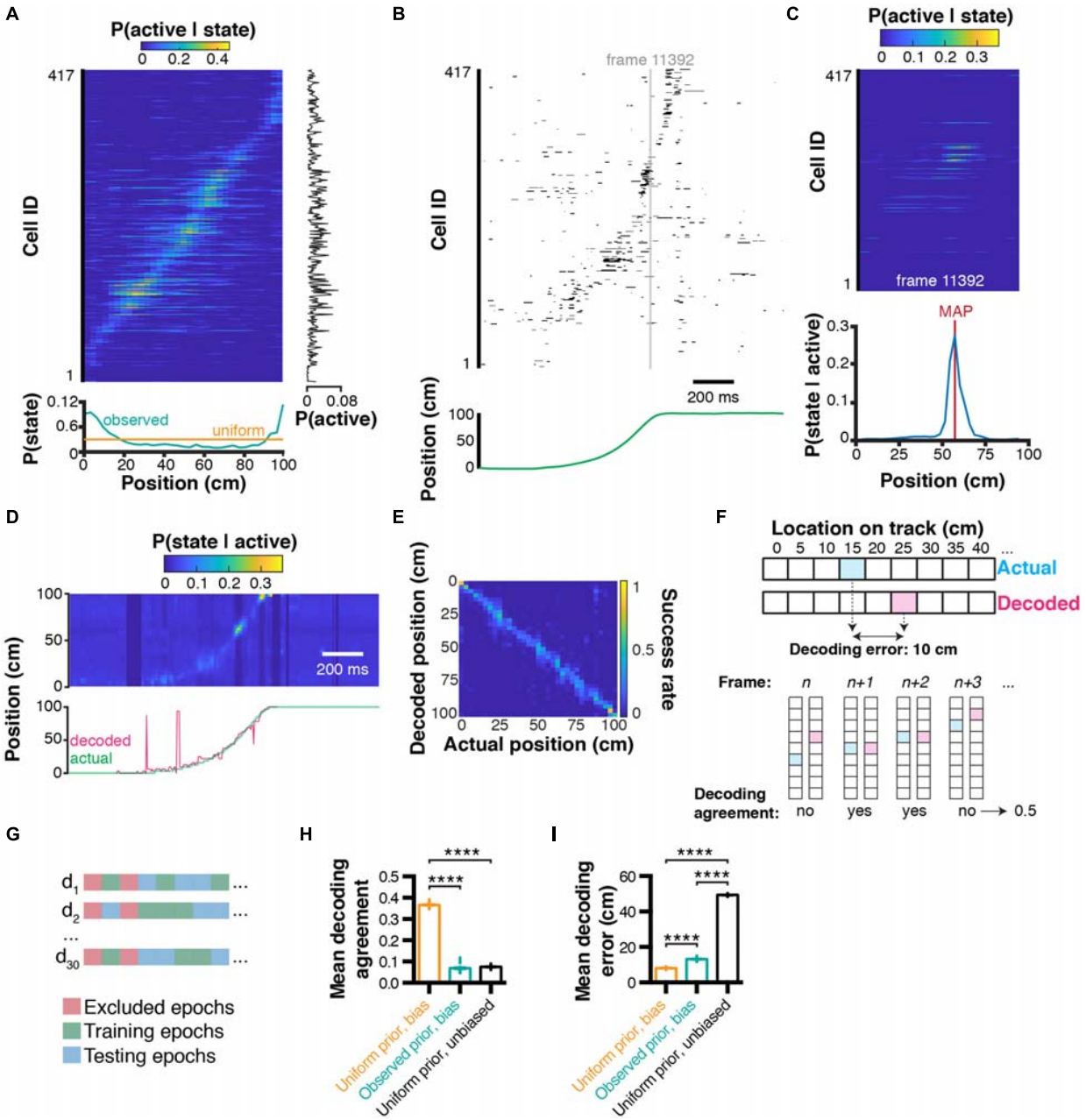

FIGURE 2 | Bayesian decoding of behavior from calcium imaging recording. **(A)** Spatial tuning curves for each individual CA1 neuron [data sorted from location of peak probability P(active|state)], and corresponding marginal likelihood of being active (right-hand side), and prior probability of being in a given state (= location; bottom). **(B)** Raster plot of binarized cell activity and corresponding position on the linear track (bottom). **(C)** Tuning curves of cells corresponding to their state at frame 11392 (in b) and subsequent posterior probability of being in a location on the linear track given cell activity (bottom). Location was estimated using maximum *a posteriori* (MAP). **(D)** Posterior probabilities for each frame estimated from ongoing binarized calcium activity, and corresponding actual (green) and decoded (pink) location estimated with MAP. **(E)** Confusion matrix of actual vs. decoded position. **(F)** Method used to compute Euclidean distance decoding error (top) and decoding agreement (bottom). **(G)** Paradigm used to train and test the decoder on different epochs of the dataset. **(H)** Effect of prior and bias (marginal likelihood of cell being active) on decoding agreement. **(I)** Same for decoding error. Color codes in a,c,d,e: dark blue = low probability, yellow = high probability.

from a small number of cells, numerical underflow will prevent decoding activity from large sets of cell assemblies. One solution to this problem is to perform computations on a log scale. Additionally, using *exp(x)-1* and *log(1+x)* allows very small values to converge toward x instead of 0. Our equation can then take the form:

$$P\,(S|A) = exp\left[\sum_{k=1}^{N} \log(1 + \frac{P\,(A_k|S)\ \times P\,(S)}{P\,(A_k)}) - 1\right] \qquad (7)$$

It is noteworthy that Eq. (7) and (8) are not formally equivalent. However, to reconstruct the position of the mouse, we will consider the location associated with the maximum *a posteriori* (MAP) which will remain the same value under such convex transform:

$$\widehat{y} = arg\ max\ exp\left[\sum_{k=1}^{N} \log(1 + \frac{P\ (A_k|S)\ \times P\ (S)}{P\ (A_k)}) - 1\right] \quad (8)$$

where $\hat{y}$ is the estimated state among all states in S.

Assessing Decoding Accuracy

In our example, we can compute the posterior probabilities for each individual timestep based on neuronal activity, and compare the actual versus decoded location on the linear track (**Figure 2D**). To visualize which states are associated with better/worse decoding error, we can compute a confusion matrix, which expresses the portion of time points where the actual state was successfully decoded (**Figure 2E**). This representation is also useful to identify which states are more difficult to decode. While confusion matrices are useful, they are not practical when it comes to summarizing decoding accuracy for large datasets and performing statistical analyzes. We thus propose two metrics: (1) decoding agreement, and (2) decoding error (**Figure 2F**). We define decoding agreement as the portion of time where the exact state of the mouse was successfully decoded:

$$decoding\ agreement\ = \frac{time\ points\ successfully\ decoded}{Total\ time} \quad (9)$$

Therefore, decoding agreement is a value between 0 and 1. For instance, a value of 0.5 means that 50 % of time points have been successfully decoded. This approach is quite conservative: when the decoded state is only one bin away from the actual behavioral state, it would lead to a null decoding agreement while still being close to reality. Therefore, another metric commonly used in decoding analyzes is decoding error, which is the distance between the decoded behavior and the actual behavior. Note that in our case, the distance is explicitly Euclidean and can be expressed in cm. For one-dimensional data, equation (16) can be used to compute decoding error:

$$decoding\ error = |decoded\ state\ - actual\ state| \quad (10)$$

The decoding error may or may not be useful depending on the variables under study. For instance, in the case of auditory stimuli, the distance between tone frequencies might not necessarily be as meaningful as an actual spatial distance, as it is the case in our example. Moreover, its computation will be different for two-dimensional space, or head orientation, to list a few of the variables commonly studied. Importantly, to assess decoding accuracy, it is recommended not to test the decoder on epochs that were used to train the Bayesian decoder. Some epochs, such as periods of immobility in our case, can be excluded for both training and testing altogether. We propose here to train and test our decoder on non-overlapping sets of random epochs, repeat the process several times, and compute the average decoding agreement and decoding error (**Figure 2G**). Using this approach, we found in our conditions that using a uniform prior *P(S)* led to higher decoding agreement (0.37 ± 0.002, n = 30 trials; data expressed as mean ± SEM) compared to using observed prior probabilities (0.07 ± 0.004, n = 30 independent trials), or replacing the marginal likelihood (bias) *P(A)* by 1 (condition which we term 'unbiased' here; 0.07 ± 0.001, n = 30 independent trials; 1ANOVA, $F_{(2,87)} = 4521$, $P < 0.0001$; **Figure 2H**). Similarly, decoding error was lower using a uniform prior (8.12 ± 0.08 cm, n = 30 independent trials) compared to using an observed prior (13.18 ± 0.15 cm, n = 30 independent trials) or in unbiased conditions (49.34 ± 0.08 cm, n = 30 trials; $F_{(2,87)} = 44710$, $P < 0.0001$; **Figure 2I**).

Adding Temporal Constraints

Although decoding can be performed for each individual time point, this temporal independence can lead to spurious results (see decoded trajectory in **Figure 2D**, pink line in the bottom panel). Rationaly, if the mouse is at one end of the linear track, it is extremely unlikely to be found at the opposite end on the next frame. There are several ways to solve this problem and improve state estimation. A first method could be to build a transition matrix (such as one that would be used in a Markov process), and attribute null values to impossible transitions (such as going from one end of the linear track to the other), as well as uniform probabilities to adjacent states. One could then replace the observed or uniform prior *P(S)* by the appropriate realistic transition values at each individual timestep. Another method consists of taking the product of temporally adjacent posteriors. In that case, we would decode the mouse state by rewriting equation (7):

$$P\ (S|A_t) = \prod_{k=1}^{N}\prod_{l=1}^{L} \frac{P\ (A_{k,t=l}|S)\ \times P\ (S)}{P\ (A_{k,t=l})} \quad (11)$$

where $P\ (S|A_t)$ is the *a posteriori* distribution of states at time t. The number of past timesteps l used to estimate the mouse state at time t is determined by L. The effect of different values of L will be detailed in the following section. The advantage of this method is that it does not require to determine transition probabilities experimentally. In our conditions, temporal filtering can greatly improve reconstruction and remove erratic 'jumps' that can sometimes occur during decoding (**Figure 3A**).

Parameter Optimization

To find the best conditions to decode neuronal activity, it is possible to optimize parameters including (but not restricted to): number of cells used, portion of training set, temporal filtering window, or spatial filtering of tuning curves. For instance, we performed decoding on 30 sets of random epochs using several temporal filtering window sizes ranging from 0 (no filtering) to 2 s, and found that better reconstructions could be achieved using a 0.5 s filtering window, leading to smaller decoding errors (4.73 ± 0.04 cm, n = 30 independent trials per filtering window; 1ANOVA, $F_{(8,261)} = 1002$, $P < 0.0001$; **Figure 3B**). Interestingly, the bigger the temporal filtering window, the lower the decoding agreement (Pearson correlation, $R^2 = 0.96$, $P < 0.0001$, n = 30 independent trials per filtering window;

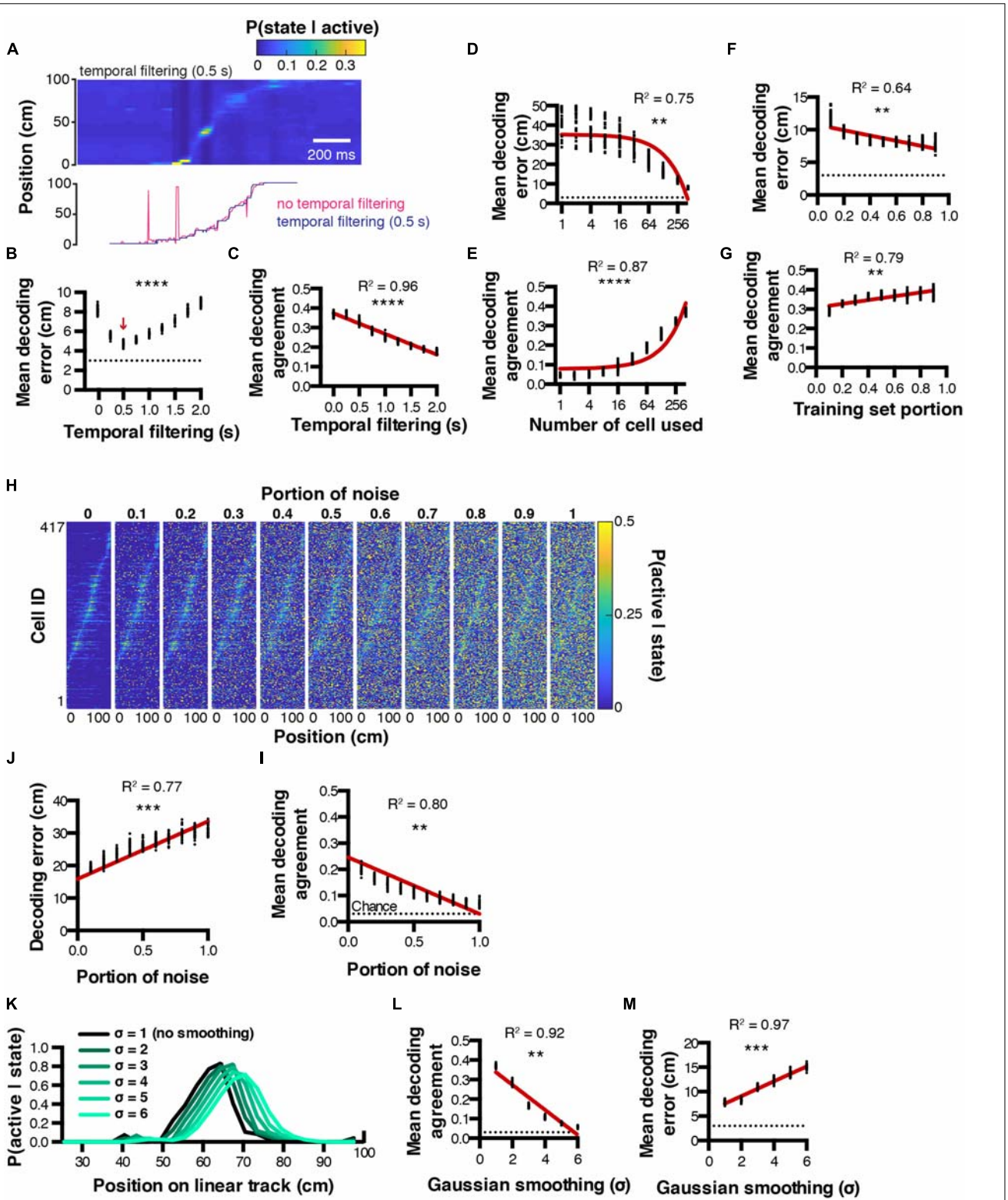

FIGURE 3 | Decoding parameter estimation. **(A)** Example posterior probabilities P(state| active) when using a 0.5 s temporal filtering window (top), and corresponding decoded location estimated from MAP (bottom). **(B,C)** Effect of temporal filtering window size on decoding error and agreement, respectively. **(D,E)** Effect of the number of cells used on decoding error and agreement, respectively. **(F,G)** Effect of training set portion on decoding error and agreement, respectively. **(H)** Effect of random noise on spatial tuning curves. **(I,J)** Corresponding decoding agreement and error, respectively. **(K)** Effect of gaussian smoothing on spatial tuning curves. **(L,M)** Corresponding decoding agreement and error, respectively. Color codes in **(A,H)**,: dark blue = low probability, yellow = high probability.

Figure 3C). As expected, considering more cells during the reconstruction resulted in decreased decoding error (Pearson correlation, $R^2 = 0.75$, $P < 0.0012$, $n = 30$ independent trials per cell number; **Figure 3D**) and increased decoding agreement (Pearson correlation, $R^2 = 0.87$, $P < 0.0001$, $n = 30$ independent trials per cell number; **Figure 3E**). We also tested the influence of the training/testing length ratio on reconstruction accuracy and found that good reconstruction can be achieved by using testing epochs that represent beyond 30 % of the total experiment length. Mean decoding error decreased as the training set portion increased (Pearson correlation, $R^2 = 0.64$, $P = 0.01$, $n = 30$ independent trials per training set portion tested; **Figure 3F**), while mean decoding agreement increased (Pearson correlation, $R^2 = 0.79$, $P = 0.0013$, $n = 30$ independent trials per training set portion tested; **Figure 3G**). We next assessed the robustness of tuning curves to random noise. To this end, we computed tuning curves as described previously, then replaced a portion (between 0 and 1, with 0.1 incremental steps) of the tuning curves data with random probability values (**Figure 3H**). Addition of noise was correlated with decreased decoding agreement (Pearson correlation, $R^2 = 0.80$, $P = 0.0014$, $n = 30$ independent trials per noise amount; **Figure 3I**), and increased decoding error (Pearson correlation, $R^2 = 0.77$, $P = 0.0004$, $n = 30$ independent trials per noise amount; **Figure 3J**). Finally, we tested the impact of smoothing tuning curves on decoding accuracy (**Figure 3K**). Gaussian smoothing is often performed in the context of place cell studies, presumably to improve the visualization of assumed place fields (O'Keefe and Burgess, 1996; Hetherington and Shapiro, 1997). In our conditions, we found that Gaussian smoothing of tuning curves was systematically associated with decreased decoding agreement (Pearson correlation, $R^2 = 0.92$, $P = 0.0025$; $n = 30$ independent trials per gaussian sigma value; **Figure 3L**), together with increasing decoding error (Pearson correlation, $R^2 = 0.97$, $P = 0.0003$, $n = 30$ independent trials per gaussian sigma value; **Figure 3M**).

Optimal Method to Binarize Neuronal Activity

In our conditions, we used a simple binarizing algorithm that transformed rising periods of calcium transients into periods of activity. We compared this method to a simple z-score threshold where all activity above 2 standard-deviations is considered active, and to a deconvolved signal using a first order autoregressive model (see methods), where all values above zero are considered as periods of activity. To quantify the accuracy of these methods, we performed *in vitro* electrophysiological recordings in the cell attached configuration, in conjunction with 1-photon calcium imaging (**Supplementary Figure 2a**). We extracted calcium transients from the recorded cell (**Supplementary Figure 2b**) so as to contrast these signals with ground truth spiking activity (**Supplementary Figure 2c**). Interestingly, calcium transients appeared much longer in these conditions, and our binarizing method only matched the later portion of transients rising periods (**Supplementary Figure 2d**). In the following analyses, we seperated the portion of action potentials successfully labeled as active periods in the corresponding calcium imaging recording frame, as well as the portion of total recorded frames that were either correctly labeled as active if they were associated with at least one action potential, or inactive if they did not. Using a deconvolved trace to estimate neuronal activity resulted in a higher number of action potentials successfully detected as corresponding calcium imaging active periods (0.94 ± 0.032) compared to our binarizing algorithm (0.49 ± 0.067) or a simple z-score threshold (0.65 ± 0.075; 1ANOVA, $F_{(2,108)} = 13.71$, $P < 0.0001$, $n = 37$ detection windows; **Supplementary Figure 2e**). Furthermore, both the portion of true negatives (calcium imaging frames binarized as inactive that indeed contained no action potential divided by the total number of recorded frames) and the portion of true positives (calcium imaging frames binarized as active that indeed contained at least one action potential, divided by total number of recorded frames) were comparable between methods (**Supplementary Figures 2f,g**, respectively).

Interestingly, these *in vitro* results did not compare to our *in vivo* conditions. When computing tuning curves for the neuron presented in **Figure 1**, using a simple threshold resulted in a larger place field, while binarizing data from a deconvolved trace resulted in two peaks (**Supplementary Figure 3a**). While there is no ground truth data to conclude which method is best to compute tuning curves, decoding analyzes can shed a light on this question, because animal behavior can be used as ground truth data (the higher the decoding accuracy, the closer to ground truth). We thus trained our decoder (Eq. 9) using tuning curves computed from binarized activity derived using a simple *z*-score threshold, a deconvolved trace, or using our binarizing method. We found that using both our binarizing method (4.74 ± 0.0039 cm) or a deconvolved trace (4.81 ± 0.048 cm) led to lower decoding errors compared to using a simple threshold (5.18 ± 0.051 cm, $F_{(2,87)} = 26.22$, $P < 0.0001$, $n = 30$ independent trials for each binarizing method; **Supplementary Figure 3b**).

Decoding Two-Dimensional Behavioral Variables

The decoding method presented above is scalable to a large variety of behaviors. However, sometimes it can be useful to represent behaviors in more than one dimension. This is for instance the case with spatial location in larger environments. We will now show that the principles presented above can easily be translated to more dimensions. To this end, we recorded neuronal activity using calcium imaging in a mouse exploring an open-field for the first time. Calcium transients are then extracted and binarized, along with the x and y mouse position (**Figure 4A**). It is possible to plot periods of activity of one cell in 2D space, and color code this activity to visualize the stability of such activity in time/space (**Figure 4B**). Relative occupancy (**Figure 4C**) and P(active| state) probabilities can be computed for each state (3×3 cm spatial bin) the same way as presented above (**Figure 4D**). The posterior probability distribution can then be derived (**Figure 4F**). To assess the confidence of the likelihood probability distribution, it is possible to shuffle data circularly and compute P(active| state) probability maps (**Figure 4E**). From these shuffled probability maps, we can derive the level of significance using a *p*-value that corresponds to the number of shuffled data points above the actual data divided by the number of shuffled surrogates (**Figure 4G**). We can then derive a thresholded place field that only retains significant values of

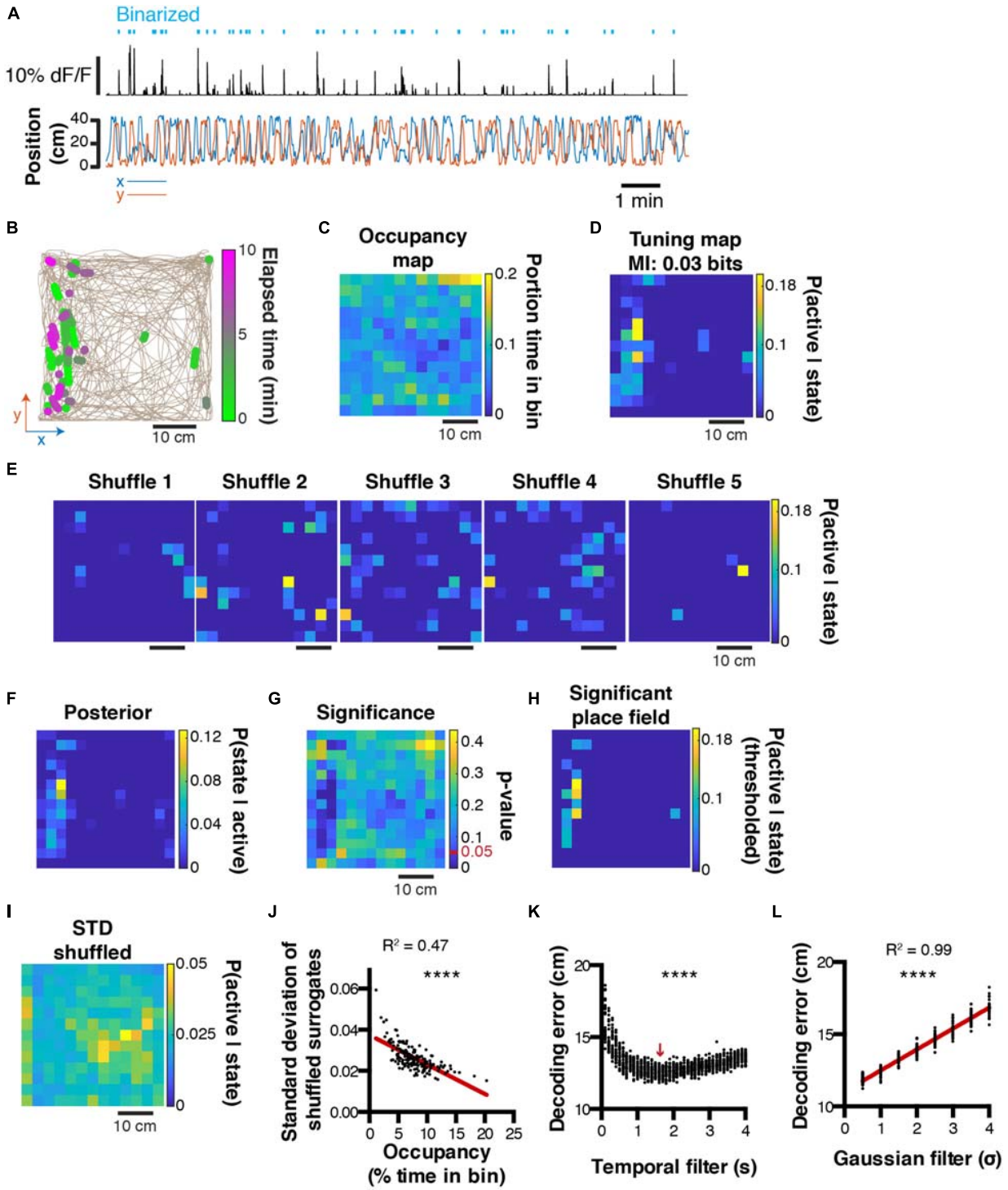

FIGURE 4 | Decoding two-dimensional behaviors. **(A)** *x,y* coordinates of mouse location in an open field (bottom) and corresponding raw calcium trace of one example cell and binarized activity (top). **(B)** Top view of mouse trajectory (beige trace) with overlaid location corresponding to neuronal activity (green, early activity; magenta, late activity). **(C)** Relative occupancy in the open field. **(D)** Tuning map (probability of being active given location) of one neuron. Top, corresponding MI index. **(E)** Example tuning maps computed from shuffled calcium traces. **(F)** Posterior probability P(state| active) for the same cell. **(G)** *P*-value computed from the actual tuning map and corresponding shuffled surrogates. **(H)** Thresholded place field using only significant P(active| state) values. **(I)** Standard-deviation of the shuffled distribution. **(J)** Scatter plot comparing the standard-deviation of the shuffled distribution, and the mouse open field occupancy. **(K)** Effect of temporal filtering on decoding error in the open field. The red arrow indicates the temporal filtering window size yielding the lower decoding error. **(L)** Effect of gaussian smoothing of tuning maps on decoding error in the open field.

P(active| state) (**Figure 4H**). Importantly, it is noteworthy that the standard-deviation of the shuffled distribution (**Figure 4I**) is negatively correlated to the relative occupancy (Pearson correlation, $R^2 = 0.47$, $P < 0.0001$; **Figure 4J**). This suggests that for states with high P(active| state) probabilities, significance can be higher if the state displays high occupancy, and lower if the state displays low occupancy. We also assessed the effect of temporal filtering on the quality of the reconstructions and found that in our conditions, a 1.6 s filtering window yielded best results (1ANOVA, $F_{(39,1160)} = 72.31$, $P < 0.0001$, $n = 30$ independent trials per temporal filter window size; **Figure 4K**). As for one-dimensional data, Gaussian filtering of tuning maps (2D tuning curves) consistently increased the decoding error (Pearson correlation, $R^2 = 0.99$, $P < 0.0001$, $n = 30$ independent trials per Gaussian sigma value; **Figure 4L**).

Refining Encoding Predictions

The ultimate goal of decoding neuronal activity is to improve our understanding of the relationship that may exist between neurons and behavior. In other terms, in addition to predicting behavior from neuronal activity, one should be able to predict neuronal activity from behavior. These encoding predictions can easily be derived from equation (3) since $P(S|A)$ represents the likelihood of a given neuron to be active while an animal is in a given state. This probability distribution can be interpreted as both a direct measure from our data, and a prediction of activity rate as a function of the animal location. Consequently, if $P(S|A)$ would take the value 1 for the given states i, we would be absolutely certain that the considered neuron would be active in these given states. In our linear track example, we can refine our encoding prediction since it has been previously shown that hippocampal place cell activity on a linear track tend to be unidirectional: some cell will fire in one given location, but only when being traversed in one direction (McNaughton et al., 1983; Markus et al., 1995). If the peak probability of being active $P(S|A)$ for a neuron that displays a prominent place field is only 0.5, it could be due to the fact that this cell fires only 50 % of the time, when the animal is running in one direction, but not in the other. We will now demonstrate that it is possible to predict neuronal activity from estimated tuning curves, and that refining our behavioral states by including directional information can increase our encoding prediction, i.e. the confidence we have that a neuron will fire given that the animal is in a given state. To this end, we extracted tuning curves from neurons being active on the linear track using either location only (**Figure 5A**), or by considering both location and direction (**Figure 5B**). Note that using the later method, the peak probability $P(S|A)$ greatly increases. When comparing probability values obtained from the same cells but using either technique, it seems that most cells' $P(S|A)$ increase when including traveling direction (Pearson correlation, $r = 0.8781$, $R^2 = 0.77$, $P < 0.0001$; **Figure 5C**). Interestingly, this is not the case for a minority of cells, indicating that some cells still display preferential activity for absolute location, regardless of direction. We then reconstructed neuronal activity using the $P(S|A)$ of each neuron for each known state i (location in our example) of the mouse. For display purposes, we only show probability values greater than 0.5 (**Figure 5D**). To estimate the confidence in neuronal activity predictions, we can use the same bootstrap method presented earlier to build 95% confidence intervals for $P(S|A)$ tuning curves computed by considering left, right, or both traveling directions (**Figure 5E**; $n = 1000$ bootstrap samples). The advantage of this method is that it gives a clear range of prediction accuracy that is easily interpretable. In our example neuron #4, it is apparent that greater encoding predictions can be achieved when only considering travels to the right (**Figure 5E**). Furthermore, we can use mutual information as a measure of how much uncertainty about neuronal activity can be reduced by knowing the state of the animal. In our example, we found that MI values were the highest when only considering travels to the right (0.22 ± 0.0005 bits), followed by considering both directions (0.09 ± 0.0002 bits), and only travels to the left (0.02 ± 0.0001 bits; 1ANOVA, $F_{(2,2997)} = 44.84$, $P < 0.0001$; $n = 1000$ bootstrap samples; **Figure 5F**).

DISCUSSION

We show here that representing neuronal activity extracted from calcium imaging data by a binary state (active vs. inactive) is sufficient to approximate the state of a neuronal assembly. While such binarization was previously proposed as an intermediate step to perform decoding (Ziv et al., 2013), here we generalize this principle and propose several additional metrics to describe the strength of neuronal tuning to behavioral variables. In particular, several methods can be used to binarize calcium activity, but because the rise time of calcium transients contains the vast majority of action potentials, binarizing methods should aim at labeling specifically these epochs as periods of activity. Importantly, optimizing methods and parameters using *in vitro* conditions cannot necessarily be translated to data acquired *in vivo* because calcium transients differ fundamentally across conditions, even if most variables are the same (animal strain/age, viral construct and dilution).

Information on neuronal coding can be extracted using simple methods and minimal data processing. Importantly, three metrics can be used to describe neurons: the likelihood of being active in a given behavioral state P(active| state), the posterior probability of the animal being in a state given neuronal activity P(state| active), and mutual information – a measure of reduction in uncertainty of the mouse state that results from knowing neuronal activity, and vice versa. Furthermore, we propose to determine significance by either computing a p-value value derived from shuffled surrogates, or estimating confidence intervals using bootstrap resampling. In particular, the later method provides confidence in encoding predictions that are easily interpretable.

While action potentials recorded with electrophysiological techniques constitute discrete temporal events, calcium imaging signals take the form of a continuous vector which prevents the direct computation of previously used information metrics: bits/s and bits/spike. On the other hand, MI values can easily be derived from probabilities computed above and provide useful insights in the amount of uncertainty that is reduced about the animal state given neuronal activity. It is noteworthy that the MI is sensitive to the number of bins used, therefore faithful comparisons between

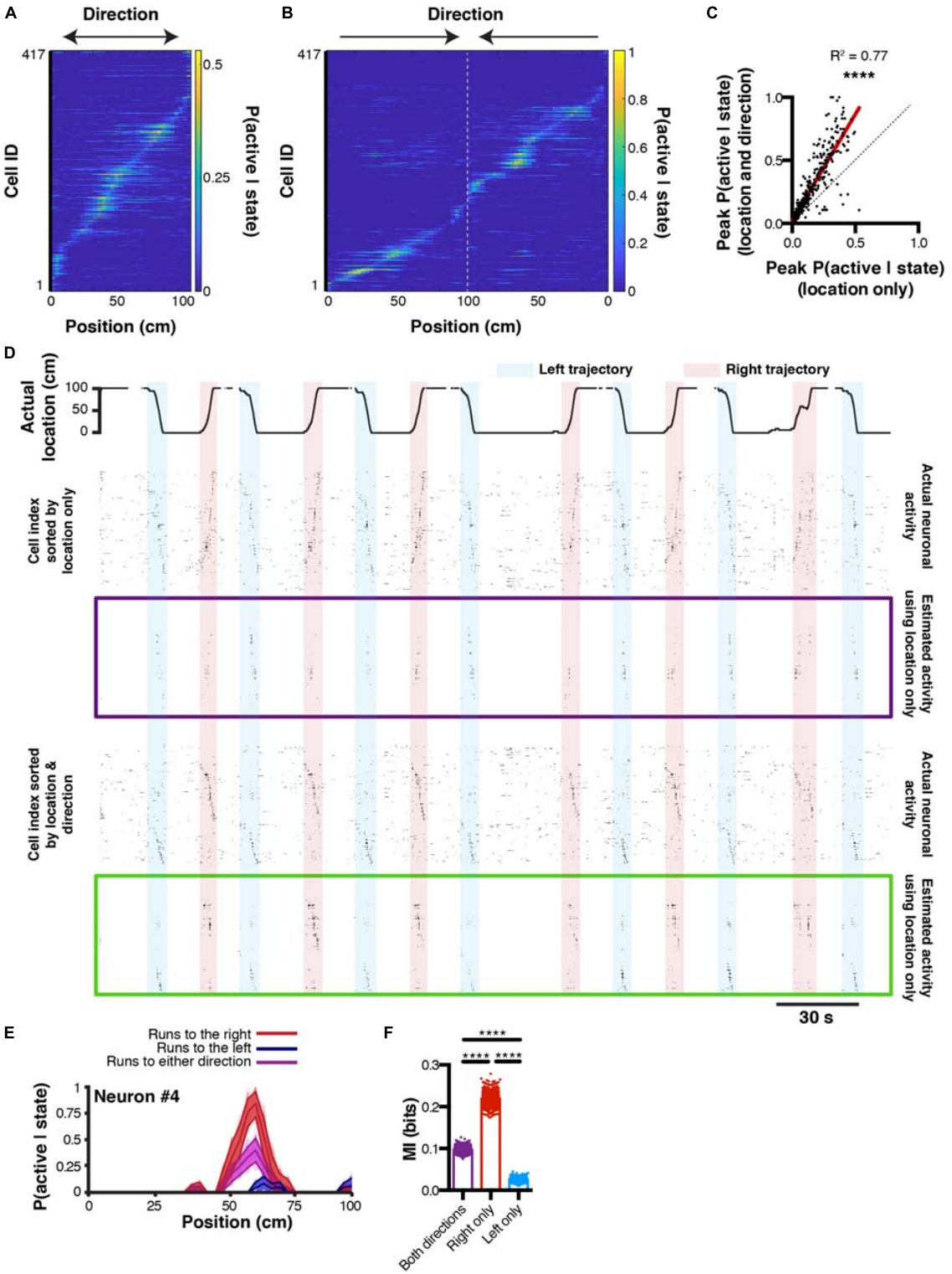

FIGURE 5 | Reconstructing neuronal activity and refining tuning curves. **(A)** Tuning curves of every neuron sorted by peak activity in the linear track. **(B)** Same, but after discriminating left and right trajectories. **(C)** Relationship between peak P(active| state) likelihood computed using either method (location only versus location and direction). **(D)** Actual location of the mouse in the linear track (top), and corresponding actual and reconstructed neuronal activity using location only (purple box), as well as actual and reconstructed neuronal activity using both location and direction (green box). **(E)** P(active| state) computed using either right (red), left (blue), or both (purple) trajectories. Thickness of curves indicate 95% confidence interval computed from n = 1000 bootstrap samples. **(F)** Corresponding MI for each bootstrap sample.

electrophysiological and calcium imaging data would require to compute MI values on electrophysiological and calcium imaging data where neuronal activity was binarized the same way as well as behavior discretized using the same binning parameters. Furthermore, while bursting activity is associated with large calcium transients that result in good decoding accuracy, single spikes might lead to changes in GCamp6 fluorescence that are too small to be detected, and could be associated with larger decoding errors in some conditions.

Unsurprisingly, we found that MI values are significantly correlated with peak P(active| state) probabilities, while in parallel, behavioral states with low occupancy display more variability in the surrogate data, which indicates that higher significance can be achieved when the sampling of behavioral states is higher. Importantly, the choice of a null hypothesis should be considered carefully. On one hand, if it is hypothesized that neurons become active in response to an external stimulus, then one should permute neuronal activity in respect to the time course of external stimuli under the null hypothesis. On the other hand, if it is hypothesized that the temporal organization of neurons (e.g. sequences) underlies certain cognitive processes (e.g. replay), then permutations should be performed so as to remove temporal patterns of neuronal activity (i.e. shuffle each neuron activity vector independently) under the null hypothesis.

Using such a probabilistic approach allows to derive predictions based on Bayes theorem. In our conditions, we found that minimal *a priori* (uniform distribution of states likelihood) yielded better results. Adding temporal constraints could decrease decoding error but not decoding agreement. Consequently, these filters have to be optimized on a case by case basis depending on the goal of the study. Interestingly, smoothing probability distributions had negative effects in our conditions, most likely due to the asymmetric nature of place fields when unfiltered. Such post-processing methods thus have to be used with caution, and while they can improve the visualization of particular phenomena such as place fields, they can result in spurious interpretations. While the method we describe here might not apply to any type of behavior, we present examples of one- and two-dimensional datasets, and the number of dimensions being studied should not be a limiting factor. One of the most significant limitations with this method arises directly from behavioral sampling, and only behaviors that are directly sampled can be reconstructed or used to predict neuronal activity. For alternative approaches that do not make assumptions about behaviors being encoded in neuronal activity, the use of dimensionality reduction techniques has been proposed (Rubin et al., 2019), and if sequential patterns are hypothesized to underlie behaviors, matrix factorization methods can be used instead (Mackevicius et al., 2018). Moreover, when multiple variables contribute to variability in neuronal activity, generalized linear models can outperform the methods presented here (Park et al., 2014), at the expense of requiring significantly more data points which may or may not be compatible with calcium imaging approaches, depending on the activity rate of neurons being studied.

Finally, we propose a simple method to characterize neuronal encoding and predict neuronal activity. This method is useful in refining the behavioral components that can determine neuronal activity. As such, the quality of models that can be drawn from observations largely depends on the very nature and accuracy of these observations. In particular, increasing the amount of information concerning a certain behavior can result in a refinement of the underlying model of neuronal activity. Perfect predictions of neuronal activity on the simple basis of behavior is a difficult endeavor, however, because such activity is not only determined by external variables (behavior) but also internal variables including animal state, and pre-synaptic activity that is often inaccessible to the observer. In this context, previous work has outlined organized patterns of neuronal activity that are usually associated with spatial location while animals did not perceive any external stimuli other than self-motion (Villette et al., 2015). Moreover, taking into account the interdependence of neuronal activity could also improve the quality of predictions. In particular, including pairwise (Pillow et al., 2008; Meshulam et al., 2017) or temporal (Naud and Gerstner, 2012) correlations of neuronal activity could reduce decoding error. Note that these temporal correlations would also be taken into account when using long short-term memory (LSTM) artificial neural networks (Tampuu et al., 2019), thus increasing reconstruction accuracy at the expense of interpretability. Rather than proposing a sophisticated analysis pipeline, the methods presented here have the advantage of remaining simple, requiring only few data points, and are easily interpretable using metrics that can facilitate the communication of results along with significance and confidence intervals, making it an appropriate tool for exploration of calcium imaging data in conjunction with behavior.

MATERIALS AND METHODS

Surgical Procedures

All procedures were approved by the McGill University Animal Care Committee and the Canadian Council on Animal Care. For the linear track and open field data, one adult mouse (∼2 months) was anesthetized with isoflurane (5% induction, 0.5–2% maintenance) and placed in a stereotaxic frame (Stoelting). The skull was completely cleared of all connective tissue, and a ∼500 μm hole was drilled. We then injected the AAV5.CamKII.GCaMP6f.WPRE.SV40 virus (Addgene # 100834; 200 nL at 1 $nl.s^{-1}$) in hippocampal CA1 using the following coordinates: anteroposterior (AP) −1.86 mm from bregma, mediolateral (ML) 1.5 mm, dorsoventral (DV) 1.5 mm. 2 weeks following the injection, the mouse was anesthetized with isoflurane and the skull was cleared. A ∼2 mm diameter hole was perforated in the skull above the injection site. An anchor screw was placed on the posterior plate above the cerebellum. The dura was removed, and the portion of the cortex above the injection site was aspirated using a vacuum pump, until the corpus callosum was visible. These fiber bundles were then gently aspirated without applying pressure on the underlying hippocampus, and a 1.8 mm diameter gradient index (GRIN; Edmund Optics) lens was lower at the following coordinates: AP −1.86 mm from bregma, ML 1.5 mm, DV 1.2 mm. The GRIN

lens was permanently attached to the skull using C&B-Metabond (Patterson dental), and Kwik-Sil (World Precision Instruments) silicone adhesive was placed on the GRIN to protect it. 4 weeks later, the silicone cap was removed and CA1 was imaged using a miniscope mounted with an aluminium base plate while the mouse was under light anesthesia (∼0.5 % isoflurane) to allow the visualization of cell activity. When a satisfying field of view was found (large neuronal assembly, visible landmarks), the base plate was cemented above the GRIN lens, the miniscope was removed, and a plastic cap was placed on the base plate to protect the GRIN lens.

Behavior and Miniscope Recordings

After baseplating, the mouse was gently handled for ∼5 min per day for 7 days. The mouse was then water-scheduled (2 h access per day), and placed on a 1 m long linear track for 15 min. 10% sucrose in water rewards were placed at each end of the linear track, and the mouse had to consume one reward before getting the next one delivered. Miniscope recordings were performed at 30 Hz for 15 min every day, and decoding was performed on the last training day (day 7). The following week, the mouse was allowed to freely explore for 15 min a 45 × 45 cm dark gray open-field that contained visual cues, and miniscope recordings were performed at 30 Hz for the entire duration of the exploration (15 min).

Miniscope and Behavior Video Acquisition

Miniscopes were manufactured using open source plans available on www.miniscope.org and as described previously (Ghosh et al., 2011; Cai et al., 2016; Aharoni and Hoogland, 2019). Imaging data was acquired using a CMOS imaging sensor (Aptina, MT9V032) and multiplexed through a lightweight coaxial cable. Data was acquired using a data acquisition (DAQ) box connected via a USB host controller (Cypress, CYUSB3013). Data was recorded using a custom written acquisition software relying on Open Computer Vision (OpenCV) librairies. Video streams were recorded at ∼30 frames per second (30 Hz) and saved as uncompressed.avi files. Animal behavior was recorded using a webcam, and the DAQ software simultaneously recorded timestamps for both the miniscope and behavior camera in order to perform subsequent alignment.

Calcium Imaging Analysis

Calcium imaging videos were analyzed using the MiniscopeAnalysis pipeline[2]. In particular, we first applied rigid motion correction using NoRMCorre (Pnevmatikakis and Giovannucci, 2017). 1000 frame videos were then concatenated into a large video file after a 2 fold spatial downsampling. Spatial components as well as calcium traces were then extracted using CNMFe (Zhou et al., 2018) using the following parameters: gSig = 3 pixels (width of gaussian kernel), gSiz = 15 pixels (approximate neuron diameter), background_model = 'ring', spatial_algorithm = 'hals', min_corr = 0.8 (minimum pixel correlation threshold), min_PNR = 8 (minimum peak-to-noise ratio threshold). When applicable, calcium traces were deconvolved with OASIS (Friedrich et al., 2017), using an autoregressive model with order $p = 1$ and using the 'constrained' method.

[2]https://github.com/etterguillaume/MiniscopeAnalysis

In vitro Patch-Clamp Electrophysiology

One adult mouse (∼2 months) was stereotaxically injected with a GCaMP6f construct (AAV5.CamKII.GCaMP6f.WPRE.SV40 virus, Addgene # 100834; 0.4 µL at 0.06 µl/min) in hippocampal CA1. 2 weeks later, it was deeply anesthetized using ketamine/xylazine/acepromazine mix (100, 16, 3 mg/kg, respectively, intraperitoneal injection), and intracardially perfused with cold N-methyl-D-glutamine (NMDG) recovery solution (4°C), oxygenated with carbogen (5% CO2/95% O2). The NMDG solution contained the following (in mM): 93 NMDG, 93 HCl, 2.5 KCl, 1.2 NaH2PO4, 30 NaHCO3, 20 HEPES, 25 glucose, 5 sodium ascorbate, 2 thiourea, 3 sodium pyruvate, pH adjusted to 7.4 with HCl before adding 10 $MgSO_4$ and 0.5 $CaCl_2$. Following NMDG perfusion, brains were quickly removed and immersed for an additional 1 min in cold NMDG recovery solution. Coronal slices (300 µm) were cut using a vibratome (Leica-VT1000S), then collected in a 32°C NMDG recovery solution for 12 min. Slices were transferred to room temperature and oxygenated artificial cerebrospinal fluid (aCSF) containing the following (in mM): 124 NaCl, 24 NaHCO3, 2.5 KCl, 1.2 NaH2PO4, 2 MgSO4, 5 HEPES, 2 $CaCl_2$ and 12.5 glucose (pH 7.4). Patch pipettes (3–5 MΩ) were filled with internal solution, containing the following (in mM): 140 K gluconate, 2 MgCl2, 10 HEPES, 0.2 EGTA, 2 NaCl, 2 mM Na2-ATP and 0.3 mM Na2-GTP, pH adjusted to 7.3 with KOH, 290 mOsm. Slices were transferred to a submerged recording chamber filled with aCSF (2–3 ml/min flow rate, 30 °C), continuously oxygenated with carbogen. All reagents were purchased from Sigma-Aldrich, unless stated otherwise. Extracellular cell-attached patch-clamp recordings were used for monitoring spontaneous cell firing activity from hippocampal pyramidal neurons expressing GcAMP6f (identified under EGFP-fluorescence). The recording pipette was held at a potential of −70 mV. Imaging of GcAMP6f-expressing pyramidal cells was performed with a 60x Olympus water immersion objective (LUMPLFLN60X/W, NA 1.0) and acquired at 10 Hz using Olympus cellSens software. Electrophysiological signals were amplified, using a Multiclamp 700B patch-clamp amplifier (Axon Instruments), sampled at 20 kHz, and filtered at 10 kHz.

Statistics

Statistical analyses were performed using GraphPad Prism version 6.00 (GraphPad Software, La Jolla, CA, United States). All data are presented as mean ± standard error of the mean (SEM) and statistical test details are described in the corresponding results. All *t*-tests are two-tailed. Normality distribution of each group was assessed using the Shapiro-Wilk normality test and parametric tests were used only when distributions were found normal (non-parametric tests are described where applicable). 1ANOVA: one-way ANOVA; 2ANOVA: two-way ANOVA; RMANOVA: repeated measure ANOVA. $p < 0.05$

was considered statistically significant. $^{*}p < 0.05$; $^{**}p < 0.01$; $^{***}p < 0.001$, $^{****}p < 0.0001$.

DATA AVAILABILITY STATEMENT

All the code and data presented here can be downloaded at the following address: https://github.com/etterguillaume/CaImDecoding.

ETHICS STATEMENT

The animal study was reviewed and approved by the McGill University Animal Care Committee Canadian Council on Animal Care.

AUTHOR CONTRIBUTIONS

GE and SW designed the study. GE performed surgeries, behavioral the experiments, and analyzes. FM performed patch clamp *in vitro* electrophysiology. GE and SW wrote the manuscript.

FUNDING

This work is supported by Brain Canada, Fonds de la recherche en Santé du Québec (FRSQ), the Canadian Institutes of Health Research (CIHR), the Natural Sciences and Engineering Research Council of Canada (NSERC), and Healthy Brains, Healthy Lives (HBHL).

ACKNOWLEDGMENTS

We thank Ke Cui for support maintaining the colony and perfusing mice, Daniel Aharoni for support using the miniaturized fluorescence microscopes (www.miniscope.org), Bruno Rivard for manufacturing the miniscopes, and Suzanne van der Veldt for helpful comments on the manuscript.

SUPPLEMENTARY MATERIAL

The Supplementary Material for this article can be found online at: https://www.frontiersin.org/articles/10.3389/fncir.2020.00019/full#supplementary-material

REFERENCES

Aharoni, D., and Hoogland, T. M. (2019). Circuit investigations with open-source miniaturized microscopes: past, present and future. *Front. Cell. Neurosci.* 13:141. doi: 10.3389/fncel.2019.00141

Belle, A. M., Enright, H. A., Sales, A. P., Kulp, K., Osburn, J., Kuhn, E. A., et al. (2018). Evaluation of in vitro neuronal platforms as surrogates for in vivo whole brain systems. *Sci. Rep.* 8:10820. doi: 10.1038/s41598-018-28950-5

Brown, E. N., Frank, L. M., Tang, D., Quirk, M. C., and Wilson, M. (1998). A statistical paradigm for neural spike train decoding applied to position prediction from ensemble firing patterns of rat hippocampal place cells. *J. Neurosci.* 18, 7411–7425. doi: 10.1523/jneurosci.18-18-07411.1998

Cai, D. J., Aharoni, D., Shuman, T., Shobe, J., Biane, J., Song, W., et al. (2016). A shared neural ensemble links distinct contextual memories encoded close in time. *Nature* 534, 115–118. doi: 10.1038/nature17955

Chen, T., Wardill, T. J., Sun, Y., Pulver, S. R., Renninger, S. L., Baohan, A., et al. (2013). Ultra-sensitive fluorescent proteins for imaging neuronal activity. *Nature* 499, 295–300.

Cohen, M. X. (2014). *Analyzing Neural Time Series Data: Theory And Practice*. Cambridge, MA: The MIT Press.

Davidson, T. J., Kloosterman, F., and Wilson, M. A. (2009). Hippocampal replay of extended experience. *Neuron* 63, 497–507. doi: 10.1016/j.neuron.2009.07.027

Deneux, T., Kaszas, A., Szalay, G., Katona, G., Lakner, T., Grinvald, A., et al. (2016). Accurate spike estimation from noisy calcium signals for ultrafast three-dimensional imaging of large neuronal populations in vivo. *Nat. Commun.* 7:12190. doi: 10.1038/ncomms12190

Diba, K., and Buzsáki, G. (2007). Forward and reverse hippocampal place-cell sequences during ripples. *Nat. Neurosci.* 10, 1241–1242. doi: 10.1038/nn1961

Dimitrov, A. G., Lazar, A. A., and Victor, J. D. (2011). Information theory in neuroscience. *J. Comput. Neurosci.* 30, 1–5. doi: 10.1007/s10827-011-0314-3

Foster, D. J., and Wilson, M. A. (2006). Reverse replay of behavioural sequences in hippocampal place cells during the awake state. *Nature* 440, 680–683. doi: 10.1038/nature04587

Friedrich, J., Zhou, P., and Paninski, L. (2017). Fast online deconvolution of calcium imaging data. *PLoS Comput. Biol.* 13:e1005423. doi: 10.1371/journal.pcbi.1005423

Gerwinn, S. (2009). Bayesian population decoding of spiking neurons. *Front. Comput. Neurosci.* 3:2009. doi: 10.3389/neuro.10.021.2009

Ghosh, K. K., Burns, L. D., Cocker, E. D., Nimmerjahn, A., Ziv, Y., Gamal, A. E., et al. (2011). Miniaturized integration of a fluorescence microscope. *Nat. Methods* 8, 871–878. doi: 10.1038/nmeth.1694

Giovannucci, A., Friedrich, J., Gunn, P., Kalfon, J., Koay, S. A., Taxidis, J., et al. (2018). CaImAn: an open source tool for scalable calcium imaging data analysis. *bioRxiv* [Preprint], doi: 10.1101/339564

Giovannucci, A., Friedrich, J., Kaufman, M., Churchland, A., Chklovskii, D., Paninski, L., et al. (2017). Onacid: online analysis of calcium imaging data in real time. *Adv. Neural Inf. Process. Syst.* 30, 2381–2391.

Gonzalez, W. G., Zhang, H., Harutyunyan, A., and Lois, C. (2019). Persistence of neuronal representations through time and damage in the hippocampus. *Science* 365, 821–825. doi: 10.1126/science.aav9199

Grewe, B. F., Gründemann, J., Kitch, L. J., Lecoq, J. A., Parker, J. G., Marshall, J. D., et al. (2017). Neural ensemble dynamics underlying a long-term associative memory. *Nature* 543, 670–675. doi: 10.1038/nature21682

Grynkiewicz, G., Poenie, M., and Tsien, R. Y. (1985). A new generation of Ca2+ indicators with greatly improved fluorescence properties. *J. Biol. Chem.* 260, 3440–3450.

Hetherington, P. A., and Shapiro, M. L. (1997). Hippocampal place fields are altered by the removal of single visual cues in a distance-dependent manner. *Behav. Neurosci.* 111, 20–34. doi: 10.1037/0735-7044.111.1.20

Hubel, D. H., and Wiesel, T. N. (1962). Receptive fields, binocular interaction and functional architecture in the cat's visual cortex. *J. Physiol.* 160, 106–154. doi: 10.1113/jphysiol.1962.sp006837

Huber, D., Gutnisky, D. A., Peron, S., O'Connor, D. H., Wiegert, J. S., Tian, L., et al. (2012). Multiple dynamic representations in the motor cortex during sensorimotor learning. *Nature* 484, 473–478. doi: 10.1038/nature11039

Kass, R. E., Eden, U., and Brown, E. N. (2014). *Analysis of Neural Data*. New York, NY: Springer, doi: 10.1007/978-1-4614-9602-1

Katsuki, Y., Uchiyama, H., Watanabe, T., and Maruyama, N. (1956). Electric responses of auditory neurons in cat to sound stimulation. *II. Proc. Jpn. Acad.* 32, 504–506. doi: 10.2183/pjab1945.32.504

Kondo, T., Saito, R., Otaka, M., Yoshino-Saito, K., Yamanaka, A., Yamamori, T., et al. (2018). Calcium transient dynamics of neural ensembles in the primary motor cortex of naturally behaving monkeys. *Cell Rep.* 24, 2191.e–2195.e. doi: 10.1016/j.celrep.2018.07.057

Koyama, S., Eden, U. T., Brown, E. N., and Kass, R. E. (2010). Bayesian decoding of neural spike trains. *Ann. Inst. Stat. Math.* 62, 37–59. doi: 10.1007/s10463-009-0249-x

Mackevicius, E. L., Bahle, A. H., Williams, A. H., Denissenko, N. I., Goldman, M. S., and Fee, M. S. (2018). Unsupervised discovery of temporal sequences in high-dimensional datasets, with applications to neuroscience. *eLife* 8:38471.

Markus, E. J., Qin, Y. L., Leonard, B., Skaggs, W. E., McNaughton, B. L., and Barnes, C. A. (1995). Interactions between location and task affect the spatial and directional firing of hippocampal neurons. *J. Neurosci.* 15, 7079–7094. doi: 10.1523/JNEUROSCI.15-11-07079.1995

Mau, W., Sullivan, D. W., Kinsky, N. R., Hasselmo, M. E., Howard, M. W., and Eichenbaum, H. (2018). The same hippocampal CA1 Population simultaneously codes temporal information over multiple timescales. *Curr. Biol.* 28, 1499–1508.e4. doi: 10.1016/j.cub.2018.03.051

McNaughton, B. L., Barnes, C. A., and O'Keefe, J. (1983). The contributions of position, direction, and velocity to single unit activity in the hippocampus of freely-moving rats. *Exp. Brain Res.* 52, 41–49. doi: 10.1007/BF00237147

Meshulam, L., Gauthier, J. L., Brody, C. D., Tank, D. W., and Bialek, W. (2017). Collective behavior of place and non-place neurons in the hippocampal network. *Neuron* 96, 1178–1191.e4. doi: 10.1016/j.neuron.2017.10.027

Nakai, J., Ohkura, M., and Imoto, K. (2001). A high signal-to-noise Ca(2+) probe composed of a single green fluorescent protein. *Nat. Biotechnol.* 19, 137–141. doi: 10.1038/84397

Naud, R., and Gerstner, W. (2012). Coding and decoding with adapting neurons: a population approach to the peri-stimulus time histogram. *PLoS Comput. Biol.* 8:e1002711. doi: 10.1371/journal.pcbi.1002711

Ohkura, M., Sasaki, T., Sadakari, J., Gengyo-Ando, K., Kagawa-Nagamura, Y., Kobayashi, C., et al. (2012). Genetically encoded green fluorescent Ca2+ indicators with improved detectability for neuronal Ca2+ signals. *PLoS One* 7:e51286. doi: 10.1371/journal.pone.0051286

O'Keefe, J., and Burgess, N. (1996). Geometric determinants of the place fields of hippocampal neurons. *Nature* 381, 425–428. doi: 10.1038/381425a0

O'Keefe, J., and Dostrovsky, J. (1971). The hippocampus as a spatial map. Preliminary evidence from unit activity in the freely-moving rat. *Brain Res.* 34, 171–175. doi: 10.1016/0006-8993(71)90358-1

Pachitariu, M., Stringer, C., and Harris, K. D. (2018). Robustness of spike deconvolution for neuronal calcium imaging. *J. Neurosci.* 38, 7976–7985. doi: 10.1523/jneurosci.3339-17.2018

Park, I. M., Meister, M. L. R., Huk, A. C., and Pillow, J. W. (2014). Encoding and decoding in parietal cortex during sensorimotor decision-making. *Nat. Neurosci.* 17, 1395–1403. doi: 10.1038/nn.3800

Persechini, A., Lynch, J. A., and Romoser, V. A. (1997). Novel fluorescent indicator proteins for monitoring free intracellular Ca2+. *Cell Calcium* 22, 209–216. doi: 10.1016/S0143-4160(97)90014-2

Pillow, J. W., Shlens, J., Paninski, L., Sher, A., Litke, A. M., Chichilnisky, E. J., et al. (2008). Spatio-temporal correlations and visual signalling in a complete neuronal population. *Nature* 454, 995–999. doi: 10.1038/nature07140

Pnevmatikakis, E. A., and Giovannucci, A. (2017). NoRMCorre: An online algorithm for piecewise rigid motion correction of calcium imaging data. *J. Neurosci. Methods* 291, 83–94. doi: 10.1016/j.jneumeth.2017.07.031

Pnevmatikakis, E. A., Soudry, D., Gao, Y., Machado, T. A., Merel, J., Pfau, D., et al. (2016). Simultaneous denoising, deconvolution, and demixing of calcium imaging data. *Neuron* 89:299. doi: 10.1016/j.neuron.2015.11.037

Quian Quiroga, R., and Panzeri, S. (2009). Extracting information from neuronal populations: Information theory and decoding approaches. *Nat. Rev. Neurosci.* 10, 173–185. doi: 10.1038/nrn2578

Rahmati, V., Kirmse, K., Holthoff, K., and Kiebel, S. J. (2018). Ultra-fast accurate reconstruction of spiking activity from calcium imaging data. *J. Neurophysiol.* 119, 1863–1878. doi: 10.1152/jn.00934.2017

Richmond, B. J., and Optican, L. M. (1990). Temporal encoding of two-dimensional patterns by single units in primate primary visual cortex. II. Information transmission. *J. Neurophysiol.* 64, 370–380. doi: 10.1152/jn.1990.64.2.370

Richmond, B. J., Optican, L. M., and Spitzer, H. (1990). Temporal encoding of two-dimensional patterns by single units in primate primary visual cortex. I. Stimulus-response relations. *J. Neurophysiol.* 64, 351–369. doi: 10.1152/jn.1990.64.2.351

Rubin, A., Sheintuch, L., Brande-Eilat, N., Pinchasof, O., Rechavi, Y., Geva, N., et al. (2019). Revealing neural correlates of behavior without behavioral measurements. *Nat. Commun.* 10, 1–14. doi: 10.1038/s41467-019-12724-2

Shannon, C. E. (1948). A mathematical theory of communication. *Bell Syst. Tech. J.* 27, 379–423. doi: 10.1002/j.1538-7305.1948.tb01338.x

Sheintuch, L., Rubin, A., Brande-Eilat, N., Geva, N., Sadeh, N., Pinchasof, O., et al. (2017). Tracking the same neurons across multiple days in ca2+ imaging data. *Cell Rep.* 21, 1102–1115. doi: 10.1016/j.celrep.2017.10.013

Skaggs, W. E., McNaughton, B. L., and Gothard, K. M. (1993). "An information-theoretic approach to deciphering the hippocampal code," in *Advances in Neural Information Processing Systems*, 1030–1037.

Souza, B. C., Pavão, R., Belchior, H., and Tort, A. B. L. (2018). On information metrics for spatial coding. *Neuroscience* 375, 62–73. doi: 10.1016/j.neuroscience.2018.01.066

Tampuu, A., Matiisen, T., Ólafsdóttir, H. F., Barry, C., and Vicente, R. (2019). Efficient neural decoding of self-location with a deep recurrent network. *PLoS Comput. Biol.* 15:e1006822. doi: 10.1371/journal.pcbi.1006822

Tegtmeier, J., Brosch, M., Janitzky, K., Heinze, H.-J., Ohl, F. W., and Lippert, M. T. (2018). CAVE: an open-source tool for combined analysis of head-mounted calcium imaging and behavior in MATLAB. *Front. Neurosci.* 12:958. doi: 10.3389/fnins.2018.00958

Tian, L., Hires, S. A., Mao, T., Huber, D., Chiappe, M. E., Chalasani, S. H., et al. (2009). Imaging neural activity in worms, flies and mice with improved GCaMP calcium indicators. *Nat. Methods* 6, 875–881. doi: 10.1038/nmeth.1398

Villette, V., Malvache, A., Tressard, T., Dupuy, N., and Cossart, R. (2015). Internally recurring hippocampal sequences as a population template of spatiotemporal information. *Neuron* 88, 357–366. doi: 10.1016/j.neuron.2015.09.052

Zhang, K., Ginzburg, I., McNaughton, B. L., and Sejnowski, T. J. (1998). Interpreting neuronal population activity by reconstruction: unified framework with application to hippocampal place cells. *J. Neurophysiol.* 79, 1017–1044. doi: 10.1152/jn.1998.79.2.1017

Zhou, P., Resendez, S. L., Rodriguez-Romaguera, J., Jimenez, J. C., Neufeld, S. Q., Giovannucci, A., et al. (2018). Efficient and accurate extraction of in vivo calcium signals from microendoscopic video data. *eLife* 7:e28728. doi: 10.7554/eLife.28728

Ziv, Y., Burns, L. D., Cocker, E. D., Hamel, E. O., Ghosh, K. K., Kitch, L. J., et al. (2013). Long-term dynamics of CA1 hippocampal place codes. *Nat. Neurosci.* 16, 264–266. doi: 10.1038/nn.3329

Conflict of Interest: The authors declare that the research was conducted in the absence of any commercial or financial relationships that could be construed as a potential conflict of interest.

frontiers in Neural Circuits

ORIGINAL RESEARCH
published: 25 May 2020
doi: 10.3389/fncir.2020.00021

Ultradian Secretion of Growth Hormone in Mice: Linking Physiology With Changes in Synapse Parameters Using Super-Resolution Microscopy

Klaudia Bednarz[1,2], Walaa Alshafie[1,3], Sarah Aufmkolk[4], Théotime Desserteaux[1], Pratap Singh Markam[3,5], Kai-Florian Storch[5,6] and Thomas Stroh[1,2]**

[1]Department of Neurology and Neurosurgery, Montreal Neurological Institute, McGill University, Montreal, QC, Canada, [2]Department of Anatomy and Cell Biology, McGill University, Montreal, QC, Canada, [3]Integrated Program in Neuroscience, McGill University, Montreal, QC, Canada, [4]Department of Genetics, Harvard Medical School, Boston, MA, United States, [5]Douglas Mental Health University Institute, Montreal, QC, Canada, [6]Department of Psychiatry, McGill University, Montreal, QC, Canada

Neuroendocrine circuits are orchestrated by the pituitary gland in response to hypothalamic hormone-releasing and inhibiting factors to generate an ultradian and/or circadian rhythm of hormone secretion. However, mechanisms that govern this rhythmicity are not fully understood. It has been shown that synaptic transmission in the rodent hypothalamus undergoes cyclical changes in parallel with rhythmic hormone secretion and a growing body of evidence suggests that rapid rewiring of hypothalamic neurons may be the source of these changes. For decades, structural synaptic studies have been utilizing electron microscopy, which provides the resolution suitable for visualizing synapses. However, the small field of view, limited specificity and manual analysis susceptible to bias fuel the search for a more quantitative approach. Here, we apply the fluorescence super-resolution microscopy approach *direct* Stochastic Optical Reconstruction Microscopy (*d*STORM) to quantify and structurally characterize excitatory and inhibitory synapses that contact growth hormone-releasing-hormone (GHRH) neurons during peak and trough values of growth hormone (GH) concentration in mice. This approach relies on a three-color immunofluorescence staining of GHRH and pre- and post-synaptic markers, and a quantitative analysis with a Density-Based Spatial Clustering of Applications with Noise (DBSCAN) algorithm. With this method we confirm our previous findings, using electron microscopy, of increased excitatory synaptic input to GHRH neurons during peak levels of GH. Additionally, we find a shift in synapse numbers during low GH levels, where more inhibitory synaptic inputs are detected. Lastly, we utilize *d*STORM to study novel aspects of synaptic structure. We show that more excitatory (but not inhibitory) pre-synaptic clusters associate with excitatory post-synaptic clusters during peaks of GH secretion and that the numbers of post-synaptic clusters increase during high hormone levels. The results presented here provide an opportunity to highlight *d*STORM as a valuable quantitative approach to study synaptic structure in the neuroendocrine circuit. Importantly, our analysis of GH circuitry sheds light on the potential mechanism that drives ultradian changes in synaptic transmission and possibly aids in GH pulse generation in mice.

Keywords: *d*STORM, SMLM, growth hormone, structural synaptic study, neuroendocrine circuits

OPEN ACCESS

Edited by:
Yves De Koninck,
Laval University, Canada

Reviewed by:
Marco Mainardi,
Institute of Neuroscience (CNR), Italy
Michael R. Akins,
Drexel University, United States

****Correspondence:***
Klaudia Bednarz
klaudia.bednarz@mail.mcgill.ca
Thomas Stroh
thomas.stroh@mcgill.ca

Received: *24 January 2020*
Accepted: *14 April 2020*
Published: *25 May 2020*

Citation:
Bednarz K, Alshafie W, Aufmkolk S, Desserteaux T, Markam PS, Storch K-F and Stroh T (2020) Ultradian Secretion of Growth Hormone in Mice: Linking Physiology With Changes in Synapse Parameters Using Super-Resolution Microscopy. Front. Neural Circuits 14:21. doi: 10.3389/fncir.2020.00021

INTRODUCTION

Growth Hormone (GH) is a major regulator of longitudinal growth during childhood and puberty, and of anabolic metabolism in mammals throughout life. It is released in a pulsatile fashion with major episodes of GH secretion occurring at approximately 3-h intervals followed by prolonged trough periods of near undetectable basal serum GH levels in most species (Tannenbaum and Martin, 1976; Bertherat et al., 1995). This rhythm of GH secretion appears to be generated by the interaction of two hypothalamic neuropeptides, excitatory GH-Releasing Hormone (GHRH) and inhibitory somatostatin (SOM, a.k.a. Somatotropin Release-Inhibiting Factor, SRIF) in the hypophysis and in the hypothalamic arcuate nucleus (ARC). In male rodents, these two regulatory peptides are released in reciprocal 3–4 h cycles in the median eminence of the hypothalamus, where they enter the hypophyseal portal blood supply and thereby reach somatotropes in the anterior lobe of the hypophysis (Tannenbaum and Ling, 1984; Plotsky and Vale, 1985). It has been hypothesized that SOM is released into the ARC with the same periodicity (Wagner et al., 1998). Recently, we have also shown that the release of the stimulating hormone from the hypothalamus together with the cellular localization of SOM receptors in pituitary cells fine-tunes the rhythms of pituitary hormone secretion (Alshafie et al., 2019).

In parallel with this ultradian cycle of GH secretion and reciprocal secretion of regulatory hypothalamic neuropeptides, it was found that the binding of radiolabeled SOM to the ARC in rodents also oscillates, exhibiting the same periodicity as GH secretion (Tannenbaum et al., 1993). This led to the hypothesis that differential plasma membrane targeting of somatostatin receptors, which are increasing the susceptibility of GHRH neurons in the ARC to inhibition by locally released SOM, may be underlying the observed ultradian rhythm of GH secretion at the hypothalamic level (Tannenbaum et al., 1993; Stroh et al., 2009). However, later electron microscopic studies in fixed tissue from rats with known plasma GH status on the subcellular localization of SOM receptors in GHRH neurons of the ARC revealed that there was no significant difference in the ratio of intracellular vs. plasma membrane-bound receptors in a GH trough vs. peak (Stroh et al., 2009). Interestingly, the relative abundance of excitatory vs. inhibitory synapses, as identified by their symmetric, i.e., inhibitory, vs. asymmetric, i.e., excitatory, morphology (Peters et al., 1991), contacting dendritic profiles of GHRH neurons, varied markedly between the phases of the GH secretion cycle, with a predominance of inhibitory synapses during trough periods. This predominance was not found during GH peak periods. However, the mechanisms behind that observation remained unknown and the small numbers dictated by the technique used, transmission electron microscopy (TEM), made the quantification and interpretation of the finding difficult.

New fluorescence microscopy methods that bisect the diffraction limit of optical resolution have summarily been termed super-resolution microscopy (Sigal et al., 2018). Single molecule localization microscopy (SMLM) in particular, permits nanoscopic resolution by clever exploitation of the photo-chemical properties of fluorophores. Identifying proteins of interest with a resolution down to 10 nm makes SMLM a competitive tool compared to TEM (Baddeley and Bewersdorf, 2018). Here, we use the SMLM technique of *direct* Stochastic Optical Reconstruction Microscopy (*d*STORM), by labeling proteins of interest with commercially available antibodies. The samples are immersed in a chemical environment favoring reversible depletion of fluorescent events enabling single fluorophore detection (Bates et al., 2007; Heilemann et al., 2008; Baddeley and Bewersdorf, 2018). This method is well established in the neuroimaging field and has been used to reveal unknown characteristics of the neuronal ultrastructure. For instance, it was shown that axons exhibit a para-crystalline arrangement of the actin cytoskeleton in which actin forms regularly spaced rings around the circumference of the axon at approximately 180 nm periodicity. Spectrin forms alternating structures with the actin rings (Xu et al., 2013; Lorenzo et al., 2019). Studies like (Nair et al., 2013; Andreska et al., 2014; Ehmann et al., 2014; Rahbek-Clemmensen et al., 2017; Siddig et al., 2020) emphasized the quantitative potential of dual-color *d*STORM by quantifying synaptic protein distribution in synapses in primary cell culture, *Drosophila* larvae and murine cerebellum tissue samples.

In the present study, we hypothesized that the change in the relative abundance of excitatory vs. inhibitory synapses contacting GHRH neurons in the ARC in parallel with the GH secretion cycle (Stroh et al., 2009) may be a result of physical uncoupling of excitatory presynaptic terminals from their postsynaptic counterparts. To test this hypothesis, we used mice from which plasma GH levels had been measured continuously at high temporal resolution using a highly sensitive sandwich ELISA (Steyn et al., 2011) to determine which animals were in either a GH secretory episode or trough at the time of fixation. Brain sections from these two groups were then stained for pre- and post-synaptic markers of excitatory or inhibitory central synapses, and a GHRH marker to identify synapses on GHRH-positive neurons. These samples were then imaged using *d*STORM, which enabled the measurement of multiple morphological parameters at the ultrastructural level and detailed quantification of the data using cluster analysis algorithms.

MATERIALS AND METHODS

Measures of Pulsatile GH Secretion and Tissue Extraction

All animal procedures were approved by the Animal Care Committee of McGill University and conducted in compliance with the guidelines of the Canadian Council of Animal Care. Pulsatile GH secretion measurements were done as described by Steyn et al. (2011). Eighteen adult male (8–10 weeks-old) C57BL/6 mice (Charles River Canada, Saint Constant, QC, Canada) were group-housed ($n = 4$) for at least 2 weeks before the experiment under a 12 h light, 12 h dark cycle (lights on at 08:00 a.m. and off at 08:00 p.m.). Room temperature was maintained at 20 ± 2°C. Mouse chow and tap water

were available *ad libitum*. To minimize stress, prior to all experiments, mice were habituated to the test environment (human handling and tail manipulation) for 10 days, 15 min each day. Habituation was done by the same person conducting all subsequent experiments. A small cardboard tube was placed in the cage 2 days before the sample collection and used during experimental procedures to assist in animal handling. Starting at 09:10, 09:20 or 09:40 a.m., sequential tail-clip blood collections were performed in 15 or 20-min intervals from each mouse, where mice were placed inside the cardboard tube and ∼2 mm of the distal portion of the tail was excised once, at the beginning of the experiment, using a surgical blade. A small volume of whole blood (2 μl) was collected with a pipette and transferred to an Eppendorf tube containing 58 μl of 0.05% phosphate-buffered saline (PBS)-Tween 20 and placed on dry ice until the end of the collection period. Gentle pressure was applied with a gauze to the wound to stop the blood flow and the mouse was placed back in its cage. For subsequent blood withdrawals, the surface of the original wound was disrupted (mechanically or by applying gauze soaked in physiological saline). Collection of each sample was performed in less than 45 s. After collecting several blood samples from each mouse (5–15 samples, end times chosen randomly), the mouse was anesthetized with an intraperitoneal injection of an anesthetic cocktail (Ketamine/Xylazine/Acepromazine), followed by a trans-aortic perfusion with 4% paraformaldehyde (PFA) in 0.1 M sodium-phosphate buffer (SPB), consisting of Na_2HPO_4 and NaH_2PO_4 in ddH_2O at pH 7.4. The time delay between the last blood collection and brain extraction was 15 min. Brains were removed immediately and post-fixed in the same fixative overnight at 4°C. The next day, brains were placed in 30% sucrose solution in 0.1 M SPB overnight, snap-frozen at −40°C in isopentane and stored at −80°C until sectioning. 30 μm coronal sections were obtained with a Leica Ultramicrotome and stored in an antifreeze solution (30% glycerol + 30% ethylene glycol in 0.12 M PBS) until *d*STORM imaging. Plasma growth hormone (GH) concentrations were measured using a modified version of the sensitive sandwich ELISA assay, originally described in Steyn et al. (2011). As such, a 96-well plate (Corning Inc., 9018) was coated overnight at 4°C with 50 μl monkey anti-rat GH antibody (AFP411S, NIDDK-NHPP, Torrance, CA, USA) at a final dilution of 1:40,000. Each well was subsequently incubated with 200 μl blocking buffer (5% skim milk powder in 0.05% PBS-Tween 20) for 2 h at room temperature. A standard curve was generated using 2-fold serial dilutions of mouse GH (reference preparation, AFP-10783B, NIDDK-NHPP) in 0.05% PBS-Tween 20 supplemented with 1 ng/ml normal goat serum (NGS) to a final concentration of 0.2% NGS-Tween 20. Fifty microliter of standard curve solutions in duplicates or blood samples in singlets were loaded to the plate and incubated for 2 h at room temperature on an orbital shaker. After washing, bound standards and samples were incubated with 50 μl detection antibody (rabbit antiserum to rGH, AFP5672099, NIDDK-NHPP) at a final dilution of 1:40,000 in a blocking buffer for 90 min. The bound complex was incubated with 50 μl horseradish peroxidase-conjugated antibody (goat anti-rabbit, BioRad, Berkley, CA, USA) at a final dilution of 1:2,000 in blocking buffer for 90 min. Addition of 100 μl O-phenylenediamine (00-2003, Invitrogen, Carlsbad, CA, USA) substrate to each well resulted in an enzymatic colorimetric reaction. This reaction was stopped by addition of 50 μl 3 M HCl, and the absorbance was read at dual wavelengths of 490 nm and 650 nm with a microplate reader. The concentration of GH in each well was calculated by the regression of the standard curve using Graph Pad Prism. **Figure 1A** graphically represents the blood collection, brain extraction and ELISA procedures.

Immunohistochemistry

Thirty micrometer mouse brain sections representing approximately Bregma –1.06 mm to –2.54 mm of a mouse brain atlas by Franklin and Paxinos (2012), containing the tuberal hypothalamus with the arcuate nucleus (harboring GHRH neurons) were used for all experiments. The sections were selected visually, according to their position within the brain and tissue morphology (shape of the third ventricle, position of lateral ventricles, distinct mound of the median eminence). Prior to immunofluorescence staining, each section was washed with 0.1 M SPB for 3 h to remove the antifreeze solution and incubated with 0.1% $NaBH_4$ in 0.1 M tris-buffered saline (TBS) to quench any autofluorescence from residual PFA. The sections were then washed three times in 0.1 M TBS and incubated in 500 μl blocking buffer containing 10% NGS, 3% BSA and 0.1% Triton X-100 in 0.1 M TBS for 2 h. This was followed by incubation with 300 μl primary antibody solution containing primary antibodies, 0.1% Triton X-100 and 2% NGS in 0.1 M TBS at 4°C overnight. Each section was labelled addressing three targets including a pair of antibodies against a pre- and post-synaptic marker of either inhibitory or excitatory synapses plus an antibody against Growth-Hormone Releasing Hormone (GHRH; **Table 1**). Control sections were incubated with two of the three primary antibodies. The following day, sections were washed three times for 5 min with 0.1 M TBS + 0.1% Triton X-100, then incubated with secondary antibody solution containing appropriate species-specific secondary antibodies (**Table 1**), 0.1% Triton X-100 and 2% NGS in 0.1 M TBS for 1.5 h. Control sections were incubated in the same manner with all three secondary antibodies. Next, sections were washed twice in a solution of 0.1 M TBS and 0.1% Triton X-100 for 5 min and three more times for 5 min with 0.1 M TBS. Sections were then post-fixed in 4% PFA in 0.1 M SPB for 30 min to immobilize the antibodies and thus avoid movement during imaging, then washed three times for 10 min in 0.1 M SPB. Finally, to reduce light scattering and allow for 3D tissue imaging, sections were stored in Scale U2 tissue clearing buffer (30% v/v glycerol, 4 M urea, 0.1% Triton X-100; Hama et al., 2011), minimum overnight at 4°C and until *d*STORM imaging (for a maximum of 7 days).

Optical Set-Up for *d*STORM Imaging and 3D Multi-color Calibration

All super-resolution imaging was performed with the commercial microscope Vutara 350 (Bruker Corp., Billerica, MA,

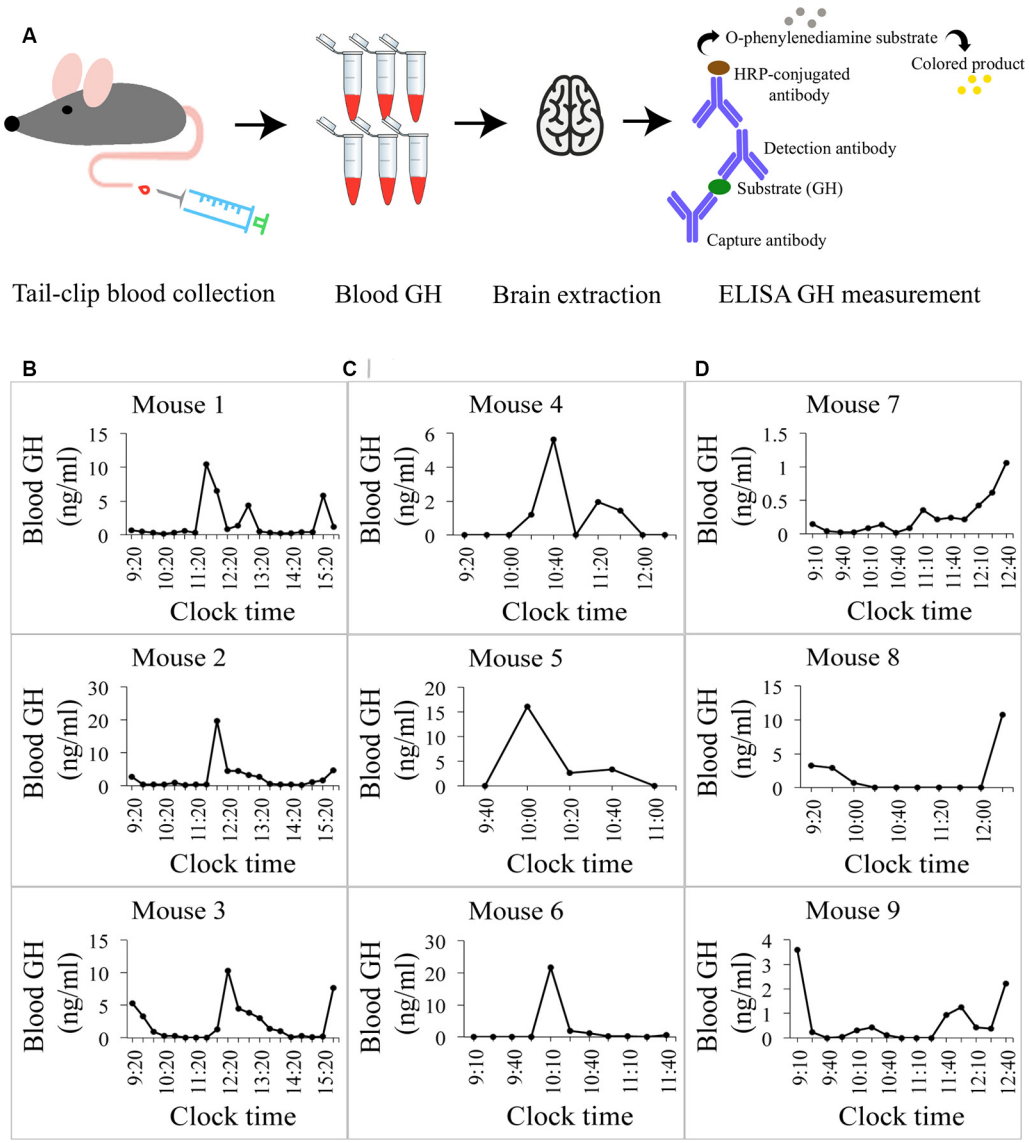

FIGURE 1 | Growth hormone (GH) profiles in mice. **(A)** A pictogram of the data collection for blood GH levels. Blood was collected from the mouse's tail at regular intervals to obtain profiles of circulating GH concentrations. The mouse was then perfused and the brain extracted. A sandwich-ELISA GH measurement from the collected blood samples followed. **(B)** Daily profiles of circulating GH levels in ng/ml in three different mice. Oscillating levels of GH are observed with a peak of GH secretion around the same time (∼13:20) and baseline levels of GH at 0 ng/ml in all mice. Detection minimum from the standard curve = 0.2 ng/ml, ELISA essay detection sensitivity 0.03 ng/ml. **(C)** Circulating GH levels in mice sacrificed at the time of baseline hormone secretion (0 ng/ml). The last point in each graph represents the final blood collection point. **(D)** Circulating GH levels in mice sacrificed at the time of high hormone secretion. Final blood GH concentrations range from 1.04 ng/ml to 11 ng/ml.

USA), equipped with Single Molecule Localization (SML) biplane technology (Juette et al., 2008). The microscope is equipped with a Hamamatsu high resolution (4 MP, 6.5 μm × 6.5 μm), high speed (up to 3,000 fps) sCMOS camera for super resolution acquisition, and a CCD camera (1,392 × 1,040 pixels) for widefield imaging. Excitation lasers include 1 W 640 nm (excitation wavelength for Alexa Fluor 647), 1 W 561 nm (for CF 568) and 1 W 488 nm (for Alexa Fluor 488), as well as a 100 mW 405 nm activation laser, enabling excitation densities of approx. 5 kW/cm^2; with epi-illumination at the sample site. All images were acquired using a 60× 1.2 NA water-immersion Olympus objective. Prior to imaging, an experimental point-spread function (PSF) was generated using 200 nm Tetraspeck microsphere beads (Thermo Fisher Scientific, Waltham, MA, USA) to create a response function of the microscope (experimental point spread function, PSF) to fit single molecule signals and align the individual biplane and color channels.

The bead-sample was prepared on a high-resolution coverslip of the thickness #1.5H (diameter 25 mm, Electron Microscopy

TABLE 1 | List of antibodies used in the study.

Primary antibodies

Antigen	Target details	Clone	Host	Supplier	Product code	Dilution
GHRH	GHRH hormone in soma	Polyclonal	Rabbit	AbClonal	A5343	1:200
VGAT	Inhibitory pre-synaptic terminal	Polyclonal	Guinea Pig	Synaptic Systems	131004	1:1000
Gephyrin	Inhibitory post-synaptic terminal	Monoclonal	Mouse	Synaptic Systems	147021	1:500
VGLUT2	Excitatory pre-synaptic terminal	Polyclonal	Guinea Pig	Synaptic Systems	135403	1:5000
PSD-95	Excitatory post-synapftic terminal	Polyclonal	Mouse	Abcam	ab18258	1:500

Secondary antibodies

Antigen	Conjugation	Host	Supplier	Product code	Dilution
Rabbit IgG	Alexa Fluor 488	Goat	Jackson ImmunoResearch	111545003	1:500
Mouse IgG	CF 568	Goat	Biotum	20100	1:800
Guinea Pig IgG	Alexa Fluor 647	Goat	Life Technologies	A21236	1:1000

Science, Hatfield, PA, USA) by coating the center of the glass with poly-L-lysine (Sigma–Aldrich St. Louis, MO, USA, 10 min incubation). Once dried, 30 µl of a well-sonicated (>10 min) 1:20 Tetraspeck dilution in ddH_2O was added to the center and aspirated with a pipette after 10 min. The sample was then immersed in a drop of Immersol W 2010 (Carl Zeiss, Jena, Germany) and sealed with a coverslip and nail-polish.

An experimental PSF from orange and red channels was acquired using the calibration module in the Vutara SRX software (6.04.02), allowing a lateral registration of the biplane focus planes and the different color channels to each other with a root mean squared error (RMSE) of <5 nm.

*d*STORM Imaging and Localization Process

Brain sections were transferred from the Scale U2 buffer to 0.1 M TBS and rinsed on an orbital shaker for 5 min before being placed flat atop a #1.5H circular cover glass (diameter 25 mm), with a small paint brush and left to dry completely. Imaging was performed in buffer containing reducing agent to enable reversible photoswitching of the utilized fluorescent dyes. The buffer consists of 20 mM β-Mercaptoethylamine (MEA) in 50 mM Tris-HCl (pH 8) + 10 mM NaCl, 1% (v/v) β-mercaptoethanol (BME; Sigma–Aldrich, St. Louis, MO, USA) and a 1× Glucose-oxidase (Gloxy) solution, all diluted in a buffer containing 50 mM Tris-HCl (pH 8), 10 mM NaCl and 10% (w/v) glucose. The Gloxy solution was prepared as a 50× stock containing 8440 AU of glucose oxidase type VII from Aspergilius (Sigma–Aldrich, St. Louis, MO, USA) and 70200 AU of catalase from bovine liver (Sigma–Aldrich) in a buffer containing 50 mM Tris-HCl (pH 8) and 10 mM NaCl. A drop of the imaging buffer was added onto the section and the tissue was left to re-hydrate and expand for 10 min to prevent movement during imaging. A second #1.5H cover glass was added on top of the section for immobilization and sealed to prevent further oxygen influx that facilitates photo damage and therefore bleaching of the fluorophores. The tissue construct was then placed into an AttoFlour imaging chamber (Thermo Fischer) and fixed on the sample holder to minimize drift. The switching buffer was replaced every 1.5 h to ensure a stable pH and therefore reproducible localization rates.

In the arcuate nucleus of the hypothalamus, the region of interest (ROI) was identified *via* fluorescence of GHRH-positive neurons and its lateral location with regards to the third ventricle (**Figure 2A**). The ROI was then randomly scanned on both sides of the third ventricle and each field exhibiting a triple labeling of GHRH with its pre-and post-synaptic markers (on average, between 13 and 20 fields (neurons) on each side of the third ventricle for a total of 26–40 neurons per section) was chosen for further super-resolution imaging, such that each super-resolved image contained synapses contacting the soma of one GHRH neuron. On average, 3–5 brain sections were imaged per animal. Widefield reference images were captured for the triple-labeled GHRH neurons before super-resolution imaging. Pre- and post-synaptic markers were then imaged sequentially with a 561 nm laser at 7.5 kW/cm^2 and a 640 nm laser at 6 kW/cm^2, both at 20 ms exposure time for 10,000 frames each. Single Molecule Localization (SML) was performed using the Vutara SRX software, allowing 3D localization by fitting biplane-signals to an experimental PSF. The fit window was set to 99.8 nm × 99.8 nm, and we allowed signal accumulation in consecutive frames if the localization center was shifted less than 4 pixels. If the same fluorophore was "on" more than 10 consecutive frames, it was considered a fiducial marker and used for drift correction. No maximum limit was set for the number of particles to be localized in a given frame.

DBSCAN Cluster Analysis

To identify and extract inhibitory and excitatory synaptic clusters from all recorded localizations, a Density-Based Spatial Clustering of Applications with Noise (DBSCAN) algorithm, proposed by Ester et al. (1996) was utilized and run through the Vutara SRX software. The DBSCAN algorithm assigns localizations to a cluster based on a threshold for the minimum particle number of neighboring localizations found within a maximum particle distance from

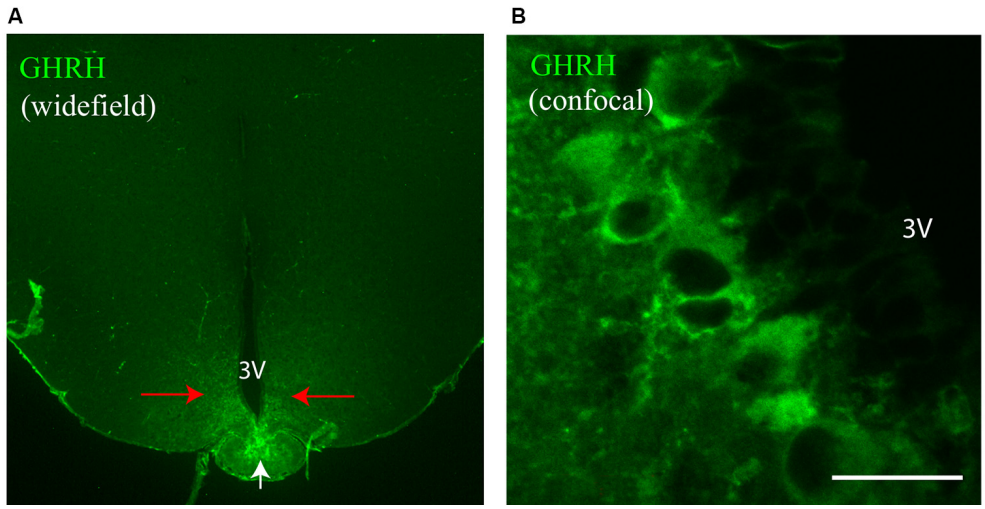

FIGURE 2 | GH-Releasing Hormone (GHRH) neurons in the mouse brain. **(A)** A widefield overview image of a mouse brain section stained with an antibody against GHRH. The staining is specific to the arcuate nucleus (red arrows) and the median eminence (white arrow). **(B)** A confocal image of GHRH-stained neuronal bodies in the arcuate nucleus. 3V, third ventricle. Scale bar = 20 μm.

the current localization. All unassigned localizations are excluded. The DBSCAN variables are determined by keeping the minimum number of neighbors constant at a value of 6 as recommended for three dimensional data in (Ester et al., 1996) and varying the distance radius. Therefore, the density of particles per μm^3 (a parameter of the determined cluster) was plotted against a series of increasing distance values (DBSCAN variable; **Figure 4B**). The advent of a plateau in the distribution indicates that a cluster population is detected and can be used to indicate a reproducible value for the distance variable of DBSCAN. Cluster parameters such as area/volume and density were computed using a non-convex alpha shape hull. The alpha shape radius was set at 0.1 μm. Next, clusters that contacted GHRH neurons were selected by overlaying the widefield GHRH reference image with the super-resolved localizations that are assigned to a cluster. Since the GHRH staining delineates the soma of neurons, cell borders were established around the hormone staining, as shown in **Figure 3B**. Synapses were identified by a co-occurrence of a pre- and post-synaptic marker clusters that are less than 250 nm apart. The distance is defined as the space in between the closest particle of each cluster identified with an algorithm that enables relative distribution assessment of STORM localizations called STORM-RLA (Veeraraghavan and Gourdie, 2016). The cluster distance filtering was executed *via* an in-house-built "R"-code. The distance was chosen by estimations of synaptic protein distances as described in Dani et al. (2010) and because protein markers used in our study included vesicular transporters (VGAT and VGLUT2) and their axial positions were not earlier reported in Dani et al. (2010), the known size of a synaptic vesicle (∼40 nm) was considered and added to the threshold for a final value of 250 nm. All data was exported into an Excel file and statistical analysis was performed using two-way ANOVA combined with a Bonferroni post-test.

RESULTS

Pulsatile GH Secretion in Mice

With this project, our goal was to quantify the numbers—and study more novel aspects—of excitatory and inhibitory synapses that contact growth hormone-releasing-hormone (GHRH) neurons during peak and trough levels of circulating growth hormone (GH) in mice. A schematic representing tissue extraction and GH level measurement is depicted in **Figure 1A**. To validate the ELISA GH measurement assay, we obtained 6-h profiles based on 20-min interval sampling of circulating GH levels of three adult male mice (**Figure 1B**). A regular periodicity of pulsatile GH secretion was observed with profiles revealing a 2-h multicomponent peak based on peak-doublets (mouse 1) or shoulders (mouse 2 and 3) and there was a strong concordance in secretion timing (between ∼11:20 and ∼13:20), followed by a low baseline secretory period of similar duration. These data are comparable to observations by Steyn et al. (2011) in mice and similar to measures obtained earlier in rats (Tannenbaum and Martin, 1976). We then sampled more mice at 15–20-min intervals with at least five GH measurements before mouse perfusion and extracted a total of six brains, three corresponding to trough- and three to peak- levels of circulating GH (**Figures 1C,D**, respectively). Circulating levels of GH, obtained 15 min prior to sacrifice and tissue extraction are represented by the last time point on each individual graph in **Figures 1C,D**.

GHRH Neurons in the Mouse Brain

Earlier studies utilizing *in situ* hybridization of GHRH gene expression in the mouse brain by Suhr et al. (1989) revealed

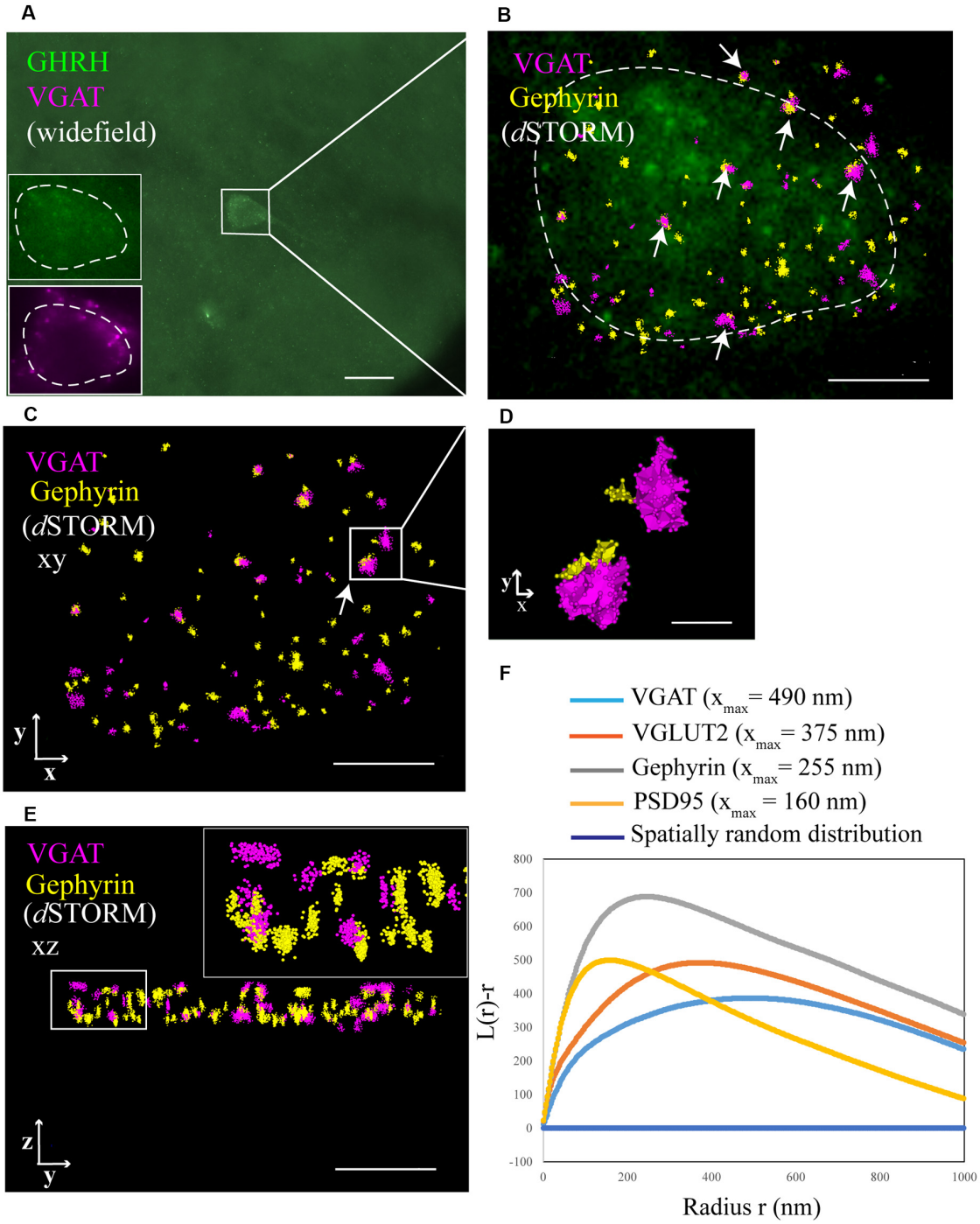

FIGURE 3 | Identification of synaptic inputs to GHRH neurons with *d*STORM. **(A)** An overview widefield image of a GHRH-positive neuron (AF488, green) in the arcuate nucleus of the hypothalamus and two widefield zoomed-in images of the same GHRH cell (left bottom corner, top insert) and of a pre-synaptic marker VGAT (AF647, magenta; bottom insert). **(B)** Enlarged view of the reference GHRH cell shown in panel **(A)**, with inhibitory VGAT and Gephyrin (post-synaptic) clusters imaged using *d*STORM and rendered with a Density-Based Spatial Clustering of Applications with Noise (DBSCAN) algorithm, displayed as pointcloud. Synaptic inputs to GHRH neurons are shown with arrows and identified as opposing pre- and post-synaptic clusters with an inter-cluster distance of <250 nm. **(C)** A pointcloud visualization of synaptic markers from panel **(B)** without the reference GHRH cell in the background, shown in the XY-plane. **(D)** Enlarged clusters of VGAT and Gephyrin from panel **(C)** to highlight lateral resolution. **(E)** YZ-plane depiction of VGAT and Gephyrin. The axial resolution allows 3D distance analysis. Scale bars: **(A)** = 20 μm **(B,C,E)** = 4 μm, **(D)** = 500 nm. **(F)** A general cluster test by Ripley's H analysis, represented as a normalized Ripley's H function (L(r)-r) for indicated synaptic proteins. The peak indicates the highest degree of aggregation at specific interacting distance r compared to a spatially random distribution with L(r)-r of 0 (dark blue line). Pre-synaptic proteins VGAT and VGLUT2 cluster at higher radii (490 nm and 375 nm, respectively), as compared to post-synaptic proteins Gephyrin and PSD95 (255 nm and 160 nm, respectively).

that the hormone's mRNA is restricted primarily to the arcuate nucleus of the hypothalamus. Furthermore, in an eGFP-GHRH transgenic mouse, it was shown that the peptide is transported from cell bodies in the arcuate nucleus to varicose fiber terminals in the median eminence, where the hormone is released (Balthasar et al., 2003). Therefore, to specifically label GHRH neurons in the mouse brain, we first collected tissue that contained the mediobasal hypothalamus (MBH) with the arcuate nucleus, as described in Materials and Methods. We then used an antibody against GHRH and observed specific staining of GHRH neurons in the arcuate nucleus (**Figure 2A**, red arrows; **Figure 2B**) and GHRH neuronal fiber terminals in the median eminence (**Figure 2A**, white arrow). No other regions of the MBH were labeled with the anti-GHRH antibody. Negative controls for all fluorescent markers used in the study were performed (GHRH, VGAT, Gephyrin, VGLUT2, PSD95 and their corresponding secondary antibodies) and revealed the absence of unspecific binding and low background fluorescence levels (**Supplementary Figures S1A,B**).

*d*STORM and DBSCAN Allow for Quantitative Imaging and Analysis of Synapses That Contact GHRH Neurons

To better understand the mechanism of GH pulsatile release, we looked at the synaptic connectivity of GHRH neurons in the arcuate nucleus of the hypothalamus during peaks and troughs of GH secretion in the mouse. **Figure 3A** represents a sample widefield image of a GHRH neuron and an inhibitory pre-synaptic marker VGAT. However, as seen in the two inserts in **Figure 3A**, due to the limited resolution of conventional fluorescence microscopy, it would be difficult to quantitatively assess synapse numbers and other cluster parameters. Therefore, we utilized *d*STORM imaging of pre-and post- synaptic inhibitory and excitatory markers of GHRH neurons combined with a DBSCAN algorithm to quantify the numbers of inhibitory and excitatory synapses, as shown in **Figures 3B,C**. The improvement in resolution can be clearly seen in **Figure 3D**. To ensure a more accurate assessment of synaptic cluster numbers, we utilized the Vutara 350 (Bruker) equipped with a biplane module allowing 3D super-resolution imaging of 1 μm sectioning, as shown in **Figure 3E** with synapses revealed at different depths. To describe the degree of clustering for the proteins of interest, we utilized the normalized Ripley's H function (**Figure 3F**). This is a descriptive statistic approach that allows to investigate the spatial homogeneity of points in a data set. Clustering is identified if the average number of points within a distance *r* of another point is statistically greater than what is expected for a random distribution (Kiskowski et al., 2009). Distribution curves of the post-synaptic density markers PSD-95 and Gephyrin follow a similar trend, showing a peak that indicates high-order clustering at small radii (160 nm for PSD 95 and 255 nm for Gephyrin). The distribution of pre-synaptic vesicular protein markers VGLUT2 and VGAT indicate bigger cluster with a maximum of aggregation at higher radii (375 nm for VGLUT2 and 490 nm for VGAT). This trend is possibly due to the size of the synaptic vesicle (40 nm) and the clustering at active zones. The difference in cluster size between pre- and post-synaptic proteins can be also seen in **Figure 3D**, with pre-synaptic clusters bigger than post-synaptic ones. The degree of clustering between animals and between the peak and trough concentration values of GH was comparable (data not shown). *d*STORM data acquisition relies on repetitive detection of a target bound fluorophore resulting in a localization nanocluster representing one fluorophore. This can aggravate the distinction of expected signal of localizations from unspecifically bound fluorophores (**Figure 4A** shows all recorded localizations surrounding the soma of a GHRH cell). Therefore, it is important to find suitable parameters for the cluster algorithm that represents the structure of interest in a reproducible manner. Here, we utilized DBSCAN, as shown in **Figure 4**. For the selection of parameters, the r_0 neighborhood graph (**Figure 4B**) was used to select a value for the maximum particle distance to form a cluster. These values varied between animals, ranging from 0.10 μm to 0.16 μm. The minimum number of particles to form a cluster was set to 6. DBSCAN analysis of the synaptic localization data facilitated a clear extraction of clusters (**Figure 4C**). In comparison, we can observe the same structure boxed in the unfiltered *d*STORM data visualized in **Figure 4A**. Removal of clusters that did not contact GHRH-positive neurons (by deleting clusters outside of the cluster overlay zone with a GHRH widefield image) allowed selection of only clusters of interest (**Figure 4D**). Various cluster data was collected in the SRX software (**Figure 4E**) and a quantitative assessment of the inter-cluster distance was used to select synapses based on a threshold of 250 nm (**Figure 4F**). As such, the data presented here underscores the potential of *d*STORM to quantitatively assess the synaptic architecture of a cell of interest in the neuroendocrine circuit.

Quantitative Assessment of Synapse Numbers and Other Synaptic Parameters

We have reported earlier that synaptic connectivity varies in parallel with the ultradian rhythm of GH secretion in rats, using an electron microscopic approach (Stroh et al., 2009), where synapses were counted visually in one plane. Here, we confirm and extend our findings to mice, revealing increased excitatory input to GHRH neurons during peak levels of circulating GH, while increased inhibitory inputs are detected when GH levels are low. Specifically, we found that when blood hormone levels were high, 69% of all synapses that contact GHRH neurons were excitatory and 31% inhibitory ($p < 0.001$; $n = 3$ animals; **Figure 5A**, "GH Peak"). However, when blood hormone levels dropped we observed a rapid GHRH circuit rewiring, where now 34% synapses were excitatory and 66% inhibitory ($p < 0.001$; $n = 3$ animals; **Figure 5A**, "GH Trough"). No change was observed in the control group, where we combined all available data of excitatory and inhibitory synapses for GH Peak and Trough to scramble peak and trough-associated differences [**Figure 5A**, "GH Peak+GH Trough (…)"]. When comparing the absolute inhibitory and excitatory synapse numbers in each mouse (**Figure 5B**), we noted a significant variation between animals (thus, the data from all mice could not

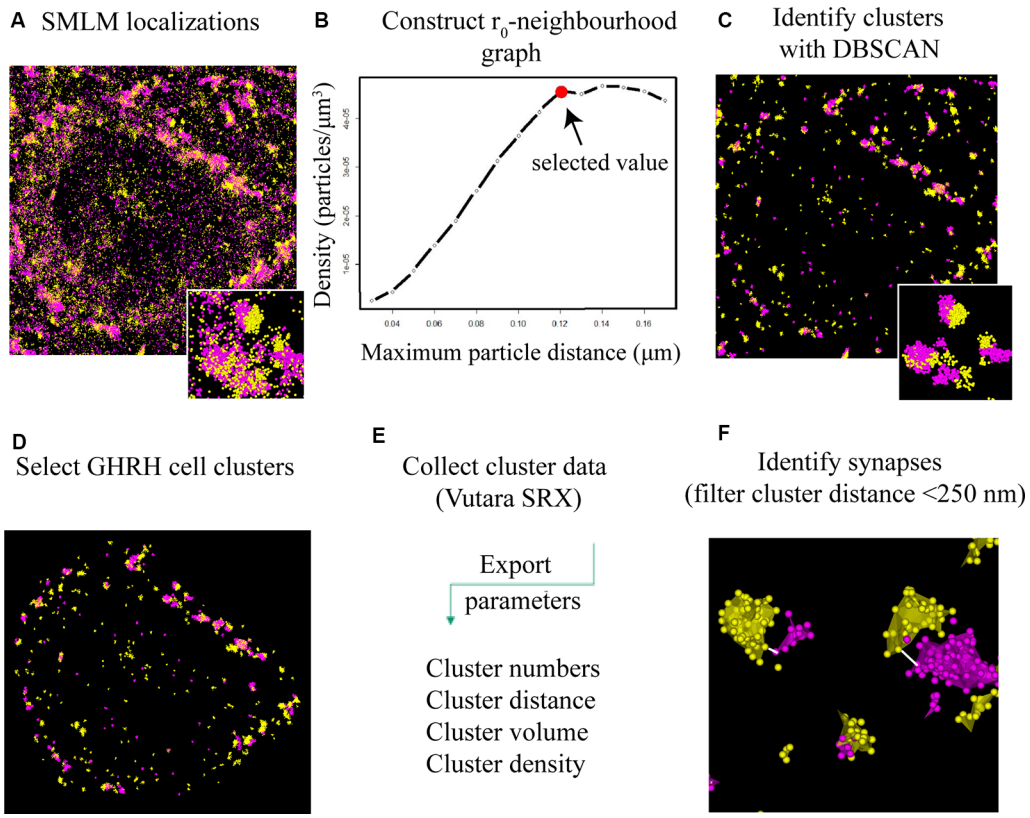

FIGURE 4 | DBSCAN extraction of synapses from SMLM localization data. **(A)** All single molecule localization microscopy (SMLM) localizations of VGLUT2 (magenta) and PSD95 (yellow), displayed as a pointcloud visualization. The data contains clusters (synaptic and non-synaptic) and single localizations (non-clustered proteins, unbound antibodies). **(B)** Serial parameter scan for DBSCAN: the mean value of the localization density per identified cluster is plotted against the increasing DBSCAN distances (r_0) while the minimum particle count is kept constant to 6. The plateauing curve indicates stable clustering parameter. We choose the beginning of the plateau as the ideal r_0 value for the specific protein population. **(C)** DBSCAN algorithm filters data based on the input parameters and displays resulting clusters. **(D)** Synaptic clusters associated with a GHRH cell are selected manually (based on an overlay with a GHRH reference image, as shown in **Figure 3B**). **(E)** Various quantitative cluster data of interest is exported to an Excel file. **(F)** An in-house-built algorithm for the software "R" filters full synapses based on their inter-cluster distance between pre-and post-synaptic clusters of <250 nm.

be combined for statistical reasons). However, the ratios of excitatory and inhibitory synapses between animals were mainly conserved. Moreover, the increase in excitatory synapse ratio during peak GH, as seen in **Figure 5A**, seems to be the result of an increase in the absolute numbers of excitatory synapses as well as the decrease in the absolute numbers of inhibitory synapses, as per visual assessment of the data from all graphs in **Figure 5B** (all bars for "Excitatory" synapses are higher at GH peak and all bars for "Inhibitory" synapses are lower during GH trough). It is known that synaptic vesicles assemble from smaller, reserve clusters situated more distal to the release site, into bigger release clusters at the release site (Pechstein and Shupliakov, 2010; Vaden et al., 2019). Thus, we hypothesized that the fast circuit rewiring observed between the peak and trough of GH release in the arcuate nucleus might be a result of mobilization and clustering of the reserve-pool of pre-synaptic vesicles into the pre-synaptic membrane. To this end, we counted the numbers of fully evolved synapses (from here-on dubbed "full synapse"). These are defined as an apposition of a pre- and post-synaptic cluster with an inter-cluster distance of <250 nm (as described earlier). The amount of full synapses has been compared to the numbers of all presynaptic clusters including free pre-synaptic clusters not associated with a synapse and those forming full synapses. All results are calculated following the equation:

$$\%\ \text{of pre-synaptic clusters associated with post-synaptic clusters} = \frac{\text{number of full synapses}}{\text{number of all pre-synaptic clusters}} * 100\%$$

We found that during GH peak secretion, 81% of pre-synaptic excitatory VGLUT2 clusters had a post-synaptic excitatory "partner" labeled with an anti-PSD95 antibody, thus forming a full synapse (**Figure 5C**, "GH Peak," Excitatory). However, during GH trough secretion, only 41% of all pre-synaptic VGLUT2 clusters had a PSD95 post-synaptic partner (**Figure 5C**, "GH Trough," Excitatory; $p < 0.001$). No differences were seen in the control group [**Figure 5C**, "GH Peak+GH Trough (. . .)"]. We found no difference in the association of pre-synaptic clusters

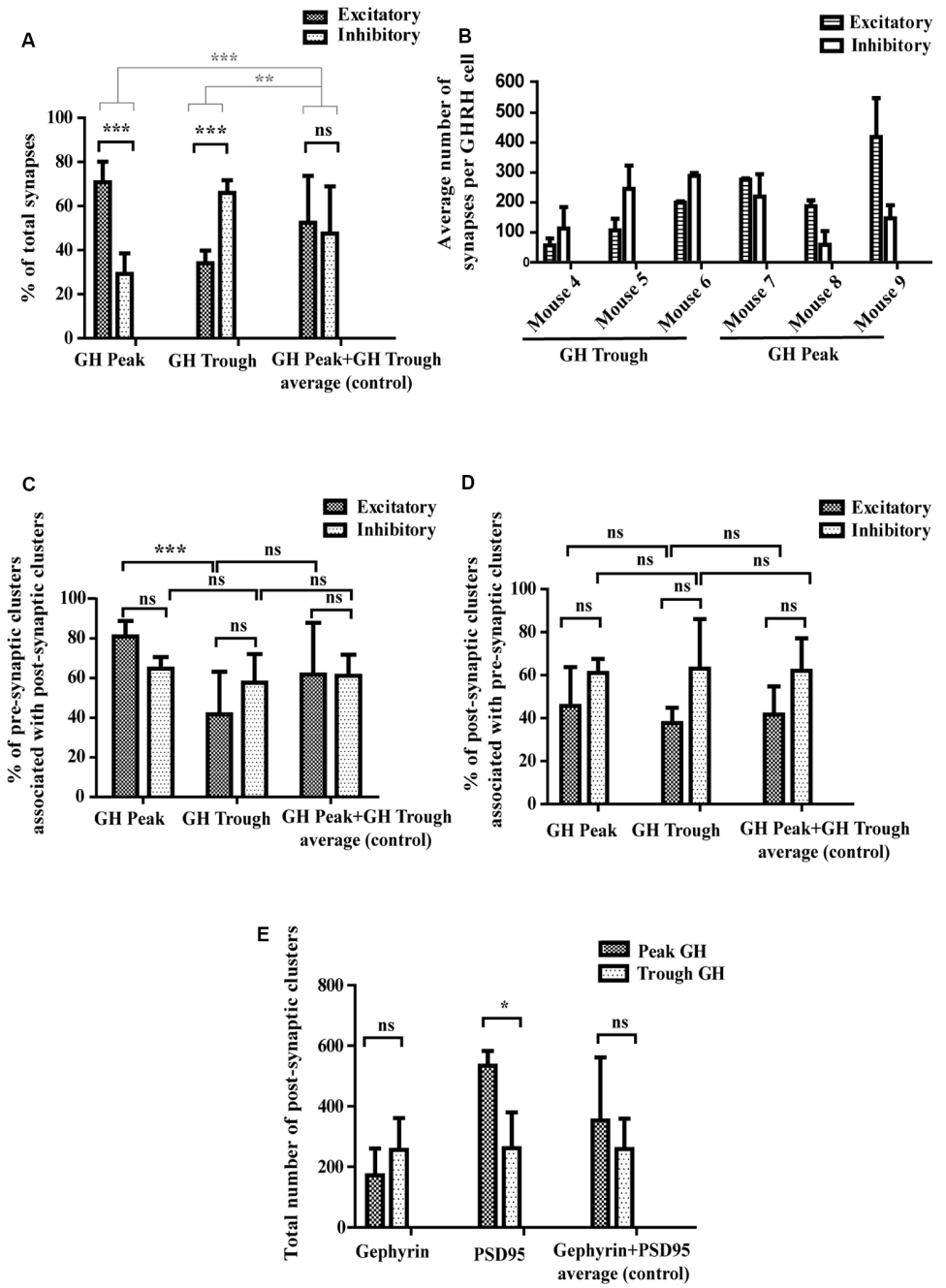

FIGURE 5 | Quantitative assessment of synaptic parameters. **(A)** Synapse numbers during peaks and troughs of GH secretion. During high hormone levels ("GH Peak"), 69% of all synapses are excitatory and 31% are inhibitory. During low hormone levels ("GH Trough"), 34% of all synapses are excitatory and 66% inhibitory. There is no significant difference in the percent of excitatory and inhibitory synapses in the control condition ("GH Peak+GH Trough"). Black significance bars represent the change in synapse numbers (as % of total synapses) between the three conditions. Gray significance bars represent the significance levels of the percent change of excitatory and inhibitory synapse numbers at GH Peak and GH Trough as compared to the percent change of the average (control). Black significance bars: ANOVA-2 $p_{(\text{interaction})} < 0.001$; after Bonferroni *post hoc* test correction $p_{(\text{GH Peak})} < 0.001$, $p_{(\text{GH Trough})} < 0.001$. Gray significance bars: ANOVA-1 $p < 0.001$; after Tukey *post hoc* test $p_{(\text{percent change GH Peak vs. percent change Average})} < 0.001$, $p_{(\text{percent change GH Trough vs. percent change Average})} = 0.005$. **(B)** Absolute synapse numbers in each mouse per GHRH cell. Although numbers of excitatory and inhibitory synapses varied between mice [excitatory synapse numbers ranged from 45 (in mouse 4) to 372 (in mouse 9) and inhibitory synapse numbers ranged from 47 (in mouse 8) to 255 (in mouse 6)], the ratios of excitatory to inhibitory synapses between each mouse were more conserved. Data displayed as means ± SD. **(C)** Synapse-forming pre-synaptic clusters. During GH Peak, 81% of excitatory pre-synaptic clusters are associated with excitatory post-synaptic clusters, forming a synapse (the remaining 19% are "free" pre-synaptic clusters). This changes during GH Trough, where only 41% of pre-synaptic clusters are associated with post-synaptic clusters (the remaining 59% are "free" pre-synaptic clusters). This is not seen in inhibitory clusters, where levels remain similar (65% of pre-synaptic clusters associate with post-synaptic clusters during peaks and 58% during troughs).

(*Continued*)

FIGURE 5 | Continued
No change is observed in the control data. ANOVA-2 $p_{(\text{GH Peak vs. GH Trough})} < 0.001$; after Bonferroni *post hoc* test correction $p_{(\text{GH Peak Excitatory vs. GH Trough Excitatory})} < 0.001$. **(D)** Synapse-forming post-synaptic clusters. No significant difference was found between the percent of post-synaptic clusters that associate with pre-synaptic clusters to form synapses during GH Peak and GH Trough. ANOVA-2 $p_{(\text{Excitatory vs. Inhibitory})} = 0.008$; after Bonferroni *post hoc* test correction $p_{(\text{all factors})} > 0.62$. However, the absolute number of post-synaptic excitatory PSD95 clusters increased during GH Peak levels from an average of 262–534 clusters, as presented in **(E)** with ANOVA-2 $p_{(\text{GH Peak vs. GH Trough})} = 0.03$; after Bonferroni *post hoc* test correction $p_{(\text{PSD95 GH Peak vs. PSD95 GH Trough})} = 0.02$. No changes were seen in the control data, in both **(D,E)**. All data is displayed as means ± SD using two-way ANOVA with significance values at 0.12 (ns), 0.033 (*), 0.002 (**), <0.001 (***).

with post-synaptic ones in the inhibitory system, where 65% and 58% of all pre-synaptic VGAT clusters formed a full synapse during high and low GH levels, respectively (**Figure 5C**, "GH Peak," Inhibitory, vs. **Figure 5C**, "GH Trough," Inhibitory). We repeated the analysis for post-synaptic clusters that associate with pre-synaptic clusters (as opposed to pre-synaptic clusters associating with post-synaptic ones, see above) and found no significant differences in both, excitatory and inhibitory synapses, between GH trough and peak levels (**Figure 5D**). This was puzzling, since we expected that the observed increase of pre-synaptic clusters that form synapses between trough and peak of GH secretion would require a parallel increase in the association of post-synaptic clusters with pre-synaptic ones to account for the changing synapse numbers. As such, we reasoned that the absolute number of post-synaptic excitatory clusters increases, such that post-synaptic clusters associating with pre-synaptic ones to form new synapses are balanced out by new post-synaptic clusters (thus maintaining a constant cluster ratio). Since cluster numbers were comparable between animals (data not shown), they could be combined for a direct comparison. Indeed, we found 262 PSD95 clusters present during trough- and 534 PSD95 clusters during peak of GH secretion (**Figure 5E**, "PSD95," Trough GH vs. Peak GH; $n = 3$ animals; $p = 0.02$). There was no significant difference in the total cluster number for Gephyrin between trough and peak of GH (**Figure 5E**, "Gephyrin," Trough GH vs. Peak GH), which supports our earlier findings of no changes in the percentage of pre-synaptic clusters that associate with post-synaptic ones in the inhibitory system.

DISCUSSION

For decades, structural synaptic studies have relied on electron microscopy, a technique providing the resolution to visualize individual synapses. In the neuroendocrine circuit, such studies were mainly done using immunogold labeling of a target cell followed by a visual analysis/quantification of associated synapses in one plane of view, with limitations in multi-component 3D analysis. As a result of extensive sample processing, the image quality suffered and a small field of view required many rounds of imaging. Fluorescence microscopy overcomes these limitations by allowing high-throughput imaging with high target specificity, but its diffraction-limited resolution does not allow for the quantitative analysis of synaptic components (Maglione and Sigrist, 2013). Therefore, protein localization at a nanometer-level is challenging. However, the advent of super-resolution fluorescence microscopy by SMLM enabled target-specific visualization of proteins at the nanometer scale resulting in a multitude of biologically-relevant discoveries (Nair et al., 2013; Andreska et al., 2014; Ehmann et al., 2014; Rahbek-Clemmensen et al., 2017; Lorenzo et al., 2019; Reinhard et al., 2019; Siddig et al., 2020). Here, we present a first-to-date super-resolution imaging of GHRH neuroendocrine cells in organotypic tissue to quantitatively assess the synaptic architecture in the GH-regulating circuit by utilizing *d*STORM paired with DBSCAN (Density-Based Spatial Clustering of Applications with Noise) cluster analysis. We employ mice with a known GH secretion status pre-measured with sandwich ELISA prior to fixation. Combining these techniques enabled us to quantitatively demonstrate that GHRH neurons in the arcuate nucleus of rodent hypothalamus receive increased excitatory input during peak levels of GH secretion. This result confirms our earlier findings by TEM measurements (Stroh et al., 2009). Additionally, we find excitatory synapse numbers dropping during periods with low levels of circulating GH, indicating rapid circuit rewiring within a single period of the GH secretion cycle. Lastly, we show that more pre-synaptic excitatory clusters associate with post-synaptic excitatory clusters forming a full excitatory synapse and that the absolute number of post-synaptic excitatory clusters increases during peak levels of GH secretion, while no increase of synapse formation is detected in the inhibitory system. We therefore propose that a mobilization of free excitatory pre-synaptic "reserve-pool" clusters towards the pre-synaptic membrane unfolds during peak hormone secretion periods. This appears to happen in conjunction with the *de novo* emergence of additional post-synaptic excitatory synaptic densities to form excitatory synapses. Ultimately, this might be a mechanism contributing to the regulation of pulsatile ultradian GH secretion.

Interestingly, GHRH neurons do not display rhythmicity at the electrical level: patch-clamp studies *in situ* did not reveal the presence of electrical oscillations in cell bodies (Baccam et al., 2007). Furthermore, factors such as hypoglycemic challenge or stimulation of the GH axis (central or peripheral) increase GHRH neuron spike discharge (Stanley et al., 2013; Osterstock et al., 2016). As such, the up- or down-regulation of the firing activity of GHRH neurons appears to play an important role in the control of pituitary GH secretion. It has been shown that agonists of somatostatin receptor irregularly suppressed GHRH neuron electrical activity leading to slow oscillations within a population, as soon as 12 min after octreotide superfusion in male mice (Osterstock et al., 2016). This happens *via* initial hyperpolarization through activation of K+ channels followed by a sst1/sst2-receptor dependent unbalancing of glutamatergic and GABAergic synaptic inputs (Osterstock et al., 2016).

At the structural level, the existence of rapid structural plasticity in neuroendocrine circuits has initially been shown in the oxytocin system by Theodosis et al. (1981), with rapid

synapse formation and elimination in response to prolonged activation (parturition, lactation, chronic dehydration). The proposed mechanism underlying this rewiring is a glial ensheathment of neurons (or lack thereof) that prevents (or allows) synapse formation. More recently, in the arcuate nucleus of the tuberal hypothalamus, synaptic structural plasticity has been shown to take place in the circuitry controlling feeding, where changes in the number of excitatory and inhibitory synapses contacting the perikarya of NPY and POMC neurons were detected 6 h post leptin injection (Pinto et al., 2004). Combined, these observations suggest that activity-dependent circuit rewiring may drive or inhibit neuronal secretion in the neuroendocrine hypothalamus.

Here, we report rapid changes in synapse numbers contacting the perikarya of GHRH neurons when circulating GH levels rise from baseline. We only analyzed synapses on the soma of GHRH, since the hormone is highly concentrated there and only low levels are present as irregularly appearing "puncta" in axons of GHRH neurons (Balthasar et al., 2003), through which GHRH is rapidly transported to varicose fibers in the median eminence (a region with the highest concentration of GHRH). Moreover, in brain sections, axons have a "curved" trajectory and it is difficult to find a single GHRH neuron with all its projections in one plane of sectioning. Furthermore, no hormone is present in the dendrites of GHRH neurons (Balthasar et al., 2003), therefore it would be hard to asses which synapses in the vicinity of cell bodies actually contact GHRH cells (without introducing a fourth immunofluorescent label). By solely assessing somatic synapses, we ensured their association with the cell of interest. Furthermore, we did not expect to see opposing effects (or opposing synapse ratios) in axons to those in soma, as it would lead to an unnecessary energy expenditure in the cell.

Because we sacrificed and extracted brains around the expected rise of circulating GH levels between 11:00 and 12:30 (see reference profiles in **Figure 1B** and sacrification time points in **Figure 1C** and **Figure 1D**), we can conclude that the inversion of excitatory to inhibitory synapse ratios that is associated with the switch from baseline to rising GH levels, may typically take place in less than 90 min. This astoundingly rapid rewiring seems to be based on a combination of recruitment of "free" clusters of pre-synaptic components and possible *de novo* assembly of post-synaptic densities. The former mode of recruitment from pre-assembled units, at least pre-synaptically, is in line with other reports (reviewed in Garner et al., 2002). Notably, the formation of a pre-synaptic terminal has been previously shown to occur in only 10–20 min and the recruitment of post-synaptic receptors takes place 90 min after cell-cell contact (Garner et al., 2002). Interestingly, by comparing the numbers or pre-synaptic "free" clusters of VGLUT2 (a putative pre-assembled component of a future glutamatergic synapse) with "full" synapses (defined as an apposition of pre- and post-synaptic clusters with an inter-cluster distance of <250 nm, as described earlier) along the GH secretion time course, we noticed that free pre-synaptic clusters drop in number while full synapse frequencies rise when GH levels are high (GHRH neurons are stimulated). We did not observe such changes for the post-synaptic side. However, values are reported as ratios of all post- (or pre-) synaptic clusters to those clusters that form synapses and although this ratio remained unchanged between peak and trough of GH levels for the post-synaptic clusters, the absolute numbers of PSD95 clusters increased during peak levels of GH secretion [and were conserved between mice (data not shown)]. It is worth noting that while reporting the absolute numbers of synapses per GHRH cell in **Figure 5B**, we noted a significant variation in the *numbers* of excitatory (or inhibitory) synapses between mice (the *ratios* of excitatory to inhibitory synapses were more conserved and served as a basis for all analysis in the present study). This variation in synapse numbers between animals could be due to many factors, from those of experimental nature (such as the density of immunolabeling) to physiological factors, such as the brain size and the size of GHRH cells, or other particular differences in the amplitude of GHRH stimulation/inhibition of each mouse (the last possibly hinted by the difference in absolute values of the plasma GH concentrations between mice). Those of experimental nature would apply equally to both excitatory and inhibitory synapses in each animal, making synapse ratios a more suitable parameter for analysis; those of physiological nature were not a subject of this study and were not measured.

Looking at the increase of PSD95 cluster numbers, it is unclear how new cluster formation could have occurred, considering the fairly short time frame. However, it is known that PSD95 is directly involved in synaptic plasticity and interestingly, as proposed by Gray et al. (2006) using *in vivo* two-photon microscopy in the neocortex, synaptic PSD95 turns over rapidly (22–63 min) and exchanges with PSD95 in neighboring spines by diffusion. Here, we solely report a rapid increase in PSD95 cluster numbers between trough and peak of GH levels. The mechanism responsible for the observed changes remains unclear and would be an interesting topic for future investigations.

DATA AVAILABILITY STATEMENT

The datasets generated for this study are available on request to the corresponding author.

ETHICS STATEMENT

The animal study was carried out according to the guidelines of the Canadian Council on Animal Care. It was reviewed and approved by the Animal Care Committee of McGill University.

AUTHOR CONTRIBUTIONS

KB, WA and TS designed all experiments, which were performed by KB. KB generated the figures. WA and TS assisted in mouse perfusions and tissue extraction. SA assisted in setting up *d*STORM imaging and analysis. TD programmed a code in the "R" statistical software. PM trained KB in mouse blood collections and ELISA procedures. K-FS provided mice for the study and assisted in interpreting results. KB and TS wrote the manuscript. WA, SA and K-FS provided input and edited the initial draft of the manuscript. KB implemented reviewer comments. SA and TS edited the final draft of the manuscript.

FUNDING

TS was supported by Natural Sciences and Engineering Research Council of Canada (NSERC; RGPIN-2016-06096). K-FS was supported by NSERC (RGPIN-2015-04034). In addition, this research was supported by a Bachynski Family Foundation grant to TS. KB was supported by the Max Stern Entrance Fellowship awarded by the Department of Anatomy and Cell Biology at McGill University and a CGS-M award from the Natural Sciences and Engineering Research Council of Canada. WA was supported by a Montreal Neurological Institute Jeanne Timmins Costello Fellowship and a Faculty of Medicine, McGill University Gerald Clavet and J.P. Giroud Fellowship. SA was supported by the Conrad F. Harrington Postdoctoral Fellowships—Canadian Scholarships.

ACKNOWLEDGMENTS

We thank Sean Goldfarb for assisting in microscope calibration, fluorescent beads generation and contributing to the final copyediting of the text. We extend our thanks to Xiang Zhou from Dr. Bernard's lab for showing us how to perform mice habituation. We wish to extend our gratitude to Carl G. Ebeling from Bruker for the best technical support on the Vutara 350 microscope. We thank Naomi Takeda for administrative assistance and to the lab of Dr. Petrides for training and allowing us to use their microtome. Last but not least, thanks to the Neuro Microscopy Imaging Facility for their support.

SUPPLEMENTARY MATERIAL

The Supplementary Material for this article can be found online at: https://www.frontiersin.org/articles/10.3389/fncir.2020.00021/full#supplementary-material.

FIGURE S1 | Negative controls for immunofluorescence stainings. **(A)** Control immunofluorescence labeling for inhibitory synapses. Each column represents a confocal image of the arcuate nucleus with an antibody staining against a specific target (GHRH neuron, pre or post-synaptic markers). Rows represent an image of an immunofluorescent staining of either all three targets (triple "+") or two targets (double "+," single "−") with all three secondary antibodies present. Clear signal is observed for the three-target immunofluorescence image and no unspecific secondary antibody binding is seen for all two-target controls. Scale bar = 50 μm. **(B)** Similar to **(A)** but for excitatory synapses.

REFERENCES

Alshafie, W., Francis, V., Bednarz, K., Pan, Y. E., Stroh, T., and McPherson, P. S. (2019). Regulated resurfacing of a somatostatin receptor storage compartment fine-tunes pituitary secretion. *J. Cell Biol.* 219:e201904054. doi: 10.1083/jcb.201904054

Andreska, T., Aufmkolk, S., Sauer, M., and Blum, R. (2014). High abundance of BDNF within glutamatergic presynapses of cultured hippocampal neurons. *Front. Cell. Neurosci.* 8:107. doi: 10.3389/fncel.2014.00107

Baccam, N., Alonso, G., Costecalde, T., Fontanaud, P., Molino, F., Robinson, I. C. A. F., et al. (2007). Dual-level afferent control of growth hormone-releasing hormone (GHRH) neurons in GHRH-green fluorescent protein transgenic mice. *J. Neurosci.* 27, 1631–1641. doi: 10.1523/JNEUROSCI.2693-06.2007

Baddeley, D., and Bewersdorf, J. (2018). Biological insight from super-resolution microscopy: what we can learn from localization-based images. *Annu. Rev. Biochem.* 87, 965–989. doi: 10.1146/annurev-biochem-060815-014801

Balthasar, N., Mery, P.-F., Magoulas, C. B., Mathers, K. E., Martin, A., Mollard, P., et al. (2003). Growth hormone-releasing hormone (GHRH) neurons in GHRH-enhanced green fluorescent protein transgenic mice: a ventral hypothalamic network. *Endocrinology* 144, 2728–2740. doi: 10.1210/en.2003-0006

Bates, M., Huang, B., Dempsey, G. T., and Zhuang, X. (2007). Multicolor super-resolution imaging with photo-switchable fluorescent probes. *Science* 317, 1749–1753. doi: 10.1126/science.1146598

Bertherat, J., Bluet-Pajot, M. T., and Epelbaum, J. (1995). Neuroendocrine regulation of growth hormone. *Eur. J. Endocrinol.* 132, 12–24. doi: 10.1530/eje.0.1320012

Dani, A., Huang, B., Bergan, J., Dulac, C., and Zhuang, X. (2010). Super-resolution imaging of chemical synapses in the brain. *Neuron* 68, 843–856. doi: 10.1016/j.neuron.2010.11.021

Ehmann, B. N., van de Linde, S., Alon, A., Ljaschenko, D., Keung, X. Z., Holm, T., et al. (2014). Quantitative super-resolution imaging of Bruchpilot distinguishes active zone states. *Nat. Commun.* 5:4650. doi: 10.1038/ncomms5650

Ester, M., Kriegel, H.-P., Sander, J., and Xu, X. (1996). "A density-based algorithm for discovering clusters a density-based algorithm for discovering clusters in large spatial databases with noise," in *Proceedings of the Second International Conference on Knowledge Discovery and Data Mining* (Portland, Oregon: AAAI Press), 226–231.

Franklin, K., and Paxinos, G. (2012). *The Mouse Brain in Stereotaxic Coordinates.* Amsterdam: Elsevier.

Garner, C. C., Zhai, R. G., Gundelfinger, E. D., and Ziv, N. E. (2002). Molecular mechanisms of CNS synaptogenesis. *Trends Neurosci.* 25, 243–250. doi: 10.1016/s0166-2236(02)02152-5

Gray, N. W., Weimer, R. M., Bureau, I., and Svoboda, K. (2006). Rapid redistribution of synaptic PSD-95 in the neocortex *in vivo*. *PLoS Biol.* 4:e370. doi: 10.1371/journal.pbio.0040370

Hama, H., Kurokawa, H., Kawano, H., Ando, R., Shimogori, T., Noda, H., et al. (2011). Scale: a chemical approach for fluorescence imaging and reconstruction of transparent mouse brain. *Nat. Neurosci.* 14, 1481–1488. doi: 10.1038/nn.2928

Heilemann, M., van de Linde, S., Schüttpelz, M., Kasper, R., Seefeldt, B., Mukherjee, A., et al. (2008). Subdiffraction-resolution fluorescence imaging with conventional fluorescent probes. *Angew. Chem. Int. Ed Engl.* 47, 6172–6176. doi: 10.1002/anie.200802376

Juette, M. F., Gould, T. J., Lessard, M. D., Mlodzianoski, M. J., Nagpure, B. S., Bennett, B. T., et al. (2008). Three-dimensional sub-100 nm resolution fluorescence microscopy of thick samples. *Nat. Methods* 5, 527–529. doi: 10.1038/nmeth.1211

Kiskowski, M. A., Hancock, J. F., and Kenworthy, A. K. (2009). On the use of Ripley's K-function and its derivatives to analyze domain size. *Biophys. J.* 97, 1095–1103. doi: 10.1016/j.bpj.2009.05.039

Lorenzo, D. N., Badea, A., Zhou, R., Mohler, P. J., Zhuang, X., and Bennett, V. (2019). βII-spectrin promotes mouse brain connectivity through stabilizing axonal plasma membranes and enabling axonal organelle transport. *Proc. Natl. Acad. Sci. U S A.* 116, 15686–15695. doi: 10.1073/pnas.1820649116

Maglione, M., and Sigrist, S. J. (2013). Seeing the forest tree by tree: super-resolution light microscopy meets the neurosciences. *Nat. Neurosci.* 16, 790–797. doi: 10.1038/nn.3403

Nair, D., Hosy, E., Petersen, J. D., Constals, A., Giannone, G., Choquet, D., et al. (2013). Super-resolution imaging reveals that ampa receptors inside synapses are dynamically organized in nanodomains regulated by PSD95. *J. Neurosci.* 33, 13204–13224. doi: 10.1523/JNEUROSCI.2381-12.2013

Osterstock, G., Mitutsova, V., Barre, A., Granier, M., Fontanaud, P., Chazalon, M., et al. (2016). Somatostatin triggers rhythmic electrical

firing in hypothalamic GHRH neurons. *Sci. Rep.* 6:24394. doi: 10.1038/srep24394

Pechstein, A., and Shupliakov, O. (2010). Taking a back seat: synaptic vesicle clustering in presynaptic terminals. *Front. Synaptic Neurosci.* 2:143. doi: 10.3389/fnsyn.2010.00143

Peters, A., Palay, S. L., and Webster, H. D. (1991). *The Fine Structure of the Nervous System: Neurons and Their Supporting Cells.* New York, NY: Oxford University Press.

Pinto, S., Roseberry, A. G., Liu, H., Diano, S., Shanabrough, M., Cai, X., et al. (2004). Rapid rewiring of arcuate nucleus feeding circuits by leptin. *Science* 304, 110–115. doi: 10.1126/science.1089459

Plotsky, P., and Vale, W. (1985). Patterns of growth hormone-releasing factor and somatostatin secretion into the hypophysial-portal circulation of the rat. *Science* 230, 461–463. doi: 10.1126/science.2864742

Rahbek-Clemmensen, T., Lycas, M. D., Erlendsson, S., Eriksen, J., Apuschkin, M., Vilhardt, F., et al. (2017). Super-resolution microscopy reveals functional organization of dopamine transporters into cholesterol and neuronal activity-dependent nanodomains. *Nat. Commun.* 8:740. doi: 10.1038/s41467-017-00790-3

Reinhard, S., Aufmkolk, S., Sauer, M., and Doose, S. (2019). Registration and visualization of correlative super-resolution microscopy data. *Biophys. J.* 116, 2073–2078. doi: 10.1016/j.bpj.2019.04.029

Siddig, C. S., Aufmkolk, S., Doose, S., Jobin, M.-L., Werner, C., Sauer, M., et al. (2020). Super-resolution imaging reveals the nanoscale organization of metabotropic glutamate receptors at presynaptic active zones. *Sci. Adv.* 6, eaay719. doi: 10.1126/sciadv.aay7193

Sigal, Y. M., Zhou, R., and Zhuang, X. (2018). Visualizing and discovering cellular structures with super-resolution microscopy. *Science* 361, 880–887. doi: 10.1126/science.aau1044

Stanley, S., Ana Domingos, I., Kelly, L., Garfield, A., Damanpour, S., Heisler, L., et al. (2013). Profiling of glucose-sensing neurons reveals that GHRH neurons are activated by hypoglycemia. *Cell Metab.* 18, 596–607. doi: 10.1016/j.cmet.2013.09.002

Steyn, F. J., Huang, L., Ngo, S. T., Leong, J. W., Tan, H. Y., Xie, T. Y., et al. (2011). Development of a method for the determination of pulsatile growth hormone secretion in mice. *Endocrinology* 152, 3165–3171. doi: 10.1210/en.2011-0253

Stroh, T., van Schouwenburg, M. R., Beaudet, A., and Tannenbaum, G. S. (2009). Subcellular dynamics of somatostatin receptor subtype 1 in the rat arcuate nucleus: receptor localization and synaptic connectivity vary in parallel with the ultradian rhythm of growth hormone secretion. *J. Neurosci.* 29, 8198–8205. doi: 10.1523/JNEUROSCI.0336-09.2009

Suhr, S. T., Rahal, J. O., and Mayo, K. E. (1989). Mouse growth hormone-releasing hormone: precursor structure and expression in brain and placenta. *Mol. Endocrinol.* 3, 1693–1700. doi: 10.1210/mend-3-11-1693

Tannenbaum, G. S., and Ling, N. (1984). The interrelationship of growth hormone (GH)-releasing factor and somatostatin in generation of the ultradian rhythm of GH secretion. *Endocrinology* 115, 1952–1957. doi: 10.1210/endo-115-5-1952

Tannenbaum, G. S., and Martin, J. B. (1976). Evidence for an endogenous ultradian rhythm governing growth hormone secretion in the rat. *Endocrinology* 98, 562–570. doi: 10.1210/endo-98-3-562

Tannenbaum, G. S., Farhadi-Jou, F., and Beaudet, A. (1993). Ultradian oscillation in somatostatin binding in the arcuate nucleus of adult male rats. *Endocrinology* 133, 1029–1034. doi: 10.1210/endo.133.3.8103446

Theodosis, D. T., Poulain, D. A., and Vincent, J. D. (1981). Possible morphological bases for synchronisation of neuronal firing in the rat supraoptic nucleus during lactation. *Neuroscience* 6, 919–929. doi: 10.1016/0306-4522(81)90173-1

Vaden, J. H., Banumurthy, G., Gusarevich, E. S., Overstreet-Wadiche, L., and Wadiche, J. I. (2019). The readily-releasable pool dynamically regulates multivesicular release. *Elife* 8:e47434. doi: 10.7554/eLife.47434.023

Veeraraghavan, R., and Gourdie, R. G. (2016). Stochastic optical reconstruction microscopy-based relative localization analysis (STORM-RLA) for quantitative nanoscale assessment of spatial protein organization. *Mol. Biol. Cell* 27, 3583–3590. doi: 10.1091/mbc.E16-02-0125

Wagner, C., Caplan, S. R., and Tannenbaum, G. S. (1998). Genesis of the ultradian rhythm of GH secretion: a new model unifying experimental observations in rats. *Am. J. Physiol.* 275, E1046–E1054. doi: 10.1152/ajpendo.1998.275.6.E1046

Xu, K., Zhong, G., and Zhuang, X. (2013). Actin, spectrin and associated proteins form a periodic cytoskeletal structure in axons. *Science* 339, 452–456. doi: 10.1126/science.1232251

Conflict of Interest: The authors declare that the research was conducted in the absence of any commercial or financial relationships that could be construed as a potential conflict of interest.

frontiers in Neural Circuits

ORIGINAL RESEARCH
published: 03 June 2020
doi: 10.3389/fncir.2020.00024

Optogenetic Manipulation of Postsynaptic cAMP Using a Novel Transgenic Mouse Line Enables Synaptic Plasticity and Enhances Depolarization Following Tetanic Stimulation in the Hippocampal Dentate Gyrus

*Thomas T. Luyben[1,2], Jayant Rai[1,2], Hang Li[1], John Georgiou[1], Ariel Avila[1,3], Mei Zhen[1,2,4,5], Graham L. Collingridge[1,4,6], Takashi Tominaga[7] and Kenichi Okamoto[1,2]**

[1]Lunenfeld-Tanenbaum Research Institute, Mount Sinai Hospital, Toronto, ON, Canada, [2]Department of Molecular Genetics, Faculty of Medicine, University of Toronto, Toronto, ON, Canada, [3]Basic Science Department, Faculty of Medicine, Universidad Católica de la Santísima Concepción (UCSC), Concepción, Chile, [4]Department of Physiology, Faculty of Medicine, University of Toronto, Toronto, ON, Canada, [5]Department of Cell and Systems Biology, Faculty of Medicine, University of Toronto, Toronto, ON, Canada, [6]TANZ Centre for Research in Neurodegenerative Diseases (CRND), University of Toronto, Toronto, ON, Canada, [7]Laboratory for Neural Circuit Systems, Institute of Neuroscience, Tokushima Bunri University, Sanuki, Japan

OPEN ACCESS

Edited by:
Edward S. Ruthazer,
McGill University, Canada

Reviewed by:
Yumiko Yoshimura,
National Institute for Physiological Sciences (NIPS), Japan
Naofumi Uesaka,
The University of Tokyo, Japan

***Correspondence:**
Kenichi Okamoto
okamoto@lunenfeld.ca

Received: 18 February 2020
Accepted: 17 April 2020
Published: 03 June 2020

Citation:
Luyben TT, Rai J, Li H, Georgiou J, Avila A, Zhen M, Collingridge GL, Tominaga T and Okamoto K (2020) Optogenetic Manipulation of Postsynaptic cAMP Using a Novel Transgenic Mouse Line Enables Synaptic Plasticity and Enhances Depolarization Following Tetanic Stimulation in the Hippocampal Dentate Gyrus. Front. Neural Circuits 14:24. doi: 10.3389/fncir.2020.00024

cAMP is a positive regulator tightly involved in certain types of synaptic plasticity and related memory functions. However, its spatiotemporal roles at the synaptic and neural circuit levels remain elusive. Using a combination of a cAMP optogenetics approach and voltage-sensitive dye (VSD) imaging with electrophysiological recording, we define a novel capacity of postsynaptic cAMP in enabling dentate gyrus long-term potentiation (LTP) and depolarization in acutely prepared murine hippocampal slices. To manipulate cAMP levels at medial perforant path to granule neuron (MPP-DG) synapses by light, we generated transgenic (Tg) mice expressing photoactivatable adenylyl cyclase (PAC) in DG granule neurons. Using these Tg(CMV-Camk2a-RFP/bPAC)3Koka mice, we recorded field excitatory postsynaptic potentials (fEPSPs) from MPP-DG synapses and found that photoactivation of PAC during tetanic stimulation enabled synaptic potentiation that persisted for at least 30 min. This form of LTP was induced without the need for GABA receptor blockade that is typically required for inducing DG plasticity. The paired-pulse ratio (PPR) remained unchanged, indicating the cAMP-dependent LTP was likely postsynaptic. By employing fast fluorescent voltage-sensitive dye (VSD: di-4-ANEPPS) and fluorescence imaging, we found that photoactivation of the PAC actuator enhanced the intensity and extent of dentate gyrus depolarization triggered following tetanic stimulation. These results

demonstrate that the elevation of cAMP in granule neurons is capable of rapidly enhancing synaptic strength and neuronal depolarization. The powerful actions of cAMP are consistent with this second messenger having a critical role in the regulation of synaptic function.

Keywords: cAMP, optogenetics, photoactivatable adenylyl cyclase (PAC), VSD imaging, electrophysiology, long-term potentiation, synaptic plasticity

INTRODUCTION

Hippocampal synapses play a critical role in learning and memory and exhibit post-synaptic NMDA receptor-dependent long-term potentiation (LTP) of synaptic transmission (Collingridge et al., 1983; Moser et al., 1998; Gilbert et al., 2001). The postsynaptic cAMP/PKA pathway at both the CA3-CA1 and medial perforant path to dentate gyrus (MPP-DG) synapses is known to be involved in protein synthesis-dependent LTP (late-phase LTP, or L-LTP or LTP2; Brandon et al., 1995; Nguyen and Kandel, 1996; Barad et al., 1998; Park et al., 2018). However, the mechanisms by how cAMP contributes to the induction of NMDA receptor-dependent LTP are still incompletely understood.

cAMP function in synaptic plasticity at excitatory synapses has conventionally been studied using pharmacological and genetic approaches (Abel et al., 1997; Barad et al., 1998; Wong et al., 1999; Navakkode et al., 2004; Govindarajan et al., 2011; Park et al., 2016). However, recent advances in optogenetic techniques have made it possible to control spatiotemporal signaling functions within living neurons (Kim et al., 2015; Murakoshi et al., 2017), thus providing powerful tools for addressing dynamic molecular processes at synapses. In this regard, optogenetic manipulation of cAMP production has begun to show promise. Endogenous photoactivatable adenylyl cyclase (PAC) has been reported from several species including *Euglena* and bacteria (Iseki et al., 2002; Stierl et al., 2011) which have been utilized to study cAMP functions (Jansen et al., 2015; Zhou et al., 2016). However, methods to control cAMP with spatiotemporal precision within intact brain tissue remain limited.

The DG is a gateway to the hippocampus where it plays a critical role in learning and memory (Moser et al., 1998; Gilbert et al., 2001). To examine the consequences of cAMP modulation in this pathway, we generated a PAC transgenic mouse line expressing a photoactivatable cAMP actuator in hippocampal DG granule neurons. We examined synaptic responses by electrophysiology and performed voltage-sensitive dye (VSD) imaging (Grinvald and Hildesheim, 2004; Homma et al., 2009; Peterka et al., 2011; Tominaga et al., 2013) to optically record activation of the entire DG at the circuit level under high temporal resolution (Chang and Jackson, 2006; Tominaga et al., 2018).

In acutely prepared hippocampal slices from PAC Tg mice, photostimulation of the cAMP actuator during MPP-DG pathway tetanic stimulation enabled potentiation of synaptic responses that lasted for at least 30 min. Furthermore, activation of PAC during the tetanus resulted in a greater depolarization within the dentate gyrus. The findings demonstrate that transiently enhanced cAMP signaling during MPP activity can potentiate synaptic transmission and facilitate the spread of neuronal depolarization. Importantly, these actions were manifest without any disinhibition, which suggests that neuromodulators acting *via* cAMP can negate the inhibitory influences on synaptic plasticity in the dentate gyrus.

MATERIALS AND METHODS

Animal Care

Acute hippocampal slices were prepared following the guidelines of the animal use protocol approved by the animal care committees at The Centre for Phenogenomics (TCP; Toronto, ON, Canada) and Tokushima-Bunri University (Japan).

Transgene Construction and Generation of PAC Mice

We generated a transgene containing the CMV enhancer-CaMKIIα promoter (1.3 kb), the coding region of RFP (tdTomato) fused with PAC which is codon-optimized for human expression (addgene ID 28134; Stierl et al., 2011) at the C-terminal and contains a polyadenylation signal. The resulting cDNA was subcloned into a custom plasmid vector (pMM403), including a gene for ampicillin resistance, for bacterial amplification. The 5.2 kb transgene was digested with SfiI +SalI to linearize the DNA and remove prokaryotic sequences. Tg(CMV-Camk2a-RFP/PAC)3Koka mice were generated by injecting the purified insert into the pronuclei of C57BL/6D2 mice at The Centre for Phenogenomics (TCP, Toronto, ON, Canada). Genotyping was performed by PCR to detect an 859 bp fragment using the following primers: 5′-TTCTCCGTTTGC ACTCAGGAGC-3′ and 5′-GATGACGGCCATGTTGTTGT-3′. Founders were backcrossed with C57BL/6J mice for at least 10 generations. The official name for the resulting mouse line that we studied is C57BL/6J.B6 × B6D2-Tg(CMV-CamK2a-RFP/PAC)3koka.

Electrophysiology

Acute hippocampal slices were prepared as previously described (Henderson et al., 2001) from adult (13–24 week-old) PAC transgenic mice and their wild-type (WT) littermates. After 1–2 h recovery, slices were transferred to a recording chamber perfused with an aCSF solution containing 124 mM NaCl, 3 mM KCl, 2.5 mM $CaCl_2$, 1.3 mM $MgSO_4$, 1.25 mM NaH_2PO_4, 26 mM $NaHCO_3$, 10 mM glucose (pH 7.4, 30°C, 1.5 ml/min) equilibrated with 5% CO_2/95% O_2. Recordings of field excitatory postsynaptic potentials (fEPSPs) were conducted as previously described (Henderson et al., 2001) in the MPP-

DG synapses without blocking inhibitory synaptic function. The stimulation electrode was positioned in the dorsal blade of the dentate molecular layer for MPP stimulation. Paired field responses were evoked by stimulating with an intensity (0.05 ms pulses, 40 ms apart) that yielded fEPSPs that were 40% of the maximum spike-free fEPSP size. Responses were evoked and acquired every 20 s throughout the experiment using an Axopatch 1D amplifier (Axon Instruments, San Jose, CA, USA) digitized at 20 kHz and measured by the slope (10–50% of fEPSP rising phase). The expressed PAC in DG granule cells was photoactivated using a blue LED light (1.5 mW, 5 min, EXFO, Canada) under an objective lens (4×, NA0.1, Nikon, Tokyo, Japan). Tetanic stimulation was induced with a bipolar matrix Pt;Ir microelectrode (FHC, Inc., CA, USA) using 100 Hz, 0.15 ms pulses delivered in four trains of 0.5 s duration, 20 s apart. In the case of photoactivation of PAC during MPP stimulation, the tetani were delivered at the end of the first minute of light exposure. In the time-course experiments, field responses were plotted by normalizing to the baseline fEPSP slope (average of the 10 min period before tetanus).

Fluorescence Imaging of RFP-PAC in Hippocampal Slices

The hippocampal slices from PAC Tg mice were incubated with aCSF at room temperature in the microscope chamber. RFP fluorescence imaging of PAC was conducted using a confocal scanning microscope (Nikon C2 equipped with a 4× and 20× objective lenses, Nikon, Tokyo, Japan) with 543 nm (excitation laser) and 575–630 nm (emission). The fluorescence image was combined across the z-stacks composed of 30–50 sections taken at 5 μm intervals, and merged with the transmitted light image collected through a separate detector. The fluorescence images collected using the 20× objective lens were further deconvoluted (cellSens, Olympus, Tokyo, Japan).

cAMP Measurement by ELISA

The hippocampal slices from PAC and WT littermate mice were homogenized in buffer (40 mM HEPES/Na, pH 8.0, 0.1 mM EGTA, 5 mM magnesium acetate, 1 mM DTT, and 0.01% Tween-20) by sonication, and centrifuged at 16,000 *g* for 15 min to clear large tissue debris. After isolation of the supernatant, the total protein concentration was measured using Bradford assay (protein assay kit, Bio-Rad, CA, USA) and adjusted the total protein concentration between PAC TG and WT for the photoactivation experiment. The lysate (100 μl) were excited for 10 min with a 455 nm LED (4.5 mW/mm^2; ThorLabs, NJ, USA) on a plastic paraffin film (Parafilm M®, Bemis, USA) covered glass slide at room temperature, and cAMP was measured by ELISA (Enzo Life Sciences, NY, USA; Ryu et al., 2010; Stierl et al., 2011).

Fluorescent Voltage-Sensitive Dye (VSD) Imaging

Fluorescent VSD imaging was carried as previously reported (Tominaga and Tominaga, 2016; Tominaga et al., 2019). Briefly, acute hippocampal slices (400 μm thick) were prepared from adult (10–21 week-old) PAC transgenic mice and maintained in aCSF, containing 124 mM NaCl, 2.5 mM KCl, 2 mM $CaCl_2$, 2 mM $MgSO_4$, 1.25 mM NaH_2PO_4, 26 mM $NaHCO_3$, and 10 mM glucose, pH 7.4, gassed with 95% O_2/5% CO_2. After incubating for 1 h, each slice was stained for 15 min with 110 μl of VSD solution, containing 0.1 mM Di-4-ANEPPS (Molecular Probes, OR, USA) in 48.1% aCSF, 48.1% fetal bovine serum (Sigma–Aldrich, MO, USA), 2.5% ethanol, 1.17% distilled water, and 0.13% Cremophor EL (Sigma–Aldrich, MO, USA). After the washout of the dye with aCSF, slices were incubated for >1 h before the start of imaging.

Hippocampal slices (supported by Plexiglass ring) were placed in an immersion-type recording chamber (Tominaga et al., 2019). Slices were continuously perfused at a rate of 1 mL/min with aCSF at 31°C, gassed with 95% O_2/5% CO_2. The fluorescence VSD signals were recorded using a MiCAM Ultima imaging system with THT-01 epifluorescence optics (BrainVision, Inc., Tokyo, Japan), consisting of a two lenses system (Tominaga et al., 2000). A custom-made objective lens (Olympus MYCAM 5×/0.6 WI, Olympus, Tokyo, Japan) and a projection lens (PLANAPO, 1×, Leica Microsystems GmbH, Wetzlar, Germany). Excitation light was provided by a 150W halogen light source (MHF-G150LR, Moritex, Saitama, Japan) with an excitation filter (530 ± 10 nm) and an emission filter (>590 nm) for VSD imaging. VSD recordings of a duration of 400 ms (0.2 ms/frame, 2,048 frames) at 14 mW of excitation light were simultaneously obtained with electrophysiological recordings evoked with the delivery of a bipolar (0.2 ms pulse width) electrical stimulation to the MPP every 20 s. The intensity of the baseline electrical stimulation was determined to yield fEPSPs that were 40% of the maximum spike-free fEPSP size. Average of eight VSD recordings were presented as an optical signal. Recordings were taken before (baseline) and immediately following (time 0) tetanic stimulation (100 pulses × 100 Hz). PAC was photoactivated using 15 × 4 s duration pulses of excitation light (3.2 mW, 482/35 nm) every 10 s immediately before tetanic stimulation. The excitation wavelength used for PAC did not photobleach di-4-ANEPPS and vice versa. The imaging system provided a resolution of 18.2 × 18.2 μm at the objective plane (100 × 100 pixels resolution).

The fluorescence signal intensity before stimulation was averaged and used as the baseline reference intensity (F_0). The change in fluorescence [$\Delta F_{(t)} = F_{(t)} - F_0$] was normalized by F_0 ($\Delta F/F_0$) and used as the optical signal. Optical signals were then Gaussian filtered in time and space by 5 × 5 × 3 (horizontal × vertical × temporal; IgorPro; WaveMetrics Inc., OR, USA). Pseudo-colored optical voltage maps were superimposed on the initial (pre-stimulation) gray-scale fluorescent image of the hippocampal DG area for a visual reference of the location. Since di-4-ANEPPS decreases in fluorescence when the membrane depolarizes, we chose to represent this change as a positive value to make the results more intuitive (Tominaga et al., 2000, 2002). The pseudo-colored 3D presentation of the VSD fluorescence changes were created using Origin Pro

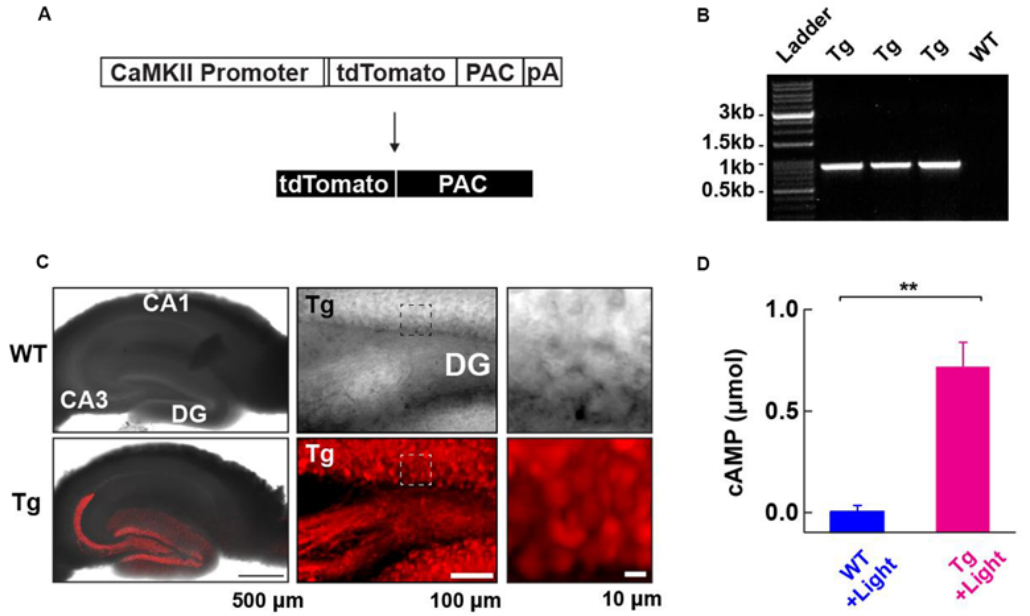

FIGURE 1 | Generation and characterization of photoactivatable adenylyl cyclase (PAC) expressing transgenic (Tg) mice. **(A)** Schematic representation of the PAC transgene construct. **(B)** Genotyping of the Tg(CMV-Camk2a-RFP/PAC)3Koka mice. The specific PCR amplification of an 859 bp band for PAC in Tg, but not wild-type (WT) mice was detected on the agarose gel. **(C)** Distribution of RFP (tdTomato)-PAC in the hippocampal slice. Left upper: WT (wild type), Left lower: Tg (PAC transgenic mouse). The RFP fluorescence (red color) on the living hippocampal slice was imaged by a confocal microscope and merged with the transmitted light image. Note: the red labeling extending into the CA3 region reflects signals in the mossy fiber axons of the DG granule neurons. Middle: a transmitted light (upper) and the corresponding red fluorescence (lower) deconvoluted confocal images of the hippocampal DG area in a living PAC Tg mouse hippocampal slice. About 85% of DG granule cells (141/163 cells) showed red fluorescence signals above the background level. Right: The transmitted light (upper) and the corresponding red fluorescence (lower) images within the boxed region in the middle images. **(D)** ELISA-based detection of the light-dependent cAMP production in the WT and Tg hippocampal lysate (per mg total protein) after illumination (455 nm LED, 4.5 mW/mm^2, 30 s; each $n = 3$). $^{**}p < 0.01$ (unpaired t-test). Data are presented as mean ± SEM.

(OriginLab, Northampton, MA, USA). The threshold levels of the signal/noise were set independently of the peak fluorescence changes, using a set threshold of 40% of the maximum signal intensity at baseline to determine the distribution area of the fluorescence changes. For fitting the plots (**Figure 5**), we used OriginPro (OriginLab, Northampton, MA, USA).

All recordings were made using a borosilicate pipette (5 µm inner diameter; filled with aCSF; ∼1 MΩ). Responses were evoked and acquired every 20 s throughout the experiment using a Model 440 amplifier (Neurophase LLC, Palo Alto, CA, USA) digitized at 10 kHz (ITC-18; InstruTech Inc., NY, USA) and measured by the slope (10–50% of fEPSP rising phase). Tetanic stimulation was induced with a single train (100 Hz for 1 s × 0.05 ms duration pulses) without blocking inhibitory synapse function. Tetanic stimulation was induced immediately after PAC photostimulation. The fEPSP change was plotted by normalizing to the baseline slope (average of the 10-min period before tetanus).

Statistical Analysis

Statistical methods are indicated in the figure legends. All data are presented as mean ± SEM. $^{***}p < 0.001$; $^{**}p < 0.01$; $^{*}p < 0.05$; NS, $p > 0.05$.

RESULTS

Generation of a PAC Expressing Transgenic Mouse Line

To address the role of cAMP in synaptic plasticity at medial perforant path (MPP) fibers synapsing onto dentate gyrus (DG) granule neurons (MPP-DG synapses), we designed transgenic (Tg) mice expressing PAC. We constructed a transgene in which the CaMKIIα promoter drives the expression of a red fluorescence protein (RFP)-tagged PAC (**Figure 1A**). After generating several founders of Tg mice we genotyped them by PCR (**Figure 1B**), analyzed the expression pattern of RFP fluorescence in the brain and selected a mouse line which showed high expression of RFP-PAC in DG granule neurons, but not their input from the entorhinal cortex (**Figure 1C**). To validate the light-dependent enzymatic function of PAC, we photoactivated brain lysate from the hippocampal slices of Tg mice for 30 s (455 nm LED, 4.5 mW/mm^2). The Tg lysates showed a light-dependent increase of cAMP compared with the brain lysate from the WT littermates, confirming that the expressed PAC actuator carries photoactivatable (cAMP generating) function within intact brain tissue

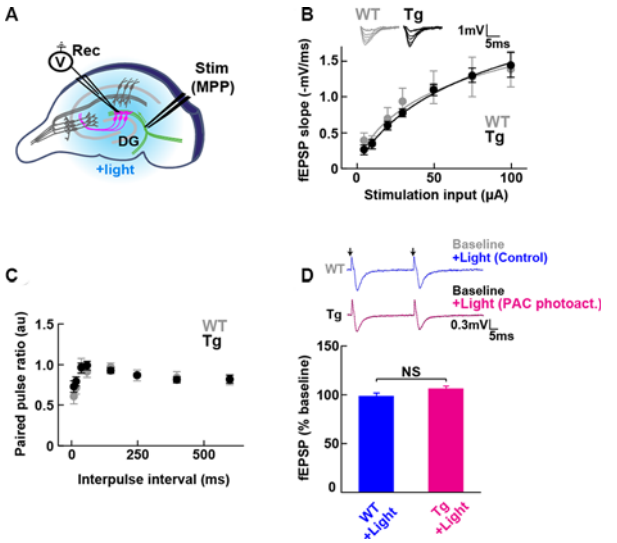

FIGURE 2 | Baseline transmission at medial perforant path to granule dentate gyrus (MPP-DG) synapses of Tg and WT mice. **(A)** Schematic of the DG recording (Rec) electrode to detect fEPSPs upon stimulation (stim) of the MPP of hippocampal brain slices. Light was delivered for photoactivation (blue light, 480 ± 15 nm) of PAC expressed within granule neurons (magenta). **(B)** Input/output relationship within MPP-DG synapses in the absence (WT) and presence of PAC (Tg; WT n = 7 slices/3 mice, Tg n = 16 slices/9 mice). Inset shows sample I/O responses superimposed. **(C)** Comparison of the paired-pulse ratio (PPR) calculated from the ratio of the second fEPSP slope to the first, at different interpulse intervals (WT n = 12 slices/4 mice, Tg n = 15 slices/7 mice). **(D)** Quantification of synaptic response with/without PAC photoactivation for 60 s during the baseline recording (Tg n = 11 slices/7 mice, WT n = 13 slices/3 mice). NS, $p > 0.05$ (unpaired t-test). Data are presented as mean ± SEM. Upper: sample paired-pulse traces show the fEPSP responses before (Baseline) and 1 min after (+Light) light stimulation. Black arrows indicate the time of the single pulses of stimulation.

(**Figure 1D**). These initial validation experiments on the Tg(CMV-Camk2a-RFP/PAC)3Koka new mouse line were carried out in the absence of any evoked axonal stimulation and set the stage for further studies on cAMP action on synaptic function *in situ*.

Expressed PAC Does Not Affect Baseline MPP-DG Synaptic Transmission

To test whether the expression of PAC (without photoactivation) has any impact on the basal synaptic transmission at intact MPP-DG synapses, we measured the field excitatory postsynaptic potentials (fEPSPs) in the acutely prepared hippocampal slices (**Figure 2A**). The input/output (I/O) curves and paired-pulse ratio (PPR) showed no significant difference between PAC Tg animals and their WT littermates (**Figures 2B,C**), suggesting no effect of PAC expression on basal synaptic properties.

To test the effect of PAC photoactivation on basal synaptic responses at MPP-DG synapses, we next illuminated the slices with LED light (480 ± 15 nm, 1.5 mW for 60 s) under a fluorescence microscope and recorded the fEPSPs (**Figure 2D**). However, photoactivation of PAC alone did not affect basal synaptic transmission at MPP-DG synapses.

Postsynaptic cAMP Enables Synaptic Potentiation

We next examined whether photoactivation of PAC has any effect on activity-dependent synaptic potentiation. The DG exhibits strong inhibition, such that tetanic stimulation of the MPP input is insufficient for generating LTP *in situ* unless GABA receptors are blocked (Wigstrom and Gustafsson, 1983; Nguyen and Kandel, 1996). However, upon photoactivation of PAC in combination with the tetanic stimulation of the MPP, we observed a robust synaptic potentiation that lasted for the entire 30 min of the post-tetanic recording period (**Figures 3A,B**, +Light, Tg). In contrast, in the absence of light delivery, tetanic stimulation of the MPP-DG synapses induced a weak and transient synaptic potentiation lasting only a few minutes (**Figures 3A,B**, −Light, Tg). Similarly, the WT littermates did not show the enhancement even with the same amount of light delivery upon tetanus (**Figures 3A,B**, +Light, WT). The PPR yields a short-term depression at MPP-DG synapses, a measure of the probability of release and short-term presynaptic plasticity. This parameter was not significantly altered 30 min after delivery of a tetanus either in the absence or presence of PAC photoactivation (**Figure 3C**). The data are consistent with an entirely postsynaptic effect, whereby tetanic potentiation in the presence of elevated cAMP leads to persistent potentiation of synaptic transmission.

Combination of Optogenetic cAMP Manipulation With VSD Imaging

To evaluate the effect of cAMP on the global depolarization associated with the tetanus-induced potentiation, we employed fast (VSD: di-4-ANEPPS; Fluhler et al., 1985; Loew et al., 1992) imaging in combination with PAC photoactivation. For the optical recordings of membrane potential changes, we set up the custom-epifluorescence optical system equipped with a CMOS camera and a LED equipped with a feedback-stabilizing controller for constant LED light output (**Figure 4A**). In this system, the excitation wavelength (530 ± 10 nm) for VSD imaging has no overlap with the photoactivation wavelength of PAC (which required wavelengths up to 500 nm light). The excitation light was minimized for capturing the sufficient amount of VSD (di-4-ANEPPS) fluorescence needed for live high-speed imaging. For the photoactivation of PAC on the slices of PAC Tg mice, we switched the filter before blue light illumination (482 ± 17.5 nm; **Figure 4B**). Using VSD imaging, we optically monitored the depolarization that spread throughout the DG and also collected fEPSPs by electrophysiology (**Figure 4C**). Since the photoactivation of PAC alone did not affect basal synaptic transmission at MPP-DG synapses (**Figure 4C** right upper inset), we optically monitored the light-dependent cAMP effect on tetanus-induced fEPSP potentiation (**Figure 4C** right lower inset, **4D**).

Effect of cAMP on Depolarization During MPP-DG Potentiation

Photoactivation of PAC followed by tetanic stimulation showed an increased fluorescence intensity change in the DG area compared with controls receiving no 482 nm light (**Figure 4E**).

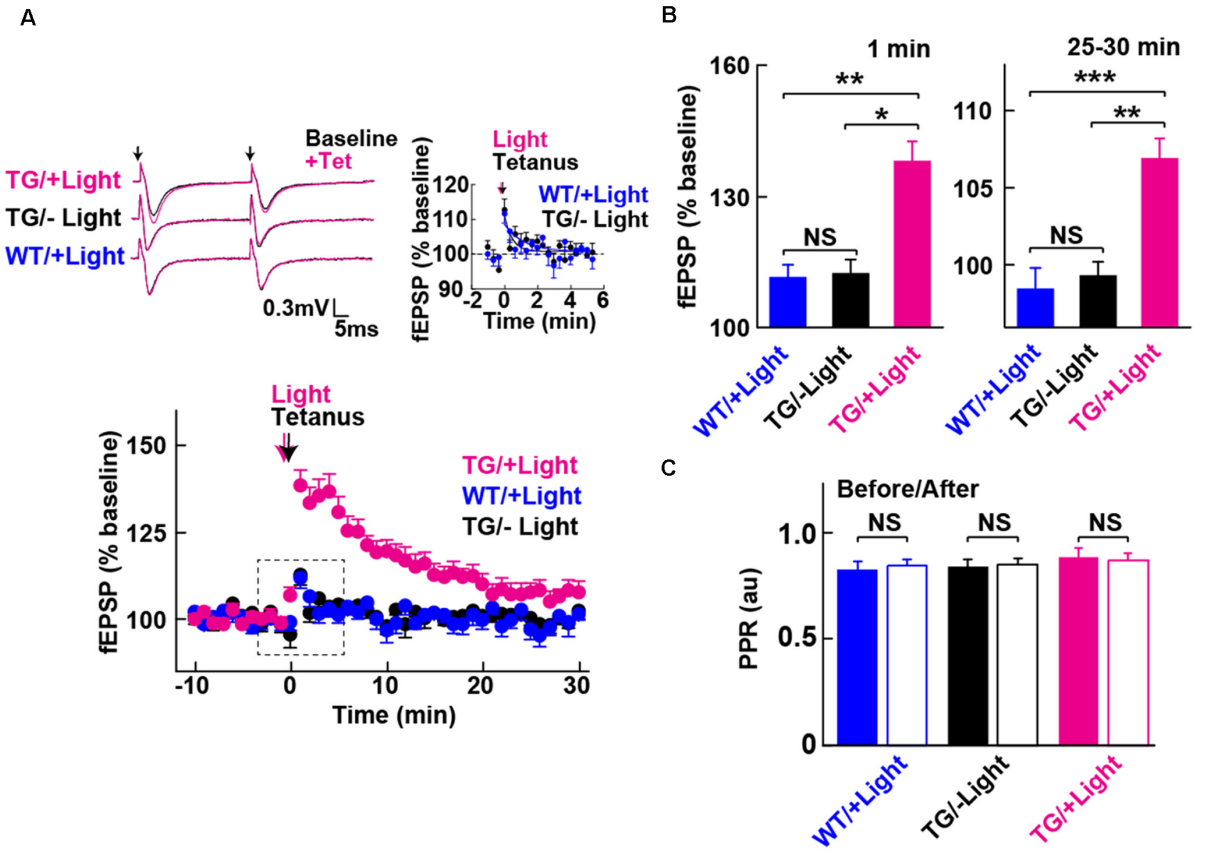

FIGURE 3 | Long-term potentiation (LTP) enabled by photoactivation of PAC. **(A)** Lower: Blue light (480 nm, 5 min) photoactivation of PAC during tetanic stimulation (100 Hz × 4 trains, arrow) of MPP-DG synapses evoked potentiation of responses that persisted for 30 min. Hippocampal slices from WT mice receiving light, as well as Tg slices not receiving light, showed a transient and relatively small potentiation lasting about a minute (−Light, TG n = 10 slices/3 mice, +Light, TG n = 11 slices/7 mice, +Light, WT n = 13 slices/3 mice). Left upper: sample paired-pulse traces (scale bar of 0.3 mV and 5 ms) show superimposition of the fEPSP response before (Baseline; black) and 1 min after (+Tet; magenta) tetanic stimulation. Black arrows indicate the time of single pulses of stimulation. Right upper: comparison of post-tetanic potentiation within the boxed region in the lower graph showing the fEPSP normalized slope in expanded detail for the two control conditions, WT littermates in the presence of blue light (cyan) and Tg animals without blue light (black). **(B)** Quantification of synaptic potentiation at 1 min and 25–30 min after tetanus **(A)**. *$p < 0.05$, **$p < 0.01$, ***$p < 0.001$ (Tukey test). **(C)** Comparison of PPR before (−10 to 0 min) and after the tetanic stimulation (10–20 min) in the three conditions revealed no statistically significant differences (sample size identical to A). NS, $p > 0.05$ (paired t-test). All data displayed are mean ± SEM.

The enhancement in depolarization occurred together with the fEPSP potentiation suggesting they are both consequences of cAMP generation (**Figure 4G**). In the absence of PAC photoactivation, the area of VSD fluorescence measured before vs. after the tetanus did not change (**Figures 4F**, **5**, −Light). However, the region of fluorescence change was significantly enlarged by a tetanus that was preceded with photoactivation of PAC (**Figures 4F**, **5**, +Light). A three-dimensional (3D) map of the averaged fluorescence changes visually shows the overall increase of both intensity and area of activity in the DG after tetanic stimulation of the MPP pathway in the presence of cAMP (photoactivation of PAC) compared with the tetanus alone (**Figure 5**). These results demonstrate that cAMP enhances the extent of dentate neuronal activation, enabling depolarization signals to propagate further.

DISCUSSION

In this study, we generated Tg mice overexpressing PAC in the granule neurons of the hippocampal DG. We prepared brain slices from the Tg mice and imaged the CaMKIIα-driven expression of PAC by way of the built-in RFP reporter. Confocal imaging revealed that the Tg(CMV-Camk2a-RFP/PAC)3Koka transgenic mice expressed abundant levels of RFP within the dentate granule cells, although further characterization is necessary to confirm the full specificity of the expression. This new mouse line did not show detectable levels of RFP expression in the DG input from the entorhinal cortex, suggesting exclusive and/or selective postsynaptic expression in the dentate granule neurons. Furthermore, the lysates from Tg slices showed photoactivity-dependent cAMP production upon delivery of blue light. In addition, tetanic activation of MPP to dentate

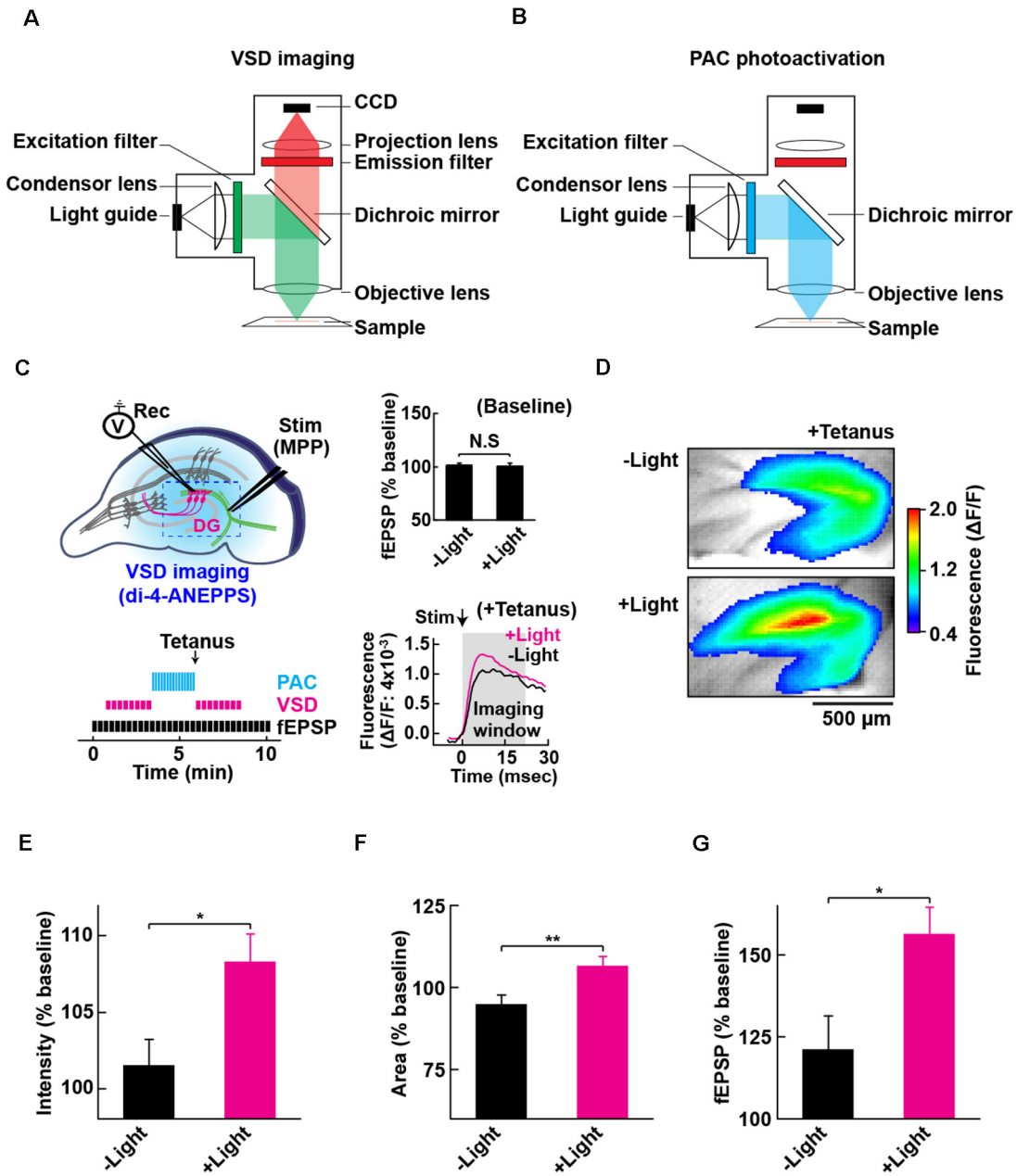

FIGURE 4 | Configuration for PAC photoactivation and voltage-sensitive dye (VSD) imaging. A schematic of the setup for VSD imaging **(A)** and PAC photoactivation **(B)** in the fluorescence microscope. After PAC photoactivation, we switched the filter cube to detect VSD optical signal by the CCD-based camera system. The excitation light (530 ± 10 nm) for VSD imaging does not photoactivate PAC (down to 500 nm). **(C)** Left upper: schematic of PAC photoactivation, fEPSP recording and VSD imaging in PAC Tg hippocampal slices. The dotted rectangle indicates an ROI region for VSD imaging of fluorescence signal (di-4-ANEPPS). Left lower: time-course of VSD imaging with fEPSP recording before and after photoactivation of PAC with tetanic stimulation. VSD fluorescence changes were recorded as an average of eight images (400 ms duration each) taken every 20 s before and after tetanic stimulation (1 train, 100 × 100 Hz, 0.05 ms duration pulses). Right upper: quantification of synaptic response before/after PAC photoactivation for 60 s during the recording of VSD imaging (n = 11 slices/3 mice. NS, $p > 0.05$ (paired t-test). Data are presented as mean ± SEM. Right lower: trace of VSD fluorescence signal with/without PAC photoactivation (+Light/−Light). The black arrow (Stim) shows the time of delivery of tetanic stimulation which evoked the optical signals (at 0 ms). Gray box (Imaging analysis window): time window (0–20 ms) used for the measurement of fluorescence changes during basal stimulation and after the tetanic stimulation. **(D)** Representative VSD images in the DG area after tetanus with (+Light) or without (−Light) PAC photoactivation. The VSD fluorescence signal changes are displayed in pseudo color at the peak change time (6.4 ms). Warmer red colors indicate higher fluorescence intensities, signifying stronger depolarization. **(E–G)** Quantification of the changes **(C,D)** in the averaged peak fluorescence intensity **(E)** and area **(F)** during 0.4–160 s after tetanus (8 × 20 ms imaging every 20 s), and the fEPSP changes 0.05 ms after tetanus **(G)** with (+Light, n = 8 slices/2 mice) or without (−Light, n = 7 slices/2 mice) PAC photoactivation. *$p < 0.05$; **$p < 0.01$ (unpaired t-test). Data are presented as mean ± SEM.

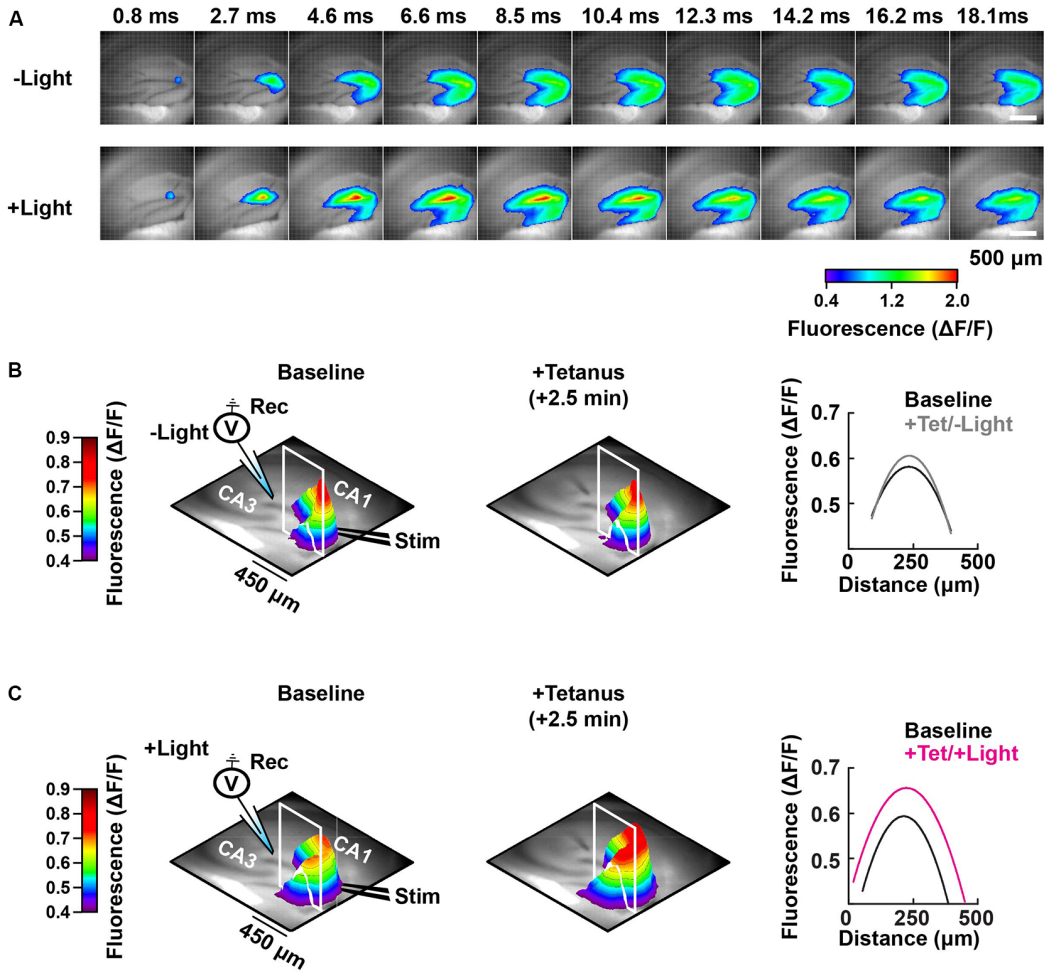

FIGURE 5 | Spatial-temporal mapping of the PAC-induced enhancement of DG depolarization. **(A)** Representative time-lapse images of the VSD fluorescence change (depicted in pseudocolor scale) after tetanus, collected either without (−Light; upper row) or with photostimulation to activate PAC (+Light; lower row). **(B)** Left and middle: pseudo-colored 3D graph of the averaged peak VSD fluorescence change in the hippocampal DG region before (Baseline) and after tetanic stimulation (+Tetanus). The 3D fluorescence images were calculated as the ratio of the fluorescence changes before and after tetanus. Right: fluorescence profiles across the lines in the 3D fluorescence distribution (white line of left and middle) fitted with a parabola. Black, before tetanic stimulation (Baseline); grey, after tetanic stimulation without photostimulation to activate PAC (+Tet/−Light); magenta, after tetanic stimulation with the photostimulation (+Tet/+Light). The same analysis shown in panel **(B)** which was performed without PAC activation (−Light; *n* = 56 images/7 slices/2 mice), was repeated in panel **(C)** with PAC (+Light; *n* = 64 images/8 slices/2 mice) activation, respectively.

synapses enabled LTP in Tg slices that received light during the tetanus. Presynaptic function was unaffected, indicating that when postsynaptic cAMP is elevated during high-frequency synaptic activity, there is a robust postsynaptic potentiation of synaptic strength that persists for at least 30 min.

Optogenetic Manipulation of cAMP in Neurons

In addition to actuators such as PAC, other light-dependent cAMP production methods have also been reported. Opto-β2AR and its derivatives are chimeric rhodopsins that light-dependently release a G-protein subunit to activate adenylyl cyclase, AC (Airan et al., 2009). Compared to PAC, which directly produces AC upon light activation, this approach is indirect and acts through G-protein signaling pathways, that may conceivably affect multiple and diverse signaling cascades. Membrane-permeant caged cAMP is another method to instantaneously release cAMP by light (Moutinho et al., 2001; Nicol et al., 2007). However, this method is not ideal for repeated application over time, and a UV-requirement for uncaging prevents tissue penetrance and spatial specificity in tissues. Our results present an effective and consistent means to control and study the role of cAMP in native tissue.

cAMP Elevation Results in the Spread of Depolarization in Granule Cells

To spatially investigate the amount and extent of granule cell activation by postsynaptic cAMP, we utilized (VSD)

imaging to record changes in global DG depolarization upon MPP stimulation in acutely prepared hippocampal slices. We applied Di-4-ANNEPS for VSD imaging in combination with photostimulation of the PAC Tg brain slices. Di-4-ANNEPS is highly soluble in lipid solutions, remains longer in the membrane, making it suitable for long-term recordings of neural activity in brain slices (Tominaga et al., 2000, 2009, 2018). The excitation wavelength (530 ± 10 nm) for VSD imaging avoids photoactivation of PAC (<500 nm). The combination of optogenetic approaches to manipulate cAMP levels and image with VSD revealed that postsynaptic cAMP serves as a rapid positive modulator of excitation at MPP-DG synapses in hippocampal slices. Furthermore, cAMP expanded the activation area in the DG further along the MPP after tetanic stimulation. The enlarged region contains the soma and dendrites of granule cells, suggesting an increased number of activated synapses on the dendrites. The enlarged DG region of fluorescence change following tetanic stimulation paired with the optically-triggered generation of cAMP may indicate an increased number of activated synapses. For instance, cAMP may enhance the activity of weakly stimulated synapses (subthreshold stimulation for activation), and/or spread to more synapses to trigger heterosynaptic facilitation of LTP (Park et al., 2019). In principle, this photostimulation method for manipulating cAMP levels will be useful for characterizing the spatial-temporal features of this phenomenon.

cAMP Elevation Enables LTP in Granule Cells Under Standard Slice Recording Conditions

Within brain slices, the strong DG inhibition normally precludes LTP to be induced by tetanic stimulation, unless GABA receptors are blocked (Wigstrom and Gustafsson, 1983; Nguyen and Kandel, 1996). It is therefore of interest that LTP could be readily induced without the need to pharmacologically remove synaptic inhibition when the tetanus was paired with cAMP elevation. Thus, cAMP circumvents the inhibitory influence of GABA-mediated synaptic inhibition. This property may be utilized by neuromodulatory systems, such as dopaminergic and noradrenergic, which can elevate cAMP within the dentate gyrus and facilitate LTP (Hamilton et al., 2010; Yang and Dani, 2014; Palacios-Filardo and Mellor, 2019). In this manner, powerful inhibitory processes restrict LTP until appropriate neuromodulatory inputs provide the necessary salience.

A potential mechanism for how cAMP reduces the influence of GABAergic inhibition relates to the spread and enhancement of depolarization of granule cells that we observed. Ordinarily, the synaptic activation of NMDA receptors is limited by the synaptic activation of GABA inhibition, which hyperpolarizes the membrane to intensify the Mg^{2+} block of NMDA receptors (Herron et al., 1985; Dingledine et al., 1986). The increase in depolarization would counteract this effect. Indeed, there was a trend towards a larger depolarizing field potential recorded immediately after the tetanic trains (PAC + light group vs. controls), which is consistent with enhanced synaptic activation of NMDA receptors. However, further experiments on current-clamped granule neurons are necessary to establish whether this is indeed the case. A candidate mechanism for this depolarization that we observed is the cyclic nucleotide-gated and -regulated channels, such as HCN1, that can be dynamically and rapidly modulated at the neuronal cell membrane (Robinson and Siegelbaum, 2003; Noam et al., 2010). An additional mechanism may involve the direct phosphorylation of NMDA receptors by PKA, following cAMP elevation (Skeberdis et al., 2006). Further experiments will need to be designed to examine these potential mechanisms.

An interesting feature of the cAMP-enabled LTP that we have described here is its rapid time-course of activation. Originally, cAMP was implicated in late-phase LTP, defined as the protein synthesis-dependent form of LTP that takes many tens of minutes to hours to develop (Frey et al., 1993; Matthies and Reymann, 1993; Huang and Kandel, 1994; Park et al., 2016). However, depending on the induction pattern, it became evident that cAMP-, AC-, and PKA are involved in early effects immediately after tetanic stimulation (Huang et al., 1994; Blitzer et al., 1995; Otmakhova et al., 2000). Furthermore, the application of rolipram, which inhibits the breakdown of cAMP, can greatly augment tetanus-induced LTP from its onset (Barad et al., 1998; Navakkode et al., 2004; Park et al., 2016). Therefore, under a variety of conditions, cAMP elevation can rapidly facilitate or permit synaptic plasticity.

In summary, we have developed a Tg mouse line expressing the actuator PAC and RFP reporter in granule neurons within hippocampal DG. We employed an optical system for photoactivation of PAC and simultaneously optically imaged membrane potential changes using the fast VSD di-4-ANEPPS in combination with electrophysiology. The work revealed that elevating postsynaptic cAMP at the same time as delivering tetanic stimulation results in a larger depolarization that spreads further within the dentate gyrus. It also enables the induction of LTP under conditions where LTP is not normally observed. We conclude that postsynaptic cAMP serves as a powerful modulator of synaptic plasticity at medial perforant path synapses onto dentate gyrus granule cells.

DATA AVAILABILITY STATEMENT

All datasets generated for this study are included in the article.

ETHICS STATEMENT

The animal study was reviewed and approved by the animal care committee at The Centre for Phenogenomics (TCP; Toronto, ON, Canada) and Tokushima-Bunri University (Japan).

AUTHOR CONTRIBUTIONS

HL constructed a transgene and genotyped the founder lines made at TCP. HL and TL selected, maintained and backcrossed the PAC transgenic mouse after confirming DG expression with JG. JG carried out the pilot LTP work in the DG, which was followed up by TL. AA and JG prepared the hippocampal slices

for the pure electrophysiology by TL in the GC lab. TL and JR performed RFP imaging studies with JG. MZ supports JR work. TL performed the combined electrophysiological and VSD imaging experiments in the TT lab. KO, JG, and TT designed the experiments. KO conceived the study. KO, TL, JG, TT, and GC wrote the manuscript.

FUNDING

This work was supported by the Canadian Institutes of Health Research (CIHR, MOP111220, PJT 156103, KO), Natural Sciences and Engineering Research Council of Canada Discovery Grants (2017-06444, KO), Canada Foundation for Innovation (KO), CIHR Foundation Scheme (CIHR 154274, MZ). This work was supported by the Brain Canada Foundation through the Canada Brain Research Fund, with the financial support of Health Canada. JG and AA were supported by Brain Canada and a CIHR Foundation grant to GC. This study was also supported by Japan Society for the Promotion of Science (JSPS) KAKENHI Grant Number (JP16H06532, JP16K21743, JP16H06524, JP19H01142, JP19K12190, JP19K22990) to TT, and grants from the Ministry of Health, Labour and Welfare [MHLW-Kagaku-ippan-H30 (18062156)] to TT.

ACKNOWLEDGMENTS

We thank Dr. Yoko Tominaga (Tokushima Bunri University) for the software development/assistance of VSD imaging. We thank all of the staff at TCP including Marina Gertsenstein (Transgenics Core), Julia Silva, Betty-Jo Edgell, all previous staff including Kyle Duffin, as well as veterinarian support (Lise Phaneuf and Amanda Healy) and the Animal Care Committee.

REFERENCES

Abel, T., Nguyen, P. V., Barad, M., Deuel, T. A., Kandel, E. R., and Bourtchouladze, R. (1997). Genetic demonstration of a role for PKA in the late phase of LTP and in hippocampus-based long-term memory. *Cell* 88, 615–626. doi: 10.1016/s0092-8674(00)81904-2

Airan, R. D., Thompson, K. R., Fenno, L. E., Bernstein, H., and Deisseroth, K. (2009). Temporally precise *in vivo* control of intracellular signalling. *Nature* 458, 1025–1029. doi: 10.1038/nature 07926

Barad, M., Bourtchouladze, R., Winder, D. G., Golan, H., and Kandel, E. (1998). Rolipram, a type IV-specific phosphodiesterase inhibitor, facilitates the establishment of long-lasting long-term potentiation and improves memory. *Proc. Natl. Acad. Sci. U S A* 95, 15020–15025. doi: 10.1073/pnas.95.25.15020

Blitzer, R. D., Wong, T., Nouranifar, R., Iyengar, R., and Landau, E. M. (1995). Postsynaptic cAMP pathway gates early LTP in hippocampal CA1 region. *Neuron* 15, 1403–1414. doi: 10.1016/0896-6273(95)90018-7

Brandon, E. P., Zhuo, M., Huang, Y. Y., Qi, M., Gerhold, K. A., Burton, K. A., et al. (1995). Hippocampal long-term depression and depotentiation are defective in mice carrying a targeted disruption of the gene encoding the RI β-subunit of cAMP-dependent protein kinase. *Proc. Natl. Acad. Sci. U S A* 92, 8851–8855. doi: 10.1073/pnas.92.19.8851

Chang, P. Y., and Jackson, M. B. (2006). Heterogeneous spatial patterns of long-term potentiation in rat hippocampal slices. *J. Physiol.* 576, 427–443. doi: 10.1113/jphysiol.2006.112128

Collingridge, G. L., Kehl, S. J., and McLennan, H. (1983). The antagonism of amino acid-induced excitations of rat hippocampal CA1 neurones *in vitro*. *J. Physiol.* 334, 19–31. doi: 10.1113/jphysiol.1983.sp014477

Dingledine, R., Hynes, M. A., and King, G. L. (1986). Involvement of N-methyl-D-aspartate receptors in epileptiform bursting in the rat hippocampal slice. *J. Physiol.* 380, 175–189. doi: 10.1113/jphysiol.1986.sp016279

Fluhler, E., Burnham, V. G., and Loew, L. M. (1985). Spectra, membrane binding, and potentiometric responses of new charge shift probes. *Biochemistry* 24, 5749–5755. doi: 10.1021/bi00342a010

Frey, U., Huang, Y. Y., and Kandel, E. R. (1993). Effects of camp simulate a late-stage of LTP in hippocampal Ca1 neurons. *Science* 260, 1661–1664. doi: 10.1126/science.8389057

Gilbert, P. E., Kesner, R. P., and Lee, I. (2001). Dissociating hippocampal subregions: a double dissociation between dentate gyrus and CA1. *Hippocampus* 11, 626–636. doi: 10.1002/hipo.1077

Govindarajan, A., Israely, I., Huang, S.-Y., and Tonegawa, S. (2011). The dendritic branch is the preferred integrative unit for protein synthesis-dependent LTP. *Neuron* 69, 132–146. doi: 10.1016/j.neuron.2010.12.008

Grinvald, A., and Hildesheim, R. (2004). VSDI: a new era in functional imaging of cortical dynamics. *Nat. Rev. Neurosci.* 5, 874–885. doi: 10.1038/nrn1536

Hamilton, T. J., Wheatley, B. M., Sinclair, D. B., Bachmann, M., Larkum, M. E., and Colmers, W. F. (2010). Dopamine modulates synaptic plasticity in dendrites of rat and human dentate granule cells. *Proc. Natl. Acad. Sci. U S A* 107, 18185–18190. doi: 10.1073/pnas.1011558107

Henderson, J. T., Georgiou, J., Jia, Z., Robertson, J., Elowe, S., Roder, J. C., et al. (2001). The receptor tyrosine kinase EphB2 regulates NMDA-dependent synaptic function. *Neuron* 32, 1041–1056. doi: 10.1016/s0896-6273(01)00553-0

Herron, C. E., Lester, R. A., Coan, E. J., and Collingridge, G. L. (1985). Intracellular demonstration of an N-methyl-D-aspartate receptor mediated component of synaptic transmission in the rat hippocampus. *Neurosci. Lett.* 60, 19–23. doi: 10.1016/0304-3940(85)90375-1

Homma, R., Baker, B. J., Jin, L., Garaschuk, O., Konnerth, A., Cohen, L. B., et al. (2009). Wide-field and two-photon imaging of brain activity with voltage- and calcium-sensitive dyes. *Methods Mol. Biol.* 489, 43–79. doi: 10.1007/978-1-59745-543-5_3

Huang, Y. Y., Li, X. C., and Kandel, E. R. (1994). cAMP contributes to mossy fiber LTP by initiating both a covalently mediated early phase and macromolecular synthesis-dependent late phase. *Cell* 79, 69–79. doi: 10.1016/0092-8674(94)90401-4

Huang, Y. Y., and Kandel, E. R. (1994). Recruitment of long-lasting and protein kinase A-dependent long-term potentiation in the CA1 region of hippocampus requires repeated tetanization. *Learn. Mem.* 1, 74–82.

Iseki, M., Matsunaga, S., Murakami, A., Ohno, K., Shiga, K., Yoshida, K., et al. (2002). A blue-light-activated adenylyl cyclase mediates photoavoidance in Euglena gracilis. *Nature* 415, 1047–1051. doi: 10.1038/4151047a

Jansen, V., Alvarez, L., Balbach, M., Strünker, T., Hegemann, P., Kaupp, U. B., et al. (2015). Controlling fertilization and cAMP signaling in sperm by optogenetics. *eLife* 4:e05161. doi: 10.7554/eLife.05161

Kim, K., Lakhanpal, G., Lu, H. E., Khan, M., Suzuki, A., Hayashi, M. K., et al. (2015). A temporary gating of actin remodeling during synaptic plasticity consists of the interplay between the kinase and structural functions of CaMKII. *Neuron* 87, 813–826. doi: 10.1016/j.neuron.2015.07.023

Loew, L. M., Cohen, L. B., Dix, J., Fluhler, E. N., Montana, V., Salama, G., et al. (1992). A naphthyl analog of the aminostyryl pyridinium class of potentiometric membrane dyes shows consistent sensitivity in a variety of tissue, cell, and model membrane preparations. *J. Membr. Biol.* 130, 1–10. doi: 10.1007/bf00233734

Matthies, H., and Reymann, K. G. (1993). Protein kinase A inhibitors prevent the maintenance of hippocampal long-term potentiation. *Neuroreport* 4, 712–714. doi: 10.1097/00001756-199306000-00028

Moser, E. I., Krobert, K. A., Moser, M. B., and Morris, R. G. M. (1998). Impaired spatial learning after saturation of long-term potentiation. *Science* 281, 2038–2042. doi: 10.1126/science.281.5385.2038

Moutinho, A., Hussey, P. J., Trewavas, A. J., and Malhó, R. (2001). cAMP acts as a second messenger in pollen tube growth and reorientation. *Proc. Natl. Acad. Sci. U S A* 98, 10481–10486. doi: 10.1073/pnas.171104598

Murakoshi, H., Shin, M. E., Parra-Bueno, P., Szatmari, E. M., Shibata, A. C. E., and Yasuda, R. (2017). Kinetics of endogenous CaMKII required for synaptic plasticity revealed by optogenetic kinase inhibitor. *Neuron* 94, 37.e5–47.e5. doi: 10.1016/j.neuron.2017.02.036

Navakkode, S., Sajikumar, S., and Frey, J. U. (2004). The type IV-specific phosphodiesterase inhibitor rolipram and its effect on hippocampal long-term potentiation and synaptic tagging. *J. Neurosci.* 24, 7740–7744. doi: 10.1523/JNEUROSCI.1796-04.2004

Nguyen, P. V., and Kandel, E. R. (1996). A macromolecular synthesis-dependent late phase of long-term potentiation requiring cAMP in the medial perforant pathway of rat hippocampal slices. *J. Neurosci.* 16, 3189–3198. doi: 10.1523/JNEUROSCI.16-10-03189.1996

Nicol, X., Voyatzis, S., Muzerelle, A., Narboux-Nême, N., Südhof, T. C., Miles, R., et al. (2007). cAMP oscillations and retinal activity are permissive for ephrin signaling during the establishment of the retinotopic map. *Nat. Neurosci.* 10, 340–347. doi: 10.1038/nn1842

Noam, Y., Zha, Q., Phan, L., Wu, R. L., Chetkovich, D. M., Wadman, W. J., et al. (2010). Trafficking and surface expression of hyperpolarization-activated cyclic nucleotide-gated channels in hippocampal neurons. *J. Biol. Chem.* 285, 14724–14736. doi: 10.1074/jbc.M109.070391

Otmakhova, N. A., Otmakhov, N., Mortenson, L. H., and Lisman, J. E. (2000). Inhibition of the cAMP pathway decreases early long-term potentiation at CA1 hippocampal synapses. *J. Neurosci.* 20, 4446–4451. doi: 10.1523/JNEUROSCI.20-12-04446.2000

Palacios-Filardo, J., and Mellor, J. R. (2019). Neuromodulation of hippocampal long-term synaptic plasticity. *Curr. Opin. Neurobiol.* 54, 37–43. doi: 10.1016/j.conb.2018.08.009

Park, P., Kang, H., Sanderson, T. M., Bortolotto, Z. A., Georgiou, J., Zhuo, M., et al. (2018). The role of calcium-permeable AMPARs in long-term potentiation at principal neurons in the rodent hippocampus. *Front. Synaptic Neurosci.* 10:42. doi: 10.3389/fnsyn.2018.00042

Park, P., Kang, H., Sanderson, T. M., Bortolotto, Z. A., Georgiou, J., Zhuo, M., et al. (2019). On the role of calcium-permeable AMPARs in long-term potentiation and synaptic tagging in the rodent hippocampus. *Front. Synaptic Neurosci.* 11:4. doi: 10.3389/fnsyn.2019.00004

Park, P., Sanderson, T. M., Amici, M., Choi, S. L., Bortolotto, Z. A., Zhuo, M., et al. (2016). Calcium-permeable AMPA receptors mediate the induction of the protein kinase A-dependent component of long-term potentiation in the hippocampus. *J. Neurosci.* 36, 622–631. doi: 10.1523/jneurosci.3625-15.2016

Peterka, D. S., Takahashi, H., and Yuste, R. (2011). Imaging voltage in neurons. *Neuron* 69, 9–21. doi: 10.1016/j.neuron.2010.12.010

Robinson, R. B., and Siegelbaum, S. A. (2003). Hyperpolarization-activated cation currents: from molecules to physiological function. *Annu. Rev. Physiol.* 65, 453–480. doi: 10.1146/annurev.physiol.65.092101.142734

Ryu, M.-H., Moskvin, O. V., Siltberg-Liberles, J., and Gomelsky, M. (2010). Natural and engineered photoactivated nucleotidyl cyclases for optogenetic applications. *J. Biol. Chem.* 285, 41501–41508. doi: 10.1074/jbc.M110.177600

Skeberdis, V. A., Chevaleyre, V., Lau, C. G., Goldberg, J. H., Pettit, D. L., Suadicani, S. O., et al. (2006). Protein kinase A regulates calcium permeability of NMDA receptors. *Nat. Neurosci.* 9, 501–510. doi: 10.1038/nn1664

Stierl, M., Stumpf, P., Udwari, D., Gueta, R., Hagedorn, R., Losi, A., et al. (2011). Light modulation of cellular cAMP by a small bacterial photoactivated adenylyl cyclase, bPAC, of the soil bacterium Beggiatoa. *J. Biol. Chem.* 286, 1181–1188. doi: 10.1074/jbc.M110.185496

Tominaga, Y., Ichikawa, M., and Tominaga, T. (2009). Membrane potential response profiles of CA1 pyramidal cells probed with voltage-sensitive dye optical imaging in rat hippocampal slices reveal the impact of $GABA_A$-mediated feed-forward inhibition in signal propagation. *Neurosci. Res.* 64, 152–161. doi: 10.1016/j.neures.2009.02.007

Tominaga, T., Kajiwara, R., and Tominaga, Y. (2013). VSD imaging method of *ex vivo* brain preparation. *J. Neurosci. Neuroeng.* 2, 211–219. doi: 10.1166/jnsne.2013.1051

Tominaga, Y., Taketoshi, M., Maeda, N., and Tominaga, T. (2019). Wide-field single-photon optical recording in brain slices using voltage-sensitive dye. *J. Vis. Exp.* 148:e59692. doi: 10.3791/59692

Tominaga, Y., Taketoshi, M., and Tominaga, T. (2018). Overall assay of neuronal signal propagation pattern with long-term potentiation (LTP) in hippocampal slices from the CA1 area with fast voltage-sensitive dye imaging. *Front. Cell. Neurosci.* 12:389. doi: 10.3389/fncel.2018.00389

Tominaga, T., and Tominaga, Y. (2016). Paired burst stimulation causes $GABA_A$ receptor-dependent spike firing facilitation in CA1 of rat hippocampal slices. *Front. Cell. Neurosci.* 10:9. doi: 10.3389/fncel.2016.00009

Tominaga, T., Tominaga, Y., and Ichikawa, M. (2002). Optical imaging of long-lasting depolarization on burst stimulation in area CA1 of rat hippocampal slices. *J. Neurophysiol.* 88, 1523–1532. doi: 10.1152/jn.2002.88.3.1523

Tominaga, T., Tominaga, Y., Yamada, H., Matsumoto, G., and Ichikawa, M. (2000). Quantification of optical signals with electrophysiological signals in neural activities of Di-4-ANEPPS stained rat hippocampal slices. *J. Neurosci. Methods* 102, 11–23. doi: 10.1016/s0165-0270(00)00270-3

Wigstrom, H., and Gustafsson, B. (1983). Large long-lasting potentiation in the dentate gyrus *in vitro* during blockade of inhibition. *Brain Res.* 275, 153–158. doi: 10.1016/0006-8993(83)90428-6

Wong, S. T., Athos, J., Figueroa, X. A., Pineda, V. V., Schaefer, M. L., Chavkin, C. C., et al. (1999). Calcium-stimulated adenylyl cyclase activity is critical for hippocampus-dependent long-term memory and late phase LTP. *Neuron* 23, 787–798. doi: 10.1016/s0896-6273(01)80036-2

Yang, K., and Dani, J. A. (2014). Dopamine D1 and D5 receptors modulate spike timing-dependent plasticity at medial perforant path to dentate granule cell synapses. *J. Neurosci.* 34, 15888–15897. doi: 10.1523/JNEUROSCI.2400-14.2014

Zhou, Z., Tanaka, K. F., Matsunaga, S., Iseki, M., Watanabe, M., Matsuki, N., et al. (2016). Photoactivated adenylyl cyclase (PAC) reveals novel mechanisms underlying cAMP-dependent axonal morphogenesis. *Sci. Rep.* 5:19679. doi: 10.1038/srep19679

Conflict of Interest: The authors declare that the research was conducted in the absence of any commercial or financial relationships that could be construed as a potential conflict of interest.

frontiers in Neural Circuits

REVIEW
published: 09 June 2020
doi: 10.3389/fncir.2020.00026

Neurophotonics Approaches for the Study of Pattern Separation

Cristian Morales[1†], Juan Facundo Morici[2†], Magdalena Miranda[2], Francisco Tomás Gallo[2], Pedro Bekinschtein[2] and Noelia V. Weisstaub[2]*

[1]Departamento de Psiquiatria, Centro Interdisciplinario de Neurociencia, Pontificia Universidad Católica de Chile, Santiago, Chile, [2]Instituto de Neurociencias Cognitiva y Traslacional (INCYT), Concejo Nacional de Investigaciones Cientificas y Tecnológicas (CONICET), Instituto de Neurología Cognitiva (INECO), Universidad Favaloro, Buenos Aires, Argentina

Successful memory involves not only remembering over time but also keeping memories distinct. Computational models suggest that pattern separation appears as a highly efficient process to discriminate between overlapping memories. Furthermore, lesion studies have shown that the dentate gyrus (DG) participates in pattern separation. However, these manipulations did not allow identifying the neuronal mechanism underlying pattern separation. The development of different neurophotonics techniques, together with other genetic tools, has been useful for the study of the microcircuit involved in this process. It has been shown that less-overlapped information would generate distinct neuronal representations within the granule cells (GCs). However, because glutamatergic or GABAergic cells in the DG are not functionally or structurally homogeneous, identifying the specific role of the different subpopulations remains elusive. Then, understanding pattern separation requires the ability to manipulate a temporal and spatially specific subset of cells in the DG and ideally to analyze DG cells activity in individuals performing a pattern separation dependent behavioral task. Thus, neurophotonics and calcium imaging techniques in conjunction with activity-dependent promoters and high-resolution microscopy appear as important tools for this endeavor. In this work, we review how different neurophotonics techniques have been implemented in the elucidation of a neuronal network that supports pattern separation alone or in combination with traditional techniques. We discuss the limitation of these techniques and how other neurophotonic techniques could be used to complement the advances presented up to this date.

Keywords: memory, pattern separation, optogenetics, calcium imagaing, granule cells, mossy cells, interneuron, adult born granule cells

OPEN ACCESS

Edited by:
Edward S. Ruthazer, McGill University, Canada

Reviewed by:
Simon Chen, University of Ottawa, Canada
Alex Dranovsky, Columbia University, United States

***Correspondence:**
Juan Facundo Morici
faq.morici@gmail.com

†These authors have contributed equally to this work

Received: *30 January 2020*
Accepted: *20 April 2020*
Published: *09 June 2020*

Citation:
Morales C, Morici JF, Miranda M, Gallo FT, Bekinschtein P and Weisstaub NV (2020) Neurophotonics Approaches for the Study of Pattern Separation. Front. Neural Circuits. 14:26. doi: 10.3389/fncir.2020.00026

INTRODUCTION

Research in the memory field has been interested not only in the ability to remember over time but also in the capacity to keep memories differentiated and resistant to confusion. To evoke a memory, our brain needs to integrate the information it receives from the environment. This integration is important for coding the general structure of the environment and abstracting it from the specificities of individual events, which allows us to generalize to novel situations. This ability to separate memory components into unique

representations was postulated to rely on a computational process known as "pattern separation" (McClelland et al., 1995; Norman and O'Reilly, 2003). Computational models define this process as a transformation of the correlated input information into an orthogonal output (Marr, 1971; Treves and Rolls, 1994; Ranganath, 2010). According to these theories, the correct storage and retrieval of memories require the stored of the information in nonoverlapping representations. Because episodic memory implies learning about unique events and avoid interference, being able to differentiate them is particularly important for this kind of memories so that storing new information does not lead to overwriting previously stored ones. For this reason, pattern separation is proposed as an essential component for the storage of differentiated representations of episodic memories and as such has been mainly studied in the hippocampus (HP; Ranganath, 2010).

The HP is one of the structures that constitute the medial temporal lobe, and it has been associated with the pattern separation process. Classically, four regions have been identified in the HP that have distinct anatomical, physiological, and genetic characteristics (**Figure 1**): the regions cornu ammonis 1, 2, and 3 (CA1, CA2, and CA3) and the dentate gyrus (DG). Computational models first suggested the potential importance of the DG for this cognitive function. The attractor system present in CA3 would be favored by a previous decorrelating process in the DG that could increase the storage capacity of the CA3 system (Amaral et al., 1990; Rolls et al., 1998). The presence of a highly inhibited DG structure or subregion, with a five-time greater number of cells than the upstream entorhinal cortex (EC), and divergent connectivity toward the CA3 region appears as the perfect structure to be able to achieve this randomizing function (Amaral et al., 1990; Jung and McNaughton, 1993; Chawla et al., 2005; Leutgeb et al., 2007). The potential adaptive role of this putative function was immediately appreciated because very similar events could lead to different outcomes and being able to judge this is crucial for our cognitive versatility.

Many tasks have been developed to show the relevance of the pattern separation process for cognition (Gilbert et al., 1998, 2001; Clelland et al., 2009; Toner et al., 2009; Creer et al., 2010; Bekinschtein et al., 2013). Gilbert et al. (2001) found that the DG ablation leads to a deficit in the discrimination of two similar positions based on distal cues. This deficit was not observed if the separation between the positions was greater. These results were confirmed in subsequent studies (Goodrich-Hunsaker et al., 2005), strongly supporting the role of the DG in pattern separation. The gradual observed impairment indicates a failure in pattern separation at the behavioral level. Consistently, McHugh et al. (2007) found, using a genetic approach, that mice lacking the essential NR1 subunit of the N-methyl-D-aspartate receptor (NMDA receptors; rNMDA) in GCs of the DG could not distinguish two similar contexts during a fear-conditioning task, although their performance in a regular task of contextual fear conditioning was normal (McHugh et al., 2007). Thus, the results indicate that DG participates in the discrimination of spatial or contextual information. The experiments commented above allowed to postulate the existence of a pattern separation process, which can be deduced from the behavioral performance (e.g., good execution on the pattern separation task) have correctly occurred and can only hypothesize about the existence of an underlying circuit-level process that supports this kind of cognitive discrimination.

Human studies indicate that patter separation takes place in the DG. In studies using high-resolution functional magnetic resonance imaging to measure brain activity during incidental memory encoding (Bakker et al., 2008; Lacy et al., 2011), authors found that CA3/DG activity was highly sensitive to small changes in the input. In such studies, the interpretation is that DG amplifies the differences between highly similar objects, thus generating highly dissimilar and nonoverlapping representations. Then, the evidence accumulated from animal and human studies supports the theoretical models proposed for the DG to be involved in pattern separation. As from the mechanism underlying this process, theoretical models proposed that the correct occurrence of the pattern separation process requires low excitability of GCs to induce the orthogonalization of memory representations (Treves and Rolls, 1992; Rolls and Kesner, 2006; Rolls, 2013) The low excitability would permit a small number of GCs to represent an episode and then decreasing the possibility of superposition between similar representations (Rolls, 2013). Also, orthogonalization could be a mechanism that forces distinct GCs to be active in the codification of similar episodes (Rolls, 2013). Lesion studies by electrolytic or histochemical techniques (Gilbert et al., 1998, 2001; Goodrich-Hunsaker et al., 2005; Hunsaker et al., 2008) and traditional electrophysiological techniques (Leutgeb et al., 2007; Neunuebel and Knierim, 2014) support this theoretical model. However, the exact mechanism by which pattern separation occurs remains unresolved mainly for technical limitations. Over the last decades, the implementation of new technologies in the study of biologically relevant questions opens a new window of opportunity to tackle in undertaking the complexity of the DG circuitry. Particularly, photonic techniques are one of the most used in neuroscience research (Torricelli et al., 2014). Their popularity comes from their characteristics, such as their adaptability to different settings and their versatility to study different problems, from the cellular to the behavioral level, as well as their high temporal and structural accuracy for cell-specific activity measurement and activity intervention (Cho et al., 2016). In this scenario, the usage of neurophotonics has shown some advantages over previous techniques in the study of the DG microcircuit involved in pattern separation. Regarding the complexity of this issue due to the cell-type variability proposed to be involved during the pattern separation process, it is important to try and contrast the theoretical models with the empirical evidence. In this review article, we focus primordially on the evidence obtained by neurophotonics techniques.

IMPLICATIONS OF MEMORY ENGRAM THEORY IN PATTERN SEPARATION PROCESS

Pattern separation computational models (Rolls and Kesner, 2006; Rolls, 2013) propose that orthogonalization implicates

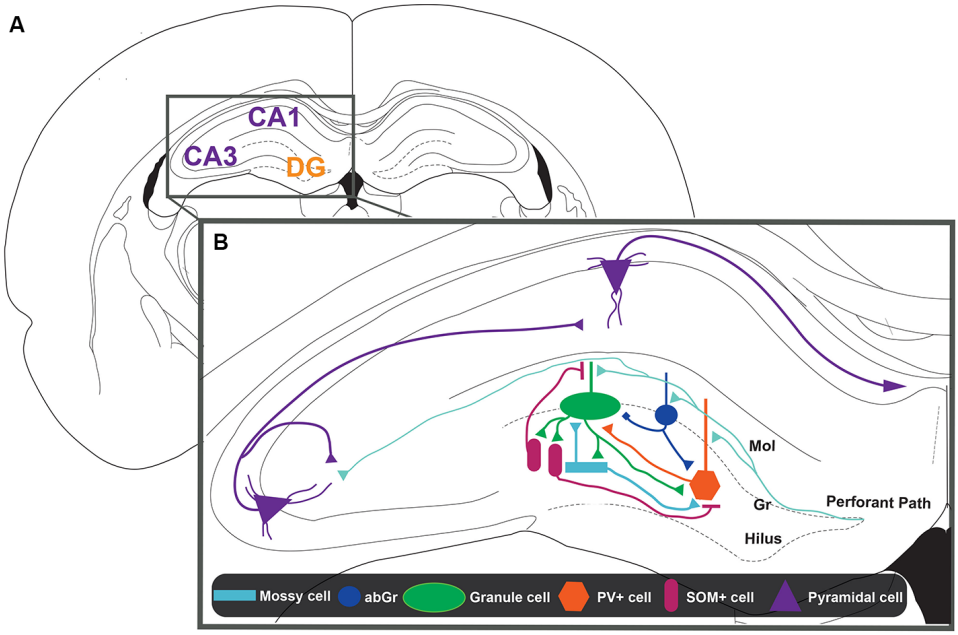

FIGURE 1 | Representation of the dentate gyrus (DG)-CA3 circuit. **(A)** Schematic representation of a coronal slice from rat brain. The hippocampus (HIP) is constituted by cornu ammonis regions 1 and 3 (CA1 and CA3, in violet) and the DG region (DG, in orange). **(B)** Zoom inset from the HIP. The main inputs to the HIP come from the layers 2/3 of the entorhinal cortex (EC) that constitute the perforant path (PP, light blue lines). The information coming from the EC could project to the CA3 pyramidal layer directly or indirectly by making and intermediate synapse on the granule cells (GCs, green ellipse) located in the granular layer (Gr) of the DG. Mossy cells (MCs, ligth blue rectangle) and adult-born GCs (abGC, blue circle) would be the first neurons activated and could initiate pattern separation. The abGCs can modulate the activation of GCs through a direct connection, which is excitatory or inhibitory, depending on the activity pattern of entorhinal input. On the other hand, abGCs and MCs can inhibit GCs by recruitment of parvalbumin containing interneurons (PV+, orange hexagon). Also, the activity of PV+ interneurons is modulated by somatostatin containing interneurons (SOM+, pink ellipse) and by GCs itself. SOM+ interneurons can directly inhibit GCs, specifically distal dendrites, where contextual information arrives. Thus, the interaction between the different cell types present in the DG defines the activity of GCs, which project to CA3. Finally, the CA3 pyramidal cells project through the Schaffer collaterals to the CA1 pyramidal cells forming the main hippocampal output into layer 5 of the EC.

the activation of different GCs within the total population in different contextual experiences. Empirical experiments have supported this statement. Using the expression of an activity-dependent gene, like the activity-regulated cytoskeleton-associated protein (ARC), Chawla et al. (2005) found that when mice were exposed to two different environments, ARC was expressed in two different sets of neurons. Similar results were obtained for ZIF268 in an experiment where mice were allowed to explore the same environments but with two different motivations (Satvat et al., 2011). Both results indicate that in the DG an orthogonalization process occurs not only to encode different contextual features but also to encode differences between the experiences *per se*. This activation of different cell populations appears to be specific to situations that require differentiation because when the mice explored the same environment with the same motivation, the sets of zif268-positive cells obtained were significantly overlapped (Satvat et al., 2011). This suggests a correspondence between the behavioral experience and the subset of cells that encode it. Interestingly, the representational differentiation also occurs in the CA3 region but not in the CA1 region (Leutgeb et al., 2005, 2007) of the HP, This differential recruitment highlights the differentiation process as a DG and/or CA3 region property.

The existence of the neural substrate of memories that make us unique and unrepeatable individuals has been a matter of discussion for over a century. Richard Semon proposed the existence of physical changes in the brain generated by the encoding of new information and called them "engrams" (Tonegawa et al., 2015). Engrams are commonly defined as a set of cells that are synchronously activated during the encoding of a particular experience resulting in the storage of this new information (Wang, 2019). Semon's idea was too progressive for his time to experimentally contrast it, although it has changed in the last decades, when several publications supporting the engrams theory have appeared (for a review see Bocchio et al., 2017; Tanaka and McHugh, 2018 and Josselyn and Tonegawa, 2020). As predicted by Martin and Morris (2002): "In our view, the final test of any hypothesis concerning memory encoding and storage must be a mimicry experiment, in which apparent memory is generated artificially without the usual requirement for sensory experience, or indeed any form of experience, during learning. [...] In another sense, such an experiment would constitute a critical test that changes in synaptic efficacy are sufficient for memory, rather than merely necessary." Neurophotonics give us, for the first time, the opportunity to test the engram hypothesis. In the following

section, we will try to address some of the advances made in the engram research area by focusing on the use of neurophotonics techniques.

Neurophotonics in the Development of Engrams Theory

It was not until a few years ago that huge steps were taken in the quest to identify memory engrams, thanks to the generation of different behavioral, molecular, genetic, and optic tools (Josselyn and Tonegawa, 2020). Particularly, optogenetics was the first neurophotonic technique used to tackle this question. Liu et al. (2012) injected an adenoassociated virus (AAV) AAV9-TRE-ChR2-EYFP in the DG of a c-fos–tTA mice. The main idea of this strategy was to express channelrhodopsin 2 (ChR2, excitatory opsin) in the DG cells that were active during the training phase of a fear-conditioning task (Liu et al., 2012; c-fos will be recruited and drive the expression of tTA.) They showed that activating this population of DG cells was enough to trigger the reactivation of the fear response. These results indicated that reactivating the cells recruited during the encoding of a fear memory was sufficient to retrieve and express this memory. This finding was supported and expanded when Ramirez et al. (2013) were able to create a false memory. By reactivating the DG cells recruited during the encoding of a neutral context (context A) while the animal received a shock at a different one (context B), the authors were able to create a false association between context A and the delivery of the electrical shock (Ramirez et al., 2013). Interestingly, this phenomenon was observed in other parts of the brain, such as the olfactory bulb (Vetere et al., 2019) and the amygdala (Redondo et al., 2014), suggesting an underlying common neural mechanism. To study the stability of the contextual component of a fear memory within the neuronal representation in the HP, Ghandour et al. (2019) performed *in vivo* Ca^{2+} imaging of putative engram and nonengram cells in the CA1 region of the HP at posttraining sessions. To do this, they injected a TRE-KikGR lentivirus into the CA1 (to label engram cells) of a Thy1-G-CaMP7 × c-fos–tTA double transgenic mice. KikGR is a highly effective fluorescent protein that could photoconvert from green to red upon the exposure to 365-nm light without affecting the Ca^{2+} imaging signal. Its expression was controlled in an activity and time-dependent manner (by the c-fos–tTA construct). G-Camp7 is a very sensitive calcium sensor. Then, by combining both tools, they could identify the activated engram cells during the recordings. They observed that the total activity pattern of the engram cells during learning was more stable across postlearning memory processing than the activity of the nonengram cells. However, as far as we know, this kind of experiments was not yet performed in the DG. Nevertheless, these results suggest that neurophotonics is a powerful instrument in the quest and identification of memory engrams and their role in the different memory stages of normal and pathological conditions (Roy et al., 2016; Denny et al., 2017).

The capacity of the brain to maintain differentiated engrams could be really useful for the storage of overlapping memories (Deng et al., 2013). Then, understanding how a particular subset of cells is recruited to be part of an engram is indeed important. It has been shown that neuron excitability could be enhanced by CREB expression (Han et al., 2009; Rao-Ruiz et al., 2019), helping with the engram allocation into that particular subset of neurons (Zhou et al., 2009; Kim et al., 2013; Yiu et al., 2014). With this background in mind, Rashid et al. (2016) asked if two fear-conditioning episodes closely in time could recruit similar neuronal populations in the lateral amygdala. They observed that the overlapping between *arc* and *homer1*, two immediate early genes, mRNA increased. Moreover, there was interest in dissecting if the excitability of a particular neuronal ensemble was sufficient to direct the memory allocation to those neurons. To do this, they guide the expression of halorhodopsin (NpHR3.0, inhibitory opsin) and ChR2 to inhibit or excite the activity of the same neuronal population before the first fear conditioning. The main objective behind this experimental design was to bidirectionally modulate the excitability of the transfected neurons to enhance or decrease the degree of overlapping between memory engrams. They observed that the optogenetics manipulations had effects over the engram overlapping outcomes only when the two fear-conditioning episodes were generated within a limited time frame. This result suggests that, depending on the temporal proximity between two slightly different experiences, the neuronal ensemble recruited by both of them could be similar. This experiment suggests that, at least in the amygdala, the time interval between two similar experiences is crucial in the ability to generate distinct memory engrams and implies that this structure might not have the computational ability to use pattern separation as a disambiguating process. This kind of experimental setting would be really useful to dissect if pattern separation happening in the DG requires the allocation of two similar experiences into different neuronal ensembles. However, to tackle this idea, future experiments should parameterize the similarity of the contexts used during training.

More recently, it has been shown that the enhancement of the engram cells excitability after reactivation is mediated by the internalization of Kir2.1 inward-rectifier potassium channels and the activation of rNMDAs (Pignatelli et al., 2019). It was shown that K2+ inward rectifier currents are negatively modulated by the activation of α-amino-3-hydroxy-5-methyl-4-isoxazolepropionic acid receptor (AMPA receptors) (Houzen et al., 1998; Jones et al., 2000; Schröder et al., 2002). Using optogenetics to tag DG engram cells associated with a fear memory, Ryan et al. (2015) have shown that engram cells present an enhancement of the spine density and rAMPA/rNMDA ratios compared with nonengram cells. Interestingly, this phenotype was depleted when the animals received a protein synthesis inhibitor, anisomycin, classically used to impair memory consolidation. To study more in detail this aspect, a technique called dual-eGRASP has been developed (Kim et al., 2012). The conventional GRASP technique requires two complementary mutant GFP fragments, which are expressed separately on presynaptic and postsynaptic membranes. When the complementary GFP fragments interact within each other

at the synaptic cleft, a functional GFP appears. Then, the GFP signal indicates a formed synapse between presynaptic and postsynaptic neurons. Using this approach, it was shown that the CA3–CA1 spine density is enhanced after the training phase (Choi et al., 2018), suggesting that the excitability changes observed happen in the entire engram cell ensemble. The increase of spine density observed in the engram cells was related to the enhancement of the rAMPA/rNMDA ratio and subsequently with the Kir2.1 inward-rectifier potassium channel internalization. Then, these results suggested that changes in the excitability of neurons (Park et al., 2016) that are part of an engram could be key in the mechanism of pattern separation of overlapping memories.

It has been proposed that engram cells from distinctive ensembles spread all over the brain (Kastellakis and Poirazi, 2019). This particularity is associated with the capacity of integrating different features of the encoding experience (Guan et al., 2016). According to this idea, activation of DG engram cells, as a hub in the pattern separation mechanism, could trigger the expression of aversive or appetitive responses that are commonly located in different downstream structures (Redondo et al., 2014; Ramirez et al., 2015; Roy et al., 2017; Chen et al., 2019). Ramirez et al. (2015) showed that chronic optogenetic reactivation of rewarded experiences reverts the depressive behavior in a mouse model. Moreover, the chronic reactivation of the dorsal DG engram cells associated with an aversive experience generates extinction response, whereas the reactivation of the ventral DG engram cells generates an enhancement of the fear response (Chen et al., 2019). However, how memory function emerges from the coordinated activity between all the engram nodes remains a mystery. It has been shown that distinct neuronal populations of the basolateral amygdala participate in giving positive or negative valence (Redondo et al., 2014; Gore et al., 2015) to a particular experience. Then, it was proposed that the reactivation of contextual engram cells located in the DG could guide the reactivation of the valence engram cells associated with guiding the behavioral outcome of a certain experience (Tonegawa et al., 2015). These results are in line with the postulation that reactivation of one of the nodes guides the reactivation of the entire engram. Understanding the mechanisms underlying this feature could be useful for the treatment of different anxiety and mood disorders.

Then, the accumulated evidence proposes that the information in the brain could be stored at specific cell ensembles. In this sense, the differentiation of similar information by generating nonoverlapping engrams is proposed as the material outcome of a pattern separation process. Most of the studies focus their attention on the interaction between excitatory neurons at the time of characterizing the intrinsic properties of engram cells. However, the GCs are not the only glutamatergic cells within the DG and neither the only population within the structure. Then, it is plausible that other cell populations might also be engram cells or at least play important modulatory roles to the main cells. In this regard, inhibitory engrams have been proposed to be important for specific memory reactivation (for a review, Barron et al., 2017). In the following sections, we discuss the role of different cell types in the DG circuit involved in pattern separation.

DENTATE GYRUS GLUTAMATERGIC CELLS PARTICIPATION IN PATTERN SEPARATION

Usage of Neurophotonics in the Study of the Spatial Codification of Granule and Mossy Cells

One of the most studied hippocampal function is its involvement in spatial memory encoding. Lesions or pharmacological interventions on the DG impair the performance in different spatial memory tasks (Gilbert et al., 1998, 2001; Goodrich-Hunsaker et al., 2005, 2008), suggesting a role of this structure during the storage or recall of this kind of memory. Moreover, electrophysiological recordings have shown the existence of place cells within the DG (Jung and McNaughton, 1993; Leutgeb et al., 2007), neurons that are selectively activated when rodents moved into a specific location within a maze (O'Keefe and Dostrovsky, 1971). A closer analysis has shown that the DG place cells present multiple place fields (Jung and McNaughton, 1993; Leutgeb et al., 2007) and, like CA1 place cells, can remap (Leutgeb et al., 2007). Remapping is a property consisting of the change of the place cell firing pattern in response to a small change in the sensory (Muller and Kubie, 1987; Colgin et al., 2008) or behavioral context (Colgin et al., 2008). In this way, it has been suggested that this remapping property allows the encoding of information emerging from similar experiences into distinct neuronal representations, which in turn is important for pattern separation. However, one of the disadvantages of the data obtained with electrophysiological recordings is the difficulty in distinguishing between other neurons that are also glutamatergic-like mossy cells (MCs; Soriano and Frotscherf, 1994). In this scenario, neurophotonic techniques have allowed researchers to separate the contribution of GCs and MCs to pattern separation.

The DG is composed primarily of GCs, whose dendrites are arranged within the molecular layer, and their cell bodies form the adjacent GC layer (Amaral et al., 2007). Between the molecular layer and the CA3 region, there is a polymorphic layer called the hilus. Mossy cells are located only in the hilus region (**Figure 1**). However, because GCs fibers and MCs coexist in this region (Scharfman, 2016), their differential contribution to the circuitry functionality has been difficult to be dissected. One possible, and elegant, setting used for the study of the differential contribution from GCs and MCs has been to perform simultaneous optical stimulation and electrophysiological recordings (Senzai and Buzsáki, 2017; Jung et al., 2019). In these studies, an optrode was used. This array allows the simultaneous recording of the voltage field while the light is delivered to the tissue, making possible to see the instantaneous effect of light in the firing rate of units recorded (Royer et al., 2010; Anikeeva et al., 2011). Senzai and Buzsáki (2017) used dopamine receptor

D2 (DRD2) promoter to drive the expression of a chloride pump called archaerhodopsin specifically to MCs. Using this strategy, neurons that suppressed their activity during the optical stimulation were classified as putative MCs. Surprisingly, this study found that MCs from the DG present one or more than one place fields, like GCs, making it necessary to reinterpret previous works (Jung and McNaughton, 1993; Leutgeb et al., 2007), but also proving the strength of the new optical techniques.

With this system, the accuracy of the study of the MCs' electrophysiological characteristics can be enhanced. However, this form of identification presents some limitations that depend on neuronal connectivity. For example, in some cases, neurons that express archaerhodopsin can activate other neurons. Then, optical stimulation can induce suppression of the activity of neurons that express archaerhodopsin but excitation of neurons that are subsequently activated by them (Senzai and Buzsáki, 2017; Morales et al., 2019). This method does not allow the identification of GCs (that excite directly the MCs) but is useful for the identification of MCs. To tackle this issue, Danielson et al. (2017) used *in vivo* two-photon calcium imaging in awake behaving mice to differentiate the role of MCs and GCs. To achieve selective manipulation of MCs, they took advantage of the anatomical properties of MCs. Specifically, they injected an AAV-expressing Cre-recombinase into the DG. Then they injected a Cre-dependent rAAV-expressing GCaMP6f, a sensitive fluorescent protein used for imaging of neuronal activity, in one of the DGs. Because MCs project to contralateral DG, this technique allows the expression of fluorescent markers only in MCs of the contralateral DG. Then a chronic imaging window was implanted above the DG to visualize Ca^{2+} activity from MCs in head-fixed mice that have to run on a treadmill in different linear environments to receive a reward. They found that MCs have place fields, as has been previously described, but while GCs have high tuning specificity, MCs have low tuning specificity indicating that MCs have multiple firing fields. This supports the finding that place cells with multiple place fields that were found in electrophysiological experiments (Jung and McNaughton, 1993; Leutgeb et al., 2007) are principally MCs. Danielson et al. (2017) showed that the fraction of place coding was bigger in MCs than in GCs, supporting the idea that, in electrophysiological recording, MCs represent an important number of place cells. Although a powerful approach, a disadvantage of this setting is that the cell specificity is given by anatomical properties. Some studies show that MCs are not the unique cells that project to contralateral DG (Scharfman, 2018). If this is confirmed, the results reviewed above required to be interpreted with caution.

The results of a recent study (Jung et al., 2019) suggest a possible driver role of MCs in remapping. They showed that when there are changes in the environment, such as those used to induce remapping, MCs' response precedes the activity change on GCs. It is important to note that, to differentiate between GCs and MCs, Jung et al. (2019) injected a CRE-inducible AAV to drive the expression of Chronos, an excitatory opsin that is faster and more light-sensitive than the conventional channelrhodopsin (Klapoetke et al., 2014), in two different transgenic mice line, DRD2-Cre and POMC-Cre mice, which allowed them to excite, MCs and GCs, respectively. Although the use of this setting to differentiate the role of MCs and GCs in the DG circuit was previously used, they argued that excitation is better than inhibition to discriminate between neuronal types.

In summary, the evidence described above suggests that both CGs and MCs may be deferentially involved in the functionality of the DG circuitry. In particular, MCs showed more sensibility to contextual changes than GCs suggesting that MCs could be part of the circuits that detect and encode the nonoverlapped information, while the GCs could be encoding the overlapped information. Although further research would be needed to completely dissect their specific function, the evidence accumulated until now proposes to MCs as important players in the mechanism of pattern separation.

What Can We Say About the "Irritable" Hypothesis Using Neurophotonic Techniques?

One of the most exciting topics on the study of the DG is related to the role of each cell type in terms of which node orchestrates the activity of the other nodes. It has been shown that MCs can excite GCs directly and can inhibit GCs indirectly through the recruitment of feedback inhibition (Scharfman, 1995; Larimer and Strowbridge, 2008). However, because of the complexity of the DG circuit, the neuronal mechanisms underlying the net effect on GC activity are still a controversial matter (Scharfman, 2018).

In the early 1980s, some seminal studies showed that the stimulation of commissural (fiber of MCs) just before stimulating the perforant path (PP) produced an inhibition over the GC spikes population (Buzsàki and Eidelberg, 1981; Douglas et al., 1983), suggesting that the activation of MCs principally inhibits the activity of GCs. Interestingly, this conclusion was confirmed by subsequent experiments (Sloviter, 1983, 1991; Scharfman, 1995), allowing the establishment of the "dormant basket cells (BCs)" hypothesis. This hypothesis proposed that the net effect of MCs on GC activity was mediated by the activation of parvalbumin (PV+) GABAergic interneurons within the DG that then inhibit GCs (Sloviter, 1991). However, in contrast to this theory, other experiments suggested that the net effect was mediated by the excitation of the GCs by the MCs (Buckmaster et al., 1996; Ratzliff et al., 2004). This alternative hypothesis, called the "irritable mossy cells" hypothesis, proposed that MCs' hyperexcitability increases the activity of the GCs affecting in this way the net effect onto the DG (Santhakumar et al., 2000). Despite that the last hypothesis was described in pathological conditions such as epilepsy, it has been extrapolated to memory function. Then, based on these two perspectives, MCs could modulate GCs' response by indirect inhibition or direct activation.

One of the problems with electrical stimulation is how to selectively and specifically stimulate MCs (Amaral et al., 2007; Leranth and Hajszan, 2007). Then, identification of MCs by other parameters than their electrophysiological properties is required.

Jackson and Scharfman (1996) used in hippocampal slice the voltage-sensitive dye technique (90–92). This technique has a better spatial resolution than traditional electrophysiological approaches and permits to study the spread of activity within DG after stimulation of PP. They showed that the spread of activity depends specifically on the hilar activation, whereas the PP damage was not related to this outcome (Jackson and Scharfman, 1996) and that electrical stimulation of the hilus induces depolarization at the inner molecular layer. Thus, they suggested that the spread of activity delivered by PP stimulation depends on positive feedback between GCs and MCs. Despite these results, other investigations that combine a laser-scanning photostimulation with a voltage-sensitive dye (Xu et al., 2010) have shown that photostimulation of the hilus does not increment the activity in GCs (Sun et al., 2017). Hsu et al. (2016) performed a series of experiments to resolve the discrepancy between these results. They injected unilaterally a CRE-inducible AAV carrying the ChR2 gene in the hilus of Grik4-cre hemizygous mice to direct the expression of ChR2 to the commissural fiber of contralateral DG. The authors found that inhibition/excitation balance in GCs was increased when commissural fibers were photostimulated. Moreover, they showed that while concurrent activation of commissural and perforant pathways increased the response of GCs, the delayed activation of PP compared with the commissural pathway decreased the percentage of responding GCs (Hsu et al., 2016). These results proposed that the optogenetic stimulation of the PP at 10 Hz, the "dormant BCs" hypothesis, seems to apply. Interestingly, the frequency of the optostimulation is quite similar to the one observed in the HP of animals during active exploration periods.

Contrasting with what was described above, another study (Hashimotodani et al., 2017) decided to address the effect of fast (30 Hz) optical stimulation of MC fiber, because this kind of stimulation can induce long-term potentiation (LTP). To generate an optical fast stimulation, they used ChIEF, a faster version of ChR2 (Lin et al., 2009). They found that fast optical stimulation induces LTP between MCs–GCs synapses, but not in mossy-interneurons synapses. This facilitation increases the excitation/inhibition balance, thereby inducing an increment in GC activity. These results obtained using a fast optostimulation protocol support the "irritable" hypothesis. Taking all this evidence together, the optostimulation frequency performed at the PP seems to be critical in defining the role of the MCs in the modulation of the GC activity. If the input is low frequency, the indirect inhibition mechanism seems to modulate the GC net effect, whereas the direct MCs–GCs excitation seems to be more preponderant when higher-frequency inputs impact into the circuit.

NEUROPHOTONICS APPLICATIONS IN THE STUDY OF THE DG INTERNEURONS ROLE IN PATTERN SEPARATION

Several models have proposed that GABAergic DG interneurons mediate the control of GC excitability and the orthogonalization of engrams that represents similar contexts (Rolls, 2013). Electrophysiological experiments have shown that GABAergic interneuron activity in the DG, unlike other hippocampal regions, is higher in a novel than in a familiar context (Nitz and McNaughton, 2004), suggesting its role in encoding novel information (**Figure 1**). Some of the GABAergic interneurons that contact GCs at the perisomatic region are BCs, whose inputs come from other GCs, the perforant pathway (Freund and Buzsáki, 1996), and MCs (Scharfman and Myers, 2012; Hsu et al., 2016; Scharfman, 2016; Danielson et al., 2017). Thus, in this way, these interneurons could control both feedback and feedforward inhibition onto GCs (Freund and Buzsáki, 1996; Savanthrapadian et al., 2014). On the other hand, within interneurons that contact the dendritic region of GCs are the hilar PP-associated interneurons (HIPPs), which correspond to a type of interneurons that have their soma in the hilus, where contact with GC axons takes place (Freund and Buzsáki, 1996; Savanthrapadian et al., 2014; Yuan et al., 2017). It has been proposed that HIPPs could control GC activity through feedback mechanisms (Houser, 2007). There has been an established relationship between the anatomical characteristics of these subpopulations and the presence of specific neuronal markers (Freund and Buzsáki, 1996; Savanthrapadian et al., 2014). The expression of neuronal markers associated with distinct GABAergic cells has allowed the use of optogenetics techniques to analyze the role of each of these GABAergic interneurons in DG networks and pattern separation. Specially, BC interneurons are PV+, whereas HIPP interneurons are SOM+ (Freund and Buzsáki, 1996; Savanthrapadian et al., 2014; Yuan et al., 2017).

The stronger inhibition mediated by the recruitment of PV+ interneurons counterbalances excitation of DG networks. In this way, stronger excited cells recruit GCs more effectively than less excited cells, allowing a "winner-takes-all" situation that would allow a good pattern separation mechanism (Sambandan et al., 2010; Guzman et al., 2019). Electrophysiological experiments have shown that this property depends on the coactivation of the perforant pathway and mossy fibers (Sambandan et al., 2010). Although there are other mechanisms capable of regulating the activity of PV+ interneurons, Hu et al. (2010), using confocal imaging and patch-clamp simultaneously, showed that some of the intrinsic properties of PV+ interneurons dendrites, such as the presence of Kv3 channels, are implicated in the rapid and precise time inhibition mediated by PV+. On the other hand, several studies (Savanthrapadian et al., 2014; Yuan et al., 2017) showed that SOM+ also contributes to the precision of the discharge of PV+. In this line of evidence, Savanthrapadian et al. (2014) injected a Cre-inducible rAAV vector containing ChR2-tdT into the DG of SOM-Cre mice. They studied the PV+ interneurons, while paired optical stimulation of SOM+ interneurons with electrical stimulation of PP. They showed that the optical stimulation of the outer molecular layer, where the axons of HIPPs are present, increases the precision of action potential generation in PV+ interneurons. Yuan et al. (2017) showed that there are two types of SOM+ interneurons within the DG, the HIPP interneurons, which were studied by Savanthrapadian et al. (2014), and SOM+ interneurons that have their axons in the

hilus and contact other interneurons such as PV+ interneurons. This last group is called hilus-associated interneuron (HIL; Yuan et al., 2017). In this study, the scientists used a similar injection protocol as described by Savanthrapadian et al. (2014), but besides stimulating the outer molecular layers for the recruitment of HIPPs, they stimulated the perisomatic region of PV+ interneurons. Using this approach, they showed that the activity of the HIL determines the activity of PV+ interneurons (Yuan et al., 2017). Thus, the activity of PV+ interneurons is regulated by SOM+ interneurons through dendritic inhibition by HIPPs and perisomatic inhibition by HIL (**Figure 1**). This complex array of inhibitory control seems to indicate a complementary role between PV+ and SOM+ interneurons and could be instrumental for pattern separation.

The EC is generally characterized as the main input to the DG (Rolls, 2013). Understanding how cortical inputs modulate DG inhibitory microcircuits is crucial to understand the processing of information in the HP. To this end, Lee et al. (2016) studied how PV+ and SOM+ interneurons affect the activity of GCs in response to cortical stimulation. They injected an AAV (AAV5)-expressing Cre-dependent enhanced halorhodopsin (eNpHR3.0). Using this experimental approach, they selectively inhibit each of these interneurons, PV+ and SOM+. They showed that inhibition of PV+ interneurons suppresses GCs' responses to single cortical stimulation. When cortical stimulation was in theta (θ) or gamma (γ) frequencies (Lee et al., 2016), that is, frequencies present during exploration (Bragin et al., 1995), they found that both types of interneurons differentially regulate GCs' responses. Interestingly, they found that PV+ regulates the onset of the spike series, whereas SOM+ interneurons regulate principally late spikes. Overall, these results are in agreement with the view that PV+ and SOM+ interneurons play complementary roles in pattern separation.

Besides regulating GC excitability, it is possible that GABAergic interneurons also participate in the orthogonalization of engrams that represents similar contexts through a lateral inhibition mechanism. By coupling the expression of td-tomato or enhanced green fluorescent protein (EGFP) reports with the expression of neurochemical marker for its identification in slice experiments, Espinoza et al. (2018) found that, in the case of GCs-PV+ connection, the ratio of lateral inhibition regarding recurrent inhibition was higher, suggesting an important role of this interneurons in lateral inhibition. On the other hand, Stefanelli et al. (2016) were interested in the size of the ensemble recruited during the encoding of contextual information and how it modulates the specificity during recall. To tackle this question, they expressed ChR2 in GCs, SOM+, and PV+ interneurons to optostimulate these cells during the encoding of a contextual fear memory paradigm. They showed that the rise time of GABAergic current response induced by PV+ stimulation was the shortest, whereas the rise time of GABAergic current response induced by SOM+ and GCs did not have significant differences. In this way, the authors conclude that, because of the similarity between GABAergic current response induced by SOM+ and GCs, the lateral inhibition induced by GCs corresponds to the recruitment of SOM+ interneurons (Stefanelli et al., 2016). Thus, in the case of orthogonalization, experimental evidence suggests that PV+ and SOM+ participate in a complementary way. These results provide evidence that integrates the role of different DG cell types in the memory allocation and how it could contribute to the pattern separation process. From this perspective, DG interneurons are recruited during the encoding of contextual fear memory. Their role during this process seems to be circumscribed to the control of the size of the ensemble. If this process is affected by blocking the activity PV+ or SOM+ cells, the number of recruited GCs would increase. This outcome could affect the selectivity of the storage and/or recall of the information because the probability of overlap with other neuronal ensembles coding other memories is enhanced.

NEUROPHOTONICS TECHNIQUES TO UNDERSTAND THE ROLE OF ADULT-BORN GRANULE CELLS IN PATTERN SEPARATION

The DG circuit, as well as the olfactory bulb, is continuously changing because of the integration of adult-born GCs (abGCs; Sahay et al., 2011b). A growing body of studies are currently focused on finding if abGCs play a particular role in pattern separation. Clelland et al. (2009) found that blocking hippocampal adult neurogenesis by X-ray irradiation altered the animal's ability to distinguish small changes in spatial discrimination, but not unmistakable changes. Consistently, Sahay et al. (2011a) observed that animals with genetically increased levels of adult neurogenesis were better at discriminating between two similar contexts (Freund and Buzsáki, 1996; Sahay et al., 2011a). Moreover, many studies suggested that these new neurons could be a preferential substrate for remapping the place cells in presence of subtle changes in the environment. This is because the immature granular neurons have higher excitability and plasticity that distinguishes them from the population of old and relatively silent neurons (Espósito et al., 2005; Marín-Burgin et al., 2012). In addition to this, it has been proposed that mature neurons could be specialized for certain, more stable characteristics of their environment because they would respond preferentially to the inputs they received during their development (Aimone et al., 2011). On the other hand, immature GCs showed a low threshold for the induction of LTP (Schmidt-Hieber et al., 2004; Ge et al., 2007). Then, the particular properties of immature GCs confer them the characteristics required to be involved in pattern separation. Consistently with this idea, Nakashiba et al. (2012) suggested that neither the larger number nor the more dispersed activity of the DG is sufficient to separate similar contexts and that young aGCs would be necessary to allow this process.

Ikrar et al. (2013) studied the DG response to electrical stimulation with a voltage-sensitive dye technique (Ebner and Chen, 1995; Chemla and Chavane, 2009; Tsytsarev et al.,

2014) using an iBax-nestin mice, a model mice in which neurogenesis can be enhanced with tamoxifen administration. They showed that photostimulation or electrical stimulation of DG induced a smaller and less-spread neuronal excitability in mice with increased adult neurogenesis compared to the controls (Ikrar et al., 2013). These results suggest that adult neurogenesis is an important factor in the control of the DG neurons' excitability. This result was supported by a different studies (Temprana et al., 2015; Drew et al., 2016). In this case, a retrovirus expressing a light-activated channel ChR2 was delivered to the DG of adult mice for its selective transduction in neural progenitor cells of the adult DG. Then, acute slices were prepared some weeks postinjection for studying the effect of photostimulation of abGCs generated at different time points. They showed that abGCs activate hilar GABAergic interneurons that in turn inhibit mature GCs (**Figure 1**). Specifically, Temprana et al. (2015) showed that recruitment of feedback inhibition is higher in abGCs of 7 weeks than in abGCs of 4 weeks. This result suggests that as time passes abGCs tend to be more integrated into inhibitory circuits that facilitate their role in controlling the excitability of surrounding neurons.

A recent study (Luna et al., 2019) showed that, besides the recruitment of feedback inhibition by abGCs (Temprana et al., 2015; Drew et al., 2016), these newborn neurons can directly inhibit mature GCs. Specifically, Luna et al. (2019) selectively expressed archaerhodopsin T in abGCs. They showed that optical inhibition of abGCs produced an increment in the DG LTP response to electrical stimulation, even when GABA antagonists were used. This could indicate that inhibition is independent of GABAergic interneuron activation in the hilus. They also studied the effect of abGC activation in mature GCs, by selectively expressing ChR2 in abGCs. They showed that low intensities of light, which produce low levels of glutamate release from abGCs, induce IPSPs in mature GCs. Moreover, high intensities of light, which produce high levels of glutamate liberation, induce EPSP in mature GCs. Finally, they showed that low glutamate liberation, that is, IPSP in mature GCs, is due to the preferential activation of the lateral EC that carries contextual information (Hargreaves et al., 2005; Wilson et al., 2013). Keeping low levels of mature GC excitability is important for pattern separation (Jinde et al., 2012; Sahay et al., 2011a). Luna et al. (2019) suggested that contextual information—besides spatial information—is relevant to promote a sparse coding in DG. Consistently, using calcium imaging, Danielson et al. (2016) differentiate the activity of abGCs from other populations that present a low spatial tuning but are good novelty detectors, supporting a fundamental role of abGCs in disambiguating contextual information through the process of pattern separation.

All the evidence described in this section proposed that abGCs could play a key role in the formation of orthogonal representations from similar inputs. This is because their high excitability during the early stages of their development is critical to determine which inputs will recruit them subsequently. Because neurogenesis is a continuous process, there are always abGCs at different stages of development. Therefore, the probability that two different experiences recruit the same subset of abGCs at the same developing time is low. This characteristic gives them a potential role in orchestrating the rest of the cells that potentially form the differentiated engrams in the DG.

FINAL REMARKS

Neurophotonic techniques allowed the study of the role of different neuronal types in the DG networks functionality. Specifically, the evidence described above suggests a differential role of each neuronal type in the mechanisms underlying pattern separation. As we have described, neurophotonic studies led to propose models that go beyond unique neuronal types for information processing and where several elements of DG network share complementary roles in the differentiation of overlapping information. Based on the body of evidence presented above, we are proposing a possible way in which all these different cell types might interact and contribute to pattern separation.

Neurophotonics have contributed to differentiate the role of three types of DG glutamatergic cells, MCs, newborn GCs (abGCs), and mature GCs. Thus, it has been shown that MCs and abGCs present more remapping than mature GCs (Danielson et al., 2016, 2017; Senzai and Buzsáki, 2017), which suggests that MCs and abGCs are more sensible than GCs to detect small environmental changes, that is, when differences must be detected in similar episodes. Besides, neurophotonics experiments suggest that these neuronal types would respond before than GCs (Marín-Burgin et al., 2012; Jung et al., 2019), suggesting that both neuronal types could initiate the process of pattern separation. Besides, both neuronal types are more sensitive to contextual changes (Danielson et al., 2016, 2017; Senzai and Buzsáki, 2017; Luna et al., 2019), which means that contextual information would be more relevant than other type of information. Thus, MCs and abGCs could initiate pattern separation through the detection of environmental changes, especially changes in contextual information. After activation of MCs and abGCs, they can initiate an inhibitory network. While abGCs can inhibit directly GCs (Luna et al., 2019), MCs and abGCs would activate PV (Scharfman, 2018; Groisman et al., 2020), which in turn produces a lateral inhibition proposed to be important for pattern separation (Espinoza et al., 2018). Interestingly, the activity of SOM modulates the activity of PV (Savanthrapadian et al., 2014; Yuan et al., 2017) and can produce itself a lateral inhibition (Stefanelli et al., 2016). On the other hand, the evidence indicates that the activity of SOM is delayed when compared with the activity of PV (Hsu et al., 2016; Stefanelli et al., 2016). Thus, both PV and SOM interneurons control the activity of GCs, but likely in a different time with PV activity preceding SOM activity. Some models propose pattern separation mechanisms that take into account and emphasize the role of PV interneurons (Guzman et al., 2019), abGCs (Sahay et al., 2011b), and MCs (Nakazawa, 2017). In this work, we make a complementary interpretation to all these models, paying special attention to the

interaction between the different cell types present in the DG (**Figure 1**). Still, more work is required to better understand the mechanism, dynamics, and constraints of pattern separation in the DG.

However, it is important to highlight that in the last years our understanding of this process advanced enormously, thanks to the development of neurophotonic techniques. We believe that the continuous advancement in this field in combination with genetic tools will prove to be a powerful strategy for ll for modeling pattern separation where a complementary role of different types could be studied.

AUTHOR CONTRIBUTIONS

CM, JM, MM, FG, PB, and NW conceived the content, wrote and organized the manuscript.

FUNDING

This work was supported by grants from the National Agency of Scientific and Technological Promotion of Argentina (Agencia Nacional de Promoción Científica y Tecnológica, ANPCyT, Argentina) PICT2015-2344 (NW).

REFERENCES

Aimone, J. B., Deng, W., and Gage, F. H. (2011). Resolving new memories: a critical look at the dentate gyrus, adult neurogenesis and pattern separation. *Neuron* 70, 589–596. doi: 10.1016/j.neuron.2011.05.010

Amaral, D. G., Ishizuka, N., and Claiborne, B. (1990). Neurons, numbers and the hippocampal network. *Prog. Brain Res.* 83, 1–11. doi: 10.1016/s0079-6123(08)61237-6

Amaral, D. G., Scharfman, H. E., and Lavenex, P. (2007). The dentate gyrus: fundamental neuroanatomical organization (dentate gyrus for dummies). *Prog. Brain Res.* 163, 3–22. doi: 10.1016/s0079-6123(07)63001-5

Anikeeva, P., Andalman, A. S., Witten, I., Warden, M., Goshen, I., Grosenick, L., et al. (2011). Optetrode: a multichannel readout for optogenetic control in freely moving mice. *Nat. Neurosci.* 15, 163–170. doi: 10.1038/nn.2992

Bakker, A., Kirwan, C. B., Miller, M., and Stark, C. E. L. (2008). Pattern separation in the human hippocampal CA3 and dentate gyrus. *Science* 319, 1640–1642. doi: 10.1126/science.1152882

Barron, H. C., Vogels, T. P., Behrens, T. E., and Ramaswami, M. (2017). Inhibitory engrams in perception and memory. *Proc. Natl. Acad. Sci. U S A* 114, 6666–6674. doi: 10.1073/pnas.1701812114

Bekinschtein, P., Kent, B. A., Oomen, C. A., Clemenson, G. D., Gage, F. H., Saksida, L. M., et al. (2013). BDNF in the dentate gyrus is required for consolidation of "pattern-separated" memories. *J. Chem. Inf. Model* 53, 1689–1699. doi: 10.1016/j.celrep.2013.09.027

Bocchio, M., Nabavi, S., and Capogna, M. (2017). Review synaptic plasticity, engrams and network oscillations in amygdala circuits for storage and retrieval of emotional memories. *Neuron* 94, 731–743. doi: 10.1016/j.neuron.2017.03.022

Bragin, A., Jandó, G., Nádasdy, Z., Hetke, J., Wise, K., Buzsáki, G., et al. (1995). γ (40–100 Hz) oscillation in the hippocampus of the behaving rat. *J. Neurosci.* 15, 47–60.

Buckmaster, P. S., Wenzel, H. J., Kunkel, D. D., and Schwartzkroin, P. A. (1996). Axon arbors and synaptic connections of hippocampal mossy cells in the rat *in vivo*. *J. Comp. Neurol.* 366, 270–292. doi: 10.1002/(sici)1096-9861(19960304)366:2<270::aid-cne7>3.0.co;2-2

Buzsàki, G., and Eidelberg, E. (1981). Commiasural projection to the dentate gyrus of the rat: evidence for feed-forward inhibition. *Brain Res.* 230, 346–350. doi: 10.1016/0006-8993(81)90413-3

Chawla, M. K., Guzowski, J. F., Ramirez-Amaya, V., Lipa, P., Hoffman, K. L., Marriott, L. K., et al. (2005). Sparse, environmentally selective expression of Arc RNA in the upper blade of the rodent fascia dentata by brief spatial experience. *Hippocampus* 15, 579–586. doi: 10.1002/hipo.20091

Chemla, S., and Chavane, F. (2009). Voltage-sensitive dye imaging: technique review and models. *J. Physiol.* 104, 40–50. doi: 10.1016/j.jphysparis.2009.11.009

Chen, B. K., Murawski, N. J., Cincotta, C., Zaki, Y., Fortin, A., Ramirez, S., et al. (2019). Artificially enhancing and suppressing report artificially enhancing and suppressing hippocampus-mediated memories. *Curr. Biol.* 29, 1885.e4–1894.e4. doi: 10.1016/j.cub.2019.04.065

Cho, Y. K., Zheng, G., Augustine, G. J., Hochbaum, D., Cohen, A., Knopfel, G., et al. (2016). Roadmap on neurophotonics. *J. Opt.* 18:093007. doi: 10.1088/2040-8978/18/9/093007

Choi, J., Sim, S., Kim, J., Choi, D. I., Oh, J., Ye, S., et al. (2018). Interregional synaptic maps among engram cells underlie memory formation. *Science* 360, 430–435. doi: 10.1126/science.aas9204

Clelland, C. D., Choi, M., Romberg, C., Clemenson, G. D., Fragniere, A., Tyers, P., et al. (2009). A functional role for adult hippocampal neurogenesis in spatial pattern separation. *Science* 325, 210–213. doi: 10.1126/science.1173215

Colgin, L. L., Moser, E. I., and Moser, M. B. (2008). Understanding memory through hippocampal remapping. *Trends Neurosci.* 31, 469–477. doi: 10.1016/j.tins.2008.06.008

Creer, D. J., Romberg, C., Saksida, L. M., van Praag, H., and Bussey, T. J. (2010). Running enhances spatial pattern separation in mice. *Proc. Natl. Acad. Sci. U S A* 107, 2367–2372. doi: 10.1073/pnas.0911725107

Danielson, N. B., Kaifosh, P., Zaremba, J. D. D., Lovett-Barron, M., Tsai, J., Denny, C. A. A., et al. (2016). Distinct contribution of adult-born hippocampal granule cells to context encoding. *Neuron* 90, 101–112. doi: 10.1016/j.neuron.2016.02.019

Danielson, N. B., Turi, G. F., Ladow, M., Chavlis, S., Petrantonakis, P. C., Danielson, N. B., et al. (2017). *in vivo* imaging of dentate gyrus mossy cells in behaving mice. *Neuron* 93, 552.e4–559.e4. doi: 10.1016/j.neuron.2016.12.019

Deng, W., Mayford, M., and Gage, F. H. (2013). Selection of distinct populations of dentate granule cells in response to inputs as a mechanism for pattern separation in mice. *Elife* 2:e00312. doi: 10.7554/elife.00312

Denny, C. A., Lebois, E., and Ramirez, S. (2017). From engrams to pathologies of the brain. *Front. Neural Circuits* 11:23. doi: 10.3389/fncir.2017.00023

Douglas, R. M., Mcnaughton, B. L., and Goddard, G. V. (1983). Commissural inhibition and facilitation of granule cell discharge in fascia dentata. *J. Comp. Neurol.* 219, 285–294. doi: 10.1002/cne.902190304

Drew, L. J., Kheirbek, M. A., Luna, V. M., Denny, C. A., Cloidt, M. A., Wu, M. V., et al. (2016). Activation of local inhibitory circuits in the dentate gyrus by adult-born neurons. *Hippocampus* 26, 763–778. doi: 10.1002/hipo.22557

Ebner, T., and Chen, G. (1995). Use of voltage-sensitive dyes ans optical recordings in the central nervous system. *Prog. Neurobiol.* 46, 463–506. doi: 10.1016/0301-0082(95)00010-s

Espinoza, C., Guzman, S. J., Zhang, X., and Jonas, P. (2018). Parvalbumin$^+$ interneurons obey unique connectivity rules and establish a powerful lateral-inhibition microcircuit in dentate gyrus. *Nat. Commun.* 9:4605. doi: 10.1038/s41467-018-06899-3

Espósito, M. S., Piatti, C., Laplagne, D. A., Morgenstern, A., Ferrari, C. C., Pitossi, F. J., et al. (2005). Neuronal differentiation in the adult hippocampus recapitulates embryonic development. *J. Neurosci.* 25, 10074–10086. doi: 10.1523/jneurosci.3114-05.2005

Freund, T. F., and Buzsáki, G. (1996). Interneurons of the hippocampus. *Hippocampus* 6, 347–470. doi: 10.1002/(sici)1098-1063(1996)6:4<347::aid-hipo1>3.0.co;2-i

Ge, S., Yang, C., Hsu, K., Ming, G., and Song, H. (2007). A critical period for enhanced synaptic plasticity in newly generated neurons of the adult brain. *Neuron* 54, 559–566. doi: 10.1016/j.neuron.2007.05.002

Ghandour, K., Ohkawa, N., Chung, C., Fung, A., Asai, H., Hayashi, Y., et al. (2019). Orchestrated ensemble activities constitute a hippocampal memory engram. *Nat. Commun.* 10:2637. doi: 10.1038/s41467-019-10683-2

Gilbert, P. E., Kesner, R. P., and DeCoteau, W. E. (1998). Memory for spatial location: role of the hippocampus in mediating spatial pattern separation. *J. Neurosci.* 18, 804–810. doi: 10.1523/jneurosci.18-02-00804.1998

Gilbert, P. E., Kesner, R. P., and Lee, I. (2001). Dissociating hippocampal subregions: a double dissociation between dentate gyrus and CA1. *Hippocampus* 636, 626–636. doi: 10.1002/hipo.1077

Goodrich-Hunsaker, N. J., Hunsaker, M. R., and Kesner, R. P. (2005). Dissociating the role of the parietal cortex and dorsal hippocampus for spatial information. *Behav. Neurosci.* 119, 1307–1315. doi: 10.1037/0735-7044.119.5.1307

Goodrich-Hunsaker, N. J., Hunsaker, M. R., and Kesner, R. P. (2008). The interactions and dissociations of the dorsal hippocampus subregions: how the dentate gyrus, CA3 and CA1 process spatial information. *Behav. Neurosci.* 122, 16–26. doi: 10.1037/0735-7044.122.1.16

Gore, F., Schwartz, E. C., Brangers, B. C., Aladi, S., Stujenske, J. M., Likhtik, E., et al. (2015). Neural representations of unconditioned stimuli in basolateral amygdala mediate innate and learned responses. *Cell* 162, 134–145. doi: 10.1016/j.cell.2015.06.027

Groisman, A., Yang, S., and Schinder, A. (2020). Differential coupling of adult-born granule cells to article differential coupling of adult-born granule cells to parvalbumin and somatostatin interneurons. *Cell Rep.* 30, 202.e4–214.e4. doi: 10.1101/598615

Guan, J., Jiang, J., Xie, H., and Liu, K. (2016). How does the sparse memory "engram" neurons encode the memory of a spatial-temporal event? *Front. Neural Circuits* 10:61. doi: 10.3389/fncir.2016.00061

Guzman, S. J., Schlogl, A., Espinoza, C., Zhang, X., Suter, B., and Jonas, P. (2019). Fast signaling and focal connectivity of PV+ interneurons ensure efficient pattern separation by lateral inhibition in a full-scale dentate gyrus network model. *biorxiv* [Preprint]. doi: 10.1101/647800

Han, J.-H., Kushner, S. A., Yiu, A. P., Hsiang, H.-L., Buch, T., Waisman, A., et al. (2009). Selective erasure of a fear memory. *Science* 323, 1492–1496. doi: 10.1126/science.1164139

Hargreaves, E. L., Rao, G., Lee, I., and Knierim, J. J. (2005). Major dissociation between medial and lateral entorhinal input to dorsal hippocampus. *Science* 308, 1792–1794. doi: 10.1126/science.1110449

Hashimotodani, Y., Nasrallah, K., Jensen, K. R., Carrera, D., and Castillo, P. E. (2017). LTP at hilar mossy cell-dentate granule cell synapses modulates dentate gyrus output by increasing excitation/inhibition balance. *Neuron* 95, 928.e3–943.e3. doi: 10.1016/j.neuron.2017.07.028

Houser, C. R. (2007). Interneurons of the dentate gyrus: an overview of cell types, terminal fields and neurochemical identity. *Prog. Brain Res.* 163, 217–233. doi: 10.1016/s0079-6123(07)63013-1

Houzen, H., Kanno, M., and Kikuchi, S. (1998). AMPA/kainate receptor activation inhibits neuronal delayed rectifier K^+ current *via* Na^+ entry in rat cortical neurons. *Biochem. Biophys. Res. Commun.* 243, 617–621. doi: 10.1006/bbrc.1998.8146

Hsu, T., Lee, C., Tai, M., and Lien, C. (2016). Differential recruitment of dentate gyrus interneuron types by commissural versus perforant pathways. *Cereb. Cortex* 26, 2715–2727. doi: 10.1093/cercor/bhv127

Hu, H., Martina, M., and Jonas, P. (2010). Dendritic mechanisms underlying rapid synaptic activation of fast-spiking hippocampal interneurons. *Science* 327, 52–58. doi: 10.1126/science.1177876

Hunsaker, M. R., Rosenberg, J. S., and Kesner, R. P. (2008). The role of the dentate gyrus, CA3a,b and CA3c for detecting spatial and environmental novelty. *Hippocampus* 18, 1064–1073. doi: 10.1002/hipo.20464

Ikrar, T., Guo, N., He, K., Besnard, A., Levinson, S., and Hill, A. (2013). Adult neurogenesis modifies excitability of the dentate gyrus. *Front. Neural Circuits* 7:204. doi: 10.3389/fncir.2013.00204

Jackson, M. B., and Scharfman, H. E. (1996). Positive feedback from hilar mossy cells to granule cells in the dentate gym revealed by voltage-sensitive dye and microelectrode recording. *J. Neurophysiol.* 76, 601–616. doi: 10.1152/jn.1996.76.1.601

Jinde, S., Zsiros, V., Jiang, Z., Nakao, K., Pickel, J., Kohno, K., et al. (2012). Hilar mossy cell degeneration causes transient dentate granule cell hyperexcitability and impaired pattern separation. *Neuron* 76, 1189–1200. doi: 10.1016/j.neuron.2012.10.036

Jones, G., Boyd, D. F., Yeung, S. Y., and Mathie, A. (2000). Inhibition of delayed rectifier K^+ conductance in cultured rat cerebellar granule neurons by activation of calcium- permeable AMPA receptors. *Eur. J. Neurosci.* 12, 935–944. doi: 10.1046/j.1460-9568.2000.00983.x

Josselyn, S., and Tonegawa, S. (2020). Memory engrams: recalling the past and imagining the future. *Science* 367:eaaw4325. doi: 10.1126/science.aaw4325

Jung, D., Kim, S., Sariev, A., Sharif, F., and Kim, D. (2019). Dentate granule and mossy cells exhibit distinct spatiotemporal responses to local change in a one-dimensional landscape of visual-tactile cues. *Sci. Rep.* 9:9545. doi: 10.1038/s41598-019-45983-6

Jung, M. W., and McNaughton, B. L. (1993). Spatial selectivity of unit activity in the hippocampal granular layer. *Hippocampus* 3, 165–182. doi: 10.1002/hipo.450030209

Kastellakis, G., and Poirazi, P. (2019). Synaptic clustering and memory formation. *Front. Mol. Neurosci.* 12:300. doi: 10.3389/fnmol.2019.00300

Kim, D., Paré, D., and Nair, S. S. (2013). Assignment of model amygdala neurons to the fear memory trace depends on competitive synaptic interactions. *J. Neurosci.* 33, 14354–14358. doi: 10.1523/jneurosci.2430-13.2013

Kim, J., Zhao, T., Petralia, R. S., Yu, Y., Peng, H., Myers, E., et al. (2012). mGRASP enables mapping mammalian synaptic connectivity with light microscopy. *Nat. Methods* 9, 96–102. doi: 10.1038/nmeth.1784

Klapoetke, N. C., Murata, Y., Kim, S. S., Pulver, S. R., Birdsey-benson, A., Cho, Y. K., et al. (2014). Independent optical excitation of distinct neural populations. *Nat. Methods* 11, 338–346. doi: 10.1038/nmeth.2836

Lacy, J. W., Yassa, M. A., Stark, S. M., Muftuler, L. T., and Stark, C. E. L. (2011). Distinct pattern separation related transfer functions in human CA3/dentate and CA1 revealed using high-resolution fMRI and variable mnemonic similarity. *Learn. Mem.* 18, 15–18. doi: 10.1101/lm.1971111

Larimer, P., and Strowbridge, B. W. (2008). Nonrandom local circuits in the dentate gyrus. *J. Neurosci.* 28, 12212–12223. doi: 10.1523/JNEUROSCI.3612-08.2008

Lee, C., Kao, M., Hou, W., Wei, Y., Chen, C., and Lien, C.-C. (2016). Causal evidence for the role of specific GABAergic interneuron types in entorhinal recruitment of dentate granule cells. *Sci. Rep.* 6:36885. doi: 10.1038/srep36885

Leranth, C., and Hajszan, T. (2007). Extrinsic afferent systems to the dentate gyrus. *Prog. Brain Res.* 163, 63–85. doi: 10.1016/S0079-6123(07)63004-0

Leutgeb, S., Leutgeb, J. K., Barnes, C. A., Moser, E. I., McNaughton, B. L., and Moser, M.-B. (2005). Independent codes for spatial and episodic memory in hippocampal neuronal ensembles. *Science* 309, 619–623. doi: 10.1126/science.1114037

Leutgeb, J. K., Leutgeb, S., Moser, M.-B., and Moser, E. I. (2007). Pattern separation in the dentate gyrus and CA3 of the hippocampus. *Science* 315, 961–966. doi: 10.1126/science.1135801

Lin, J. Y., Lin, M. Z., Steinbach, P., and Tsien, R. Y. (2009). Characterization of engineered channelrhodopsin variants with improved properties and kinetics. *Biophys. J.* 96, 1803–1814. doi: 10.1016/j.bpj.2008.11.034

Liu, X., Ramirez, S., Pang, P. T., Puryear, C. B., Govindarajan, A., Deisseroth, K., et al. (2012). Optogenetic stimulation of a hippocampal engram activates fear memory recall. *Nature* 484, 381–385. doi: 10.1038/nature11028

Luna, V. M., Anacker, C., Burghardt, N. S., Khandaker, H., Andreu, V., Millette, A., et al. (2019). Adult-born hippocampal neurons bidirectionally modulate entorhinal inputs into the dentate gyrus. *Science* 364, 578–583. doi: 10.1126/science.aat8789

Marín-Burgin, A., Mongiat, L. A., Pardi, M. B., and Schinder, A. F. (2012). Unique processing during a period of high excitation/inhibition balance in adult- born neurons. *Science* 335, 1238–1242. doi: 10.1126/science.1214956

Marr, D. (1971). Simple memory: a theory for archicortex. *Philos. Trans. R. Soc. Lond. B Biol. Sci.* 262, 23–81. doi: 10.1098/rstb.1971.0078

Martin, S. J., and Morris, R. G. M. (2002). New life in an old idea: the synaptic plasticity and memory hypothesis revisited. *Hippocampus* 12, 609–636. doi: 10.1002/hipo.10107

McClelland, J. L., McNaughton, B. L., and O'Reilly, R. C. (1995). Why there are complementary learning system in the hippocampus and neocortex: insights from the successes and failures of connectionist models of learning and memory. *Psychol. Rev.* 102, 419–457. doi: 10.1037/0033-295x.102.3.419

McHugh, T. J., Jones, M. W., Quinn, J. J., Balthasar, N., Coppari, R., Elmquist, J. K., et al. (2007). Dentate gyrus NMDA receptors mediate rapid pattern separation in the hippocampal network. *Science* 317, 94–99. doi: 10.1126/science.1140263

Morales, C., Morici, J. F., Espinosa, N., Sacson, A., Lara-Vasquez, A., Garcia-Perez, A., et al. (2019). Dentate gyrus somatostatin cells are required

for contextual discrimination during episodic memory encoding. *biorxiv* [Preprint].

Muller, R. U., and Kubie, J. L. (1987). The effects of changes in the environment hippocampal cells on the spatial firing of hippocampal complex-spike cells. *J. Neurosci.* 7, 1951–1968. doi: 10.1523/JNEUROSCI.07-07-01951.1987

Nakashiba, T., Cushman, J. D., Pelkey, K. A., Renaudineau, S., Buhl, D. L., McHugh, T. J., et al. (2012). Young dentate granule cells mediate pattern separation, whereas old granule cells facilitate pattern completion. *Cell* 149, 188–201. doi: 10.1016/j.cell.2012.01.046

Nakazawa, K. (2017). Dentate mossy cell and pattern separation kazu. *Neuron* 93, 465–467. doi: 10.1016/j.neuron.2017.01.021

Neunuebel, J. P., and Knierim, J. J. (2014). CA3 retrieves coherent representations from degraded input: direct evidence for CA3 pattern completion and dentate gyrus pattern separation. *Neuron* 81, 416–427. doi: 10.1016/j.neuron.2013.11.017

Nitz, D., and McNaughton, B. (2004). Differential modulation of CA1 and dentate gyrus interneurons during exploration of novel environments. *J. Neurophysiol.* 91, 863–872. doi: 10.1152/jn.00614.2003

Norman, K. A., and O'Reilly, R. C. (2003). Modeling hippocampal and neocortical contributions to recognition memory: a complementary-learning-systems approach. *Psychol. Rev.* 110, 611–646. doi: 10.1037/0033-295x.110.4.611

O'Keefe, J., and Dostrovsky, J. (1971). The hippocampus as a spatial map. Preliminary evidence from unit activity in the freely-moving rat. *Brain Res.* 34, 171–175. doi: 10.1016/0006-8993(71)90358-1

Park, S., Kramer, E. E., Mercaldo, V., Rashid, A. J., Insel, N., Frankland, P. W., et al. (2016). Neuronal allocation to a hippocampal engram. *Neuropsychopharmacology* 41, 2987–2993. doi: 10.1038/npp.2016.73

Pignatelli, M., Ryan, T. J., Roy, D. S., Lovett, C., Smith, L. M., Muralidhar, S., et al. (2019). Engram cell excitability state determines the efficacy of memory retrieval. *Neuron* 101, 274.e5–284.e5. doi: 10.1016/j.neuron.2018.11.029

Ramirez, S., Liu, X., MacDonald, C. J., Moffa, A., Zhou, J., Redondo, R. L., et al. (2015). Activating positive memory engrams suppresses depression-like behaviour. *Nature* 522, 335–339. doi: 10.1038/nature14514

Ramirez, S., Tonegawa, S., and Liu, X. (2013). Identification and optogenetic manipulation of memory engrams in the hippocampus. *Front. Behav. Neurosci.* 7:226. doi: 10.3389/fnbeh.2013.00226

Ranganath, C. (2010). A unified framework for the functional organization of the medial temporal lobes and the phenomenology of episodic memory. *Hippocampus* 20, 1263–1290. doi: 10.1002/hipo.20852

Rao-Ruiz, P., Couey, J. J., Marcelo, I. M., Bouwkamp, C. G., Slump, D. E., Matos, M. R., et al. (2019). Engram-specific transcriptome profiling of contextual memory consolidation. *Nat. Commun.* 10:2232. doi: 10.1038/s41467-019-09960-x

Rashid, A. J., Yan, C., Mercaldo, V., Hsiang, H. L., Park, S., Cole, C. J., et al. (2016). Competition between engrams influences fear memory formation and recall. *Science* 353, 383–388. doi: 10.1126/science.aaf0594

Ratzliff, A. H., Howard, A. L., Santhakumar, V., Osapay, I., and Soltesz, I. (2004). Rapid deletion of mossy cells does not result in a hyperexcitable dentate gyrus: implications for epileptogenesis. *J. Neurosci.* 24, 2259–2269. doi: 10.1523/JNEUROSCI.5191-03.2004

Redondo, R. L., Kim, J., Arons, A. L., Ramirez, S., Liu, X., and Tonegawa, S. (2014). Bidirectional switch of the valence associated with a hippocampal contextual memory engram. *Nature* 513, 426–430. doi: 10.1038/nature13725

Rolls, E. T. (2013). The mechanisms for pattern completion and pattern separation in the hippocampus. *Front. Syst. Neurosci.* 7:74. doi: 10.3389/fnsys.2013.00074

Rolls, E. T., and Kesner, R. P. (2006). A computational theory of hippocampal function and empirical tests of the theory. *Prog. Neurobiol.* 79, 1–48. doi: 10.1016/j.pneurobio.2006.04.005

Rolls, E. T., Treves, A., Robertson, R. G., Georges-François, P., and Panzeri, S. (1998). Information about spatial view in an ensemble of primate hippocampal cells. *J. Neurophysiol.* 79, 1797–1813. doi: 10.1152/jn.1998.79.4.1797

Roy, D. S., Arons, A., Mitchell, T. I., Pignatelli, M., and Tonegawa, S. (2016). Memory retrieval by activating engram cells in mouse models of early Alzheimer's disease. *Nature* 531, 508–512. doi: 10.1038/nature17172

Roy, D. S., Muralidhar, S., Smith, L. M., and Tonegawa, S. (2017). Silent memory engrams as the basis for retrograde amnesia. *Proc. Natl. Acad. Sci. U S A* 114, E9972–E9979. doi: 10.1073/pnas.1714248114

Royer, S., Zemelman, B. V., Barbic, M., Losonczy, A., Buzsáki, G., and Magee, J. C. (2010). Multi-array silicon probes with integrated optical fibers: light-assisted perturbation and recording of local neural circuits in the behaving animal. *Eur. J. Neurosci.* 31, 2279–2291. doi: 10.1111/j.1460-9568.2010.07250.x

Ryan, T., Roy, D. S., Pignatelli, M., Arons, A., and Tonegawa, S. (2015). Engram cells retain memory under retrograde amnesia. *Science* 348, 1007–1013. doi: 10.1126/science.aaa5542

Sahay, A., Scobie, K. N., Hill, A. S., O'Carroll, C. M., Kheirbek, M. A., Burghardt, N. S., et al. (2011a). Increasing adult hippocampal neurogenesis is sufficient to improve pattern separation. *Nature* 472, 466–470. doi: 10.1038/nature09817

Sahay, A., Wilson, D. A., and Hen, R. (2011b). Pattern separation: a common function for new neurons in hippocampus and olfactory bulb. *Neuron* 70, 582–588. doi: 10.1016/j.neuron.2011.05.012

Sambandan, S., Sauer, J., Vida, I., and Bartos, M. (2010). Associative plasticity at excitatory synapses facilitates recruitment of fast-spiking interneurons in the dentate gyrus. *J. Neurosci.* 30, 11826–11837. doi: 10.1523/JNEUROSCI.2012-10.2010

Santhakumar, V., Bender, R., Frotscher, M., Ross, S. T., Hollrigel, G. S., Toth, Z., et al. (2000). Granule cell hyperexcitability in the early post-traumatic rat dentate gyrus: the 'irritable mossy cell' hypothesis. *J. Physiol.* 524, 117–134. doi: 10.1111/j.1469-7793.2000.00117.x

Satvat, E., Schmidt, B., Argraves, M., Marrone, D. F., and Markus, E. J. (2011). Changes in task demands alter the pattern of zif268 expression in the dentate gyrus. *J. Neurosci.* 31, 7163–7167. doi: 10.1523/JNEUROSCI.0094-11.2011

Savanthrapadian, S., Meyer, T., Elgueta, C., Booker, S. A., Vida, I., and Bartos, M. (2014). Synaptic properties of SOM- and CCK-expressing cells in dentate gyrus interneuron networks. *J. Neurosci.* 34, 8197–8209. doi: 10.1523/JNEUROSCI.5433-13.2014

Scharfman, H. E. (1995). Electrophysiological evidence that dentate hilar mossy cells are excitatory and innervate both granule cells and interneurons. *J. Neurophysiol.* 74, 179–194. doi: 10.1152/jn.1995.74.1.179

Scharfman, H. E. (2016). The enigmatic mossy cell of the dentate gyrus. *Nat. Rev. Neurosci.* 17, 562–575. doi: 10.1038/nrn.2016.87

Scharfman, H. E. (2018). Advances in understanding hilar mossy cells of the dentate gyrus. *Cell Tissue Res.* 373, 643–652. doi: 10.1007/s00441-017-2750-5

Scharfman, H. E., and Myers, C. E. (2012). Hilar mossy cells of the dentate gyrus: a historical perspective. *Front. Neural Circuits* 6:106. doi: 10.3389/fncir.2012.00106

Schmidt-Hieber, C., Jonas, P., and Bischofberger, J. (2004). Enhanced synaptic plasticity in newly generated granule cells of the adult hippocampus. *Nature* 429, 184–187. doi: 10.1038/nature02553

Schröder, W., Seifert, G., Hüttmann, K., Hinterkeuser, S., and Steinhäuser, C. (2002). MCN AMPA receptor-mediated modulation of inward rectifier K^+ channels in astrocytes of mouse hippocampus. *Mol. Cell. Neurosci.* 19, 447–458. doi: 10.1006/mcne.2001.1080

Senzai, Y., and Buzsáki, G. (2017). Physiological properties and behavioral correlates of hippocampal granule cells and mossy cells. *Neuron* 93, 691.e5–704.e5. doi: 10.1016/j.neuron.2016.12.011

Sloviter, R. S. (1983). "Epileptic" brain damage in rats induced by sustained electrical stimulation of the perforant path. I. Acute electrophysiological and light microscopic studies. *Brain Res. Bull.* 10, 675–697. doi: 10.1016/0361-9230(83)90037-0

Sloviter, R. S. (1991). Permanently altered hippocampal structure, excitability, and inhibition after experimental status epilepticus in the rat: the "dormant basket cell" hypothesis and its possible relevance to temporal lobe epilepsy. *Hippocampus* 1, 41–66. doi: 10.1002/hipo.450010106

Soriano, E., and Frotscherf, M. (1994). Mossy cells of the rat fascia dentata are glutamate-immunoreactive. *Hippocampus* 4, 65–70. doi: 10.1002/hipo.450040108

Stefanelli, T., Bertollini, C., Lüscher, C., Muller, D., and Mendez, P. (2016). Hippocampal somatostatin interneurons control the size of neuronal memory ensembles. *Neuron* 89, 1074–1085. doi: 10.1016/j.neuron.2016.01.024

Sun, Y., Grieco, S. F., Holmes, T. C., and Xu, X. (2017). Local and long-range circuit connections to hilar mossy cells in the dentate gyrus. *eNeuro* 4:ENEURO.0097-17.2017. doi: 10.1523/eneuro.0097-17.2017

Tanaka, K. Z., and McHugh, T. J. (2018). The hippocampal engram as a memory index. *J. Exp. Neurosci.* 12:1179069518815942. doi: 10.1177/1179069518815942

Temprana, S. G., Mongiat, L. A., Yang, S. M., Trinchero, M. F., Alvarez, D. D., Kropff, E., et al. (2015). Delayed coupling to feedback inhibition during a critical period for the integration of adult-born granule cells. *Neuron* 85, 116–130. doi: 10.1016/j.neuron.2014.11.023

Tonegawa, S., Liu, X., Ramirez, S., and Redondo, R. (2015). Memory engram cells have come of age. *Neuron* 87, 918–931. doi: 10.1016/j.neuron.2015.08.002

Toner, C. K., Pirogovsky, E., Kirwan, C. B., and Gilbert, P. E. (2009). Visual object pattern separation deficits in nondemented older adults. *Learn. Mem.* 16, 338–342. doi: 10.1101/lm.1315109

Torricelli, A., Contini, D., Dalla Mora, A., Pifferi, A., Re, R., Zucchelli, L., et al. (2014). Neurophotonics: non-invasive optical techniques for monitoring brain functions. *Funct. Neurol.* 29, 223–230. doi: 10.11138/fneur/2014.29.4.223

Treves, A., and Rolls, E. T. (1992). Computational constraints suggest the need for two distinct input systems to the hippocampal CA3 network. *Hippocampus* 2, 189–199. doi: 10.1002/hipo.450020209

Treves, A., and Rolls, E. T. (1994). Computational analysis of the role of the hippocampus in memory. *Hippocampus* 4, 374–391. doi: 10.1002/hipo.450040319

Tsytsarev, V., Liao, L., Kong, K. V., Liu, Y., Erzurumlu, R. S., Olivo, M., et al. (2014). Recent progress in voltage-sensitive dye imaging for neuroscience recent progress in voltage-sensitive dye imaging for neuroscience. *J. Nanosci. Nanotechnol.* 14, 4733–4744. doi: 10.1166/jnn.2014.9531

Vetere, G., Tran, L. M., Moberg, S., Steadman, P. E., Restivo, L., Morrison, F. G., et al. (2019). Memory formation in the absence of experience. *Nat. Neurosci.* 22, 940–940. doi: 10.1038/s41593-019-0389-0

Wang, J. (2019). Searching basic units in memory traces: associative memory cells. *F1000Research* 8:457. doi: 10.12688/f1000research.18771.1

Wilson, D. I. G., Langston, R. F., Schlesiger, M. I., Wagner, M., Watanabe, S., and Ainge, J. A. (2013). Lateral entorhinal cortex is critical for novel object-context recognition. *Hippocampus* 23, 352–366. doi: 10.1002/hipo.22095

Xu, X., Olivas, N. D., Levi, R., Ikrar, T., and Nenadic, Z. (2010). High precision and fast functional mapping of cortical circuitry through a novel combination of voltage sensitive dye imaging and laser scanning photostimulation. *J. Neurophysiol.* 103, 2301–2312. doi: 10.1152/jn.00992.2009

Yiu, A. P., Mercaldo, V., Yan, C., Richards, B., Rashid, A. J., Hsiang, H. L., et al. (2014). Neurons are recruited to a memory trace based on relative neuronal excitability immediately before training. *Neuron* 83, 722–735. doi: 10.1016/j.neuron.2014.07.017

Yuan, M., Meyer, T., Benkowitz, C., Savanthrapadian, S., Ansel-bollepalli, L., Foggetti, A., et al. (2017). Somatostatin-positive interneurons in the dentate gyrus of mice provide local- and long-range septal synaptic inhibition. *Elife* 6:e21105. doi: 10.7554/eLife.21105

Zhou, Y., Won, J., Karlsson, M. G., Zhou, M., Balaji, J., Neve, R., et al. (2009). CREB regulates excitability and the allocation of memory to subsets of neurons in the amygdala. *Nat. Neurosci.* 12, 1438–1443. doi: 10.1038/nn.2405

Conflict of Interest: The authors declare that the research was conducted in the absence of any commercial or financial relationships that could be construed as a potential conflict of interest.

frontiers in Neural Circuits

REVIEW
published: 12 June 2020
doi: 10.3389/fncir.2020.00031

Insights Into Spinal Dorsal Horn Circuit Function and Dysfunction Using Optical Approaches

Erika K. Harding[1,2], *Samuel Wanchi Fung*[1] *and Robert P. Bonin*[1,3]*

[1]*Department of Pharmaceutical Sciences, Leslie Dan Faculty of Pharmacy, University of Toronto, Toronto, ON, Canada,* [2]*Department of Comparative Biology and Experimental Medicine, University of Calgary, Calgary, AB, Canada,* [3]*University of Toronto Centre for the Study of Pain, University of Toronto, Toronto, ON, Canada*

Somatosensation encompasses a variety of essential modalities including touch, pressure, proprioception, temperature, pain, and itch. These peripheral sensations are crucial for all types of behaviors, ranging from social interaction to danger avoidance. Somatosensory information is transmitted from primary afferent fibers in the periphery into the central nervous system *via* the dorsal horn of the spinal cord. The dorsal horn functions as an intermediary processing center for this information, comprising a complex network of excitatory and inhibitory interneurons as well as projection neurons that transmit the processed somatosensory information from the spinal cord to the brain. It is now known that there can be dysfunction within this spinal cord circuitry in pathological pain conditions and that these perturbations contribute to the development and maintenance of pathological pain. However, the complex and heterogeneous network of the spinal dorsal horn has hampered efforts to further elucidate its role in somatosensory processing. Emerging optical techniques promise to illuminate the underlying organization and function of the dorsal horn and provide insights into the role of spinal cord sensory processing in shaping the behavioral response to somatosensory input that we ultimately observe. This review article will focus on recent advances in optogenetics and fluorescence imaging techniques in the spinal cord, encompassing findings from both *in vivo* and *in vitro* preparations. We will also discuss the current limitations and difficulties of employing these techniques to interrogate the spinal cord and current practices and approaches to overcome these challenges.

Keywords: spinal cord, dorsal horn, optogenetics, calcium imaging, *in vivo*, pain, somatosensation

OPEN ACCESS

Edited by:
Edward S. Ruthazer, McGill University, Canada

Reviewed by:
Andrew J. Todd, University of Glasgow, United Kingdom
Reza Sharif-Naeini, McGill University, Canada

***Correspondence:**
Robert P. Bonin
rob.bonin@utoronto.ca

Received: *15 March 2020*
Accepted: *01 May 2020*
Published: *12 June 2020*

Citation:
Harding EK, Fung SW and Bonin RP (2020) Insights Into Spinal Dorsal Horn Circuit Function and Dysfunction Using Optical Approaches. Front. Neural Circuits 14:31. doi: 10.3389/fncir.2020.00031

INTRODUCTION

Our physical connection to the world through sensation is essential for our health and wellbeing. Somatosensation is a broad term encompassing many modalities including touch, pressure, proprioception, temperature, pain, and itch. It is through these peripheral sensations that we can recognize and remove ourselves from danger, to sense warmth or cold for thermoregulation, and to detect and respond to socially relevant physical gestures such as a gentle caress. An inability to detect physical sensations can be severely debilitating and lead to increased risk of injury and a shortened lifespan, as can be seen in patients with congenital insensitivity to pain (Nagasako et al., 2003).

Somatosensory information is first transduced in the peripheral nervous system by specialized receptors on primary afferent neurons. This information then travels along primary afferent fibers, whose cell bodies reside in the dorsal root ganglia, and into the dorsal horn of the spinal cord. Historically, primary afferent fibers have been classified by conduction velocity and degree of myelination into four types (Aα, Aβ, Aδ, and C), and it was originally believed that each type transmits different modalities of sensory information to the spinal dorsal horn (Roberts and Elardo, 1986; McGlone and Reilly, 2010).

C fibers terminate predominantly in laminae I–II, the outermost laminae, and transmit nociceptive information including noxious heat and noxious mechanical perturbations to tissue (Basbaum et al., 2009), as well as information related to itch and low threshold, pleasant mechanical stimuli (Olausson et al., 2002; Ikoma et al., 2006; Wooten et al., 2014; Huang et al., 2018). Aδ fibers transmit a mixture of noxious and innocuous tactile and cold information and terminate predominantly within laminae I and V, with a subset of Aδ fibers corresponding to low-threshold mechanosensation terminating within lamina III (Li et al., 2011; Arcourt et al., 2017; Koch et al., 2018). However, Aβ fibers carry the bulk of innocuous tactile information, including touch, vibration, texture, and pressure (Mackenzie et al., 1975; Basbaum et al., 2009). Aβ fibers transmit information *via* the dorsal column into the cuneate and gracile nuclei, and send a branch into the dorsal horn, terminating in laminae III–V (Basbaum et al., 2009; Niu et al., 2013). Proprioceptive information is transmitted predominantly by Aα fibers, which terminate widely throughout lamina IV–VI and the ventral horn, where they contribute to sensory-motor loops (Maxwell and Bannatyne, 1983; Mears and Frank, 1997; Maxwell and Riddell, 1999). It should be noted that there is increasing evidence that this classification of primary afferent types by conduction velocity and modality of information is not as discrete as once believed, and there are many exceptions to these general rules. Instead, classification by molecular markers is increasingly used to differentiate primary afferent populations, often aligning to specific roles in somatosensation (Usoskin et al., 2015; Arcourt et al., 2017; Huang et al., 2018).

The dorsal horn is divided into six layers, referred to as laminae, and has long been recognized as a key site for somatosensory processing (Rexed, 1952; Molander et al., 1984). Integrated processing of different somatosensory modalities is achieved through a combination of organizational specificity of primary afferent fiber termination (**Figure 1**), and through complex circuitry that allows for communication between the laminae of the dorsal horn (Dubner and Ren, 1999; Duan et al., 2014; Bourane et al., 2015; Pagani et al., 2019). The most famous example of this is the gate control theory, which was first theorized by Melzack and Wall (1965) over 50 years ago, and suggests the presence of a network which allows for innocuous stimuli to affect the transmission of noxious stimuli to the brain, rather than these stimuli being separated in distinct networks. Indeed, connections between the deeper dorsal horn layers and lamina I have been defined, which, under pathological pain conditions, allow for a light touch to activate nociceptive projection neurons; a possible neural correlate for allodynia (Takazawa and MacDermott, 2010; Lu et al., 2013; Peirs et al., 2015; Petitjean et al., 2015; Cheng et al., 2017).

Primary afferent fibers may form synapses with excitatory and inhibitory neurons within the spinal cord, and with both interneurons and projection neurons (Lu and Perl, 2003, 2005; Takazawa and MacDermott, 2010). The patterns by which different primary afferent fibers synapse onto which type of dorsal horn neuron, or whether a defined pattern exists, is not definitively known. Part of the reason for this is the high degree of neuronal heterogeneity in the dorsal horn and a lack of information regarding the functional roles of the many types of dorsal horn neurons. Also, no set classification scheme of dorsal horn neurons has been agreed upon. Most early attempts to classify dorsal horn neurons used a classification scheme based on action potential firing patterns or cellular morphology (Prescott and De Koninck, 2002; Punnakkal et al., 2014). However, there can be considerable overlap across these parameters.

More modern classification schemes based on the expression of specific molecular markers have proven more fruitful, with markers such as somatostatin effectively labeling excitatory neurons (Gutierrez-Mecinas et al., 2016, 2019), and markers such as parvalbumin effectively labeling inhibitory neurons (Boyle et al., 2017). It has also recently been found that two classes of neurons, differentiated by expression of substance P or gastrin-releasing peptide, correspond to previously identified morphologically- and electrophysiologically-distinct populations of neurons, namely radial cells and transient central cells, respectively (Grudt and Perl, 2002; Dickie et al., 2019). This provides further evidence that molecular markers can differentiate functionally distinct populations of neurons. However, it should be noted that in some cases molecular markers label both excitatory and inhibitory neurons, as is the case with calretinin (Gutierrez-Mecinas et al., 2016; Boyle et al., 2017), suggesting the need to better understand the heterogeneity of expression of potential molecular markers within this diverse population, in order to find better candidates that align to functionally distinct populations. Recent attempts to use single-cell RNA-sequencing have begun to offer considerable clarity into the complex neuronal heterogeneity in the dorsal horn (Usoskin et al., 2015; Häring et al., 2018; Sathyamurthy et al., 2018; Zeisel et al., 2018), but it is still unknown if these molecularly distinct populations align to different functional populations of neurons within the dorsal horn, representing an open opportunity for research.

The spinal dorsal horn also receives direct descending modulation from several brainstem regions including the rostral ventromedial medulla (RVM) and locus coeruleus (LC; Ren and Dubner, 2002; Gebhart, 2004). These connections serve to modulate the excitability of neurons within the spinal cord, often by decreasing the excitation of cortically-projecting neurons (**Figure 1**). For example, adrenergic, opioidergic, and cannabinergic signaling from the brainstem can directly inhibit dorsal horn neurons, reduce neurotransmitter release

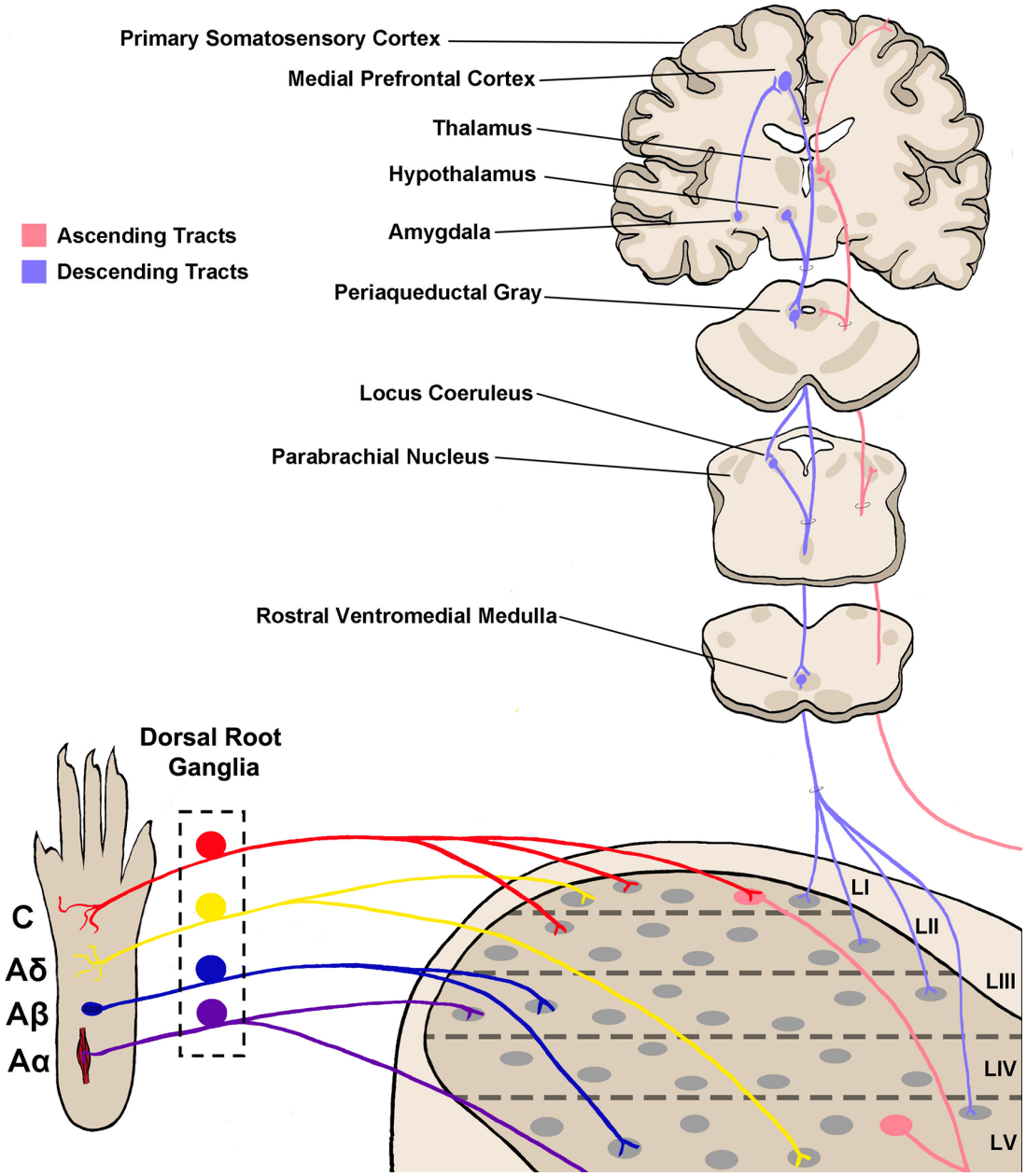

FIGURE 1 | Somatosensory circuitry from the periphery to the brain. Somatosensory information is first transmitted into the spinal dorsal horn by primary afferent neuron fibers, which extend from peripheral tissue into the spinal cord and synapse onto neurons within the dorsal horn. There are four main types of primary afferent fiber, separated by transduction velocity, and each type (Aα, Aβ, Aδ, C) shows some selectivity in somatosensory modality transmitted and synapses into different laminae as shown here (Roberts and Elardo, 1986; McGlone and Reilly, 2010; Koch et al., 2018). This produces selectivity in the modality processed in each lamina of the dorsal horn. Projection neurons within lamina I and V send axons up to the brain *via* ascending tracts including the spinothalamic tract and dorsal column–medial lemniscal tract (not shown in the figure; Willis, 1985; Niu et al., 2013). Briefly, axons decussate at the spinal level, then ascend on the contralateral side towards the thalamus. Some projections terminate within other brainstem regions including the parabrachial nucleus and periaqueductal gray. Descending tracts originate from several brain regions including the medial prefrontal cortex, hypothalamus, and amygdala, and project first to the periaqueductal gray (Gebhart, 2004; Huang et al., 2019). From here, descending projections then synapse within the rostral ventromedial medulla (RVM), and join with locus coeruleus (LC) descending projections. RVM/LC projection targets including the superficial dorsal horn and lamina V (D'Mello and Dickenson, 2008; François et al., 2017).

from primary afferents, and ultimately decrease pain behaviors (Ossipov and Gebhart, 1986; Porreca et al., 2002; Huang et al., 2019). Within the dorsal horn, both pre- and postsynaptic sites of action of inhibitory and excitatory neuronal populations have been implicated in descending pain modulation; however, the complete picture of how descending modulation of dorsal horn sensory processing occurs at a systems-level remains unclear (Lau and Vaughan, 2014).

Techniques that allow for manipulation of and recording from specific neuronal populations are ideal for determining how the circuitry of the dorsal horn processes and modulates somatosensory information in normal and pathological conditions. Of increasing utility are recently developed small molecules and genetically-encoded proteins that are activated by light, which allow for either the optical manipulation or detection of activity within spatially or genetically-defined cellular populations; namely optogenetic actuators, and activity sensors such as calcium indicators. The advantages of these tools can be demonstrated by the wide variety of usages they have, both *in vivo* and *in vitro*, from the single cell to population/circuit level; and in the insights that we are deriving from them. They can be used to understand how specifically defined populations of neurons or glia are active during or contribute to the various modalities of somatosensation, how they contribute to crosstalk between these modalities, and how they are affected by descending modulation and/or disorders of sensation including pathological pain conditions.

Here, we will review the current literature on the use of optogenetics for investigation of sensory processing, as well as calcium imaging of both neuronal and glial activity for probing spinal cord circuitry, discuss technologies and limitations, and new advances in both these techniques that could be employed in the future within the spinal dorsal horn.

APPLYING OPTOGENETIC TECHNIQUES TO PROBE SPINAL CORD CIRCUITRY

An Overview of Available Optogenetic Tools

Optogenetic tools utilize engineered and artificially introduced ion channels for rapid non-invasive activation or inactivation of specific cellular populations using light (Nagel et al., 2003; Zemelman et al., 2003; Banghart et al., 2004; Boyden et al., 2005; Lima and Miesenböck, 2005; Fenno et al., 2011). These ion channels were first derived from microbial opsins and allow for a wide degree of temporal and spatial sensitivity for manipulation of activity in specific populations of many types of cells, ranging from neurons to HEK cells, and even astrocytes and microglia. They are often referred to as optogenetic actuators, or simply as opsins. The most commonly used excitatory opsin is Channelrhodopsin-2 (ChR2), which upon activation by 488 nm (blue) light allows cations into any cell expressing it (Boyden et al., 2005). Other excitatory optogenetic ion channels have been developed beyond ChR2 that have different or improved functionality, such as oChIEF and Chronos (can be activated at high frequency), Chrimson and C1V1 (activated by a red light), CatCh (permeable to calcium ions), and ChloC (permeable to anions; see Tye and Deisseroth, 2012; Klapoetke et al., 2014, or Lin, 2011 for extensive reviews of different types of opsins and their utilities). However, ChR2 remains the most commonly used excitatory opsin, particularly for interrogation of somatosensation.

The main inhibitory ionotropic opsin is Archerhodopsin-3 (ArchT), which is maximally activated by 530 nm (green) light to allow protons to efflux from the cell, hyperpolarizing the membrane (Han et al., 2011). Halorhodopsin (NpHr) is another commonly used inhibitory opsin, which rather than being an ion channel, functions instead by pumping chloride ions into the cell upon activation with 570 nm (yellow) light (Gradinaru et al., 2008).

To investigate the circuitry of the dorsal horn as well as its function, opsins may be delivered into primary afferent neurons to drive or silence input into the spinal cord, into the brain or brainstem to control descending modulation, or into the spinal cord itself to manipulate the excitability of specific molecularly distinct cellular populations (see **Table 1** for an overview of all known usage of opsins for interrogation of spinal dorsal horn somatosensation). Since different opsins are activated by different wavelengths, this allows for the possibility of bidirectional control of excitability in the same preparation (Iyer et al., 2014; Bonin et al., 2016).

Delivery of Opsins Into Neuronal and Nonneuronal Targets

Through the use of site-specific recombinase technology, opsins can be expressed in subsets of cells by using a specific promoter to selectively express a recombinase such as cre within that subset (Rossant and McMahon, 1999; Nagy, 2000). This technique can be used to drive expression of opsins in a variety of cell types, including neurons, microglia, and astrocytes. However, this does require *a priori* knowledge of the cell type that will be modulated, which is still difficult in the spinal cord where molecularly defined neuronal subtypes are relatively poorly characterized. Recent advances in unbiased molecular screening tools such as single-cell RNA sequencing are beginning to be used to define spinal cord neuronal subtypes and develop atlases of potential target molecular markers for these groupings. This represents a powerful tool for functional characterization, whereby opsins can be expressed within these newly-defined populations to better understand their contributions to dorsal horn circuit function and eventual behavioral output (Abraira et al., 2017; Häring et al., 2018; Sathyamurthy et al., 2018).

Opsins can be delivered into target tissue either through viral transduction or by use of transgenic mouse lines, or through a combination of both technologies (Fenno et al., 2011). Transgenic lines are typically the least invasive method for expression of opsins; however, they are predominantly only available in mice, take time to develop, and are not capable of producing spatially selective expression, save for that given through careful promoter selection (Daou et al., 2013; Liske et al., 2013). Conversely, viral injections can be performed in most animal models and produce spatial selectivity, but do require invasive surgery, and may suffer from sparse expression (Iyer et al., 2014). Along the somatosensory pathways, viral-driven expression of opsins has been achieved with virus injections in the periphery and directly in the sciatic nerve to transduce DRG neurons (Christensen et al., 2016; Wang et al., 2018), by intraperitoneal injection of the virus in neonatal mouse pups to achieve a long-lasting and relatively high degree of DRG transduction (Machida et al., 2013; Vrontou et al., 2013; Bonin et al., 2016; Masuda et al., 2016), by intrathecal injection

(Boada et al., 2014), by direct intraspinal injection after laminectomy (Bonin et al., 2016; Mondello et al., 2018) by using a less invasive non-laminectomy approach (Kohro et al., 2015; Petitjean et al., 2019), by injection in the brain to target sensory regions in the brain (Cardin et al., 2009), or through descending pathways (François et al., 2017; Huang et al., 2019). Other approaches, such as intravenous injection of AAVs, can produce low or highly variable transduction efficiencies of the central and peripheral nervous system (Schuster et al., 2014), making them generally less suitable for the optogenetic study of somatosensation.

Advances in Spinal Cord Optogenetics

Peripheral Stimulation

Optogenetic interrogation of spinal cord circuitry can be achieved by using light delivery at several locations, depending on the circuitry that the experimenter is interested in manipulating (**Figure 2**). Early optogenetic studies began with the insertion of ChR2 into primary afferent neurons, allowing for 488 nm light stimulation of the hind paw to indirectly stimulate circuitry in the spinal cord (Daou et al., 2013). Some of these first sets of experiments targeted ChR2 expression to neurons expressing the sodium channel Nav1.8, which is preferentially found in nociceptive C fiber primary afferent neurons (Agarwal et al., 2004; Daou et al., 2013; Uhelski et al., 2017, but see Shields et al., 2012). Acute stimulation of the hind paw of these animals with 488 nm light led to nocifensive responses such as licking and biting, and enhanced responses to both mechanical and thermal stimuli, suggesting a possible degree of multimodality of these fibers (Daou et al., 2013; Bonin and De Koninck, 2014; Bonin et al., 2016; Daou et al., 2016; DeBerry et al., 2018). Repeated patterned stimulation of the hind paw led to long-lasting mechanical and thermal hyperalgesia, suggestive of potentiation within the spinal cord circuitry. This was further supported by the presence of facilitated dorsal root field potentials after persistent 488 nm light stimulation in a spinal cord explant model (Daou et al., 2013; Bonin and De Koninck, 2014).

A similar technique was used to investigate the effect of activation of two other genetically distinct primary afferent neuron populations on nocifensive behaviors *in vivo*, specifically those that express TrpV1 and those that express MrgD, which are thought to be selectively expressed in peptidergic and nonpeptidergic C fibers, respectively (Zylka et al., 2005; Beaudry et al., 2017). Stimulation of the hind paw with 488 nm light in each of these transgenic mouse lines both resulted in nocifensive responses. However, behaviors were slightly different, suggesting that molecularly distinct populations of C fiber either carry slightly different somatosensory information into the brain or that there is differential processing of information from these fibers within the spinal cord or brain. Conversely, expression of the inhibitory opsin ArchT in primary sensory neurons that express TrpV1 decreases nocifensive responses in a hind paw during 532 nm light stimulation (Li et al., 2015), and activation of eNpHR expressed in C fiber afferents with 570 nm light decreased both thermal and mechanical nocifensive responses, both in naive and nerve-injured animals (Iyer et al., 2014; Bonin et al., 2016).

Expression of ChR2 in the VGLUT3 population of primary afferents, which drives expression within low threshold C fibers, results in 488 nm light-evoked mechanical hypersensitivity in mice with chemotherapy-induced pathological pain but not in naive mice (Seal et al., 2009; Lou et al., 2013; Draxler et al., 2014). This selective pain phenotype adds to evidence that input from these fibers is normally innocuous, and only contributes to nociception in certain pathological pain conditions, possibly through the unmasking of otherwise silent or inhibited synapses within the spinal cord (Li and Zhuo, 1998; Li et al., 1999; Seal et al., 2009; Zhang et al., 2018b). Interestingly, a similar phenomenon was observed when ChR2 was expressed selectively in Thy1+ Aβ fibers, suggesting a similar role (Tashima et al., 2018).

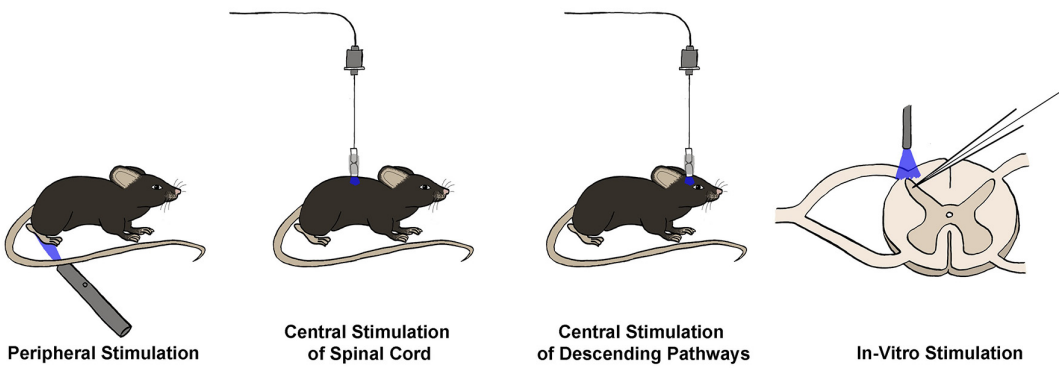

FIGURE 2 | Techniques for optogenetic interrogation of spinal circuitry. Opsins may be stimulated in four main ways to interrogate spinal circuitry. First, opsins can be expressed in primary afferent terminals, and peripheral stimulation can be used to stimulate or silence primary sensory neurons and observe real-time changes in behavioral output *in vivo*. Similarly, opsins can be expressed in neuronal populations within the spinal cord or brain, allowing for *in vivo* central stimulation of either spinal cord neuron populations or neurons involved in descending modulation, respectively. Finally, opsins may be expressed within primary afferents or spinal cord neuron populations, and then stimulation can occur in an *in vitro* slice preparation, often combined with electrophysiological recordings to measure the effect of activation or silencing of a given neuronal population on the excitability of the recorded neuron.

While many of these techniques for peripheral optogenetic stimulation drive opsin expression in molecularly distinct primary sensory neuron populations, some serotypes of AAV have been shown to selectively infect distinct subsets of primary afferent fibers. For example, intrathecal injection of AAV8 encoding ArchT under the ubiquitous CAG promoter was found to selectively induce opsin expression in only Aδ fibers (Boada et al., 2014). Using this technique, Boada et al. (2014) were able to inhibit Aδ fibers *via* activation of ArchT with 532 nm light, which decreased nocifensive responses both in naive animals and after nerve injury, indicating a role for Aδ fibers in both acute and pathological pain conditions. Similarly, Iyer et al. (2014) used an intrasciatic injection of AAV6 encoding ArchT under the CAG promoter to selectively transduce unmyelinated C- fibers, enabling light-induced analgesia.

In summary, peripheral stimulation is the most cost-effective and straightforward method for optogenetic stimulation of spinal cord circuitry and can be accomplished without the need for surgical intervention, depending on the method of opsin expression. Using this technique, the role of different primary afferent populations in various modalities of somatosensation is beginning to be understood and has demonstrated the capacity for light-activated primary afferent stimulation to induce central sensitization within the spinal cord. Unfortunately, peripheral stimulation is primarily suitable for the study of the effect of activation or inactivation of primary sensory afferents on spinal cord functional output in the form of behavioral readouts, and thus central stimulation is required to dissect the circuitry within the spinal cord itself.

Central Stimulation

Over the past decade, vast improvements have been made in the utility of optogenetics for manipulating cellular activity. A major advancement has been the capability to stimulate specific cellular populations *in vivo*, using fibreoptic implants for delivery of fixed wavelength light, typically *via* an LED (Aravanis et al., 2007). Initially, fibreoptic implants for the rodent brain suffered from instability and rigidity, necessitating keeping animals in a sedated state during experiments (Adamantidis et al., 2007; Aravanis et al., 2007; Gradinaru et al., 2007). However, new hardware has allowed for awake, *in vivo* optogenetic stimulation of the brain, giving real-time behavioral output (Lima and Miesenböck, 2005; Aravanis et al., 2007; Montgomery et al., 2015).

Researchers have now adapted this fibreoptic technology for direct central stimulation of the spinal cord. Though an initial technique was to use a fibreoptic implant that threads down from the head to the spinal cord (Bonin et al., 2016), a more commonly used approach utilizes a chronic spinal implant in which a short fibreoptic filament and ferrule are cemented into a burr hole in the T13 or L1 vertebre above the L4/L5 spinal segments (Christensen et al., 2016; Pagani et al., 2019). A fibreoptic cable can then be attached to the ceramic ferrule with a ferrule sleeve for stimulation sessions (**Figure 2**). Using this methodology, one can either directly stimulate primary afferents within the dorsal root ganglia or stimulate spinal cord neurons themselves, with the added benefit of being able to stimulate while the animal is freely moving, which is difficult to achieve with peripheral stimulation.

Central stimulation of primary afferents has been employed by Bonin et al. (2016), who expressed either ArchT or ChR2 in Nav1.8+ primary afferents and delivered light into the spinal cord *via* fiber optic implant. Using this technique, the authors were able to bidirectionally control mechanical nocifensive reflex sensitivity, as measured by Von Frey filaments. Continual excitation of Nav1.8+ afferents led to long-term changes in mechanical sensitivity, measured up to 3 h after stimulation, suggesting the presence of central sensitization.

However, the greatest strength provided by the capability to directly illuminate the spinal cord lies in the capacity to target and either activate or silence specific spinal cord neuronal and glial populations, by expressing opsins in molecularly distinct populations. As technology improves, this will prove to be a very fruitful technique, as many of the newly defined molecularly distinct dorsal horn neuronal populations still have unknown functions in regards to somatosensation in general, and disorders of somatosensation such as pathological pain (Häring et al., 2018). An early study that exemplifies the utility of *in vivo* spinal cord neuron population stimulation using optogenetics found that inhibition of GAD2+ inhibitory spinal cord neurons *via* stimulation of ArchT by 530 nm light produces an immediate increase in mechanical but not thermal sensitivity in otherwise naïve mice (Bonin et al., 2016). This indicates that inhibitory neurons within the spinal cord significantly dampen activation of nociceptive neurons and decrease nociceptive signaling to the brain, giving evidence for how the loss of inhibition could contribute to increased pain sensitivity in pathological pain conditions (Coull et al., 2003, 2005).

A more selective study of interneuron populations found a critical role for the somatostatin positive (SOM+) excitatory neuron population in the circuitry of processing of itch, such that activation of SOM+ neurons *via* ChR2 increased itching behavior *in vivo* (Christensen et al., 2016). Similarly, activation of GRP+ neurons in the spinal cord *via* ChR2 revealed that burst firing within these neurons is required to induce itch-related behaviors *in vivo*, providing evidence that a buildup of GRP neuron activity is required for itch (Pagani et al., 2019).

Finally, a recent study has demonstrated a role for calretinin positive (CR+) neurons in the intersection between innocuous touch perception and nociception. CR+ neurons receive input from multiple sensory afferents responsive to innocuous or noxious stimuli and synapse onto projection neurons within lamina I, providing a direct pathway for elicitation of pain behaviors (Petitjean et al., 2019). Indeed, optogenetic activation of this pathway alone is sufficient to result in mechanical nocifensive responses, without changing thermal sensitivity, suggesting a selective role in mechanical nociception (Petitjean et al., 2019).

It should also be noted that these techniques are not limited to the expression of opsins within neurons, and opsins can also be expressed in nonneuronal cells including astrocytes, for example using the GFAP promoter as done by Nam et al. (2016). By expressing ChR2 in astrocytes in this manner, the authors were able to selectively stimulate spinal astrocytes

in vivo, finding that astrocyte activation *via* ChR2 leads to pain hypersensitivity, demonstrating a clear link between astrocyte activity and behavioral pain output, possibly through activity-dependent ATP release (Bardoni et al., 2010; Nam et al., 2016).

In the above studies, the light was delivered to the spinal cord *via* a fibreoptic wire attached to a light source external to the animal, such that the wire may interfere with an animal's native behavior, through the weight or tension of the wire, or through movement restriction (Daou et al., 2013; Towne et al., 2013; Iyer et al., 2014). Therefore, it is of great interest to develop technologies that allow for wireless optogenetic activation, to allow for truly free moving behavior. Wireless light delivery to the spinal cord is still an early technology with only a few successful examples of central modulation of primary afferent terminals in the dorsal horn (Montgomery et al., 2015; Park et al., 2015; Samineni et al., 2017b). However, wireless approaches are thus far unable to consistently deliver sufficient light intensity to activate opsins expressed in the spinal cord parenchyma beneath the myelin and dorsal root entry zone. Continued development of this technology to improve the efficiency of wireless power delivery over larger distances from the power transmitter array and the incorporation of brighter LEDs that can deliver light to deeper laminae will allow this approach to be more broadly applied to the study of spinal somatosensory processing.

A potential complication of utilizing optogenetic tools that must be considered is that there is a risk of exciting not just a desired target cell population, but also neurons or other cell types within the spinal cord itself that also express the chosen molecular target. For example, there are some TRPV1+ neurons within the spinal cord, that could be stimulated during the central stimulation of TRPV1+ primary afferents (Valtschanoff et al., 2001; Roberts et al., 2004; Cristino et al., 2006). Another possibility is that there may be developmental changes in the expression of proteins, resulting in the opsin being expressed in populations of a neuron that previously expressed the molecular marker of interest during an unknown developmental time point, but do not normally express the molecular marker of interest at adult timepoints (Heffner et al., 2012; Song and Palmiter, 2018). Therefore, care should be used both in choosing a genetic marker for a population and in the interpretation of results (Nimmerjahn and Bergles, 2015; Otchy et al., 2015). Another potential strategy to avoid expression in populations with transient, developmental expression would be to only perform viral transfection in adult animals, or to drive recombination only once adulthood has been reached, such as can be achieved with the CreERT2 tamoxifen-dependent recombination system.

Thus far, the results obtained by both central and peripheral stimulation of primary afferent fibers are largely similar, providing encouraging evidence that the location of optical stimulation does not affect the obtained experimental results, and that these potential complications are minimal (Iyer et al., 2014; Nam et al., 2016; François et al., 2017; Samineni et al., 2017a).

Finally, the delivery of light to the spinal cord at an adequate intensity to activate opsins is a major hurdle of spinal cord optogenetics. Unlike the brain, it is not possible to insert a GRIN lens or other optical material directly into the spinal cord parenchyma without severe damage to the spinal cord that can lead to paralysis. Thus, light must be delivered from above the spinal cord, as seen with a vertebral lens or epidural optic fiber implants (Bonin et al., 2016). Also, the spinal cord contains highly myelinated dorsal white matter that can potently scatter light and greatly reduce intensity beyond depths of approximately 100 μm below the surface of the spinal cord (Sekiguchi et al., 2016). The scattering of light by myelin is much greater with short wavelengths (e.g., 488 nm) than long wavelengths of light (e.g., 594 nm), allowing long wavelengths of light to penetrate deeper into the tissue, providing a potential means to mitigate this issue (Zhang et al., 2008; Lin et al., 2013; Chuong et al., 2014; Inoue et al., 2019). Moreover, the degree of light scattering is twice as great when light is delivered from above the spinal cord and perpendicularly to the longitudinal orientation of myelin tracts than if the light is delivered parallel to the tracts (DePaoli et al., 2020). Another complication to light delivery in the spinal cord is that it is much more mobile than the brain and can move up to 50 μm along the rostral-caudal axis during locomotion in mice (Sekiguchi et al., 2016). This necessitates a larger area of illumination to ensure that the light intensity within the spinal region of interest remains sufficiently high to activate opsins as the region moves through the spot of light. Therefore, the intensity of spinally delivered light required to activate opsins expressed by intrinsic spinal cord neurons is higher than that required to activate opsins expressed by sensory afferents, and much higher than that required for opsin activation *via* proximity GRIN lens implantation in the brain.

An alternative method to investigate spinal cord function *in vivo* using optogenetics is through stimulation of the brainstem or brain to determine the effects of descending modulation on behavioral output. The spinal cord receives a great deal of descending input *via* tracts from many key brain and brainstem areas, including the prefrontal cortex, hypothalamus, amygdala, and periaqueductal gray (PAG; Hopkins and Holstege, 1978; Gebhart, 2004; François et al., 2017; Huang et al., 2019). These inputs converge at the LC and RVM, which synapse directly into the spinal cord (Proudfit and Clark, 1991; D'Mello and Dickenson, 2008; François et al., 2017). Input from the LC and RVM is thought to modulate excitability through both facilitation and inhibition, depending on the neuronal populations involved. To dissect out these roles, opsins can be selectively expressed in the spinally-projecting brainstem or brain neurons. Using this technique, a novel basolateral amygdala—medial prefrontal cortex—PAG—spinal cord pathway has been identified, that when optogenetically activated, inhibits nocifensive behaviors in mice with a pathological pain condition (Huang et al., 2019). Conversely, rostral ventromedial medulla GABAergic interneurons appear to function to increase nocifensive behaviors in mice, with activation of ChR2 increasing nocifensive behaviors, and activation of NpHR decreasing nocifensive behaviors *in vivo* (François et al., 2017).

In vitro Spinal Cord Optogenetics

In addition to observing the effect of stimulation or inhibition of neuronal populations on behavioral output *in vivo*, valuable

information can be gained from combining optogenetic stimulation with the recording of the electrical activity of dorsal horn neurons, either through field or patch-clamp recordings. While a few labs have successfully been able to perform electrophysiology from the spinal cord *in vivo*, albeit under anesthesia (Light and Willcockson, 1999; Sokal and Chapman, 2003; Urch and Dickenson, 2003; Keller et al., 2007), for most practical applications either a semi-intact preparation (Hachisuka et al., 2016), spinal cord explant (Bonin and De Koninck, 2014), or spinal cord slices are used (**Figure 2**; Daou et al., 2013; Christensen et al., 2016; Pagani et al., 2019).

Though the semi-intact and explant preparations allow for dorsal roots to remain intact, in some cases dorsal roots are removed during the preparation of spinal cord slices. However, even with dorsal roots removed, optogenetic excitation of central terminals of primary afferent neurons is sufficient to produce postsynaptic responses in spinal cord neurons (Wang and Zylka, 2009; Foster et al., 2015). For an investigation of primary afferent-evoked responses within the spinal cord, optogenetic stimulation provides the benefit of selectively stimulating a genetically distinct subset of primary afferents, as compared to electrical stimulation (Tashima et al., 2018; Kubota et al., 2019). This provides unparalleled specificity to define circuitry within the spinal cord. For example, Wang and Zylka (2009) expressed ChR2 in MrgD+ primary afferents that are nonpeptidergic multimodal C fiber primary afferents (Rau et al., 2009) and then recorded from a large number of substantia gelatinosa neurons. The authors found that 50% of all recorded substantia gelatinosa neurons receive monosynaptic input from MrgD+ afferents and that all morphologically defined classes of substantia gelatinosa neurons receive these inputs, as evidenced by light-evoked excitatory postsynaptic potentials (EPSCs).

As described earlier, opsins can also be expressed directly within molecularly distinct spinal cord populations, for example within inhibitory VGAT+ or GAD2+ neurons (Foster et al., 2015; Bonin et al., 2016). In a spinal cord slice preparation, this allows for dissection of circuitry through activation or suppression of neuronal populations during patch-clamp electrophysiology, or possibly in combination with calcium imaging. The former technique has been employed to determine the connections from pruritogenic primary afferents to the spinal cord, which synapse onto GRP+ neurons, then on to GRP receptor-containing neurons, and finally onto glutamatergic parabrachial nucleus-projecting neurons (Mu et al., 2017; Pagani et al., 2019), elucidating a full circuit from the periphery to the brain for the flow of itch information. This technique has also been employed in conjunction with *in vivo* optogenetics extensively, to determine presynaptic and postsynaptic connections between populations like CR+ and SOM+ neurons (Daou et al., 2013; Bonin and De Koninck, 2014; Christensen et al., 2016; François et al., 2017; Petitjean et al., 2019).

Overall, these insights are beginning to unravel the complex circuitry of the spinal cord and allow for dissection of the contributions of specific neuronal populations to somatosensory processing, and especially that involved in acute and pathological pain conditions. In the future, it will also be of interest to investigate the intersection between innocuous touch and pain, and how these connections have been hypothesized to be altered in pathological pain conditions.

FLUORESCENCE IMAGING FOR MEASUREMENT OF SPINAL DORSAL HORN NEURONAL AND GLIAL ACTIVITY

Tools for Fluorescence Imaging of Neuronal and Glial Activity

Historically, the only way to measure the activity of individual neurons has been through electrophysiology. However, fluorophores have now been engineered to undergo conformational changes leading to increased fluorescence in the presence of biologically relevant stimuli, such as a change in voltage or calcium concentration. This allows for non-invasive monitoring of relative cellular activity with single-neuron precision; with the additional benefit of the capability to record from up to hundreds of neurons simultaneously. These powerful tools give insight into the activity of ensembles of neurons, to better understand their function within complex circuitry such as the spinal cord.

The most common activity-sensing fluorophores are calcium and voltage indicators, which upon binding of calcium ions or a change in voltage across the membrane, respectively, proportionally increase fluorescence intensity within a set linear dynamic range (Grynkiewicz et al., 1985; Minta et al., 1989; Tsien, 1989; Chanda et al., 2005; Fromherz et al., 2008; Bradley et al., 2009). These fluorophores may either be chemical indicators or genetically-encoded proteins; and the degree of increase in fluorescence intensity upon binding, the wavelength of light required to cause this conformational change, and the sensitivity of fluorophores differs widely, creating a vast toolbox of possible indicators for any desired application (see Grienberger and Konnerth, 2012 for the table of common chemical indicators, see Lin and Schnitzer, 2016 for a table of common genetically-encoded calcium indicators).

It should be noted that fluorophores have also been created for imaging of other molecules relevant to cellular activity, such as the fluorescent chemical indicator MQAE and genetically-encoded protein Chlomeleon for chloride measurement (Arosio and Ratto, 2014), iGluSnFr for fluorescent measurement of glutamate (Marvin et al., 2013, 2018), and Epac-based FRET sensors for cAMP measurement (Ponsioen et al., 2004; Klarenbeek and Jalink, 2014). Additionally, fluorescent false neurotransmitters have been developed to study the release and recycling of neurotransmitters such as dopamine (Gubernator et al., 2009). However, imaging data obtained using these molecules are not as strongly associated with the cellular activity as calcium or voltage imaging and thus will not be discussed further in this review.

The best proxy for electrophysiology currently available is the imaging of voltage-sensitive fluorophores, which are capable of detecting both action potentials and subthreshold changes in voltage (Xu et al., 2017). Unfortunately, most voltage indicators suffer from poor signal-to-noise ratios (SNRs) and require a high intensity of light for stimulation, which is particularly difficult

to overcome in the spinal cord. Part of the necessity for higher intensity light is because voltage indicators are only expressed on the cell membrane, which accounts for only a small portion of the overall volume of a neuron. Newer indicators such as Voltron (Abdelfattah et al., 2019), QuasAR2 (Hochbaum et al., 2014), and ASAP3 (Villette et al., 2019) provide better SNR and show greater promise for use in living tissue. All three of these newer generation voltage indicators have successfully been expressed *in vivo* in the mouse cortex, with ASAP3 and Voltron capable of discerning single action potentials on the millisecond timescale (Lou et al., 2016; Bando et al., 2019). Unfortunately, there has only been one publication performing voltage imaging within the spinal cord, using the voltage-sensitive dye Di-4-ANEPPS, which lacked single-neuron resolution (Mizuno et al., 2019), leaving voltage imaging in the spinal cord an open avenue for innovation. Instead, most researchers use calcium imaging as a proxy to estimate neuronal activity.

Considerations When Using Calcium Imaging as a Proxy for Neuronal Activity

Calcium imaging takes advantage of the large, rapid flow of calcium into neurons as a result of voltage-gated calcium channel (VGCC) opening during action potential firing (Grynkiewicz et al., 1985; Minta et al., 1989; Tsien, 1989; Hahn et al., 1990). Because calcium concentration within neurons rises from the nanomolar to the micromolar range after firing of a single action potential, and because calcium indicators can be expressed within the entire cytosol rather than just on the cellular membrane, calcium imaging has typically provided an intrinsically higher SNR than voltage imaging (Grienberger and Konnerth, 2012; Kulkarni and Miller, 2017). As a result, calcium imaging has become the gold standard for fluorescence imaging of both neuronal and glial activity.

Using calcium imaging as an indirect readout of action potential firing in a neuron requires consideration of several factors regarding the time course of calcium signals. First, the kinetics of calcium concentration changes within a neuron during action potential firing differ widely from the kinetics of the action potential itself. Whereas an action potential occurs on a millisecond time scale—with voltage rapidly depolarizing *via* sodium entry and subsequently hyperpolarizing *via* potassium exodus from the neuron—calcium responses to action potential firing are both much slower to rise and much slower to return to basal concentration after action potential firing (**Figure 3**; Yang and Wang, 2006; Bean, 2007). The rise in calcium is delayed because calcium entry is typically through activation of VGCCs, which will only open once a threshold depolarization has been reached, and which have slower activation kinetics than voltage-gated sodium channels (Carbone and Swandulla, 1989; Bean, 2007). The voltage threshold for activation can vary depending on VGCC subtype, but typically would be near the end of the rising phase of the action potential itself; as is the case for the highly abundant L-type VGCCs, which have an activation threshold around −20 to 0 mV (Catterall, 2011; Striessnig et al., 2014). Slower rise times in intracellular calcium concentration will also be observed depending on the affinity and concentration of the calcium indicator. This is because every calcium indicator is also a calcium buffer, and increased buffering will subsequently increase the duration for molecules of a calcium indicator to bind to all available calcium ions, and reach peak fluorescence (Borst and Abarbanel, 2007; Hires et al., 2008).

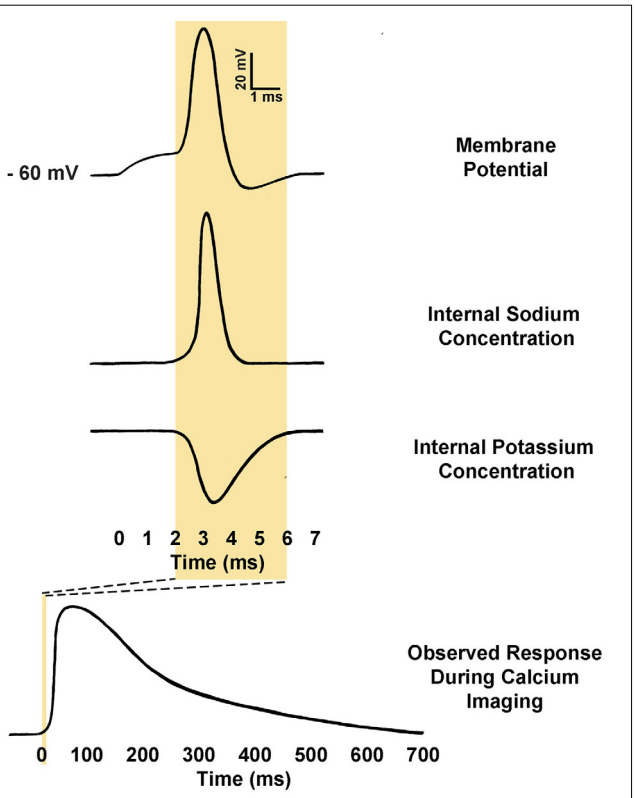

FIGURE 3 | Comparison of action potential kinetics and calcium imaging responses. Calcium indicators are used to measure relative calcium concentration, and this is often used as a proxy for action potential firing. Action potentials consist of an initial depolarization to action potential threshold, which opens voltage-gated sodium channels, causing rapid depolarization of membrane potential. The membrane potential is then rapidly repolarized by the opening of voltage-gated potassium channels. As a result, a typical action potential may only last from 2 to 5 ms. Conversely, observed calcium responses within the somatic cytosol of neurons during action potential firing may require anywhere from 500 to 1000 ms to return to baseline fluorescence (Rahmati et al., 2016). The kinetics of the response is determined in part by the calcium buffering of the neuron itself as well as the affinity and concentration of the calcium indicator present (Borst and Abarbanel, 2007; Hires et al., 2008).

In addition to slower rise times as compared to the native action potential they are reporting on, calcium indicators are also much slower to decay and return to basal calcium concentration. Typically, the calcium response to a single action potential will decay within a neuron over hundreds of milliseconds, or perhaps even seconds with high-affinity indicators (Rahmati et al., 2016). This slow decay time becomes especially problematic with high-frequency firing, where it can become impossible to resolve the peaks of individual action potentials (Smetters et al., 1999). The capacity of a given calcium indicator to accurately report on the number of action potentials fired in the sequence depends on a multitude of factors, including the calcium indicator's

affinity for calcium, the native calcium buffering present within the neuron, and extrusion rates present within that neuronal cell type (Mank and Griesbeck, 2008; Paredes et al., 2008; Tian et al., 2009; Akerboom et al., 2013; Podor et al., 2015). A final technical consideration is the frequency of image collection. For example, if one is measuring action potentials at 100 Hz, the frame sampling rate must at minimum exceed 200 Hz to resolve individual peaks, as per the Nyquist theorem. An inability to resolve individual peaks can also be an issue even at lower firing frequencies if there is a large train of action potentials, as calcium can begin to accumulate quickly within the intracellular space and exceed the linear range of the given calcium indicator (Hires et al., 2008). Thus, one must put careful consideration into the choice of calcium indicator and pick one optimal for their research parameters.

Choosing a Calcium Indicator

Three main considerations determine the type of calcium indicator to employ in an experimental paradigm: the wavelength of activation, the method of delivery into the tissue, and the affinity of the indicator. Indicators activated by blue light still have the best signal to noise ratio (SNR) properties and should be considered first (Dana et al., 2019). However, these indicators may not be possible for certain applications; for example, when combining calcium imaging with optogenetics, a red-shifted calcium indicator would be required to avoid activation of ChR2 during imaging of the calcium-sensitive fluorophore. A red-shifted calcium indicator may also be preferable for imaging at depths below 100 μm, whenever two-photon imaging is not possible, as longer wavelengths are capable of penetrating deeper into tissue (Sanderson et al., 2014).

Next, one must consider the method of delivery of the calcium indicator into tissue (**Figure 4**). Transgenic mouse lines and viral injections of genetically-encoded calcium indicators (GECIs) are becoming increasingly common, especially with the significant advances in the caliber of GECIs in recent years; particularly the GCaMP6 line of GECIs, which have SNRs similar to the best chemical calcium indicators (Chen et al., 2013b). The new jGCaMP7 line promises even better SNR, exceeding the capability of traditional chemical indicators like Fura-2 or OGB-1 (Dana et al., 2019). For red-shifted GECIs, jrGECO1a (Dana et al., 2016) or KGECO1 (Shen et al., 2018) could be employed.

For some applications, chemical calcium indicators may still be preferred. These include experiments involving animals in which transgenic lines are less common or not possible, such as rats or primates, or situations in which a viral injection may not be possible. For these types of experiments, bulk loading of a membrane-permeable AM ester-attached calcium indicator may be employed. In these experiments, the indicator will load into many neurons simultaneously and remain trapped within the neuron for hours afterward upon cleaving of the AM ester by native esterases. One other method that may be employed is single-cell loading *via* a patch pipette, which is often preferred for detailed investigation of dendritic arbor as it provides superior SNR because of reduced background (Helmchen et al., 1999; Grienberger and Konnerth, 2012).

Finally, as described above, the affinity of the chosen indicator will determine the kinetics of the measured calcium response. For experiments where single action potentials need to be resolved, a high-affinity indicator should be used, with the caveat that the decay of the response will be longer. However, for experiments where a train of action potentials need to be resolved—especially with a high-frequency train—a lower affinity indicator should be used to improve the kinetics of the response, and for the indicator to be performing within its linear dynamic range for the duration of the stimulus (Pologruto et al., 2004; Hollingworth et al., 2009).

Advances in Spinal Cord Fluorescence Imaging of Activity

Calcium Imaging of Spinal Cord Neurons *in vitro*

Calcium imaging has thus far not been employed as widely within the spinal dorsal horn as in the brain, largely because of technical limitations that have hindered its utility. This is especially true for *in vivo* studies, of which only a handful have been conducted in the spinal cord. One of the first calcium imaging experiments used epifluorescence microscopy to show that overall basal calcium indicator fluorescence was higher on the ipsilateral side of a transverse spinal cord slice from an animal with the chronic constriction injury model of pathological pain, suggestive of either increased resting calcium concentration or increased neuronal activity in the absence of external stimulation within the ipsilateral dorsal horn (Kawamata and Omote, 1996). Using a similar technique, it was also found that the calcium response to dorsal root stimulation on the superficial dorsal horn ipsilateral to nerve injury was larger, indicative of increased neuronal activity for the same stimulation, mirroring the hyperalgesia present in pathological pain conditions (Luo et al., 2008).

Since these first studies, improvements both in calcium indicators and in microscope technology now allow for single neuron and single event resolution. This provides the capacity to use calcium imaging for the measurement of discrete calcium signals within dorsal horn neurons, such as those due to action potential firing, and neuronal responses to an applied stimulus like capsaicin (Merighi et al., 2008), or electrical stimulation (Kim et al., 2015; see **Table 2** for a full list of all known applications of calcium imaging within the spinal dorsal horn).

Calcium imaging can also be used to investigate the relative function of calcium-permeable ion channels, including calcium-permeable AMPA receptors, NMDA receptors, and VGCCs within the spinal dorsal horn, especially concerning the spatial distribution of calcium. Recent investigations have utilized calcium imaging to study how calcium enters into neurons during activity. Using a bulk-loaded calcium indicator and high-resolution epifluorescence imaging, Doolen et al. (2012) were able to measure spontaneous action potentials as calcium responses in single dorsal horn neurons. They subsequently developed a technique to use calcium imaging to quantify relative glutamate receptor function by measuring glutamate-evoked calcium events in single superficial dorsal horn neurons from transverse slices. Using this technique, they found that calcium events to the same glutamate stimulus were larger on the side ipsilateral to nerve injury, indicative of either upregulation of

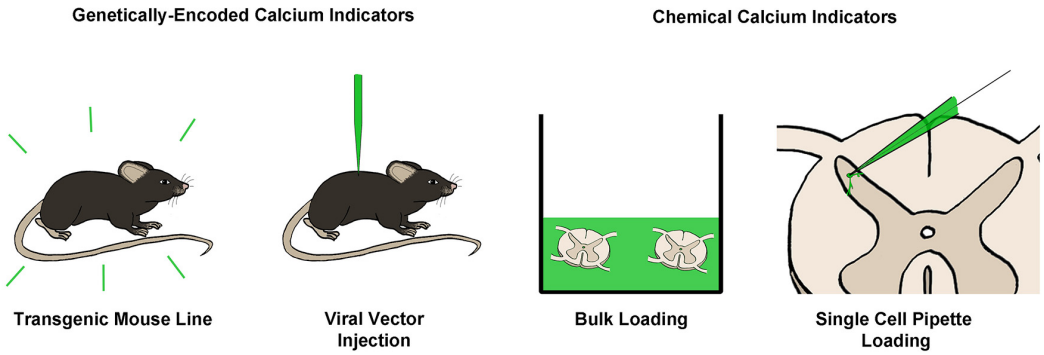

FIGURE 4 | Common techniques for loading of calcium indicators. Calcium indicators can broadly be categorized into genetically-encoded (GECIs) or chemical calcium indicators. GECIs can be introduced *via* transgenic mouse lines or through the injection of a viral vector containing a GECI into the target tissue. Chemical calcium indicators can be introduced in several ways, however, the most common is through bulk loading with an AM-ester bound indicator, or *via* single-cell pipette loading. Both of these techniques can be performed *in vitro* or *in vivo*.

glutamate receptor density or an increase in glutamate receptor conductance. Later, they found that these calcium events could be further boosted in a pain model by blocking opioid receptors (Corder et al., 2013). A similar study by Skorput et al. (2018) found that glutamate-evoked calcium responses in superficial dorsal horn neurons were significantly higher upon application of a peptide derived from VGF nerve growth factor, indicating that VGF is capable of potentiating glutamatergic signaling in the spinal cord.

In addition to measuring the activity of calcium-permeable glutamate receptors, calcium imaging has also been used to define relative contributions of VGCC subtypes to activity-evoked calcium responses. The first study to investigate this introduced the calcium indicator Fura-2 into spinal cord lamina I neurons *via* a patch pipette and measured calcium responses within the soma in response to current injection-evoked 40 Hz action potential firing (Ikeda et al., 2003). However, the authors were not able to identify discrete intracellular action potential-induced calcium responses due to the firing frequency and properties of Fura-2, which has a high calcium-binding affinity and reaches saturation below a calcium concentration of 1 μM (Paredes et al., 2008). Rather, it was observed that the total calcium response to the stimulation protocol was larger in projection neurons, largely due to the expression of additional T-type VGCC channels in these neurons that enhanced depolarization and increased total calcium influx component. This finding was then expanded to determine the relative contributions of various VGCCs to the somatic calcium response induced by the burst of action potentials. In unlabeled lamina-I neurons, of which the majority are likely interneurons, the major contributor to this calcium response was L-type VGCCs with significant T-type and N-type contributions (Heinke et al., 2004).

A key strength of calcium imaging is the ability to investigate the spatial dynamics of calcium with subcellular resolution. Within the brain, calcium imaging has been extensively used to investigate postsynaptic calcium entry (Harvey et al., 2008; Lee et al., 2009; Zito et al., 2009), dendritic calcium signaling (Spruston et al., 1995; Gulledge et al., 2005; Larkum et al., 2009; Harnett et al., 2012), and nuclear calcium dynamics (Eder and Bading, 2007; Bengtson and Bading, 2012) using two-photon calcium imaging. In superficial dorsal horn neurons, calcium imaging has been used to observe calcium entering into the nuclei of neurons during repetitive primary afferent stimulation (Simonetti et al., 2013). Inhibiting nuclear calcium signaling through the expression of CaMBP4, which binds calcium-bound calmodulin and thereby prevents calmodulin-dependent downstream signaling cascades, significantly reduced hypersensitivity in mice exposed to a Complete Freund's Adjuvant model of chronic inflammatory pain, suggesting that the development of pathological pain requires calcium to enter into the nucleus to initiate downstream signaling cascades. Thus far, there have been no other studies investigating the subcellular calcium dynamics of dorsal horn spinal cord neurons, and this represents an open field of study.

Together, these studies demonstrate the utility of calcium imaging for more than measuring neuronal activity, but also for the visualization and measurement of calcium itself within cells, including both neurons and glia. As demonstrated above, subcellular calcium imaging can provide important information on calcium's role as a critical second messenger for initiating downstream signaling cascades that lead to changes in protein expression and cellular function. Another emerging opportunity involves combining optogenetics to drive specific neuronal populations with calcium imaging to monitor resultant cellular activity within the spinal cord. This combination would be especially helpful when measuring population ensemble activity (Ruscheweyh and Sandkuhler, 2005), or when animals are freely moving and electrophysiological recordings would not be possible.

Challenges to Achieving Freely Behaving *in vivo* Calcium Imaging in the Spinal Cord

Effective calcium imaging requires precise spatial and temporal resolution, which can be difficult to achieve *in vivo* in the spinal

TABLE 1 | Summary of all publications utilizing optogenetics for interrogation of spinal cord somatosensory circuitry.

		Optical stimulation method			
		In vitro	**Peripheral**	**Central stimulation of spinal cord**	**Central stimulation of descending pathways**
Method of opsin expression in tissue	Transgenic	• Wang and Zylka (2009) • Foster et al. (2015) • Honsek et al. (2015) • Hachisuka et al. (2016) • Bellardita et al. (2017) • Uhelski et al. (2017) • Pagani et al. (2019) • Smith-Edwards et al. (2019) • Hachisuka et al. (2020)	• Ji et al. (2012) • Daou et al. (2013) • Bonin and De Koninck (2014) • Draxler et al. (2014) • Bonin et al. (2016) • Christensen et al. (2016) • Daou et al. (2016) • Stemkowski et al. (2016) • Beaudry et al. (2017) • Ghitani et al. (2017) • Samineni et al. (2017a) • Sun et al. (2017) • DeBerry et al. (2018) • Tashima et al. (2018)	• Bonin and De Koninck (2014) • Montgomery et al. (2015) • Park et al. (2015) • Bonin et al. (2016) • Bellardita et al. (2017) • Lu et al. (2017) • Samineni et al. (2017b) • Chen et al. (2018) • Pagani et al. (2019) • Petitjean et al. (2019)	• Chen et al. (2018)
	Viral vector	• Boada et al. (2014) • Yang et al. (2015) • Christensen et al. (2016) • Hachisuka et al. (2016)	• Boada et al. (2014) • Iyer et al. (2014) • Li et al. (2015) • Barik et al. (2018) • Mayer et al. (2019)	• Iyer et al. (2014) • Montgomery et al. (2015) • Bonin et al. (2016) • Christensen et al. (2016) • Nam et al. (2016) • François et al. (2017) • Mu et al. (2017) • Chen et al. (2018) • Mondello et al. (2018) • Wang et al. (2018)	• François et al. (2017) • Gao et al. (2019) • Huang et al. (2019)

This table combines all examples of optogenetic interrogation in the dorsal horn on the spinal cord, grouped by the site of stimulation and by the method of opsin delivery.

cord, and considerably more difficult to achieve in a freely moving animal. Several attempts to achieve this goal have utilized miniscope or endoscope systems (Johannssen and Helmchen, 2010; Sekiguchi et al., 2016). These types of systems allow for free movement in the mouse, restricted only by a cable leading to a computer, and the connected miniscope or endoscope itself, which often weighs only a few grams (Yang and Yuste, 2017; Zhang et al., 2018b). However, this type of system suffers from lack of tissue penetration and decreased resolution as compared to imaging under a two-photon microscope. This resolution is likely not sufficient for the monitoring of subcellular events, and in the case of endoscope systems, is often insufficient to differentiate and record from individual neurons. Additionally, as described earlier, light scattering in the spinal cord due to myelination can prevent epifluorescent and single-photon imaging from detecting fluorescent cell bodies deeper than the outer part of lamina II (Sekiguchi et al., 2016), making two-photon imaging a necessity for investigating deeper laminae. Two-photon microscopy also benefits from superior spatial resolution, reduced phototoxicity, and can be used to achieve subcellular resolution of calcium dynamics (Dana et al., 2019).

Unfortunately, with greater spatial resolution comes the need for stability in the imaging field. Therefore, with current technology, almost all *in vivo* two-photon calcium imaging in the brain has been performed on head-fixed animals (Chen et al., 2013a; Leinweber et al., 2014; Yang and Yuste, 2017; but see Helmchen et al., 2013 and Zong et al., 2017). Translating these techniques to the spinal cord has been met with middling success, partially because it is significantly more difficult to fix the spinal cord in place for imaging, with breathing and movement producing significant imaging artifacts that are difficult to compensate for while allowing for enough spinal flexibility for free movement.

This fine yet necessary balance of movement and fixation that must be achieved for *in vivo* two-photon calcium imaging represents such an obstacle that only one research group has thus far successfully achieved this, by placing a mouse mounted on a spherical treadmill under a two-photon microscope (Sekiguchi et al., 2016). For this study, the authors tested several methods of head and vertebral restraint to optimize imaging conditions, finding that a dual head and vertebral restraint provided a maximum reduction in motion artifacts while maintaining locomotor activity, and demonstrating the feasibility of the technique.

The authors then performed two-photon imaging of axonal arbor, as well as calcium imaging of astrocytic processes, and importantly found that pinch-evoked astrocytic calcium responses were depressed under anesthesia (Sekiguchi et al., 2016). This finding provides crucial evidence that within the spinal cord, there is a necessity for further refining techniques to allow for two-photon imaging that does not require anesthesia. The potential impact of anesthesia is of special interest in the context of another recent study that expressed GCaMP6m in spinal cord astrocytes using a viral vector injection

TABLE 2 | Summary of all publications utilizing calcium imaging for interrogation of spinal cord somatosensory circuitry.

		Imaging method		
		Epifluorescence	**1-photon**	**2-photon**
Method of delivery of the calcium-sensitive indicator	Transgenic	• Bellardita et al. (2017)	• Sun et al. (2017)	• Tang et al. (2015)* • Zhang et al. (2018a)* • Olivares-Moreno et al. (2019)
	Viral Vector	• Simonetti et al. (2013) • Aresh et al. (2017) • Freitag et al. (2019)	• Nishida et al., 2014* • Sekiguchi et al., 2016*	• Yoshihara et al. (2018)* • Sekiguchi et al. (2016)* • Chen et al. (2018)*
	Bulk Loading	• Kyrozis et al. (1995) • Kawamata and Omote (1996) • Coull et al. (2003) • Tsuzuki et al. (2004) • Cordero-Erausquin et al. (2005) • Coull et al. (2005) • Ruscheweyh and Sandkuhler (2005) • Shutov et al. (2006) • Luo et al. (2008) • Schoffnegger et al. (2008) • Miyano et al. (2010) • Flynn et al. (2011) • Doolen et al. (2012) • Corder et al. (2013) • Petitjean et al. (2014) • Baba et al. (2016) • Gao et al. (2016) • Doolen et al. (2017) • Potter et al. (2018) • Skorput et al. (2018) • Taylor et al. (2019)	• Gustafson-Vickers et al. (2008) • Merighi et al. (2008) • Bardoni et al. (2010) • Lu et al. (2018)	• Wilson et al. (2007) • Johannssen and Helmchen (2010)* • Laffray et al. (2011) • Cirillo et al. (2012)* • Cirillo et al. (2015)* • Ran et al. (2016)* • Skorput et al. (2018)
	Single Cell Pipette Loading	• Isaev et al. (2000) • Ikeda et al. (2003) • Heinke et al. (2004) • Kopach et al. (2011) • Yan et al. (2014) • Kim et al. (2015) • Yan et al. (2019)	• Drdla et al. (2009)*	• Ikeda et al. (2006)* • Drdla et al. (2009)

*This table amalgamates all examples of calcium imaging in the spinal dorsal horn, with references grouped by imaging technique and by the method of delivery of the calcium-sensitive indicator. *Beside a citation indicates that some or all of the experiments were performed in vivo.*

and performed *in vivo* two-photon calcium imaging under anesthesia. Here, the authors found no astrocytic calcium responses to pinch or brush in naive animals but surprisingly found astrocytic calcium responses to these innocuous stimuli after animals received a formalin injection (Yoshihara et al., 2018). It is therefore, possible that these findings could be even more pronounced in awake animals.

Additionally, through the implantation of a spinal imaging chamber attached to a miniscope, it has been found that anesthesia decreases spontaneous calcium events in superficial dorsal horn neurons from 0.52 Hz to 0.08 Hz, representing a marked depression in circuit activity (Sekiguchi et al., 2016). This calcium event rate measured using calcium imaging is remarkably close to the average action potential firing rate measured using *in vivo* extracellular single-unit recordings of superficial dorsal horn neurons under anesthesia (0.05 Hz; Keller et al., 2007), and provides further support that a system of activity measurement not requiring anesthesia represents a fundamental advance for decoding and understanding the circuitry of the spinal cord.

However, due to the many difficulties outlined above, the majority of *in vivo* two-photon imaging experiments in the spinal cord have thus far been performed under anesthesia (Ikeda et al., 2006; Davalos et al., 2008; Drdla et al., 2009; Laffray et al., 2011; Cirillo et al., 2012; Farrar et al., 2012; Fenrich et al., 2013; Nishida et al., 2014; Cirillo et al., 2015; Ran et al., 2016; Chen et al., 2018; Wang et al., 2018). Several early studies focused on technique development to determine the best approaches for exposing spinal cord tissue to the microscope and for limiting breathing artifacts. One of the first such studies expressed fluorescent molecules in the axons, microglia, and blood vessels of mouse spinal cord to monitor structural changes over time, and developed a spinal stabilization device that provided a high degree of stability for imaging (Davalos et al., 2008). This method was utilized to perform the first two-photon *in vivo* calcium imaging within the superficial dorsal horn in which OGB-1 AM was injected into the dorsal horn and bulk loaded into superficial dorsal horn cells (Johannssen and Helmchen, 2010). In this study, the authors found many cells to have spontaneous calcium responses, as well as evoked

calcium responses to electrical and mechanical stimulation of the hind paw.

In vivo two-photon calcium imaging has also been used to monitor long-term potentiation (LTP) in superficial dorsal horn neurons, using calcium responses as a proxy for neuronal activity. Interestingly, the authors found that calcium responses were slower to rise and fall in PAG-projecting spinal cord neurons, as opposed to PBN-projecting neurons, and that this slower, longer calcium response was correlated with a greater degree of LTP in that neuron (Ikeda et al., 2006).

Unfortunately, all of these studies required a head-support, spinal column, and tail-clamping, as well as deep anesthesia. As a result, these imaging sessions were terminal and precluded long term imaging of cellular changes accompanying chronification of hyperalgesia. Newer techniques have been developed in which a glass chronic spinal imaging window is implanted, which allows for chronic imaging at multiple time points over the course of months (Farrar et al., 2012; Fenrich et al., 2013; Chen et al., 2018). An added benefit of a chronic spinal imaging window is that after implantation, and at later time points, the inflammatory response is minimal, giving better insight into the native function of the spinal cord (Fenrich et al., 2013).

Three recent studies have investigated *in vivo* dorsal horn neuron calcium responses to several different modalities of hind paw stimuli, including pinch, brush, cold, and heat (Nishida et al., 2014; Ran et al., 2016; Chen et al., 2018). These studies have found significant overlap in the modalities that can activate individual neurons, as well as grading in both the percentage of neurons active and the amplitude of the ultimate measured calcium response. Notably, one study found that stimulating the anterior cingulate cortex resulted in potentiation of the calcium response in over 50% of pinch-responding neurons in the dorsal horn, indicating rapid descending modulation of spinal cord neuron excitability (Chen et al., 2018). These initial results will be incredibly interesting to investigate further through combination with optogenetic stimulation, or with the labeling of genetically distinct neuronal populations, to begin to delineate which spinal cord cell types contribute to the processing of different sensory modalities.

Although not strictly within the spinal cord, two complementary studies to the ones above were recently performed for primary afferent neuron cell bodies within the dorsal root ganglia (DRG), measuring *in vivo* calcium responses in DRG cell bodies to various stimuli (Chisholm et al., 2018; Wang et al., 2018). In these studies, GCaMP6 was introduced into DRG cell bodies through injection of the AAV9 or AAV8 viral vectors, respectively, under a general CAG promoter. Various thermal and mechanical stimuli were presented to the hind paw while the mice were under anesthesia and spinal restraint. By studying the responses of a large population of cells to multiple stimuli, both studies concluded that many primary afferent neurons were polymodal, responding both to thermal and noxious mechanical stimulation. Wang et al. additionally found that heat and cold are differentially encoded by DRG activity, such that increasing heat produced a graded response in a subset of heat-sensitive neurons, while increasingly cold temperatures activate distinct subsets of cells to reveal a population level encoding. In the future, it is hopeful that these types of study will also be performed within the spinal cord, and without the necessity for anesthesia.

In summary, fluorescence imaging is a powerful tool for the monitoring of cellular activity. Although several considerations must be taken into account to most effectively employ this technology, imaging remains an ideal way to monitor the activity of hundreds of neurons or glial cells simultaneously at the overall network level or in genetically defined subpopulations, providing invaluable information about neuronal circuitry and function. Calcium imaging can effectively be adapted for a wide variety of paradigms, owing to the multitude of ways that calcium indicators can be introduced into cells, and the many experimental paradigms in which it can be employed; ranging from single-cell patch pipette loading to two-photon *in vivo* imaging of genetically-encoded calcium indicators. While there are fewer examples of imaging with voltage-sensitive indicators, likely owing to the relatively new development of indicators with sufficient SNR for use in tissue, advances in imaging technology and novel voltage indicator development have paved the way for wider use of this imaging modality.

SUMMARY AND OUTLOOK

Optical approaches allow for less invasive and highly selective manipulation and measurement of cellular activity. Given the complexity of the circuitry involved in the processing of somatosensory information, these tools promise to aid in unraveling how somatosensory information is encoded and integrated within the spinal cord, and how these processes change in conditions such as pathological pain.

Optogenetic tools such as ChR2 and ArchT have been effectively utilized to rapidly and non-invasively activate and inactivate specific neuronal populations, respectively. Molecular genetic approaches have allowed for directed, tissue-specific opsin expression with the cre-lox system, and surgical advances have paved the way for precise, stereotaxic injections for virally-mediated transduction. The ability to transgenically or virally introduce both excitatory and inhibitory opsins to the same population of neurons has opened new possibilities to study the role of discrete spinal cord neuronal populations with remarkable resolution. Using these techniques, optogenetics has been used in a multitude of studies, from defining the contributions of various distinct primary afferent fibers in somatosensation to single-neuron interrogation of spinal dorsal horn circuitry.

As the gold standard for fluorescence imaging of cellular activity, calcium imaging provides the capacity to detect discrete events within single cells, while simultaneously recording from ensembles of neurons in the spinal cord. This is especially powerful when utilizing genetically-encoded calcium indicators that can be driven to molecularly distinct populations of neurons or glia, and can be used to answer many outstanding questions in the field, including the possibility of neuronal synchrony, and how activity in populations of spinal cord neurons and glia determine freely moving behaviors in real-time.

Given the high diversity of calcium indicators, we have presented three major considerations in choosing a calcium indicator: the desired activation wavelength, tissue delivery technique, and indicator affinity. By considering these variables, calcium imaging experiments can be utilized optimally within the spinal cord. Technological advances in both calcium indicators and microscopy now allow for single-cell, and subcellular resolution with an *in vivo* approach, but major challenges concerning microscope stability and anesthetic conditions remain. Nonetheless, the utility of calcium imaging as a measure of cellular activity, and the relative degree of non-invasiveness compared to electrophysiology, makes this technique invaluable for elucidating spinal cord circuitry function at both single-cell and network-level resolution.

The determination of brain circuitry in behavior is moving towards all-optical interrogation, which combines the comprehensive readout of cellular activity *via* calcium imaging with the spatial and temporal precision of neuronal activation *via* optogenetics. While the technical difficulties are substantial, and especially so within the spinal cord, this approach could provide the opportunity to define somatosensory circuitry with unprecedented detail. Through combining expression of blue-shifted and red-shifted indicators and opsins, such as the combination of ChR2 with jrGECO1a or Chrimson with GCaMP7, experimenters will be able to activate or silence one population of cells at one wavelength and measure the changes in the activity of another population, all *in vivo*, allowing for simultaneous readout of behavior (Rickgauer et al., 2014; Packer et al., 2015; Stamatakis et al., 2018; Zhang et al., 2018c). Together, these tools provide the future possibility for closed-loop interrogation of spinal cord circuitry and function *in vivo*, to understand how somatosensory information is processed in this incredibly complex network.

AUTHOR CONTRIBUTIONS

All authors planned the structure of the manuscript. All authors wrote and edited the manuscript.

FUNDING

This work was supported by a Brain and Behavior Foundation NARSAD Young Investigator Grant and a Natural Sciences and Engineering Research Council of Canada (NSERC) grant (RGPIN-2016-05538) to RB.

REFERENCES

Abdelfattah, A. S., Kawashima, T., Singh, A., Novak, O., Liu, H., Shuai, Y., et al. (2019). Bright and photostable chemigenetic indicators for extended *in vivo* voltage imaging. *Science* 365, 699–704. doi: 10.1126/science.aav6416

Abraira, V. E., Kuehn, E. D., Chirila, A. M., Springel, M. W., Toliver, A. A., Zimmerman, A. L., et al. (2017). The cellular and synaptic architecture of the mechanosensory dorsal horn. *Cell* 168, 295.e19–310.e19. doi: 10.1016/j.cell.2016.12.010

Adamantidis, A. R., Zhang, F., Aravanis, A. M., Deisseroth, K., and de Lecea, L. (2007). Neural substrates of awakening probed with optogenetic control of hypocretin neurons. *Nature* 450, 420–424. doi: 10.1038/nature06310

Agarwal, N., Offermanns, S., and Kuner, R. (2004). Conditional gene deletion in primary nociceptive neurons of trigeminal ganglia and dorsal root ganglia. *Genesis* 38, 122–129. doi: 10.1002/gene.20010

Akerboom, J., Carreras Calderon, N., Tian, L., Wabnig, S., Prigge, M., Tolo, J., et al. (2013). Genetically encoded calcium indicators for multi-color neural activity imaging and combination with optogenetics. *Front. Mol. Neurosci.* 6:2. doi: 10.3389/fnmol.2013.00002

Aravanis, A. M., Wang, L. P., Zhang, F., Meltzer, L. A., Mogri, M. Z., Schneider, M. B., et al. (2007). An optical neural interface: *in vivo* control of rodent motor cortex with integrated fiberoptic and optogenetic technology. *J. Neural Eng.* 4, S143–S156. doi: 10.1088/1741-2560/4/3/s02

Arcourt, A., Gorham, L., Dhandapani, R., Prato, V., Taberner, F. J., Wende, H., et al. (2017). Touch receptor-derived sensory information alleviates acute pain signaling and fine-tunes nociceptive reflex coordination. *Neuron* 93, 179–193. doi: 10.1016/j.neuron.2016.11.027

Aresh, B., Freitag, F. B., Perry, S., Blümel, E., Lau, J., Franck, M. C. M., et al. (2017). Spinal cord interneurons expressing the gastrin-releasing peptide receptor convey itch through vglut2-mediated signaling. *Pain* 158, 945–961. doi: 10.1097/j.pain.0000000000000861

Arosio, D., and Ratto, G. M. (2014). Twenty years of fluorescence imaging of intracellular chloride. *Front. Cell. Neurosci.* 8:258. doi: 10.3389/fncel.2014.00258

Baba, H., Petrenko, A. B., and Fujiwara, N. (2016). Clinically relevant concentration of pregabalin has no acute inhibitory effect on excitation of dorsal horn neurons under normal or neuropathic pain conditions: an intracellular calcium-imaging study in spinal cord slices from adult rats. *Brain Res.* 1648, 445–458. doi: 10.1016/j.brainres.2016.08.018

Bando, Y., Sakamoto, M., Kim, S., Ayzenshtat, I., and Yuste, R. (2019). Comparative evaluation of genetically encoded voltage indicators. *Cell Rep.* 26, 802.e4–813.e4. doi: 10.1016/j.celrep.2018.12.088

Banghart, M., Borges, K., Isacoff, E., Trauner, D., and Kramer, R. H. (2004). Light-activated ion channels for remote control of neuronal firing. *Nat. Neurosci.* 7, 1381–1386. doi: 10.1038/nn1356

Bardoni, R., Ghirri, A., Zonta, M., Betelli, C., Vitale, G., Ruggieri, V., et al. (2010). Glutamate-mediated astrocyte-to-neuron signalling in the rat dorsal horn. *J. Physiol.* 588, 831–846. doi: 10.1113/jphysiol.2009.180570

Barik, A., Thompson, J. H., Seltzer, M., Ghitani, N., and Chesler, A. T. (2018). A brainstem-spinal circuit controlling nocifensive behavior. *Neuron* 100, 1491.e3–1503.e3. doi: 10.1016/j.neuron.2018.10.037

Basbaum, A., Bautista, D., Scherrer, G., and Julius, D. (2009). Cellular and molecular mechanisms of pain. *Cell* 139, 267–284. doi: 10.1016/j.cell.2009.09.028

Bean, B. P. (2007). The action potential in mammalian central neurons. *Nat. Rev. Neurosci.* 8, 451–465. doi: 10.1038/nrn2148

Beaudry, H., Daou, I., Ase, A. R., Ribeiro-da-Silva, A., and Séguéla, P. (2017). Distinct behavioral responses evoked by selective optogenetic stimulation of the major TRPV1^{+} and MrgD^{+} subsets of C-fibers. *Pain* 158, 2329–2339. doi: 10.1097/j.pain.0000000000001016

Bellardita, C., Caggiano, V., Leiras, R., Caldeira, V., Fuchs, A., Bouvier, J., et al. (2017). Spatiotemporal correlation of spinal network dynamics underlying spasms in chronic spinalized mice. *Elife* 6:e23011. doi: 10.7554/eLife.23011

Bengtson, C. P., and Bading, H. (2012). Nuclear calcium signaling. *Adv. Exp. Med. Biol.* 970, 377–405. doi: 10.1007/978-3-7091-0932-8_17

Boada, M. D., Martin, T. J., Peters, C. M., Hayashida, K., Harris, M. H., Houle, T. T., et al. (2014). Fast-conducting mechanoreceptors contribute to withdrawal behavior in normal and nerve injured rats. *Pain* 155, 2646–2655. doi: 10.1016/j.pain.2014.09.030

Bonin, R. P., and De Koninck, Y. (2014). A spinal analog of memory reconsolidation enables reversal of hyperalgesia. *Nat. Neurosci.* 17, 1043–1045. doi: 10.1038/nn.3758

Bonin, R. P., Wang, F., Desrochers-Couture, M., Ga Secka, A., Boulanger, M. E., Cote, D. C., et al. (2016). Epidural optogenetics for controlled analgesia. *Mol. Pain* 12:1744806916629051. doi: 10.1177/1744806916629051

Borst, A., and Abarbanel, H. D. (2007). Relating a calcium indicator signal to the unperturbed calcium concentration time-course. *Theor. Biol. Med. Model.* 4:7. doi: 10.1186/1742-4682-4-7

Bourane, S., Duan, B., Koch, S. C., Dalet, A., Britz, O., Garcia-Campmany, L., et al. (2015). Gate control of mechanical itch by a subpopulation of spinal cord interneurons. *Science* 350, 550–554. doi: 10.1126/science.aac8653

Boyden, E. S., Zhang, F., Bamberg, E., Nagel, G., and Deisseroth, K. (2005). Millisecond-timescale, genetically targeted optical control of neural activity. *Nat. Neurosci.* 8, 1263–1268. doi: 10.1038/nn1525

Boyle, K. A., Gutierrez-Mecinas, M., Polgár, E., Mooney, N., O'Connor, E., Furuta, T., et al. (2017). A quantitative study of neurochemically defined populations of inhibitory interneurons in the superficial dorsal horn of the mouse spinal cord. *Neuroscience* 363, 120–133. doi: 10.1016/j.neuroscience.2017.08.044

Bradley, J., Luo, R., Otis, T. S., and DiGregorio, D. A. (2009). Submillisecond optical reporting of membrane potential *in situ* using a neuronal tracer dye. *J. Neurosci.* 29, 9197–9209. doi: 10.1523/jneurosci.1240-09.2009

Carbone, E., and Swandulla, D. (1989). Neuronal calcium channels: kinetics, blockade and modulation. *Prog. Biophys. Mol. Biol.* 54, 31–58. doi: 10.1016/0079-6107(89)90008-4

Cardin, J. A., Carlen, M., Meletis, K., Knoblich, U., Zhang, F., Deisseroth, K., et al. (2009). Driving fast-spiking cells induces gamma rhythm and controls sensory responses. *Nature* 459, 663–667. doi: 10.1038/nature08002

Catterall, W. (2011). Voltage-gated calcium channels. *Cold Spring Harb. Perspect. Biol.* 3:a003947. doi: 10.1101/cshperspect.a003947

Chanda, B., Blunck, R., Faria, L. C., Schweizer, F. E., Mody, I., and Bezanilla, F. (2005). A hybrid approach to measuring electrical activity in genetically specified neurons. *Nat. Neurosci.* 8, 1619–1626. doi: 10.1038/nn1558

Chen, J. L., Andermann, M. L., Keck, T., Xu, N. L., and Ziv, Y. (2013a). Imaging neuronal populations in behaving rodents: paradigms for studying neural circuits underlying behavior in the mammalian cortex. *J. Neurosci.* 33, 17631–17640. doi: 10.1523/jneurosci.3255-13.2013

Chen, T., Taniguchi, W., Chen, Q. Y., Tozaki-Saitoh, H., Song, Q., Liu, R. H., et al. (2018). Top-down descending facilitation of spinal sensory excitatory transmission from the anterior cingulate cortex. *Nat. Commun.* 9:1886. doi: 10.1038/s41467-018-04309-2

Chen, T., Wardill, T., Sun, Y., Pulver, S., Renninger, S., Baohan, A., et al. (2013b). Ultrasensitive fluorescent proteins for imaging neuronal activity. *Nature* 498, 295–300. doi: 10.1038/nature12354

Cheng, L., Duan, B., Huang, T., Zhang, Y., Chen, Y., Britz, O., et al. (2017). Identification of spinal circuits involved in touch-evoked dynamic mechanical pain. *Nat. Neurosci.* 20, 804–814. doi: 10.1038/nn.4549

Chisholm, K. I., Khovanov, N., Lopes, D. M., La Russa, F., and McMahon, S. B. (2018). Large scale *in vivo* recording of sensory neuron activity with gcamp6. *eNeuro* 5:ENEURO.0417-17.2018. doi: 10.1523/eneuro.0417-17.2018

Christensen, A. J., Iyer, S. M., Francois, A., Vyas, S., Ramakrishnan, C., Vesuna, S., et al. (2016). *In vivo* interrogation of spinal mechanosensory circuits. *Cell Rep.* 17, 1699–1710. doi: 10.1016/j.celrep.2016.10.010

Chuong, A. S., Miri, M. L., Busskamp, V., Matthews, G. A., Acker, L. C., Sorensen, A. T., et al. (2014). Noninvasive optical inhibition with a red-shifted microbial rhodopsin. *Nat. Neurosci.* 17, 1123–1129. doi: 10.1038/nn.3752

Cirillo, G., Colangelo, A. M., Berbenni, M., Ippolito, V. M., De Luca, C., Verdesca, F., et al. (2015). Purinergic modulation of spinal neuroglial maladaptive plasticity following peripheral nerve injury. *Mol. Neurobiol.* 52, 1440–1457. doi: 10.1007/s12035-014-8943-y

Cirillo, G., De Luca, D., and Papa, M. (2012). Calcium imaging of living astrocytes in the mouse spinal cord following sensory stimulation. *Neural Plast.* 2012:425818. doi: 10.1155/2012/425818

Corder, G., Doolen, S., Donahue, R. R., Winter, M. K., Jutras, B. L., He, Y., et al. (2013). Constitutive mu-opioid receptor activity leads to long-term endogenous analgesia and dependence. *Science* 341, 1394–1399. doi: 10.1126/science.1239403

Cordero-Erausquin, M., Coull, J. A., Boudreau, D., Rolland, M., and De Koninck, Y. (2005). Differential maturation of gaba action and anion reversal potential in spinal lamina i neurons: impact of chloride extrusion capacity. *J. Neurosci.* 25, 9613–9623. doi: 10.1523/jneurosci.1488-05.2005

Coull, J., Beggs, S., Boudreau, D., Boivin, D., Tsuda, M., Inoue, K., et al. (2005). Bdnf from microglia causes the shift in neuronal anion gradient underlying neuropathic pain. *Nature* 438, 1017–1021. doi: 10.1038/nature04223

Coull, J., Boudreau, D., Bachand, K., Prescott, S., Nault, F., Sik, A., et al. (2003). Trans-synaptic shift in anion gradient in spinal lamina I neurons as a mechanism of neuropathic pain. *Nature* 424, 938–942. doi: 10.1038/nature01868

Cristino, L., de Petrocellis, L., Pryce, G., Baker, D., Guglielmotti, V., and Di Marzo, V. (2006). Immunohistochemical localization of cannabinoid type 1 and vanilloid transient receptor potential vanilloid type 1 receptors in the mouse brain. *Neuroscience* 139, 1405–1415. doi: 10.1016/j.neuroscience.2006.02.074

Dana, H., Mohar, B., Sun, Y., Narayan, S., Gordus, A., Hasseman, J. P., et al. (2016). Sensitive red protein calcium indicators for imaging neural activity. *Elife* 5:e12727. doi: 10.7554/eLife.12727

Dana, H., Sun, Y., Mohar, B., Hulse, B. K., Kerlin, A. M., Hasseman, J. P., et al. (2019). High-performance calcium sensors for imaging activity in neuronal populations and microcompartments. *Nat. Methods* 16, 649–657. doi: 10.1038/s41592-019-0435-6

Daou, I., Beaudry, H., Ase, A. R., Wieskopf, J. S., Ribeiro-da-Silva, A., Mogil, J. S., et al. (2016). Optogenetic silencing of nav1.8-positive afferents alleviates inflammatory and neuropathic pain. *eNeuro* 3:ENEURO.0140-15.2016. doi: 10.1523/eneuro.0140-15.2016

Daou, I., Tuttle, A. H., Longo, G., Wieskopf, J. S., Bonin, R. P., Ase, A. R., et al. (2013). Remote optogenetic activation and sensitization of pain pathways in freely moving mice. *J. Neurosci.* 33, 18631–18640. doi: 10.1523/JNEUROSCI.2424-13.2013

Davalos, D., Lee, J. K., Smith, W. B., Brinkman, B., Ellisman, M. H., Zheng, B., et al. (2008). Stable *in vivo* imaging of densely populated glia, axons and blood vessels in the mouse spinal cord using two-photon microscopy. *J. Neurosci. Methods* 169, 1–7. doi: 10.1016/j.jneumeth.2007.11.011

DeBerry, J. J., Samineni, V. K., Copits, B. A., Sullivan, C. J., Vogt, S. K., Albers, K. M., et al. (2018). Differential regulation of bladder pain and voiding function by sensory afferent populations revealed by selective optogenetic activation. *Front. Integr. Neurosci.* 12:5. doi: 10.3389/fnint.2018.00005

DePaoli, D., Gasecka, A., Bahdine, M., Deschenes, J. M., Goetz, L., Perez-Sanchez, J., et al. (2020). Anisotropic light scattering from myelinated axons in the spinal cord. *Neurophotonics* 7:015011. doi: 10.1117/1.nph.7.1.015011

Dickie, A. C., Bell, A. M., Iwagaki, N., Polgár, E., Gutierrez-Mecinas, M., Kelly, R., et al. (2019). Morphological and functional properties distinguish the substance, P. and gastrin-releasing peptide subsets of excitatory interneuron in the spinal cord dorsal horn. *Pain* 160, 442–462. doi: 10.1097/j.pain.0000000000001406

D'Mello, R., and Dickenson, A. H. (2008). Spinal cord mechanisms of pain. *Br. J. Anaesth.* 101, 8–16. doi: 10.1093/bja/aen088

Doolen, S., Blake, C. B., Smith, B. N., and Taylor, B. K. (2012). Peripheral nerve injury increases glutamate-evoked calcium mobilization in adult spinal cord neurons. *Mol. Pain* 8:56. doi: 10.1186/1744-8069-8-56

Doolen, S., Cook, J., Riedl, M., Kitto, K., Kohsaka, S., Honda, C. N., et al. (2017). Complement 3a receptor in dorsal horn microglia mediates pronociceptive neuropeptide signaling. *Glia* 65, 1976–1989. doi: 10.1002/glia.23208

Draxler, P., Honsek, S. D., Forsthuber, L., Hadschieff, V., and Sandkuhler, J. (2014). Vglut3^{+} primary afferents play distinct roles in mechanical and cold hypersensitivity depending on pain etiology. *J. Neurosci.* 34, 12015–12028. doi: 10.1523/jneurosci.2157-14.2014

Drdla, R., Gassner, M., Gingl, E., and Sandkühler, J. (2009). Induction of synaptic long-term potentiation after opioid withdrawal. *Science* 325, 207–210. doi: 10.1126/science.1171759

Duan, B., Cheng, L., Bourane, S., Britz, O., Padilla, C., Garcia-Campmany, L., et al. (2014). Identification of spinal circuits transmitting and gating mechanical pain. *Cell* 159, 1417–1432. doi: 10.1016/j.cell.2014.11.003

Dubner, R., and Ren, K. (1999). Endogenous mechanisms of sensory modulation. *Pain* 6, S45–S53. doi: 10.1016/s0304-3959(99)00137-2

Eder, A., and Bading, H. (2007). Calcium signals can freely cross the nuclear envelope in hippocampal neurons: somatic calcium increases generate nuclear calcium transients. *BMC Neurosci.* 8:57. doi: 10.1186/1471-2202-8-57

Farrar, M. J., Bernstein, I. M., Schlafer, D. H., Cleland, T. A., Fetcho, J. R., and Schaffer, C. B. (2012). Chronic *in vivo* imaging in the mouse spinal cord using an implanted chamber. *Nat. Methods* 9, 297–302. doi: 10.1038/nmeth.1856

Fenno, L., Yizhar, O., and Deisseroth, K. (2011). The development and application of optogenetics. *Annu. Rev. Neurosci.* 34, 389–412. doi: 10.1146/annurev-neuro-061010-113817

Fenrich, K. K., Weber, P., Rougon, G., and Debarbieux, F. (2013). Implanting glass spinal cord windows in adult mice with experimental autoimmune encephalomyelitis. *J. Vis. Exp.* 82:e50826. doi: 10.3791/50826

Flynn, J. R., Brichta, A. M., Galea, M. P., Callister, R. J., and Graham, B. A. (2011). A horizontal slice preparation for examining the functional connectivity of dorsal column fibres in mouse spinal cord. *J. Neurosci. Methods* 200, 113–120. doi: 10.1016/j.jneumeth.2011.06.017

Foster, E., Wildner, H., Tudeau, L., Haueter, S., Ralvenius, W. T., Jegen, M., et al. (2015). Targeted ablation, silencing, and activation establish glycinergic dorsal horn neurons as key components of a spinal gate for pain and itch. *Neuron* 85, 1289–1304. doi: 10.1016/j.neuron.2015.02.028

François, A., Low, S. A., Sypek, E. I., Christensen, A. J., Sotoudeh, C., Beier, K. T., et al. (2017). A brainstem-spinal cord inhibitory circuit for mechanical pain modulation by gaba and enkephalins. *Neuron* 93, 822.e6–839.e6. doi: 10.1016/j.neuron.2017.01.008

Freitag, F. B., Ahemaiti, A., Jakobsson, J. E. T., Weman, H. M., and Lagerstrom, M. C. (2019). Spinal gastrin releasing peptide receptor expressing interneurons are controlled by local phasic and tonic inhibition. *Sci. Rep.* 9:16573. doi: 10.1038/s41598-019-52642-3

Fromherz, P., Hübener, G., Kuhn, B., and Hinner, M. J. (2008). Annine-6plus, a voltage-sensitive dye with good solubility, strong membrane binding and high sensitivity. *Eur. Biophys. J.* 37, 509–514. doi: 10.1007/s00249-007-0210-y

Gao, Z. R., Chen, W. Z., Liu, M. Z., Chen, X. J., Wan, L., Zhang, X. Y., et al. (2019). Tac1-expressing neurons in the periaqueductal gray facilitate the itch-scratching cycle *via* descending regulation. *Neuron* 101, 45.e9–59.e9. doi: 10.1016/j.neuron.2018.11.010

Gao, X., Xia, J., Munoz, F. M., Manners, M. T., Pan, R., Meucci, O., et al. (2016). Stims and orai1 regulate cytokine production in spinal astrocytes. *J. Neuroinflammation* 13:126. doi: 10.1186/s12974-016-0594-7

Gebhart, G. F. (2004). Descending modulation of pain. *Neurosci. Biobehav. Rev.* 27, 729–737. doi: 10.1016/j.neubiorev.2003.11.008

Ghitani, N., Barik, A., Szczot, M., Thompson, J. H., Li, C., Le Pichon, C. E., et al. (2017). Specialized mechanosensory nociceptors mediating rapid responses to hair pull. *Neuron* 95, 944.e4–954.e4. doi: 10.1016/j.neuron.2017.07.024

Gradinaru, V., Thompson, K. R., and Deisseroth, K. (2008). Enphr: a natronomonas halorhodopsin enhanced for optogenetic applications. *Brain Cell Biol.* 36, 129–139. doi: 10.1007/s11068-008-9027-6

Gradinaru, V., Thompson, K. R., Zhang, F., Mogri, M., Kay, K., Schneider, M. B., et al. (2007). Targeting and readout strategies for fast optical neural control *in vitro* and *in vivo*. *J. Neurosci.* 27, 14231–14238. doi: 10.1523/jneurosci.3578-07.2007

Grienberger, C., and Konnerth, A. (2012). Imaging calcium in neurons. *Neuron* 73, 862–885. doi: 10.1016/j.neuron.2012.02.011

Grudt, T. J., and Perl, E. R. (2002). Correlations between neuronal morphology and electrophysiological features in the rodent superficial dorsal horn. *J. Physiol.* 540, 189–207. doi: 10.1113/jphysiol.2001.012890

Grynkiewicz, G., Poenie, M., and Tsien, R. Y. (1985). A new generation of Ca^{2+} indicators with greatly improved fluorescence properties. *J. Biol. Chem.* 260, 3440–3450.

Gubernator, N. G., Zhang, H., Staal, R. G., Mosharov, E. V., Pereira, D. B., Yue, M., et al. (2009). Fluorescent false neurotransmitters visualize dopamine release from individual presynaptic terminals. *Science* 324, 1441–1444. doi: 10.1126/science.1172278

Gulledge, A., Kampa, B., and Stuart, G. (2005). Synaptic integration in dendritic trees. *J. Neurobiol.* 64, 75–90. doi: 10.1002/neu.20207

Gustafson-Vickers, S. L., Lu, V. B., Lai, A. Y., Todd, K. G., Ballanyi, K., and Smith, P. A. (2008). Long-term actions of interleukin-1beta on delay and tonic firing neurons in rat superficial dorsal horn and their relevance to central sensitization. *Mol. Pain* 4:63. doi: 10.1186/1744-8069-4-63

Gutierrez-Mecinas, M., Bell, A., Polgar, E., Watanabe, M., and Todd, A. J. (2019). Expression of neuropeptide ff defines a population of excitatory interneurons in the superficial dorsal horn of the mouse spinal cord that respond to noxious and pruritic stimuli. *Neuroscience* 416, 281–293. doi: 10.1016/j.neuroscience.2019.08.013

Gutierrez-Mecinas, M., Furuta, T., Watanabe, M., and Todd, A. J. (2016). A quantitative study of neurochemically defined excitatory interneuron populations in laminae i-iii of the mouse spinal cord. *Mol. Pain* 12:1744806916629065. doi: 10.1177/1744806916629065

Hachisuka, J., Baumbauer, K. M., Omori, Y., Snyder, L. M., Koerber, H. R., and Ross, S. E. (2016). Semi-intact *ex vivo* approach to investigate spinal somatosensory circuits. *Elife* 5:e22866. doi: 10.7554/eLife.22866

Hachisuka, J., Koerber, H. R., and Ross, S. E. (2020). Selective-cold output through a distinct subset of lamina i spinoparabrachial neurons. *Pain* 161, 185–194. doi: 10.1097/j.pain.0000000000001710

Hahn, K. M., Waggoner, A. S., and Taylor, D. L. (1990). A calcium-sensitive fluorescent analog of calmodulin based on a novel calmodulin-binding fluorophore. *J. Biol. Chem.* 265, 20335–20345.

Han, X., Chow, B. Y., Zhou, H., Klapoetke, N. C., Chuong, A., Rajimehr, R., et al. (2011). A high-light sensitivity optical neural silencer: development and application to optogenetic control of non-human primate cortex. *Front. Syst. Neurosci.* 5:18. doi: 10.3389/fnsys.2011.00018

Häring, M., Zeisel, A., Hochgerner, H., Rinwa, P., Jakobsson, J. E. T., Lönnerberg, P., et al. (2018). Neuronal atlas of the dorsal horn defines its architecture and links sensory input to transcriptional cell types. *Nat. Neurosci.* 21, 869–880. doi: 10.1038/s41593-018-0141-1

Harnett, M. T., Makara, J. K., Spruston, N., Kath, W. L., and Magee, J. C. (2012). Synaptic amplification by dendritic spines enhances input cooperativity. *Nature* 491, 599–602. doi: 10.1038/nature11554

Harvey, C. D., Yasuda, R., Zhong, H., and Svoboda, K. (2008). The spread of ras activity triggered by activation of a single dendritic spine. *Science* 321, 136–140. doi: 10.1126/science.1159675

Heffner, C. S., Herbert Pratt, C., Babiuk, R. P., Sharma, Y., Rockwood, S. F., Donahue, L. R., et al. (2012). Supporting conditional mouse mutagenesis with a comprehensive cre characterization resource. *Nat. Commun.* 3:1218. doi: 10.1038/ncomms2186

Heinke, B., Balzer, E., and Sandkühler, J. (2004). Pre- and postsynaptic contributions of voltage-dependent Ca^{2+} channels to nociceptive transmission in rat spinal lamina i neurons. *Eur. J. Neurosci.* 19, 103–111. doi: 10.1046/j.1460-9568.2003.03083.x

Helmchen, F., Denk, W., and Kerr, J. N. (2013). Miniaturization of two-photon microscopy for imaging in freely moving animals. *Cold Spring Harb. Protoc.* 2013, 904–913. doi: 10.1101/pdb.top078147

Helmchen, F., Svoboda, K., Denk, W., and Tank, D. W. (1999). *In vivo* dendritic calcium dynamics in deep-layer cortical pyramidal neurons. *Nat. Neurosci.* 2, 989–996. doi: 10.1038/14788

Hires, S. A., Tian, L., and Looger, L. L. (2008). Reporting neural activity with genetically encoded calcium indicators. *Brain Cell Biol.* 36, 69–86. doi: 10.1007/s11068-008-9029-4

Hochbaum, D. R., Zhao, Y., Farhi, S. L., Klapoetke, N., Werley, C. A., Kapoor, V., et al. (2014). All-optical electrophysiology in mammalian neurons using engineered microbial rhodopsins. *Nat. Methods* 11, 825–833. doi: 10.1038/nmeth.3000

Hollingworth, S., Gee, K. R., and Baylor, S. M. (2009). Low-affinity Ca^{2+} indicators compared in measurements of skeletal muscle Ca^{2+} transients. *Biophys J.* 97, 1864–1872. doi: 10.1016/j.bpj.2009.07.021

Honsek, S. D., Seal, R. P., and Sandkühler, J. (2015). Presynaptic inhibition of optogenetically identified VGluT3+ sensory fibres by opioids and baclofen. *Pain* 156, 243–251. doi: 10.1097/01.j.pain.0000460304.63948.40

Hopkins, D. A., and Holstege, G. (1978). Amygdaloid projections to the mesencephalon, pons and medulla oblongata in the cat. *Exp. Brain Res.* 32, 529–547. doi: 10.1007/bf00239551

Huang, J., Gadotti, V. M., Chen, L., Souza, I. A., Huang, S., Wang, D., et al. (2019). A neuronal circuit for activating descending modulation of neuropathic pain. *Nat. Neurosci.* 22, 1659–1668. doi: 10.1038/s41593-019-0481-5

Huang, J., Polgár, E., Solinski, H. J., Mishra, S. K., Tseng, P. Y., Iwagaki, N., et al. (2018). Circuit dissection of the role of somatostatin in itch and pain. *Nat. Neurosci.* 21, 707–716. doi: 10.1038/s41593-018-0119-z

Ikeda, H., Heinke, B., Ruscheweyh, R., and Sandkühler, J. (2003). Synaptic plasticity in spinal lamina I projection neurons that mediate hyperalgesia. *Science* 299, 1237–1241. doi: 10.1126/science.1080659

Ikeda, H., Stark, J., Fischer, H., Wagner, M., Drdla, R., Jäger, T., et al. (2006). Synaptic amplifier of inflammatory pain in the spinal dorsal horn. *Science* 312, 1659–1662. doi: 10.1126/science.1127233

Ikoma, A., Steinhoff, M., Ständer, S., Yosipovitch, G., and Schmelz, M. (2006). The neurobiology of itch. *Nat. Rev. Neurosci.* 7, 535–547. doi: 10.1038/nrn1950

Inoue, M., Takeuchi, A., Manita, S., Horigane, S. I., Sakamoto, M., Kawakami, R., et al. (2019). Rational engineering of XCaMPS, a multicolor GECI suite for *in vivo* imaging of complex brain circuit dynamics. *Cell* 177, 1346.e24–1360.e24. doi: 10.1016/j.cell.2019.04.007

Isaev, D., Gerber, G., Park, S. K., Chung, J. M., and Randik, M. (2000). Facilitation of nmda-induced currents and ca2+ transients in the rat substantia gelatinosa neurons after ligation of l5–l6 spinal nerves. *Neuroreport* 11, 4055–4061. doi: 10.1097/00001756-200012180-00030

Iyer, S. M., Montgomery, K. L., Towne, C., Lee, S. Y., Ramakrishnan, C., Deisseroth, K., et al. (2014). Virally mediated optogenetic excitation and inhibition of pain in freely moving nontransgenic mice. *Nat. Biotechnol.* 32, 274–278. doi: 10.1038/nbt.2834

Ji, Z. G., Ito, S., Honjoh, T., Ohta, H., Ishizuka, T., Fukazawa, Y., et al. (2012). Light-evoked somatosensory perception of transgenic rats that express channelrhodopsin-2 in dorsal root ganglion cells. *PLoS One* 7:e32699. doi: 10.1371/journal.pone.0032699

Johannssen, H., and Helmchen, F. (2010). *In vivo* calcium imaging of dorsal horn neuronal populations in mouse spinal cord. *J. Physiol.* 588, 3397–3404. doi: 10.1113/jphysiol.2010.191833

Kawamata, M., and Omote, K. (1996). Involvement of increased excitatory amino acids and intracellular Ca^{2+} concentration in the spinal dorsal horn in an animal model of neuropathic pain. *Pain* 68, 85–96. doi: 10.1016/s0304-3959(96)03222-8

Keller, A. F., Beggs, S., Salter, M. W., and De Koninck, Y. (2007). Transformation of the output of spinal lamina i neurons after nerve injury and microglia stimulation underlying neuropathic pain. *Mol. Pain* 3:27. doi: 10.1186/1744-8069-3-27

Kim, H., Jun, J., Wang, J., Bittar, A., Chung, K., and Chung, J. (2015). Induction of long-term potentiation and long-term depression is cell-type specific in the spinal cord. *Pain* 156, 618–625. doi: 10.1097/01.j.pain.0000460354.09622.ec

Klapoetke, N. C., Murata, Y., Kim, S. S., Pulver, S. R., Birdsey-Benson, A., Cho, Y. K., et al. (2014). Independent optical excitation of distinct neural populations. *Nat. Methods* 11, 338–346. doi: 10.1038/nmeth.2836

Klarenbeek, J., and Jalink, K. (2014). Detecting camp with an epac-based fret sensor in single living cells. *Methods Mol. Biol.* 1071, 49–58. doi: 10.1007/978-1-62703-622-1_4

Koch, S. C., Acton, D., and Goulding, M. (2018). Spinal circuits for touch, pain, and itch. *Annu. Rev. Physiol.* 80, 189–217. doi: 10.1146/annurev-physiol-022516-034303

Kohro, Y., Sakaguchi, E., Tashima, R., Tozaki-Saitoh, H., Okano, H., Inoue, K., et al. (2015). A new minimally-invasive method for microinjection into the mouse spinal dorsal horn. *Sci. Rep.* 5:14306. doi: 10.1038/srep14306

Kopach, O., Kao, S. C., Petralia, R. S., Belan, P., Tao, Y. X., and Voitenko, N. (2011). Inflammation alters trafficking of extrasynaptic ampa receptors in tonically firing lamina ii neurons of the rat spinal dorsal horn. *Pain* 152, 912–923. doi: 10.1016/j.pain.2011.01.016

Kubota, S., Sidikejiang, W., Kudo, M., Inoue, K. I., Umeda, T., Takada, M., et al. (2019). Optogenetic recruitment of spinal reflex pathways from large-diameter primary afferents in non-transgenic rats transduced with aav9/channelrhodopsin 2. *J. Physiol.* 597, 5025–5040. doi: 10.1113/jp278292

Kulkarni, R. U., and Miller, E. W. (2017). Voltage imaging: pitfalls and potential. *Biochemistry* 56, 5171–5177. doi: 10.1021/acs.biochem.7b00490

Kyrozis, A., Goldstein, P. A., Heath, M. J., and MacDermott, A. B. (1995). Calcium entry through a subpopulation of ampa receptors desensitized neighbouring nmda receptors in rat dorsal horn neurons. *J. Physiol.* 485, 373–381. doi: 10.1113/jphysiol.1995.sp020736

Laffray, S., Pagès, S., Dufour, H., De Koninck, P., De Koninck, Y., and Cote, D. (2011). Adaptive movement compensation for *in vivo* imaging of fast cellular dynamics within a moving tissue. *PLoS One* 6:e19928. doi: 10.1371/journal.pone.0019928

Larkum, M., Nevian, T., Sandler, M., Polsky, A., and Schiller, J. (2009). Synaptic integration in tuft dendrites of layer 5 pyramidal neurons: a new unifying principle. *Science* 325, 756–760. doi: 10.1126/science.1171958

Lau, B. K., and Vaughan, C. W. (2014). Descending modulation of pain: the gaba disinhibition hypothesis of analgesia. *Curr. Opin. Neurobiol.* 29, 159–164. doi: 10.1016/j.conb.2014.07.010

Lee, S., Escobedo-Lozoya, Y., Szatmari, E., and Yasuda, R. (2009). Activation of camkii in single dendritic spines during long-term potentiation. *Nature* 458, 299–304. doi: 10.1038/nature07842

Leinweber, M., Zmarz, P., Buchmann, P., Argast, P., Hubener, M., Bonhoeffer, T., et al. (2014). Two-photon calcium imaging in mice navigating a virtual reality environment. *J. Vis. Exp.* 84:e50885. doi: 10.3791/50885

Li, P., Kerchner, G. A., Sala, C., Wei, F., Huettner, J. E., Sheng, M., et al. (1999). Ampa receptor-pdz interactions in facilitation of spinal sensory synapses. *Nat. Neurosci.* 2, 972–977. doi: 10.1038/14771

Li, L., Rutlin, M., Abraira, V. E., Cassidy, C., Kus, L., Gong, S., et al. (2011). The functional organization of cutaneous low-threshold mechanosensory neurons. *Cell* 147, 1615–1627. doi: 10.1016/j.cell.2011.11.027

Li, B., Yang, X. Y., Qian, F. P., Tang, M., Ma, C., and Chiang, L. Y. (2015). A novel analgesic approach to optogenetically and specifically inhibit pain transmission using trpv1 promoter. *Brain Res.* 1609, 12–20. doi: 10.1016/j.brainres.2015.03.008

Li, P., and Zhuo, M. (1998). Silent glutamatergic synapses and nociception in mammalian spinal cord. *Nature* 393, 695–698. doi: 10.1038/31496

Light, A. R., and Willcockson, H. H. (1999). Spinal laminae i-ii neurons in rat recorded *in vivo* in whole cell, tight seal configuration: properties and opioid responses. *J. Neurophysiol.* 82, 3316–3326. doi: 10.1152/jn.1999.82.6.3316

Lima, S. Q., and Miesenböck, G. (2005). Remote control of behavior through genetically targeted photostimulation of neurons. *Cell* 121, 141–152. doi: 10.1016/j.cell.2005.02.004

Lin, J. Y. (2011). A user's guide to channelrhodopsin variants: features, limitations and future developments. *Exp. Physiol.* 96, 19–25. doi: 10.1113/expphysiol.2009.051961

Lin, J. Y., Knutsen, P. M., Muller, A., Kleinfeld, D., and Tsien, R. Y. (2013). Reachr: a red-shifted variant of channelrhodopsin enables deep transcranial optogenetic excitation. *Nat. Neurosci.* 16, 1499–1508. doi: 10.1038/nn.3502

Lin, M. Z., and Schnitzer, M. J. (2016). Genetically encoded indicators of neuronal activity. *Nat. Neurosci.* 19, 1142–1153. doi: 10.1038/nn.4359

Liske, H., Qian, X., Anikeeva, P., Deisseroth, K., and Delp, S. (2013). Optical control of neuronal excitation and inhibition using a single opsin protein, chr2. *Sci. Rep.* 3:3110. doi: 10.1038/srep03110

Lou, S., Adam, Y., Weinstein, E. N., Williams, E., Williams, K., Parot, V., et al. (2016). Genetically targeted all-optical electrophysiology with a transgenic cre-dependent optopatch mouse. *J. Neurosci.* 36, 11059–11073. doi: 10.1523/JNEUROSCI.1582-16.2016

Lou, S., Duan, B., Vong, L., Lowell, B. B., and Ma, Q. (2013). Runx1 controls terminal morphology and mechanosensitivity of vglut3-expressing c-mechanoreceptors. *J. Neurosci.* 33, 870–882. doi: 10.1523/jneurosci.3942-12.2013

Lu, Y., Dong, H., Gao, Y., Gong, Y., Ren, Y., Gu, N., et al. (2013). A feed-forward spinal cord glycinergic neural circuit gates mechanical allodynia. *J. Clin. Invest.* 123, 4050–4062. doi: 10.1172/jci70026

Lu, A., Lei, H., Li, L., Lai, L., Liang, W., and Xu, S. (2018). Role of mitochondrial Ca^{2+} uniporter in remifentanil-induced postoperative allodynia. *Eur. J. Neurosci.* 47, 305–313. doi: 10.1111/ejn.13842

Lu, C., Park, S., Richner, T. J., Derry, A., Brown, I., Hou, C., et al. (2017). Flexible and stretchable nanowire-coated fibers for optoelectronic probing of spinal cord circuits. *Sci. Adv.* 3:e1600955. doi: 10.1126/sciadv.1600955

Lu, Y., and Perl, E. R. (2003). A specific inhibitory pathway between substantia gelatinosa neurons receiving direct c-fiber input. *J. Neurosci.* 23, 8752–8758. doi: 10.1523/jneurosci.23-25-08752.2003

Lu, Y., and Perl, E. R. (2005). Modular organization of excitatory circuits between neurons of the spinal superficial dorsal horn (laminae I and II). *J. Neurosci.* 25, 3900–3907. doi: 10.1523/JNEUROSCI.0102-05.2005

Luo, C., Seeburg, P. H., Sprengel, R., and Kuner, R. (2008). Activity-dependent potentiation of calcium signals in spinal sensory networks in inflammatory pain states. *Pain* 140, 358–367. doi: 10.1016/j.pain.2008.09.008

Machida, A., Kuwahara, H., Mayra, A., Kubodera, T., Hirai, E., Sunaga, F., et al. (2013). Intraperitoneal administration of AAV9-shRNA inhibits target gene expression in the dorsal root ganglia of neonatal mice. *Mol. Pain* 9:36. doi: 10.1186/1744-8069-9-36

Mackenzie, R. A., Burke, D., Skuse, N. F., and Lethlean, A. K. (1975). Fibre function and perception during cutaneous nerve block. *Proc. Aust. Assoc. Neurol.* 12, 65–73.

Mank, M., and Griesbeck, O. (2008). Genetically encoded calcium indicators. *Chem. Rev.* 108, 1550–1564. doi: 10.1021/cr078213v

Marvin, J. S., Borghuis, B. G., Tian, L., Cichon, J., Harnett, M. T., Akerboom, J., et al. (2013). An optimized fluorescent probe for visualizing glutamate neurotransmission. *Nat. Methods* 10, 162–170. doi: 10.1038/nmeth.2333

Marvin, J. S., Scholl, B., Wilson, D. E., Podgorski, K., Kazemipour, A., Müller, J. A., et al. (2018). Stability, affinity, and chromatic variants of the glutamate sensor iglusnfr. *Nat. Methods* 15, 936–939. doi: 10.1038/s41592-018-0171-3

Masuda, T., Ozono, Y., Mikuriya, S., Kohro, Y., Tozaki-Saitoh, H., Iwatsuki, K., et al. (2016). Dorsal horn neurons release extracellular ATP in a VNUT-dependent manner that underlies neuropathic pain. *Nat. Commun.* 7:12529. doi: 10.1038/ncomms12529

Maxwell, D. J., and Bannatyne, B. A. (1983). Ultrastructure of muscle spindle afferent terminations in lamina vi of the cat spinal cord. *Brain Res.* 288, 297–301. doi: 10.1016/0006-8993(83)90106-3

Maxwell, D. J., and Riddell, J. S. (1999). Axoaxonic synapses on terminals of group ii muscle spindle afferent axons in the spinal cord of the cat. *Eur. J. Neurosci.* 11, 2151–2159. doi: 10.1046/j.1460-9568.1999.00632.x

Mayer, P., Sivakumar, N., Pritz, M., Varga, M., Mehmann, A., Lee, S., et al. (2019). Flexible and lightweight devices for wireless multi-color optogenetic experiments controllable *via* commercial cell phones. *Front. Neurosci.* 13:819. doi: 10.3389/fnins.2019.00819

McGlone, F., and Reilly, D. (2010). The cutaneous sensory system. *Neurosci. Biobehav. Rev.* 34, 148–159. doi: 10.1016/j.neubiorev.2009.08.004

Mears, S. C., and Frank, E. (1997). Formation of specific monosynaptic connections between muscle spindle afferents and motoneurons in the mouse. *J. Neurosci.* 17, 3128–3135. doi: 10.1523/jneurosci.17-09-03128.1997

Melzack, R., and Wall, P. D. (1965). Pain mechanisms: a new theory. *Science* 150, 971–979. doi: 10.1126/science.150.3699.971

Merighi, A., Bardoni, R., Salio, C., Lossi, L., Ferrini, F., Prandini, M., et al. (2008). Presynaptic functional trkb receptors mediate the release of excitatory neurotransmitters from primary afferent terminals in lamina ii (substantia gelatinosa) of postnatal rat spinal cord. *Dev. Neurobiol.* 68, 457–475. doi: 10.1002/dneu.20605

Minta, A., Kao, J. P., and Tsien, R. Y. (1989). Fluorescent indicators for cytosolic calcium based on rhodamine and fluorescein chromophores. *J. Biol. Chem.* 264, 8171–8178.

Miyano, K., Morioka, N., Sugimoto, T., Shiraishi, S., Uezono, Y., and Nakata, Y. (2010). Activation of the neurokinin-1 receptor in rat spinal astrocytes induces Ca2+ release from IP3-sensitive Ca2+ stores and extracellular Ca2+ influx through TRPC3. *Neurochem. Int.* 57, 923–934. doi: 10.1016/j.neuint.2010.09.012

Mizuno, M., Kato, G., and Strassman, A. M. (2019). Spatial organization of activity evoked by focal stimulation within the rat spinal dorsal horn as visualized by voltage-sensitive dye imaging in the slice. *J. Neurophysiol.* 122, 1697–1707. doi: 10.1152/jn.00697.2018

Molander, C., Xu, Q., and Grant, G. (1984). The cytoarchitectonic organization of the spinal cord in the rat. I. The lower thoracic and lumbosacral cord. *J. Comp. Neurol.* 230, 133–141. doi: 10.1002/cne.902300112

Mondello, S. E., Sunshine, M. D., Fischedick, A. E., Dreyer, S. J., Horwitz, G. D., Anikeeva, P., et al. (2018). Optogenetic surface stimulation of the rat cervical spinal cord. *J. Neurophysiol.* 120, 795–811. doi: 10.1152/jn.00461.2017

Montgomery, K. L., Yeh, A. J., Ho, J. S., Tsao, V., Mohan Iyer, S., Grosenick, L., et al. (2015). Wirelessly powered, fully internal optogenetics for brain, spinal and peripheral circuits in mice. *Nat. Methods* 12, 969–974. doi: 10.1038/nmeth.3536

Mu, D., Deng, J., Liu, K. F., Wu, Z. Y., Shi, Y. F., Guo, W. M., et al. (2017). A central neural circuit for itch sensation. *Science* 357, 695–699. doi: 10.1126/science.aaf4918

Nagasako, E. M., Oaklander, A. L., and Dworkin, R. H. (2003). Congenital insensitivity to pain: an update. *Pain* 101, 213–219. doi: 10.1016/s0304-3959(02)00482-7

Nagel, G., Szellas, T., Huhn, W., Kateriya, S., Adeishvili, N., Berthold, P., et al. (2003). Channelrhodopsin-2, a directly light-gated cation-selective membrane channel. *Proc. Natl. Acad. Sci. U S A* 100, 13940–13945. doi: 10.1073/pnas.1936192100

Nagy, A. (2000). Cre recombinase: the universal reagent for genome tailoring. *Genesis* 26, 99–109. doi: 10.1002/(sici)1526-968x(200002)26:2<99::aid-gene1>3.0.co;2-b

Nam, Y., Kim, J. H., Kim, J. H., Jha, M. K., Jung, J. Y., Lee, M. G., et al. (2016). Reversible induction of pain hypersensitivity following optogenetic stimulation of spinal astrocytes. *Cell Rep.* 17, 3049–3061. doi: 10.1016/j.celrep.2016.11.043

Nimmerjahn, A., and Bergles, D. E. (2015). Large-scale recording of astrocyte activity. *Curr. Opin. Neurobiol.* 32, 95–106. doi: 10.1016/j.conb.2015.01.015

Nishida, K., Matsumura, S., Taniguchi, W., Uta, D., Furue, H., and Ito, S. (2014). Three-dimensional distribution of sensory stimulation-evoked neuronal activity of spinal dorsal horn neurons analyzed by *in vivo* calcium imaging. *PLoS One* 9:e103321. doi: 10.1371/journal.pone.0103321

Niu, J., Ding, L., Li, J. J., Kim, H., Liu, J., Li, H., et al. (2013). Modality-based organization of ascending somatosensory axons in the direct dorsal column pathway. *J. Neurosci.* 33, 17691–17709. doi: 10.1523/jneurosci.3429-13.2013

Olausson, H., Lamarre, Y., Backlund, H., Morin, C., Wallin, B. G., Starck, G., et al. (2002). Unmyelinated tactile afferents signal touch and project to insular cortex. *Nat. Neurosci.* 5, 900–904. doi: 10.1038/nn896

Olivares-Moreno, R., López-Hidalgo, M., Altamirano-Espinoza, A., González-Gallardo, A., Antaramian, A., Lopez-Virgen, V., et al. (2019). Mouse corticospinal system comprises different functional neuronal ensembles depending on their hodology. *BMC Neurosci.* 20:50. doi: 10.1186/s12868-019-0533-5

Ossipov, M. H., and Gebhart, G. F. (1986). Opioid, cholinergic and alpha-adrenergic influences on the modulation of nociception from the lateral reticular nucleus of the rat. *Brain Res.* 384, 282–293. doi: 10.1016/0006-8993(86)91164-9

Otchy, T. M., Wolff, S. B., Rhee, J. Y., Pehlevan, C., Kawai, R., Kempf, A., et al. (2015). Acute off-target effects of neural circuit manipulations. *Nature* 528, 358–363. doi: 10.1038/nature16442

Packer, A. M., Russell, L. E., Dalgleish, H. W., and Häusser, M. (2015). Simultaneous all-optical manipulation and recording of neural circuit activity with cellular resolution in vivo. *Nat. Methods* 12, 140–146. doi: 10.1038/nmeth.3217

Pagani, M., Albisetti, G. W., Sivakumar, N., Wildner, H., Santello, M., Johannssen, H. C., et al. (2019). How gastrin-releasing peptide opens the spinal gate for itch. *Neuron* 103, 102.e5–117.e5. doi: 10.1016/j.neuron.2019.04.022

Paredes, R. M., Etzler, J. C., Watts, L. T., Zheng, W., and Lechleiter, J. D. (2008). Chemical calcium indicators. *Methods* 46, 143–151. doi: 10.1016/j.ymeth.2008.09.025

Park, S. I., Brenner, D. S., Shin, G., Morgan, C. D., Copits, B. A., Chung, H. U., et al. (2015). Soft, stretchable, fully implantable miniaturized optoelectronic systems for wireless optogenetics. *Nat. Biotechnol.* 33, 1280–1286. doi: 10.1038/nbt.3415

Peirs, C., Williams, S., Zhao, X., Walsh, C., Gedeon, J., Cagle, N., et al. (2015). Dorsal horn circuits for persistent mechanical pain. *Neuron* 87, 797–812. doi: 10.1016/j.neuron.2015.07.029

Petitjean, H., Bourojeni, F. B., Tsao, D., Davidova, A., Sotocinal, S. G., Mogil, J. S., et al. (2019). Recruitment of spinoparabrachial neurons by dorsal horn calretinin neurons. *Cell Rep.* 28, 1429.e4–1438.e4. doi: 10.1016/j.celrep.2019.07.048

Petitjean, H., Hugel, S., Barthas, F., Bohren, Y., Barrot, M., Yalcin, I., et al. (2014). Activation of transient receptor potential vanilloid 2-expressing primary afferents stimulates synaptic transmission in the deep dorsal horn of the rat spinal cord and elicits mechanical hyperalgesia. *Eur. J. Neurosci.* 40, 3189–3201. doi: 10.1111/ejn.12688

Petitjean, H., Pawlowski, S. A., Fraine, S. L., Sharif, B., Hamad, D., Fatima, T., et al. (2015). Dorsal horn parvalbumin neurons are gate-keepers of touch-evoked pain after nerve injury. *Cell Rep.* 13, 1246–1257. doi: 10.1016/j.celrep.2015.09.080

Podor, B., Hu, Y. L., Ohkura, M., Nakai, J., Croll, R., and Fine, A. (2015). Comparison of genetically encoded calcium indicators for monitoring

action potentials in mammalian brain by two-photon excitation fluorescence microscopy. *Neurophotonics* 2:021014. doi: 10.1117/1.nph.2.2.021014

Pologruto, T. A., Yasuda, R., and Svoboda, K. (2004). Monitoring neural activity and [Ca2+] with genetically encoded Ca2+ indicators. *J. Neurosci.* 24, 9572–9579. doi: 10.1523/JNEUROSCI.2854-04.2004

Ponsioen, B., Zhao, J., Riedl, J., Zwartkruis, F., van der Krogt, G., Zaccolo, M., et al. (2004). Detecting cAMP-induced epac activation by fluorescence resonance energy transfer: Epac as a novel cAMP indicator. *EMBO Rep.* 5, 1176–1180. doi: 10.1038/sj.embor.7400290

Porreca, F., Ossipov, M. H., and Gebhart, G. F. (2002). Chronic pain and medullary descending facilitation. *Trends Neurosci.* 25, 319–325. doi: 10.1016/s0166-2236(02)02157-4

Potter, L. E., Doolen, S., Mifflin, K., Tenorio, G., Baker, G., Taylor, B. K., et al. (2018). Antinociceptive effects of the antidepressant phenelzine are mediated by context-dependent inhibition of neuronal responses in the dorsal horn. *Neuroscience* 383, 205–215. doi: 10.1016/j.neuroscience.2018.04.047

Prescott, S. A., and De Koninck, Y. (2002). Four cell types with distinctive membrane properties and morphologies in lamina i of the spinal dorsal horn of the adult rat. *J. Physiol.* 539, 817–836. doi: 10.1113/jphysiol.2001.013437

Proudfit, H. K., and Clark, F. M. (1991). The projections of locus coeruleus neurons to the spinal cord. *Prog. Brain Res.* 88, 123–141. doi: 10.1016/s0079-6123(08)63803-0

Punnakkal, P., von Schoultz, C., Haenraets, K., Wildner, H., and Zeilhofer, H. U. (2014). Morphological, biophysical and synaptic properties of glutamatergic neurons of the mouse spinal dorsal horn. *J. Physiol.* 592, 759–776. doi: 10.1113/jphysiol.2013.264937

Rahmati, V., Kirmse, K., Markovic, D., Holthoff, K., and Kiebel, S. J. (2016). Inferring neuronal dynamics from calcium imaging data using biophysical models and bayesian inference. *PLoS Comput. Biol.* 12:e1004736. doi: 10.1371/journal.pcbi.1004736

Ran, C., Hoon, M. A., and Chen, X. (2016). The coding of cutaneous temperature in the spinal cord. *Nat. Neurosci.* 19, 1201–1209. doi: 10.1038/nn.4350

Rau, K. K., McIlwrath, S. L., Wang, H., Lawson, J. J., Jankowski, M. P., Zylka, M. J., et al. (2009). Mrgprd enhances excitability in specific populations of cutaneous murine polymodal nociceptors. *J. Neurosci.* 29, 8612–8619. doi: 10.1523/jneurosci.1057-09.2009

Ren, K., and Dubner, R. (2002). Descending modulation in persistent pain: an update. *Pain* 100, 1–6. doi: 10.1016/s0304-3959(02)00368-8

Rexed, B. (1952). The cytoarchitectonic organization of the spinal cord in the cat. *J. Comp. Neurol.* 96, 414–495. doi: 10.1002/cne.900960303

Rickgauer, J. P., Deisseroth, K., and Tank, D. W. (2014). Simultaneous cellular-resolution optical perturbation and imaging of place cell firing fields. *Nat. Neurosci.* 17, 1816–1824. doi: 10.1038/nn.3866

Roberts, J. C., Davis, J. B., and Benham, C. D. (2004). [^{3}H]resiniferatoxin autoradiography in the cns of wild-type and TRPV1 null mice defines trpv1 (VR-1) protein distribution. *Brain Res.* 995, 176–183. doi: 10.1016/j.brainres.2003.10.001

Roberts, W. J., and Elardo, S. M. (1986). Clustering of primary afferent fibers in peripheral nerve fascicles by sensory modality. *Brain Res.* 370, 149–152. doi: 10.1016/0006-8993(86)91115-7

Rossant, J., and McMahon, A. (1999). "Cre"-ating mouse mutants-a meeting review on conditional mouse genetics. *Genes Dev.* 13, 142–145. doi: 10.1101/gad.13.2.142

Ruscheweyh, R., and Sandkuhler, J. (2005). Long-range oscillatory calcium waves in rat spinal dorsal horn. *Eur. J. Neurosci.* 22, 1967–1976. doi: 10.1111/j.1460-9568.2005.04393.x

Samineni, V. K., Mickle, A. D., Yoon, J., Grajales-Reyes, J. G., Pullen, M. Y., Crawford, K. E., et al. (2017a). Optogenetic silencing of nociceptive primary afferents reduces evoked and ongoing bladder pain. *Sci. Rep.* 7:15865. doi: 10.1038/s41598-017-16129-3

Samineni, V. K., Yoon, J., Crawford, K. E., Jeong, Y. R., McKenzie, K. C., Shin, G., et al. (2017b). Fully implantable, battery-free wireless optoelectronic devices for spinal optogenetics. *Pain* 158, 2108–2116. doi: 10.1097/j.pain.0000000000000968

Sanderson, M. J., Smith, I., Parker, I., and Bootman, M. D. (2014). Fluorescence microscopy. *Cold Spring Harb. Protoc.* 2014:pdb.top071795. doi: 10.1101/pdb.top071795

Sathyamurthy, A., Johnson, K. R., Matson, K. J. E., Dobrott, C. I., Li, L., Ryba, A. R., et al. (2018). Massively parallel single nucleus transcriptional profiling defines spinal cord neurons and their activity during behavior. *Cell Rep.* 22, 2216–2225. doi: 10.1016/j.celrep.2018.02.003

Schoffnegger, D., Ruscheweyh, R., and Sandkühler, J. (2008). Spread of excitation across modality borders in spinal dorsal horn of neuropathic rats. *Pain* 135, 300–310. doi: 10.1016/j.pain.2007.12.016

Schuster, D. J., Dykstra, J. A., Riedl, M. S., Kitto, K. F., Belur, L. R., McIvor, R. S., et al. (2014). Biodistribution of adeno-associated virus serotype 9 (aav9) vector after intrathecal and intravenous delivery in mouse. *Front. Neuroanat.* 8:42. doi: 10.3389/fnana.2014.00042

Seal, R. P., Wang, X., Guan, Y., Raja, S. N., Woodbury, C. J., Basbaum, A. I., et al. (2009). Injury-induced mechanical hypersensitivity requires C-low threshold mechanoreceptors. *Nature* 462, 651–655. doi: 10.1038/nature08505

Sekiguchi, K., Shekhmeyster, P., Merten, K., Arena, A., Cook, D., Hoffman, E., et al. (2016). Imaging large-scale cellular activity in spinal cord of freely behaving mice. *Nat. Commun.* 7:11450. doi: 10.1038/ncomms11450

Shen, Y., Dana, H., Abdelfattah, A. S., Patel, R., Shea, J., Molina, R. S., et al. (2018). A genetically encoded Ca^{2+} indicator based on circularly permutated sea anemone red fluorescent protein eqFP578. *BMC Biol.* 16:9. doi: 10.1186/s12915-018-0480-0

Shields, S. D., Ahn, H. S., Yang, Y., Han, C., Seal, R. P., Wood, J. N., et al. (2012). Nav1.8 expression is not restricted to nociceptors in mouse peripheral nervous system. *Pain* 153, 2017–2030. doi: 10.1016/j.pain.2012.04.022

Shutov, L., Kruglikov, I., Gryshchenko, O., Khomula, E., Viatchenko-Karpinski, V., Belan, P., et al. (2006). The effect of nimodipine on calcium homeostasis and pain sensitivity in diabetic rats. *Cell. Mol. Neurobiol.* 26, 1541–1557. doi: 10.1007/s10571-006-9107-z

Simonetti, M., Hagenston, A., Vardeh, D., Freitag, H., Mauceri, D., Lu, J., et al. (2013). Nuclear calcium signaling in spinal neurons drives a genomic program required for persistent inflammatory pain. *Neuron* 77, 43–57. doi: 10.1016/j.neuron.2012.10.037

Skorput, A. G. J., Zhang, X., Waataja, J. J., Peterson, C. D., Riedl, M. S., Kitto, K. F., et al. (2018). Involvement of the vgf-derived peptide tlqp-62 in nerve injury-induced hypersensitivity and spinal neuroplasticity. *Pain* 159, 1802–1813. doi: 10.1097/j.pain.0000000000001277

Smetters, D., Majewska, A., and Yuste, R. (1999). Detecting action potentials in neuronal populations with calcium imaging. *Methods* 18, 215–221. doi: 10.1006/meth.1999.0774

Smith-Edwards, K. M., Najjar, S. A., Edwards, B. S., Howard, M. J., Albers, K. M., and Davis, B. M. (2019). Extrinsic primary afferent neurons link visceral pain to colon motility through a spinal reflex in mice. *Gastroenterology* 157, 522.e2–536.e2. doi: 10.1053/j.gastro.2019.04.034

Sokal, D. M., and Chapman, V. (2003). Effects of spinal administration of muscimol on c- and a-fibre evoked neuronal responses of spinal dorsal horn neurones in control and nerve injured rats. *Brain Res.* 962, 213–220. doi: 10.1016/s0006-8993(02)04057-x

Song, A. J., and Palmiter, R. D. (2018). Detecting and avoiding problems when using the cre-lox system. *Trends Genet.* 34, 333–340. doi: 10.1016/j.tig.2017.12.008

Spruston, N., Schiller, Y., Stuart, G., and Sakmann, B. (1995). Activity-dependent action potential invasion and calcium influx into hippocampal ca1 dendrites. *Science* 268, 297–300. doi: 10.1126/science.7716524

Stamatakis, A. M., Schachter, M. J., Gulati, S., Zitelli, K. T., Malanowski, S., Tajik, A., et al. (2018). Simultaneous optogenetics and cellular resolution calcium imaging during active behavior using a miniaturized microscope. *Front. Neurosci.* 12:496. doi: 10.3389/fnins.2018.00496

Stemkowski, P., García-Caballero, A., Gadotti, V. M., M'Dahoma, S., Huang, S., Black, S. A. G., et al. (2016). Trpv1 nociceptor activity initiates usp5/t-type channel-mediated plasticity. *Cell Rep.* 17, 2901–2912. doi: 10.1016/j.celrep.2016.11.047

Striessnig, J., Pinggera, A., Kaur, G., Bock, G., and Tuluc, P. (2014). L-type Ca^{2+} channels in heart and brain. *Wiley Interdiscip. Rev. Membr. Transp. Signal.* 3, 15–38. doi: 10.1002/wmts.102

Sun, S., Xu, Q., Guo, C., Guan, Y., Liu, Q., and Dong, X. (2017). Leaky gate model: intensity-dependent coding of pain and itch in the spinal cord. *Neuron* 93, 840.e5–853.e5. doi: 10.1016/j.neuron.2017.01.012

Takazawa, T., and MacDermott, A. B. (2010). Synaptic pathways and inhibitory gates in the spinal cord dorsal horn. *Ann. N Y Acad. Sci.* 1198, 153–158. doi: 10.1111/j.1749-6632.2010.05501.x

Tang, P., Zhang, Y., Chen, C., Ji, X., Ju, F., Liu, X., et al. (2015). *In vivo* two-photon imaging of axonal dieback, blood flow and calcium influx with methylprednisolone therapy after spinal cord injury. *Sci. Rep.* 5:9691. doi: 10.1038/srep09691

Tashima, R., Koga, K., Sekine, M., Kanehisa, K., Kohro, Y., Tominaga, K., et al. (2018). Optogenetic activation of non-nociceptive abeta fibers induces neuropathic pain-like sensory and emotional behaviors after nerve injury in rats. *eNeuro* 5:ENEURO.0450-17.2018. doi: 10.1523/eneuro.0450-17.2018

Taylor, B. K., Sinha, G. P., Donahue, R. R., Grachen, C. M., Morón, J. A., and Doolen, S. (2019). Opioid receptors inhibit the spinal ampa receptor Ca^{2+} permeability that mediates latent pain sensitization. *Exp. Neurol.* 314, 58–66. doi: 10.1016/j.expneurol.2019.01.003

Tian, L., Hires, S. A., Mao, T., Huber, D., Chiappe, M. E., Chalasani, S. H., et al. (2009). Imaging neural activity in worms, flies and mice with improved gcamp calcium indicators. *Nat. Methods* 6, 875–881. doi: 10.1038/nmeth.1398

Towne, C., Montgomery, K. L., Iyer, S. M., Deisseroth, K., and Delp, S. L. (2013). Optogenetic control of targeted peripheral axons in freely moving animals. *PLoS One* 8:e72691. doi: 10.1371/journal.pone.0072691

Tsien, R. Y. (1989). Fluorescent indicators of ion concentrations. *Methods Cell Biol.* 30, 127–156. doi: 10.1016/s0091-679x(08)60978-4

Tsuzuki, K., Xing, H., Ling, J., and Gu, J. G. (2004). Menthol-induced Ca^{2+} release from presynaptic Ca^{2+} stores potentiates sensory synaptic transmission. *J. Neurosci.* 24, 762–771. doi: 10.1523/jneurosci.4658-03.2004

Tye, K. M., and Deisseroth, K. (2012). Optogenetic investigation of neural circuits underlying brain disease in animal models. *Nat. Rev. Neurosci.* 13, 251–266. doi: 10.1038/nrn3171

Uhelski, M. L., Bruce, D. J., Séguéla, P., Wilcox, G. L., and Simone, D. A. (2017). *In vivo* optogenetic activation of $Na_v1.8^+$ cutaneous nociceptors and their responses to natural stimuli. *J. Neurophysiol.* 117, 2218–2223. doi: 10.1152/jn.00083.2017

Urch, C. E., and Dickenson, A. H. (2003). *In vivo* single unit extracellular recordings from spinal cord neurones of rats. *Brain Res. Protoc.* 12, 26–34. doi: 10.1016/s1385-299x(03)00068-0

Usoskin, D., Furlan, A., Islam, S., Abdo, H., Lönnerberg, P., Lou, D., et al. (2015). Unbiased classification of sensory neuron types by large-scale single-cell rna sequencing. *Nat. Neurosci.* 18, 145–153. doi: 10.1038/nn.3881

Valtschanoff, J. G., Rustioni, A., Guo, A., and Hwang, S. J. (2001). Vanilloid receptor vr1 is both presynaptic and postsynaptic in the superficial laminae of the rat dorsal horn. *J. Comp. Neurol.* 436, 225–235. doi: 10.1002/cne.1063

Villette, V., Chavarha, M., Dimov, I. K., Bradley, J., Pradhan, L., Mathieu, B., et al. (2019). Ultrafast two-photon imaging of a high-gain voltage indicator in awake behaving mice. *Cell* 179, 1590.e23–1608.e23. doi: 10.1016/j.cell.2019.11.004

Vrontou, S., Wong, A. M., Rau, K. K., Koerber, H. R., and Anderson, D. J. (2013). Genetic identification of c fibres that detect massage-like stroking of hairy skin *in vivo*. *Nature* 493, 669–673. doi: 10.1038/nature11810

Wang, F., Bélanger, E., Côté, S. L., Desrosiers, P., Prescott, S. A., Côté, D. C., et al. (2018). Sensory afferents use different coding strategies for heat and cold. *Cell Rep.* 23, 2001–2013. doi: 10.1016/j.celrep.2018.04.065

Wang, H., and Zylka, M. J. (2009). Mrgprd-expressing polymodal nociceptive neurons innervate most known classes of substantia gelatinosa neurons. *J. Neurosci.* 29, 13202–13209. doi: 10.1523/jneurosci.3248-09.2009

Willis, W. D. (1985). Nociceptive pathways: anatomy and physiology of nociceptive ascending pathways. *Philos. Trans. R. Soc. Lond. B Biol. Sci.* 308, 253–270. doi: 10.1098/rstb.1985.0025

Wilson, J., Dombeck, D., Diaz-Ross, M., Harris-Warrick, R., and Brownstone, R. (2007). Two-photon calcium imaging of network activity in xfp-expressing neurons in the mouse. *J. Physiol.* 97, 3118–3127. doi: 10.1152/jn.01207.2006

Wooten, M., Weng, H. J., Hartke, T. V., Borzan, J., Klein, A. H., Turnquist, B., et al. (2014). Three functionally distinct classes of c-fibre nociceptors in primates. *Nat. Commun.* 5:4122. doi: 10.1038/ncomms5122

Xu, Y., Zou, P., and Cohen, A. E. (2017). Voltage imaging with genetically encoded indicators. *Curr. Opin. Chem. Biol.* 39, 1–10. doi: 10.1016/j.cbpa.2017.04.005

Yan, X., Li, F., Maixner, D. W., Yadav, R., Gao, M., Ali, M. W., et al. (2019). Interleukin-1β released by microglia initiates the enhanced glutamatergic activity in the spinal dorsal horn during paclitaxel-associated acute pain syndrome. *Glia* 67, 482–497. doi: 10.1002/glia.23557

Yan, X., Yadav, R., Gao, M., and Weng, H. R. (2014). Interleukin-1 beta enhances endocytosis of glial glutamate transporters in the spinal dorsal horn through activating protein kinase c. *Glia* 62, 1093–1109. doi: 10.1002/glia.22665

Yang, K., Ma, R., Wang, Q., Jiang, P., and Li, Y. Q. (2015). Optoactivation of parvalbumin neurons in the spinal dorsal horn evokes gaba release that is regulated by presynaptic gabab receptors. *Neurosci. Lett.* 594, 55–59. doi: 10.1016/j.neulet.2015.03.050

Yang, W., and Yuste, R. (2017). *In vivo* imaging of neural activity. *Nat. Methods* 14, 349–359. doi: 10.1038/nmeth.4230

Yang, Y. M., and Wang, L. Y. (2006). Amplitude and kinetics of action potential-evoked ca2+ current and its efficacy in triggering transmitter release at the developing calyx of held synapse. *J. Neurosci.* 26, 5698–5708. doi: 10.1523/jneurosci.4889-05.2006

Yoshihara, K., Matsuda, T., Kohro, Y., Tozaki-Saitoh, H., Inoue, K., and Tsuda, M. (2018). Astrocytic Ca^{2+} responses in the spinal dorsal horn by noxious stimuli to the skin. *J. Pharmacol. Sci.* 137, 101–104. doi: 10.1016/j.jphs.2018.04.007

Zeisel, A., Hochgerner, H., Lonnerberg, P., Johnsson, A., Memic, F., van der Zwan, J., et al. (2018). Molecular architecture of the mouse nervous system. *Cell* 174, 999.e22–1014.e22. doi: 10.1016/j.cell.2018.06.021

Zemelman, B. V., Nesnas, N., Lee, G. A., and Miesenbock, G. (2003). Photochemical gating of heterologous ion channels: remote control over genetically designated populations of neurons. *Proc. Natl. Acad. Sci. U S A* 100, 1352–1357. doi: 10.1073/pnas.242738899

Zhang, J., Liu, X., Xu, W., Luo, W., Li, M., Chu, F., et al. (2018a). Stretchable transparent electrode arrays for simultaneous electrical and optical interrogation of neural circuits *in vivo*. *Nano Lett.* 18, 2903–2911. doi: 10.1021/acs.nanolett.8b00087

Zhang, Y., Liu, S., Zhang, Y. Q., Goulding, M., Wang, Y. Q., and Ma, Q. (2018b). Timing mechanisms underlying gate control by feedforward inhibition. *Neuron* 99, 941.e4–955.e4. doi: 10.1016/j.neuron.2018.07.026

Zhang, F., Prigge, M., Beyrière, F., Tsunoda, S. P., Mattis, J., Yizhar, O., et al. (2008). Red-shifted optogenetic excitation: a tool for fast neural control derived from volvox carteri. *Nat. Neurosci.* 11, 631–633. doi: 10.1038/nn.2120

Zhang, Z., Russell, L. E., Packer, A. M., Gauld, O. M., and Häusser, M. (2018c). Closed-loop all-optical interrogation of neural circuits *in vivo*. *Nat. Methods* 15, 1037–1040. doi: 10.1038/s41592-018-0183-z

Zito, K., Scheuss, V., Knott, G., Hill, T., and Svoboda, K. (2009). Rapid functional maturation of nascent dendritic spines. *Neuron* 61, 247–258. doi: 10.1016/j.neuron.2008.10.054

Zong, W., Wu, R., Li, M., Hu, Y., Li, Y., Li, J., et al. (2017). Fast high-resolution miniature two-photon microscopy for brain imaging in freely behaving mice. *Nat. Methods* 14, 713–719. doi: 10.1038/nmeth.4305

Zylka, M. J., Rice, F. L., and Anderson, D. J. (2005). Topographically distinct epidermal nociceptive circuits revealed by axonal tracers targeted to mrgprd. *Neuron* 45, 17–25. doi: 10.1016/j.neuron.2004.12.015

Conflict of Interest: The authors declare that the research was conducted in the absence of any commercial or financial relationships that could be construed as a potential conflict of interest.

frontiers in Neural Circuits

ORIGINAL RESEARCH
published: 16 June 2020
doi: 10.3389/fncir.2020.00033

Comprehensive Imaging of Sensory-Evoked Activity of Entire Neurons Within the Awake Developing Brain Using Ultrafast AOD-Based Random-Access Two-Photon Microscopy

Kelly D. R. Sakaki[1], *Kaspar Podgorski*[2], *Tristan A. Dellazizzo Toth*[1], *Patrick Coleman*[1] *and Kurt Haas*[1]*

[1] *Department of Cellular and Physiological Sciences, Djavad Mowafaghian Centre for Brain Health, University of British Columbia, Vancouver, BC, Canada,* [2] *Janelia Research, Ashburn, VA, United States*

Determining how neurons transform synaptic input and encode information in action potential (AP) firing output is required for understanding dendritic integration, neural transforms and encoding. Limitations in the speed of imaging 3D volumes of brain encompassing complex dendritic arbors *in vivo* using conventional galvanometer mirror-based laser-scanning microscopy has hampered fully capturing fluorescent sensors of activity throughout an individual neuron's entire complement of synaptic inputs and somatic APs. To address this problem, we have developed a two-photon microscope that achieves high-speed scanning by employing inertia-free acousto-optic deflectors (AODs) for laser beam positioning, enabling random-access sampling of hundreds to thousands of points-of-interest restricted to a predetermined neuronal structure, avoiding wasted scanning of surrounding extracellular tissue. This system is capable of comprehensive imaging of the activity of single neurons within the intact and awake vertebrate brain. Here, we demonstrate imaging of tectal neurons within the brains of albino *Xenopus laevis* tadpoles labeled using single-cell electroporation for expression of a red space-filling fluorophore to determine dendritic arbor morphology, and either the calcium sensor jGCaMP7s or the glutamate sensor iGluSnFR as indicators of neural activity. Using discrete, point-of-interest scanning we achieve sampling rates of 3 Hz for saturation sampling of entire arbors at 2 μm resolution, 6 Hz for sequentially sampling 3 volumes encompassing the dendritic arbor and soma, and 200–250 Hz for scanning individual planes through the dendritic arbor. This system allows investigations of sensory-evoked information input-output relationships of neurons within the intact and awake brain.

Keywords: comprehensive imaging, random-access, multi-photon, acousto-optics, *in-vivo* calcium imaging, encoding, dendritic integration

OPEN ACCESS

Edited by:
Edward S. Ruthazer, McGill University, Canada

Reviewed by:
Carlos D. Aizenman, Brown University, United States
Laurent Bourdieu, Centre National de la Recherche Scientifique (CNRS), France

***Correspondence:**
Kurt Haas
kurt.haas@ubc.ca

Received: *29 February 2020*
Accepted: *07 May 2020*
Published: *16 June 2020*

Citation:
Sakaki KDR, Podgorski K, Dellazizzo Toth TA, Coleman P and Haas K (2020) Comprehensive Imaging of Sensory-Evoked Activity of Entire Neurons Within the Awake Developing Brain Using Ultrafast AOD-Based Random-Access Two-Photon Microscopy. Front. Neural Circuits 14:33. doi: 10.3389/fncir.2020.00033

INTRODUCTION

Neurons within brain circuits receive inputs from hundreds to thousands of upstream neurons at synaptic contacts distributed across their elaborate dendritic arbors. Information received in synaptic currents is integrated within dendrites and transformed into neural output encoded in action potential (AP) firing at the soma, which is then transmitted via the axon to downstream targets. Information carried by neural activity can be deciphered by tracking synaptic events or APs evoked by controlled sensory stimuli in awake animals. However, our understanding of neural information processing and encoding is limited due to technical challenges in simultaneously tracking activity throughout complex three dimensional (3D) dendritic arbor structures and the soma, which is needed to establish full input-output relationships.

Approaches to this problem have been aided by the development of fluorescent sensors of neural activity, particularly those capable of detecting rapid changes in intracellular free calcium. Neurons tightly control the transmembrane calcium gradient with intracellular concentrations being on the order of 10,000 times lower than extracellular levels (Gleichmann and Mattson, 2013). Synaptic and AP activity evoke distinct spatiotemporal elevations in intracellular calcium (reviewed in Sabatini et al., 2002; Redmond and Ghosh, 2005). Excitatory, glutamatergic synaptic transmission induces calcium influx by activation of calcium-permeable N-Methyl-D-aspartate (NMDA) and GluA2 subunit-lacking α-amino-3-hydroxy-5-methyl-4-isoxazolepropionic acid (AMPA) subtypes of glutamate receptors (Burnashev et al., 1992), and secondary opening of voltage-gated calcium channels (Sabatini and Svoboda, 2000; Cowan et al., 2001; Oertner and Svoboda, 2002; Sabatini et al., 2002). Transients within the soma from voltage-gated calcium channels are also triggered by AP-mediated depolarization (Nakai et al., 2001; Chen et al., 2013; Gleichmann and Mattson, 2013). Thus, calcium transients can be imaged as a proxy for neural activity using calcium-sensitive fluorescent dyes or genetically-encoded calcium indicators (GECIs) (Nakai et al., 2001; Rose et al., 2014), such as the family of engineered GCaMPs (Chen et al., 2013). These indicators inherently slow neural activity signals due to their calcium binding kinetics (Nakai et al., 2001; Chen et al., 2013), but require sampling rates on the order of milliseconds to adequately measure transient rise times and signal intensity (Katona et al., 2011), and seconds for decay times (Chen et al., 2013; Sun et al., 2013). An alternative strategy for detecting synaptic input has been the development of sensors of neurotransmitters. For sensing glutamate, the genetically encoded protein iGluSnFR can be expressed on the surface of neurons and increases fluorescence upon binding to pre-synaptically-released glutamate (Marvin et al., 2013, 2018).

In order to fully capture a neuron's synaptic and AP neural activity within the intact brain one must image the complex 3D dendritic arbor morphology and soma relatively deep within light-scattering brain tissue at sample rates sufficiently fast to track activity. Conventional two-photon laser scanning microscopy (TPLSM) systems achieve deep imaging up to 600–800 μm into brain through use of long-wavelength excitation light which can penetrate further into the brain than wavelengths used for single-photon absorption in confocal microscopy (Denk et al., 1994; Svoboda et al., 1997). However, the most significant obstacles of conventional TPLSM systems in achieving full imaging of brain neuronal activity is their slow rate of 3D-volume imaging. Inertia-induced latencies are incurred by the galvanometer mirrors used to deflect the laser between imaging points. Conventional systems image brain neurons (e.g., within volumes of 100 μm^3) using numerous sequences of line-scans (i.e., "rastering") to image a single 2D X-Y image-plane. Repeating this 2D sampling at multiple incremental steps throughout the Z-axis is employed to fully capture the 3D-volume encompassing the neuron's cell body and dendritic arbor. Although conducting line-scans using galvanometer mirror-based systems is relatively fast between two points of interest (POIs) on one X-Y plane, requiring only single-axis transitions, scanning rates slow dramatically as the number of non-linear POIs increase due to multiple X-, and Y-axis transitions. For example, imaging two points on a 10-μm line on the same plane can achieve scanning rates of 1 attainable reduces to 20 Hz, yet decreases to 1 Hz or slower when the points are spread over an area of 100 μm^2. Thus, imaging a 3D volume of 100 μm^3, with 1 μm interval steps per plane on the Z-axis (i.e., 100 X-Y image planes) requires in excess of 100 s per cycle to complete, which is significantly below the rate required for tracking neural activity using calcium biosensors. Critically, the vast majority of sample time conducted by such conventional TPLSM volume imaging of brain neurons is wasted since the structure of neurons comprises a small fraction of the image space. Since neuronal morphology is comprised of long, thin and often highly branched dendrites, the majority of the 3D volume is composed of irrelevant unlabeled extracellular tissue surrounding the target neuron.

Significant recent advances in microscopy have improved the spatial and temporal sampling rates of conventional imaging systems, which have been critical steps toward achieving comprehensive imaging of brain neurons. To increase the ability to change focal depths piezo-actuators have been employed, such as driving the actuator with a sinusoidal voltage, to produce rapid mechanical oscillation of the microscope objective (Göbel et al., 2007). Combined with galvanometer mirror control of the focal point in the X-Y plane, such systems proved capable of capturing somatic calcium transients from a volume containing several hundred cell neurons at 10 Hz. Incremental increases in imaging speeds can be achieved by replacing X-Y rastering with a faster spiral scan pattern, or restricting imaging areas to pre-defined areas containing neuronal elements. Further improvements were achieved by synchronizing the X-Y positioning by the galvanometer mirror with the Z-axis oscillatory motion of a piezo-actuator to scan 3D neuron structures (Katona et al., 2011).

Significantly increased rates of imaging complex 3D neuronal structures have been achieved using "random-access" sampling, which allows discrete POI sampling, and scanning multiple POIs in 2- or 3D without scanning the intervening space between them (**Figure 1**). Random access microscopy takes

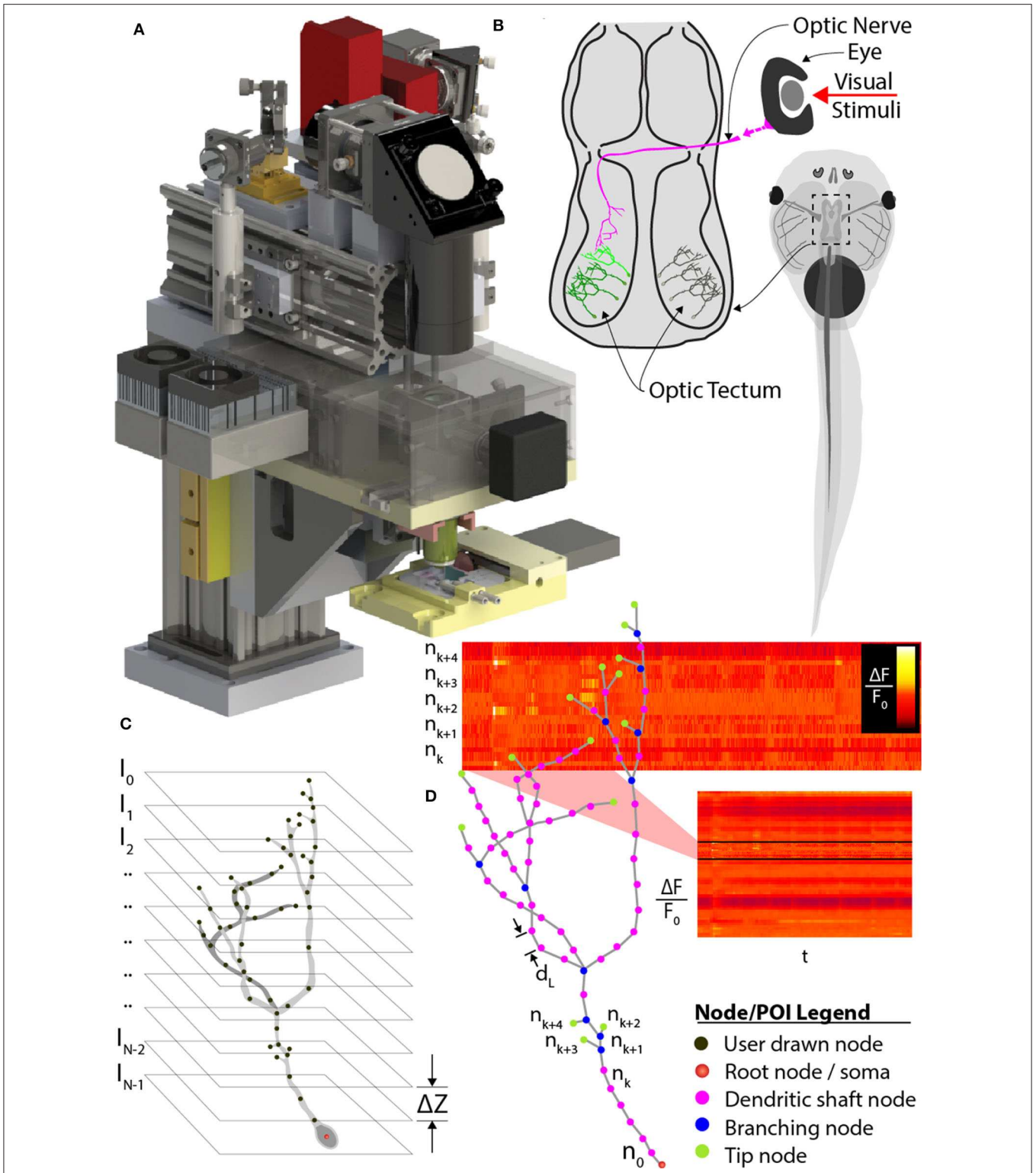

FIGURE 1 | Comprehensive imaging. **(A)** The random-access, two-photon laser-scanning system used to analyze neuron morphology and functional activity. **(B)** Schematic of *Xenopus* tadpole brain visual circuit showing tectal neurons targets (green) for comprehensive imaging *in vivo*. Neurons are labeled with a space-filling fluorophore to capture morphology and a calcium indicator to monitor activity. Neuronal morphology is first determined using a stack of 2D planes encompassing the entire neuron. **(C)** Next, the user traces the 3D dendritic arbor of the neuron, from which points-of-interest (POI) along the entire dendritic arbor and cell body are converted to a 3D tree-structure relationship, and **(D)** automatically interpolated at 2 μm intervals. A "rapid-scan" executes a routine employing AOD-based random-access imaging to simultaneously sample the interpolated POIs to record the AP and all synaptic activity across the neuron.

advantage of acousto-optic deflectors (AODs) in place of galvanometer mirrors (Bullen and Saggau, 1997, 1999; Iyer et al., 2005; Salomé et al., 2006; Reddy et al., 2008; Grewe et al., 2010; Katona et al., 2012; Nadella et al., 2016; Szalay et al., 2016). Soundwave-mediated changes in the AOD crystal refractive index acts as a diffraction grating to refract the path of the laser, producing a rapid, inertia-free laser position transition system. Systems using pairs of AODs can achieve kHz-rate sampling in X-Y planes for both one- and two-photon imaging (Bullen and Saggau, 1997, 1999; Iyer et al., 2005; Salomé et al., 2006), and two pairs of AODs can be used for X-Y and Z-axes transitions (Reddy et al., 2008; Katona et al., 2012; Nadella et al., 2016; Szalay et al., 2016). AODs have also been recently applied as laser beam shapers, which could serve systems that require very fast wavefront control (Akemann et al., 2015). AOD-based microscopy has been applied to imaging multiple dendrites and the soma of individual neurons *in vivo* in rodents (Szalay et al., 2016). Fast imaging of cubes or rectangular volumes encompassing the target neuronal compartments was used to compensate for the motion artifacts inherent in mammalian models due to blood flow and respiration. Other approaches incorporate remote focusing to speed Z-axis positioning enabling line-scanning *in vivo* within a volume spanning over two hundred microns (Nadella et al., 2016).

However, application of fast-scanning technologies for comprehensive imaging of fluorescent indicators of sensory-evoked neural activity across an entire neuron *in vivo* remains a challenge. Here, we approached this problem by designing a random-access AOD-based TPLSM system with a variable-speed piezo-actuator system for Z-axis focus, combined with *a priori* determination of the neuronal structure to direct the image path, as well as by selecting a model system with minimal drift and brain neurons with relatively small dendritic arbors. We have selected the albino *Xenopus laevis* tadpole as a model system since they are readily immobilized under awake conditions, and their transparency allows direct visualization of neurons without the brain tissue movement intrinsic to mammals. We fluorescently label tadpole brain neurons using *in vivo* single-cell electroporation to transfect neurons with space-filling fluorophores or biosensors of activity (Haas et al., 2001). Our approach involves first imaging the brain volume encompassing a target neuron using serial sectioning (**Figure 1C**), and then creating a schematic rending of the soma and dendritic arbor to provide the *a priori* knowledge of the full 3D neuronal structure to direct discrete fast random-access sampling (**Figure 1D**). This *a priori* structure must be determined for each neuron imaged, since individual brain neurons have unique patterns of dendritic branches extending in non-uniform paths (Haas et al., 2006; Chen et al., 2010; Romand et al., 2011; Hossain et al., 2012). We provide examples for application of our AOD-based random access TPLSM system for imaging of visual-evoked neural activity of individual brain neurons within the optic tectum of awake, immobilized tadpoles. We describe the software driving this microscope and alternative modes of sampling neural activity to optimize coverage or sample rate.

METHODS

AOD-Based Random-Access Microscope Optical Train

The optical train (**Figure 2**) of the random-access system achieves high-throughput POI scanning as well as volume imaging (i.e., multiple X-Y images within a volume region) by using a piezo-actuator, for Z-axis motion, and two AODs to provide *X*-, *Y*-axis scanning. In combination, this allows for sampling at any possible scan points in three dimensions. In our system, the X and Y axes were scanned using two wide-scan angle AODs, $AOD_{1,2}$ (OAD1121-XY deflector / DA104-2 power driver, Isomet) for NIR with a scan angle of 5.4 degrees, an T_{ACC} of 13 μs, 40 MHz bandwidth and 9 mm apertures. Transitioning between any two points on the image plane using the AODs executes at rates up to 100 kHz. A Ti:Sapphire laser (Chameleon Vision II, Coherent), with tuned, temporal-dispersion compensation, provides femtosecond pulses and enters the preprocessing optical train through a dichroic mirror D_1 (T660LPXR-UF2, Chroma) and overfilling the back-aperture of a water immersion objective (60X, 1.1 NA, 0.150 kg, LUMPL, Olympus). The objective is mounted on a piezo-actuator (PA_1, QNP-250-250L, 250 μm range, 1 kg maximum payload, Aerotech Inc.) to adjust the focal plane.

The fluorescent light emitted from the sample returns through the objective and exits from the back aperture pupil, reflects off D_1 and is then filtered through a shortpass filter (SPF_1, 700SP-2P, Chroma) to prevent stray laser emissions. The emitted and collimated light is focused using the relay lens L_5, and then separated into green and red wavelengths by a dichroic mirror, D_2 (565LPXR, Chroma). The green channel, to measure the jGCaMP7s signal, is filtered using a bandpass emission filter (EF_1, ET525/50m-2P, Chroma) and red channel is filtered using a bandpass emission filter (EF_2, ET620/60m-2P (Chroma). The emitted light from each channel passes through the relay lenses, L_6 and $L_{7,8}$, to fit through the apertures of the GaAsP photo-multiplier tubes (H7422-40, Hamamatsu). The PMT signals are amplified using low-noise current amplifiers (SR570, Stanford Research Systems). The signal output of the amplifier was acquired using a 12-bit analog input (PCI-6110 DAQ; National Instruments), at a rate of 2.5 MHz.

Piezo-Actuator and POI-Based Trajectory

The primary role of the Z-axis actuator for comprehensive imaging is to move the focal plane of the objective to each POI between $[Z_{min}, Z_{max}]$ on the interpolated neuron in 3D space (**Figure 3A**). Piezo-actuators are capable of large accelerations with heavy loads over relatively large distances and can provide sub-micrometer repeatability. For these reasons, a piezo-actuator was used to provide stable position-control for planned, POI trajectories during the *RS*. In contrast with certain previous fast-scanning approaches in which a piezo-actuator was used to adjust the focal plane through employing a sinusoidal vibration of the objective for the purposes of sampling a populations of multiple neurons (Göbel et al., 2007), we chose to implement a unique single "sweep" trajectory for each neuron. This method was chosen because of the non-uniform distribution of POIs on the

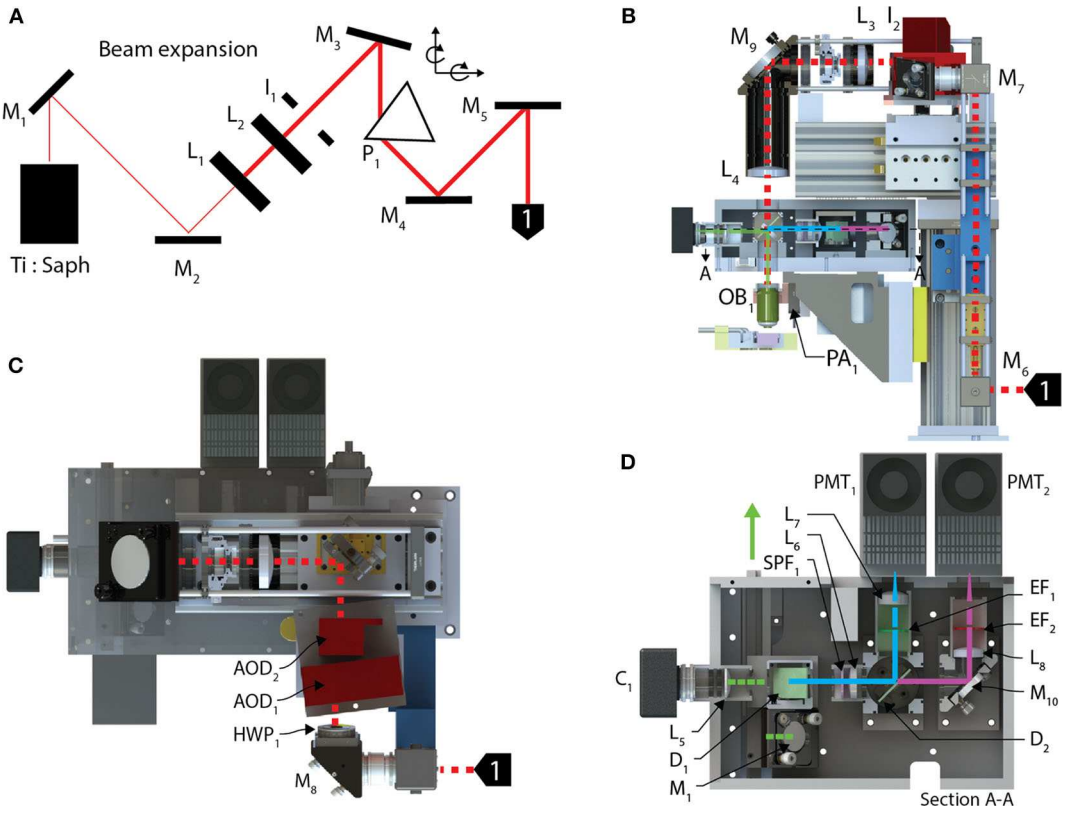

FIGURE 2 | Optical train and the stimulation module. **(A)** The pre-processing optical train for the AOD TPLSM undergoes 4X beam expansion and is passed through a prism used to spatially compensate for the dispersion created in the acousto-optic deflectors deflecting the beam into the back aperture of a 60X objective. **(B)** The beam enters the optical train of the AOD-TPLSM, passes through **(C)** two AODs orientated 90 degrees with respect to each other and provides X-Y scanning. Two lenses collimate the laser at the pupil of the back aperture of the microscope objective. The fluorescence light returns through the objective and **(D)** enters the post-processing optics by reflecting off a dichroic mirror. The emission path on the AOD-TPLSM is split between two channels using a short-pass dichroic mirror. Channel 1, filtered green emissions, and Channel 2 captures red emissions. Calcium transients were observed using jGCaMP7s on the Channel 1. The fluorescence light is detected by a PMT dedicated to each channel.

Z-axis due to unique and sporadic patterns of dendrite branching of each brain neuron's dendritic arbor. Our routine calculates the required trajectory to scan all POIs using a monotonically increasing path from Z_{min} to Z_{max} (Z-axis distance encapsulating all of the POIs) varying the position of the piezo-actuator to adjust the focal plane. The duration of the trajectory is based on the mechanical limitations (maximum velocity and acceleration) of the piezo-actuator and the required time the focal plane should exist at any particular position on the Z-axis to scan one or more POIs.

AODs and High Speed POI Scanning

AODs are "solid-state" devices that can provide random-access control of laser beam positioning at high speeds and have negligible fly-back delay in comparison to scan mirrors. The "laser-scanning" mechanism of an AOD consists of passing a soundwave through a piezoelectric transducer coupled to a crystal (e.g., TeO_2). Controlled changes in the piezoelectric modulate the crystal causing contractions and rarefactions in the substrate resulting in periodic changes in the refractive index similar to a diffraction grating, to refract the path of the laser. The deflection angle of the AODs, θ_{scan}, can be modulated using the following relation,

$$\theta_{scan} = \frac{\lambda f_{mod}}{v}$$

where λ is the wavelength of the laser, and f_{mod}, is the modulating frequency passing through the AOD crystal and v is the intrinsic, acoustic velocity of the material. The rate of change of the AOD is limited to the "access time," T_{ACC}, the time for the radio-frequency wave to propagate completely through the beam waist of the laser in the AOD deflecting the path of the laser to a different angle. T_{ACC} is defined as,

$$T_{ACC} = \frac{\varnothing_L}{v}$$

where $\varnothing_L$ is the laser beam diameter.

POI Scan

Each POI scan (**Figure 3B**) consists of a short line scan of 11 pixels, and 5 samples per pixel. The 5 measurement samples

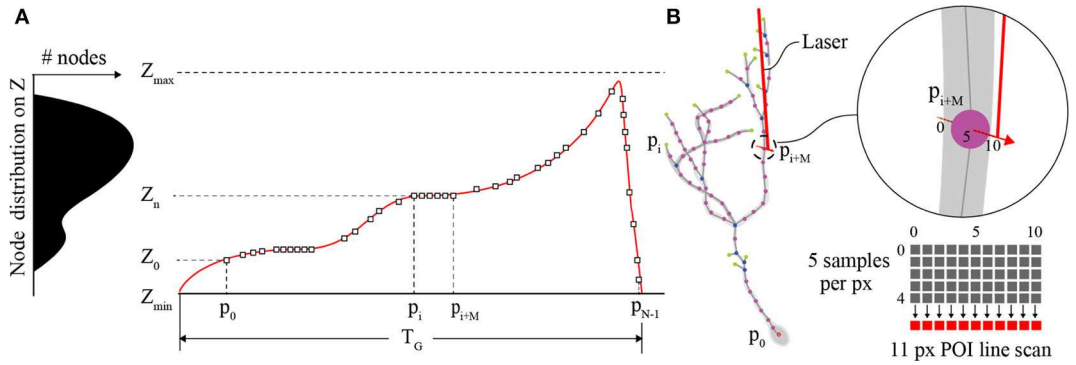

FIGURE 3 | POI distribution and Z-actuator schedule and trajectory. **(A)** A typical distribution of POIs in a tectal neuron and the scanning schedule of POIs synchronizing the activity of the Z-actuator and the AODs. **(B)** An illustration of the neuron structure representing the POIs scanned in A, and an example of three generic POIs on the neuron in 3D space and how they relate to a possible Z-stage trajectory planned for scanning and synchronization with the AODs (inset). The "short" line scan of each POI is created in image space using 11 pixels. The center pixel exists at the location of the POI and each pixel is created from 5 summed samples of the PMT output.

per pixel site are summed, and the combined intensity $I(k)$ is then mapped to image space $I(x,y)$. This is done to account for the spatial drift and noise that is inherent in *in vivo* imaging experiments. The minimum time required to scan a POI is defined by the following sum,

$$T_{POI} = T_{Buffer} + T_{ACC} + T_{SCAN}$$

where T_{BUFFER} is the time required between samples and T_{SCAN} is the time for the AODs to scan from f_0 to f_1 shifting the path of the laser. The maximum allowable velocity of the piezo actuator, V_{Z_MAX}, is constrained by T_{POI} where a required tolerance, d_{TOL}, is defined to ensure the laser excites the coordinates of the POI to capture the fluorescent signal. V_{Z_MAX}, is defined as follows,

$$V_{Z\_MAX} = \frac{2d_{TOL}}{T_{POI}}$$

AOD POI Laser Deflection Programming

The relationship between image space coordinates and the AOD frequency input converts image POI coordinates to AOD instructions, which control the random-access, laser excitation position on the focal plane. Image space coordinates (i.e., locations of the POIs) are converted to AOD frequencies using the following,

$$\begin{bmatrix} f_0 \\ f_1 \end{bmatrix} = \begin{bmatrix} \frac{f_{max} - f_{min}}{f_{BW}} \end{bmatrix} \begin{bmatrix} u_0 - \frac{L_{POI}}{2} - 0.5 \\ u_1 + \frac{L_{POI}}{2} + 0.5 \end{bmatrix} + \begin{bmatrix} f_{min} \end{bmatrix}$$

where each pair of frequency instructions $\langle f_0, f_1 \rangle$, commands the AODs to execute a swept range from f_0 to f_1, between the minimum frequency of the AOD, f_{min} to the maximum frequency, f_{max}. The swept range represents a short line scan and directs the laser through the POI on the arbor of the neuron to excite fluorophores and capture the resulting fluorescence light sample, $I(k)$. u_0 is the start of the line scan and u_1 is the end of the line scan in image space. L_{POI} is the length of the line scan, 11 pixels in image space. Since AODs are mounted orthogonally with-respect-to each other, duplicate coordinate pairs are sent to each other resulting in a diagonal sweep across the imaged points u_0, u_1, in the X-Y plane.

Piezo-Actuator and AOD Synchronization

The position of the piezo-actuator and deflection angle of the AOD are synchronized to coordinate the laser focal point on the neuron's dendritic arbor and cell body in 3D space to excite the fluorophores and detect the fluorescence emissions (**Figure 4**). This is achieved by acquiring a template sweep trajectory scan (prior to executing the *RS*) and scheduling each frequency pair instruction (i.e., X-Y-position of the laser on the focal plane) according to the time of the known position of the piezo-actuator (i.e., Z-position of the focal plane). The template scan is generated by executing the planned trajectory repeatedly over a 4 s interval providing a recorded output of the piezo-actuator position feedback. Using the position feedback, an AOD start-pulse signal schedule is generated for each frequency pair. Each start-pulse synchronizes the start of the frequency pair instruction in the AODs with the position of the piezo-actuator to ensure each 11-pixel line scan crosses through each POI.

System Requirements

We experimentally determined the key temporal and spatial system requirements using image sampling of neural activity evoked by visual stimuli in the developing brain of the *Xenopus laevis* tadpole (**Figure 1B**). Baseline measurements were conducted on a conventional galvanomirror-based TPLSM (custom-designed, modified Olympus BX61, running Olympus Fluoview 1000).

Temporal Sampling Considerations

Four temporal measurements were required in order to determine temporal scanning rates necessary to sample brain neuron synaptic and AP activity. These included:

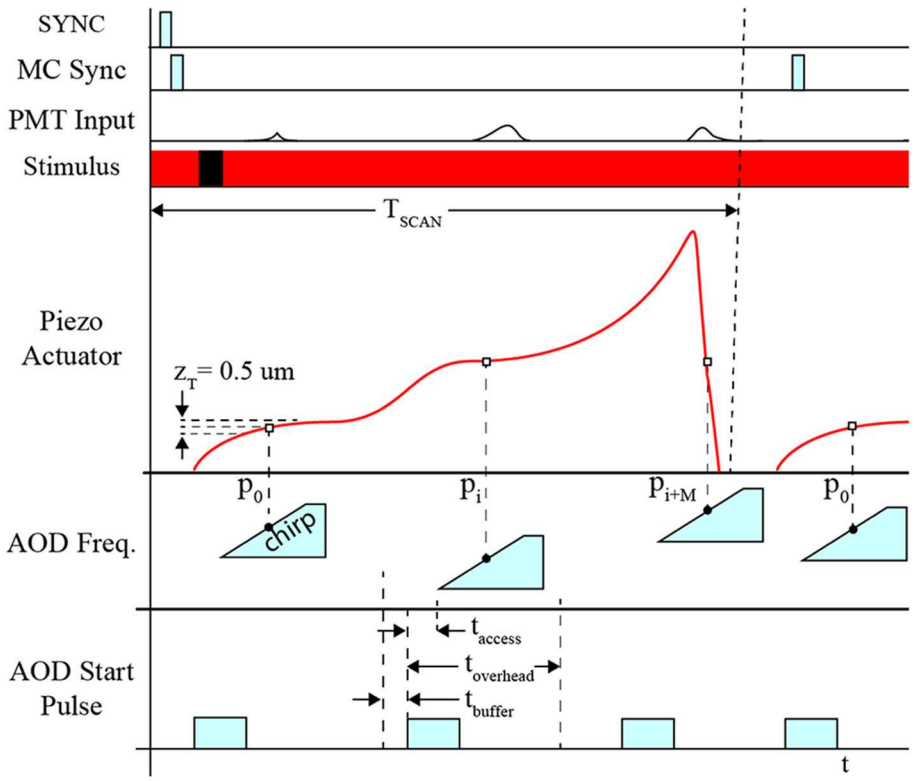

FIGURE 4 | Timing diagram for system synchronization. Synchronization between devices is coordinated using the sample clock signal, T_{CLK}. Initially, the start signal (*START*) is activated indicating the beginning of the measurement sequence. All PMT channels initiate recording and AOD "chirps," which are responsible for deflecting the path of the laser for line scans for F3D or FS measurement sequences. The Z-stage command signal, *CMD-Z*, begins after *START*, and feedback is recorded providing an absolute comparison between the desired position and actual position measured.

1) $\overline{\tau_{Delay}}$; the average delay time between the beginning of the visual stimuli and the peak amplitude of the evoked intracellular calcium transient response,
2) $\overline{\tau_R}$ and $\overline{\tau_F}$; the mean time constants of the rising and falling times of the calcium transients;
3) $\overline{f_{\max}}$; the frequency bandwidth of the evoked, calcium signals.

When initially designing our random-access TPLSM system, we calculated the temporal sampling considerations based on the 6th generation GCaMPs that were at the time, the latest publicly available. We experimentally obtained the temporal data of the system from neurons expressing GCaMP6m in the optic tectum of head-mounted tadpoles. Calcium transients in dendrites and the soma were evoked by light stimuli produced by an LED. We subjected the tadpoles to repeated 50 ms OFF square pulses presented at 8–10 s intervals. Evoked responses were sampled at five locations on the neuron's dendritic arbor and at the soma. Averaged responses from 4 OFF events were used to determine the delay between stimulus onset and event peak ($\overline{\tau_{Delay}}$) as well as the parameters for the temporal rise to peak ($\overline{\tau_R}$) and fall to the baseline ($\overline{\tau_F}$). $\overline{\tau_{Delay}}$, $\overline{\tau_R}$ and $\overline{\tau_F}$ were recorded experimentally as 0.404, 0.237, and 2.907 s, respectively (**Figure 5A**).

A Fast Fourier Transform (FFT) was then applied to each time-domain signal to acquire the frequency domain response. The average of all FFTs (**Figure 5B**) indicated most of the signals existed around 3 Hz. Thus the Nyquist sampling rate, f_{Nyq}, during comprehensive imaging should be at least 6 Hz. Subsequent to the release of the 7th generation of GCaMPs we switched to using jGCaMP7s, which has both superior sensitivity and a slower decay rate then the 6th generation GCaMPs (dal Maschio et al., 2012; Dana et al., 2019). This allows for a potentially slower Nyquist sampling rate than previously calculated. When advanced spike deconvolution methods are required to achieve millisecond-precision on spike timings (Deneux et al., 2016), the faster planar scans are recommended due to the 200 Hz time resolution, and faster indicators such as jGCaMP7f can be used.

Spatial Sampling Considerations

The requirement to capture POIs distributed across an entire neuron within the intact and awake brain requires imaging a large enough field-of-view to encompass the entire 3D dendritic arbor and the cell body over long periods. The minimum POI spatial resolution (d_L) along the dendritic arbor is experiment-dependent and limited by scanning speed; however, should be $<5\,\mu m$ to identify neuronal subcompartments (Biess et al., 2011) and to saturate the domains of calcium transients allowing us to discriminate individual events. Thus, the optical resolution is required to be $<2.5\,\mu m$ to satisfy the Nyquist spatial sampling requirement.

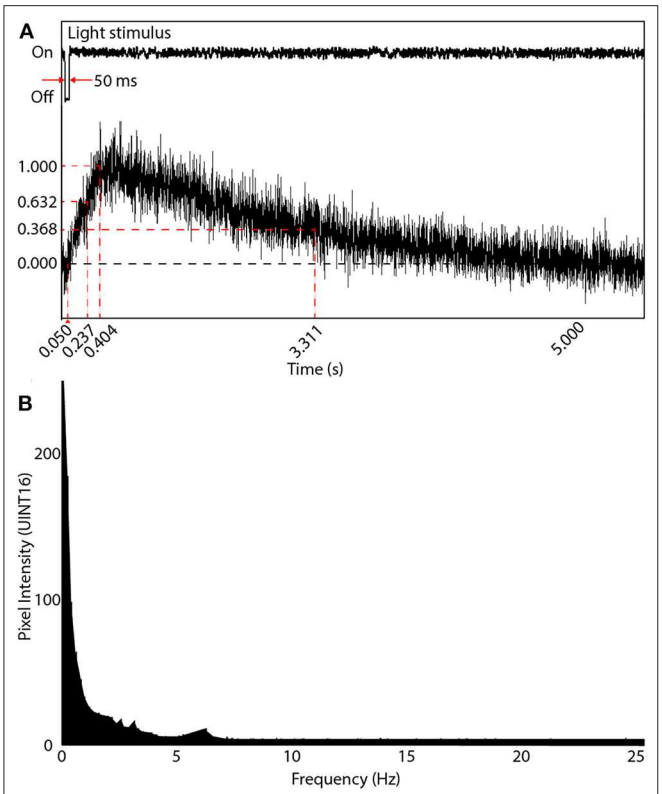

FIGURE 5 | Visual-evoked calcium responses in a brain neuron using GCaMP6m. **(A)** A line scan of the neuron's soma was acquired at 1,000 Hz showing the evoked response following a 50 ms light OFF stimulus. The maximum intensity peak was 0.404 s after the OFF pulse. The rise time parameter (at intensity 1-1/e of peak) was measured 0.237 s after the OFF pulse, and the decay time parameter (intensity 1/e of peak) occurred 2.907 s after the peak of the signal rising transient. **(B)** Frequency response of **(A)** after applying the Fourier transform. Most information is in the very low frequency range (under 2 Hz), with diminishing power until 7 Hz, and noise thereafter.

Temporal and Spatial Scanning Limitations

The temporal and spatial scanning limitations define the rates for the minimum scanning frequency, f_{Nyq}, required for calcium imaging. This rate will vary based on the number of POIs, N_{POI}, on each unique neuron arbor and is a function of the total dendritic branch length, L_T and the spatial resolution, d_L. The minimum POI scanning frequency, f_s, required can be calculated as follows,

$$f_s \geq 2f_{Nyq}$$

$$f_{Nyq} = \left(N_{POI} \cdot T_{POI_{SCAN}}\right)^{-1} \approx \left(\frac{L_T}{d_L} \cdot T_{POI_{SCAN}}\right)^{-1}$$

$$f_s \geq 2\left(\frac{L_T}{d_L} \cdot T_{POI_{SCAN}}\right)^{-1}$$

where $T_{POI_{SCAN}}$ is the time required for the system to scan one POI.

Microscope Driver Software Design

One of the overarching goals for our random-access TPLSM system design was to create a modular and flexible architecture. We believed that by partitioning the system's responsibilities and by maintaining a loosely coupled design, we would greatly simplify and expedite system modifications in response to future needs or technological innovations. For this reason, the system was designed using the Actor Framework (AF) concept (Hewitt et al., 1973), which supports implementing large, queued-message handler systems. The system was implemented using object-oriented design/programming for the AF [e.g., National Instruments LabVIEW (Kerry, 2012)], and allows for scalability and easier maintenance as the system expands over time. In general, the AF subdivides the system routines into "actors" or primitives that respond to messages from other actors and execute local routines with a minimal amount of overhead. By keeping routines fast, this avoids long synchronous processing, which enables asynchronous event-based processing that can require precise timings.

Graphical User Interfaces

Interactions between the operator and the system are facilitated through a measurement user interface (i.e., "*Msmt. UI*", **Figure 6A**), and the Cell Trace and Analysis Kit user interface (i.e., "*CTAK UI*", **Figure 6B**) to define experiments (i.e., individual or sequential sets of measurements) and draw the 3D neuron morphologies for experiments. These interfaces provide access to hardware parameters, and experiment design/post-processing tools respectively.

The *Msmt. UI* allows the operator to design scanning experiments, and set parameters required by the hardware peripherals. Experimental measurements (e.g., type of scan and number of repetitions of each type of scan) are arranged in order of execution, defined by the operator, and stored as an instance of the "*Experiment*" class. Each *Msmt.* in the *Experiment* executes the following sequence of overridden methods:

1. *Initialize*: preliminary settings for the measurement
2. *Configure*: requests resources to execute the measurement
3. *Acquire*: records the data from the input channel(s)
4. *Measure*: performs calculations using the raw data
5. *Close*: Releases resources held during the acquisition stage and signals completion.

The *CTAK UI* acquires operator input during experiments and provides a visual display of the results of each *Msmt.* During experiments, the operator can draw/modify the spatial organization of the POIs defining the neuron's dendritic arbor. This 3D structure is stored within an instance of the *Neuron* class and relates the spatial information, such as the locations of each POI, to the synaptic/AP patterns of activity recorded during comprehensive imaging (**Figure 1D**). The *Neuron* class is a descendant of the *Tree* class and stores POIs as a conventional tree structure comprised of a doubly linked list of *Branch Node* objects.

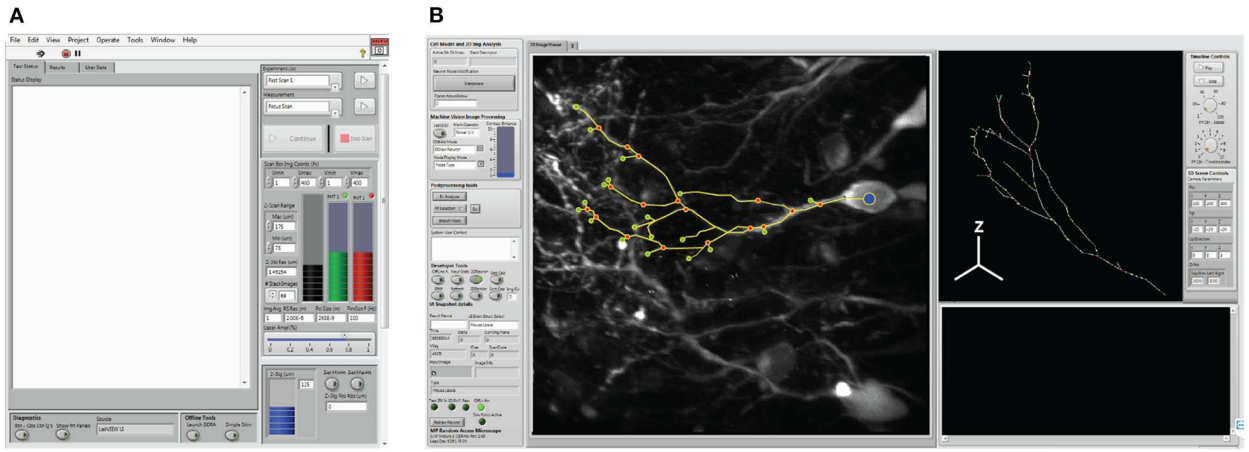

FIGURE 6 | System user interfaces. **(A)** The measurement user interface (i.e., *Msmt. UI*) provides user access for hardware selection, and experimental design. **(B)** The cell trace and analysis toolkit user interface (*CTAK UI*) serves as an interface for drawing the initial 3D structure of the neuron, correcting minor positional errors following scans, and for post-analysis following either the *F3DS* or *FSS* routines.

Proposed Event Sequence for Comprehensive Imaging

Our system separates comprehensive imaging of brain neurons into a sequence of pre-defined *Msmts*. executed by the system actors. These measurements are designed to be composable, extendable steps, and those available with the system are illustrated in **Figure 7**. An initialization routine begins by executing a focus-scan (*FS,* **Figure 7A**), a repeating X-Y scan allowing the operator to adjust the X, Y or Z-position of the specimen and set the imaging volume-boundaries encapsulating the neuron. These boundaries define the maximum limits to all scanning routines acquired during the experiment. A full 3D scan (*F3DS,* **Figure 7B**) is acquired and consists of a stack of N_{IMG} images with a resolution of $S_X \times S_Y$ pixels and separation distance, Z_{INT}. This first *F3DS* provides the operator a representation of the neuron's 3D arbor on X-Y image planes. In **Figure 7C**, an illustration of one X-Y image in the stack shows the acquired cross-section of the neuron residing on one image plane.

The stack of X-Y image planes allow the operator to manually trace the neuron's full dendritic arbor and cell body in the *CTAK UI*, creating a skeletonized, 3D-frame (**Figures 1C**, **7D**). The initial 3D-frame defines key registration points along each branch on the neuron. The initial drawing of the neuron typically requires approximately 15 min. Given the delay following the conclusion of the operator tracing the neuron, a second *F3DS* routine is executed to provide minor adjustments to the position of the neuron on X, Y, and Z-axes to account for sample drift. Further ancillary *F3DS's* are employed typically at 10 min intervals throughout the experiment to detect and accommodate growth or position drift. Following the second *F3DS*, the operator-drawn, skeletonized, neuron is linearly interpolated along the dendritic arbor at an operator-selected resolution (e.g., 2 μm spacing) in 3D-scanned space defining the location of the POIs intended for scanning (**Figure 7E**).

The rapid scan (*RS,* **Figure 7F***)* is the comprehensive, 3D scan used to acquire the synaptic activity and AP firing information along the arbor and cell body of the neuron at all of the POIs on the neuron. The *RS* is initiated concurrently with the visual stimulation routine. During the visual stimulation routine, stimuli are presented to the eye contralateral to the optic tectum containing the neuron. While the stimuli are being presented to the eye, functional activity is acquired. At the end of the stimulation sequence, a focus-and-shift routine (*FSS,* **Figure 7G**) is executed to accommodate minor shifts with respect to the expected position of the cell body. A *F3DS* is then acquired and the operator can adjust either the location of individual POIs or the location of the entire neuron if required. This sequential set of measurements, (*RS*, *FSS*, and *F3DS)* and the visual stimulation routine continues as scheduled in *Experiment*.

Rapid Scanning Scheme

To achieve comprehensive analysis of the entire neuron, the system requires a scanning routine to sample all POIs and minimize the period, $\mathbf{T_G}$, between POIs. Sufficiently fast sampling rates are required to detect the fast calcium transients mediated by synaptic activity throughout the expanse of the dendritic arbor and APs in the soma. Scanning routines must take into account that dendritic arbor morphologies are complex and the POIs along the arbor have a non-uniform spatial distribution along the Z-axis. Fully imaging a neuron's entire set of POIs requires rapidly repositioning the relatively heavy microscope objective from focal plane-to-focal plane, and coordinating the AOD laser-deflection angle with the position of the focal plane in order to capture all POI in each plane.

System Validation

Comprehensive imaging of sensory-evoked calcium activity in a visual stimulus processing neuron in the brain of the

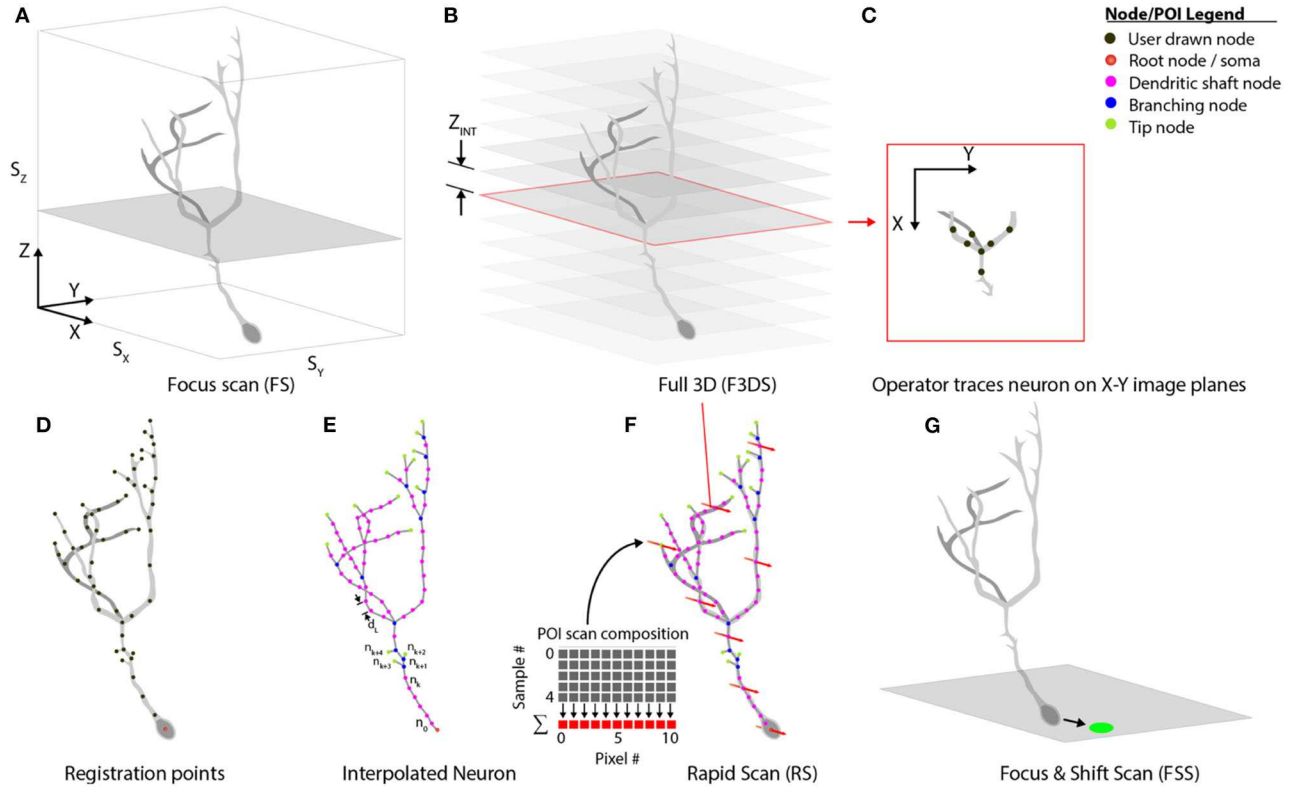

FIGURE 7 | Scan class hierarchy and scan types. **(A)** The focus scan (*FS*) allows the operator to adjust the position of the neuron in 3D-space, and defines the boundaries during scanning. **(B)** The Full 3D scan (*F3DS*) images the volume defined in the *FS* at an interval along the Z-axis, Z_{INT}, which is defined by the operator. **(C)** After the *F3DS* is acquired, the operator traces the neuron on each X-Y image planes forming a **(D)** skeletonized frame of the neuron in 3D space. **(E)** The registration points, drawn by the operator, are then linearly interpolated over the entire arbor using a spatial separation distance of d_L. **(F)** The POIs are scheduled for scanning and the volume rapid scan (*V-RS*) is executed scanning all interpolated POIs at calcium imaging rates. **(G)** Following the RS, the user has an opportunity to make adjustments to the position of the neuron in 3D space to account for minor position shifts.

awake albino *Xenopus laevis* tadpole was used to validate this new microscope system. This model animal was selected due to its transparency, which allows direct imaging of brain neurons in awake and immobilized specimens. Moreover, the external development of tadpoles permits imaging of early vertebrate brain developmental events that typically occur in the womb in mammals (Sin et al., 2002; Ruthazer and Aizenman, 2010). Development of the tadpole visual system has been extensively studied (Engert et al., 2002; Sin et al., 2002; Dunfield and Haas, 2009; Li et al., 2011). The experimental routine in **Figure 8**, for system validation, was used to identify a tectal neuron's dendritic arbor morphology and observe the functional activity in response to a controlled, visual stimuli paradigm (Dunfield and Haas, 2009). The first epoch consists of 8 measurement cycles of the rapid-scan, N_{RS}, with each cycle presenting 9 stimuli−−4 light-off pulses (OFF) on a bright background, a gradual transition shift from a bright background to a dark background and 4 light-on pulses (ON) on opposing background. A simplified variation of this routine removing the ON pulses and the gradual transition shift and instead having 9 OFF pulses on a bright background was subsequently created.

Xenopus laevis Preparation

Freely swimming albino *Xenopus laevis* tadpoles were reared and maintained in 10% Steinberg's solution (Dunfield and Haas, 2009). In order to transfect brain neurons for expression of calcium sensors we used single-cell electroporation of plasmid DNA (Haas et al., 2001). Seven days post-fertilization, tadpoles were anesthetized using 0.01% solution of MS-222 (A5040-25G, Sigma-Aldrich). A borosilicate micropipette (BF150-75-10, Sutter Inc.) pulled on a micropipette puller (P-97, Sutter Inc.) was backfilled with a solution containing 3 μg/μL plasmid DNA encoding the a green calcium-sensitive fluorophore, jGCaMP7s and a red space-filling fluorophore mCyRFP in calcium-free, ringers solution (in mM: 116 NaCl, 1.2 KCl, 2.7 $NaHCO_3$). The filled micropipette was then inserted into the optic tectum of the tadpole and an Axon 800A Electroporator delivered a train of voltage pulses to induce electroporative transfection. Prior to experimentation, tadpoles were paralyzed in a bath using 2 mM panacronium dibromide (0693/50, Tocris). All experimental procedures were conducted on Stage 49 tadpoles (Nieuwkoop and Faber, 1994) according to the guidelines of the CCAC and were approved by the Animal Care Committee of the University of British Columbia's Faculty of Medicine.

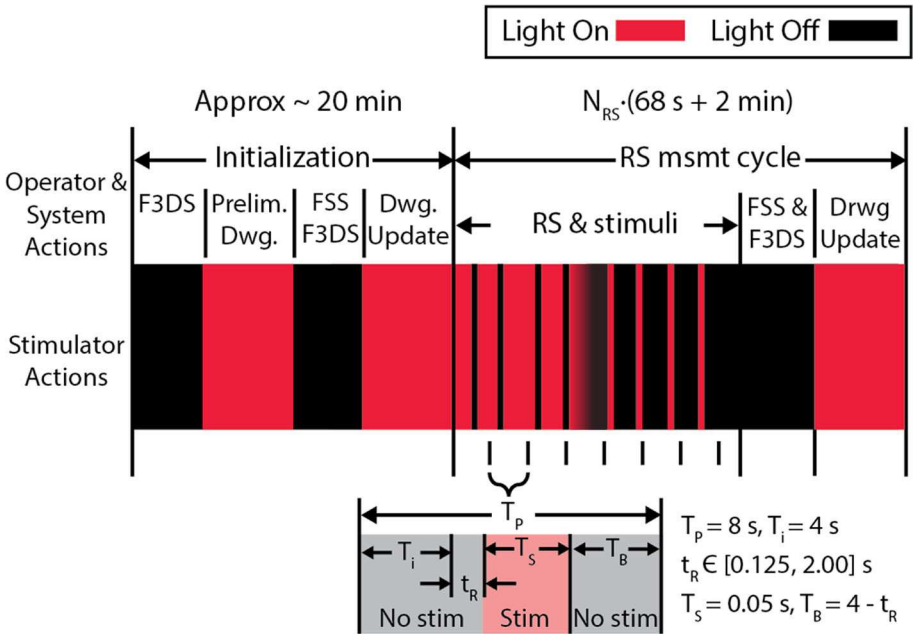

FIGURE 8 | The experiment protocol used to validate the microscope. An initial stimulus, consisting of alternating screens "ON" and "OFF" are displayed during the initial *F3DS*, after which the user draws the initial morphology in the *CTAK UI*. The *RS* executes immediately after the initial drawing of the neuron structure, and stimuli are displayed while recording the 3D, evoked activity in the dendritic arbor AP firing. In this stimulation routine, 9 stimuli are presented in sequence-–4 OFF pulses on a bright background a transition shift from the bright background to the dark background and 4 ON pulses on a dark background. Each stimulus is displayed within an 8 s interval (T_P) and has a buffer time, T_B, before and after the stimulus.

Animal Stimulation Chamber With Visual Stimulator

A custom-designed imaging chamber (**Figure 9**) is used to stabilize the head of the tadpole while imaging, to provide the specimen with oxygenated solution, and to provide visual stimuli to the contralateral eye. Stabilization of the animal is required during imaging routines to prevent positional drift by minimizing tadpole movement using a formfitting chamber. The design of the chamber was based on tadpole morphology and tested using *in vivo* time-lapse imaging of neuronal structures. Physical dimensions of Stage 49 *Xenopus laevis* were used to determine the spatial requirements. Tadpoles with on overall body length of 11.0 ± 0.5 mm have head diameters of 3.3 ± 0.2 mm, and eyes are offset by 17.4 ± 2.5 degrees from the transverse axis. *Xenopus laevis* brain neurons fit within a cubic volume of 100 μm^3. Thus, we set the minimum FOV (S_X and S_Y), and the axial requirements, S_z to ensure that the neurons will fit into a volume with sides of at least 100 µm. The stimulation chamber was created by printing a negative mold using polyactide (PLA) using a 3D-printer (Creatr Dual Extruder, Leapfrog), and filling the mold with polydimethylsiloxane (PDMS, Sylgard 184, Dow Corning). The head of the *Xenopus laevis* was stabilized in the chamber using a 0.2 mm thick, square sheet of cellulose acetate secured by a 3D-printed, PLA, C-clip. The *Xenopus laevis*'s eye was coaxial with the normal of the visual stimulator screen. The resulting field of view of the screen available to the eye is 78° on the horizontal and 44° on the vertical plane, while being submersed with several millimeters of physiological solution. Clearance between the screen and the optical axis of the microscope allows a water immersion objective with a diameter ≤33 mm, with shank angle greater or equal to 26° from the aperture of the objective. Objectives this size can accommodate a maximum of 9 mm motion of the objective in X, or Y directions controlled via three manual stages (X_M, Y_M, and Z_M) before obstruction with the chamber or screen. A mini laser-projector (ShowWX+/PicoP, Microvision), mounted directly to the stimulation chamber, projects the stimulus image on a diffuser film (Inventables, 23114-08) that is mounted on a section of a glass slide (VWR, 16004-386) with PDMS, which is the interface between the physiological solution and the project image.

RESULTS

Validating the Optical Train

The optical train was evaluated with measurements acquiring the amount of power reaching the back aperture, the axial and lateral optical resolution, and the field-of-view of the microscope. The power of the laser was measured before and after the prism used for spatial compensation and at back aperture of the objective. The power being emitted from the Ti-Sapphire, using maximum dispersion compensation was 1.94 W out of the Ti-Sapphire laser, 1.35 W after the beam expansion, and 0.35 W maximum at the back aperture of the objective using a wavelength of 910 nm to maximize the excitation of jGCaMP7s.

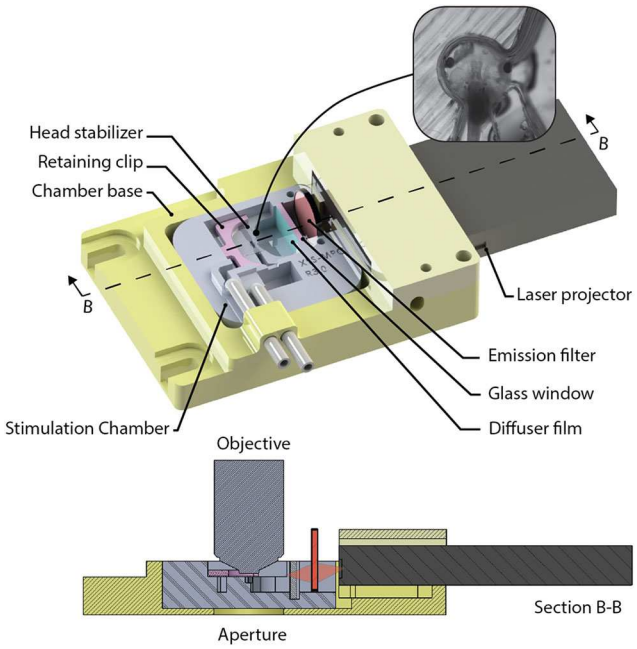

FIGURE 9 | The visual stimulation chamber was designed to allow simultaneous imaging and visual stimulation by projecting red and black images to screen (diffuser film) using a laser projector (inset). The head of a tadpole is stabilized inside a small cavity that has an opening allowing the tadpoles eye to view the screen.

The axial and lateral resolution of the microscope, using two-photon excitation at 910 nm was measured using 0.1 μm diameter green fluorospheres (F-8803, Thermo Fisher Scientific). The lateral resolution was measured to be an average of 0.34 ± 0.3 μm full-width at half maximum (FWHM, N = 9) by 1.24 ± 0.3 μm FWHM ($N = 9$), which were the major and minor axes over the entire FOV of the image. The difference accounts for the spatial dispersion caused by the AODs due to the varied frequencies over the scan. This value remains constant between *RS* and *F3DS* since the same frequency dwell time is used. The axial resolution was measured to be 2.5 ± 0.7 μm.

Tracking the edges of a fluorescent standard (1951 USAF Target #57-855, Edmund Optics, Group 4—Element 6), determined a maximum FOV using the AODs and the 60X objective to be 112 × 112 μm. Using the same standard, the FOV of the digital camera was measured to be 288 × 216 μm at a resolution of 2,560 × 1,920 pixels.

Piezo-Actuator Validation

The performance of the piezo-actuator was evaluated for its dynamic range and response to a step-input to determine the velocity, acceleration and settling response to define the limitations during the *RS* and *F3DS* scans. The dynamic range of the Z-actuator and 0.176 Kg payload (objective and mount, **Figure 10A**) was measured using the vendor's onboard parameter tuning application for piezo actuators (Aerotech EasyTune™) and found to be stable up to approximately 125 Hz (**Figure 10B**). The maximum velocity, V_{Z_MAX}, of the Z-stage was experimentally determined by observing the output to a step-response by observing the settling time, T_S, with an error <0.5 μm. The piezoactuator was subjected to a step response of 100 μm (**Figure 10C**). Under the loaded conditions, a maximum velocity of 0.043 m/s was obtained in both directions with a settling time of $<2.1 \times 10^{-3}$ s. Acceleration values of <60,000 m/s/s were found to provide stability ensuring following errors of $<0.5 \times 10^{-6}$ m.

Rapid-Scan Position Validation

The *RS* was validated to ensure that the X-Y position of the laser was synchronized with the position of the focal plane ensuring that the laser excited the 3D-position in space defined by the coordinates of the POI. Fluorospheres, 0.1 μm in diameter (F-8803, Thermo Fisher Scientific), were embedded and distributed within a 300 μm thick layer of Sylgard 184 providing sufficiently spaced, and immobile targets for analysis. A *F3DS* scan captured a volume of 112 × 112 × 125 μm (slightly greater than the volume of neurons sampled for analysis) and a total of 10 beads were drawn in the *CTAK UI*. The *RS* scan was executed and the Z-actuator provided position feedback from its capacitive sensor with an average relative error of ± 3.9% $\Delta F/F_0$ ($N = 10$ beads). The capacitive feedback from the Z-actuator was compared with the desired position of the POIs and an error of $0.375 \times 10^{-6} \pm 0.125 \times 10^{-6}$ m ($N = 8$ motion trials of the same trajectory, 68 s per motion trial) was measured with respect to the entire motion profile with an error of $0.375 \times 10^{-6} \pm 0.125 \times 10^{-6}$ m ($N = 1270$ measurements) on the Z-axis for all nodes.

Experimental Validation and 4D Data Collection

Visually evoked calcium activity was recorded in individual *Xenopus* tectal neurons expressing jGCaMP7s and mCyRFP1 through single-cell electroporation and used to demonstrate the system's capabilities of the routine. We initially validated the platform's capability to record stimulus-evoked calcium events with a temporal resolution necessary to be accurately registered as evoked events by automated detectors in *Xenopus* tectal neurons expressing GCaMP6m (Sakaki et al., 2018). However, upon release of the 7th generation of GCaMPs we switched to jGCaMP7s due to its superior sensitivity and longer decay time which improves the platform's capability of detecting short duration, local calcium transients across a large number of points in a 3D space, such as is the case with synaptic inputs (Dana et al., 2019). Both the higher $\Delta F/F_0$ and slower decay rate of jGCaMP7s maximize the number of samples collected above noise, giving high confidence that transients are detected in response to a stimulus. A typical result set, shown in **Figure 11**, shows a standard deviation projection of a neuron (**Figures 11A,B**) for images collected during the *F3DS*. The user-drawn, computer interpolated 3D-structure is shown in **Figure 11C**. Calcium data for each of the 609 POI collected at a rate of 3 Hz is shown for the initial time period in **Figure 11C**i and shows $\Delta F/F_0$ traces for each of the POI recorded representing each raw "line-scan" for each POI on

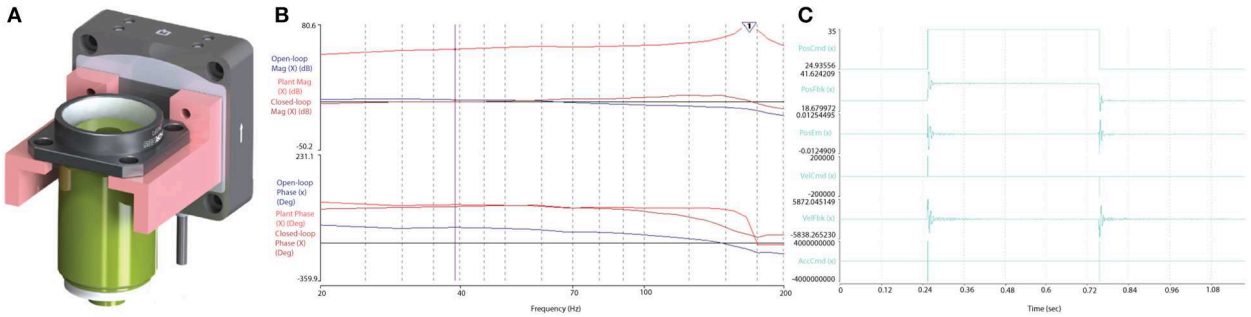

FIGURE 10 | Optical train and piezoactuator performance validation. **(A)** The 0.176 Kg objective assembly mounted on the Aerotech, piezo actuator, and **(B)** the Bode plot output following a stability test proved the actuator stable up to ∼125 Hz. **(C)** The Z-stage, piezo actuator's response to a step command over 100 and 10 μm, respectively. The Piezo achieved a maximum velocity of 0.043 m/s with a following error less than $\pm$ 5 × 10^{-6} m, and a settling time of <5.3 × 10^{-3} s.

the neuron. As indicated immediately beneath each of the line-scans four 50 ms OFF stimuli are presented at pseudorandom time points on a bright background, the background is gradually shifted from bright to dark over several seconds and then four 50 ms ON stimulus are presented at pseudorandom time points. An in-house designed automated event detection system (Sakaki et al., 2018) was employed to detect the number of stimulus that evoked action potentials in this neuron (2/4 OFF stimuli, 1/1 transition shift stimulus and 0/4 ON stimuli). Four separate planar *RS* (i.e., no moving Z-stage, scanning is exclusively provided by the X-axis and Y-axis AODs) were performed on this same neuron using a similar experimental protocol as was used in the *F3DS* scan (**Figures 11D–G,D**i**–G**i). While the planar *RS* lack the comprehensive imaging capability of the *F3DS* scan, they provide greater temporal resolution, recorded at scanning rates between 204 and 246 Hz, each recording POIs on a single Z-plane cutting through the neuron. A comparison of the individual traces for a section of the neuron sampled both with a 3 Hz *F3DS* scan (**Figures 11H,J**) and a 232 Hz planar *RS* (**Figures 11I,K**) demonstrate the advantage of an increased sampling rate for recording stimulus-evoked calcium microdomains that are potentially synaptic.

To improve temporal resolution relative to the *F3DS* scanning method while still maintaining a dataset containing recordings from across the dendritic arbor a "Segmented Scanning" was developed. In this method, the 3D structure of the neuron (**Figures 12A,B**) is divided into 3 compartments (**Figure 12C**). Furthermore, the majority of interstitial nodes are excluded from scanning, with sampling only occurring at the soma, branch points, filopodia bases and filopodia tips (a total number of 324 POIs for this neuron), where previous studies demonstrate there is an enrichment in the density of synapses in these neurons (Li et al., 2011). Fluorescence data from each third is serially collected in three imaging epochs and the data from all three scans is then combined to produce a reconstructed recording of both OFF-stimulus evoked (**Figure 12D**) and ON stimulus evoked calcium transients (**Figure 12E**). **Figures 12F,G** shows a the $\Delta F/F_0$ traces of series of POIs at the tips and bases of filopodia recorded using a Segmented Scan at a rate of 6 Hz (4 filopodia out of a total of 174 on the neuron), where spatially restricted (2 μm) stimulus-driven calcium currents are present at the tips of filopodia that represent synaptic activity.

The ability of this platform to record stimulus-evoked neuronal glutamate release onto a neuron was also tested using *Xenopus* tectal neurons expressing the non-ratiometric fluorescence based glutamate sensor Super-folder-GFP-iGluSnFR-A184S (Marvin et al., 2013, 2018) through employing single-cell electroporation, with a result set shown in **Figure 13**. Segmented Scanning using 9 OFF stimuli was performed on an individual neuron expressing the construct (**Figure 13A**) and a total of 259 POIs were collected at a rate of 6 Hz. Active areas of glutamate release could be analyzed by calculating the stimulus-evoked response for each POI, using the average $\Delta F/F_0$ change between 0 and 3 s after the 9 stimuli (**Figure 13C**). Responses were identified using a matched filter algorithm (Sakaki et al., 2018), to the expected iGluSnFR dynamics ($\overline{\tau_R}$ = 5 ms, $\overline{\tau_F}$ = 150 ms) using a window size of 8 samples (**Figure 13D**) and localized back to their position in the arbor (**Figure 13E**). **Figures 13F,G** show the traces of a subset of 6 POI on 4 filopodia demonstrating recordings of spatially restricted, stimulus driven glutamate release onto filopodia tips.

DISCUSSION

Our AOD TPLSM achieved comprehensive imaging of brain neurons while providing an open-source blueprint for the full software and hardware systems. The system successfully detected activity at subcellular resolution on regions of the neuron's dendritic arbor and cell body. We demonstrated that that our system can capture calcium-based, fluorescence activity at 2 μm resolution at 3 Hz over an entire neuron's dendritic arbor (**Figure 11**). Through employing Segmented Scanning (**Figures 12**, **13**) this system is able to increase the sampling rate to 6 Hz while generating trace data from across all filopodia and branchpoints across the dendritic arbor. Furthermore, through the planar *RS* this TPLSM can provide higher temporal resolution sampling (i.e., >100 Hz) in continuous sections of the neuron within single focal planes (**Figure 11**). In conjunction, these multiple scanning modes accord users of this platform a

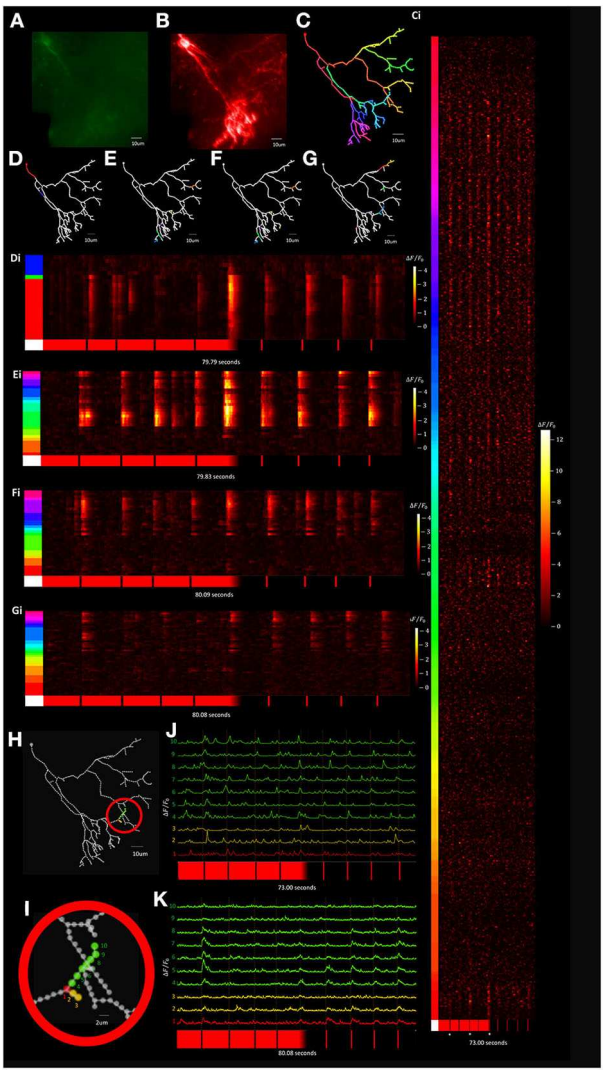

FIGURE 11 | Visually evoked tectal neural activity can be recorded across the complete dendritic arbor and soma using random access TPLSM. **(A,B)** A standard deviation projection image in the green **(A)** and red channels **(B)** of a *Xenopus* tectal neuron expressing jGCaMP7s and mCyRFP created from a *F3DS* stack of images is shown. **(C)** The user-drawn POIs tracing out the structure of the neuron. A total of 609 POIs are drawn located at 2 μm distances from their nearest neighbor. **(Ci)** $\Delta F/F_0$ output from the resulting *F3DS* of the 609 POIs, collected at 3 Hz over a 73 second interval. Responses can be seen for four 50 ms "OFF" stimuli, a "transition shift" stimulus and four 50 ms "ON" stimuli at spaced at pseudorandom time points. White asterisks indicate evoked somatic events. **(D–G)** The user-drawn POIs tracing out the structure of the neuron with the colored POIs sampled using a series of planar *RS* **(Di-Gi)** collected between 204 and 246 Hz with a similar experimental protocol as used previously (C-Ci). **(H–I)** A series of POIs that were recorded in both a 3 Hz *F3DS* scan and 232 Hz planar *RS*. **(J)** The traces for the POIs recorded at 3 Hz over 73.00 s. **(K)** The traces for the POIs recorded at 232 Hz over 80.08 s.

substantial degree of flexibility in tailoring its function to their experimental design.

One of the major goals of this work was to provide a software, mechanical and electrical framework to serve as a template for comprehensive imaging, as well as for future TPLSM development. We achieved this by partitioning this system into modules with distinct areas of responsibility. The low dependency between modules allowed tasks to run independently from each other (e.g., measurement tasks such as the *RS*) while system maintenance/monitoring was consecutively handled. It is evident that the overhead throughout the development of the system using LVOOP/Actor Framework was initially high. However, the benefit of the system's versatility with respect to the scalability of the platform (e.g., other measurements, additional hardware configurations, other modes of imaging) greatly overshadows the burden of the initial, implementation investment.

Our UI designs (*Msmt UI* and the *CTAK UI*) handled the system/experiment administration and seamlessly integrated the operator's user-in-the-loop tasks into the experiment (e.g., drawing the neuron, updating POI positions). Up-to-date, *F3DS* and *FSS* information from the scanned neuron provided the user with the means to identify and maintain the relationship between the neuron's morphology and the TPLSM system analyzing each POI extracted from the morphology. It is apparent that having a user-in-the-loop will have obvious advantages, depending on the skill of the operator (e.g., quickly identifying small cell features, tracing the neuron), and disadvantages depending on the duration of the experiment (e.g., operator fatigue and fatigue-related mistakes). However, given the current limitations of machine vision algorithms' accuracy in localizing the topography of the neuron's arborization (Peng et al., 2011), we hope to develop or encourage the development of fully automated methods of identifying and maintaining the neuron's structure and eliminate the need for the user-in-the-loop.

Our *RS* utilizes a hybrid AOD-piezoactuator combination to acquire calcium-related activity from POI scans in 3D by acquiring all of the POIs using a planned trajectory. The planned trajectory synchronizes the motion of the piezoactuator with the laser deflection angle of the AODs on the X-Y plane. Using this method, we have achieved comprehensive imaging rates up to 4 Hz and have sustained this method over durations of 68 s with measured errors of no more than $0.375 \times 10^{-6} \pm 0.125 \times 10^{-6}$ m throughout the duration of the experimental trials.

We acknowledge that an obvious bottleneck exists at the piezoactuator as a result of the mechanical motion. However, we believe we achieved the overarching goal of developing a versatile system for comprehensive imaging, which can be optimized through further design improvements and minimal effort, as current research has demonstrated that incorporating compact remote focusing technologies with acousto-optics has become feasible (Nadella et al., 2016). Furthermore, the simplicity of the design requires only basic skills for implementation to achieve initial imaging as opposed to more complex systems where remote focus designs are used or where optical trains are designed and dedicated to compensating for the dispersion of AODs.

In this work, we described an open-source, rapid-access, two-photon laser-scanning system for comprehensive sampling and analysis of neuronal activity. We demonstrated a system capable of extracting and creating a structural representation of a neuron and converting that structure into points-of-interest (POIs) to

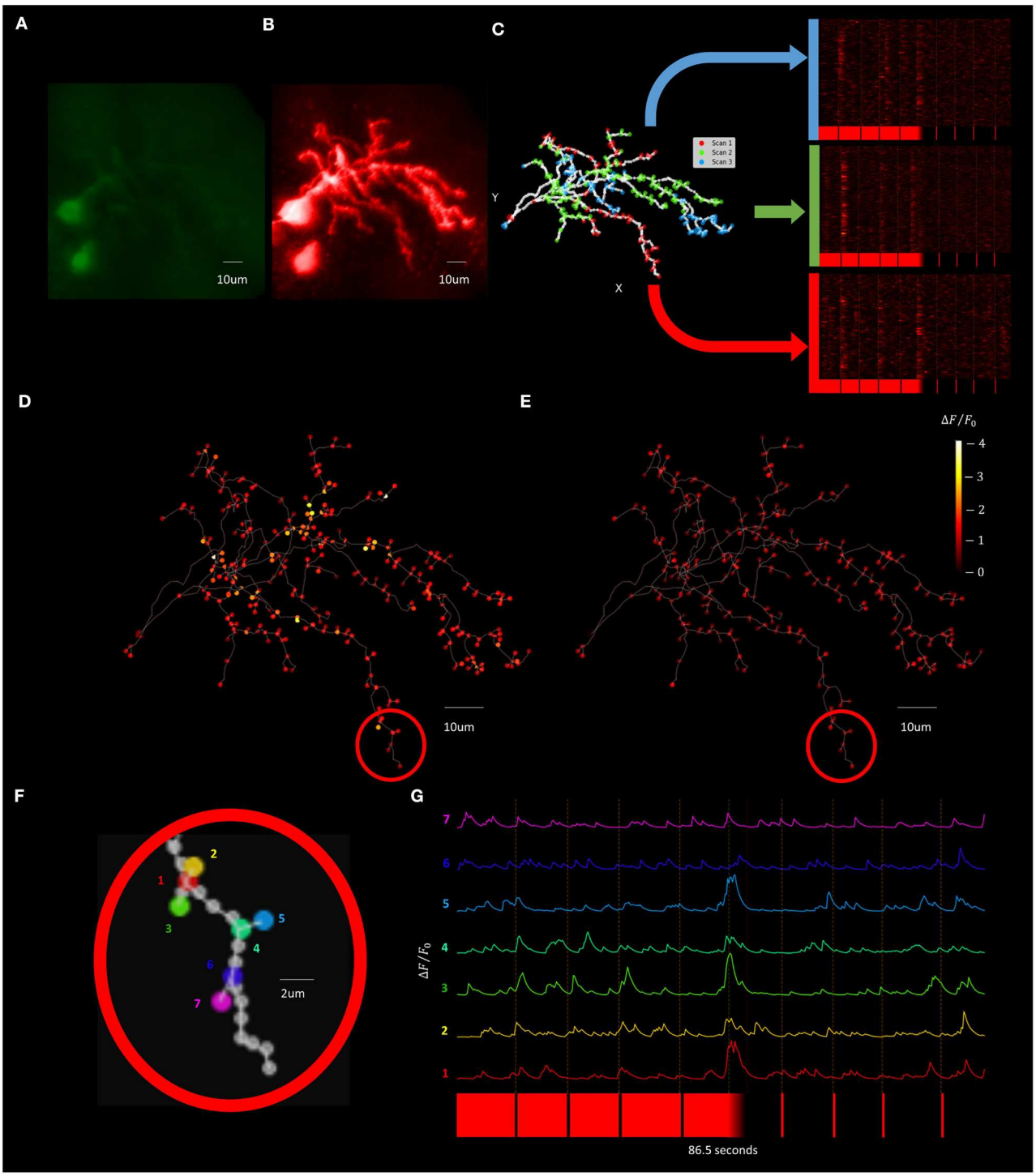

FIGURE 12 | Visually evoked synaptic calcium transients across the neuron can be recorded with increased temporal resolution using Segmented Scanning. **(A,B)** A standard deviation projection image in the green **(A)** and red channels **(B)** of a *Xenopus* tectal neuron expressing jGCaMP7s and mCyRFP created from a *F3DS* stack of images is shown. **(C)** The user-drawn POIs tracing out the structure of the neuron with the POIs that are sampled in each sub-scan of the Segmented scan are colored and the subsequent visually evoked calcium activity is shown. A total of 324 POIs located at the soma, branch points, filopodia bases and tips are collected at a rate of 6 Hz. **(D,E)** The maximum of the average $\Delta F/F_0$ evoked responses for both a series of four pseudorandom 50 ms "OFF" **(D)** and four 50 ms "ON" stimuli **(E)**. **(F)** A series of POIs recorded corresponding to filopodia tips and bases and **(G)** the individual calcium traces of those POIs.

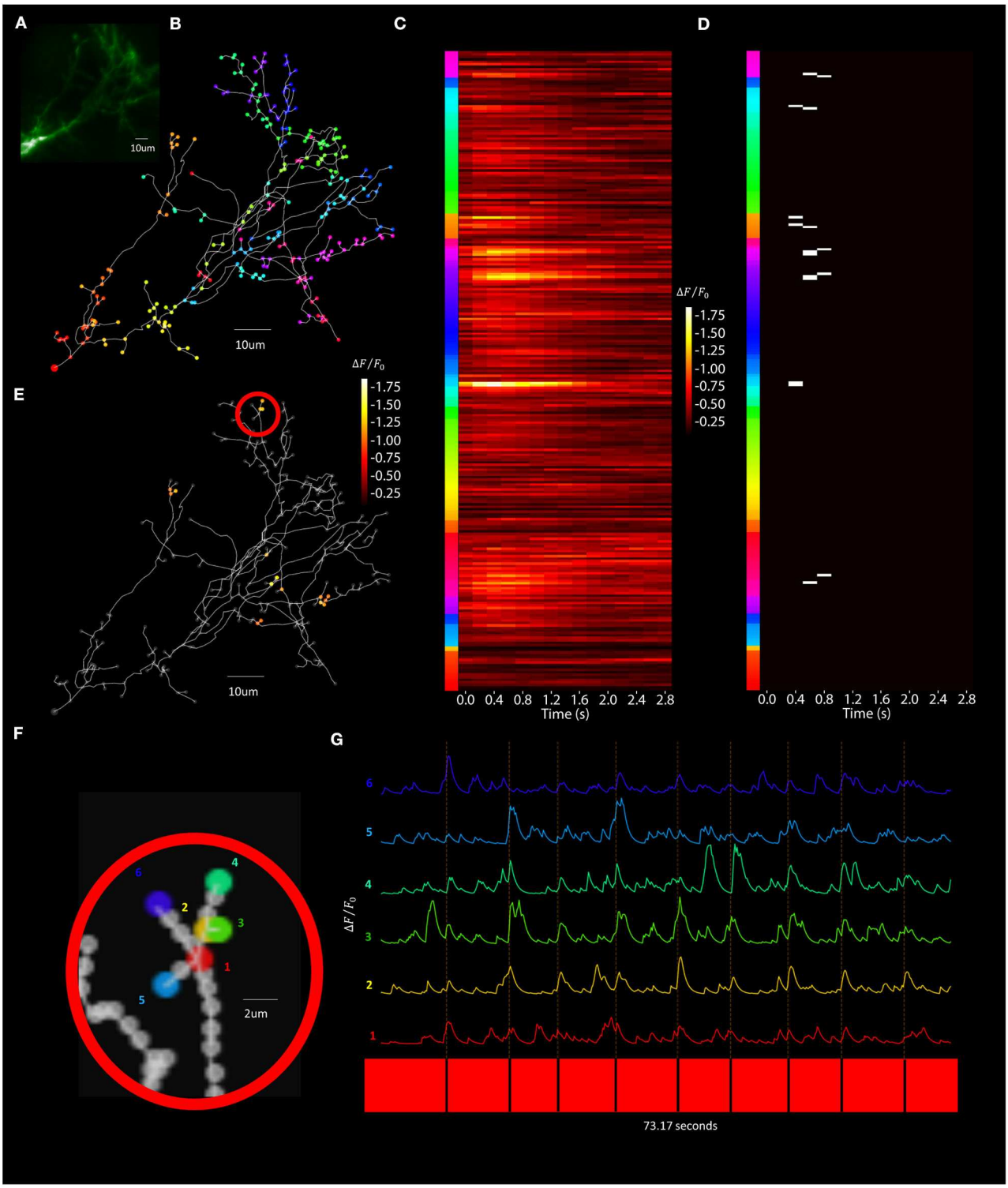

FIGURE 13 | Visually evoked synaptic-localized glutamate transients across the neuron can be detected using Segmented Scanning. **(A)** A standard deviation projection image in the green channel of a *Xenopus* tectal neuron expressing shown sfGFP-iGluSnFR-A184S. **(B)** Locations of a total of 259 POIs sampled across the soma, dendritic branch points, filopodia bases and tips. **(C)** Stimulus-evoked iGluSnFr $\Delta F/F_0$ response for 3 s post-stimulus at each POI, collected at a rate of 6 Hz and averaged over 9 50 ms "OFF" stimuli. **(D)** Transient events detected using a matched filter algorithm (Sakaki et al., 2018), identifying evoked increases that match Super-folder-GFP-iGluSnFR-A184S dynamics ($\overline{\tau_R} = 5$ ms, $\overline{\tau_F} = 150$ ms) and a window size of 8. **(E)** Locations and strengths of the responses located spatially across the arbor. **(F)** A series of POIs recorded corresponding to filopodia tips and bases and **(G)** the individual iGluSnFr traces of those POIs.

saturate sampling of activity in the cell body and throughout the entire dendritic arbor. Our system, using the list of POIs, creates a schedule for rapid-scanning, and coordinates acousto-optics and a high-speed, piezo linear-actuator to position a laser on each POI for rapid-scanning. We devised a 3D-printed chamber, and visual stimulator system to provide controlled sensory stimuli to awake immobilized animals. In conjunction, this enables us to record visually-evoked responses across the complete dendritic arbor and soma of an individual neuron with in an intact, awake developing brain. This is a novel capability and has broader appeal for the developmental neuroscience community, in particular allowing for the investigation of experience-driven neuronal growth and development of tuning.

Our versatile, open-source object-oriented, system software architecture was built using Actor Framework and LabVIEW "G" architecture using a powerful, established and commercially maintained API. This system architecture can be easily adapted for further experimental design as well as easily adapting the routines for other architectures, lending itself for future rapid prototyping as well as more mature designs in either research or for industrial purposes.

Our validated AOD-based random-access TPLSM with software is specifically designed to capture calcium biosensor fluorescence of neural activity throughout a neuron's entire dendritic arbor and soma in the intact and awake brain. Together, this hardware and software platform is capable of comprehensive imaging, required for understanding synaptic integration and neural encoding.

Additional documentation for this platform and instructions for further access to relevant resources is located at the UBC Dynamic Brain Circuits in Health and Disease GitHub page: https://github.com/ubcbraincircuits.

DATA AVAILABILITY STATEMENT

The datasets generated for this study are available on request to the corresponding author.

ETHICS STATEMENT

The animal study was reviewed and approved by UBC Animal Care Committee and were in accordance with the Canadian Council on Animal Care (CCAC) guidelines.

AUTHOR CONTRIBUTIONS

KS redesigned and fully tested the AOD-based random access microscope and accompanying software for driving microscope and analysis and wrote the first draft of manuscript. KP produced initial design of the AOD-based random-access microscope and driver software. TD designed and tested the plasmid constructs optimized for this platform and performed the system validation experiments. PC developed segmented scanning, software for the microscope, and performed imaging analysis of the resulting data. KH supervised all design, construction and implementation efforts, and rewrote the manuscript.

FUNDING

This work was supported by a Foundation Award number FDN-148468 from the Canadian Institute of Health Research (CIHR).

REFERENCES

Akemann, W., Léger, J.-F., Ventalon, C., Mathieu, B., Dieudonné, S., and Bourdieu, L. (2015). Fast spatial beam shaping by acousto-optic diffraction for 3D non-linear microscopy. *Optics Exp.* 23, 28191–28205. doi: 10.1364/OE.23.028191

Biess, A., Korkotian, E., and Holcman, D. (2011). Barriers to diffusion in dendrites and estimation of calcium spread following synaptic inputs. *PLoS Comput. Biol.* 7:e1002182. doi: 10.1371/journal.pcbi.1002182

Bullen, A., and Saggau, P. (1997). High-speed, random-access fluorescence microscopy: I. High-resolution optical recordings with voltage-sensitive dyes and ion indicators. *Biophys. J.* 73, 477–491. doi: 10.1016/S0006-3495(97)78086-X

Bullen, A., and Saggau, P. (1999). High-speed, random-access fluorescence microscopy: II. Fast quantitative measurements with voltage-sensitive dyes. *Biophys. J.* 76, 2272–2287. doi: 10.1016/S0006-3495(99)77383-2

Burnashev, N., Monyer, H., Seeburg, P. H., and Sakmann, B. (1992). Divalent ion permeability of AMPA receptor channels is dominated by the edited form of a signal subunit. *Neuron* 8, 189–198. doi: 10.1016/0896-6273(92)90120-3

Chen, S. X., Tari, P. K., She, K., and Haas, K. (2010). Neurexin-neuroligin cell adhesion complexes contribute to synaptotropic dendritogenesis via growth stabilization mechanisms *in vivo*. *Neuron* 67, 967–983. doi: 10.1016/j.neuron.2010.08.016

Chen, T., Wardill, T. J., Sun, Y., Pulver, S. R., Renninger, S. L., Baohan, A., et al. (2013). Ultrasensitive fluorescent proteins for imaging neuronal activity. *Nature* 499, 295–300. doi: 10.1038/nature12354

Cowan, M. W., Südhof, T. C., and Stevens, C. F. (2001). *Synapses*. Baltimore, MD: Johns Hopkins University Press.

dal Maschio, M., Ghezzi, D., Bony, G., Alabastri, A., Deidda, G., Brondi, M., et al. (2012). High-performance and site-directed in utero electroporation by a triple-electrode probe. *Nat. Commun.* 3, 960–961. doi: 10.1038/ncomms1961

Dana, H., Sun, Y., Mohar, B., Hulse, B. K., Kerlin, A. M., Hasseman, J. P., et al. (2019). High-performance calcium sensors for imaging activity in neuronal populations and microcompartments. *Nat. Methods* 16, 649–657. doi: 10.1038/s41592-019-0435-6

Deneux, T., Kaszas, A., Szalay, G., Katona, G., Lakner, T., Grinvald, A., et al. (2016). Accurate spike estimation from noisy calcium signals for ultrafast three-dimensional imaging of large neuronal populations *in vivo*. *Nat. Commun.* 7:12190. doi: 10.1038/ncomms12190

Denk, W., Delaney, K. R., Gelperin, A., Kleinfeld, D., Strowbridge, B. W., Tank, D. W., et al. (1994). Anatomical and functional imaging of neurons using 2-photon laser scanning microscopy. *J. Neurosci. Methods* 54, 151–162. doi: 10.1016/0165-0270(94)90189-9

Dunfield, D., and Haas, K. (2009). Metaplasticity governs natural experience-driven plasticity of nascent embryonic brain circuits. *Neuron* 64, 240–250. doi: 10.1016/j.neuron.2009.08.034

Engert, F., Tao, H. W., Zhang, L. I., and Poo, M. (2002). Moving visual stimuli rapidly induce direction sensitivity of developing tectal neurons. *Nature* 419, 470–475. doi: 10.1038/nature00988

Gleichmann, M., and Mattson, M. P. (2013). Neuronal calcium homeostasis and dysregulation, *Antioxid. Redox Signal.* 14, 1261–1273. doi: 10.1089/ars.2010.3386

Göbel, W., Kampa, B. M., and Helmchen, F. (2007). Imaging cellular network dynamics in three dimensions using fast 3D laser scanning. *Nat. Methods* 4, 73–79. doi: 10.1038/nmeth989

Grewe, B. F., Langer, D., Kasper, H., Kampa, B. M., and Helmchen, F. (2010). High-speed *in vivo* calcium imaging reveals neuronal network activity with near-millisecond precision. *Nat. Methods* 7, 399–405. doi: 10.1038/nmeth.1453

Haas, K., Li, J., and Cline, H. T. (2006). AMPA receptors regulate experience-dependent dendritic arbor growth *in vivo*. *Proc. Natl. Acad. Sci. U.S.A.* 103, 12127–12131. doi: 10.1073/pnas.0602670103

Haas, K., Sin, W. C., Javaherian, A., Li, Z., and Cline, H. T. (2001). Single-cell electroporation for gene transfer *in vivo*. *Neuron* 29, 583–591. doi: 10.1016/S0896-6273(01)00235-5

Hewitt, C., Bishop, P., and Steiger, R. (1973). "A universal modular ACTOR formalism for artificial intelligence," in *Proceedings of the 3rd International Joint Conference on Artificial Intelligence* (Stanford, CA), 235–245.

Hossain, S., Sesath Hewapathirane, D., and Haas, K. (2012). Dynamic morphometrics reveals contributions of dendritic growth cones and filopodia to dendritogenesis in the intact and awake embryonic brain. *Dev. Neurobiol.* 72, 615–627. doi: 10.1002/dneu.20959

Iyer, V., Hoogland, T. M., and Saggau, P. (2005). Fast functional imaging of single neurons using random-access multiphoton (RAMP) microscopy. *J. Neurophysiol.* 95, 535–545. doi: 10.1152/jn.00865.2005

Katona, G., Kaszás, A., Turi, G. F., Hájos, N., Tamás, G., Vizi, E. S., et al. (2011). Roller coaster scanning reveals spontaneous triggering of dendritic spikes in CA1 interneurons. *Proc. Natl. Acad. Sci. U.S.A.* 108, 2148–2153. doi: 10.1073/pnas.1009270108

Katona, G., Szalay, G., Maák, P., Kaszás, A., Veress, M., Hillier, D., et al. (2012). Fast two-photon *in vivo* imaging with three-dimensional random-access scanning in large tissue volumes. *Nat. Methods* 9, 201–208. doi: 10.1038/nmeth.1851

Kerry, E. (2012). *Measurement Abstraction Plugin Framework With Optional Test Stand Interface.* Available online at: https://forums.ni.com/t5/LabVIEW-Development-Best/Measurement-Abstraction-Plugin-Framework-with-Optional-TestStand/ta-p/3531389 (accessed May 13, 2015)

Li, J., Erisir, A., and Cline, H. (2011). *In vivo* time-lapse imaging and serial section electron microscopy reveal developmental synaptic rearrangements. *Neuron* 69, 273–286. doi: 10.1016/j.neuron.2010.12.022

Marvin, J. S., Borghuis, B. G., Tian, L., Cichon, J., Harnett, M. T., Akerboom, J., et al. (2013). An optimized fluorescent probe for visualizing glutamate neurotransmission. *Nat. Methods* 10, 162–170. doi: 10.1038/nmeth.2333

Marvin, J. S., Scholl, B., Wilson, D. E., Podgorski, K., Kazemipour, A., Müller, J. A., et al. (2018). Stability, affinity and chromatic variants of the glutamate sensor iGluSnFR. *Nat. Methods* 15, 936–939. doi: 10.1038/s41592-018-0171-3

Nadella, K. M. N. S., Roš, H., Baragli, C., Griffiths, V. A., Konstantinou, G., Koimtzis, T., et al. (2016). Random-access scanning microscopy for 3D imaging in awake behaving animals. *Nat. Methods* 13, 1001–1004. doi: 10.1038/nmeth.4033

Nakai, J., Ohkura, M., and Imoto, K. (2001). A high signal-to-noise Ca2+ probe composed of a single green fluorescent protein. *Nat. Biotechnol.* 19:137. doi: 10.1038/84397

Nieuwkoop, P. D., and Faber, J. (eds.). (1994). *Normal Table of Xenopus laevis (Daudin): A Systematical and Chronological Survey of the Development From the Fertilized Egg Till the End of Metamorphosis*. New York, NY: Garland Pub.

Oertner, T. G., and Svoboda, K. (2002). Subliminal messages in hippocampal pyramidal cells. *J. Physiol.* 543:397. doi: 10.1113/jphysiol.2002.023606

Peng, H., Long, F., Zhao, T., and Myers, E. (2011). Proof-editing is the bottleneck of 3D neuron reconstruction: The problem and solutions. *Neuroinformatics* 9, 103–105. doi: 10.1007/s12021-010-9090-x

Reddy, G. D., Kelleher, K., Fink, R., and Saggau, P. (2008). Three-dimensional random access multiphoton microscopy for functional imaging of neuronal activity. *Nat. Neurosci.* 11, 713–720. doi: 10.1038/nn.2116

Redmond, L., and Ghosh, A. (2005). Regulation of dendritic development by calcium signaling. *Cell Calcium* 37, 411–416. doi: 10.1016/j.ceca.2005.01.009

Romand, S., Wang, Y., Toledo-Rodriguez, M., and Markram, H. (2011). Morphological development of thick-tufted layer V pyramidal cells in the rat somatosensory cortex. *Front. Neuroanat.* 5:5. doi: 10.3389/fnana.2011.00005

Rose, T., Goltstein, P. M., Portugues, R., and Griesbeck, O. (2014). Putting a finishing touch on GECIs. *Front. Mol. Neurosci.* 7:88. doi: 10.3389/fnmol.2014.00088

Ruthazer, E. S., and Aizenman, C. D. (2010). Learning to see: patterned visual activity and the development of visual function. *Trends Neurosci.* 33, 183–192. doi: 10.1016/j.tins.2010.01.003

Sabatini, B. L., Oertner, T. G., and Svoboda, K. (2002). The life cycle of ca(2+) ions in dendritic spines. *Neuron* 33, 439–453. doi: 10.1016/S0896-6273(02)00573-1

Sabatini, B. L., and Svoboda, K. (2000). Analysis of calcium channels in single spines using optical fluctuation analysis. *Nature* 408, 589–593. doi: 10.1038/35046076

Sakaki, K. D. R., Coleman, P., Toth, T. D., Guerrier, C., and Haas, K. (2018). "Automating event-detection of brain neuron synaptic activity and action potential firing *in vivo* using a random-access multiphoton laser scanning microscope for real-time analysis," in *2018 40th Annual International Conference of the IEEE Engineering in Medicine and Biology Society* (Honolulu, HI: EMBC), 1–7.

Salomé, R., Kremer, Y., Dieudonné, S., Léger, J.-F., Krichevsky, O., Wyart, C., et al. (2006). Ultrafast random-access scanning in two-photon microscopy using acousto-optic deflectors. *J. Neurosci. Methods* 154, 161–174. doi: 10.1016/j.jneumeth.2005.12.010

Sin, W. C., Haas, K., Ruthazer, E. S., and Cline, H. T. (2002). Dendrite growth increased by visual activity requires NMDA receptor and Rho GTPases. *Nature* 419, 475–480. doi: 10.1038/nature00987

Sun, X. R., Badura, A., Pacheco, D. A., Lynch, L. A., Schneider, E. R., Taylor, M. P., et al. (2013). Fast GCaMPs for improved tracking of neuronal activity. *Nat. Commun.* 4:10. doi: 10.1038/ncomms3170

Svoboda, K., Denk, W., Kleinfield, D., and Tank, D. W. (1997). *In vivo* dendritic calcium dynamics in neocortical pyramidal neurons. *Nature* 385, 161–165. doi: 10.1038/385161a0

Szalay, G., Judák, L., Katona, G., Ócsai, K., Juhász, G., Veress, M., et al. (2016). Fast 3D imaging of spine, dendritic, and neuronal assemblies in behaving animals. *Neuron* 92, 723–738. doi: 10.1016/j.neuron.2016.10.002

Conflict of Interest: The authors declare that the research was conducted in the absence of any commercial or financial relationships that could be construed as a potential conflict of interest.

frontiers in Neural Circuits

ORIGINAL RESEARCH
published: 03 July 2020
doi: 10.3389/fncir.2020.00038

Mesoscopic Mapping of Stimulus-Selective Response Plasticity in the Visual Pathways Modulated by the Cholinergic System

Guillaume Laliberté[1], *Rahmeh Othman*[1,2] *and Elvire Vaucher*[1]*

[1] *Laboratoire de Neurobiologie de la Cognition Visuelle, École d'Optométrie, Université de Montréal, Montréal, QC, Canada,*
[2] *Département de Pharmacologie et Physiologie, Faculté de Médecine, Université de Montréal, Montréal, QC, Canada*

The cholinergic potentiation of visual conditioning enhances visual acuity and discrimination of the trained stimulus. To determine if this also induces long-term plastic changes on cortical maps and connectivity in the visual cortex and higher associative areas, mesoscopic calcium imaging was performed in head-fixed awake GCaMP6s adult mice before and after conditioning. The conditioned stimulus (0.03 cpd, 30°, 100% contrast, 1 Hz-drifting gratings) was presented 10 min daily for a week. Saline or Donepezil (DPZ, 0.3 mg/kg, s.c.), a cholinesterase inhibitor that potentiates cholinergic transmission, were injected prior to each conditioning session and compared to a sham-conditioned group. Cortical maps of resting state and evoked response to the monocular presentation of conditioned or non-conditioned stimulus (30°, 50 and 75% contrast; 90°, 50, 75, and 100% contrast) were established. Amplitude, duration, and latency of the peak response, as well as size of activation were measured in the primary visual cortex (V1), secondary visual areas (AL, A, AM, PM, LM, RL), retrosplenial cortex (RSC), and higher cortical areas. Visual stimulation increased calcium signaling in all primary and secondary visual areas, the RSC, but no other cortices. There were no significant effects of sham-conditioning or conditioning alone, but DPZ treatment during conditioning significantly decreased the integrated neuronal activity of superficial layers evoked by the conditioned stimulus in V1, AL, PM, and LM. The activity of downstream cortical areas was not changed. The size of the activated area was decreased in V1 and PM, and the signal-to-noise ratio was decreased in AL and PM. Interestingly, signal correlation was seen only between V1, the ventral visual pathway, and the RSC, and was decreased by DPZ administration. The resting state activity was slightly correlated and rarely affected by treatments, except between binocular and monocular V1 in both hemispheres. In conclusion, cholinergic potentiation of visual conditioning induced change in visual processing in the superficial cortical layers. This effect might be a key mechanism in the establishment of the fine cortical tuning in response to the conditioned visual stimulus.

Keywords: cholinergic potentiation, mesoscale calcium imaging, visual conditioning, acetylcholinesterase inhibitors, visual cortex

OPEN ACCESS

Edited by:
Edward S. Ruthazer, McGill University, Canada

Reviewed by:
Ayako Wendy Ishikawa, Keio University, Japan
Laura Baroncelli, National Research Council (CNR), Italy

***Correspondence:**
Elvire Vaucher
elvire.vaucher@umontreal.ca

Received: *11 March 2020*
Accepted: *22 May 2020*
Published: *03 July 2020*

Citation:
Laliberté G, Othman R and Vaucher E (2020) Mesoscopic Mapping of Stimulus-Selective Response Plasticity in the Visual Pathways Modulated by the Cholinergic System. Front. Neural Circuits 14:38. doi: 10.3389/fncir.2020.00038

INTRODUCTION

Vision is a primary sense that drives one's assessment of the external world and guides behavioral responses. Visual perception results from an interplay between various cortical areas. These areas are hierarchically organized, starting in the primary visual cortex (V1) (Glickfeld and Olsen, 2017). In mice, 12 associative visual areas, sharing close anatomical, and functional relationships with V1 (Wang and Burkhalter, 2007), process the information of complex visual stimuli. This processing starts with very selective responses of visual neurons for specific parameters of stimuli, such as orientation, spatial and temporal frequencies, and direction, which are associated with the visual hierarchy (Andermann et al., 2011). The functional selectivity of neurons and cortical areas defines visual pathways that follow a dorsal and a ventral stream in mice, as observed in greater mammals (Mishkin et al., 1982; Glickfeld et al., 2013a). The examination of circuitry between visual areas has revealed that the murine dorsal pathway, which sustains spatial perception, is composed of the latero-medial area (LM), laterointermediate area (LI), posterior area (P), and postrhinal area (Por) (**Figure 1**). The ventral pathway, which allows for the recognition of stimulus attributes, consists of the anterolateral area (AL), anterior area (A), anteromedial area (AM), rostrolateral area (RL), and posteriomedial area (PM) (Huberman and Niell, 2011; Wang et al., 2012). The dense projections from V1 to the LM and AL areas suggest that these areas could represent the entries of the dorsal and ventral visual pathways in mice, respectively.

The extraction of important visual information from the external environment requires neurons to respond with a differential strength and, consequently, involve specific visual microcircuits. A specific stimulus might require a high level of processing, thanks to neuronal gain modulation (Soma et al., 2012, 2013a) and neuronal plasticity, which would result in the persistent change of the neuronal response to this stimulus, as well as structural changes. Neuronal plasticity is defined as the principle of learning and the permanent improvement of perception. It is highly expressed in the developing brain, but it is rather latent after brain maturation when plasticity brakes such as Lynx1 (Morishita et al., 2010) are upregulated, or during the perineuronal net development (Hensch, 2005). Plasticity has to be reactivated in adults, specifically by manipulating the excitatory-inhibitory cortical balance via neuromodulation or by eliciting the long-term potentiation of the synapse strength. Also, neuronal plasticity could be reactivated via expression of plasticity factors that enhance plasticity, e.g., Lypd6 (Darvas et al., 2009; Sadahiro et al., 2016), or that structurize neuronal connectivity, such as the tissue plasminogen protein tPa (Mataga et al., 2002), and the synaptic proteins GAP43 (Han et al., 2013) or PSD95 (Kim and Sheng, 2004).

Stimulus-specific response plasticity is induced by conditioning in which a repetition of the stimulus enables the consolidation of neuronal reactivity. In the visual pathway, stimulus-specific response potentiation in V1 has been shown to involve gamma oscillations, the GABAergic microcircuits, and long-term potentiation of the response according to an Hebbian pattern (Cooke and Bear, 2010; Chen N. et al., 2012). It has also been shown to be enhanced by the cholinergic system (Kilgard and Merzenich, 1998; Rokem and Silver, 2013; Chen et al., 2015; Galuske et al., 2019; Vaucher et al., 2019), which strongly interacts with both the cortical GABAergic and glutamatergic microcircuits, inducing long-term potentiation-like mechanisms and refining circuitry efficiency. For these reasons, the cholinergic system has been proposed to be a key player in experience-induced plasticity. Acetylcholine (ACh) modulates the inhibitory GABAergic response through cholinergic nicotinic and muscarinic receptors (Mcclure-Begley et al., 2009; Disney et al., 2012; Demars and Morishita, 2014; Groleau et al., 2015). Additionally, ACh has multiple effects on the visual response, including effects on the latency (Turchi and Sarter, 1997), spread (Kimura et al., 1999; Voss et al., 2016), and signal gain (Minces et al., 2017) of the cortical response. From a behavioral point of view, it has been demonstrated that this neuromodulator enhances visual acuity (Kang et al., 2014) and recognition (Chubykin et al., 2013; Gavornik and Bear, 2014), as well as contrast detectability (Bhattacharyya et al., 2013; Soma et al., 2013c). These changes were measured in layer 4 of V1, or MT (Chen X. et al., 2012) in rodents and primates, and in associative areas. Notably, donepezil (DPZ, a cholinesterase inhibitor that potentiates cholinergic transmission) administration was found to reduce functional connectivity between cortical areas of the visual hierarchy in order to favor automated processing (Ricciardi et al., 2013). The cholinergic system controls cortical processing in defined cortical areas, though it can also coordinate cortical function as the cholinergic input comes from the basal forebrain. This cholinergic system sends wide but organized projections to the cortical mantle (Gaykema et al., 1990; Coppola et al., 2016; Huppé-Gourgues et al., 2018).

In the present study, the regional distribution of the effects of visual conditioning and DPZ was investigated in awake head-fixed Thy1-GCaMP6s mice. The goal of the study was to evaluate whether the cholinergic system would change the correlation of neural activity between areas to enhance efficiency and automation of the processing of the trained stimulus. The cholinergic system was potentiated through systemic administration of 0.3 mg/kg DPZ (Bontempi et al., 2003; Geerts et al., 2005; Bretin et al., 2018). A monocular conditioning to an oblique pattern was performed daily for a week. We used mesoscale calcium imaging (mCaI), which assesses the calcium influx from the excitatory (expressing Thy-1) neurons bodies and neurites of the superficial cortical layers (Chen et al., 2013; Dana et al., 2014), and allows for the establishment of whole-brain cortical maps. The focus was placed on the most reactive cortical areas, particularly V1, in both hemispheres, contralateral and ipsilateral to the stimulation (cV1 and iV1), as well as five areas of the ventral pathway (AL, A, AM, RL, and PM) that show great tuning for oriented gratings (Smith et al., 2017), and one area of the dorsal pathway (LM). The activity of the retrosplenial cortex (RSC) was assessed because of its role in contextual learning and memory (Makino and Komiyama, 2015; Leaderbrand et al., 2016). High-level areas were also analyzed but not reported as the signal was not significantly

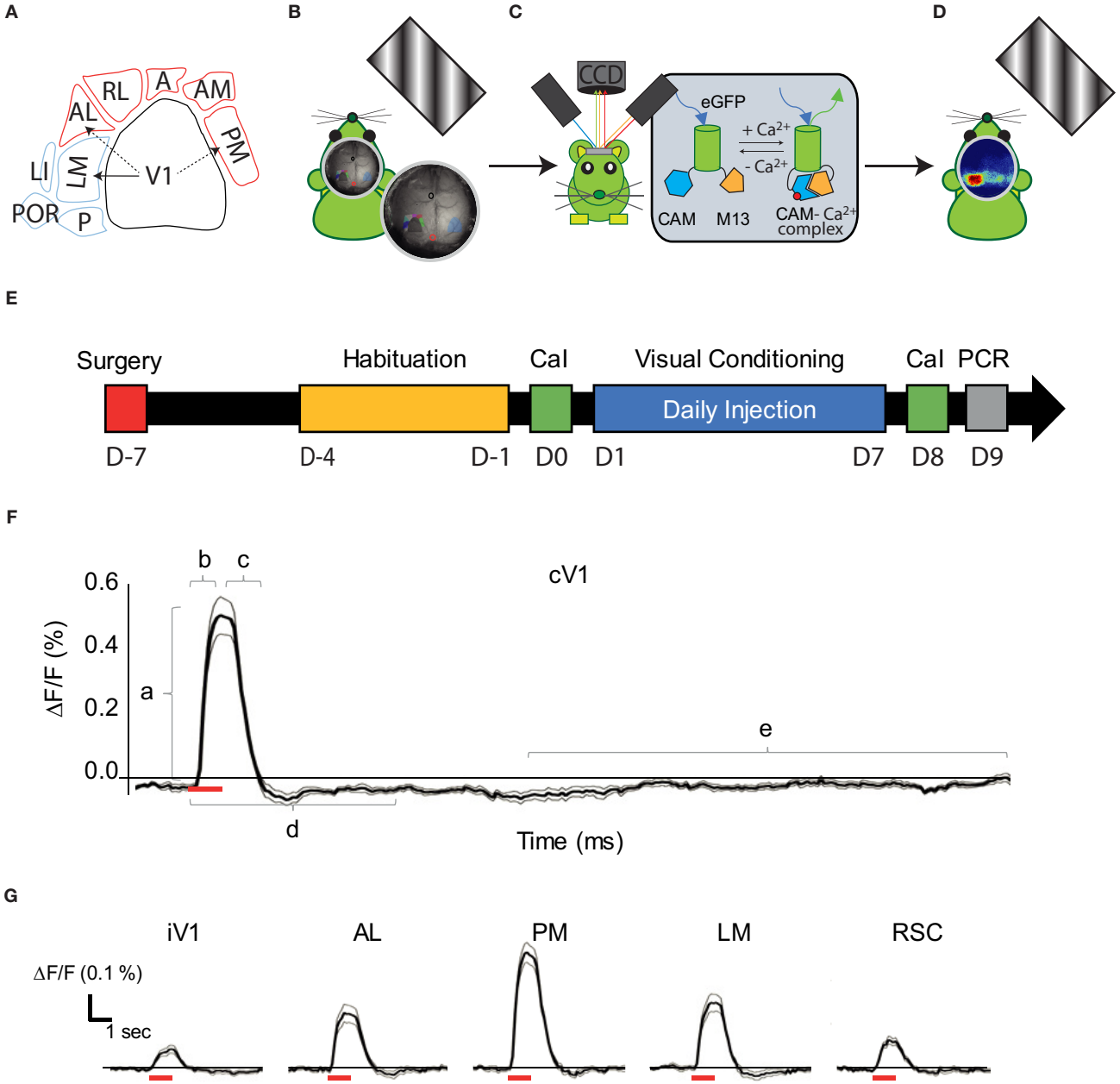

FIGURE 1 | Visual pathways and methodology. **(A)** Schematic representation of the visual cortical areas adapted from (Zhuang et al., 2017) and their belonging to the dorsal (purple) or ventral (blue) stream. The density of V1's projections to LM, AL, and PM are greater (arrows) in these areas compared to adjacent areas, suggesting that LM and AL are the gateway for each visual stream. **(B)** Schematic representation of the experimental set-up: a monitor was placed on the right side (120°) of the head-fixed mouse to monocularly stimulate the right visual field by drifting oriented gratings. **(C)** A CCD camera was placed dorsal to the mouse skull to acquire light absorbance and fluorescent signal fluctuations in the cortex through an optic chamber. During the acquisition, the brain of the mouse was sequentially illuminated by three LED lights (see text for details). **(D)** Representation of cortical map in response to the monocular visual stimulation. **(E)** Timeline for the mice treatment and experimentation (mCaI, mesoscale Calcium Imaging; V.C., Visual Conditioning; RT-qPCR, retro-transcription quantitative polymerase chain reaction). **(F)** Trace of the mean CaS in function of time ($n = 18$ mice; 15 repetitions each, mean in dark, ± SEM in gray) in response to the 30 H visual stimulation (represented by a red bar) in cV1. Representation of the parameters examined is shown: *Amplitude* (a), *Latency* (b), *Persistence* (c), *Activation correlation* window (d) and the baseline (e). **(G)** Traces of the CaS mean response to the visual stimulation (red bar) in function of time ($n = 18$ mice; 15 repetitions each, mean in dark, ± SEM in gray), during the time window used for *activation correlation* calculation in iV1, AL, PM, LM, and RSC. cV1, contralateral primary visual cortex; iV1, ipsilateral primary visual cortex; PM, posterior-median cortex; LM, latero-median cortex; A, anterior cortex; AL, anterio-lateral cortex; AM, anterio-median cortex; RL: rostro-lateral cortex; RSC, retrosplenial cortex.

affected by the visual stimulation. Different parameters of the fluorescent calcium signal (CaS, representing ΔF/F, %) were measured: the *amplitude*, the *size* of the activated area, the signal-to-noise ratio (*SNR*), the *latency*, and the *persistence* of the maximal signal, which is indicative of the strength, rapidity and efficiency of the neural processing. The resting state functional connectivity was calculated before and after visual conditioning to assess the reorganization of circuitry efficiency. Finally, to investigate through which plasticity mechanisms the cholinergic enhancement and conditioning affect the visual cortex, the expression of Lypd6, Lynx1, tPa, GAP43, and PSD95 were examined by RT-qPCR after treatments.

MATERIALS AND METHODS

Mice

All procedures were approved by the Animal Care Committee of the University of Montreal (CDEA, protocol 19-024) and conformed to the guidelines of the Canadian Council on Animal Care. Transgenic heterozygous GCaMP6s mice ($n = 18$, 9 males and 9 females equally distributed in three groups) were produced in our colony by breeding C57BL/6J-Tg(Thy1-GCaMP6s)GP4.3Dkim/J (IMSR Cat# JAX:024275, RRID:IMSR_JAX:024275) males with C57BL/6J wild type (IMSR Cat# JAX:000664, RRID:IMSR_JAX:000664) females, in agreement with the university's reproduction protocol (CDEA, 19-025). The GCaMP6s expression was determined by genotyping each animal with PCR amplification, in accordance with the Jackson Laboratory (RRID:SCR_004633) procedures for this strain. Mice were kept in a 12 h-light cycle room with *ad libitum* access to food and water. To prevent any potential bias caused by the circadian cycle, daily experiments (habituation, mCaI acquisition, drugs administration, and visual conditioning) were performed within the same daily time period (between 8 and 12 AM) for each mouse. The testing order was randomly determined on the first day using one mouse from each experimental group [non-conditioned group [Sham], control conditioned [CS], or 0.3 mg/kg DPZ conditioned [CS/DPZ] group; six series of experiments were performed]. Three (one in each group) out of the 18 initial mice were removed after complications following the surgery or during the treatment, thus there were $n = 5$ per group.

Surgical Procedures

For chronic implantation of the imaging chamber, animals were anesthetized with isoflurane (induction at 5%, maintain in 1.5%; in medical O_2) and placed in a stereotaxic frame. Body temperature was maintained at 37°C using a heating pad and monitored with a rectal thermometer throughout the procedure. The scalp was shaved, decontaminated with ethanol (70% v/v) and iodine (16% v/v), and locally anesthetized with subcutaneous injection of lidocaine (32 mg/kg). The skin covering the skull was removed and replaced with transparent dental cement (C&B MetaBond, Parkell, Edgewood, NY, USA), a cover glass (Carolina, Burlington, NC, USA), and an 11 mm diameter titanium head fixation chamber. At the end of the procedure, mice were injected subcutaneously with a non-steroidal anti-inflammatory drug, carprofen (0.5 mg/kg), in saline (injection volume equivalent to a ratio of 0.1 mL/10 g of the mouse's weight) solution and allowed to recover for 30 min in a red-light warmed cage. They were then placed individually in a clean cage. A second and third subcutaneous injection of carprofen (0.5 mg/kg) were performed at 24 and 48 h after the surgery. The animal was allowed to recover 5 days after the surgery before beginning any head-fixed procedure.

Mesoscale Calcium Imaging Recordings

The fluorescent CaS recording was performed on awake head-fixed mice at day 0 (D0, before the conditioning) and day 8 (D8, 1 day after conditioning) (**Figure 1**). No recording of the CaS in response to a visual stimulation was performed during conditioning (7 consecutive days). For the resting state cortical activity, the CaS was acquired at D0 and D8 during a period of 10 min prior to visual stimulation.

During mCaI acquisition, the mice stand inside a fenestrated PVC tube on a height-adjustable stage placed within a dark cabinet. A computer monitor (60 Hz refresh time; 250 cd/m^2, main luminance) was positioned at 21 cm from the mouse's side (120°) to stimulate its entire monocular visual field (**Figure 1B**). To minimize stress, mice were progressively habituated to the head-fixation apparatus over 5 days: 5, 10, 20, and 40 min head fixation periods without brain illumination for the first 4 days, respectively, and then 40 min with brain illumination and gray screen presentation for the last day of habituation. This habituation abolished signs of stress in the cage and on the stage (mice showed adequate grooming, diminution of vocalization, diminution of movements during the head fixation, and no weight loss). The mice were placed in a dark room for 30 min prior any CaI recording including 5 min head-fixation at rest. The CaI recording was synchronized to the visual stimulation with the Datapixx3 device (Vpixx Technologies Inc., St Bruno, QC, Canada).

The CaS was recorded through a CCD camera (NIKKOR 50 mm f/1.2, Nikon, Minato, Tokyo, Japan) positioned vertically above the skull (**Figure 1C**). A dark opaque screen was placed between the monitor displaying the visual stimulation and the imaging chamber/camera to ensure there was no light contamination. Sequential 472, 590, and 623 nm brain illumination was produced by three LEDs contained in two adjustable illumination arms (**Figure 1C**) directly on the skull of the mouse. Calcium indicators were excited at 472 nm (Blue LED, Cree XLamp XP-E2 LEDs, Cree, Durhamm, NC, USA) and intrinsic signals (absorbance of oxy- and deoxy- hemoglobin) were extracted from modifications in the absorption of the 590 and 623 nm wavelengths (Amber LED, LZ4-00MA00 and Red LED, LZ4-00MA00, respectively, OSRAM, Markham, Ontario, Canada). The reflectance of intrinsic signals and the fluorescence emission were collected at a frame rate of 30 Hz (10 Hz by wavelength) with a full resolution of 512 × 512 pixels (21.5 μm/pixel). Illumination was adjusted to avoid under or over saturation of any wavelengths. The exposure time of the camera was set to 18 ms. Filters (long pass filter at 496 nm adjusted to the objective) were used to minimize any contamination from other wavelengths.

Image Processing and Analysis of Calcium Signals

All data were imported and analyzed with Labeo Technologies, Inc. and MATLAB codes (MathWorks, Natick, MA, USA, RRID:SCR_001622). Prior to data analysis, recorded images of the whole cortex were corrected for the camera's electronic noise. In addition, each pixel's intensity time course was filtered with a low pass filter to remove high frequency artifacts related to respiration and heart rate. Pixels were fused 1:2, so CaI analysis was performed over a 256 × 256 pixel window (43 μm/pixels). Tissue absorbance due to the hemodynamic response (assessed by the at 590 and 623 nm illumination) was subtracted from the fluorescence signal using a modified Beer-Lambert equation (Guevara et al., 2013). The corrected CaS (ΔF/F, %) of each pixel was normalized by subtracting the current CaS with the CaS baseline over the CaS baseline ×100. The CaS of each pixel (CaS_p) was then spatially normalized using the Z-score to create cortical activity maps (Gias et al., 2005) (**Figures 1D**, **2**).

$$Z-score = \frac{CaS_p - mean(CaS_p)}{SD(CaS_p)}$$

The size and position of the regions of interest (ROIs) were adapted from the Allen Brain Institute (Zhuang et al., 2017) and other anatomical and functional studies imaging the mouse visual cortex (Andermann et al., 2011; Marshel et al., 2011; Wang et al., 2012; Glickfeld et al., 2013a; Groleau et al., 2014; Wekselblatt et al., 2016). A ROI template was generated, manually centered, and fitted to Bregma and Lambda (**Figures 1B**, **2B**). The size and position of the ROIs were automatically corrected according to the Bregma and Lamda distance for each mouse at D0 to avoid misidentification and cross-contamination between secondary visual areas. The CaS of each pixel contained in the ROIs was averaged in response to each visual stimulation (15 times). The resultant ROIs' CaS was then averaged across animals ($n = 18$). The CaS response in a particular ROI was considered an outlier and removed from the analysis when the CaS simultaneously measured in control areas (primary motor and somatosensory cortex) varied from the mean CaS calculated across the whole cortex (calculated with a 95% confidence interval).

Various stimulation parameters were calculated (**Figure 1F**):

The *Amplitude* was calculated by subtracting the baseline recorded during gray screen presentation from the maximal fluorescent signal during the stimulus presentation.

$$Amplitude = CaS_{Max} - CaS_{Baseline}$$

The *Size* was defined as the surface (number of pixels) of each ROI activated by the visual stimulation. We considered that the ROI was activated when the z-score of the pixel's CaSmax was >1.282. The number of activated pixels was normalized by the surface of the ROI to minimize the impact of the ROI dimensions.

$$Size = \frac{Pixels_{\ Z-score\ >1.282}}{Pixels_{\ Total\ in\ ROI}}$$

The *Latency* represented the time interval from the beginning of the visual presentation to CaS_{Max}.

The *Persistence* was the time interval between the end of the stimulation presentation and the end of the CaS, i.e., when the fluorescent signal corresponded to <2 SD of the baseline.

$$Persistence\ (ms) \rightarrow\ CaS\ \leq\ (CaS_{Baseline} + 2\sigma_{Baseline})$$

The *signal-noise ratio* (SNR) of local activation was calculated by measuring the ratio between the maximal response for the stimulation and the standard deviation of the signal baseline.

$$SNR = \frac{(CaS_{Max})}{\sigma_{Baseline}}$$

The *activation correlation* between the nine ROIs was determined using the MATLAB function *corrcoef* over a 40 ms window starting at the beginning of the stimulus presentation and represented by a matrix.

The *resting state correlation* was determined by measuring the cross-correlation coefficient r values between the temporal profiles of each of the 11 seed pixels (LM, V1b, V1m, AL, PM, RL, A, AM, RSC, AC, and M1 where AC and M1 are the anterior cingulate cortex and primary motor cortex, respectively) in each hemisphere (and all others over 10 min of resting state acquisition). Their locations were defined according to the Allen Institute Atlas (Allen Reference Atlas—Mouse Brain, RRID:SCR_013286) and were corrected by the distance between the manually selected Bregma and Lambda as previously described.

Visual Stimulation

The visual stimulation provided during CaI acquisition consisted of a series of drifting gratings (spatial frequency: 0.03 cpd, temporal frequency: 1 Hz, orientation: 30 or 90°, contrast: 50, 75, or 100 %) produced by a Vpixx software (Vpixx Technologies Inc.) and displayed on an LCD screen (23″ ACER LCD monitor S230HL, Refresh Rate 60 Hz, Brightness 250 cd/m^2) positioned in the right monocular field at 21 cm from the mice (**Figure 1B**). Each stimulus was randomly presented 15 times during 1 s with 25 s of inter-stimulation intervals (gray screen). The CaS parameters were calculated for each distinct visual stimulation condition.

Visual Conditioning

The visual conditioning of awake head-fixed mice consisted of a unilateral left exposure to a specific stimulus every day over 7 consecutive days (**Figure 1E**). A unilateral presentation of a gray screen was used for the non-conditioned group, while a drifting grating (S.F.: 0.03 cpd, T.F.: 1 Hz, Ori.: 30°, Con.: 100%) was presented to both conditioned groups during 50 s for 12 presentations with 10 s intervals of presentation (for a total stimulation time of 10 min).

Drug Administration

Mice were injected subcutaneously behind the neck with 0.1 mL/10 g (mouse weight) of sterile saline (Sham and CS, $n = 5$ per group) or with 0.3 mg/kg DPZ (Bontempi et al., 2003; Bretin et al., 2018) diluted in 0.1 mL/10 g (mouse weight) of sterile saline (CS/DPZ; $n = 5$) 15 min prior to the visual conditioning

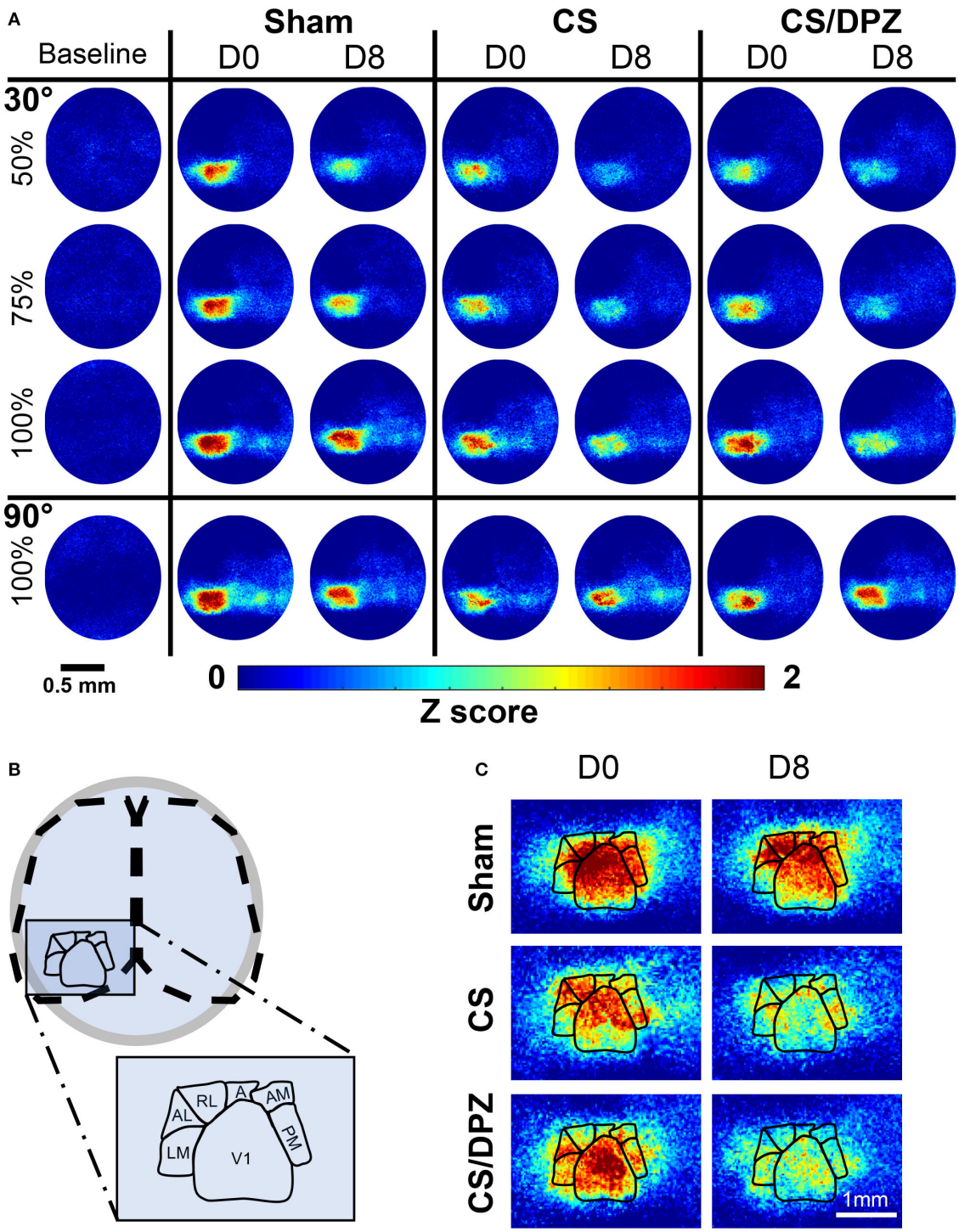

FIGURE 2 | Cortical activation maps of adult Thy1-GCaMP6s mice. **(A)** Color-coded maps show the effect of a sham-conditioning (Sham) visual conditioning coupled with saline (CS) or cholinergic potentiation (CS/DPZ) on the cortical response in superficial layers. Response to a conditioned oriented visual stimulation in different contrast (30 L, 50%, 30 M, 75%, and 30 H, 100%, top panel) and a non-conditioned orientation (90 H, 100%, bottom panel) are represented at day 0 (D0) and day8 (D8) after the conditioning. The cortical response to the conditioned stimulus and its lower contrast- equivalent is reduced for both injection groups (Data represented in *z*-score median, $n = 5$/experimental groups). **(B)** Schematic representation of the ROI mask used to extract CaS from the different visual cortices. **(C)** Magnification of the visual areas (for the 30 H stimulation). The reduction of cortical response has a general occurrence across the visual areas, while the ventral stream (AL, RL, A, AM, and PM) express more initial (D0) activation than the dorsal path (LM) for the visual stimulation.

TABLE 1 | Primers list.

		Sequence
GCaMP6s	Forward	5′-ACA AGC AGA AGA ACG GCA TC-3′
	Reverse	5′-TGG TAG TGG TAG GCG AGC TG-3′
18S	Forward	5′-GTA ACC CGT TGA ACC CCA TT-3′
	Reverse	5′-CCA TCC AAT CGG TAG TAG CG-3′
Lynx1	Forward	5′-CCA CCT ACT GTA TGA CCA CAC G-3′
	Reverse	5′-CAA CAG CAG GTG GCA GAT GCA T-3′
Lypd6	Forward	5′-CAC TCC GTA TCC TGG TGG GTT T-3′
	Reverse	5′-GAC TTC CAT CGT GTG CTG AGT G-3′
tPa	Forward	5′-TGG TGC TGT TGG TAA GTT GT-3′
	Reverse	5′-TGC CTG ACC AGG GAA TAC AT-3′
PSD95	Forward	5′-TCA ACA CGG ACA CCC TAG AA-3′
	Reverse	5′-TGA GTT ACC CCT TTC CAA TG-3′
GAP43	Forward	5′-TGG AAC AAG ATG GTG TCA AG-3′
	Reverse	5′-CCT TTG AGC TTT TTC CTT GT-3′
M2	Forward	5′-AAG TCA ACC GCC ACC TTC AGA C-3′
	Reverse	5′ GTA GCC AAT CAC AGT GTA GAG GG-3′

session in order to reach the maximal cortical effect of the drug (Geerts et al., 2005).

RNA Extraction

Immediately after the last CaI session, mice were deeply anesthetized with pentobarbital and sacrificed by decapitation. The brain was collected on a cold plate and placed in RNAlater stabilization reagent (QIAGEN, Valencia, CA, USA) for 24–48 h. The contralateral primary visual cortex (1 mm^3 centered on Bregma: −4 mm, Interaural: 2.5 mm) was dissected on ice within 60 s with RNAzap-treated instruments and stored at −80°C. Total RNA was extracted from the contralateral V1 using Qiazol reagent and the RNeasy®Lipid Tissue Mini Kit (QIAGEN, Valencia, CA, USA) according to the manufacturer's protocol. RNA concentration was determined using Nanodrop (ThermoFisher Scientific, Waltham, MA, USA), measuring 260/280 nm and 260/230 nm absorbance ratios. Real-time qPCR of 80 ng extracted RNA and specific primers (**Table 1**) was made using Quantifast® SYBR® Green RT-qPCR (QIAGEN, Valencia, CA, USA) using the manufacturer's protocol. Both targeted and referenced genes were amplified in duplicate on the same run. The relative quantification of each gene was determined using the MxProTM Q-PCR software version 3.00 (Stratagene, La Jolla, CA, USA), where the average of each duplicate mRNA levels was normalized by the $2^{-\Delta\Delta Ct}$ methods (Livak and Schmittgen, 2001) using housekeeping genes 18S and the non-conditioned group (naïve animal) as a control.

Statistical Analysis

The data were analyzed using GraphPad Prism software version 8 (GraphPad Software, San Diego, CA, USA). For the first experiment assessing sensitivity of the CaS to contrast and orientation ($n = 18$), outliers were detected and removed using the ROUT method (Q = 1%) (Motulsky and Brown, 2006). To determine whether there was a significant modification in the area responses (*Amplitude, Size, Latency, Persistence*, and *SNR)* for the stimuli contrast (L, M, H), a Kruskal-Wallis test was performed individually for both orientations (30° and 90°) in each area (cV1, iV1, PM, LM, RL, A, AM, AL, and RSC). To evaluate the difference between both orientation (30 and 90 H) responses, we used a one-tail Wilcoxon test as we expected a better response at 90°.

For the conditioning experiment, to investigate the treatments (i.e., Sham, CS and CS/DPZ, $n = 5$ per group) and effects on the cortical response, we used the Wilcoxon matched pairs signed rank test on pre and post-conditioning responses for both orientations (30 vs. 90 H). Then, Kruskal-Wallis and uncorrected Dunn's tests were used to compare experimental groups in terms of post-pre responses for each stimulation pattern.

The *activation*- and *resting state correlations* were normalized using the Fisher Z-Transformation, then compared pre vs. post effects using *t*-tests ($n = 5$). A *t*-test was used to compare the post-conditioning of both conditioned groups. To enhance the clarity of the connectivity matrix, the heatmap was reorganized by putting high r values closer to the diagonal line using the *reorderMAT* function (Brain Connectivity Toolbox, RRID:SCR_004841) on the pre-conditioning (30 H) activation correlation ($n = 18$) and resting state ($n = 18$) matrices.

The normal distribution of RT-qPCR data was confirmed with the Kolmogorov-Smirnov test and compared using a two-way ANOVA and the Bonferroni's multiple comparisons test. Results were illustrated using bars graph representing mean ± S.E.M., with a Pearson-coefficient correlation heatmap for clarity.

The statistical analysis was not corrected for multiple comparisons since this correction could lead to robust under-evaluation of changes for a large number of comparisons (Rothman, 1990), as required for the statistical analysis of multiple cortical regions as seen here. All of the data and statistical results were presented instead. The data sets generated and/or analyzed during the current study are available from the corresponding author upon reasonable request.

RESULTS

Selectivity of the Cortical Response Assessed by Mesoscale Calcium Imaging

The sensitivity of the CaS to various contrasts or orientations was first evaluated in naïve animals ($n = 18$), in nine selected cortical areas involved at different levels of visual processing (cV1, iV1, PM, LM, RL, A, AM, AL, and RSC). These areas were selected because of their responsiveness to the stimulation (0.03 cpd, 1 Hz sinusoidal grating). The responsiveness of other cortical areas was negligible and not reported. Note that the calcium signal in this Thy1-GCAMP6s line of mice mainly arises from the excitatory neurons and neurites of the superficial layers, although the GCaMP6s marker is expressed by 80% of pyramidal neurons in cortical layers 2/3 and 5 (Dana et al., 2014). The CaS is negligible in GABAergic cells. Due to the density of the cortical tissue, the fluorescent signal from the superficial layers will have a stronger influence on the acquired signal compared to the signal from deeper layers, which will be more diffuse (Ma et al.,

2016). Different parameters were assessed to detect any change in neuronal encoding, i.e., the amplitude of the signal response (*Amplitude*) (Hendel et al., 2008), the proportion of the activated area (*Size*) (Kimura et al., 1999), the time before the maximal response (*Latency*) (Mentis et al., 2001), the persistence of the calcium response (*Persistence*) after the stimulus presentation, and the Signal-Noise ratio (*SNR*) (Rieke et al., 1999).

The pattern visual stimulation elicited a CaS increase in the majority of the observed areas, which was not significantly different between the stimulation conditions (orientation or contrast) in AL, AM, LM, RL, and RSC, but significantly affected by the stimulation conditions in PM and V1 according to the Kruskal-Wallis analysis. An increase in neuronal activity (*amplitude*) upon visual stimulation was detected in all examined regions (**Table 2**, **Figures 2A**, **3**). Visually induced CaS was sensitive to contrast, particularly in cV1, iV1, PM, LM, and RSC (**Figure 3**). The *amplitude* of the CaS was identical for the two orientations of the grating (30° or 90°). The other parameters studied were rarely affected by the contrast or orientation changes, though some isolated significant changes were detected: the *size* was significantly increased in PM for the 30° orientation, and in cV1 for the 90° orientation with higher contrast of the stimulation (**Table 2**, **Figure 3**), the *latency* of the peak response was dependent on the orientation in certain cortical areas (V1, AL, and RSC), and the 90° orientation induced a higher latency of the CaS_{Max}. Our results showed that the *Persistence* was also significantly higher for the 90° orientation in V1 and AL (**Table 2**, **Figure 3**). *SNR* was affected by the contrast for both orientations only in cV1 (**Table 2**, **Figure 3**).

Cortical Activation Mesoscale Maps After a Visual Conditioning Coupled With Saline or Cholinergic Potentiation

The effect of the passive 1-week monocular visual conditioning associated or not with cholinergic potentiation on the cortical calcium response features (*Amplitude*, *Size, Latency*, and *SNR*) was then examined, as well as sham-conditioning (gray screen instead of gratings) (**Figure 4**, **Tables 3–6**). The normalized activation maps (via spatial Z-score transformation, see methods) showed a clear and localized activation of contralateral visual cortices in response to each visual stimulation for all of the mice. The ipsilateral cortex activity was not altered, except occasionally and faintly in the bilateral part of V1. The post-conditioning CaS *Amplitude* values had a tendency to decrease compared to pre-values in all contralateral cortical areas for the CS/DPZ group, with the exception of stimulation contrast in cV1 (**Figure 4A**) and PM (**Figure 4C**) and for the conditioned stimulus in AL (**Figure 4B**) and LM (**Figure 4D**). The *Amplitude* for the conditioned stimulus in the CS and sham groups decreased only for the lowest stimulation contrast (30 and 90 L) after the conditioning, and there was no change in response to the non-conditioned stimulus (**Table 3**). The post-conditioning *Size* (**Table 4**) only decreased in cV1 (**Figure 4A**) and PM (**Figure 4C**). The other parameters were virtually unaffected by the conditioning, except for the *SNR* (**Table 6**) which was affected in the secondary visual area AL (**Figure 4B**) and PM (**Figure 4C**) in the CS/DPZ group. The changes observed for the lower contrast of 50%, even for Sham animals (**Tables 3–6**), were considered irrelevant as mice have poor visual acuity at this contrast, and that this low contrast pattern stimulus might be seen as a gray screen. Thus, the gray screen presented to the non-conditioned group might behave like a conditioned stimulus.

For the CS group, the changes elicited by the conditioning were highly variable between mice. The cortical response to the conditioned stimulus (30 H) was in some cases reduced post-conditioning compared to the pre-values for every contrast (30 L, 30 M, and 30 H), but this change was not significant (**Figure 4B**). In contradistinction, activation in the ipsilateral V1 (iV1) was measured when presenting the highest contrast stimuli (30 and 90 H). This activation was located in the upper-lateral region of iV1, corresponding to the binocular region of this cortex (**Figure 2**). There was no observable modification of the CaS after the 1-week conditioning for the non-conditioned stimulus (90 H, **Figures 4A–D**). The monocular visual conditioning caused a significant decrease in the *Amplitude* on D8 for the lowest contrast of the conditioned orientation (30 L), only in the cV1, PM, and RL cortices (**Table 3**). The modification in the *Size* (**Table 4**) of the responses was highly variable between mice in AL (**Figure 4B**) and LM (**Figure 4D**), but none were significantly diminished. The *Latency* (**Table 5**) was not significantly modified in any areas for any stimulation. The *SNR* (**Table 6**) was significantly reduced in response to the lowest stimulation contrast (30 L) in A and RL.

For the CS/DPZ group, the variability of the results was much lower. The *Amplitude* in response to the conditioned stimuli was significantly decreased on D8 in cV1 (**Figure 4A**) and PM (**Figure 4C**) (30 L, 30 M, and 30 H), AM and RL (30 M and 30 H), and AL (**Figure 4B**) and LM (**Figure 4D**) (30 H) (**Table 3**). The non-conditioned stimulus (90 H) was not affected in any visual areas (**Figure 4**). The comparison of the response amplitude of both orientations (30 vs. 90 H) at D8 showed a significant difference in iV1, AM, PM, RL, and RSC following the DPZ treatment, whereas this difference was not observable on D0. Additionally, the Friedman analysis showed that the *Amplitude* response to the different contrasts (30 L, 30 M, and 30 H) was not significant after the treatment in cV1, AL, PM, and LM (**Figure 4**), even though it was before the conditioning. The *Size* was significantly reduced in response to the CS/DPZ group in cV1 (**Figure 4A**) (30 H), AM and RL (30 M), and in the PM cortex (30 L, 30 M, and 30 H, **Figure 4C**). A significant difference in the *size* between both orientations (30 vs. 90 H) was observable on D8, only in PM. Finally, the cholinergic potentiation of the conditioning had a significant influence on the *SNR* (**Table 6**) in multiple visual cortices and the PM cortex (30 L, 30 M, and 30 H, **Figure 4C**), as well as in cV1 (30 L and 30 M), AL (**Figure 4B**), AM and RL (30 M and 30 H), and A (30 H). The *Latency* and the *Persistence* were not affected following the cholinergic potentiation. Finally, no significant modification of any CaS parameters was observed in response to the 90 H stimulation (**Figure 4**, **Tables 3–6**).

When comparing of the post-pre variation, the *Amplitude* was significantly modified by treatments in PM for all contrasts

TABLE 2 | Response parameters in function of the stimulation contrast and orientation.

Area	Stim.	Amplitude (ΔF/F, %)	Size (Prop.)	Latency (ms)	Persistence (ms)	SNR
cV1	30 L	**0.39 ± 0.04**	**0.85 ± 0.03**	11.22 ± 0.44	20.59 ± 0.45	**13.26 ± 1.08**
	30 M	0.47 ± 0.05	0.86 ± 0.03	11.06 ± 0.44	20.69 ± 0.44	15.26 ± 1.18
	30 H	0.56 ± 0.06	0.88 ± 0.03	10.72 ± 0.38	20.41 ± 0.38	17.33 ± 0.88
	90 L	**0.38 ± 0.04**	0.75 ± 0.06	12.83 ± 0.50	22.25 ± 1.20	14.32 ± 1.50
	90 M	0.46 ± 0.06	0.86 ± 0.03	11.50 ± 0.51	22.13 ± 0.90	10.17 ± 1.25
	90 H	0.55 ± 0.06	0.95 ± 0.01	12.06 ± 0.51	22.94 ± 0.99	14.81 ± 0.79
PM	30 L	**0.37 ± 0.03**	**0.87 ± 0.03**	11.33 ± 0.33	19.59 ± 0.76	6.53 ± 1.05
	30 M	0.46 ± 0.04	0.96 ± 0.01	10.33 ± 0.40	19.94 ± 0.51	8.51 ± 1.49
	30 H	0.56 ± 0.05	0.97 ± 0.01	10.33 ± 0.32	20.63 ± 0.54	9.22 ± 1.62
	90 L	**0.38 ± 0.04**	0.89 ± 0.03	12.33 ± 0.50	21.07 ± 1.10	7.08 ± 1.25
	90 M	0.45 ± 0.04	0.96 ± 0.01	11.50 ± 0.47	19.63 ± 1.03	6.48 ± 1.28
	90 H	0.54 ± 0.05	0.92 ± 0.02	11.56 ± 0.57	21.18 ± 0.89	8.76 ± 1.67
LM	30 L	0.23 ± 0.03	0.73 ± 0.06	11.50 ± 0.51	18.80 ± 0.39	6.06 ± 1.02
	30 M	0.28 ± 0.04	0.80 ± 0.05	12.17 ± 0.47	18.88 ± 0.46	6.69 ± 1.26
	30 H	0.32 ± 0.04	0.92 ± 0.02	11.72 ± 0.37	19.71 ± 0.40	7.36 ± 1.46
	90 L	**0.17 ± 0.02**	0.65 ± 0.08	12.50 ± 0.65	19.35 ± 1.68	4.77 ± 0.92
	90 M	0.23 ± 0.03	0.69 ± 0.07	11.06 ± 0.70	17.19 ± 0.98	4.87 ± 1.01
	90 H	0.27 ± 0.03	0.72 ± 0.06	12.71 ± 0.49	19.41 ± 1.30	6.16 ± 1.23
A	30 L	0.18 ± 0.02	0.34 ± 0.08	10.06 ± 1.00	15.59 ± 0.91	3.60 ± 0.70
	30 M	0.20 ± 0.04	0.40 ± 0.08	8.50 ± 0.44	14.18 ± 1.49	3.90 ± 0.94
	30 H	0.20 ± 0.04	0.33 ± 0.07	9.83 ± 0.82	14.00 ± 1.21	3.10 ± 0.61
	90 L	0.17 ± 0.03	0.21 ± 0.03	11.39 ± 0.70	14.53 ± 1.76	2.57 ± 0.52
	90 M	0.18 ± 0.03	0.33 ± 0.07	11.72 ± 0.80	15.00 ± 1.61	2.54 ± 0.48
	90 H	0.22 ± 0.03	0.30 ± 0.07	11.17 ± 0.97	16.71 ± 1.23	3.36 ± 0.69
AL	30 L	0.27 ± 0.03	0.71 ± 0.07	10.56 ± 0.62	19.07 ± 0.38	5.52 ± 0.96
	30 M	0.31 ± 0.05	0.72 ± 0.07	10.94 ± 0.45	18.36 ± 0.52	5.45 ± 1.01
	30 H	0.36 ± 0.06	0.84 ± 0.05	10.50 ± 0.47	17.25 ± 0.82	5.59 ± 1.08
	90 L	0.24 ± 0.04	0.63 ± 0.08	12.33 ± 0.67	17.76 ± 1.57	3.99 ± 0.72
	90 M	0.28 ± 0.05	0.68 ± 0.07	11.17 ± 0.61	16.53 ± 1.56	4.84 ± 0.79
	90 H	0.33 ± 0.05	0.70 ± 0.07	11.94 ± 0.78	19.59 ± 1.12	5.74 ± 1.03
AM	30 L	0.20 ± 0.02	0.37 ± 0.07	10.44 ± 0.79	17.53 ± 0.94	4.02 ± 0.75
	30 M	0.23 ± 0.03	0.44 ± 0.06	9.78 ± 0.72	18.18 ± 1.21	4.69 ± 1.04
	30 H	0.25 ± 0.04	0.41 ± 0.06	10.61 ± 0.70	16.47 ± 1.33	4.18 ± 0.79
	90 L	0.21 ± 0.03	0.40 ± 0.07	12.00 ± 0.67	17.69 ± 1.78	3.94 ± 0.84
	90 M	0.22 ± 0.04	0.39 ± 0.07	12.28 ± 0.66	19.00 ± 1.54	2.93 ± 0.52
	90 H	0.26 ± 0.04	0.34 ± 0.06	12.00 ± 0.94	18.29 ± 1.42	4.45 ± 0.979
RL	30 L	0.21 ± 0.02	0.59 ± 0.07	9.72 ± 0.80	17.41 ± 0.62	4.38 ± 0.76
	30 M	0.20 ± 0.02	0.64 ± 0.08	11.67 ± 0.56	18.18 ± 0.69	4.86 ± 1.00
	30 H	0.25 ± 0.04	0.63 ± 0.05	11.67 ± 0.56	16.88 ± 0.69	4.53 ± 0.86
	90 L	**0.17 ± 0.02**	0.56 ± 0.06	11.61 ± 0.81	17.53 ± 1.54	3.52 ± 0.63
	90 M	0.23 ± 0.03	0.59 ± 0.07	10.28 ± 0.74	16.69 ± 1.12	3.08 ± 0.56
	90 H	0.27 ± 0.03	0.58 ± 0.07	11.61 ± 0.82	18.47 ± 1.01	4.74 ± 0.93
RSC	30 L	**0.10 ± 0.01**	0.39 ± 0.03	10.89 ± 0.52	13.53 ± 0.72	3.16 ± 0.52
	30 M	0.14 ± 0.02	0.44 ± 0.04	10.59 ± 0.46	16.41 ± 1.21	3.52 ± 0.62
	30 H	0.16 ± 0.02	0.48 ± 0.04	9.39 ± 0.43	15.06 ± 0.59	3.28 ± 0.52
	90 L	**0.10 ± 0.01**	0.39 ± 0.05	11.06 ± 0.93	12.94 ± 1.67	2.74 ± 0.40
	90 M	0.13 ± 0.02	0.43 ± 0.05	10.28 ± 0.74	14.07 ± 0.85	2.36 ± 0.40
	90 H	0.15 ± 0.02	0.46 ± 0.04	11.06 ± 0.59	15.94 ± 1.02	3.62 ± 0.67

Values represent parameters (Amplitude, Size, Latency, Persistence and SNR) of response to the visual stimulation (30 L: 30°, 50%; 30 M: 30°, 75%; 30 H: 30°, 100%; 90 L: 90°, 50%; 90 M: 90°, 75%; 90 H: 90°, 100%) (means ± S.E.M.), 30 L or 90 L. Bold characters represent significant value. $p \leq 0.05$ compared to low contrast counterparts; Underline characters represent significant values comparing 30H response to 90H. $p \leq 0.05$ compared to 90 H.

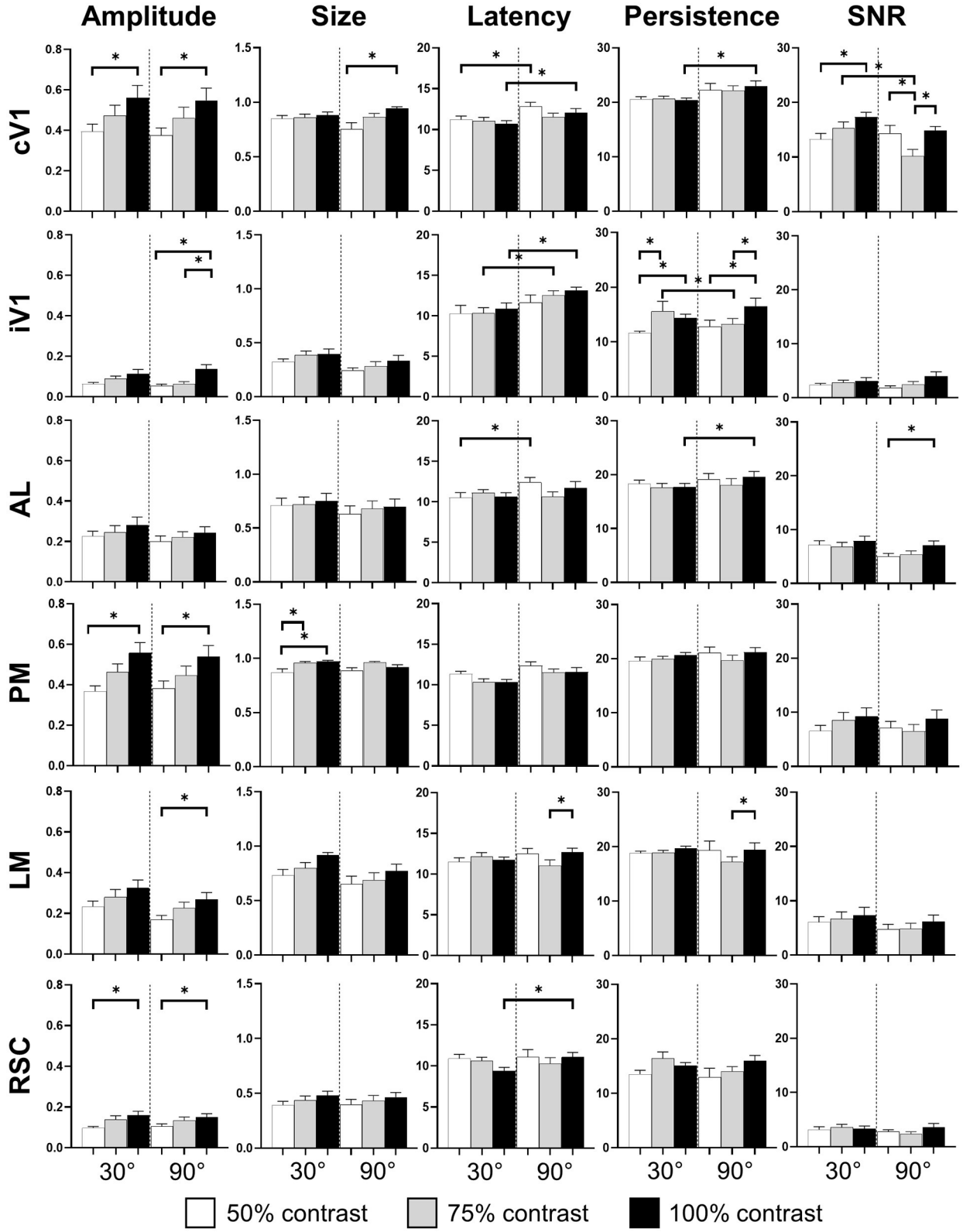

FIGURE 3 | Cortical response in function of orientation and contrast of the stimulus. The contrast of the stimulation influences the amplitude response (*Amplitude*) in almost every area. The proportion of area activated (*Size*) seems to be influenced by the contrast only in PM. The response latency (*Latency*) is influenced by the grating orientation in V1 and RSC while the response duration (*Persistence*) is only influence in V1 by this stimulus parameter. Finally, contrast and orientation of the grating influence the signal-noise ratio (*SNR*) only in V1 ($n = 18$, Kruskal-Wallis and multiple *t*-test, $^*p < 0.05$).

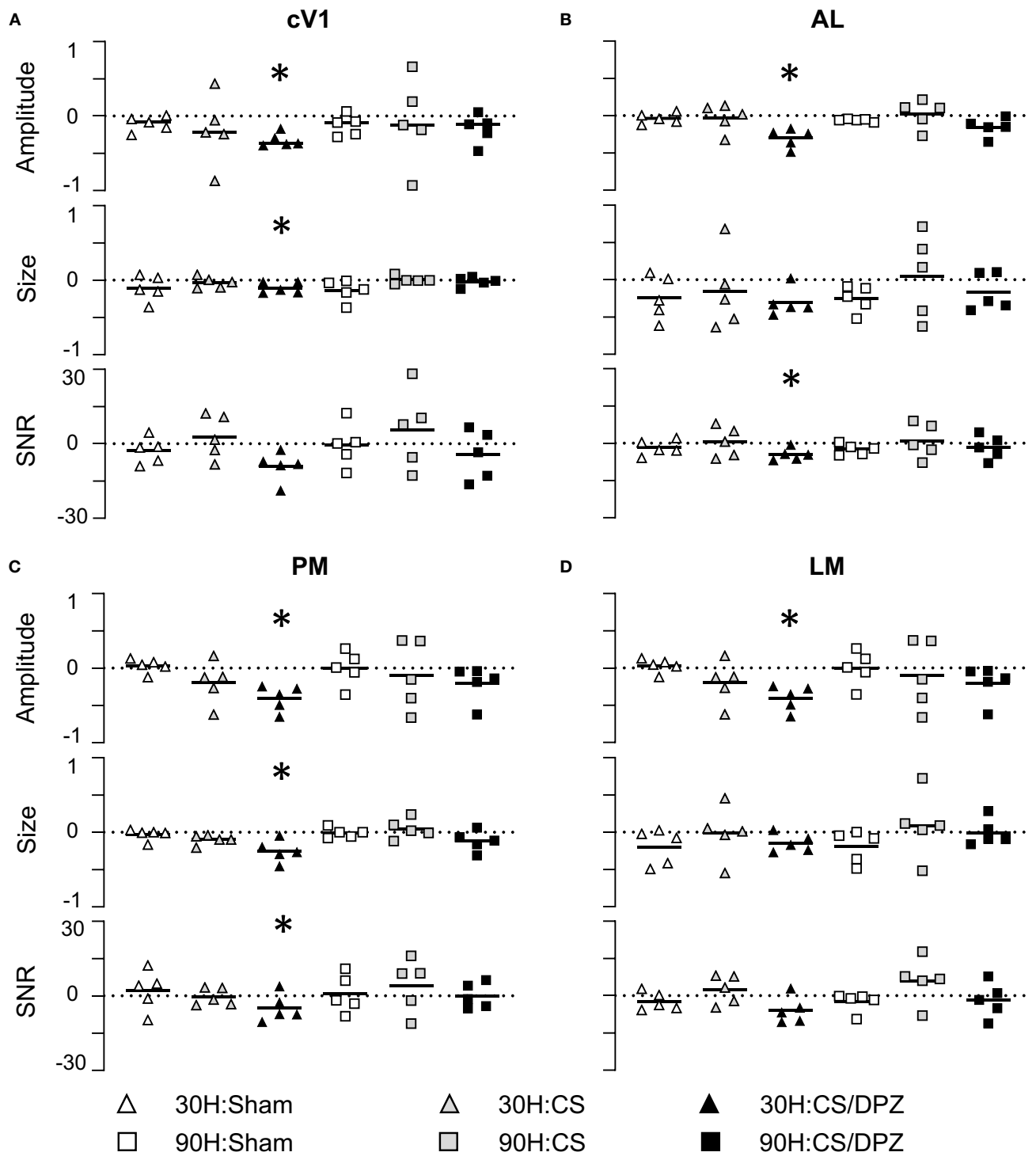

FIGURE 4 | Conditioning and cholinergic potentiation effect on the cortical calcium response in cV1, AL, LM, and PM areas for the conditioned stimulus 30 H and non-conditioned stimulus 90 H After conditioning, the *Amplitude* showed a significant decrease for the conditioned stimuli in cV1 **(A)**, AL **(B)**, PM **(C)**, and LM **(D)** for the CS/DPZ group but not the other conditions. The *Size* showed a significant decrease for the conditioned stimuli (30 H) in cV1 **(A)** and PM **(C)** for the CS/DPZ group. The *SNR* showed a significant decrease for the conditioned orientation in cV1 **(A)**, AL **(B)**, and in PM **(C)** (30 H) for the CS/DPZ group ($n = 5$ for each group; One tail Wilcoxon test, $^*p < 0.05$, comparing D8 to D0, one tail Wilcoxon test).

TABLE 3 | Modification in the *Amplitude* (ΔPost-Pre cortical response) of the visual stimulation.

Area	Stim.	Treatment					
		Sham		CS		CS/DPZ	
cV1	30 L	**−0.188 ± 0.007**	**(−0.188)**	**−0.214 ± 0.059**	**(−0.162)**	**−0.106 ± 0.018**	**(−0.116)**
	30 M	**−0.193 ± 0.013**	**(−0.186)**	−0.190 ± 0.076	(−0.078)	**−0.198 ± 0.036**	**(−0.158)**
	30 H	−0.179 ± 0.024	(−0.205)	−0.188 ± 0.074	(−0.088)	**−0.216 ± 0.043**	**(−0.145)**
	90 H	−0.195 ± 0.021	(0.198)	−0.043 ± 0.084	(0.168)	−0.041 ± 0.038	(−0.098)
iV1	30 L	−0.012 ± 0.008	(−0.020)	−0.011 ± 0.020	(0.000)	0.055 ± 0.040	(0.008)
	30 M	−0.043 ± 0.014	(−0.042)	0.020 ± 0.012	(0.030)	−0.053 ± 0.012	(0.012)
	30 H	−0.023 ± 0.031	(0.010)	0.018 ± 0.015	(−0.006)	−0.023 ± 0.009	(−0.005)
	90 H	−0.058 ± 0.019	(−0.088)	−0.014 ± 0.033	(0.006)	−0.040 ± 0.020	(0.031)
AL	30 L	**−0.120 ± 0.018**	**(−0.123)**	−0.115 ± 0.045	(−0.072)	−0.074 ± 0.024	(−0.028)
	30 M	−0.099 ± 0.028	(−0.122)	−0.062 ± 0.060	(−0.003)	−0.143 ± 0.033	(−0.157)
	30 H	−0.057 ± 0.031	(−0.072)	−0.067 ± 0.059	(0.028)	**−0.204 ± 0.037**	**(−0.209)**
	90 H	−0.077 ± 0.019	(−0.076)	0.016 ± 0.043	(0.024)	−0.079 ± 0.039	(−0.106)
A	30 L	−0.030 ± 0.020	(−0.036)	−0.120 ± 0.035	(−0.149)	−0.009 ± 0.042	(0.002)
	30 M	0.003 ± 0.045	(−0.179)	−0.045 ± 0.050	(−0.015)	−0.066 ± 0.022	(−0.034)
	30 H	0.074 ± 0.015	(0.075)	−0.070 ± 0.037	(−0.118)	**−0.137 ± 0.034**	**(−0.102)**
	90 H	0.049 ± 0.041	(0.009)	0.035 ± 0.026	(0.058)	0.067 ± 0.090	(0.194)
AM	30 L	−0.025 ± 0.030	(−0.012)	−0.091 ± 0.039	(−0.050)	−0.045 ± 0.027	(−0.014)
	30 M	0.001 ± 0.041	(0.025)	−0.041 ± 0.060	(−0.021)	**-0.124 ± 0.024**	**(−0.116)**
	30 H	0.063 ± 0.040	(0.063)	−0.051 ± 0.049	(−0.098)	**-0.192 ± 0.038**	**(−0.123)**
	90 H	0.045 ± 0.060	(0.014)	0.031 ± 0.044	(0.007)	−0.011 ± 0.065	(0.004)
PM	30 L	−0.080 ± 0.019	(−0.103)	**-0.211 ± 0.032**	**(−0.174)**	**-0.182 ± 0.039**	**(−0.144)**
	30 M	−0.094 ± 0.031	(−0.067)	−0.206 ± 0.058	(−0.201)	**-0.257 ± 0.043**	**(−0.194)**
	30 H	−0.040 ± 0.041	(−0.002)	−0.230 ± 0.068	(−0.239)	**-0.300 ± 0.059**	**(−0.354)**
	90 H	−0.074 ± 0.030	(−0.057)	−0.108 ± 0.062	(−0.195)	−0.068 ± 0.065	(−0.038)
LM	30 L	**-0.098 ± 0.019**	**(−0.093)**	−0.128 ± 0.045	(−0.062)	−0.004 ± 0.027	(0.009)
	30 M	−0.094 ± 0.023	(−0.113)	−0.075 ± 0.055	(−0.002)	−0.110 ± 0.052	(−0.078)
	30 H	−0.073 ± 0.042	(−0.139)	−0.063 ± 0.047	(0.009)	**-0.139 ± 0.043**	**(−0.144)**
	90 H	−0.079 ± 0.025	(−0.106)	0.041 ± 0.055	(0–.078)	−0.011 ± 0.028	(−0.028)
RL	30 L	**−0.076 ± 0.013**	**(−0.062)**	**−0.138 ± 0.038**	**(−0.077)**	−0.070 ± 0.036	(−0.089)
	30 M	−0.064 ± 0.030	(−0.096)	−0.067 ± 0.062	(−0.001)	**−0.139 ± 0.027**	**(−0.188)**
	30 H	0.003 ± 0.026	(−0.036)	−0.082 ± 0.050	(−0.070)	**−0.216 ± 0.034**	**(−0.213)**
	90 H	−0.056 ± 0.027	(−0.086)	0.026 ± 0.047	(−0.001)	−0.031 ± 0.058	(−0.016)
RSC	30 L	−0.024 ± 0.012	(−0.051)	−0.063 ± 0.021	(−0.054)	−0.013 ± 0.009	(−0.022)
	30 M	−0.032 ± 0.015	(−0.034)	−0.024 ± 0.037	(−0.021)	−0.014 ± 0.015	(−0.071)
	30 H	0.023 ± 0.010	(0.036)	−0.067 ± 0.029	(−0.066)	−0.061 ± 0.023	(−0.046)
	90 H	−0.011 ± 0.019	(0.010)	0.026 ± 0.013	(0.035)	0.068 ± 0.017	(0.080)

Values represent the cortical Amplitude response to the visual stimulation (n = 5) (30 L: 30°, 50%; 30 M: 30°, 75%; 30 H: 30°, 100%; 90 H: 90°, 100%) cortical response [means ± sem (median)], significant change, $p \leq 0.05$ are represented in bold, t-test compared to ΔPre-Post cortical response (cV1, contralateral primary visual cortex; iV1, ipsilateral primary visual cortex; PM, posterior-median cortex; LM, latero-median cortex; A, anterior cortex; AL, anterio-lateral cortex; AM, anterio-median cortex; RL, rostro-lateral cortex; RS, retrosplenial cortex). The values corresponding to the conditioned stimulus (30 H) are underlined in gray.

of the conditioned orientation (30 L, 30 M, and 30 H), but not for the non-conditioned stimulus (90 H). The multiple comparisons showed that this modification occurred between the non-conditioned group and the DPZ conditioning group, while no significant difference was observable between both conditioned groups. This modification was also observable in AL (30 M and 30 H) and RL (30 H). Despite the Kruskal-Wallis test not showing any significant effect of the treatments in cV1 and AM, multiple comparisons showed a clear significant effect between non-conditioned and DPZ groups (30 H). The only significant differences between CS and CS/DPZ groups were observed in RL and AL for the conditioned stimulus (30 H). For the *Size*, our results showed that there was a significant modification in PM for two contrasts of the conditioned stimulus (30 M and 30 H), both significant diminutions occurring between the non-conditioned and the CS/DPZ group. For the

TABLE 4 | Modification in the *Size* (ΔPost-Pre cortical response) in response of the visual stimulation.

Area	Stim.	Treatment					
		Sham		CS		CS/DPZ	
cV1	30 L	−0.004 ± 0.145	(−0.124)	−0.169 ± 0.190	(−0.301)	−0.048 ± 0.014	(−0.054)
	30 M	0.024 ± 0.166	(−0.128)	−0.009 ± 0.192	(−0.018)	−0.083 ± 0.030	(−0.046)
	30 H	0.022 ± 0.173	(−0.146)	−0.008 ± 0.198	(0.073)	**−0.088 ± 0.017**	**(−0.101)**
	90 H	−0.005 ± 0.162	(−0.157)	0.019 ± 0.183	(0.082)	0.006 ± 0.019	(−0.007)
iV1	30 L	−0.041 ± 0.054	(0.026)	−0.051 ± 0.069	(−0.155)	−0.009 ± 0.037	(−0.008)
	30 M	−0.100 ± 0.032	(−0.060)	0.077 ± 0.030	(0.091)	−0.013 ± 0.038	(−0.014)
	30 H	−0.090 ± 0.090	(−0.072)	0.062 ± 0.051	(0.067)	0.063 ± 0.024	(0.070)
	90 H	−0.086 ± 0.050	(−0.095)	0.076 ± 0.064	(0.035)	0.127 ± 0.041	(0.154)
AL	30 L	−0.217 ± 0.134	(−0.336)	−0.074 ± 0.171	(0.041)	−0.164 ± 0.071	(−0.068)
	30 M	−0.093 ± 0.129	(−0.143)	0.027 ± 0.165	(0.300)	**−0.228 ± 0.042**	**(−0.212)**
	30 H	−0.164 ± 0.156	(−0.344)	−0.029 ± 0.224	(−0.059)	−0.276 ± 0.065	(−0.328)
	90 H	−0.178 ± 0.147	(−0.414)	0.164 ± 0.200	(0.412)	−0.065 ± 0.139	(−0.213)
A	30 L	0.245 ± 0.095	(0.124)	0.131 ± 0.080	(0.108)	0.073 ± 0.152	(−0.008)
	30 M	0.195 ± 0.089	(0.058)	0.255 ± 0.081	(0.172)	−0.182 ± 0.073	(−0.164)
	30 H	0.214 ± 0.076	(0.171)	0.100 ± 0.138	(−0.021)	−0.045 ± 0.131	(−0.138)
	90 H	0.262 ± 0.113	(0.125)	0.263 ± 0.129	(0.101)	0.018 ± 0.154	(0.010)
AM	30 L	0.197 ± 0.114	(0.123)	0.178 ± 0.096	(0.223)	0.045 ± 0.130	(0.129)
	30 M	0.170 ± 0.134	(0.160)	0.217 ± 0.104	(0.235)	**−0.208 ± 0.031**	**(−0.191)**
	30 H	0.199 ± 0.116	(0.129)	0.127 ± 0.151	(−0.184)	−0.210 ± 0.101	(−0.246)
	90 H	0.231 ± 0.140	(0.080)	0.295 ± 0.131	(0.256)	−0.051 ± 0.125	(0.024)
PM	30 L	0.139 ± 0.133	(0.000)	−0.170 ± 0.180	(−0.316)	**−0.273 ± 0.033**	**(−0.239)**
	30 M	0.118 ± 0.149	(−0.014)	−0.034 ± 0.175	(−0.047)	**−0.268 ± 0.045**	**(−0.240)**
	30 H	0.143 ± 0.147	(0.000)	−0.088 ± 0.191	(−0.041)	**−0.260 ± 0.050**	**(−0.265)**
	90 H	0.150 ± 0.142	(−0.054)	0.048 ± 0.211	(0.099)	−0.076 ± 0.047	(−0.067)
LM	30 L	−0.059 ± 0.125	(−0.230)	−0.118 ± 0.181	(−0.230)	−0.044 ± 0.055	(−0.119)
	30 M	−0.058 ± 0.159	(−0.351)	0.075 ± 0.195	(0.049)	−0.124 ± 0.068	(−0.068)
	30 H	−0.141 ± 0.183	(−0.495)	0.087 ± 0.207	(0.053)	−0.099 ± 0.044	(−0.048)
	90 H	−0.142 ± 0.161	(−0.479)	0.175 ± 0.225	(0.117)	0.099 ± 0.066	(0.039)
RL	30 L	0.022 ± 0.132	(−0.127)	0.027 ± 0.161	(0.120)	−0.178 ± 0.095	(−0.257)
	30 M	0.095 ± 0.125	(−0.069)	0.090 ± 0.152	(0.234)	**−0.242 ± 0.057**	**(−0.304)**
	30 H	0.069 ± 0.140	(−0.044)	−0.077 ± 0.176	(−0.258)	−0.381 ± 0.104	(−0.598)
	90 H	0.054 ± 0.145	(−0.127)	0.177 ± 0.182	(0.143)	−0.070 ± 0.149	(0.017)
RSC	30 L	−0.038 ± 0.052	(−0.074)	−0.012 ± 0.082	(0.057)	−0.022 ± 0.054	(−0.065)
	30 M	−0.029 ± 0.055	(−0.119)	0.098 ± 0.052	(0.159)	−0.031 ± 0.043	(−0.009)
	30 H	0.068 ± 0.051	(0.051)	−0.030 ± 0.085	(−0.168)	−0.073 ± 0.039	(−0.062)
	90 H	−0.059 ± 0.090	(−0.227)	0.101 ± 0.094	(0.149)	0.134 ± 0.014	(0.132)

Values represent the cortical Size response to the visual stimulation (n = 5) (30 L: 30°, 50%; 30 M: 30°, 75%; 30 H: 30°, 100%; 90 H: 90°, 100%) cortical response [means ± sem (median)], significant change, $p \leq 0.05$ are represented in bold, t-test compared to ΔPre-Post cortical response (cV1, contralateral primary visual cortex; iV1, ipsilateral primary visual cortex; PM, posterior-median cortex; LM, latero-median cortex; A, anterior cortex; AL, anterio-lateral cortex; AM, anterio-median cortex; RL, rostro-lateral cortex; RS, retrosplenial cortex). The values corresponding to the conditioned stimulus (30 H) are underlined in gray.

Latency, only the response in AM was significantly changed for the conditioned stimulus (30 H), expressed by a significant diminution of *Latency* between the non-conditioned and the CS/DPZ group. Lastly, for the *SNR*, we observed a significant change for the conditioned stimulus (30 H) in cV1 and LM; this significant diminution of the *SNR* was shown between both conditioned groups (CS vs. DPZ). Interestingly, while the variation was low for the sham and CS/DPZ groups, the conditioning alone caused high interindividual variability in the treatment effect.

Activation Correlations

The co-activation of the cortical areas elicited by the conditioned (30°) or non-conditioned (90°) orientation presentation was evaluated using the Pearson's Correlation analysis (**Figure 5**) at D0 and D8. To highlight significant modifications in the activation correlation, results from both days were transformed using the Fisher Z-Transformation, allowing for *t*-test comparisons.

Before the conditioning, the activation correlation was similar for 30 H or 90 H. All selected areas of the visual system were

TABLE 5 | Modification in the *Latency* (ΔPost-Pre cortical response) in response of the visual stimulation.

Area	Stim.	Treatment					
		Sham		CS		CS/DPZ	
cV1	30 L	1.800 ± 0.611	(2.000)	0.000 ± 0.699	(1.000)	0.400 ± 0.806	(0.000)
	30 M	1.400 ± 0.686	(1.000)	0.000 ± 0.558	(0.000)	−0.200 ± 1.020	(−2.000)
	30 H	1.000 ± 0.632	(1.000)	−0.600 ± 0.581	(−2.000)	0.600 ± 0.452	(0.000)
	90 H	2.000 ± 0.558	(2.000)	1.000 ± 1.054	(1.000)	−1.200 ± 0.998	(−1.000)
iV1	30 L	−1.600 ± 1.024	(−3.000)	1.800 ± 1.638	(5.000)	−2.800 ± 2.736	(−3.000)
	30 M	0.200 ± 0.998	(−1.000)	0.000 ± 0.760	(1.000)	−2.400 ± 0.618	(−2.000)
	30 H	0.200 ± 0.879	(0.000)	0.600 ± 0.777	(2.000)	0.800 ± 1.143	(0.000)
	90 H	−1.000 ± 0.869	(0.000)	0.200 ± 1.806	(−1.000)	−1.000 ± 0.789	(0.000)
AL	30 L	0.800 ± 1.718	(2.000)	2.000 ± 0.760	(2.000)	−0.600 ± 0.884	(−1.000)
	30 M	−0.200 ± 0.573	(0.000)	−0.600 ± 0.581	(0.000)	−0.600 ± 0.618	(−1.000)
	30 H	1.000 ± 0.422	(2.000)	−1.400 ± 1.258	(−2.000)	−1.400 ± 1.514	(−2.000)
	90 H	2.400 ± 0.542	(2.000)	0.800 ± 1.356	(2.000)	−2.600 ± 2.237	(−1.000)
A	30 L	0.800 ± 1.611	(−1.000)	1.400 ± 1.166	(2.000)	−1.800 ± 1.971	(−2.000)
	30 M	5.600 ± 1.694	(4.000)	1.000 ± 2.055	(−1.000)	0.200 ± 1.254	(−1.000)
	30 H	1.800 ± 0.827	(1.000)	3.200 ± 1.855	(2.000)	−4.000 ± 1.660	(−5.000)
	90 H	−2.000 ± 1.174	(−2.000)	1.800 ± 1.451	(2.000)	−4.200 ± 1.718	(−5.000)
AM	30 L	2.200 ± 0.533	(2.000)	−1.400 ± 1.046	(−1.000)	−0.400 ± 1.939	(−1.000)
	30 M	1.600 ± 0.581	(3.000)	4.000 ± 1.592	(3.000)	0.800 ± 1.236	(3.000)
	30 H	3.000 ± 1.414	(3.000)	1.600 ± 0.653	(0.000)	−4.600 ± 1.833	(−3.000)
	90 H	0.000 ± 1.193	(−2.000)	0.400 ± 1.833	(−1.000)	−2.000 ± 2.211	(1.000)
PM	30 L	2.200 ± 0.490	(3.000)	0.000 ± 0.596	(0.000)	−0.200 ± 0.442	(0.000)
	30 M	2.000 ± 0.843	(3.000)	−0.400 ± 0.400	(−1.000)	0.200 ± 0.929	(−1.000)
	30 H	0.200 ± 0.533	(−1.000)	0.000 ± 0.558	(1.000)	0.400 ± 0.653	(−1.000)
	90 H	1.000 ± 0.966	(1.000)	0.200 ± 1.482	(−2.000)	0.600 ± 1.002	(1.000)
LM	30 L	1.400 ± 1.408	(1.000)	−1.200 ± 1.181	(−3.000)	−2.200 ± 0.327	(−3.000)
	30 M	−0.800 ± 0.742	(−1.000)	−0.400 ± 0.618	(−1.000)	−1.000 ± 0.471	(−1.000)
	30 H	2.200 ± 0.646	(2.000)	−1.400 ± 0.542	(−1.000)	0.000 ± 0.760	(0.000)
	90 H	1.400 ± 0.618	(1.000)	2.000 ± 1.789	(1.000)	−2.800 ± 1.555	(−2.000)
RL	30 L	1.400 ± 1.586	(3.000)	−0.800 ± 1.597	(−4.000)	0.200 ± 1.541	(1.000)
	30 M	−1.600 ± 0.833	(−1.000)	−0.800 ± 0.389	(−1.000)	−1.800 ± 0.975	(−1.000)
	30 H	0.400 ± 0.400	(1.000)	−0.200 ± 0.929	(−1.000)	−2.000 ± 1.874	(−2.000)
	90 H	−1.000 ± 1.155	(−2.000)	3.000 ± 1.414	(2.000)	2.000 ± 0.869	(1.000)
RSC	30 L	0.000 ± 1.054	(1.000)	−0.600 ± 0.806	(−1.000)	−1.800 ± 1.467	(−1.000)
	30 M	−0.200 ± 1.020	(−1.000)	1.000 ± 2.055	(−2.000)	1.000 ± 1.317	(2.000)
	30 H	1.800 ± 0.573	(1.000)	2.200 ± 0.573	(2.000)	−1.000 ± 0.816	(−1.000)
	90 H	−1.200 ± 1.569	(−2.000)	−0.800 ± 0.975	(−2.000)	0.800 ± 1.181	(2.000)

Values represent the cortical Latency response to the visual stimulation (n = 5) (30 L: 30°, 50%; 30 M: 30°, 75%; 30 H: 30°, 100%; 90 H: 90°, 100%) cortical response [means ± sem (median)], There were no significant differences between groups. (cV1, contralateral primary visual cortex; iV1, ipsilateral primary visual cortex; PM, posterior-median cortex; LM, latero-median cortex; A, anterior cortex; AL, anterio-lateral cortex; AM, anterio-median cortex; RL, rostro-lateral cortex; RS, retrosplenial cortex). The values corresponding to the conditioned stimulus (30 H) are underlined in gray.

strongly correlated with each other (r = 0.69–0.99), with the lowest correlation was expressed between the activation of AL and LM (r = 0.69) and the highest between cV1 and iV1 (r = 0.99). The correlation between cV1 and the ventral visual stream (A, AM, AL, PM, RL) was stronger (r = 0.84–0.98) than for the dorsal stream (LM; r = 0.70). After the conditioning, the highest effect for the conditioned stimulus (30 H) was seen in areas AL and RSC. In fact, a weaker correlation between both areas (and most of the cortical areas) was observed for this conditioned stimulus (30 H) in the CS group. However, the correlation diminution was significant only between AL and A/RSC, and between RSC and AM. No substantial alteration was observed in response to the non-conditioned stimulus (90 H). Interestingly, while using DPZ, this decorrelation between RSC and visual areas was not observable, except for in PM and RL. Despite the lack of significance, the correlation between LM and other areas was heavily diminished (r = −0.25 vs. 0.60). A similar but weaker decorrelation was also observed between AL, PM,

TABLE 6 | Modification in the *SNR* (ΔPost-Pre cortical response) in response of the visual stimulation.

Area	Stim.	Treatment					
		Sham		CS		CS/DPZ	
cV1	30 L	**−5.504 ± 0.939**	**(−6.355)**	−1.907 ± 1.768	(−3.996)	**−3.306 ± 0.501**	**(−5.837)**
	30 M	−4.327 ± 1.539	(−4.141)	−3.725 ± 3.237	(−2.985)	**−4.766 ± 0.662**	**(−11.005)**
	30 H	−5.766 ± 1.486	(−8.209)	2.983 ± 2.863	(−0.047)	−9.187 ± 1.766	(−2.867)
	90 H	−2.594 ± 0.959	(−2.473)	7.242 ± 3.414	(3.423)	−1.487 ± 1.629	(0.603)
iV1	30 L	0.058 ± 0.442	(0.440)	−0.854 ± 0.508	(−0.211)	0.367 ± 0.178	(0.085)
	30 M	−1.101 ± 0.571	(−0.779)	0.340 ± 0.628	(1.567)	0.295 ± 0.430	(−1.238)
	30 H	0.499 ± 0.709	(1.279)	2.775 ± 0.818	(2.652)	−0.609 ± 0.485	(0.623)
	90 H	−1.934 ± 0.938	(−2.564)	2.819 ± 0.750	(2.850)	1.653 ± 0.981	(−2.278)
AL	30 L	**−4.161 ± 0.917**	**(−3.268)**	−3.528 ± 1.243	(−3.304)	−2.162 ± 1.031	(−2.411)
	30 M	−3.300 ± 0.930	(−3.170)	−0.658 ± 1.554	(−1.325)	**−2.020 ± 0.321**	**(−4.938)**
	30 H	−2.525 ± 1.475	(−2.129)	0.056 ± 1.580	(−0.851)	**−5.234 ± 0.403**	**(−0.635)**
	90 H	−3.407 ± 1.386	(−4.288)	2.025 ± 0.734	(1.851)	−0.655 ± 1.501	(0.031)
A	30 L	−0.144 ± 1.189	(−0.480)	**−2.874 ± 0.800**	**(−1.170)**	0.773 ± 1.161	(−0.308)
	30 M	−0.512 ± 1.363	(−0.520)	−1.088 ± 0.935	(−0.018)	−0.408 ± 0.627	(−1.397)
	30 H	2.965 ± 0.779	(2.308)	−0.354 ± 0.667	(−0.769)	**−1.519 ± 0.226**	**(0.332)**
	90 H	1.111 ± 1.156	(0.113)	4.870 ± 1.985	(2.017)	1.008 ± 1.144	(−0.019)
AM	30 L	0.185 ± 1.218	(−0.603)	−1.956 ± 1.227	(−0.496)	−0.877 ± 1.074	(−1.856)
	30 M	−0.361 ± 1.240	(−1.507)	−0.606 ± 1.568	(−0.028)	**−2.107 ± 0.452**	**(−2.772)**
	30 H	2.696 ± 1.585	(2.715)	0.194 ± 1.310	(−1.336)	**−3.147 ± 0.524**	**(0.173)**
	90 H	1.131 ± 1.599	(1.388)	4.603 ± 1.724	(3.499)	−0.831 ± 1.035	(−2.344)
PM	30 L	−1.261 ± 0.916	(−2.382)	−3.458 ± 1.226	(−5.494)	**−3.958 ± 0.818**	**(−3.910)**
	30 M	−0.477 ± 0.847	(0.156)	−3.034 ± 1.772	(−5.262)	**−4.272 ± 0.556**	**(−8.087)**
	30 H	0.054 ± 1.575	(2.053)	0.177 ± 1.799	(−0.835)	**−6.313 ± 1.139**	**(−2.341)**
	90 H	−0.384 ± 1.063	(−0.400)	6.196 ± 2.226	(4.214)	−0.942 ± 1.939	(−0.114)
LM	30 L	**−4.189 ± 0.472**	**(−4.626)**	−1.521 ± 1.612	(−1.382)	0.095 ± 0.730	(−1.288)
	30 M	−3.416 ± 1.276	(−4.333)	−0.116 ± 2.088	(0.060)	−1.540 ± 0.706	(−6.654)
	30 H	−4.055 ± 1.884	(−6.771)	2.858 ± 2.120	(0.285)	−5.189 ± 1.370	(−0.990)
	90 H	−3.593 ± 0.825	(−5.035)	7.007 ± 3.201	(0.956)	1.232 ± 1.013	(−2.942)
RL	30 L	−1.623 ± 1.146	(−0.233)	**−3.190 ± 0.893**	**(−2.021)**	−1.334 ± 1.462	(−1.824)
	30 M	−2.034 ± 1.059	(−2.743)	−1.453 ± 1.530	(−0.398)	**−1.982 ± 0.200**	**(−3.940)**
	30 H	0.586 ± 1.028	(0.708)	−1.045 ± 1.074	(−1.691)	**−4.368 ± 0.332**	**(1.019)**
	90 H	−1.250 ± 1.559	(−2.217)	3.876 ± 1.626	(2.352)	−0.132 ± 1.395	(0.334)
RSC	30 L	−0.883 ± 0.622	(0.254)	−2.924 ± 0.758	(−2.125)	0.274 ± 0.566	(−0.936)
	30 M	−1.326 ± 0.450	(−1.482)	−0.712 ± 0.956	(−1.337)	−0.043 ± 0.423	(−2.072)
	30 H	0.820 ± 0.429	(1.683)	−0.373 ± 0.871	(−1.383)	−1.210 ± 0.584	(0.513)
	90 H	−0.002 ± 0.914	(−0.129)	2.018 ± 0.884	(1.010)	0.285 ± 0.594	(−5.837)

Values represent the cortical signal-noise-ratio (SNR) response to the visual stimulation (n = 5) (30 L: 30°, 50%; 30 M: 30°, 75%; 30 H: 30°, 100%; 90 H: 90°, 100%) cortical response [means ± sem (median)], significant change, $p \leq 0.05$ are represented in bold, t-test compared to ΔPre-Post cortical response (cV1, contralateral primary visual cortex; iV1, ipsilateral primary visual cortex; PM, posterior-median cortex; LM, latero-median cortex; A, anterior cortex; AL, anterio-lateral cortex; AM, anterio-median cortex; RL, rostro-lateral cortex; RS, retrosplenial cortex). The values corresponding to the conditioned stimulus (30 H) are underlined in gray.

RL, and most of the cortical visual areas. However, the activation correlation was generally diminished in this group for the non-conditioned stimulus (90 H), but those changes were discrete and not significant. Comparing the post-conditioning activation correlation of both conditioned groups (CS vs. CS/DPZ), there were changes in the correlation, but none were significant in response to each stimulus (30 and 90 H) (**Figure 5**). For the sham group, there were also rare isolated changes, i.e., the activation correlation for the 30 H stimulus was significantly decreased between RSC and AM, and between cV1 and both iV1 and AM for the non-conditioned stimulus (90 H).

Resting State Correlations

To evaluate the effect of conditioning on the resting state activity, which may reflect the long-term modification of the cortical network occurring in response to the conditioning, the change in the correlation between CaS was measured at rest. Our results showed that the monocular visual conditioning

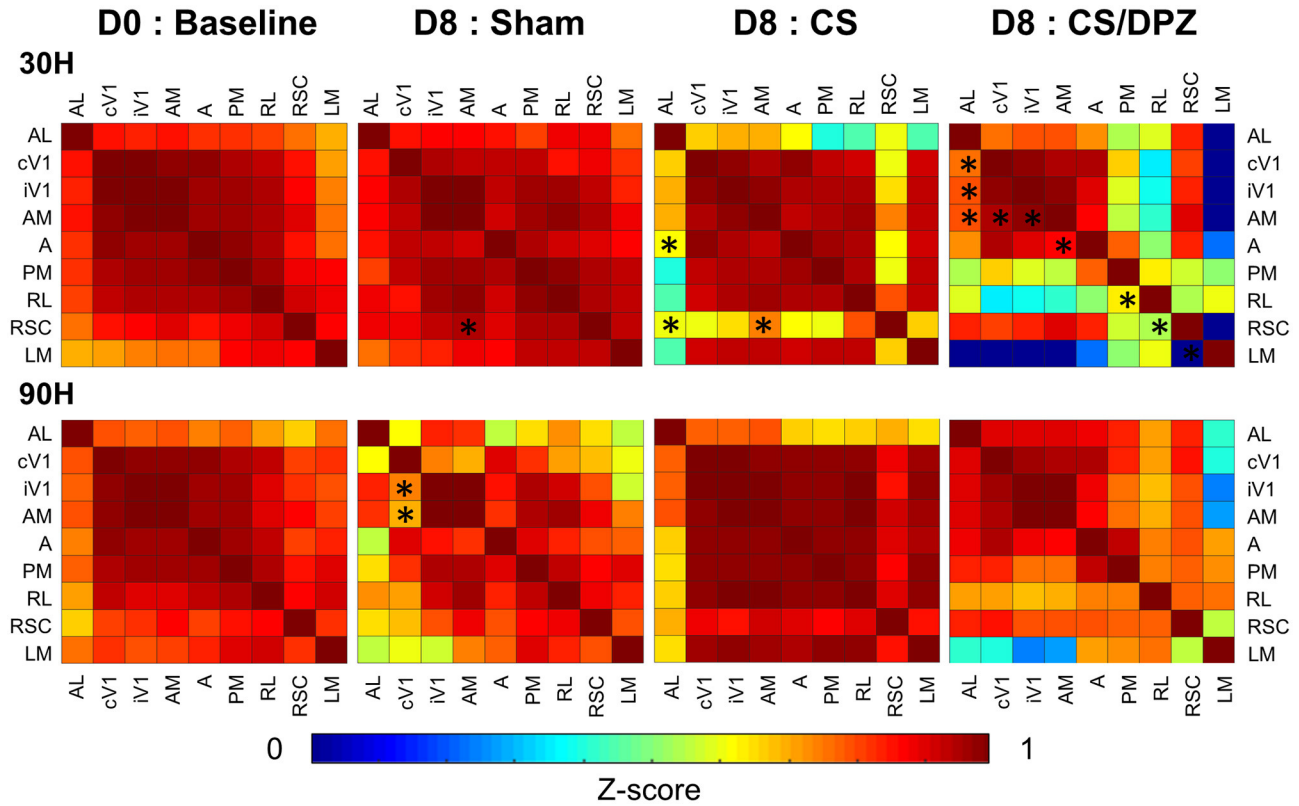

FIGURE 5 | Activation correlation matrix of cortical visual areas. Conditioning weakens the activation correlation between V1 and RSC/AL/PM/A and between A/AM and PM in DPZ group while only between V1/AL and PM in CS. The correlation between AL and LM/PM is also weakened for the non-conditioned stimulus in CS but not in CS/DPZ group ($n = 5$ for each group, Fischer Z-transform and paired T-test, $^*p < 0.05$, compared to the group baseline).

weakened the correlation between the binocular region of the ipsilateral V1 (iV1b) and cV1m, cA, iV1m, iLM, and iA. The cholinergic potentiation through DPZ injection during the conditioning partially restored the correlation between both hemispheres. We observed a diminution of the correlations only between iV1b and both cA and iAC in this group. While comparing the post-conditioning for both conditioned groups, a significant change in correlation between both hemispheres' AL, iV1b, and cV1m, and between cPM and cV1b was observed. For the non-conditioned group, there was no major modification in the resting state correlation over the experiment period (**Figure 6**).

Gene Expression Modification

The expression of plasticity markers was quantified by RT-qPCR after our treatment. Our results showed that the conditioning enhanced the expression of tPa in V1 for both conditioned groups (CS group $= 3.45 \pm 0.54$, $p = 0.0001$; CS/DPZ group $= 2.91 \pm 0.72$, $p = 0.0005$), but caused no modification in the expression of Lynx1, Lypd6, PSD95, and GAP43 compared to the non-conditioned group (**Figure 7**). While comparing both conditioned groups (CS vs. DPZ), no significant difference in tPa expression was observed ($p = 0.6377$), nor in any other gene's expression.

DISCUSSION

In this study, we examined the effects of a 7-day visual monocular conditioning on the mesoscopic map of the entire cortex, as well as cortical correlations with or without cholinergic potentiation via systemic DPZ administration (0.3 mg/kg). As the responses in other cortical areas were negligible, we centered our analysis on nine reactive cortical areas related to vision: A, AL, RL, AM, PM, LM, cV1, and iV1, as well as in the RSC. Our results showed that there was a neuronal activity decrease in the superficial layers after conditioning, enhanced by the DPZ treatment. The significant effects were located in the contralateral visual areas and in the RSC. The functional connectivity between visual areas also decreased following the conditioning potentiated by DPZ. However, those modifications were observed predominantly in the ventral visual pathway. Additionally, an upregulation of tPa, a proteolytic factor involved in plasticity, was observed in the conditioned V1 regardless of the cholinergic potentiation, suggesting the involvement of synaptic plasticity in the conditioning process.

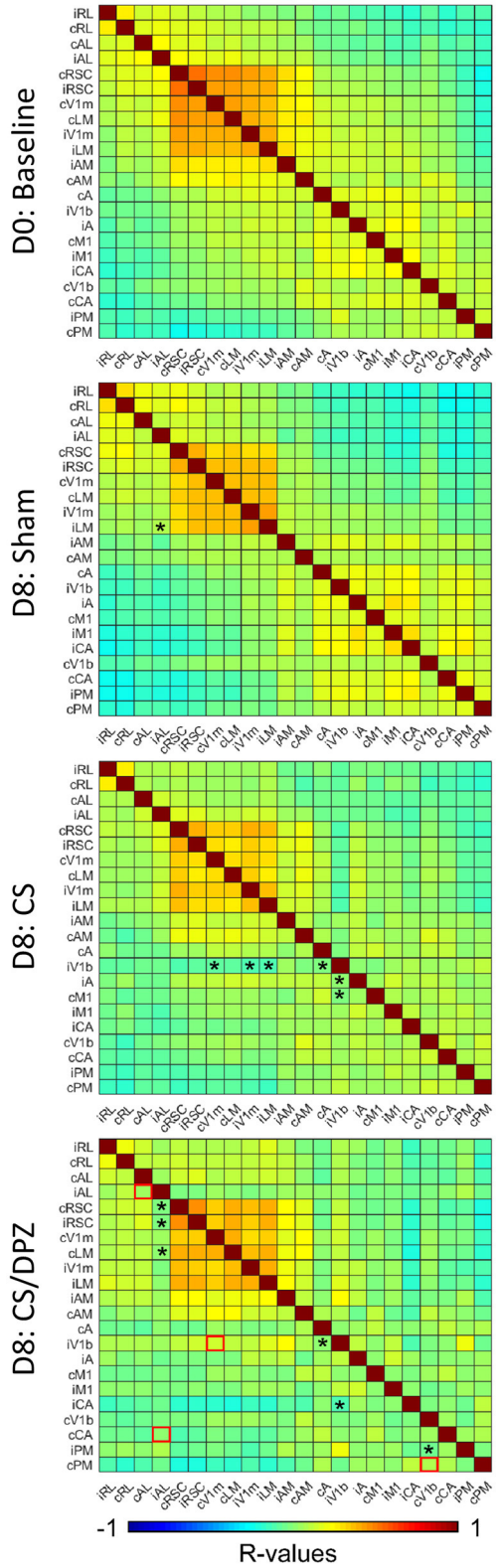

FIGURE 6 | Resting state correlation. Conditioning with saline weakens the correlation of ipsilateral binocular V1 (iV1b) with cV1M, cA, cM1, and iV1M. *(Continued)*

FIGURE 6 | Injection of DPZ during the conditioning diminish this effect on iV1b, while in DPZ group, only the correlation between iV1b and cA and cM1 are weakened ($n = 5$ for each group, Fischer Z-transform and paired T-test, $^*p < 0.05$, compared to the baseline; unpaired T-test, red square=$p < 0.05$, comparing D8 CS to D8 CS/DPZ resting state correlation).

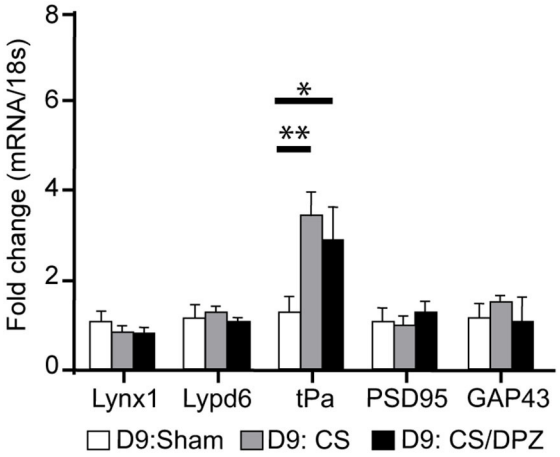

FIGURE 7 | Gene expression modification through conditioning. Conditioning enhanced the expression of tPa in both conditioned groups but caused no modification in the expression of Lynx1, Lypd6, mAChR M2, PSD95, and GAP43 ($n = 5$ for each group, multiple t-test, $^*p = 0.004$, $^{**}p = 0.0001$, compared to Sham group).

This is the first report showing mesoscale CaI mapping in the cortex upon visual stimulation with full field drifting gratings, and after a visual conditioning. The CaS was increased by a visual stimulation and was sensitive to the contrast but not the orientation of the gratings. The CaS was strikingly restricted to the cortical areas involved in vision. These areas were highly correlated during visual stimulation with drifting patterns in naïve animals. However, the CaS was not increased by the visual stimulation of other areas, including the ipsilateral V1. The downstream neural transmission of V1 to the prefrontal cortex was thus not detectable in Thy1-GCaMP6s mice with these experimental conditions. In the resting state, the CaS was only slightly correlated between bilateral cortices, except in the case of the primary visual cortex. The main result shows a strong reduction in the CaS for the conditioned stimulus in most of the cortical areas after CS/DPZ treatment, although a slight tendency for a decreased signal was also seen with sham or CS conditions.

The decrease in cortical activity induced by CS/DPZ is surprising, as previous studies rather demonstrated an enhancement of visual-evoked activity in similar conditions (Cooke and Bear, 2010; Kang et al., 2014; Chamoun et al., 2016). First, this discrepancy might be explained by experimental considerations, i.e., the level of signal collection or arousal

state of the animal. The mCaI technique using GP4.3 Thy1-GCaMP6s mice is an amalgamation of the CaS from excitatory cell bodies, axons, and dendrites located in the superficial layers covering large areas of the cortex. On the other hand, previous electrophysiology recordings have been restricted to one site of layer 4 in V1 and result from the firing of both excitatory and inhibitory neurons. Moreover, recordings in the present study were performed on awake animals, as opposed to animals under anesthesia as seen in previous studies, which may change the neuronal activity, connectivity, or responsiveness to cholinergic input (Galuske et al., 2019). Specifically, awareness and the behavioral states of the animal such as arousal, attention, and locomotion (Niell and Stryker, 2010; Pakan et al., 2016) may influence the duration, dynamics of the evoked response, and cortico-cortical interactions (Sellers et al., 2015). It is possible, although we did not measure it, that repetitive administration of DPZ might slightly change the brain states of the animal although not detected in sleep duration for rats at this dose (Ishida and Kamei, 2009). Finally, mCaI measures the global rather than single-cell response. Due to the salt-and-pepper organization of the neurons in the rodent V1, it is possible that the CaS was augmented in conditioned and tuned neurons, but this signal could have been masked by the suppression of activity in the more numerous non-conditioned and un-tuned neurons by ACh, which suppresses irrelevant neuronal activation (Castro-Alamancos and Oldford, 2002). The decrease of the fluorescent signal in superficial layers, rather than an enhancement in layer 4 neuronal activity, might also be explained by the functional organization of the visual cortex, particularly the layer-dependent neural activity. For example, a layer-specific response to visual stimulation and to cholinergic activation has been previously demonstrated (Obermayer et al., 2017; Yildirim et al., 2019). The excitatory effect of sensory input is stronger in layer 4 (Verdier and Dykes, 2001), which is explained by the endings of the thalamocortical fibers and by fewer GABAergic cells in this layer compared to layers 2/3 (Gonchar et al., 2007). The activation of the layers 2/3 depends on layer 4 feedforward input, layer 5 recurrent circuits, as well as layer 1 feedback from other cortical layers; this connectivity is orchestrated by the inhibition from GABAergic cells (Makino and Komiyama, 2015; D'souza et al., 2016). It is possible that, in our study, both conditioning groups (CS and DPZ-CS) showed inhibition of layer 2/3 pyramidal cells due to either this GABAergic drive or a top-down modulation. This is in line with the calcium activity diminution in layers 2/3 after passive visual conditioning that has been previously observed (Makino and Komiyama, 2015; Henschke et al., 2020). It is also well-documented that cholinergic influence differs from one layer to another according to the receptors involved (Disney et al., 2012; Pfeffer et al., 2013; Obermayer et al., 2017), causing a differential effect of ACh (Oldford and Castro-Alamancos, 2003; Giocomo and Hasselmo, 2007; Soma et al., 2013b; Shimegi et al., 2016; Minces et al., 2017). In addition, it is possible that conditioning partially reduced cell firing, or a reduction of the CaS results from afferent axons, including projecting fibers in layer 1 (although the contribution of axons in the mesoscale CaS recorded is probably minor).

Our findings thus agree with previous studies showing that the conditioning might increase activation of GABAergic neurons in sensory cortices (Gierdalski et al., 2001; Jiao et al., 2006, 2011), leading to an upregulation of the inhibitory drive (Tokarski et al., 2007; Saar et al., 2012; Mckay et al., 2013). This inhibitory drive has been demonstrated as essential for the induction of condition-dependent synaptic plasticity and its maintenance (Posluszny et al., 2015). It is therefore possible that conditioning reduces the number of activated excitatory neurons in layers 2/3 or their level of excitation, which would be exacerbated by ACh. Accordingly, ACh increases inhibitory drive and suppresses lateral spreading (Kimura and Baughman, 1997; Zinke et al., 2006; Obermayer et al., 2018). Furthermore, the spread of a CaS response to the visual stimulation (reduced size of activated area and restriction of the correlation to primary visual areas) was reduced only by CS/DPZ treatment, confirming previous results with ACh administration (Kimura et al., 1999; Silver et al., 2008). Our previous studies have also shown a strong dependency of cholinergic potentiation on M2-type muscarinic and nicotinic receptors (Kang et al., 2015) associated with GABAergic neurons (Disney and Aoki, 2008; Groleau et al., 2015). However, cholinergic fibers modulate various inhibitory circuits, i.e., feed-forward inhibition, lateral inhibition and disinhibition (Obermayer et al., 2018), so we cannot directly infer the effect on GABAergic circuits induced by enhanced cholinergic transmission from our experiment. On the other hand, a decreased response following conditioning might reflect an experience-dependent adaptation of neurons, in which the reduction of activity corresponds to an increase in neuronal efficiency, as the cortical response to visual stimulation is not affected in the upstream secondary cortical areas.

The CS/DPZ reduced the *amplitude* response to the conditioned stimulus in V1, AM, LM, AL, and RSC. The correlation of cortical areas that respond to the pattern stimulation was also affected by our treatment, but only in V1 and in the ventral pathway, while the dorsal path (represented by LM) remained unaffected. This is likely due to the visual stimulus used, i.e., drifting gratings, which are processed by the ventral pathway (Marshel et al., 2011; Smith et al., 2017). The greatest effects occur in V1 and PM, which is unsurprising considering the fact that neuron selectivity in V1 is essential to orientation and contrast changes (Glickfeld et al., 2013b) and because PM is one of the most innervated visual areas, along with LM and AL (Wang et al., 2012). The low temporal frequency of our stimuli (1 Hz) might explain why PM, which responds to low temporal but high spatial frequencies, expresses more modifications in its response post-conditioning than AL, which has preferential affinity to high temporal and low spatial frequencies. These results might also suggest that the temporal frequency of the stimulation has a greater effect on the mouse's neuronal tuning than the spatial frequency. In fact, our stimulation (S.F.: 0.03 cpd, T.F.: 1 Hz, sinusoidal grating) is closer to the preferred spatial frequency of AL (S.F.: 0.045 cpd) and the preferred temporal frequency of PM (T.F.: 1.2 Hz) (Andermann et al., 2011).

Aside from PM, the subsequent extrastriate visual area responses were not significantly affected, while V1 responses were

reduced, suggesting an improved efficiency in V1 feedforward neurons projecting to those areas. The effect of the CS/DPZ did not seem to be related to the release of plasticity brakes Lynx1 and LypD6, which affects nicotinic transmission, since the expression of these molecules was not modified. The increased expression of tPa during CS, combined with a weakening of the conditioned-stimulus response, suggests the involvement of LTD and/or LTP mechanisms. In fact, this plasticity marker is well-known to be essential in experience-dependent plasticity (Mataga et al., 2004). Additionally, its expression is upregulated during long-term potentiation (Qian et al., 1993) and long-term depression (Calabresi et al., 2000). In contradistinction, the expression of GAP43, which has an influence on AMPA receptor endocytosis and LTD (Han et al., 2013), was not modified by any treatments. It is therefore possible that LTP was involved in the mechanism of conditioning, improving the efficiency of neurons in superficial layers. Despite our hypothesis, the effect of cholinergic potentiation does not seem to be related to the release of the plasticity brakes Lynx1 and LypD6, reducing nicotinic transmission, as the expression of these molecules were not modified. Knowing that the cholinergic system plays a key role in visual attentional processes (Herrero et al., 2008), the administration of DPZ might have contributed to an improved beneficial effect on visual transmission. Consequently, DPZ reduced the increased inter-individual variability in the CS groups, suggesting an attentional effect of increased levels of ACh.

DPZ also abolished the CS-induced decorrelation between interhemispheric binocular and monocular zones of V1 during resting state, suggesting an effect of ACh on binocular interaction. These results are also concomitant with a recent human study showing that DPZ administration reduces the ocular dominance shift normally observed after a monocular deprivation (Sheynin et al., 2019) and reduce interocular suppression (Sheynin et al., 2020). Knowing that the binocular response is influenced by multiple factors such as the thalamocortical input from both eyes, the GABAergic modulation, and the corticocortical projections, it might be further explained by the influence of ACh on each of these factors (Disney et al., 2012; Groleau et al., 2015; Vaucher et al., 2019). This result may reflect the modification in perceptual strength in the conditioned eye over the other in the binocular region as observed in a monocular deprivation experiment (Scholl et al., 2017).

In regard to present and previous results, we suggest that the global decrease observed in cortical calcium responses in the superficial layers of V1 and PM might be due to the attenuation of pyramidal neuron activation in layers 2/3, even if layer 4 is activated, and thus reduces conscious perception of the conditioned stimulus. Accordingly, a similar repetitive passive visual stimulation causes a reduction of the calcium signals to the passive stimulation, whereas a rewarded presentation leads to an increased calcium response (Makino and Komiyama, 2015; Henschke et al., 2020). This may result from a suppression of the neurons' response to the passive conditioned stimulus in layers 2/3 from direct activation of the GABAergic neurons by feedforward inputs, or through top-down feedback activation of layer 1 inhibitory interneurons (Makino and Komiyama, 2015). It is also possible that the decreased activity resulted from reduced attention or motivation in the mice. It is tempting to speculate that this reduction of neuronal response in superficial layers probably reflects the habituation of the neurons to irrelevant stimuli, and prevents the upstream processing of this stimulus to high order cortices. Accordingly, we do not report any change in the high-level cortical areas. In that case, this suppression would diminish the perception of this signal, in line with previous studies suggesting the attenuation of the conscious perception of redundant signals that are irrelevant for survival (Briggs et al., 2013; Galuske et al., 2019). It is, however, contradictory to the effect of ACh in previous studies. First, ACh usually mediates visual attentional processes (Herrero et al., 2008; Li et al., 2018), therefore improving ACh cortical levels should alleviate the suppression effect of passive conditioning. ACh is usually considered as responsible for shifting the dynamics of the cortical circuits to a signal significant mode and enhancing cue detection (Sarter and Lustig, 2020). Second, the coupling of passive visual stimulation to electrical stimulation of cholinergic neurons or DPZ administration has been shown to selectively improve the detection of the conditioned grating after the training. This is in favor of an improved perception. In this regard, the effect of ACh on neuronal plasticity is highly relevant. First, the increase of tPA in this study suggests an LTP process, which is in line with previous studies showing the triggering of long-lasting events by ACh in V1 (Kang and Vaucher, 2009). Altogether, our results and these studies could argue for a processing of this passive stimulus for an automatic mode that does not require attentional demand and neuronal resources, but rather relies on improve neuronal efficiency. This would be in line with Furey and Ricciardi results proposing improved circuitry dynamics by DPZ in humans (Furey et al., 2000; Ricciardi et al., 2013).

DATA AVAILABILITY STATEMENT

The datasets generated for this study are available on request to the corresponding author.

ETHICS STATEMENT

The animal study was reviewed and approved by Comité de déontologie de l'expérimentation sur les animaux (CDEA) de l'université de Montréal.

AUTHOR CONTRIBUTIONS

GL performed the experiments, wrote the MATLAB script supervised by Labeo Technologies, analyzed the data, and wrote the first draft of the paper. RO contributed to RT-qPCR experiments. GL and EV designed the experiments, interpreted the results, and finalized writing.

All authors contributed to the article and approved the submitted version.

FUNDING

This work was supported by a grant from the NSERC (RGPIN-2016-06634) to EV and from the FRQS Research Quebec Bio-Imaging Network (QBIN, Innovation Program) to EV, in partnership with Labeo Technologies (Montreal, QC, Canada). GL was the recipient of a scholarship from the QBIN and from the École d'Optométrie of Université de Montréal.

ACKNOWLEDGMENTS

The authors are grateful to Drs. Matthieu Vanni (School of Optometry) and Samuel Bélanger (Labeo Technologies Inc.) for their valuable assistance in mesoscopic calcium imaging, including in the development of the scripts for the analysis.

REFERENCES

Andermann, M. L., Kerlin, A. M., Roumis, D. K., Glickfeld, L. L., and Reid, R. C. (2011). Functional specialization of mouse higher visual cortical areas. *Neuron* 72, 1025–1039. doi: 10.1016/j.neuron.2011.11.013

Bhattacharyya, A., Veit, J., Kretz, R., Bondar, I., and Rainer, G. (2013). Basal forebrain activation controls contrast sensitivity in primary visual cortex. *BMC Neurosci.* 14:55. doi: 10.1186/1471-2202-14-55

Bontempi, B., Whelan, K. T., Risbrough, V. B., Lloyd, G. K., and Menzaghi, F. (2003). Cognitive enhancing properties and tolerability of cholinergic agents in mice: a comparative study of nicotine, donepezil, and SIB-1553A, a subtype-selective ligand for nicotinic acetylcholine receptors. *Neuropsychopharmacology* 28, 1235–1246. doi: 10.1038/sj.npp.1300150

Bretin, S., Krazem, A., Henkous, N., Froger-Colleaux, C., Mocaer, E., Louis, C., et al. (2018). Synergistic enhancing-memory effect of donepezil and S 47445, an AMPA positive allosteric modulator, in middle-aged and aged mice. *Psychopharmacology* 235, 771–787. doi: 10.1007/s00213-017-4792-5

Briggs, F., Mangun, G. R., and Usrey, W. M. (2013). Attention enhances synaptic efficacy and the signal-to-noise ratio in neural circuits. *Nature* 499, 476–480. doi: 10.1038/nature12276

Calabresi, P., Napolitano, M., Centonze, D., Marfia, G. A., Gubellini, P., Teule, M. A., et al. (2000). Tissue plasminogen activator controls multiple forms of synaptic plasticity and memory. *Eur. J. Neurosci.* 12, 1002–1012. doi: 10.1046/j.1460-9568.2000.00991.x

Castro-Alamancos, M. A., and Oldford, E. (2002). Cortical sensory suppression during arousal is due to the activity-dependent depression of thalamocortical synapses. *J. Physiol.* 541, 319–331. doi: 10.1113/jphysiol.2002.016857

Chamoun, M., Groleau, M., Bhat, M., and Vaucher, E. (2016). Dose-dependent effect of donepezil administration on long-term enhancement of visually evoked potentials and cholinergic receptor overexpression in rat visual cortex. *J. Physiol. Paris* 110, 65–74. doi: 10.1016/j.jphysparis.2016.11.010

Chen, N., Sugihara, H., Sharma, J., Perea, G., Petravicz, J., Le, C., et al. (2012). Nucleus basalis-enabled stimulus-specific plasticity in the visual cortex is mediated by astrocytes. *Proc. Natl. Acad. Sci. U.S.A.* 109, E2832–E2841. doi: 10.1073/pnas.1206557109

Chen, N., Sugihara, H., and Sur, M. (2015). An acetylcholine-activated microcircuit drives temporal dynamics of cortical activity. *Nat. Neurosci.* 18, 892–902. doi: 10.1038/nn.4002

Chen, T. W., Wardill, T. J., Sun, Y., Pulver, S. R., Renninger, S. L., Baohan, A., et al. (2013). Ultrasensitive fluorescent proteins for imaging neuronal activity. *Nature* 499, 295–300. doi: 10.1038/nature12354

Chen, X., Hoffmann, K. P., Albright, T. D., and Thiele, A. (2012). Effect of feature-selective attention on neuronal responses in macaque area MT. *J. Neurophysiol.* 107, 1530–1543. doi: 10.1152/jn.01042.2010

Chubykin, A. A., Roach, E. B., Bear, M. F., and Shuler, M. G. (2013). A cholinergic mechanism for reward timing within primary visual cortex. *Neuron* 77, 723–735. doi: 10.1016/j.neuron.2012.12.039

Cooke, S. F., and Bear, M. F. (2010). Visual experience induces long-term potentiation in the primary visual cortex. *J. Neurosci.* 30, 16304–16313. doi: 10.1523/JNEUROSCI.4333-10.2010

Coppola, J. J., Ward, N. J., Jadi, M. P., and Disney, A. A. (2016). Modulatory compartments in cortex and local regulation of cholinergic tone. *J. Physiol. Paris* 110, 3–9. doi: 10.1016/j.jphysparis.2016.08.001

Dana, H., Chen, T. W., Hu, A., Shields, B. C., Guo, C., Looger, L. L., et al. (2014). Thy1-GCaMP6 transgenic mice for neuronal population imaging *in vivo*. *PLoS ONE* 9:e108697. doi: 10.1371/journal.pone.0108697

Darvas, M., Morsch, M., Racz, I., Ahmadi, S., Swandulla, D., and Zimmer, A. (2009). Modulation of the Ca^{2+} conductance of nicotinic acetylcholine receptors by Lypd6. *Eur. Neuropsychopharmacol.* 19, 670–681. doi: 10.1016/j.euroneuro.2009.03.007

Demars, M. P., and Morishita, H. (2014). Cortical parvalbumin and somatostatin GABA neurons express distinct endogenous modulators of nicotinic acetylcholine receptors. *Mol. Brain* 7:75. doi: 10.1186/s13041-014-0075-9

Disney, A. A., and Aoki, C. (2008). Muscarinic acetylcholine receptors in macaque V1 are most frequently expressed by parvalbumin-immunoreactive neurons. *J. Comp. Neurol.* 507, 1748–1762. doi: 10.1002/cne.21616

Disney, A. A., Aoki, C., and Hawken, M. J. (2012). Cholinergic suppression of visual responses in primate V1 is mediated by GABAergic inhibition. *J. Neurophysiol.* 108, 1907–1923. doi: 10.1152/jn.00188.2012

D'souza, R. D., Meier, A. M., Bista, P., Wang, Q., and Burkhalter, A. (2016). Recruitment of inhibition and excitation across mouse visual cortex depends on the hierarchy of interconnecting areas. *Elife* 5:e19332. doi: 10.7554/eLife.19332.018

Furey, M. L., Pietrini, P., and Haxby, J. V. (2000). Cholinergic enhancement and increased selectivity of perceptual processing during working memory. *Science* 290, 2315–2319. doi: 10.1126/science.290.5500.2315

Galuske, R. A. W., Munk, M. H. J., and Singer, W. (2019). Relation between gamma oscillations and neuronal plasticity in the visual cortex. *Proc. Natl. Acad. Sci. U.S.A.* 116, 23317–23325. doi: 10.1073/pnas.1901277116

Gavornik, J. P., and Bear, M. F. (2014). Learned spatiotemporal sequence recognition and prediction in primary visual cortex. *Nat. Neurosci.* 17, 732–737. doi: 10.1038/nn.3683

Gaykema, R. P., Luiten, P. G., Nyakas, C., Traber, J. (1990). Cortical projection patterns of the medial septum-diagonal band complex. *J. Comp. Neurol.* 293, 103–124. doi: 10.1002/cne.902930109

Geerts, H., Guillaumat, P.-O., Grantham, C., Bode, W., Anciaux, K., and Sachak, S. (2005). Brain levels and acetylcholinesterase inhibition with galantamine and donepezil in rats, mice, and rabbits. *Brain Res.* 1033, 186–193. doi: 10.1016/j.brainres.2004.11.042

Gias, C., Hewson-Stoate, N., Jones, M., Johnston, D., Mayhew, J. E., and Coffey, P. J. (2005). Retinotopy within rat primary visual cortex using optical imaging. *Neuroimage* 24, 200–206. doi: 10.1016/j.neuroimage.2004.08.015

Gierdalski, M., Jablonska, B., Siucinska, E., Lech, M., Skibinska, A., and Kossut, M. (2001). Rapid regulation of GAD67 mRNA and protein level in cortical neurons after sensory learning. *Cereb. Cortex* 11, 806–815. doi: 10.1093/cercor/11.9.806

Giocomo, L. M., and Hasselmo, M. E. (2007). Neuromodulation by glutamate and acetylcholine can change circuit dynamics by regulating the relative influence of afferent input and excitatory feedback. *Mol. Neurobiol.* 36, 184–200. doi: 10.1007/s12035-007-0032-z

Glickfeld, L. L., Andermann, M. L., Bonin, V., and Reid, R. C. (2013a). Cortico-cortical projections in mouse visual cortex are functionally target specific. *Nat. Neurosci.* 16, 219–226. doi: 10.1038/nn.3300

Glickfeld, L. L., Histed, M. H., and Maunsell, J. H. (2013b). Mouse primary visual cortex is used to detect both orientation and contrast changes. *J. Neurosci.* 33, 19416–19422. doi: 10.1523/JNEUROSCI.3560-13.2013

Glickfeld, L. L., and Olsen, S. R. (2017). Higher-order areas of the mouse visual cortex. *Annu. Rev. Vis. Sci.* 3, 251–273. doi: 10.1146/annurev-vision-102016-061331

Gonchar, Y., Wang, Q., and Burkhalter, A. (2007). Multiple distinct subtypes of GABAergic neurons in mouse visual cortex identified by triple immunostaining. *Front. Neuroanat.* 1:3. doi: 10.3389/neuro.05.003.2007

Groleau, M., Kang, J. I., Huppe-Gourgues, F., and Vaucher, E. (2015). Distribution and effects of the muscarinic receptor subtypes in the primary visual cortex. *Front. Synaptic Neurosci.* 7:10. doi: 10.3389/fnsyn.2015.00010

Groleau, M., Nguyen, H. N., Vanni, M. P., Huppe-Gourgues, F., Casanova, C., and Vaucher, E. (2014). Impaired functional organization in the visual cortex of muscarinic receptor knock-out mice. *Neuroimage* 98, 233–242. doi: 10.1016/j.neuroimage.2014.05.016

Guevara, E., Sadekova, N., Girouard, H., and Lesage, F. (2013). Optical imaging of resting-state functional connectivity in a novel arterial stiffness model. *Biomed. Opt. Express* 4, 2332–2346. doi: 10.1364/BOE.4.002332

Han, M.-H., Jiao, S., Jia, J.-M., Chen, Y., Chen, C. Y., Gucek, M., et al. (2013). The novel caspase-3 substrate Gap43 is involved in AMPA receptor endocytosis and long-term depression. *Mol. Cell. Proteomics* 12, 3719–3731. doi: 10.1074/mcp.M113.030676

Hendel, T., Mank, M., Schnell, B., Griesbeck, O., Borst, A., and Reiff, D. F. (2008). Fluorescence changes of genetic calcium indicators and OGB-1 correlated with neural activity and calcium *in vivo* and *in vitro*. *J. Neurosci.* 28, 7399–7411. doi: 10.1523/JNEUROSCI.1038-08.2008

Hensch, T. K. (2005). Critical period plasticity in local cortical circuits. *Nat. Rev. Neurosci.* 6, 877–888. doi: 10.1038/nrn1787

Henschke, J. U., Dylda, E., Katsanevaki, D., Dupuy, N., Currie, S. P., Amvrosiadis, T., et al. (2020). Reward association enhances stimulus-specific representations in primary visual cortex. *Curr. Biol.* 30, 1–15. doi: 10.1016/j.cub.2020.03.018

Herrero, J. L., Roberts, M. J., Delicato, L. S., Gieselmann, M. A., Dayan, P., and Thiele, A. (2008). Acetylcholine contributes through muscarinic receptors to attentional modulation in V1. *Nature* 454, 1110–1114. doi: 10.1038/nature07141

Huberman, A. D., and Niell, C. M. (2011). What can mice tell us about how vision works? *Trends Neurosci.* 34, 464–473. doi: 10.1016/j.tins.2011.07.002

Huppé-Gourgues, F., Jegouic, K., Vaucher, E., (2018). Topographic organization of cholinergic innervation from the basal forebrain to the visual cortex in the rat. *Front. Neural Circuits.* 12:19. doi: 10.3389/fncir.2018.00019

Ishida, T., and Kamei, C. (2009). Characteristic effects of anti-dementia drugs on rat sleep patterns. *J. Pharmacol. Sci.* 109, 449–455. doi: 10.1254/jphs.08229FP

Jiao, Y., Zhang, C., Yanagawa, Y., and Sun, Q.-Q. (2006). Major effects of sensory experiences on the neocortical inhibitory circuits. *J. Neurosci.* 26, 8691–8701. doi: 10.1523/JNEUROSCI.2478-06.2006

Jiao, Y., Zhang, Z., Zhang, C., Wang, X., Sakata, K., Lu, B., et al. (2011). A key mechanism underlying sensory experience-dependent maturation of neocortical GABAergic circuits *in vivo*. *Proc. Natl. Acad. Sci. U.S.A.* 108, 12131–12136. doi: 10.1073/pnas.1105296108

Kang, J. I., Groleau, M., Dotigny, F., Giguere, H., and Vaucher, E. (2014). Visual training paired with electrical stimulation of the basal forebrain improves orientation-selective visual acuity in the rat. *Brain Struct. Funct.* 219, 1493–1507. doi: 10.1007/s00429-013-0582-y

Kang, J. I., Huppe-Gourgues, F., and Vaucher, E. (2015). Pharmacological mechanisms of cortical enhancement induced by the repetitive pairing of visual/cholinergic stimulation. *PLoS ONE* 10:e0141663. doi: 10.1371/journal.pone.0141663

Kang, J. I., and Vaucher, E. (2009). Cholinergic pairing with visual activation results in long-term enhancement of visual evoked potentials. *PLoS ONE* 4:e5995. doi: 10.1371/journal.pone.0005995

Kilgard, M. P., and Merzenich, M. M. (1998). Cortical map reorganization enabled by nucleus basalis activity. *Science* 279, 1714–1718. doi: 10.1126/science.279.5357.1714

Kim, E., and Sheng, M. (2004). PDZ domain proteins of synapses. *Nat. Rev. Neurosci.* 5, 771–781. doi: 10.1038/nrn1517

Kimura, F., and Baughman, R. W. (1997). Distinct muscarinic receptor subtypes suppress excitatory and inhibitory synaptic responses in cortical neurons. *J. Neurophysiol.* 77, 709–716. doi: 10.1152/jn.1997.77.2.709

Kimura, F., Fukuda, M., and Tsumoto, T. (1999). Acetylcholine suppresses the spread of excitation in the visual cortex revealed by optical recording: possible differential effect depending on the source of input. *Eur. J. Neurosci.* 11, 3597–3609. doi: 10.1046/j.1460-9568.1999.00779.x

Leaderbrand, K., Chen, H. J., Corcoran, K. A., Guedea, A. L., Jovasevic, V., Wess, J., et al. (2016). Muscarinic acetylcholine receptors act in synergy to facilitate learning and memory. *Learn. Memory* 23, 631–638. doi: 10.1101/lm.043133.116

Li, X., Yu, B., Sun, Q., Zhang, Y., Ren, M., Zhang, X., et al. (2018). Generation of a whole-brain atlas for the cholinergic system and mesoscopic projectome analysis of basal forebrain cholinergic neurons. *Proc. Natl. Acad. Sci. U.S.A.* 115, 415–420. doi: 10.1073/pnas.1703601115

Livak, K. J., and Schmittgen, T. D. (2001). Analysis of relative gene expression data using real-time quantitative PCR and the 2(-Delta Delta C(T)) method. *Methods* 25, 402–408. doi: 10.1006/meth.2001.1262

Ma, Y., Shaik, M. A., Kim, S. H., Kozberg, M. G., Thibodeaux, D. N., Zhao, H. T., et al. (2016). Wide-field optical mapping of neural activity and brain haemodynamics: considerations and novel approaches. *Philos. Trans. R. Soc. Lond. B Biol. Sci.* 371:20150360. doi: 10.1098/rstb.2015.0360

Makino, H., and Komiyama, T. (2015). Learning enhances the relative impact of top-down processing in the visual cortex. *Nat. Neurosci.* 18, 1116–1122. doi: 10.1038/nn.4061

Marshel, J. H., Garrett, M. E., Nauhaus, I., and Callaway, E. M. (2011). Functional specialization of seven mouse visual cortical areas. *Neuron* 72, 1040–1054. doi: 10.1016/j.neuron.2011.12.004

Mataga, N., Mizuguchi, Y., and Hensch, T. K. (2004). Experience-dependent pruning of dendritic spines in visual cortex by tissue plasminogen activator. *Neuron* 44, 1031–1041. doi: 10.1016/j.neuron.2004.11.028

Mataga, N., Nagai, N., and Hensch, T. K. (2002). Permissive proteolytic activity for visual cortical plasticity. *Proc. Natl. Acad. Sci. U.S.A.* 99, 7717–7721. doi: 10.1073/pnas.102088899

Mcclure-Begley, T. D., King, N. M., Collins, A. C., Stitzel, J. A., Wehner, J. M., and Butt, C. M. (2009). Acetylcholine-stimulated [3H]GABA release from mouse brain synaptosomes is modulated by alpha4beta2 and alpha4alpha5beta2 nicotinic receptor subtypes. *Mol. Pharmacol.* 75, 918–926. doi: 10.1124/mol.108.052274

Mckay, B. M., Oh, M. M., and Disterhoft, J. F. (2013). Learning increases intrinsic excitability of hippocampal interneurons. *J. Neurosci.* 33, 5499–5506. doi: 10.1523/JNEUROSCI.4068-12.2013

Mentis, M. J., Sunderland, T., Lai, J., Connolly, C., Krasuski, J., Levine, B., et al. (2001). Muscarinic versus nicotinic modulation of a visual task. a pet study using drug probes. *Neuropsychopharmacology* 25, 555–564. doi: 10.1016/S0893-133X(01)00264-0

Minces, V., Pinto, L., Dan, Y., and Chiba, A. A. (2017). Cholinergic shaping of neural correlations. *Proc. Natl. Acad. Sci. U.S.A.* 114, 5725–5730. doi: 10.1073/pnas.1621493114

Mishkin, M., Lewis, M. E., and Ungerleider, L. G. (1982). Equivalence of parieto-preoccipital subareas for visuospatial ability in monkeys. *Behav. Brain Res.* 6, 41–55. doi: 10.1016/0166-4328(82)90080-8

Morishita, H., Miwa, J. M., Heintz, N., and Hensch, T. K. (2010). Lynx1, a cholinergic brake, limits plasticity in adult visual cortex. *Science* 330, 1238–1240. doi: 10.1126/science.1195320

Motulsky, H. J., and Brown, R. E. (2006). Detecting outliers when fitting data with nonlinear regression – a new method based on robust nonlinear regression and the false discovery rate. *BMC Bioinformatics* 7:123. doi: 10.1186/1471-2105-7-123

Niell, C. M., and Stryker, M. P. (2010). Modulation of visual responses by behavioral state in mouse visual cortex. *Neuron* 65, 472–479. doi: 10.1016/j.neuron.2010.01.033

Obermayer, J., Heistek, T. S., Kerkhofs, A., Goriounova, N. A., Kroon, T., Baayen, J. C., et al. (2018). Lateral inhibition by Martinotti interneurons is facilitated by cholinergic inputs in human and mouse neocortex. *Nat. Commun.* 9:4101. doi: 10.1038/s41467-018-06628-w

Obermayer, J., Verhoog, M. B., Luchicchi, A., and Mansvelder, H. D. (2017). Cholinergic modulation of cortical microcircuits is layer-specific: evidence from rodent, monkey and human brain. *Front. Neural Circuits* 11:100. doi: 10.3389/fncir.2017.00100

Oldford, E., and Castro-Alamancos, M. (2003). Input-specific effects of acetylcholine on sensory and intracortical evoked responses

in the "barrel cortex" *in vivo*. *Neuroscience* 117, 769–778. doi: 10.1016/S0306-4522(02)00663-2

Pakan, J. M. P., Lowe, S. C., Dylda, E., Keemink, S. W., Currie, S. P., Coutts, C. A., et al. (2016). Behavioral-state modulation of inhibition is context-dependent and cell type specific in mouse visual cortex. *Elife* 5:e14985. doi: 10.7554/eLife.14985.013

Pfeffer, C. K., Xue, M., He, M., Huang, Z. J., and Scanziani, M. (2013). Inhibition of inhibition in visual cortex: the logic of connections between molecularly distinct interneurons. *Nat. Neurosci*. 16, 1068–1076. doi: 10.1038/nn.3446

Posluszny, A., Liguz-Lecznar, M., Turzynska, D., Zakrzewska, R., Bielecki, M., and Kossut, M. (2015). Learning-dependent plasticity of the barrel cortex is impaired by restricting GABA-ergic transmission. *PLoS ONE* 10:e0144415. doi: 10.1371/journal.pone.0144415

Qian, Z., Gilbert, M. E., Colicos, M. A., Kandel, E. R., and Kuhl, D. (1993). Tissue-plasminogen activator is induced as an immediate-early gene during seizure, kindling and long-term potentiation. *Nature* 361, 453–457. doi: 10.1038/361453a0

Ricciardi, E., Handjaras, G., Bernardi, G., Pietrini, P., and Furey, M. L. (2013). Cholinergic enhancement reduces functional connectivity and BOLD variability in visual extrastriate cortex during selective attention. *Neuropharmacology* 64, 305–313. doi: 10.1016/j.neuropharm.2012.07.003

Rieke, F., Warland, D., Steveninck, R. D. R. V., and Bialek, W. (1999). *Spikes: Exploring the Neural Code*. Cambridge, MA; MIT Press.

Rokem, A., and Silver, M. A. (2013). The benefits of cholinergic enhancement during perceptual learning are long-lasting. *Front. Comput. Neurosci*. 7:66. doi: 10.3389/fncom.2013.00066

Rothman, K. J. (1990). No adjustments are needed for multiple comparisons. *Epidemiology* 1, 43–46. doi: 10.1097/00001648-199001000-00010

Saar, D., Reuveni, I., and Barkai, E. (2012). Mechanisms underlying rule learning-induced enhancement of excitatory and inhibitory synaptic transmission. *J. Neurophysiol*. 107, 1222–1229. doi: 10.1152/jn.00356.2011

Sadahiro, M., Sajo, M., and Morishita, H. (2016). Nicotinic regulation of experience-dependent plasticity in visual cortex. *J. Physiol. Paris* 110, 29–36. doi: 10.1016/j.jphysparis.2016.11.003

Sarter, M., and Lustig, C. (2020). Forebrain cholinergic signaling: wired and phasic, not tonic, and causing behavior. *J. Neurosci*. 40, 712–719. doi: 10.1523/JNEUROSCI.1305-19.2019

Scholl, B., Pattadkal, J. J., and Priebe, N. J. (2017). Binocular disparity selectivity weakened after monocular deprivation in mouse V1. *J. Neurosci*. 37, 6517–6526. doi: 10.1523/JNEUROSCI.1193-16.2017

Sellers, K. K., Bennett, D. V., Hutt, A., Williams, J. H., and Fröhlich, F. (2015). Awake vs. anesthetized: layer-specific sensory processing in visual cortex and functional connectivity between cortical areas. *J. Neurophysiol*. 113, 3798–3815. doi: 10.1152/jn.00923.2014

Sheynin, Y., Chamoun, M., Baldwin, A. S., Rosa-Neto, P., Hess, R. F., and Vaucher, E. (2019). Cholinergic potentiation alters perceptual eye dominance plasticity induced by a few hours of monocular patching in adults. *Front. Neurosci*. 13:22. doi: 10.3389/fnins.2019.00022

Sheynin, Y., Rosa-Neto, P., Hess, R. F., and Vaucher, E. (2020). Cholinergic modulation of binocular vision. *J. Neurosci*. doi: 10.1523/JNEUROSCI.2484-19.2020

Shimegi, S., Kimura, A., Sato, A., Aoyama, C., Mizuyama, R., Tsunoda, K., et al. (2016). Cholinergic and serotonergic modulation of visual information processing in monkey V1. *J. Physiol. Paris* 110, 44–51. doi: 10.1016/j.jphysparis.2016.09.001

Silver, M. A., Shenhav, A., and D'esposito, M. (2008). Cholinergic enhancement reduces spatial spread of visual responses in human early visual cortex. *Neuron* 60, 904–914. doi: 10.1016/j.neuron.2008.09.038

Smith, I. T., Townsend, L. B., Huh, R., Zhu, H., and Smith, S. L. (2017). Stream-dependent development of higher visual cortical areas. *Nat. Neurosci*. 20, 200–208. doi: 10.1038/nn.4469

Soma, S., Shimegi, S., Osaki, H., and Sato, H. (2012). Cholinergic modulation of response gain in the primary visual cortex of the macaque. *J. Neurophysiol*. 107, 283–291. doi: 10.1152/jn.00330.2011

Soma, S., Shimegi, S., Suematsu, N., and Sato, H. (2013a). Cholinergic modulation of response gain in the rat primary visual cortex. *Sci. Rep*. 3:1138. doi: 10.1038/srep01138

Soma, S., Shimegi, S., Suematsu, N., Tamura, H., and Sato, H. (2013b). Modulation-specific and laminar-dependent effects of acetylcholine on visual responses in the rat primary visual cortex. *PLoS ONE* 8:e68430. doi: 10.1371/journal.pone.0068430

Soma, S., Suematsu, N., and Shimegi, S. (2013c). Cholinesterase inhibitor, donepezil, improves visual contrast detectability in freely behaving rats. *Behav. Brain Res*. 256, 362–367. doi: 10.1016/j.bbr.2013.08.022

Tokarski, K., Urban-Ciecko, J., Kossut, M., and Hess, G. (2007). Sensory learning-induced enhancement of inhibitory synaptic transmission in the barrel cortex of the mouse. *Eur. J. Neurosci*. 26, 134–141. doi: 10.1111/j.1460-9568.2007.05629.x

Turchi, J., and Sarter, M. (1997). Cortical acetylcholine and processing capacity: effects of cortical cholinergic deafferentation on crossmodal divided attention in rats. *Brain Res. Cogn. Brain Res*. 6, 147–158. doi: 10.1016/S0926-6410(97)00027-X

Vaucher, E., Laliberte, G., Higgins, M. C., Maheux, M., Jolicoeur, P., and Chamoun, M. (2019). Cholinergic potentiation of visual perception and vision restoration in rodents and humans. *Restor. Neurol. Neurosci*. 37, 553–569. doi: 10.3233/RNN-190947

Verdier, D., and Dykes, R. W. (2001). Long-term cholinergic enhancement of evoked potentials in rat hindlimb somatosensory cortex displays characteristics of long-term potentiation. *Exp. Brain Res*. 137, 71–82. doi: 10.1007/s002210000646

Voss, P., Thomas, M., Chou, Y. C., Cisneros-Franco, J. M., Ouellet, L., and De Villers-Sidani, E. (2016). Pairing cholinergic enhancement with perceptual training promotes recovery of age-related changes in rat primary auditory cortex. *Neural. Plast*. 2016:1801979. doi: 10.1155/2016/1801979

Wang, Q., and Burkhalter, A. (2007). Area map of mouse visual cortex. *J. Comp. Neurol*. 502, 339–357. doi: 10.1002/cne.21286

Wang, Q., Sporns, O., and Burkhalter, A. (2012). Network analysis of corticocortical connections reveals ventral and dorsal processing streams in mouse visual cortex. *J. Neurosci*. 32, 4386–4399. doi: 10.1523/JNEUROSCI.6063-11.2012

Wekselblatt, J. B., Flister, E. D., Piscopo, D. M., and Niell, C. M. (2016). Large-scale imaging of cortical dynamics during sensory perception and behavior. *J. Neurophysiol*. 115, 2852–2866. doi: 10.1152/jn.01056.2015

Yildirim, M., Sugihara, H., So, P. T. C., and Sur, M. (2019). Functional imaging of visual cortical layers and subplate in awake mice with optimized three-photon microscopy. *Nat. Commun*. 10:177. doi: 10.1038/s41467-018-08179-6

Zhuang, J., Ng, L., Williams, D., Valley, M., Li, Y., Garrett, M., et al. (2017). An extended retinotopic map of mouse cortex. *Elife* 6:e18372. doi: 10.7554/eLife.18372

Zinke, W., Roberts, M. J., Guo, K., Mcdonald, J. S., Robertson, R., and Thiele, A. (2006). Cholinergic modulation of response properties and orientation tuning of neurons in primary visual cortex of anaesthetized Marmoset monkeys. *Eur. J. Neurosci*. 24, 314–328. doi: 10.1111/j.1460-9568.2006.04882.x

Conflict of Interest: The authors declare that the research was conducted in the absence of any commercial or financial relationships that could be construed as a potential conflict of interest.

frontiers in Neural Circuits

ORIGINAL RESEARCH
published: 15 July 2020
doi: 10.3389/fncir.2020.00042

Automated Curation of CNMF-E-Extracted ROI Spatial Footprints and Calcium Traces Using Open-Source AutoML Tools

Lina M. Tran[1,2,3], *Andrew J. Mocle*[1,2], *Adam I. Ramsaran*[1,4], *Alexander D. Jacob*[1,4], *Paul W. Frankland*[1,2,4,5,6] *and Sheena A. Josselyn*[1,2,4,5,7]*

[1]*Hospital for Sick Children, Neurosciences and Mental Health, Toronto, ON, Canada,* [2]*Department of Physiology, University of Toronto, Toronto, ON, Canada,* [3]*Postgraduate Affiliates Program, Vector Institute, Toronto, ON, Canada,* [4]*Department of Psychology, University of Toronto, Toronto, ON, Canada,* [5]*Institute of Medical Sciences, University of Toronto, Toronto, ON, Canada,* [6]*Child & Brain Development Program, Canadian Institute for Advanced Research (CIFAR), Toronto, ON, Canada,* [7]*Brain, Mind & Consciousness Program, Canadian Institute for Advanced Research (CIFAR), Toronto, ON, Canada*

In vivo 1-photon (1p) calcium imaging is an increasingly prevalent method in behavioral neuroscience. Numerous analysis pipelines have been developed to improve the reliability and scalability of pre-processing and ROI extraction for these large calcium imaging datasets. Despite these advancements in pre-processing methods, manual curation of the extracted spatial footprints and calcium traces of neurons remains important for quality control. Here, we propose an additional semi-automated curation step for sorting spatial footprints and calcium traces from putative neurons extracted using the popular constrained non-negative matrix factorization for microendoscopic data (CNMF-E) algorithm. We used the automated machine learning (AutoML) tools TPOT and AutoSklearn to generate classifiers to curate the extracted ROIs trained on a subset of human-labeled data. AutoSklearn produced the best performing classifier, achieving an F1 score >92% on the ground truth test dataset. This automated approach is a useful strategy for filtering ROIs with relatively few labeled data points and can be easily added to pre-existing pipelines currently using CNMF-E for ROI extraction.

Keywords: calcium imaging, open-source, machine learning, microendoscopy, 1-photon, CNMF-E

OPEN ACCESS

Edited by:
Edward S. Ruthazer, McGill University, Canada

Reviewed by:
Kurt Haas, University of British Columbia, Canada
Mark Brandon, University of California, San Diego, United States

***Correspondence:**
Sheena A. Josselyn
sheena.josselyn@sickkids.ca

Received: *13 March 2020*
Accepted: *19 June 2020*
Published: *15 July 2020*

Citation:
Tran LM, Mocle AJ, Ramsaran AI, Jacob AD, Frankland PW and Josselyn SA (2020) Automated Curation of CNMF-E-Extracted ROI Spatial Footprints and Calcium Traces Using Open-Source AutoML Tools. Front. Neural Circuits 14:42. doi: 10.3389/fncir.2020.00042

INTRODUCTION

Advances in 1-photon (1p) miniaturized fluorescence microscopy in terms of utility, cost, and ease-of-use have increased the accessibility and popularity of *in vivo* calcium imaging in freely behaving rodents (Ghosh et al., 2011; Hamel et al., 2015; Cai et al., 2016; Jacob et al., 2018). Consequently, researchers can track the activity of neuronal populations across days, weeks, or even months (Rubin et al., 2015; Gonzalez et al., 2019). Concurrent with the growing usage of 1p microendoscopy in neuroscience, there is an increasing demand for high-throughput software that can accurately and efficiently process the very large raw calcium imaging datasets now being produced. To address this challenge, several algorithms and analysis pipelines have been developed to automate the extraction of cells and calcium activity traces across time in a robust manner—necessary step for downstream analyses (Pnevmatikakis, 2019).

Motion correction, source extraction, and cell registration (across multiple recording sessions) are important steps involved in pre-processing raw 1p calcium imaging data. Source extraction, the task of identifying the locations and activity of neurons in the imaged field of view (FOV), is arguably the most challenging of these steps, as evidenced by the number of different algorithms published to improve this step. Nevertheless, two main methods of source extraction have been widely adopted in the field: principal component analysis/independent component analysis (PCA/ICA; Mukamel et al., 2009) and the more recent extended constrained non-negative matrix factorization for microendoscopic data (CNMF-E; Zhou et al., 2018). CNMF-E explicitly models background signals present in 1p microendoscopic recordings and therefore results in more accurate signal detection from neurons compared to PCA/ICA (Zhou et al., 2018).

Our lab has successfully applied CNMF-E to recordings from our open-source Compact Head-mounted Endoscope (CHEndoscope) to identify neuron locations (or spatial footprints) and extract their calcium activity traces from freely-behaving mice performing different behavioral tasks. CNMF-E has proven to be a reliable tool across multiple imaging sessions and experimental paradigms conducted in the lab with minimal parameter tuning in our hands (Jacob et al., 2018). However, like PCA/ICA, CNMF-E may still produce some false-positives in the output of detected cells (i.e., non-neuronal spatial footprints or calcium traces), which can be filtered out of the final dataset manually. We initially found success in filtering CNMF-E-extracted spatial footprints and traces by adding a manual curation step that involved visual inspection of each ROI and calcium trace (previously described in Jacob et al., 2018). While this type of manual curation can reduce the number of false-positives in CNMF-E's output, visual inspection of potentially tens of thousands of extracted cells can be time-consuming, and this method is not free from human error. Here, we propose an automated machine learning (AutoML) approach built on top of the CNMF-E algorithm's outputs to filter out potential false-positives. We implemented a semi-automated classification tool to limit the amount of manual curation required during pre-processing, without completely removing the ability to fine-tune the process with human-labeled datasets.

The main outputs of CNMF-E's source extraction algorithm are: 1. the extracted calcium traces representing cellular activity and 2. the spatial footprint of putative neurons. As mentioned previously, manual curation of these outputs involves identifying both aberrant traces that do not have stable baseline fluorescence (Resendez et al., 2016), transient durations inconsistent with the expressed calcium indicator (e.g., GCAMP6f; Badura et al., 2014), and/or spatial footprints that are not consistent with the shape and size of neurons in the brain region being recorded (Resendez et al., 2016). We trained and validated our classifiers on a dataset of 14,000 manually curated spatial footprints and traces output from CNMF-E. The final model chosen was then used to automate the curation of ROIs from other recording sessions. From the two AutoML libraries, we chose the best performing model to train on the full training set to evaluate on the test set. We find our model can accurately predict whether a cell would be included or excluded at a rate of 92%. We further validated the performance of our models on an additional ground truth dataset derived from 2-photon (2p) imaging source ROIs of mouse visual cortex (Stringer et al., 2019a,b), where ROIs were downsampled to emulate 1p images and modified to simulate a proportion of "negative" labeled ROIs for ground truth labels. The AutoML classifier was able to accurately predict >98% of the correct labels on the 2p simulated ground-truth dataset.

The potential time savings of manually curating thousands of cells makes this approach a method worth employing as part of a typical 1p calcium imaging pipeline. While our AutoML-based curation pipeline was primarily developed to be used with CHEndoscope data, our model takes the output of CNMF-E and as a result, allows this method to be readily applied to data acquired using other 1p miniature microscopes.

MATERIALS AND METHODS

Dataset Preparation and Pre-processing

The dataset used for model training was acquired from multiple hippocampal CA1 recordings captured across different mice and recording sessions using methods described in Jacob et al., 2018. From these recordings, we used CNMF-E (Zhou et al., 2018) to extract spatial footprints and calcium traces of 14,000 ROIs. We then manually reviewed and labeled these ROIs as neuronal (included for further analysis) or artifact (excluded from analysis). The labels were generated by two human expert raters that inspected the calcium transients and spatial footprints based on previously reported criteria:

1. Fast rise and slow decay of calcium transients with stable baseline fluorescence (Resendez et al., 2016).
2. Calcium transient durations consistent with GCaMP6f (or appropriate GCaMP variant; Badura et al., 2014).
3. Spatial footprints consistent with appropriate neuronal shape and size (Resendez et al., 2016).

Each label in the ground truth dataset was derived from a single rater's annotations. Interrater agreement was 87% across the two raters on a subset of the data (1,073 putative ROIs extracted from CNMF-E; **Figure 1**).

Spatial footprints consisted of the maximum projection of the identified cell from all frames in the video. We found that the location of the footprint in the FOV was not important in our labeling criteria (compared to the shape and size of footprint), we cropped the spatial footprints to remove empty space. Each spatial footprint was reduced to an 80 × 80 pixel image centered on the peak intensity of the footprint. Furthermore, recordings were of varying lengths, so all trace data was cropped at 500 frames (equivalent to 100 s of recording at 5 fps) and normalized such that the values. To combine the spatial and trace data into a single dataset for classification, the 2-dimensional spatial footprint images were flattened and the trace data were concatenated to the end of the image data to create a single 1-dimensional vector for each ROI.

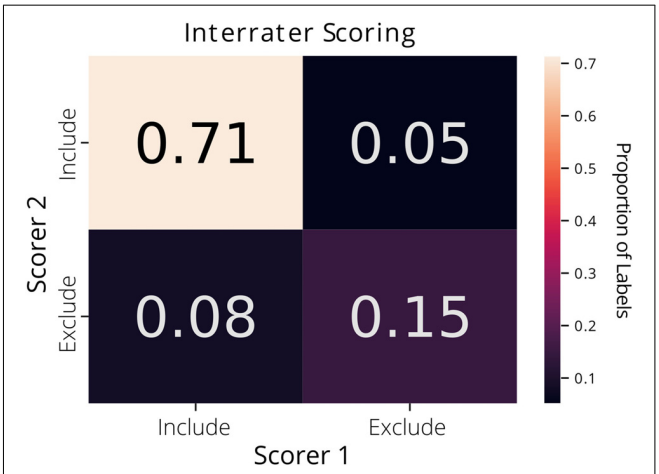

FIGURE 1 | Interrater agreement of ROI labels. A confusion matrix comparing the manually reviewed labels (include or exclude) for putative ROIs extracted from constrained non-negative matrix factorization for microendoscopic data (CNMF-E) determined by two different raters. Each cell of the matrix is annotated with the proportion of ROIs.

We aggregated the labeled ROIs into a dataset split into training and test sets, which comprised 80% (∼11,000 ROIs) and 20% (∼3,000 ROIs) of the data, respectively.

To further validate this AutoML approach, we also used an open dataset of ROIs imaged in the mouse primary visual cortex acquired using 2p microscopy (Stringer et al., 2019a). This ground-truth dataset contained 19,000 ROIs, from which we randomly selected 7,200 ROIs to use in the analysis to reduce compute time. We spatially and temporally downsampled the 2p ROI spatial footprint images and calcium traces, respectively, to better emulate 1p imaging data. Spatial footprints were cropped to 40 × 40 pixel images around the ROI centers, and trace data were cropped to a 500-frame time window.

Next, to generate true "negative" labels in our dataset, we manipulated 15% of ROIs (to match the proportion of positive and negative labels in our 1p dataset) using one or a combination of the following methods:

1. Modify the size of the spatial footprint by a scaling factor randomly chosen from ($\frac{1}{2}$, $\frac{1}{3}$, 2, 3; "spatial")
2. Add gaussian noise to the calcium trace ("trace")
3. Both methods #1 and #2 ("both")
4. Combine two ROIs to simulate the incorrect merging of two separate ROIs detected as one ROI ("merged")

The spatial footprints were flattened into a 1-dimensional vector and the trace data was concatenated to the end. The final 2p simulated ground truth dataset was split into training and test sets, which comprised 80% (6,000 ROIs) and 20% (1,000 ROIs) of the data, respectively.

Model Optimization and Selection

We used two automated machine learning (AutoML) methods, TPOT (Olson et al., 2016; Olson and Moore, 2019) and AutoSklearn (Feurer et al., 2015) that are based on the popular Python machine learning toolbox, scikit-learn (Pedregosa et al., 2011) to select optimal classification models. While other AutoML tools exist that may outperform the ones we chose (Truong et al., 2019), TPOT and AutoSklearn are both free open-source, and easy to use, making them accessible for labs to incorporate into their existing analysis pipelines. To benchmark the results of the AutoML methods on the ROI curation task, we trained two types of out-of-the-box scikit-learn classifiers, Decision Tree, and K-Nearest Neighbors, with and without PCA-transformed inputs for dimensionality reduction.

The key advantage of AutoML tools such as TPOT and AutoSklearn is that they do the extensive work of finding the best type(s) of data transformation and models to build a pipeline for classifying the input data, as well as the hyperparameters associated with these steps. TPOT is an evolutionary algorithm that works with the scikit-learn API to find the best parameters and model pipelines through searching "genetic lineages" of the best performing pipelines. It will try a pipeline, evaluate its performance, and then randomly modify various parameters in search of a better pipeline (Olson et al., 2016; Olson and Moore, 2019). TPOT generates pipelines of pre-processing steps and classification models to maximize classification performance while prioritizing simpler pipelines. For example, a pipeline may consist of PCA for dimensionality reduction and a support vector machine to perform the classification, though they do not necessarily need to have multiple components. AutoSklearn performs algorithm selection and hyperparameter tuning using Bayesian optimization, meta-learning, and ensemble construction (Feurer et al., 2015) and as a result, the final classifier is an ensemble of many different model types and their associated hyperparameters. We primarily used default TPOT and AutoSklearn parameters, with a max evaluation time for a single pipeline of 10 min, and a total search time of 2 days.

During training, we used 10-fold cross-validation using stratified folds that preserved the relative proportions of "include" and "exclude" labels (i.e., during each run of training, 9 of 10 folds were used for training, and the 10th fold was used to test the performance of the model). This process was repeated for all 10 folds, resulting in an averaged performance metric for the data. We optimized the models to maximize the F1 score, the harmonic average of precision and recall, where high precision indicates a low false-positive rate and high recall indicates a low false-negative rate. In our dataset, a true positive is an extracted ROI that both the trained model and a "ground truth" human scorer define as suitable to be included for further analysis (i.e., it satisfies the three selection criteria listed above). A true negative is an extracted ROI that is excluded for further analysis by both the model and our ground truth scoring.

RESULTS

To define a benchmark for classifier performance on CNMF-E extracted ROIs and the utility of using trace and spatial data together, we used two conventional machine learning algorithms [Decision Trees and K-Nearest Neighbors (KNN)] trained on:

TABLE 1 | ROI classification F1 scores in different ML and automated machine learning (AutoML) methods tested on 1p ground truth and 2p simulated ground truth data.

Classifier	1p Spatial	1p Trace	1p Combined	2p Simulated ground truth (combined)
Decision Tree	0.856	0.822	0.868	0.988
Decision Tree + PCA	0.806	0.813	0.835	0.935
K Nearest Neighbours	0.873	0.877	0.881	0.929
K Nearest Neighbours + PCA	0.814	0.815	0.885	0.953
TPOT	-	-	0.904	0.954
AutoSklearn	-	-	0.922	0.994

(1) only spatial footprint data, (2) only trace data or (3) the combined spatial and trace data. Our spatial and trace data had a large number of features, 6,400 and 500, respectively. To test whether the classifiers would perform better using dimensionality reduction, we also compared the performance of classifiers with and without Principal Component Analysis (PCA) as a data preprocessing step. We trained and tested the Decision Tree, or the KNN classifiers on each of the three types of data listed above, with and without PCA to reduce the dimensionality of our data. The F1 scores on the test set for each of these classifiers are reported in **Table 1**. Notably, both the Decision Tree and K-Nearest Neighbors classifiers generalized best on the test set when trained on the combined spatial and trace data, compared to the trace only or spatial only data. The highest F1 score achieved by any of these models on our 1p ground truth dataset was the KNN (with PCA) classifier with a score of 0.885 trained on the combined data.

Next, to determine the efficacy of an AutoML approach for classification of our ROI curation task, we tested the ability of TPOT and AutoSklearn to build classifiers that can label the pre-processed spatial footprints and calcium traces of putative ROIs. Both TPOT and AutoSklearn were trained on the 11,000 labeled ROIs in the training set, split into 10 folds for cross-validation, repeated five times. The best models obtained during training were used to determine the F1 score on the test set. **Table 1** reports the performance of the best models obtained by TPOT and AutoSklearn across the training folds and on the test set.

We then tested the transferability of the best classifier pipelines identified by TPOT and AutoSklearn using fewer samples. We used the top-performing classifier pipelines and hyperparameters chosen by TPOT and AutoSklearn and trained the initialized pipelines using datasets of increasing ROI numbers. The training set size ranged from 150–10,000 ROIs. Using a change point analysis algorithm (PELT, Killick et al., 2012), we determined that AutoSklean and TPOT classifiers approached a maximal F1 score with 719 and 1,000 labeled ROIs, respectively (**Figure 2**). The pipelines found using our much larger labeled dataset may be easily incorporated into other pipelines with a minimal computational effort to train and finetune on CNMF-E extracted ROIs from other 1p experiments, using fewer labeled ROIs.

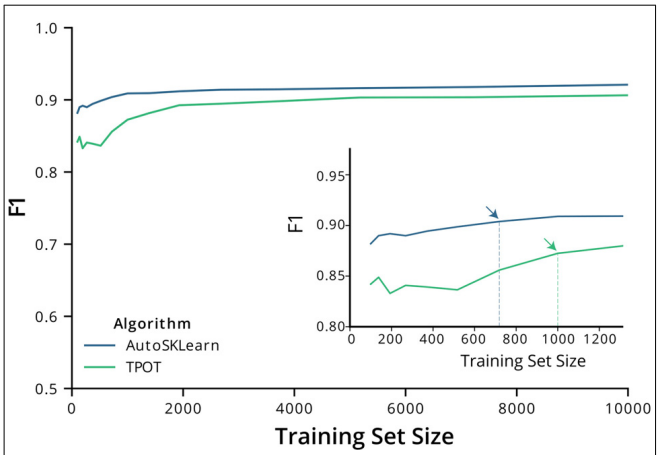

FIGURE 2 | F1 score performance with increasing training size. Graph of the F1 test scores vs. the number of training samples used to train the best models output by AutoSklearn (blue) and TPOT (green). (Inset) A graph of the same plot with a smaller range of training sizes and the change point is marked with arrows on each algorithm type.

To examine the classifier performance in terms of false positives and false negatives, we created confusion matrices to visualize the rate of true positives, true negatives, false positives, and false negatives from the TPOT and AutoSklearn predictions compared to the ground truth. We found that the classifier built with AutoSklearn (0.922 F1, **Table 1**) performs better in terms of both reducing false positives and false negatives (**Figure 3**).

To further assess the nature of the classification errors, we looked at the class confidences or probabilities of the test set predictions from the trained TPOT and AutoSklearn models (**Figure 4**). Class probabilities indicate the classifier's certainty (using confidence score for TPOT and class probability for AutoSklearn) that a sample belongs to a particular class label. We tested whether mislabeled ROIs were also those in which the classifiers expressed less confidence in classifying. We examined the size of the difference between certainty scores (true positives vs. false positives, true negatives vs. false negatives) in TPOT and AutoSklearn using Cohen's d (Sawilowsky, 2009; Cohen, 2013; **Table 2**). The AutoSklearn classifier which outperformed the TPOT classifier based on F1 scores showed large differences in certainty scores when labeling ROIs as positive (d = 1.36) or negative (d = 2.34). By contrast, the TPOT classifier was relatively less confident in both types of classification (positive d = 0.63, negative d = 1.68). In other words, the AutoSklearn classifier was more certain in applying labels to ROIs than was the TPOT classifier. This indicates that false negatives and false positives in the higher-performing AutoSklearn classifier may arise from "edge-cases" ROIs in the dataset which the classifier was not as certain about the label. In contrast, the poorer performance of the TPOT classifier may simply be due to poor generalization on the test set.

To investigate the nature of the false positives and false negatives from the best TPOT and AutoSklearn models, we looked at the underlying spatial footprints and calcium traces for mislabeled ROIs from both AutoML tools (**Figure 5**).

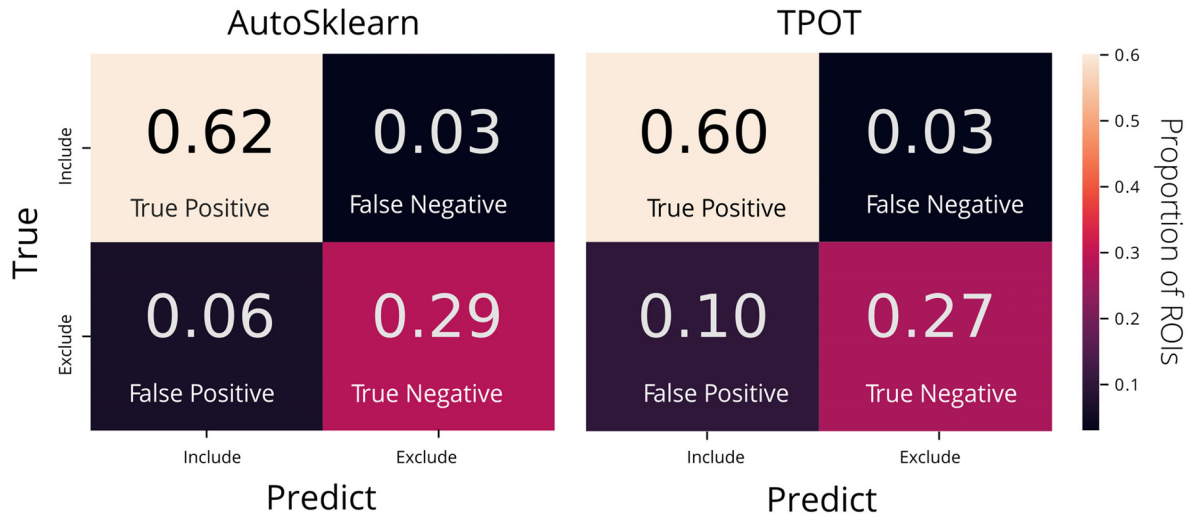

FIGURE 3 | Confusion matrices of AutoML tools: TPOT and AutoSklearn. Each cell in the matrix is annotated with the proportion of ROIs labeled as Include or Exclude according to the predicted and true labels. Colors indicate the relative proportions of the labels where lower proportions are darker in color and higher proportions are lighter in color. The confusion matrices were made from predictions on the test set from the best models output by AutoSklearn (left) and TPOT (right).

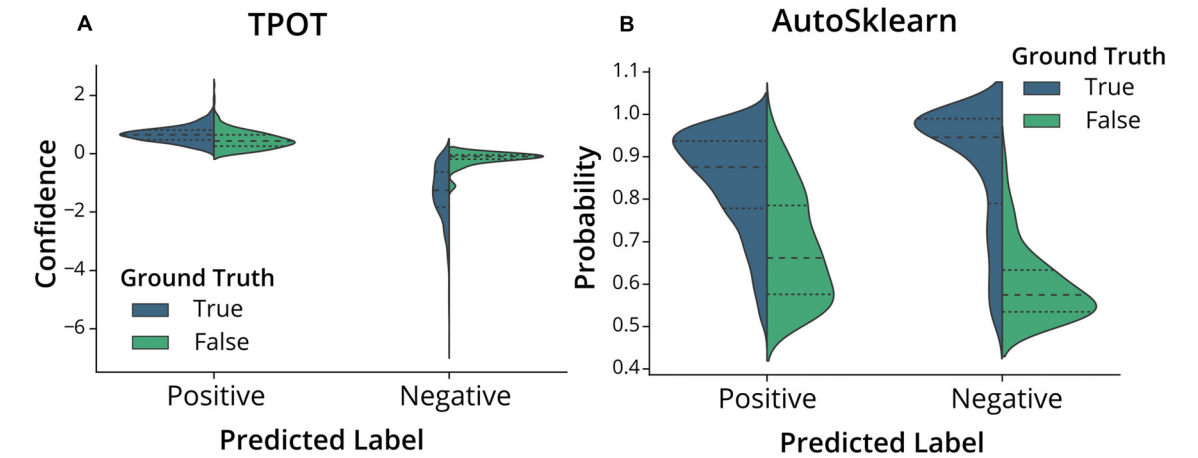

FIGURE 4 | Classifier confidence (TPOT) and class probabilities (AutoSklearn) on predicted false positives and false negatives. Violin plots of the distribution of **(A)** TPOT classifier confidence or **(B)** AutoSklearn class probabilities on predicted ROI labels (Positive for Include, or Negative for Exclude) in the test set. Each half of the violin plot is the distribution of values for correct labels (True, left/blue) or incorrect (False, right/green) based on the ground truth labels.

Representative examples of excluded ROIs from the ground truth dataset show that some cells may be excluded (i.e., true negatives) because of poor trace data and/or poor spatial footprints, which possibly represent non-neuronal imaging artifacts and/or ROIs representing areas of background fluorescence. While some false positives from AutoSklearn shared similar features with true negative ROIs, others were more ambiguous. Upon inspection, these ROIs sometimes were high-quality spatial footprints with poor-quality calcium traces, or vice versa, or were composed of spatial footprints and calcium traces of true neuronal origin mixed with additional non-neuronal noise. These examples represent "edge-cases" which may be difficult to judge even by a human rater.

To validate the utility of the AutoML models on a different set of calcium imaging data, we trained and tested our out-of-the-box scikit-learn classifiers and the final ensemble classifiers output by TPOT and AutoSklearn on an open 2p calcium imaging dataset of 7,200 ROIs (a randomly chosen subset from the original 19,000 ROIs) from mouse visual cortex cells (Stringer et al., 2019a,b). We modified ROIs by downsampling the spatial footprints, and traces to simulate 1p data that has been analyzed by CNMF-E, and generated a subset of "bad" ROIs where we modified the trace, spatial footprint, both

TABLE 2 | Cohen's *d* effect size of certainty scores between predicted labels that were correct or incorrect compared to ground truth in TPOT or AutoSklearn.

	Include (Positive)		Exclude (Negative)	
	TPOT	**AutoSklearn**	**TPOT**	**AutoSklearn**
Cohen's *d*	0.63	1.36	1.68	2.34

trace, and footprint modification, or simulated the merging of two separate ROIs into one ROI, a common issue in calcium imaging ROI extraction (**Figure 6A**). Of the conventional scikit-learn models, we found that a Decision Tree classifier achieved an F1 score of 0.988 on the 2p simulated ground truth test set (**Table 1**). Surprisingly, the Decision Tree classifier outperformed the TPOT Linear Support Vector Machine which had an F1 score of 0.954. However, the final AutoSklearn ensemble was achieved the best F1 score of 0.994, and notably had a far lower proportion of false positives than the TPOT classifier, and no false negatives were labeled in the test set (**Figure 6B**).

DISCUSSION

Automated curation of ROIs provides a fast, accurate method for classifying neural data generated in 1p calcium imaging experiments. We show that AutoML tools such as the open-source TPOT and AutoSklearn packages provide an easy way to build effective classifiers for ROIs extracted from the widely used CNMF-E algorithm. Spatial footprints and calcium traces from CNMF-E can be used to train these models with minimal data preprocessing. Furthermore, it may be possible to apply the top-performing classifiers generated from this work to other experimental datasets taken from different 1p imaging setups, while requiring relatively few labeled samples. Other analyses pipelines such as MIN1PIPE (Lu et al., 2018) have been developed to improve source extraction by reducing false-positive ROIs without increasing the rate of false negatives. However, given the more widespread adoption of CNMF-E, the approach described here prevents labs from having to adopt entirely new analysis pipelines. Our approach provides a balance between the need to manually review the output of CNMF-E ROIs to maximize the number of detected cells, while still allowing some further automation of the otherwise laborious curation process.

While great advancements have been made in widefield 1p imaging, fundamental constraints (e.g poor axial resolution, light scattering) limit the number of high-quality cells that can be detected compared to 2p imaging (Svoboda and Yasuda, 2006). As a result, being able to accurately detect as many "true" ROIs as possible is crucial for downstream analyses. If false positives make it through ROI extraction, or if data is lost due to false negatives, analyses of these datasets will suffer from increased variability and reduced statistical power.

AutoML may be a useful approach for curating CNMF-E extracted ROIs and can be implemented on top of pre-existing analysis pipelines without much need to adapt the software. However, there are several limitations to this approach. First, we emphasize the automated aspect of this machine learning classifier approach and little need for hand-tuning, but we recognize that the best models still make errors. Cases in which the best performing classifier generated by AutoSklearn failed to detect true positives or true negatives were further reviewed and were typically seen to be edge cases where it may be difficult for a human reviewer to make a judgment. Similarly, we found that a second expert scorer looking at the same data may not make the same judgments on such edge cases (having an interrater reliability score of 87%). While the AutoML classifiers were trained on data that had relatively little preprocessing beyond cropping and downsampling, future work could address whether feature engineering over the spatial footprints and trace data could further improve accuracy and reduce training time for model selection and hyperparameter tuning. Better curation of a training dataset for the models may help reduce ambiguous cases that make it difficult for a classifier to make accurate predictions.

Ultimately, automated methods for source extraction are still likely to be imperfect, resulting in some small proportion of false positives in the final dataset, and/or false negatives not detected during source extraction. In practice, it may be useful to be able to prioritize precision (proportion of positive labels by the classifier that are true positives), over recall (proportion of all true positives that were correctly labeled), or vice versa. For example, the loss of some small proportion of ROIs from a large dataset (i.e., false negatives) may not be as harmful as a small number of highly active false-positive ROIs that could disproportionately impact downstream analyses. We used the F1 metric, which equally weights precision and recall, to optimize our AutoML classifiers. However, one could instead use an F Beta score which is a weighted F1 score where the beta parameter determines the weight of recall (penalty on false negatives) relative to the precision (penalty on false positives). This could be used to bias the autoML search for an optimal classifier in either direction.

To reduce computing time and complexity of ROI classifiers, we flattened and concatenated our 2d spatial footprints with our 1d trace data to create a single dataset to train the classifiers on. Perhaps there are alternative machine learning methods that preserve the originally structured inputs in the spatial images and calcium trace time-series data could provide more accurate classification results. Variations on residual neural networks (ResNets) and Hierarchical Vote Collective of Transformation-based Ensembles (HIVE-COTE) have achieved a state of the art performance on image classification and time series classification, respectively (He et al., 2016; Lines et al., 2016). However, the simplicity of exported pipelines from TPOT, AutoSklearn, and conventional scikit-learn algorithms do not require as much computational power and runtime as HIVE-COTE (an ensemble of typically 37 classifiers that need to be trained and tuned for each use-case) or ResNet which typically requires a GPU to finetune the model on one's dataset. Furthermore, the strong performance of the final extracted AutoSklearn and TPOT ensemble classifiers found using our 1p data and retrained/tested on the 2p simulated

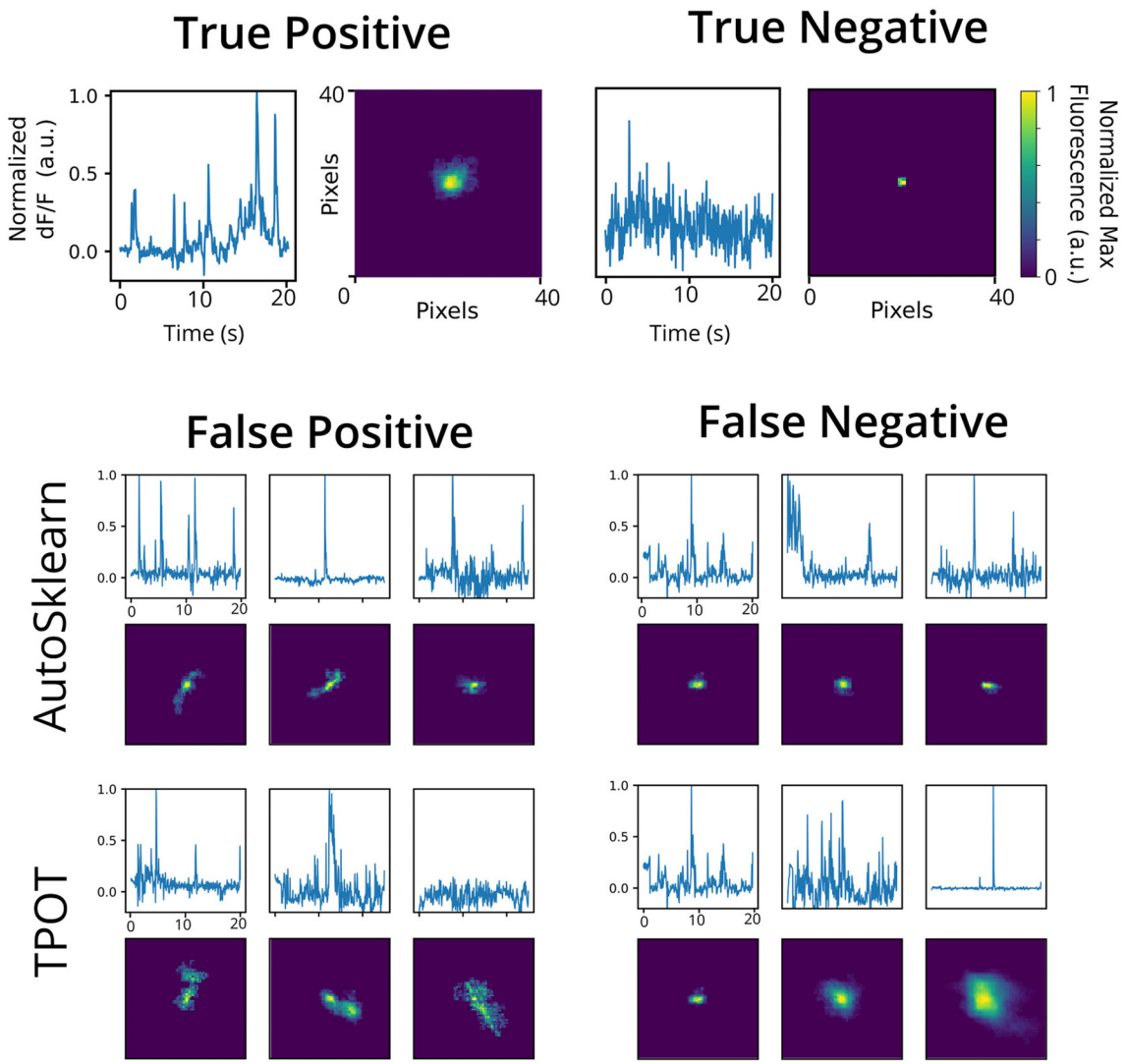

FIGURE 5 | Representative false positives and negatives compared to ground truth ROIs. Example calcium traces (top) and spatial footprints (bottom) from ground truth positive- (left) and negative-labeled (right) ROIs. Example calcium traces (top) and spatial footprints (bottom) of false positive and false negative ROIs predicted from the AutoSklearn (middle row) or TPOT (bottom row) classifiers.

ground truth dataset demonstrates the transferable capabilities of these models with ROIs from different brain regions and different imaging set-up.

In conclusion, we present here a demonstration and benchmark of an AutoML approach for the curation of CNMF-E extracted ROIs. The data show that simple, out-of-the-box ML methods can also be trained to curate ROIs to a relatively high degree of accuracy, but the final ensemble model found by AutoSklearn was consistently able to outperform other classifiers in both the 1p and 2p simulated ground truth datasets. The methods described here can provide a flexible, free open-source, and easy-to-incorporate curation step for other researchers using CNMF-E for source extraction of their 1p datasets, while requiring few changes to their existing analysis pipelines.

DATA AVAILABILITY STATEMENT

The datasets and code generated for this study can be found in the cnmfe-reviewer GitHub repository (https://github.com/jf-lab/cnmfe-reviewer).

ETHICS STATEMENT

The studies involving animals were reviewed and approved by Animal Care and Use Committee (ACC) of the Hospital for Sick Children. All procedures were conducted in accordance with policies of the Canadian Council on Animal Care (CCAC) and National Institutes of Health (NIH) Guidelines on Care and Use of Laboratory Animals.

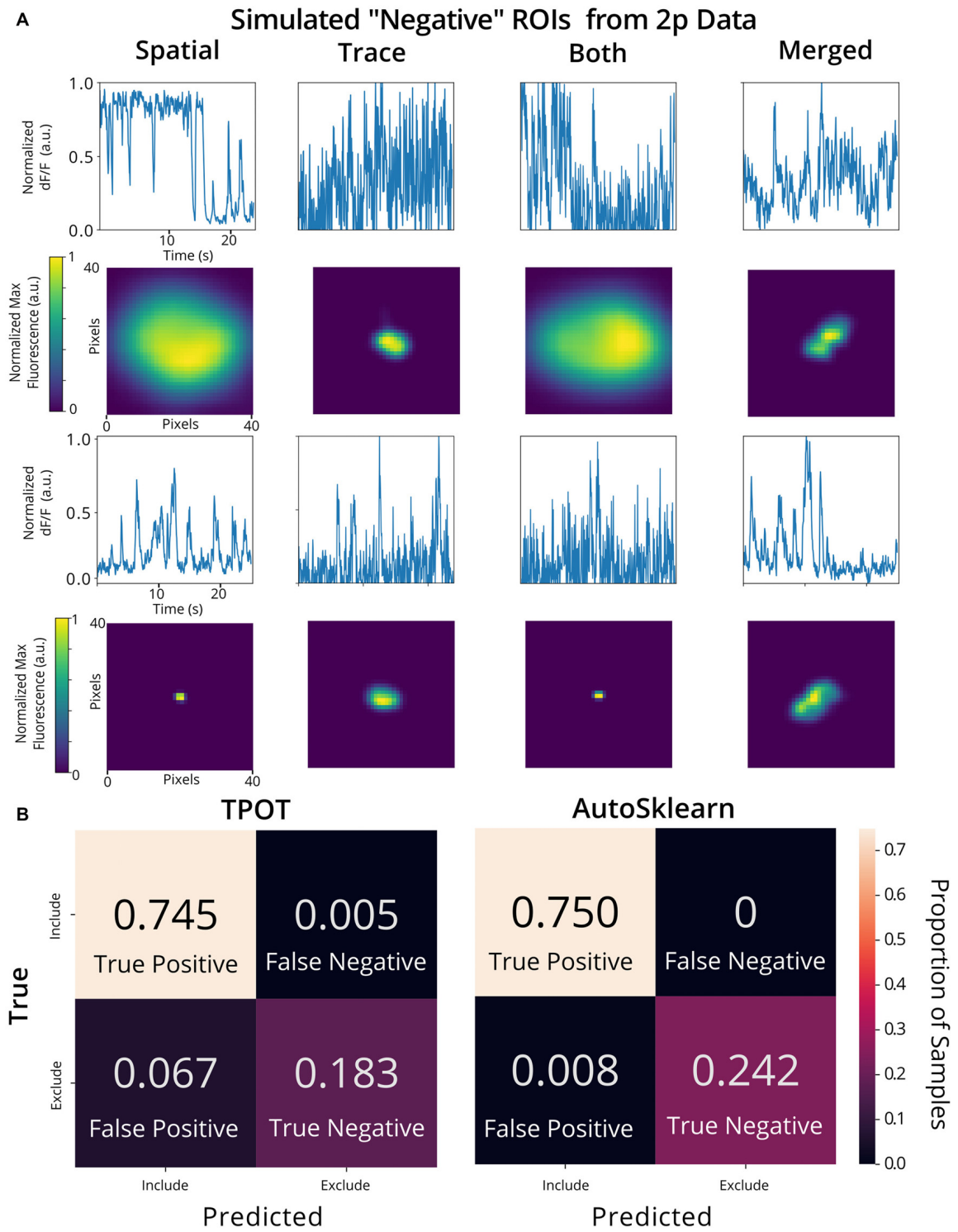

FIGURE 6 | Validation of AutoML methods on modified 2p calcium imaging data. **(A)** Examples of ROIs extracted from 2p calcium imaging modified to resemble 1p data and to simulate ROIs that should be excluded from the analysis. Example trace data (top) and spatial footprints (bottom) of simulated negative ROIs that were modified using various methods: "spatial" (spatial footprints were upscaled or downscaled beyond the range of typical neuronal size in the dataset), "trace" (traces with Gaussian noise added), "both" (where both "spatial" and "trace" modifications were made) or merged" (where two ROIs are incorrectly identified as a single ROI by combining the spatial footprint and trace of two separate cells). **(B)** Confusion matrices of the TPOT (left) and AutoSklearn (right) test predictions on the 2p simulated ground truth dataset (where the test set size is 1,080 ROIs).

AUTHOR CONTRIBUTIONS

LT, PF, and SJ contributed to the study design. AJ designed and constructed the CHEndoscopes. AR and AM conducted surgeries, behavior experiments, CNMF-E processing, and manual ROI labeling. LT performed analyses using automated machine learning pipelines. LT, AM, AR, and AJ performed the statistical analyses and wrote the article. All authors discussed and commented on the manuscript.

FUNDING

This work was supported by grants from the Canadian Institutes of Health Research (CIHR, grant numbers FDN-388455 to SJ, FDN143227 to PF), Natural Science and Engineering Council of Canada (NSERC to SJ and PF), CIFAR catalyst award (SJ, PF) and an NIH (NIMH, 1 R01 MH119421-01; SJ, PF). LT was supported by a SickKids Research Training Centre Restracomp Fellowship, Natural Science and Engineering Council of Canada Scholarship (NSERC, PGSD), AM by an NSERC CGSD, AR by an NSERC CGSD and NIH (NIMH, 1 F31 MH120920-01), AJ by a Canadian Open Neuroscience Platform Student Scholar Award (in partnership with Brain Canada).

ACKNOWLEDGMENTS

Compute resources provided by Compute Ontario and Compute Canada (www.computecanada.ca) were used to perform this research.

REFERENCES

Badura, A., Sun, X. R., Giovannucci, A., Lynch, L. A., and Wang, S. S.-H. (2014). Fast calcium sensor proteins for monitoring neural activity. *Neurophotonics* 1:025008. doi: 10.1117/1.nph.1.2.025008

Cai, D. J., Aharoni, D., Shuman, T., Shobe, J., Biane, J., Song, W., et al. (2016). A shared neural ensemble links distinct contextual memories encoded close in time. *Nature* 534, 115–118. doi: 10.1038/nature17955

Cohen, J. (2013). *Statistical Power Analysis for the Behavioral Sciences*. New York, NY: Routledge.

Feurer, M., Klein, A., Eggensperger, K., Springenberg, J. T., Blum, M., and Hutter, F. (2015). "Auto-sklearn: efficient and robust automated machine," in *Advances in Neural Information Processing Systems* (Montreal, CA: NIPS 2015), 28, 2962–2970.

Ghosh, K. K., Burns, L. D., Cocker, E. D., Nimmerjahn, A., Ziv, Y., Gamal, A. E., et al. (2011). Miniaturized integration of a fluorescence microscope. *Nat. Methods* 8, 871–878. doi: 10.1038/nmeth.1694

Gonzalez, W. G., Zhang, H., Harutyunyan, A., and Lois, C. (2019). Persistence of neuronal representations through time and damage in the hippocampus. *Science* 365, 821–825. doi: 10.1126/science.aav9199

Hamel, E. J. O., Grewe, B. F., Parker, J. G., and Schnitzer, M. J. (2015). Cellular level brain imaging in behaving mammals: an engineering approach. *Neuron* 86, 140–159. doi: 10.1016/j.neuron.2015.03.055

He, K., Zhang, X., Ren, S., and Sun, J. (2016). "Deep residual learning for image recognition," in *2016 IEEE Conference on Computer Vision and Pattern Recognition (CVPR)*, (Las Vegas, NV: IEEE), 770–778.

Jacob, A. D., Ramsaran, A. I., Mocle, A. J., Tran, L. M., Yan, C., Frankland, P. W., et al. (2018). A compact head-mounted endoscope for *in vivo* calcium imaging in freely behaving mice. *Curr. Protoc. Neurosci.* 84:e51. doi: 10.1002/cpns.51

Killick, R., Fearnhead, P., and Eckley, I. A. (2012). Optimal detection of changepoints with a linear computational cost. *J. Am. Stat. Assoc.* 107, 1590–1598. doi: 10.1080/01621459.2012.737745

Lines, J., Taylor, S., and Bagnall, A. (2016). "HIVE-COTE: the hierarchical vote collective of transformation-based ensembles for time series classification," in *2016 IEEE 16th International Conference on Data Mining (ICDM)*, (Barcelona: IEEE), 1041–1046.

Lu, J., Li, C., Singh-Alvarado, J., Zhou, Z. C., Fröhlich, F., Mooney, R., et al. (2018). MIN1PIPE: A miniscope 1-photon-based calcium imaging signal extraction pipeline. *Cell Reports* 23, 3673–3684. doi: 10.1016/j.celrep.2018.05.062

Mukamel, E. A., Nimmerjahn, A., and Schnitzer, M. J. (2009). Automated analysis of cellular signals from large-scale calcium imaging data. *Neuron* 63, 747–760. doi: 10.1016/j.neuron.2009.08.009

Olson, R. S., Bartley, N., Urbanowicz, R. J., and Moore, J. H. (2016). "Evaluation of a tree-based pipeline optimization tool for automating data science," in *Proceedings of the 2016 on Genetic and Evolutionary Computation Conference—GECCO '16*, (New York, NY: ACM), 485–492.

Olson, R. S., and Moore, J. H. (2019). "TPOT: a tree-based pipeline optimization tool for automating machine learning," in *Automated Machine Learning*, eds F. Hutter, L. Kotthoff and J. Vanschoren (Cham: Springer), 151–160.

Pedregosa, F., Varoquaux, G., Gramfort, A., Michel, V., Thirion, B., Grisel, O., et al. (2011). Scikit-learn: machine learning in Python, pedregosa. *JMLR* 12, 2825–2830.

Pnevmatikakis, E. A. (2019). Analysis pipelines for calcium imaging data. *Curr. Opin. Neurobiol.* 55, 15–21. doi: 10.1016/j.conb.2018.11.004

Resendez, S. L., Jennings, J. H., Ung, R. L., Namboodiri, V. M. K., Zhou, Z. C., Otis, J. M., et al. (2016). Visualization of cortical, subcortical and deep brain neural circuit dynamics during naturalistic mammalian behavior with head-mounted microscopes and chronically implanted lenses. *Nat. Protoc.* 11, 566–597. doi: 10.1038/nprot.2016.021

Rubin, A., Geva, N., Sheintuch, L., and Ziv, Y. (2015). Hippocampal ensemble dynamics timestamp events in long-term memory. *eLife* 4:e12247. doi: 10.7554/eLife.12247

Sawilowsky, S. S. (2009). New effect size rules of thumb. *J. Mod. Appl. Statist. Methods* 8, 597–599. doi: 10.22237/jmasm/1257035100

Stringer, C., Michaelos, M., and Pachitariu, M. (2019a). *Recording of 19,000 Neurons Across Mouse Visual Cortex During Sparse Noise Stimuli [Data set]*. Janelia Research Campus: Figshare.

Stringer, C., Pachitariu, M., Steinmetz, N., Carandini, M., and Harris, K. D. (2019b). High-dimensional geometry of population responses in visual cortex. *Nature* 571, 361–365. doi: 10.1038/s41586-019-1346-5

Svoboda, K., and Yasuda, R. (2006). Principles of two-photon excitation microscopy and its applications to neuroscience. *Neuron* 50, 823–839. doi: 10.1016/j.neuron.2006.05.019

Truong, A., Walters, A., Goodsitt, J., Hines, K., Bayan Bruss, C., and Farivar, R. (2019). "Towards automated machine learning: evaluation and comparison of auto ML approaches and tools," in *2019 IEEE 31st International Conference on Tools with Artificial Intelligence (ICTAI)*, (Portland: IEEE), 1471–1479.

Zhou, P., Resendez, S. L., Rodriguez-Romaguera, J., Jimenez, J. C., Neufeld, S. Q., Giovannucci, A., et al. (2018). Efficient and accurate extraction of *in vivo* calcium signals from microendoscopic video data. *eLife* 7:e28728. doi: 10.7554/eLife.28728

Conflict of Interest: The authors declare that the research was conducted in the absence of any commercial or financial relationships that could be construed as a potential conflict of interest.

frontiers in Neural Circuits

MINI REVIEW
published: 15 July 2020
doi: 10.3389/fncir.2020.00041

Challenges for Therapeutic Applications of Opsin-Based Optogenetic Tools in Humans

Yi Shen[1], *Robert E. Campbell*[1,2], *Daniel C. Côté*[3,4] *and Marie-Eve Paquet*[3,5]*

[1]*Department of Chemistry, University of Alberta, Edmonton, AB, Canada,* [2]*Department of Chemistry, Graduate School of Science, The University of Tokyo, Tokyo, Japan,* [3]*Centre de Recherche CERVO, Université Laval, Quebec City, QC, Canada,* [4]*Département de Physique et Génie Physique, Université Laval, Quebec City, QC, Canada,* [5]*Département de Biochimie, Microbiologie et Bioinformatique, Université Laval, Quebec City, QC, Canada*

As the technological hurdles are overcome and optogenetic techniques advance to have more control over neurons, therapies based on these approaches will begin to emerge in the clinic. Here, we consider the technical challenges surrounding the transition of this breakthrough technology from an investigative tool to a true therapeutic avenue. The emerging strategies and remaining tasks surrounding genetically encoded molecules which respond to light as well as the vehicles required to deliver them are discussed.The use of optogenetics in humans would represent a completely new paradigm in medicine and would be associated with unprecedented technical considerations. To be applied for stimulation of neurons in humans, an ideal optogenetic tool would need to be non-immunogenic, highly sensitive, and activatable with red light or near-infrared light (to maximize light penetration while minimizing photodamage). To enable sophisticated levels of neuronal control, the combined use of optogenetic actuators and indicators could enable closed-loop all-optical neuromodulation. Such systems would introduce additional challenges related to spectral orthogonality between actuator and indicator, the need for decision making computational algorithms and requirements for large gene cassettes. As in any gene therapy, the therapeutic efficiency of optogenetics will rely on vector delivery and expression in the appropriate cell type. Although viral vectors such as those based on AAVs are showing great potential in human trials, barriers to their general use remain, including immune responses, delivery/transport, and liver clearance. Limitations associated with the gene cassette size which can be packaged in currently approved vectors also need to be addressed.

Keywords: optogenetics, viral vectors, therapeutic applications, technical challenges, opsins

OPEN ACCESS

Edited by:
Jean-Claude Béïque, University of Ottawa, Canada

Reviewed by:
Daniel Llano, University of Illinois at Urbana-Champaign, United States
Anna Beyeler, Institut National de la Santé et de la Recherche Médicale (INSERM), France

***Correspondence:**
Marie-Eve Paquet
marie-eve.paquet@bcm.ulaval.ca

Received: *13 March 2020*
Accepted: *16 June 2020*
Published: *15 July 2020*

Citation:
Shen Y, Campbell RE, Côté DC and Paquet M-E (2020) Challenges for Therapeutic Applications of Opsin-Based Optogenetic Tools in Humans. Front. Neural Circuits 14:41. doi: 10.3389/fncir.2020.00041

INTRODUCTION

Therapeutic applications of optogenetic techniques, which take advantage of the exquisite levels of cellular control that are enabled using the combination of light and genetic targeted constructs, are increasingly plausible. In particular, the ambitious goal to cure diseases of the nervous system would take a substantial step forward if researchers and clinicians were empowered to safely introduce and control optogenetic tools in humans. While there are several different

classes of optogenetic tools (e.g., LOV domains, phytochromes, photocleavable proteins; Rost et al., 2017; Zhang et al., 2017), genetically encoded opsins (light-activated ion channels or pumps; Zhang et al., 2006; Deisseroth, 2015), are of the most relevance for therapeutic control of the nervous system. Optogenetic opsins are proteins that were borrowed from various microbial species and re-engineered or otherwise adapted for mammalian expression. Illumination with the appropriate wavelength of light allows ions to flow (or be actively pumped) across the membrane, leading to reversible activation or inhibition of a neural cell. Although not the focus of this review article, it is important to mention the existence of chemogenetic tools, which are genetically-encoded receptors that can activate or inhibit neurons upon small molecule agonists binding (Magnus et al., 2019). This approach offers significant therapeutic potential with the advantage of targeting that comes with gene therapy and the convenience of pharmacology. While optogenetics may have to overcome challenges of light delivery, the added spacial control and time resolution are critical components of this transformative technology.

A key stepping stone towards bringing optogenetic tools to the clinic will be intensive testing and validation in non-human primates (NHP). To date, there have been relatively few reports of using optogenetics in NHP (Galvan et al., 2017), likely due to both cost constraints and ethical considerations. Given the limited examples reported to date, it is apparent that open data sharing within the academic community will be an important aspect of moving the field forward. To help facilitate data sharing, researchers at the University of Pennsylvania are leading an initiative to put together a database of positive and negative results for various studies involving optogenetics in different species of NHP (Tremblay, S., NHP Optogenetics Open Database, retrieved from osf.io/mknfu August 7, 2019). This effort has already helped to highlight the very large number of variables and the many technical challenges that come with the use of this technology in larger species. Addressing these issues will advance primate neuroscience research and further translation to human medicine.

Here, we consider the technical challenges yet to be overcome to translate optogenetics from a tool for the investigation of model organisms to a therapeutic for the treatment of human diseases. The use of optogenetic tools for human gene therapies would represent a completely new paradigm in medicine and is associated with a combination of challenges, some of which are novel and some of which have precedent in the development of other clinical treatments. For example, precedent for aspects of optogenetic therapies can be found in gene therapy, and chronic brain implants used for Deep Brain Stimulation (DBS). An example of an entirely novel aspect would be light delivery deep into the tissue. We discuss a select number of these challenges that researchers from the fields of protein engineering, optics, genetics, virology, process optimization, and even economics will need to address to bring the therapeutic potential of optogenetics closer to patients.

At a minimum, to be applied for stimulation of neurons in human patients, an ideal optogenetic therapy would require: (1) a safe and efficient gene delivery vehicle; (2) Targeting of the gene delivery vehicle to the tissue of interest; (3) a delivery vehicle, transgene, and therapeutic protein gene-product, that is non-immunogenic and non-mutagenic; and (4) an optogenetic protein that is highly sensitive to light in the red to near-infrared wavelength range (to keep light doses low, maximize light penetration, and minimize photodamage). Additionally, the delivery of light itself also becomes a major issue when dealing with humans and primates compared to more commonly used animal models such as rodents. Overall, the large size of the primate brain, and the human brain, in particular, means that strategies optimized in mice models will need to be entirely rethought and redesigned.

NEAR-FUTURE PROSPECTS FOR CLINICAL APPLICATIONS OF OPTOGENETICS

Clinical applications for optogenetics are diverse but the field of vision restoration has shown particular promise with two clinical trials already ongoing (NCT02556736; NCT03326336). Many of the hurdles discussed in this review article are diminished in the case of treating retinal degeneration, which is the cause of most cases of blindness. Indeed, the affected cells are accessible to both light and transgene delivery, which has already contributed to the success of optogenetics to restore light sensitivity in various species (Baker and Flannery, 2018). Another promising application area is the treatment of severe epilepsy (Walker and Kullmann, 2020). In this case, traditional gene therapy, which is based on the replacement of a defective gene with a functional one, is associated with complications due to issues of dosage. Indeed, gene expression levels are difficult to control but the use of light to activate a genetically encoded channel provides a "dosage dial" that can be turned up or down as need be. There is also hope that optogenetics may replace the traditional electrode-based cochlear implants used to treat certain forms of hearing loss. Although electrical stimulation has been used extensively and successfully in the cochlea, the use of light could improve upon the number of cells effectively stimulated by the implant. Spiral ganglion cells expressing an activating opsin could be illuminated by a simple LED implanted locally and restore auditory function (DiGuiseppi and Zuo, 2019). The idea of repairing muscle paralysis with light is also appealing and promising results are already emerging. Functional optical stimulation has already been demonstrated in rodents and very recently the feasibility of light stimulation of peripheral motor nerves has been shown in NHP (Williams et al., 2019).

Applications in the treatment of Parkinson's disease are also emerging through technologies based on neuromodulation such as opto-deep brain stimulation (Opto-DBS). Current DBS protocols are based on electrical stimulation delivered to a target brain area through a surgically implanted electrode. Despite being an approved therapy for Parkinson's, the exact mechanism for DBS is not fully understood and protocols rely on clinical outcomes for optimization of the electrical strength and polarity of the neurostimulator. Another important issue with DBS is related to the absence of neuronal targeting during stimulation.

Optical stimulation offers an attractive solution to this problem as it is possible to target the genetically encoded light-sensitive tools to particular cell types or a specific cellular compartment. Opto-DBS treatments would require the insertion of an optical probe delivering light to a large number of cells of which only a desirable fraction would respond (Lüscher et al., 2015; Gittis and Yttri, 2018).

Chronic pain continues to be one of the most common causes of disability that impairs quality of life. It remains difficult to treat; complete pain control with available drug treatment is rarely achieved and disabling side effects are common, including addiction, dependence, or even paradoxical hyperalgesia (Wang et al., 2012; Ferrini et al., 2013; Burma et al., 2017). In the context of the opioid crisis, non-pharmacological approaches for pain relief hold much therapeutic potential (Mickle and Gereau, 2018). While conventional electrical stimulation at the spinal level or in the skin show efficacy, the full potential of these approaches is not achieved because the stimulation approach is nonspecific and targets multiple cell types (e.g., different classes of sensory fibers during transcutaneous electrical nerve stimulation; different classes of afferents, local spinal interneurons, or ascending/descending pathways for spinal cord stimulation). Cell-specific optogenetic-based treatments for pain relief have been explored successfully in preclinical paradigms (Wang et al., 2016). Although far from being used in humans, strategies using an epidural optic fiber to deliver light to the spinal cord and sensory afferents expressing opsins are successful in mice (Bonin et al., 2016). Also, the use of miniature bio-optoelectronic implants to generate a closed loop of optoelectronic stimulation presents highly promising results in rodent models of bladder dysfunctions (Mickle et al., 2019). Translatability potential of the approach was also demonstrated by using viral transduction in dorsal root ganglion neurons *in vivo* (Spencer et al., 2018) but before these strategies can be safely used clinically, issues of transgene targeting remain to be completely solved.

CHOICE OF GENE DELIVERY VEHICLE

As with other types of gene therapies, therapeutic applications of optogenetics will necessitate the expression of a genetically encoded protein in a specific cell type, organ or anatomical location and thus requires a delivery vehicle for the transgene. Such a targeted introduction of foreign genes is now done routinely in model organisms. However, translating such approaches to humans is, of course, associated with much higher ethical and safety standards and much lower tolerance of risk. Many approaches that are routinely used for transgenic animals, such as *in vivo* electroporation, are probably not translatable to humans. Other techniques, like the use of nanoparticles or carbon dots as gene carriers, show potential for therapeutic applications but research remains a relatively early stage (Zhou et al., 2016; Trigueros et al., 2019). Currently, viral vector-based transduction is the most advanced, powerful, and commonly used method to constitutively deliver foreign genes to specific tissues in mammals (Naso et al., 2017).

Viral vectors have a long track record in therapeutic gene delivery and research efforts are starting to bear even more fruit, as an increasing number of viral vector-based therapies are reaching the later stages of clinical studies (Keeler and Flotte, 2019). The approval of these strategies for the treatment of Lipoprotein Lipase Deficiency and hemophilia are landmark achievements of modern medicine (Gaudet et al., 2013; Chapin and Monahan, 2018). Amongst the many types of viral vectors, adeno-associated virus (AAV) is already being used in neural tissue to treat vision disorders (Bennett et al., 2016; FDA Briefing Document on Voretigene Neparvovec from Spark Therapeutics)[1] and, based on current trends, is the frontrunner to be the method of choice for optogenetic applications in humans. However, even for AAVs, there remain major barriers to their widespread use in humans, including immune responses, specificity delivery/transport to the target cells, clearance of the vector through the liver, and the limited size of the gene cassette size which can be packaged in currently approved vectors.

For many clinical applications, lifelong expression of the optogenetic tool might be required and thus, maintenance of the transgene over time is an important consideration. AAV vectors do not consistently integrate their DNA into the host's genome but persist episomally and have been shown to lead to prolonged gene expression with very low toxicity in various cell types including neurons (Gil-Farina and Schmidt, 2016; Hordeaux et al., 2019; Bravo-Hernandez et al., 2020). Although additional data is required, studies in rhesus macaques suggest that virally delivered opsins can remain functional for several months post-injection (Williams et al., 2019).

Other barriers to this fast-advancing field are the constraint of high regulatory scrutiny on production as well as the prohibitive costs associated with the use of patented gene delivery vectors. RegenxBio currently holds exclusive rights to most known AAV serotypes such as AAV7, 8, 9 and Rh10 and over 100 more through their NAV platform but other components such as the therapeutic transgene itself, and its mechanism of action (e.g., RNA interference, CRISPR) are often linked to licensing rights. Identifying exactly what intellectual property is owned by what inventor or institution and properly attributing rights and credit for all facets of potential gene therapy could be a complicated task. Obtaining the required rights can also quickly become costly and highly time-consuming (Kaemmerer, 2018).

One important constraint to the use of AAVs as gene delivery vehicles is the relatively small DNA packaging size. An AAV vector is limited to a single-stranded DNA cargo of approximately 5,000 bases (5 kb), which includes the necessary elements such as inverted terminal repeat (ITRs), polyadenylation sequence, and promoter. Generally speaking, most current optogenetic transgenes, fused to the gene encoding a fluorescent protein, span about 1.6–2.0 kb and thus fit within the rAAV constraints. As human applications may benefit from the combined use of multiple actuators (i.e., for two-color activation and silencing; Han and Boyden, 2007), or the combination of an optogenetic actuator and activity biosensors

[1] www.fda.gov/media/108375/download

(Hochbaum et al., 2014), the size restriction of AAVs could limit their use as a delivery vehicle. Existing serotypes have been "over-packaged" with mixed success and varying reproducibility and the consensus appears to be that AAV can be overpackaged by ∼10%, but with a concomitant reduction in both viral titers and *in vivo* transduction (Chamberlain et al., 2016). Trans-splicing is the favored approach currently used to increase the size of transgenes delivered through AAVs (Tornabene and Trapani, 2020). This approach relies on the splitting of the gene of interest and its separate packaging in two different vectors followed by their co-infection in the same cell. Since AAVs genomes will form concatemers, the two portions of the transgenes delivered separately usually end up being expressed as one gene (Colella et al., 2018). The challenge related to the implementation of such a strategy is the successful co-infection of the same target cell at levels high enough to obtain significant expression of the gene of interest. Molecular methods such as the use of protein trans-splicing mechanisms appear to increase the efficiency of the approach (Tornabene et al., 2019) but the issue remains particularly relevant when working with optogenetics tools which need to be expressed at relatively high levels to affect cellular processes.

Though not a technical constraint, another barrier to the use of currently available AAVs is restrictive multi-party intellectual property agreements resulting from the long chains of technical improvements made by different laboratories. Each contributor may impose intellectual property conditions that, collectively, preempt future developments. The challenge of costs thus relates to the development of new business models or funding mechanisms allowing for the development of these therapies as well as their usage within our health care systems.

GENE DELIVERY AND TARGETING TO THE TISSUE OF INTEREST

Although other approaches have been reported (Dalkara et al., 2013), AAV-mediated delivery of optogenetic tools to the central and peripheral nervous systems of animal models has been mostly done with local injection. Relative to systemic administration, local injection avoids some of the issues described above. Indeed, immune responses are most problematic when the AAV is delivered into the bloodstream where it comes into direct contact with circulating antibodies. Neurosensory organs are particularly well suited for local administration of AAVs and monitoring of therapeutic effects. As such, ophthalmic disorders are among the most practical first targets for therapeutic optogenetics in humans.

In the central nervous system, the delivery of AAV through stereotaxic injection involves risks of viral or bacterial infection, hemorrhage, and edema. Also, as opposed to rodents for which detailed atlases of the brain exist and coordinates are well defined, surgical delivery in the human brain requires imaging and expert analysis immediately before the intervention which adds to the duration and cost of the process. The restricted spread of the injected vector can also be limiting, especially for the treatment of diseases that affect large areas of the CNS. Engineered AAV capsids such as the AAVDJ have shown increased spreading capacity with promising perspectives (Jollé et al., 2019). An alternative to stereotaxic injection is to deliver AAVs to the cerebrospinal fluid (CSF), which allows for more widespread gene transfer throughout the brain and spinal cord with a lower degree of precision required for injection (Hardcastle et al., 2018). However, the presence of tight junctions between ependymal cells can prevent AAV entry into brain parenchyma and will restrict such applications. In rodents, this technique has been used with the most success in newborns and young animals, which is also not applicable to humans (Hudry and Vandenberghe, 2019).

Due to the inherent challenges associated with stereotaxic injection and delivery *via* CSF, much effort has been directed towards the development of AAVs suitable for peripheral delivery in adult mammals. To obtain efficient targeting to the CNS from intravenous injections in adult mice, mutations have been introduced into the capsid of AAV9 to generate new serotypes such as PHP.B and PHP.S (Deverman et al., 2016; Chan et al., 2017; Challis et al., 2019). The efficiency of these engineered vectors for CNS targeting in mice has improved dramatically, but there is almost certainly further room for improvement. Initial efforts to use these serotypes in NHPs have demonstrated that these vectors do not exhibit the same targeting properties as observed in rodents and that toxicity is an issue (Hordeaux et al., 2018; Liguore et al., 2019). Indeed, with the high dose of vector required to achieve relevant transduction, adverse effects become significant. These results emphasize the importance of developing highly efficient viruses for human applications, such that the therapeutic window is associated with low viral titers. Hepatotoxicity represents a particularly significant risk as most AAVs are hepatotropic and considerable proportions of the vectors distribute to the liver. The most promising future direction to obtain the ideal delivery vehicle for optogenetics tools in the CNS is to undertake systematic testing in NHP to identify new vectors with the ability to cross the blood-brain barrier (BBB) while being excluded from various organs. Capsid engineering, *in vivo* selections, and directed evolution are all promising strategies for developing further improved AAV vehicles. An alternative could be the use of focussed ultrasound to disrupt the BBB and allow entry of AAVs into the brain (Chen et al., 2019). Fortunately, the natural biological diversity of AAV serotypes, which is diverse and displays remarkable differences in gene transfer and vector tropism between serotypes, remains a rich resource that should continue to be mined to discover improved tools for gene delivery.

Although a broad AAV biodistribution throughout the CNS could be desirable for some applications, targeting specific anatomical areas or cell types is often important for the specificity of treatment. Efficient long-distance anterograde and retrograde axonal transport of certain AAV serotypes has been demonstrated in various animal models (Tervo et al., 2016; Zingg et al., 2017). Assuming that there is a connected area that is easily reachable for local injection and associated with minimal risks of infection, this type of transport could be used as a means to promote the introduction of viral particles, and their payloads, across anatomically connected areas of the brain. However, considering that our knowledge of the human

neuronal connectome remains relatively sparse, it is unlikely that this strategy will be applicable on a large scale shortly. Of course, one of the main advantages of optogenetics is that activation requires both gene delivery and illumination. Accordingly, even in cases where tissue-specific gene delivery is imperfect or not possible, spatially confined illumination will provide a means of activating specific tissue areas.

Beyond general tissue specificity, AAV serotypes can exhibit unique cellular tropisms, though there is still much progress that needs to be made to achieve high levels of cell-type specificity. Indeed, despite numerous studies reported on the life cycle of AAVs, the molecular basis of the varied tropisms of AAV vectors is still being elucidated (Srivastava, 2016). Although most natural AAVs have been shown to use cell surface glycans as primary receptors, structure differences in both the AAV capsids and receptor glycans have been linked to variations in transduction efficiencies and tropism (Asokan et al., 2012; Murlidharan et al., 2014). A recently identified cellular receptor (AAVR) has been shown to bind most AAVs (Summerford et al., 2016) but the role, if any, that this receptor plays in larger animals and humans remains to be shown. Interestingly, the identification of a new class of receptors that binds the engineered PHP-B capsids (Huang et al., 2019) independently of previously known receptors, may improve our understanding of variations in tropisms between species and provide new ways to exploit the use of cellular receptors in AAV targeting.

Another approach to achieving cell-type specificity in rodents and NHPs is to drive optogenetic tool expression using cell-specific eukaryotic promoters (Galvan et al., 2017). Inherent challenges for promoter development are the contradictory requirements for small size (constrained by the packaging limitations of the AAV capsid) and high expression level (required to impact cell function). Although initiatives such as the "Pleiades promoter project" have contributed to the elaboration of databases of mini-promoters with potential for human brain gene therapy (de Leeuw et al., 2014), only a few are well characterized and drive expression levels strong enough for the needs of optogenetics applications. Our ever-increasing understanding of gene regulation has led to the emergence of optimized "tailor-made" expression cassettes with improved efficacy which are exploiting strategies such as miRNA or nucleotide structure-based control (Papadakis et al., 2004; de Leeuw et al., 2014; Domenger and Grimm, 2019; Zhong et al., 2020). A promising strategy is the addition of strong distal enhancer elements upstream of the core-specific promoter which can increase the level of transgene expression while maintaining a small size promoter and the tissue specificity (Blankvoort et al., 2018, 2020). Challenges remain, however, in the translation of these developments to humans. Although it is known that the same promoters can drive gene expression in different animal species, the specificity of a given promoter can vary between species.

While there remains a tremendous potential for engineered promoters for therapeutic applications, detailed characterization of *in vivo* expression patterns in humans seems impractical or impossible. For this reason, the use of human-induced pluripotent stem cells or cerebral organoids (Shiri et al., 2019) to validate transduction efficiency driven by cell-specific promoters could be considered. Though, they are far from perfect models of *in vivo* biology, these quickly evolving technologies are extremely promising and should be included in promoter and vector validation pipelines.

IMMUNOGENICITY AND GENOTOXICITY

Human optogenetic-based therapies, like many other cell-, gene-, and protein-based therapies, will be complicated by the possibility of immune responses. The introduction and expression of foreign molecules, such as a light-activated opsin, comes with the risk of eliciting a response from our immune cells. Furthermore, the AAV delivery vehicle itself could also be targeted by our immune system through pre-existing immunity (PEI; Bartel et al., 2011). PEI occurs due to prior exposure to an AAV, which introduces a lasting memory immune response. Since AAV is endemic in humans and most AAV serotypes currently in use came from primates, most patients will have likely been pre-exposed and may carry circulating anti-AAV neutralizing antibodies secreted by memory B cells. As these antibodies can, even at low levels, prevent the AAV particle from reaching its intended tissue or cell target, PEI needs to be considered when developing AAV based therapies (Meadows et al., 2019; Nidetz et al., 2019).

To develop AAVs that are minimally or negligibly inactivated due to PEI, it might be necessary to develop AAV vectors from isolates and serotypes not found in humans or NHP and with sequence differences significant enough that the circulating antibodies would not recognize and neutralize the viral particles. Alternatively, as regions of the AAV capsid important for antibody binding have been identified, inserting mutations in these residues could abolish epitope recognition (Kotterman and Schaffer, 2014), or the AAV could be pegylated to shield the virus capsid from the immune system (Yao et al., 2017). Strategies involving the manipulation of the host may also be considered. For example, using plasmapheresis, which could remove most antibodies against AAV, or suppressing innate immunity could potentially mitigate the effect of a possible antibody response (Tse et al., 2015).

In addition to potential immune responses against the viral delivery vehicle, immune responses against the optogenetic protein itself are a major concern. Notably, microbial opsins are membrane-spanning proteins so they necessarily present non-human epitopes to the extracellular environment. This hypothesis has so far been mostly examined in the context of vision restoration therapy (Sugano et al., 2011, 2016). It was shown that in the retina, which is a known immune-privileged site, the specific reaction to ChR2 or mVChR1 is minimal and does not affect its expression. However, when Maimon et al. (2018) recently tested the immunogenicity of ChR2 following intramuscular injection in rats (AAV delivery), significant levels of anti-ChR2 antibodies were detected in the serum. More importantly, they observed loss of expression and cell death induced by the immune reaction, suggesting that researchers should be cautious when using optogenetic

tools of microbial origins. Protein engineering to remove the most immunogenic epitopes or "humanize" opsin proteins may be one approach to addressing this challenge. Yet another approach would be to re-purpose human opsins as optogenetic tools. Proof-of-concept for this approach comes from the work of Berry et al. (2019), who restored vision in a mouse by AAV-mediated delivery of the gene for mammalian medium wavelength cone opsin (MW-opsin) in the retina.

In addition to immunogenicity, close attention must be paid to the possibility of AAV gene delivery-induced mutagenicity or genotoxicity that could serve as a driver for tumor formation. Fortunately, relative to other potential viral delivery vehicles, AAV-delivered transgenes rarely insert into the host's genomic DNA (Colella et al., 2018). Rather, the AAV-delivered DNA cargo tends to exist as a nuclear-localized circular double-stranded DNA known as an episome. Accordingly, AAVs have relatively low mutagenicity or genotoxicity. Even though the insertion rate is low, the fact that AAVs used for therapeutic purposes would likely deliver very strong promoters to drive high-level expression, even rare genomic integration events could drive increased expression levels of adjacent oncogenes.

IMPROVED OPTOGENETIC TOOLS OF POTENTIAL UTILITY FOR THERAPEUTIC APPLICATIONS

In parallel with efforts to develop improved gene delivery methods, ongoing efforts are providing improved optogenetic tools with higher light sensitivity and sensitivity to longer wavelength (lower energy) light. To realize these improvements, researchers have used multiple approaches including mutagenesis, chimera-genesis, and discovery of improved genes in nature. For example, early efforts to further improve the light-gated cation channel channelrhodopsin-2 (ChR2) produced several variants with higher light sensitivity, larger photocurrent, and/or faster kinetics (Lin et al., 2009; Gunaydin et al., 2010; Berndt et al., 2011). As another example, a bioinformatic search against the sequenced genome of cryptophyte *Guillardia theta* led to the discovery of light-activated opsins that are highly light-sensitive and efficiently hyperpolarize the membrane and silence the neuron through anion conduction (Govorunova et al., 2015). More recently, machine learning has been applied to guide opsin engineering to simultaneously optimize multiple properties including localization, kinetics, photocurrents, and light sensitivity (Bedbrook et al., 2019).

In addition to efforts to increase the light sensitivity, substantial efforts have been invested in the discovery and engineering of optogenetic tools with higher sensitivity to red-shifted wavelengths of light. The use of more red-shifted activation light is associated with reduced potential for tissue photodamage and greater tissue penetration of the light. The red-shifted channelrhodopsin variant VChR1 (∼550 nm activation peak) was first identified from *Volvox carteri* using a genomic screening strategy. However, weak expression and small photocurrents initially limited its practical utility (Zhang et al., 2008). A chimeric opsin variant, C1V1, composed of sequences from both ChR1 and VChR1, retained the red-shifted spectrum but also exhibited improved membrane trafficking and enhanced photocurrents (Yizhar et al., 2011). A further red-shift was realized with the ReaChR variant (∼600 nm activation peak) which was also engineered using chimera-genesis and rationally designed mutations (Lin et al., 2013). In the ongoing search for further improved red-shifted opsins with large photocurrents and high light-sensitivity, genome screens have helped to identify new variants such as Chrimson from *Stigeoclonium helveticum* (Klapoetke et al., 2014), and ChRmine from *Tiarina fusus* (Marshel et al., 2019). GenSight Bioscience is currently performing a clinical trial (NCT03326336) in which a Chrimson variant is being explored for vision restoration (**Supplementary Table S1**; **Figure 1**).

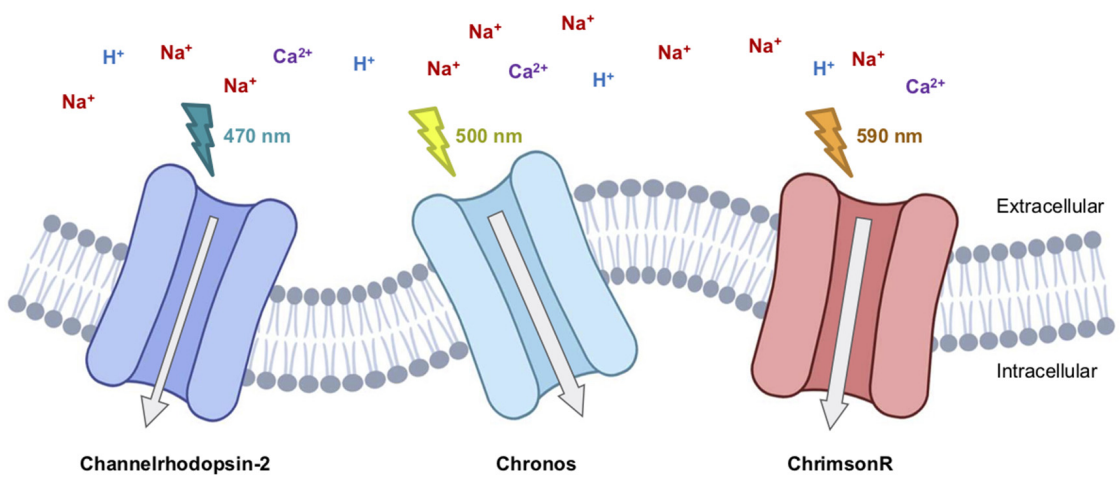

FIGURE 1 | Therapeutic-relevant opsins currently involved in clinical trials. Channelrhodopsin2 (Clinical Trial #NCT02556736), Chronos (Clinical Trial #NCT04278131), and ChrimsonR (Clinical Trial #NCT03326336) are excitatory light-gated cation channelrhodopsins.

The issue of the alteration of ion balance which can be induced by the activity of certain opsins should also be considered when designing tools for therapeutic applications (Wang et al., 2016). It is known that inhibitory opsins, which have mostly been based on ion pumps (Cl^- for NpHR; H^+ for Arch and ArchT) may result in undesirable side effects such as the collapse in Cl^- gradients and pH changes. Rebound excitation, due to the accumulation of Cl^- ions following the end of NpHR activation, for example, has been found (Gradinaru et al., 2007; Raimondo et al., 2012). This caveat may be further compounded in disorders associated with Cl^- imbalance such as chronic pain (Coull et al., 2003), drug dependence (Ferrini et al., 2013; Ostroumov et al., 2016), and certain symptoms of autism (Anacker et al., 2019). In this context, the recent advent of Cl^- permeable opsins may be more promising (Govorunova et al., 2015; Wietek et al., 2015).

LIGHT DELIVERY

Light delivery is at the heart of the technical challenges of human optogenetics: the sampling volume within which the irradiance is sufficient for stimulation is essentially the same in rodents and humans because the tissue properties are similar. However, the number of neurons that need to be excited in humans is larger than in rodents, and therefore the volume of tissue that must be illuminated is also larger. Therefore, the strategies that have worked in rodents (e.g., point excitation from multimode fibers) are likely going to be insufficient to trigger a response in humans. There are two options to maximize the number of illuminated neurons: the use of volume diffusers or longer wavelength illumination. Here, we can learn from other fields where light delivery to large volumes is also a challenge. For example, photodynamic therapy must also maximize the excitation volume for tumor treatment and many solutions have been proposed such as fiber diffusers (Mizeret and van den Bergh, 1996; Selm et al., 2007) or multi-fiber geometries. In Diffuse Optical Tomography, reflectance measurements are routinely performed up to a few centimeters through the skull thanks to the use of infrared light (800 nm; White et al., 2009). The required power for photodynamic therapy and tomography experiments is lower than for optogenetics stimulation, but they provide additional arguments for red-shifted channels. In as much as the volume of excitation is maximized, we still required a minimum irradiance to generate an action potential: when local expression levels are sufficient, the threshold irradiance is nominally 10 mW/mm^2 for ChR2 in rodents (Boyden et al., 2005), which can be achieved with LEDs or lasers alike fairly easily, even with wirelessly charged μ-LED (Shin et al., 2017). However, it is not trivial to estimate the necessary power that will be sufficient for humans: even if several milliwatts of power are incident on the tissue, it will be quickly redistributed due to scattering and will be removed from the tissue with absorption.

Although, it is outside the scope of this review article to explain the details of light scattering calculations in tissue, we can still provide important guidelines and even tools for the interested researchers. The light distribution within tissue depends on the scattering and the absorption coefficients, two properties that depend on the light wavelength and that are difficult to characterize accurately. In addition to the uncertainty in their exact values, the random scattering and absorption processes lead to a light distribution that is a rapidly varying

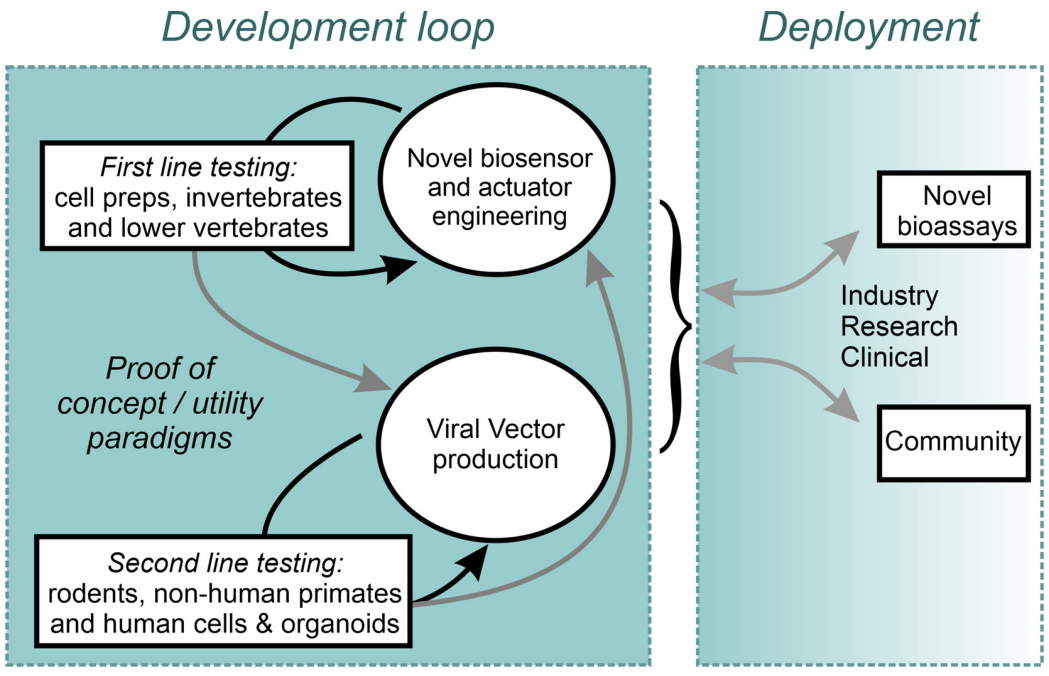

FIGURE 2 | An open science Design-Build-Test model implemented within the Canadian Neurophotonics Platform, giving rise to the Canadian Optogenetics and Vectorology Foundry project (neurophotonics.ca).

function of space with intricate reflections from surrounding tissue. The reduced scattering coefficient (i.e., the scattering coefficient multiplied by (1-g) where g is the anisotropy factor) ranges from 10 cm^{-1} to 100 cm^{-1} in nervous tissue and varies only mildly with a wavelength in the visible (Cheong et al., 1990). On the other hand, the absorption coefficient is essentially zero above a wavelength of 600 nm but is over 1,000 cm^{-1} due to hemoglobin absorption around 488 nm. The great variability and the large values of these coefficients make the final distribution of light very difficult to estimate accurately. The tools used to perform such estimates are Monte Carlo simulations, with the most common and validated software being MCML (Wang et al., 1995). Today, it is even possible to use web-based calculations to obtain reasonable estimates sufficient to choose a laser adequately (Doronin and Meglinski, 2011). It is expected that the typical illumination volume from a point source in the brain will increase from 1 mm^3 to 1 cm^3 (a thousandfold increase) when going from 488 nm to 600 nm excitation wavelength (DePaoli et al., 2020), indicating that other solutions such as volume diffusers may be necessary to trigger a response if red-shifted channels are not available.

CONCLUSIONS

Ultimately, to enable the most sophisticated levels of neuronal control, the combined use of optogenetic actuators and genetically encoded biosensors of cellular activity indicators could enable closed-loop all-optical activity neuromodulation. Such systems would introduce additional challenges related to spectral orthogonality between actuator and indicator, the need for decision making computational algorithms, and the need to deliver large gene cassettes. As highlighted above, there is not a single strategy which appears to fulfill all the requirements for the ideal delivery method of optogenetics tools in humans. As such, likely, combining multiple approaches (light, serotype, delivery route, promoter, etc.) will be needed to obtain the proper level of targeting and cellular specificity. Moving the field forward will require researchers to address an extremely large number of challenges that will only be overcome by testing in NHP as well as human *in vitro* models. This monumental task will far exceed the capabilities of any one team and will succeed only if a proper structure of data sharing is put in place and the whole of the vested research community is compelled to contribute. A proposal to accelerate this effort is the rapid, unencumbered, dissemination of open-source constructs, combined with open communication of both positive findings and setbacks. An example of such an enterprise is the effort developed within the Canadian Neurophotonics Platform project (**Figure 2**; neurophotonics.ca). Through the combined efforts and transdisciplinary expertise of the research community, therapeutic applications of optogenetics no longer need to be "just over the horizon," and can be made into a therapeutic reality in the here and now.

AUTHOR CONTRIBUTIONS

YS contributed the entire text related to improved genetic tools for therapeutic applications. RC contributed to all sections of the text and M-EP initiated the project and wrote sections pertaining to viral vectors and near-future prospects for therapeutic applications. DC wrote the section on light.

FUNDING

The authors are members of the Canadian Neurophotonics Platform which is supported in part by the Canada Brain Research Fund, administered by Brain Canada and the Canada Foundation for Innovation. Research in the lab of RC is also supported by grants from the Natural Sciences and Engineering Research Council of Canada (NSERC), the Canadian Institutes of Health Research (CIHR), and the Japan Society for the Promotion of Science (JSPS). DC's research is funded by NSERC and CIHR. M-EP is supported by the Québec Pain Research Network of the Fonds de Recherche du Québec-Santé and the Ministère de l'Économie et de l'Innovation du Québec.

ACKNOWLEDGMENTS

We would like to thank Yves De Koninck for fruitful discussions and suggestions as well as contribution to the last figure of the article.

SUPPLEMENTARY MATERIAL

The Supplementary Material for this article can be found online at: https://www.frontiersin.org/articles/10.3389/fncir.2020.00041/full#supplementary-material.

REFERENCES

Anacker, A. M. J., Moran, J. T., Santarelli, S., Forsberg, C. G., Rogers, T. D., Stanwood, G. D., et al. (2019). Enhanced social dominance and altered neuronal excitability in the prefrontal cortex of male KCC2b mutant mice. *Autism Res.* 12, 732–743. doi: 10.1002/aur.2098

Asokan, A., Schaffer, D. V., and Samulski, R. J. (2012). The AAV vector toolkit: poised at the clinical crossroads. *Mol. Ther.* 20, 699–708. doi: 10.1038/mt.2011.287

Baker, C. K., and Flannery, J. G. (2018). Innovative optogenetic strategies for vision restoration. *Front. Cell. Neurosci.* 12:316. doi: 10.3389/fncel.2018.00316

Bartel, M., Schaffer, D., and Büning, H. (2011). Enhancing the clinical potential of AAV vectors by capsid engineering to evade pre-existing immunity. *Front. Microbiol.* 2:204. doi: 10.3389/fmicb.2011.00204

Bedbrook, C. N., Yang, K. K., Robinson, J. E., Mackey, E. D., Gradinaru, V., and Arnold, F. H. (2019). Machine learning-guided channelrhodopsin engineering enables minimally invasive optogenetics. *Nat. Methods.* 16, 1176–1184. doi: 10.1038/s41592-019-0583-8

Bennett, J., Wellman, J., Marshall, K. A., McCague, S., Ashtari, M., DiStefano-Pappas, J., et al. (2016). Safety and durability of effect of contralateral-eye administration of AAV2 gene therapy in patients with childhood-onset blindness caused by RPE65 mutations: A follow-on phase 1 trial. *Lancet*. 388, 661–672. doi: 10.1016/S0140-6736(16)30371-3

Berndt, A., Schoenenberger, P., Mattis, J., Tye, K. M., Deisseroth, K., Hegemann, P., et al. (2011). High-efficiency channelrhodopsins for fast neuronal stimulation at low light levels. *Proc. Natl. Acad. Sci. U S A* 108, 7595–7600. doi: 10.1073/pnas.1017210108

Berry, M. H., Holt, A., Salari, A., Veit, J., Visel, M., Levitz, J., et al. (2019). Restoration of high-sensitivity and adapting vision with a cone opsin. *Nat. Commun.* 10:1221. doi: 10.1038/s41467-019-09124-x

Blankvoort, S., Descamps, L. A. L., and Kentros, C. (2020). Enhancer-driven gene expression (EDGE) enables the generation of cell type specific tools for the analysis of neural circuits. *Neurosci. Res.* 152, 78–86. doi: 10.1016/j.neures.2020.01.009

Blankvoort, S., Witter, M. P., Noonan, J., Cotney, J., and Kentros, C. (2018). Marked diversity of unique cortical enhancers enables neuron-specific tools by enhancer-driven gene expression. *Curr. Biol.* 28, 2103.e5–2114.e5. doi: 10.1016/j.cub.2018.05.015

Bonin, R. P., Wang, F., Desrochers-Couture, M., Ga Secka, A., Boulanger, M.-E., Côté, D. C., et al. (2016). Epidural optogenetics for controlled analgesia. *Mol. Pain* 12:1744806916629051. doi: 10.1177/1744806916629051

Boyden, E., Zhang, F., Bamberg, E., Nagel, G., and Deisseroth, K. (2005). Millisecond-timescale, genetically targeted optical control of neural activity. *Nat. Neurosci.* 8, 1263–1268. doi: 10.1038/nn1525

Bravo-Hernandez, M., Tadokoro, T., Navarro, M. R., Platoshyn, O., Kobayashi, Y., Marsala, S., et al. (2020). Spinal subpial delivery of AAV9 enables widespread gene silencing and blocks motoneuron degeneration in ALS. *Nat. Med.* 26, 118–130. doi: 10.1038/s41591-019-0674-1

Burma, N. E., Bonin, R. P., Leduc-Pessah, H., Baimel, C., Cairncross, Z. F., Mousseau, M., et al. (2017). Blocking microglial pannexin-1 channels alleviates morphine withdrawal in rodents. *Nat. Med.* 23, 355–360. doi: 10.1038/nm.4281

Challis, R. C., Kumar, S. R., Chan, K. Y., Challis, C., Beadle, K., Jang, M. J., et al. (2019). Publisher correction: systemic AAV vectors for widespread and targeted gene delivery in rodents. *Nat. Protoc.* 14:2597. doi: 10.1038/s41596-019-0155-5

Chamberlain, K., Riyad, J. M., and Weber, T. (2016). Expressing transgenes that exceed the packaging capacity of adeno-associated virus capsids. *Hum. Gene Ther. Methods* 27, 1–12. doi: 10.1089/hgtb.2015.140

Chan, K. Y., Jang, M. J., Yoo, B. B., Greenbaum, A., Ravi, N., Wu, W.-L., et al. (2017). Engineered AAVs for efficient noninvasive gene delivery to the central and peripheral nervous systems. *Nat. Neurosci.* 20, 1172–1179. doi: 10.1038/nn.4593

Chapin, J. C., and Monahan, P. E. (2018). Gene therapy for hemophilia: progress to date. *BioDrugs* 32, 9–25. doi: 10.1007/s40259-017-0255-0

Chen, K.-T., Wei, K.-C., and Liu, H.-L. (2019). Theranostic strategy of focused ultrasound induced blood-brain barrier opening for CNS disease treatment. *Front. Pharmacol.* 10:86. doi: 10.3389/fphar.2019.00086

Cheong, W., Prahl, S., and Welch, A. (1990). A review of the optical properties of biological tissues. *IEEE J. Quantum Electron.* 26, 2166–2185.

Colella, P., Ronzitti, G., and Mingozzi, F. (2018). Emerging issues in AAV-mediated *in vivo* gene therapy. *Mol. Ther. Methods Clin. Dev.* 8, 87–104. doi: 10.1016/j.omtm.2017.11.007

Coull, J. A. M., Boudreau, D., Bachand, K., Prescott, S. A., Nault, F., Sík, A., et al. (2003). Trans-synaptic shift in anion gradient in spinal lamina I neurons as a mechanism of neuropathic pain. *Nature* 424, 938–942. doi: 10.1038/nature01868

Dalkara, D., Byrne, L. C., Klimczak, R. R., Visel, M., Yin, L., Merigan, W. H., et al. (2013). *In vivo*-directed evolution of a new adeno-associated virus for therapeutic outer retinal gene delivery from the vitreous. *Sci. Transl. Med.* 5:189ra76. doi: 10.1126/scitranslmed.3005708

Deisseroth, K. (2015). Optogenetics: 10 years of microbial opsins in neuroscience. *Nat. Neurosci.* 18, 1213–1225. doi: 10.1038/nn.4091

de Leeuw, C. N., Dyka, F. M., Boye, S. L., Laprise, S., Zhou, M., Chou, A. Y., et al. (2014). Targeted CNS delivery using human minipromoters and demonstrated compatibility with adeno-associated viral vectors. *Mol. Ther. Methods Clin. Dev.* 1:5. doi: 10.1038/mtm.2013.5

DePaoli, D., Gasecka, A., Bahdine, M., Deschenes, J. M., Goetz, L., Perez-Sanchez, J., et al. (2020). Anisotropic light scattering from myelinated axons in the spinal cord. *Neurophotonics* 7:015011. doi: 10.1117/1.nph.7.1.015011

Deverman, B. E., Pravdo, P. L., Simpson, B. P., Kumar, S. R., Chan, K. Y., Banerjee, A., et al. (2016). Cre-dependent selection yields AAV variants for widespread gene transfer to the adult brain. *Nat. Biotechnol.* 34, 204–209. doi: 10.1038/nbt.3440

DiGuiseppi, J., and Zuo, J. (2019). The awesome power of optogenetics in hearing research. *Neurosci. Lett.* 701, 175–179. doi: 10.1016/j.neulet.2019.02.037

Domenger, C., and Grimm, D. (2019). Next-generation AAV vectors-do not judge a virus (only) by its cover. *Hum. Mol. Genet.* 28, R3–R14. doi: 10.1093/hmg/ddz148

Doronin, A., and Meglinski, I. (2011). Online object oriented Monte Carlo computational tool for the needs of biomedical optics. *Biomed. Opt. Express* 2, 2461–2469. doi: 10.1364/boe.2.002461

Ferrini, F., Trang, T., Mattioli, T.-A. M., Laffray, S., Del'Guidice, T., Lorenzo, L.-E., et al. (2013). Morphine hyperalgesia gated through microglia-mediated disruption of neuronal Cl^- homeostasis. *Nat. Neurosci.* 16, 183–192. doi: 10.1038/nn.3295

Galvan, A., Stauffer, W. R., Acker, L., El-Shamayleh, Y., Inoue, K.-I., Ohayon, S., et al. (2017). Nonhuman primate optogenetics: recent advances and future directions. *J. Neurosci.* 37, 10894–10903. doi: 10.1523/JNEUROSCI.1839-17.2017

Gaudet, D., Méthot, J., Déry, S., Brisson, D., Essiembre, C., Tremblay, G., et al. (2013). Efficacy and long-term safety of alipogene tiparvovec (AAV1-LPLS447X) gene therapy for lipoprotein lipase deficiency: an open-label trial. *Gene Ther.* 20, 361–369. doi: 10.1038/gt.2012.43

Gil-Farina, I., and Schmidt, M. (2016). Interaction of vectors and parental viruses with the host genome. *Curr. Opin. Virol.* 21, 35–40. doi: 10.1016/j.coviro.2016.07.004

Gittis, A. H., and Yttri, E. A. (2018). Translating insights from optogenetics to therapies for Parkinson's disease. *Curr. Opin. Biomed. Eng.* 8, 14–19. doi: 10.1016/j.cobme.2018.08.008

Govorunova, E. G., Sineshchekov, O. A., Janz, R., Liu, X., and Spudich, J. L. (2015). NEUROSCIENCE. Natural light-gated anion channels: a family of microbial rhodopsins for advanced optogenetics. *Science* 349, 647–650. doi: 10.1126/science.aaa7484

Gradinaru, V., Thompson, K. R., Zhang, F., Mogri, M., Kay, K., Schneider, M. B., et al. (2007). Targeting and readout strategies for fast optical neural control *in vitro* and *in vivo*. *J. Neurosci.* 27, 14231–14238. doi: 10.1523/jneurosci.3578-07.2007

Gunaydin, L. A., Yizhar, O., Berndt, A., Sohal, V. S., Deisseroth, K., and Hegemann, P. (2010). Ultrafast optogenetic control. *Nat. Neurosci.* 13, 387–392. doi: 10.1038/nn.2495

Han, X., and Boyden, E. S. (2007). Multiple-color optical activation, silencing and desynchronization of neural activity, with single-spike temporal resolution. *PLoS One* 2:e299. doi: 10.1371/journal.pone.0000299

Hardcastle, N., Boulis, N. M., and Federici, T. (2018). AAV gene delivery to the spinal cord: serotypes, methods, candidate diseases, and clinical trials. *Expert Opin. Biol. Ther.* 18, 293–307. doi: 10.1080/14712598.2018.1416089

Hochbaum, D. R., Zhao, Y., Farhi, S. L., Klapoetke, N., Werley, C. A., Kapoor, V., et al. (2014). All-optical electrophysiology in mammalian neurons using engineered microbial rhodopsins. *Nat. Methods* 11, 825–833. doi: 10.1038/nmeth.3000

Hordeaux, J., Hinderer, C., Buza, E. L., Louboutin, J.-P., Jahan, T., Bell, P., et al. (2019). Safe and sustained expression of human iduronidase after intrathecal administration of adeno-associated virus serotype 9 in infant rhesus monkeys. *Hum. Gene Ther.* 30, 957–966. doi: 10.1089/hum.2019.012

Hordeaux, J., Wang, Q., Katz, N., Buza, E. L., Bell, P., and Wilson, J. M. (2018). The neurotropic properties of AAV-PHP.B are limited to C57BL/6J Mice. *Mol. Ther.* 26, 664–668. doi: 10.1016/j.ymthe.2018.01.018

Huang, Q., Chan, K. Y., Tobey, I. G., Chan, Y. A., Poterba, T., Boutros, C. L., et al. (2019). Delivering genes across the blood-brain barrier: LY6A, a novel cellular receptor for AAV-PHP.B capsids. *PLoS One* 14:e0225206. doi: 10.1371/journal.pone.0225206

Hudry, E., and Vandenberghe, L. H. (2019). Therapeutic AAV gene transfer to the nervous system: a clinical reality. *Neuron* 102:263. doi: 10.1016/j.neuron.2019.03.020

Jollé, C., Déglon, N., Pythoud, C., Bouzier-Sore, A.-K., and Pellerin, L. (2019). Development of efficient AAV2/DJ-based viral vectors to selectively downregulate the expression of neuronal or astrocytic target proteins in the rat

central nervous system. *Front. Mol. Neurosci.* 12:201. doi: 10.3389/fnmol.2019.00201

Kaemmerer, W. F. (2018). How will the field of gene therapy survive its success? *Bioeng. Transl. Med.* 3, 166–177. doi: 10.1002/btm2.10090

Keeler, A. M., and Flotte, T. R. (2019). Recombinant adeno-associated virus gene therapy in light of luxturna (and zolgensma and glybera): where are we and how did we get here? *Ann. Rev. Virol.* 6, 601–621. doi: 10.1146/annurev-virology-092818-015530

Klapoetke, N. C., Murata, Y., Kim, S. S., Pulver, S. R., Birdsey-Benson, A., Cho, Y. K., et al. (2014). Independent optical excitation of distinct neural populations. *Nat. Methods* 11, 338–346. doi: 10.1038/nmeth.2836

Kotterman, M. A., and Schaffer, D. V. (2014). Engineering adeno-associated viruses for clinical gene therapy. *Nat. Rev. Genet.* 15, 445–451. doi: 10.1038/nrg3742

Liguore, W. A., Domire, J. S., Button, D., Wang, Y., Dufour, B. D., Srinivasan, S., et al. (2019). AAV-PHP.B Administration results in a differential pattern of CNS biodistribution in non-human primates compared with mice. *Mol. Ther.* 27, 2018–2037. doi: 10.1016/j.ymthe.2019.07.017

Lin, J. Y., Knutsen, P. M., Muller, A., Kleinfeld, D., and Tsien, R. Y. (2013). ReaChR: a red-shifted variant of channelrhodopsin enables deep transcranial optogenetic excitation. *Nat. Neurosci.* 16, 1499–1508. doi: 10.1038/nn.3502

Lin, J. Y., Lin, M. Z., Steinbach, P., and Tsien, R. Y. (2009). Characterization of engineered channelrhodopsin variants with improved properties and kinetics. *Biophys. J.* 96, 1803–1814. doi: 10.1016/j.bpj.2008.11.034

Lüscher, C., Pascoli, V., and Creed, M. (2015). Optogenetic dissection of neural circuitry: from synaptic causalities to blue prints for novel treatments of behavioral diseases. *Curr. Opin. Neurobiol.* 35, 95–100. doi: 10.1016/j.conb.2015.07.005

Magnus, C. J., Lee, P. H., Bonaventura, J., Zemla, R., Gomez, J. L., Ramirez, M. H., et al. (2019). Ultrapotent chemogenetics for research and potential clinical applications. *Science* 364:eaav5282. doi: 10.1126/science.aav5282

Maimon, B. E., Diaz, M., Revol, E. C. M., Schneider, A. M., Leaker, B., Varela, C. E., et al. (2018). Optogenetic peripheral nerve immunogenicity. *Sci. Rep.* 8:14076. doi: 10.1038/s41598-018-32075-0

Marshel, J. H., Kim, Y. S., Machado, T. A., Quirin, S., Benson, B., Kadmon, J., et al. (2019). Cortical layer-specific critical dynamics triggering perception. *Science* 365:eaaw5202. doi: 10.1126/science.aaw5202

Meadows, A. S., Pineda, R. J., Goodchild, L., Bobo, T. A., and Fu, H. (2019). Threshold for pre-existing antibody levels limiting transduction efficiency of systemic rAAV9 gene delivery: relevance for translation. *Mol. Ther. Methods Clin. Dev.* 13, 453–462. doi: 10.1016/j.omtm.2019.04.004

Mickle, A. D., and Gereau, R. W. IV. (2018). A bright future? Optogenetics in the periphery for pain research and therapy. *Pain* 159, S65–S73. doi: 10.1097/j.pain.0000000000001329

Mickle, A. D., Won, S. M., Noh, K. N., Yoon, J., Meacham, K. W., Xue, Y., et al. (2019). A wireless closed-loop system for optogenetic peripheral neuromodulation. *Nature* 565, 361–365. doi: 10.1038/s41586-018-0823-6

Mizeret, J. C., and van den Bergh, H. E. (1996). Cylindrical fiberoptic light diffuser for medical applications. *Lasers Surg. Med.* 19, 159–167. doi: 10.1002/(sici)1096-9101(1996)19:2<159::aid-lsm6>3.0.co;2-r

Murlidharan, G., Samulski, R. J., and Asokan, A. (2014). Biology of adeno-associated viral vectors in the central nervous system. *Front. Mol. Neurosci.* 7:76. doi: 10.3389/fnmol.2014.00076

Naso, M. F., Tomkowicz, B., Perry, W. L. III., and Strohl, W. R. (2017). Adeno-associated virus (AAV) as a vector for gene therapy. *BioDrugs* 31, 317–334. doi: 10.1007/s40259-017-0234-5

Nidetz, N. F., McGee, M. C., Tse, L. V., Li, C., Cong, L., Li, Y., et al. (2019). Adeno-associated viral vector-mediated immune responses: understanding barriers to gene delivery. *Pharmacol. Ther.* 207:107453. doi: 10.1016/j.pharmthera.2019.107453

Ostroumov, A., Thomas, A. M., Kimmey, B. A., Karsch, J. S., Doyon, W. M., and Dani, J. A. (2016). Stress increases ethanol self-administration *via* a shift toward excitatory GABA signaling in the ventral tegmental area. *Neuron* 92, 493–504. doi: 10.1016/j.neuron.2016.09.029

Papadakis, E. D., Nicklin, S. A., Baker, A. H., and White, S. J. (2004). Promoters and control elements: designing expression cassettes for gene therapy. *Curr. Gene Ther.* 4, 89–113. doi: 10.2174/1566523044578077

Raimondo, J. V., Kay, L., Ellender, T. J., and Akerman, C. J. (2012). Optogenetic silencing strategies differ in their effects on inhibitory synaptic transmission. *Nat. Neurosci.* 15, 1102–1104. doi: 10.1038/nn.3143

Rost, B. R., Schneider-Warme, F., Schmitz, D., and Hegemann, P. (2017). Optogenetic tools for subcellular applications in neuroscience. *Neuron* 96, 572–603. doi: 10.1016/j.neuron.2017.09.047

Selm, B., Rothmaier, M., Camenzind, M., Khan, T., and Walt, H. (2007). Novel flexible light diffuser and irradiation properties for photodynamic therapy. *J. Biomed. Opt.* 12:034024. doi: 10.1117/1.2749737

Shin, G., Gomez, A. M., Al-Hasani, R., Jeong, Y. R., Kim, J., Xie, Z., et al. (2017). Flexible near-field wireless optoelectronics as subdermal implants for broad applications in optogenetics. *Neuron* 93, 509.e3–521.e3. doi: 10.1016/j.neuron.2016.12.031

Shiri, Z., Simorgh, S., Naderi, S., and Baharvand, H. (2019). Optogenetics in the era of cerebral organoids. *Trends Biotechnol.* 37, 1282–1294. doi: 10.1016/j.tibtech.2019.05.009

Spencer, N. J., Hibberd, T. J., Lagerström, M., Otsuka, Y., and Kelley, N. (2018). Visceral pain - Novel approaches for optogenetic control of spinal afferents. *Brain Res.* 1693, 159–164. doi: 10.1016/j.brainres.2018.02.002

Srivastava, A. (2016). *in vivo* tissue-tropism of adeno-associated viral vectors. *Curr. Opin. Virol.* 21, 75–80. doi: 10.1016/j.coviro.2016.08.003

Sugano, E., Isago, H., Wang, Z., Murayama, N., Tamai, M., and Tomita, H. (2011). Immune responses to adeno-associated virus type 2 encoding channelrhodopsin-2 in a genetically blind rat model for gene therapy. *Gene Ther.* 18, 266–274. doi: 10.1038/gt.2010.140

Sugano, E., Tabata, K., Takahashi, M., Nishiyama, F., Shimizu, H., Sato, M., et al. (2016). Local and systemic responses following intravitreous injection of AAV2-encoded modified Volvox channelrhodopsin-1 in a genetically blind rat model. *Gene Ther.* 23, 158–166. doi: 10.1038/gt.2015.99

Summerford, C., Johnson, J. S., and Samulski, R. J. (2016). AAVR: a multi-serotype receptor for AAV. *Mol. Ther.* 24, 663–666. doi: 10.1038/mt.2016.49

Tervo, D. G. R., Hwang, B.-Y., Viswanathan, S., Gaj, T., Lavzin, M., Ritola, K. D., et al. (2016). A designer AAV variant permits efficient retrograde access to projection neurons. *Neuron* 92, 372–382. doi: 10.1016/j.neuron.2016.09.021

Tornabene, P., and Trapani, I. (2020). Can adeno-associated viral vectors deliver effectively large genes? *Hum. Gene Ther.* 31, 47–56. doi: 10.1089/hum.2019.220

Tornabene, P., Trapani, I., Minopoli, R., Centrulo, M., Lupo, M., de Simone, S., et al. (2019). Intein-mediated protein trans-splicing expands adeno-associated virus transfer capacity in the retina. *Sci. Transl. Med.* 11:eaav4523. doi: 10.1126/scitranslmed.aav4523

Trigueros, S., Domènech, E. B., Toulis, V., and Marfany, G. (2019). *in vitro* gene delivery in retinal pigment epithelium cells by plasmid DNA-wrapped gold nanoparticles. *Genes* 10:289. doi: 10.3390/genes10040289

Tse, L. V., Moller-Tank, S., and Asokan, A. (2015). Strategies to circumvent humoral immunity to adeno-associated viral vectors. *Expert Opin. Biol. Ther.* 15, 845–855. doi: 10.1517/14712598.2015.1035645

Walker, M. C., and Kullmann, D. M. (2020). Optogenetic and chemogenetic therapies for epilepsy. *Neuropharmacology* 168:107751. doi: 10.1016/j.neuropharm.2019.107751

Wang, Y., Barker, K., Shi, S., Diaz, M., Mo, B., and Gutstein, H. B. (2012). Blockade of PDGFR-β activation eliminates morphine analgesic tolerance. *Nat. Med.* 18, 385–387. doi: 10.1038/nm.2633

Wang, F., Bélanger, E., Paquet, M.-E., Côté, D. C., and De Koninck, Y. (2016). Probing pain pathways with light. *Neuroscience* 338, 248–271. doi: 10.1016/j.neuroscience.2016.09.035

Wang, L., Jacques, S., and Zheng, L. (1995). MCML - Monte Carlo modeling of light transport in multilayered tissue. *Comput. Methods Programs Biomed.* 47, 131–146. doi: 10.1016/0169-2607(95)01640-f

White, B. R., Snyder, A. Z., Cohen, A. L., Petersen, S. E., Raichle, M. E., Schlaggar, B. L., et al. (2009). Resting-state functional connectivity in the human brain revealed with diffuse optical tomography. *NeuroImage* 47, 148–156. doi: 10.1016/j.neuroimage.2009.03.058

Wietek, J., Beltramo, R., Scanziani, M., Hegemann, P., Oertner, T. G., and Wiegert, J. S. (2015). An improved chloride-conducting channelrhodopsin for light-induced inhibition of neuronal activity *in vivo*. *Sci. Rep.* 5:14807. doi: 10.1038/srep14807

Williams, J. J., Watson, A. M., Vazquez, A. L., and Schwartz, A. B. (2019). Viral-mediated optogenetic stimulation of peripheral motor nerves in non-human primates. *Front. Neurosci.* 13:759. doi: 10.3389/fnins.2019.00759

Yao, T., Zhou, X., Zhang, C., Yu, X., Tian, Z., Zhang, L., et al. (2017). Site-specific PEGylated adeno-associated viruses with increased serum stability and reduced immunogenicity. *Molecules* 22:1155. doi: 10.3390/molecules22071155

Yizhar, O., Fenno, L. E., Prigge, M., Schneider, F., Davidson, T. J., O'Shea, D. J., et al. (2011). Neocortical excitation/inhibition balance in information processing and social dysfunction. *Nature* 477, 171–178. doi: 10.1038/nature10360

Zhang, F., Prigge, M., Beyrière, F., Tsunoda, S. P., Mattis, J., Yizhar, O., et al. (2008). Red-shifted optogenetic excitation: a tool for fast neural control derived from Volvox carteri. *Nat. Neurosci.* 11, 631–633. doi: 10.1038/nn.2120

Zhang, F., Wang, L.-P. P., Boyden, E. S., and Deisseroth, K. (2006). Channelrhodopsin-2 and optical control of excitable cells. *Nat. Methods* 3, 785–792. doi: 10.1038/nmeth936

Zhang, W., Lohman, A. W., Zhuravlova, Y., Lu, X., Wiens, M. D., Hoi, H., et al. (2017). Optogenetic control with a photocleavable protein, PhoCl. *Nat. Methods* 14, 391–394. doi: 10.1038/nmeth.4222

Zhong, G., Wang, H., He, W., Li, Y., Mou, H., Tickner, Z. J., et al. (2020). A reversible RNA on-switch that controls gene expression of AAV-delivered therapeutics *in vivo*. *Nat. Biotechnol.* 38, 169–175. doi: 10.1038/s41587-019-0357-y

Zhou, J., Deng, W., Wang, Y., Cao, X., Chen, J., Wang, Q., et al. (2016). Cationic carbon quantum dots derived from alginate for gene delivery: one-step synthesis and cellular uptake. *Acta Biomater.* 42, 209–219. doi: 10.1016/j.actbio.2016.06.021

Zingg, B., Chou, X.-L., Zhang, Z.-G., Mesik, L., Liang, F., Tao, H. W., et al. (2017). AAV-mediated anterograde transsynaptic tagging: mapping corticocollicular input-defined neural pathways for defense behaviors. *Neuron* 93, 33–47. doi: 10.1016/j.neuron.2016.11.045

Conflict of Interest: The authors declare that the research was conducted in the absence of any commercial or financial relationships that could be construed as a potential conflict of interest.

frontiers in Neural Circuits

ORIGINAL RESEARCH
published: 28 July 2020
doi: 10.3389/fncir.2020.00047

A Simple and Efficient Method for Visualizing Individual Cells *in vivo* by Cre-Mediated Single-Cell Labeling by Electroporation (CREMSCLE)

*Anne Schohl, Zahraa Chorghay and Edward S. Ruthazer**

Department of Neurology and Neurosurgery, Montreal Neurological Institute-Hospital, McGill University, Montreal, QC, Canada

Efficient methods for visualizing cell morphology in the intact animal are of great benefit to the study of structural development in the nervous system. Quantitative analysis of the complex arborization patterns of brain cells informs cell-type classification, dissection of neuronal circuit wiring, and the elucidation of growth and plasticity mechanisms. Time-lapse single-cell morphological analysis requires labeling and imaging of single cells *in situ* without contamination from the ramified processes of other nearby cells. Here, using the *Xenopus laevis* optic tectum as a model system, we describe CRE-Mediated Single-Cell Labeling by Electroporation (CREMSCLE), a technique we developed based on bulk co-electroporation of Cre-dependent inducible expression vectors, together with very low concentrations of plasmid encoding Cre recombinase. This method offers efficient, sparse labeling in any brain area where bulk electroporation is possible. Unlike juxtacellular single-cell electroporation methods, CREMSCLE relies exclusively on the bulk electroporation technique, circumventing the need to precisely position a micropipette next to the target cell. Compared with viral transduction methods, it is fast and safe, generating high levels of expression within 24 h of introducing non-infectious plasmid DNA. In addition to increased efficiency of single-cell labeling, we confirm that CREMSCLE also allows for efficient co-expression of multiple gene products in the same cell. Furthermore, we demonstrate that this method is particularly well-suited for labeling immature neurons to follow their maturation over time. This approach therefore lends itself well to time-lapse morphological studies, particularly in the context of early neuronal development and under conditions that prevent more difficult visualized juxtacellular electroporation.

Keywords: transfection, morphology, neuron, multiphoton, loxP, *Xenopus laevis*, optic tectum

OPEN ACCESS

Edited by:
Graziella DiCristo,
Université de Montréal, Canada

Reviewed by:
Simon Chen,
University of Ottawa, Canada
Anthony Holtmaat,
Université de Genève, Switzerland

***Correspondence:**
Edward S. Ruthazer
edward.ruthazer@mcgill.ca

Received: *16 May 2020*
Accepted: *08 July 2020*
Published: *28 July 2020*

Citation:
Schohl A, Chorghay Z and Ruthazer ES (2020) A Simple and Efficient Method for Visualizing Individual Cells in vivo by Cre-Mediated Single-Cell Labeling by Electroporation (CREMSCLE). Front. Neural Circuits 14:47. doi: 10.3389/fncir.2020.00047

"Against a clear background stood black threadlets, some slender and smooth, some thick and thorny in a pattern punctuated by small dense spots. All was sharp as a sketch with Chinese ink on transparent Japanese paper. And to think that this was the same tissue which, when stained with carmine or logwood left the eye in a tangled thicket where sight may stare and grope ever fruitlessly, baffled in its efforts to unravel confusion, and lost forever in twilit doubt. Here, on the contrary, all was clear and plain as a diagram. A look was enough. Dumbfounded, I could not take my eyes from the microscope."

Translation based on Santiago Ramon y Cajal's "Histologia del Sistema Nervioso", recounting his first encounter with Golgi-stained brain tissue (Glickstein, 2006).

INTRODUCTION

The nature of the chaotic complexity of intermingled fibers and cellular structures in the nervous system constituted one of the great mysteries of anatomy, until Camillo Golgi's serendipitous discovery of his "black reaction" in 1873 (Golgi, 1873). Golgi's stain, which miraculously produced sparse, but highly contrasted labeling of cells in nervous tissue, prompted the brilliant Spanish neuroanatomist Santiago Ramon y Cajal to embrace the "neuron doctrine," which states that individual brain cells, or neurons, are the fundamental units from which nervous tissue is formed (Jones, 2010).

Modern neuroanatomists have a far more diverse and powerful armamentarium at their disposal than Cajal might ever have imagined, including the use of genetically encoded labels like enhanced green fluorescent protein (EGFP) to visualize brain cells in the living organism. However, our efforts to dissect and decipher the nervous system continue to rely heavily on techniques that permit the labeling, observation and quantitative analysis of single cells within the richly complex network of brain cells and their elaborate processes from which neural circuits are constructed.

Single-cell electroporation (SCE) is a juxtacellular labeling technique that has been used successfully to transfect and visualize individual cells with Golgi-like contrast in intact brain tissue and in organotypic slice cultures (Haas et al., 2001; Uesaka et al., 2005). SCE is achieved by carefully positioning the fine (∼1 μm diameter) tip of a glass micropipette in close proximity to the cell of interest and then applying current pulses through the pipette tip. By locally disrupting the plasma membrane of the cell while iontophoretically expelling the charged contents of the micropipette, the contents of the pipette are efficiently delivered into the cell, which promptly reseals its plasma membrane and traps the material within.

Electroporation has numerous advantages compared to other transfection methods such as viral transduction. There is no strict size limitation for DNA constructs transferred by electroporation. The same cells can be electroporated repeatedly and a large number of different constructs can be electroporated into a cell at the same time, including the co-electroporation of fluorescent dye, mRNA, protein, or antisense oligonucleotides, together with plasmid DNA to permit immediate live cell imaging and manipulation. Moreover, most likely because of the high copy number of plasmids delivered, electroporation can drive high levels of expression of proteins such as EGFP within just a few hours of treatment, in many cases reaching peak levels within 1 day post-electroporation.

The main shortcoming of SCE is that successful labeling depends on the micropipette tip being positioned very precisely next to the targeted cell. If the tip is too far away it may transfect multiple nearby cells or fail to transfect any cells at all. Naturally, this is impractical in the majority of *in vivo* situations where the targeted cells are difficult to visualize under a microscope or so sparsely distributed that blind electroporation attempts are unlikely to succeed. In addition, the success rate of SCE is heavily dependent on micropipette tip shape. Optimization of tip shape requires a process of trial-and-error, which for DNA plasmid delivery cannot provide immediate reliable feedback until the next day when protein expression is (or is not) evident.

An alternative to SCE is bulk electroporation, which takes advantage of the same principles as SCE for delivery of genetic material into cells, but instead of delivering plasmid and current through the same pipette, it utilizes large plate electrodes that are positioned on opposite sides of the structure targeted for transfection and simple pressure injection to deliver plasmid into the extracellular space between the electrodes (Muramatsu et al., 1998; Falk et al., 2007). This method permits the efficient transfection of multiple plasmids or other charged materials just like SCE, but instead of targeting only one cell it is used to target many cells within larger tissue volumes. One common example of this technique is *in utero* electroporation, in which plasmid is injected into the brain ventricles of embryonic animals and electroporation pulses are delivered through forceps-like paddle electrodes that bracket the uterus to generate an electric field within the brain of the embryo (Tabata and Nakajima, 2001; Shimogori and Ogawa, 2008). The obvious advantage of this approach is that it does not require clear visualization or precise positioning of the electrode and is therefore applicable in nearly any tissue.

In the current paper, we describe CRE-Mediated Single-Cell Labeling by Electroporation (CREMSCLE), an innovative method that utilizes bulk electroporation to achieve the benefits of single-cell labeling for *in vivo* time-lapse imaging. CREMSCLE involves a binary co-expression approach that takes advantage of the ability of extremely low levels of Cre recombinase protein to edit many copies of a plasmid containing a neomycin "stop cassette" flanked by loxP sites that has been inserted into the 5′ end of the open reading frame of a gene of interest. This cre-mediated editing event effectively releases translation suppression of the downstream gene of interest. Using this binary approach, we show that co-electroporation of high concentrations of plasmid containing a gene of interest preceded by the stop cassette, together with extremely low amounts of plasmid encoding Cre recombinase, results in high levels of gene expression in very sparsely distributed individual cells, which constitutes ideal cell labeling conditions for live imaging. We previously published an application of this method to express EGFP in individual retinal ganglion cells in neonatal mouse eyes (Dhande et al., 2011). Here, using the *Xenopus* tadpole, which permits easy access for electroporation and *in vivo* visualization of fluorescent protein expression, we compare and contrast CREMSCLE with SCE and demonstrate its effectiveness for sparse co-expression of multiple gene products in the same cells.

MATERIALS AND METHODS

Animal Breeding and Husbandry

All animal experiments were approved by the Montreal Neurological Institute (MNI) Animal Care Committee in accordance with the guidelines of the Canadian Council on Animal Care. Tadpoles were bred by HCG-induced mating of albino *Xenopus laevis* frogs (NASCO) in the MNI Animal Care Facility. Embryos were then reared with regular solution

changes in bowls containing Modified Barth Solution with HEPES (MBS-H) buffer.

Constructs

pCAG-Cre, pCALNL-EGFP, pCALNL-DsRed are a generous gift from T. Matsuda & C. L. Cepko and are currently available through Addgene (plasmids 13775, 13770, 13769). pEGFP-N1 was from Clontech. mCherry was a generous gift from Dr. Roger Tsien. All plasmids were grown in DH5a competent cells (Life Technologies) and purified using endotoxin-free maxiprep kits (Qiagen).

Bulk Electroporation

Albino tadpoles at stage 44–46 according to the criteria of Nieuwkoop and Faber (1956) were used for electroporation. Animals were anesthetized by immersion in MS222 (0.02% in 0.1 × MBS-H). DNA solution containing various concentrations of either pEGFP-N1 or a mixture of pCAG-Cre with 1 μg/μL pCALNL-GFP and/or pCALNL-DsRed suspended in distilled water with a small amount of fast green dye for visualization was pressure injected in the brain ventricle with a glass micropipette (Borosilicate glass with filament, 1 mm OD, 0.78 mm ID, Sutter) pulled using a Sutter P-97 puller. Care was taken to load the ventricle without visibly distending it. Two custom-built platinum plate electrodes (cut to approximately 1 mm width strips from Sutter FB-330B platinum filaments) were placed on each side of the tectal lobe and current was applied using an electrical stimulator (SD 9, Grass Instruments), with a 3 μF capacitor connected in parallel. Two pulses of 37 V, 1.6 ms duration were applied in both directions. The animals were then placed in fresh rearing solution (MBS-H) and kept in bowls for at least 24 h before screening for EGFP expression under an epifluorescence microscope.

Single-Cell Electroporation

Tadpoles at stage 42–44 were anesthetized in MS222 (0.02% in 0.1x MBS-H) and placed on a Kimwipe under a fluorescent microscope. A micropipette filled with pEGFP-N1 plasmid (1 μg/μL) was positioned within the cell body layer of the optic tectum to perform single cell electroporation of tectal cells (Haas et al., 2001; Bestman et al., 2006; Liu and Haas, 2011). A 1 s train of 1 ms pulses at 200 Hz was passed through the micropipette with an electrical stimulator (SD 9, Grass Instruments) and monitored by an oscilloscope (Tektronix). Pulse trains were repeated twice and each hemisphere of the tadpole optic tectum was electroporated at two sites to increase yield.

Live Imaging

Animals were screened for *in vivo* imaging at 48 h after electroporation. Screened animals were anesthetized in MS222 (0.02% in 0.1x MBS-H), placed in a custom-made Sylgard chamber that fit the tadpole's body and sealed under a cover glass. A custom built two-photon microscope was used for all live imaging experiments. The microscope consisted of a converted Fluoview FV300 confocal microscope mounted on a BX61WI base (Olympus, Japan) with external R3896 multialkali PMTs (Hamamatsu, Japan) for detection of emission signal. Red and green emission light was simultaneously collected after passing through a 565DCLPXR beam splitter with HQ525/50 and HQ607/45 filters specially blocked for two-photon excitation (Chroma Technology, Brattleboro, VT, United States). Excitation was provided either by a Maitai-BB or InSight X3 Ti:Sapphire femtosecond pulsed IR laser at 910 nm or 990 nm (Spectra Physics, Mountain View, CA, United States). Optical z-series were collected at 1 μm intervals using either a 60x 1.1 NA LUMFL or 60x 1.0 NA LUM Plan FL N water immersion objective (Olympus), or for larger field imaging at 3 μm intervals using a 20x 0.5NA U Plan FL N air objective. After imaging, the animals were placed in an isolated well that contained 0.1x MBS-H, and imaged every 24 h up to 5 days post-electroporation.

Analysis

Two-photon image stacks of dendritic arbors were denoised using CANDLE non-local means denoising software implemented in MATLAB (Coupé et al., 2012). For daily imaging data, cells were reconstructed in 3D from z-series two-photon stacks using the autodepth feature of Imaris 6.0 (Bitplane). All data are expressed as mean ± SEM, and *n* values refer to the number of cells for the morphology experiments. Arbor size and branch tip number were analyzed by repeated-measures two-way ANOVA using Prism 7.0 software (Graphpad).

RESULTS

Bulk electroporation of the optic tectum of *Xenopus* tadpoles can be performed by injecting a plasmid solution into the brain ventricle, and briefly passing current across a pair of platinum plate electrodes positioned on opposite sides of the brain (**Figure 1A**). Alternatively, the electrodes can be positioned over just one hemisphere. Since DNA is negatively charged, it will preferentially transfect the brain hemisphere closest to the positive electrode (**Figure 1B**). This method typically results in a large number of brain cells that express high levels of the gene product encoded by the electroporated plasmids (**Figure 1C**). In the case of EGFP plasmid electroporation, bright green cells are typically apparent within 24 h. The number of positive cells and apparent expression levels increase only incrementally over subsequent days.

In an effort to determine whether it would be possible to attain sparse EGFP expression, suitable for single-cell morphometric reconstruction, by simply reducing the concentration of plasmid injected, we compared tadpoles injected with a range of plasmid concentrations from 2 μg/μL to 0.1 μg/μL (**Figure 1B**). Although there was an apparent decrease in the number of transfected neurons expressing EGFP, the most obvious consequence of reducing plasmid concentration was that cells expressed lower levels of EGFP, making it difficult to visualize their full morphologies (**Figures 1D,E**). The cytomegalovirus immediate early (CMV) promoter used to drive EGFP expression on this plasmid is one of the strongest promoters available, suggesting that a strategy of simply trying

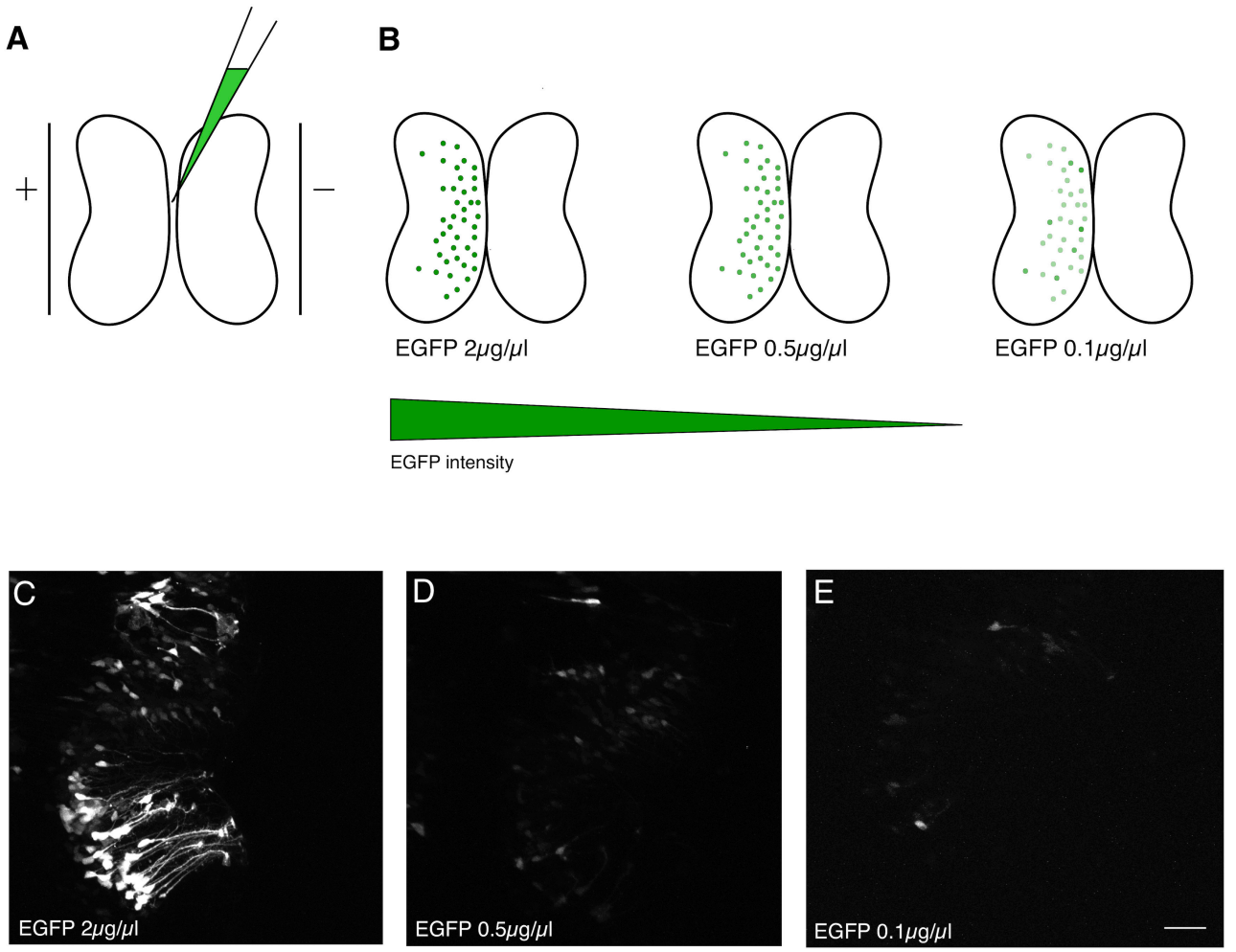

FIGURE 1 | Dilution of electroporated plasmid reduces expression level. **(A)** Bulk electroporation of the Xenopus optic tectum involves the injection of a plasmid solution into the tectal ventricle followed by passing current pulses across plate electrodes that span the targeted brain region. Transduction occurs on the side toward the positive electrode due to the negative charge of plasmid DNA. **(B–E)** Reducing the concentration of EGFP plasmid mainly lowers the levels of expression per cell. **(C–E)** Two-photon z-series projections through the optic tectum of an intact Xenopus tadpole collected using the same laser excitation intensity. **(C)** At 2 μg/μL a large number of bright cells, especially radial glial progenitors, are labeled. **(D)** 0.5 μg/μL or **(E)** 0.1 μg/μL labels fewer cells, which are also much fainter. Scale bar, 50 μm.

different promoters would be unlikely to lead to enhanced brightness of EGFP fluorescence.

This relationship of plasmid concentration to EGFP expression level suggests that the brightly expressing cells are likely to be those that received a high number of copies of the plasmid. Therefore, we reasoned that high plasmid copy number contributed to bright EGFP expression. In order to express high amounts of EGFP in a very small number of cells, we devised a binary strategy in which the EGFP expression vector contained an upstream stop cassette, in this case part of a neomycin selectable marker, flanked by loxP sites and driven by the strong synthetic CAG promoter (pCALNL-EGFP). EGFP translation is thus prevented in all cells except those expressing both pCALNL-EGFP and a Cre recombinase vector (pCAG-Cre) (**Figure 2A**). Even very small amounts of Cre recombinase are able to effectively remove loxP-flanked sequences from a large number of plasmids, so the co-expression of very low concentrations of a plasmid expressing Cre recombinase together with high concentrations of LNL-EGFP plasmid ought to induce sparse but bright EGFP expression in the electroporated tissue (**Figure 2B**).

We used this co-electroporation strategy to label cells in tadpoles at developmental stage 44–46 with pCALNL-GFP at a concentration of 1 μg/μL, together with varying concentrations of pCAG-Cre (100, 10, 1, 0.2, and 0.1 ng/μL). At the highest concentrations of pCAG-Cre, a large number of cells with relatively simple but overlapping processes expressed EGFP in the optic tectum at 2 days post-electroporation (**Figures 3A–C**), including many radial glial cells (**Figure 3C**). Electroporations of lower concentrations of Cre recombinase plasmid, less than 1 ng/μL, clearly labeled individual cells with more easily discriminable processes (**Figures 3D,E**). Over subsequent days,

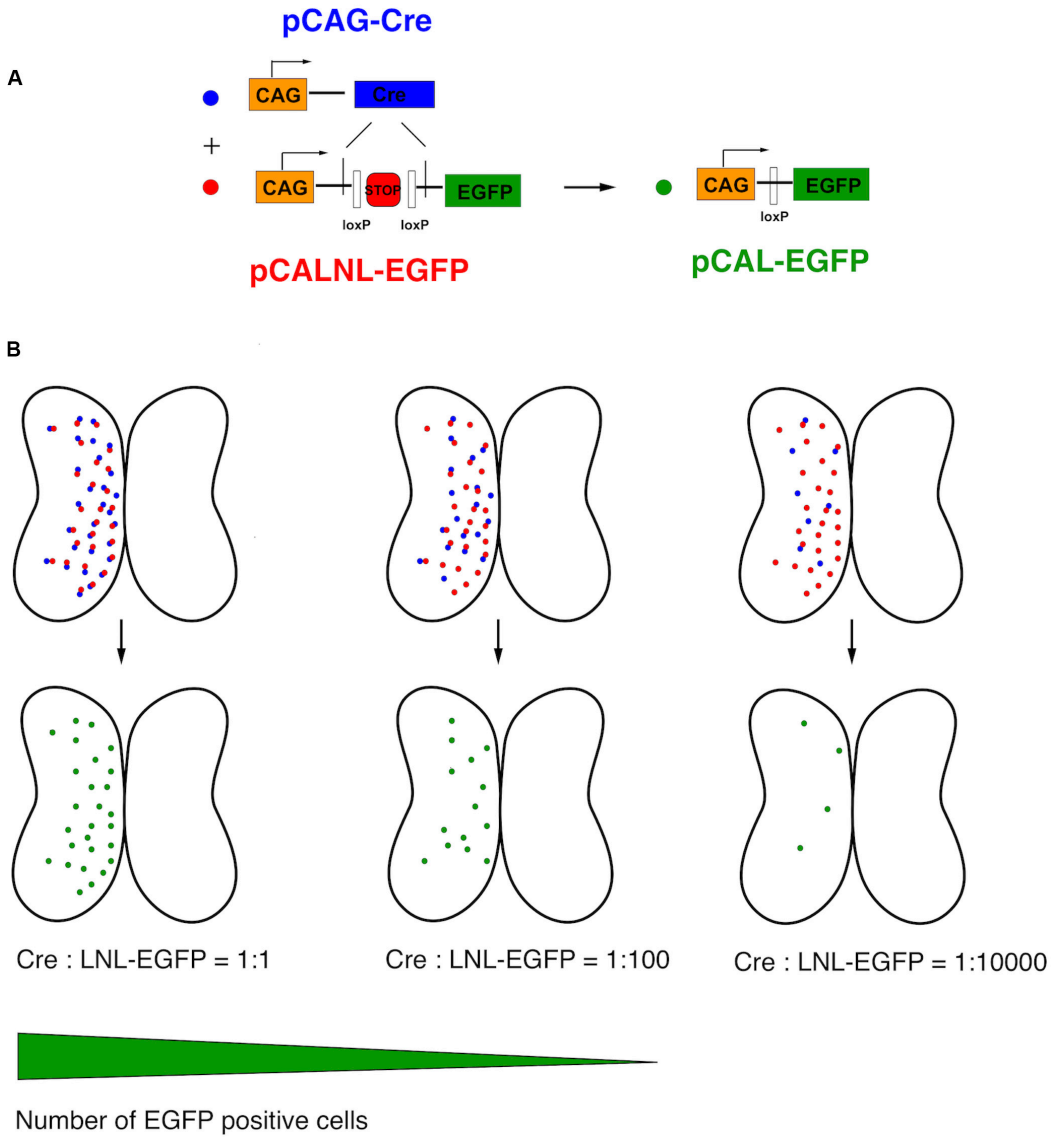

FIGURE 2 | Schematic of CREMSCLE method. **(A)** Electroporation of large amounts of pCALNL-EGFP containing a floxed neogenin "stop cassette" does not lead to EGFP expression unless pCAG-Cre plasmid is co-expressed. The Cre recombinase removes the stop cassette flanked by loxP sites to allow the translation of EGFP. **(B)** When pCAG-Cre and pCALNL-EGFP are coexpressed in roughly equimolar ratios most cells will express EGFP. As the concentration of pCAG-Cre plasmid is reduced, keeping pCALNL-EGFP levels constant, only the very few cells that express Cre recombinase will activate pCALNL-EGFP to allow high levels of EGFP expression.

expression levels increased, resulting in brighter labeling, but also a larger number of cells visibly expressing EGFP. By 5 days post-electroporation, dendritic processes had elaborated considerably in all cases (**Figures 3A′–E′**), but in the animals electroporated with less than 1 ng/μL of Cre plasmid, the low density of cells permitted clear visualization of the full morphologies of the labeled neurons and their dendrites at higher magnification (**Figures 3F,G**). In the example electroporated with the lowest concentration of Cre plasmid, 10,000 times more dilute than the pCALNL-EGFP, single cells were sparse enough to permit complete morphological segmentation without any overlap with another labeled cell (**Figure 3G**).

To assess optimal concentrations of pCAG-Cre to co-electroporate with pCALNL-EGFP to label cells efficiently and at low enough densities for morphological characterization of individual cells, we performed bilateral electroporations in 60 animals divided evenly into three groups of 20 animals, each with 1 μg/μL pCALNL-EGFP plus a different concentration of Cre plasmid: 1, 0.2, and 0.1 ng/μL. All but one out of the 60 animals survived the electroporation procedure and recovered fully from anesthesia within a few minutes following the procedure. The number of EGFP-expressing cells per animal was quantified to assess density of labeling over 3 days of daily time-lapse imaging starting at 2 days post-electroporation (**Figure 4A**). The ideal

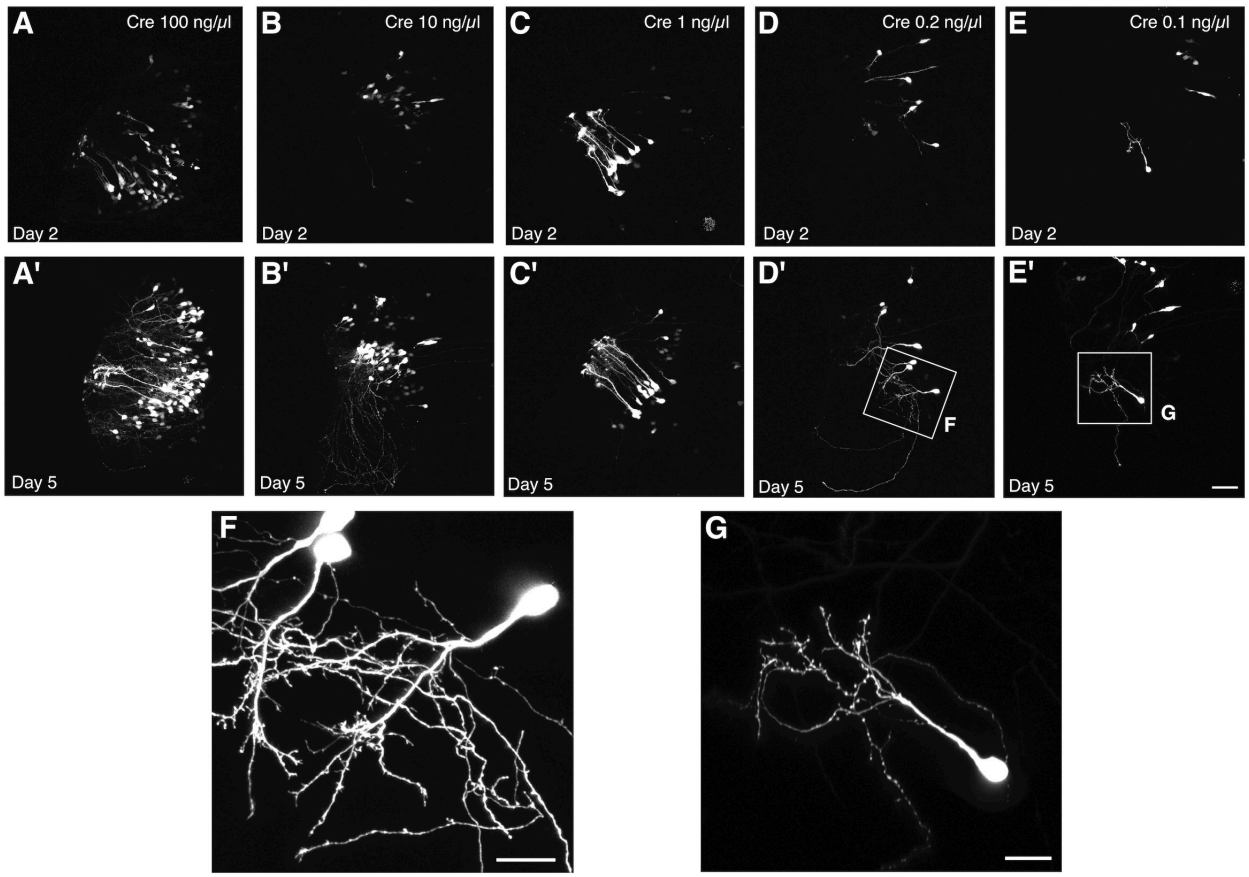

FIGURE 3 | Titration of Cre permits single cell labeling without decreasing signal intensity. Two-photon z-projections of the transfected lobe of the tadpole optic tectum demonstrate that electroporation of 1 μg/μL pCALNL-EGFP plasmid together with increasingly dilute concentrations of pCAG-Cre plasmid results in a decreasing number of labeled tectal cells with little apparent decrease in the brightness of EGFP expression. Animals were imaged **(A–E)** 2 and **(A′–E′)** 5 days after electroporation with 1 μg/μL pCALNL-EGFP plus pCAG-Cre concentrations of **(A,A′)** 100 ng/μL, **(B,B′)** 10 ng/μL, **(C,C′)** 1 ng/μL, **(D,D′)** 0.2 ng/μL, or **(E,E′)** 0.1 ng/μL. **(F,G)** Cells continue to mature and develop complex dendritic arbors over this time as can be seen in higher magnification z-series projections. Only the lowest dilution of Cre plasmid produced cells with completely non-overlapping dendritic arbors by day 5, which would be suitable for single-cell reconstruction. Scale bar, **(A–E)** 50 μm, **(F,G)** 20 μm.

case for morphometric analysis would be a single EGFP-labeled neuron per hemisphere (2 per animal). On average, 1 ng/μL of Cre plasmid resulted in well over 20 labeled cells per animal, which we found to be too high to reliably perform unambiguous single-cell morphological analysis. On the other hand, 0.2 ng/μL gave a much lower labeled cell density per animal, reaching 1.5 (range: 0–6) by 4 days post-electroporation, corresponding nearly to the ideal yield of one labeled cell per hemisphere on average. In these animals the cells started out relatively immature, with only 5.0 ± 5.0% of labeled cells per animal having a distinct neuronal morphology on day 2 after electroporation. But by day 3 and day 4, respectively, 41.1 ± 13.6% and 45.5 ± 13.9% of labeled cells had started to exhibit typical neuronal morphologies, with the remaining cells likely being radial glia and ependymocytes. The labeled cell density per animal dropped to 0.2 (range: 0–2) when the Cre plasmid concentration was halved to 0.1 ng/μL, reflecting a much lower probability that the animal had been successfully transfected to express EGFP. These findings demonstrate that with the appropriate ratio of Cre and reporter plasmid transfection, CREMSCLE has the potential to be a practical and highly efficient method for sparse labeling of cells.

We further quantified the proportion of animals under each of these conditions in which at least one isolated EGFP-expressing cell body, potentially suitable for subsequent reconstruction and quantitative analysis was present (**Figure 4B**). The efficiency of single-cell labeling was fairly low (15–20% of animals) when 0.1 ng/μL Cre plasmid was co-electroporated with LNL-EGFP. However, in the higher concentration cases, about half of the animals had at least one isolated, single cell present on day 4 (0.2 ng/μL:50%; 1 ng/μL:63% of animals). In this particular experiment, using a mix of 0.2 ng/μL pCAG-Cre with 1 μg/μL pCALNL-EGFP we were able to achieve both high numbers of labeled animals and sparse overall cell densities within each animal, which together are close to ideal for studying morphometry. This is imperative because even a well-isolated neuron can, over time, extend its dendritic processes into fields of labeled dendrites from other nearby cells, limiting

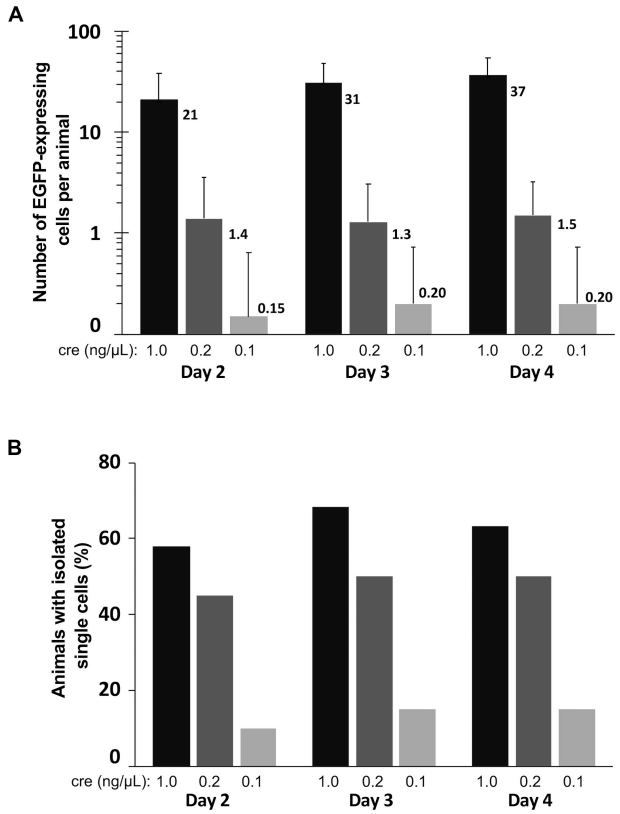

FIGURE 4 | Quantification of labeled cells imaged over three consecutive days. Tadpoles were bilaterally electroporated with 1 μg/μL pCALNL-EGFP mixed with 1.0, 0.2, and 0.1 ng/μL pCAG-Cre plasmid (n = 19, 20, 20) and subsequently screened daily for EGFP-expressing cells from 2 to 4 days post-electroporation. **(A)** The number of EGFP-positive cells per animal was substantially lower with decreased levels of Cre plasmid. **(B)** A single isolated cell could be found in nearly half of the animals from the 1.0 and 0.2 ng/μL groups on all days of imaging, but much less frequently in the 0.1 ng/μL group. In this case the 0.2 ng/μL group had the most useful optimization, with sparse expression in a large proportion of animals (high-efficiency of single cell labeling).

its usefulness for quantitative reconstruction. Achieving this goal requires careful titration of the mix of Cre and LNL-EGFP expressing plasmid, depending upon the developmental stage of the animal and the efficiency of the specific set of electrodes used for electroporation, as small differences in the plate electrode shapes and the distance between electrode poles can alter transfection efficiency.

It can be advantageous in certain studies, to be able to image very immature, recently differentiated neurons, and although this has been carried out with great skill using SCE (Hossain et al., 2012), it is straightforward with CREMSCLE. During electroporation of plasmids injected into the ventricular space, radial glia progenitors are more susceptible than postmitotic neurons to incorporating the plasmid, since they have their cell somata in the subependymal layer of the optic tectum in close proximity to the ventricle (Sharma and Cline, 2010). Differentiated neurons migrate away from the ventricular zone after they are born (Bestman et al., 2012). Consequently, bulk electroporation is more likely to target glia and immature newborn neurons than is SCE through a micropipette positioned in the cell body layer of the tectum. CREMSCLE is therefore a particularly useful method for following the life cycle of individual neurons from birth to full integration into the neuronal circuit. To ascertain whether more immature neurons are labeled using CREMSCLE than by SCE, we labeled single cells using both methods and performed daily two-photon imaging of their dendritic arbors over a 4 days period, starting from 2 days after electroporation (**Figure 5A**). Based on the empirically determined transfection efficiency with this set of electrodes, we decided to use pCAG-Cre at 0.25 ng/μL for this experiment. Two-photon z-series stacks of tectal neurons were used to manually reconstruct dendritic arbors in 3-dimensions for morphometric analysis. The dendritic arbor lengths of neurons labeled by CREMSCLE were significantly smaller than those labeled by SCE ($p < 0.0001$ repeated-measures ANOVA main effect, $n = 7$ cells per group), consistent with their being more immature (**Figure 5B**). Indeed, day 2 SCE-labeled cells appeared to be closest in size to day 5 CREMSCLE cells. Similarly, dendritic branch tip number also appeared to be slightly, but non-significantly, lower in the CREMSCLE neurons (**Figure 5C**). Robust EGFP expression in cells imaged a week or more after electroporation, suggests that the earlier developmental onset of expression did not limit subsequent imaging as the cells matured. These results indicate that CREMSCLE is suitable for labeling recently born immature neurons and following their development over time as they integrate into the circuit.

One of the strengths of SCE, for example over viral transduction, is the ability to co-transfect multiple plasmids into the same cell and achieve high probability of co-expression (Haas et al., 2001). We tested the CREMSCLE method to confirm that high rates of co-expression are also possible. It can be achieved either by simple bulk co-electroporation of a second expression vector (**Figure 6A**) or by placing the second gene of interest downstream of its own LNL stop cassette (**Figure 6B**). The first configuration is useful when it is desirable to densely express one of the two constructs in a large number of cells, for example to study the effects of intercellular signaling or competition for a secreted factor on single cell morphogenesis. In the second configuration, low-concentration Cre plasmid can activate both plasmids, resulting in a sparse distribution of predominantly double-labeled cells. To assess the efficiency of co-expression in sparsely labeled cells, we electroporated a mixture of 0.1 ng/μL pCAG-Cre with 1 μg/μL pLNL-EGFP and 3 μg/μL pLNL-dsRed, choosing a ratio of 1:3 in an effort to ensure that each EGFP-positive cell also expresses dsRed. On the first day following electroporation, each tadpole had an average of 3.0 ± 0.8 labeled cells, the majority (74%) of which appeared to exclusively have green fluorescence at this time point (**Figure 6C**). However, by the next day the number of labeled cells had increased to 4.0 ± 1.1 per animal, and 98% of the cells were now expressing both EGFP and dsRed. The perceived increase in double-labeling is likely due to the slower maturation rate of dsRed protein compared to EGFP (Baird et al., 2000). By day 3, a small number of cells appeared to

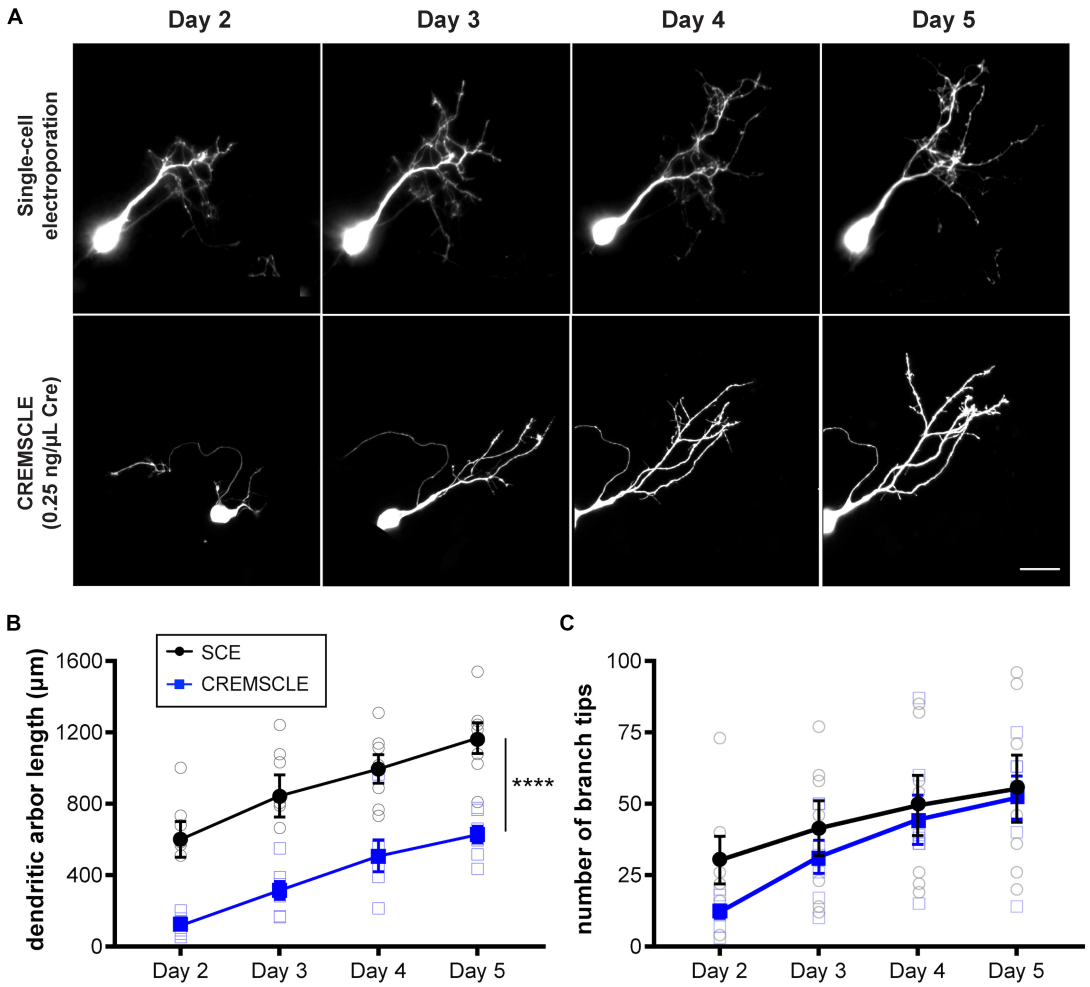

FIGURE 5 | CREMSCLE tends to label more immature tectal neurons than SCE. Tadpoles were electroporated by SCE with pEGFP-N1 (1 μg/μL) or by CREMSCLE with pCAG-Cre (0.25 ng/μl) and pCALNL-EGFP (1 μg/μL), and subsequently imaged daily for EGFP-expressing cells from 2 to 5 days post-electroporation. **(A)** Two-photon z-projections of single cells following labeling by SCE or CREMSCLE. **(B,C)** Quantification of total dendritic arbor length **(B)** and number of dendritic branch tips **(C)** over 4 days of consecutive 2-photon imaging. Scale bar, 20 μm. ****$p < 0.0001$ for main effect, RM ANOVA, $n = 7$ cells per group.

exhibit exclusively green (2%) or red (4%) fluorescence emission though a majority of cells (94%) continued to clearly express both fluorophores. These results show a very high rate of double-labeling for the vast majority of cells, and many of these cells were well-isolated and bright enough to fully visualize dendritic morphology (**Figure 6B**).

DISCUSSION

We have presented a quantitative characterization of the CREMSCLE technique for sparse but bright labeling of single cells through the co-electroporation of extremely low concentrations of plasmid encoding Cre recombinase together with an EGFP or other expression vector into which a stop cassette has been inserted upstream of the open reading frame to inhibit protein translation in cells lacking Cre expression. This method, which benefits from the versatility and ease of bulk electroporation, provides bright labeling of sparsely distributed cells, which is an ideal condition for *in vivo* imaging of cellular morphology and time lapse imaging of axonal and dendritic branch remodeling. We first introduced this technique in a 2011 paper that examined the morphologies of individual retinal ganglion cell axon arbors in the thalamus and superior colliculus of the neonatal mouse (Dhande et al., 2011). The current study expands on that initial report with valuable technical details to help investigators select the right ratios of Cre to expression plasmid for efficient single cell imaging. Sparse labeling is particularly important to allow unambiguous discrimination of single neurons and their fine processes from the complex mesh of neuropil into which they are embedded. Furthermore, it facilitates time-lapse imaging over many days, during which time cell morphologies can change significantly, normally making it extremely difficult to find the same cell in a densely labeled field. We also demonstrate that CREMSCLE is particularly advantageous for visualizing stem cells, neuroblasts,

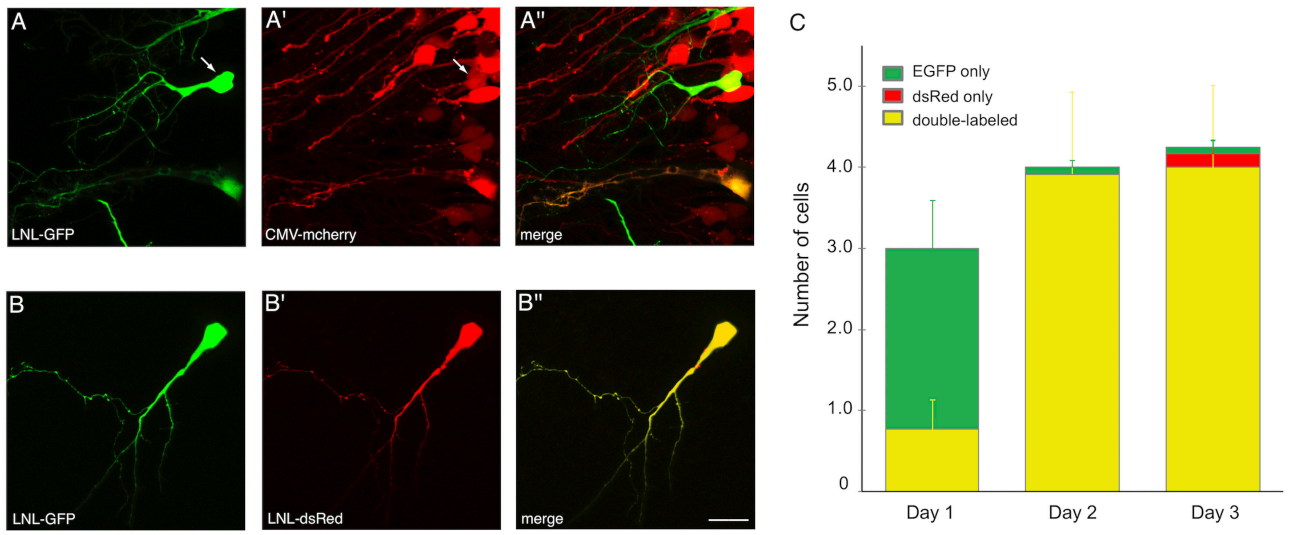

FIGURE 6 | CREMSCLE can be used for co-expression of two proteins. **(A,B)** Two-photon z-projections of double labeled cells at 3 days post-electroporation. **(A)** pCAG-Cre (0.5 ng/μL) co-electroporated with pLNL-EGFP (1 μg/μL) and **(A′)** pCMV-mCherry (3 μg/μL) leads to **(A′′)** double labeling of sparse EGFP-expressing cells within a field of mCherry-labeled cells. Most cells labeled by EGFP are also positive for mCherry. **(B)** Co-electroporation of pCAG-Cre (0.1 ng/μL) with pLNL-EGFP (1 μg/μL) and **(B′)** pLNL-dsRed (3 μg/μL) results in nearly all cells expressing **(B′′)** both EGFP and dsRed by 3 days post-electroporation. **(C)** Number of cells per animal that expressed EGFP fluorescence (green), dsRed fluorescence (red), or both (yellow). By 2 days post-electroporation nearly every cell was double-labeled. *n* = 12 animals. Scale bar, 20 μm.

and immature neurons in the brain. Finally, we show that double-labeling and co-expression of genes-of-interest occur with very high frequency using CREMSCLE.

CRE-mediated single-cell labeling by electroporation represents an effort to simplify and generalize the innovative methods originally developed for sparse labeling in transgenic mice, such as Mosaic Analysis with Double Markers (MADM; Zong et al., 2005) and Single-neuron Labeling with Inducible Cre-mediated Knockout (SLICK; Young et al., 2008). These powerful genetic approaches were limited by the substantial investment of time and resources needed to generate suitable transgenic animals, and the lack of availability of transgenic lines in non-model organisms. By relying entirely on electroporation for gene expression, CREMSCLE mitigates these limitations. Furthermore, because bench-ready electroporation constructs can be generated by simple subcloning of plasmids, any gene of interest can be prepared for CREMSCLE in just a matter of days, making it equally suitable for single-cell expression of fusion proteins for subcellular targeting, genetically encoded functional indicators like pHluorins, calcium- or voltage-indicators, as well as constructs for RNA interference (LoTurco et al., 2009; Sun et al., 2019).

The major advantage of CREMSCLE over juxtacellular labeling methods like SCE is the ability to get sparse gene expression in a large fraction of electroporated animals without the need to visualize the precise placement of an electroporation micropipette. Although sophisticated visualization techniques have been developed, such as "shadowpatching," in which the extracellular space is filled with a fluorescent dye to reveal negative images of somata by two-photon imaging to guide electroporation or recording pipettes (Kitamura et al., 2008), this is time consuming and requires expensive hardware compared with the CREMSCLE technique. These issues can be circumvented by using a bulk electroporation approach. The inspiration for CREMSCLE came from a technique for temporal control of expression of bulk electroporated genes developed by Matsuda and Cepko (2007), which used co-electroporation of LNL constructs together with an estrogen-receptor-tagged (ER) Cre recombinase that requires tamoxifen to induce excision of the stop cassette and drive gene expression.

Bulk electroporation has become extremely popular in recent years due to its low cost, versatility and applicability across many animal models, including tadpole, chick, rat, mouse, and ferret (Fukuchi-Shimogori and Grove, 2001; Gal et al., 2006; Shimogori and Ogawa, 2008; LoTurco et al., 2009; Kawasaki et al., 2012). In particular, transfecting and labeling cortical excitatory neurons by *in utero* electroporation offers a high success rate and lamina specificity, exploiting the staggered birthdates and inside-out migration of neurons within the cortex. A recent study applied a variant of the CREMSCLE method for imaging single neurons in the mouse visual cortex labeled by *in utero* co-electroporation of plasmids for Cre recombinase and Cre-dependent flip-excision (FLEX) expression of fluorescent protein (Sun et al., 2019). The advantage of the FLEX approach is that because the gene-of-interest is double-floxed and inverted in the original vector, there is no possible way for faint, leaky expression of the gene to occur in the absence of Cre recombinase. Another clever approach for overcoming possible faint background expression of the silenced construct is the Supernova system, which utilizes a positive feedback loop to drive expression of both the gene-of-interest along with a tetracycline transactivator (Luo et al., 2016). The transactivator acts back on the tetracycline response element

on the Cre plasmid to enhance Cre expression levels, activating further copies of the gene-of-interest.

In the current study, we used the strong CAG promoter to drive gene expression. Other studies have taken advantage of electroporation of constructs with cell-type specific promoters to target expression to different cell classes (Gal et al., 2006). In the Xenopus system we have observed that cell type specificity is often difficult to achieve by conventional bulk electroporation or SCE, most likely because the high plasmid copy number that must be delivered to achieve adequate *in vivo* visualization of cells may overwhelm endogenous promotor specificity. Although we have not systematically tested it, we predict that use of a cell-type specific promoter for the highly diluted Cre plasmid would be more likely to undergo normal promoter control and produce better cell type specificity. In addition to cell type specificity, better temporal specificity of sparse gene expression could also be achieved by using ER-Cre with tamoxifen dosing in CREMSCLE (Matsuda and Cepko, 2007; LoTurco et al., 2009).

One of the main shortcomings of the CREMSCLE method compared with SCE, concerns the co-electroporation of non-genetically encoded materials, such as antisense Morpholino oligonucleotide (MO) for knockdown of gene expression. When plasmid DNA and fluorescently tagged MO are delivered by SCE though the same micropipette, both materials are jointly targeted to a single cell with high probability, labeling the single cell that is subject to gene knockdown (Bestman et al., 2006). In contrast, bulk electroporation of MO causes knockdown in a large number of cells in the zone of electroporation, thus in combination with CREMSCLE knockdown in the labeled single cell is likely to occur, but will not be restricted to just the one cell, much like co-electroporation with an expression vector that does not contain a floxed stop cassette (**Figure 6A**). Because bulk electroporation efficiently targets stem cells in the ventricular zone, one area for future development could be the merging of CREMSCLE with genome editing approaches like Clustered Regularly Interspaced Short Palindromic Repeats (CRISPR) (Mikuni et al., 2016). This would allow for targeted gene knockout or tagging by homology-directed repair, which could potentially be achievable by including a floxed stop cassette in the co-electroporated Cas9 or single guide RNA expressing vectors.

DATA AVAILABILITY STATEMENT

The raw data supporting the conclusions of this article will be made available by the authors, without undue reservation.

ETHICS STATEMENT

The animal study was reviewed and approved by the Montreal Neurological Institute Animal Care Committee.

AUTHOR CONTRIBUTIONS

ER conceived the experiments. AS performed the experiments, except for **Figure 5**, executed by ZC. All authors contributed to writing the manuscript.

FUNDING

ER received grant FDN-143238 from the Canadian Institutes of Health Research (CIHR). ZC received a Natural Sciences and Engineering Research Council Master's Canada Graduate Scholarship and an IPN Returning Student Award.

ACKNOWLEDGMENTS

We thank Dr. Connie Cepko for providing the Cre and LNL plasmids used in this study. We are also grateful to Drs. Onkar Dhande, Michael Crair, and Marla Feller for initial collaborations applying our CREMSCLE technique in the mouse retina (Dhande et al., 2011).

REFERENCES

Baird, G. S., Zacharias, D. A., and Tsien, R. Y. (2000). Biochemistry, mutagenesis, and oligomerization of DsRed, a red fluorescent protein from coral. *Proc. Natl. Acad. Sci. U.S.A.* 97, 11984–11989. doi: 10.1073/pnas.97.22.11984

Bestman, J., Ewald, R., Chiu, S., and Cline, H. T. (2006). In vivo single-cell electroporation for transfer of DNA and macromolecules. *Nat. Protoc.* 1, 1267–1272. doi: 10.1038/nprot.2006.186

Bestman, J. E., Lee-Osbourne, J., and Cline, H. T. (2012). In vivo time-lapse imaging of cell proliferation and differentiation in the optic tectum of Xenopus laevis tadpoles. *J. Comp. Neurol.* 520, 401–433. doi: 10.1002/cne.22795

Coupé, P., Munz, M., Manjon, J. V., Ruthazer, E. S., and Collins, D. L. (2012). A CANDLE for deeper in vivo insight. *Med. Image Anal.* 16, 849–864. doi: 10.1016/j.media.2012.01.002

Dhande, O., Hua, E., Guh, E., Yeh, J., Bhatt, S., Zhang, Y., et al. (2011). Development of single retinofugal axon arbors in normal and ß2 knock-out mice. *J. Neurosci.* 31, 3384–3399. doi: 10.1523/jneurosci.4899-10.2011

Falk, J., Drinjakovic, J., Leung, K. M., Dwivedy, A., Regan, A. G., Piper, M., et al. (2007). Electroporation of cDNA/morpholinos to targeted areas of embryonic CNS in Xenopus. *BMC Dev. Biol.* 7:107. doi: 10.1186/1471-213X-7-107

Fukuchi-Shimogori, T., and Grove, E. A. (2001). Neocortex patterning by the secreted signaling molecule FGF8. *Science* 294, 1071–1074. doi: 10.1126/science.1064252

Gal, J. S., Morozov, Y. M., Ayoub, A. E., Chatterjee, M., Rakic, P., and Haydar, T. F. (2006). Molecular and morphological heterogeneity of neural precursors in the mouse neocortical proliferative zones. *J. Neurosci.* 26, 1045–1056. doi: 10.1523/jneurosci.4499-05.2006

Glickstein, M. (2006). Golgi and cajal: the neuron doctrine and the 100th anniversary of the 1906 Nobel Prize. *Curr. Biol.* 16, R147–R151.

Golgi, C. (1873). Sulla struttura della sostanza grigia del cervello. *Gaz. Med. Ital. Lombardia.* 6, 244–246.

Haas, K., Sin, W. C., Javaherian, A., Li, Z., and Cline, H. T. (2001). Single-cell electroporation for gene transfer in vivo. *Neuron* 29, 583–591.

Hossain, S., Hewapathirane, D. S., and Haas, K. (2012). Dynamic morphometrics reveals contributions of dendritic growth cones and filopodia to dendritogenesis in the intact and awake embryonic brain. *Dev. Neurobiol.* 72, 615–627. doi: 10.1002/dneu.20959

Jones, E. G. (2010). Cajal's debt to golgi. *Brain Res. Rev.* 66, 83–91.

Kawasaki, H., Iwai, L., and Tanno, K. (2012). Rapid and efficient genetic manipulation of gyrencephalic carnivores using in utero electroporation. *Mol. Brain* 5:24. doi: 10.1186/1756-6606-5-24

Kitamura, K., Judkewitz, B., Kano, M., Denk, W., and Häusser, M. (2008). Targeted patch-clamp recordings and single-cell electroporation of unlabeled neurons in vivo. *Nat. Methods* 5, 61–67. doi: 10.1038/nmeth1150

Liu, X. F., and Haas, K. (2011). Single-cell electroporation of Xenopus tadpole tectal neurons. *Cold Spring Harb Protoc.* 2011:db.rot065615.

LoTurco, J., Manent, J. B., and Sidiqi, F. (2009). New and improved tools for in utero electroporation studies of developing cerebral cortex. *Cereb. Cortex* 19(Suppl. 1), i120–i125. doi: 10.1093/cercor/bhp033

Luo, W., Mizuno, H., Iwata, R., Nakazawa, S., Yasuda, K., Itohara, S., et al. (2016). Supernova: a versatile vector system for single-cell labeling and gene function studies in vivo. *Sci. Rep*. 6:35747.

Matsuda, T., and Cepko, C. L. (2007). Controlled expression of transgenes introduced by in vivo electroporation. *Proc. Natl. Acad. Sci. U.S.A.* 104, 1027–1032. doi: 10.1073/pnas.0610155104

Mikuni, T., Nishiyama, J., Sun, Y., Kamasawa, N., and Yasuda, R. (2016). High-throughput, high-resolution mapping of protein localization in mammalian brain by in vivo genome editing. *Cell* 165, 1803–1817. doi: 10.1016/j.cell.2016.04.044

Muramatsu, T., Nakamura, A., and Park, H. M. (1998). In vivo electroporation: a powerful and convenient means of nonviral gene transfer to tissues of living animals. *Int. J. Mol. Med.* 1, 55–62.

Nieuwkoop, P. D., and Faber, J. (1956). *Normal Table of Xenopus Laevis (daudin): A Systematical and Chronologica Survey of the Development From the Fertilized Egg Till the End of Metamorphosis*. Amsterdam: North-Holland.

Sharma, P., and Cline, H. T. (2010). Visual activity regulates neural progenitor cells in developing xenopus CNS through musashi. *Neuron* 68, 442–455. doi: 10.1016/j.neuron.2010.09.028

Shimogori, T., and Ogawa, M. (2008). Gene application with in utero electroporation in mouse embryonic brain. *Dev. Growth. Differ* 50, 499–506.

Sun, Y. J., Espinosa, J. S., Hoseini, M. S., and Stryker, M. P. (2019). Experience-dependent structural plasticity at pre- and postsynaptic sites of layer 2/3 cells in developing visual cortex. *Proc. Natl. Acad. Sci. U.S.A.* 116, 21812–21820. doi: 10.1073/pnas.1914661116

Tabata, H., and Nakajima, K. (2001). Efficient in utero gene transfer system to the developing mouse brain using electroporation: visualization of neuronal migration in the developing cortex. *Neuroscience.* 103, 865–872. doi: 10.1016/s0306-4522(01)00016-1

Uesaka, N., Hirai, S., Maruyama, T., Ruthazer, E. S., and Yamamoto, N. (2005). Activity dependence of cortical axon branch formation: a morphological and electrophysiological study using organotypic slice cultures. *J. Neurosci.* 25, 1–9. doi: 10.1523/jneurosci.3855-04.2005

Young, P., Qiu, L., Wang, D., Zhao, S., Gross, J., and Feng, G. (2008). Single-neuron labeling with inducible Cre-mediated knockout in transgenic mice. *Nat. Neurosci.* 11, 721–728. doi: 10.1038/nn.2118

Zong, H., Espinosa, J. S., Su, H. H., Muzumdar, M. D., and Luo, L. (2005). Mosaic analysis with double markers in mice. *Cell* 121, 479–492. doi: 10.1016/j.cell.2005.02.012

Conflict of Interest: The authors declare that the research was conducted in the absence of any commercial or financial relationships that could be construed as a potential conflict of interest.

frontiers in Neural Circuits

REVIEW
published: 06 August 2020
doi: 10.3389/fncir.2020.00044

New Optical Tools to Study Neural Circuit Assembly in the Retina

*Aline Giselle Rangel Olguin, Pierre-Luc Rochon and Arjun Krishnaswamy**

Department of Physiology, McGill University, Montreal, QC, Canada

During development, neurons navigate a tangled thicket of thousands of axons and dendrites to synapse with just a few specific targets. This phenomenon termed wiring specificity, is critical to the assembly of neural circuits and the way neurons manage this feat is only now becoming clear. Recent studies in the mouse retina are shedding new insight into this process. They show that specific wiring arises through a series of stages that include: directed axonal and dendritic growth, the formation of neuropil layers, positioning of such layers, and matching of co-laminar synaptic partners. Each stage appears to be directed by a distinct family of recognition molecules, suggesting that the combinatorial expression of such family members might act as a blueprint for retinal connectivity. By reviewing the evidence in support of each stage, and by considering their underlying molecular mechanisms, we attempt to synthesize these results into a wiring model which generates testable predictions for future studies. Finally, we conclude by highlighting new optical methods that could be used to address such predictions and gain further insight into this fundamental process.

Keywords: retina, neural circuits, synaptic specificity, circuit development, recognition molecules

OPEN ACCESS

Edited by:
Yves De Koninck,
Laval University, Canada

Reviewed by:
Kara Geo Pratt,
University of Wyoming, United States
Michael R. Akins,
Drexel University, United States
Jean-Francois Bouchard,
Université de Montréal, Canada

****Correspondence:***
Arjun Krishnaswamy
arjun.krishnaswamy@mcgill.ca

Received: *15 March 2020*
Accepted: *23 June 2020*
Published: *06 August 2020*

Citation:
Rangel Olguin AG, Rochon P-L and Krishnaswamy A (2020) New Optical Tools to Study Neural Circuit Assembly in the Retina. Front. Neural Circuits 14:44. doi: 10.3389/fncir.2020.00044

INTRODUCTION

Our mental abilities depend critically on the concerted function of many distinct neural circuits. While each is functionally specialized and therefore computationally separate from its neighbors, their wiring entangles them and embeds their synapses at micrometer scales. This proximity benefits function for a variety of reasons, ranging from a need to share neurons across circuits to a need to fit the brain's wiring within the fixed volume of the skull. However, this dense arrangement poses serious challenges for circuit assembly because it requires developing neurons to select appropriate synaptic targets from several equally proximate alternatives. This selectivity creates specific wiring, but how a developing neuron chooses its synaptic partners is not entirely clear.

One possibility is that synaptic partners are genetically pre-programmed to synapse, an idea that came out of pioneering studies by Sperry (1943) and Langley (1892). Their vision was that axons possess ligands that match up with cognate receptors on targets and initiate the process of synaptogenesis. Their hypothesis, termed chemoaffinity, received enormous attention in the decades following its proposal and, in many cases, accurately predicts the synapses formed by developing neurons. *Sperry and Langley's* chemical

matchmakers would turn out to belong to large families of cell adhesion molecules, whose properties let neurons adhere tightly with appropriate targets (Sanes and Yamagata, 2009; Zipursky and Sanes, 2010; Lefebvre et al., 2015). Yet, concern grew over the completeness of this idea because the genome encodes too few of these "recognition" molecules to specify every unique connection in the nervous system. How is this disparity resolved?

One solution could be to use a single molecule to match partners separated by anatomical space or developmental time. In this scenario, each reuse subtracts from the total number of recognition molecules needed to wire a population of neurons. Another solution could be to use combinations of recognition molecules to match synaptic partners. Here, the power of combinatorics generates the required number of synaptic matchmakers from a handful of unique recognition molecules. Yet another solution could be to use recognition molecules to position partners in geometric arrangements that lead to specific matching. Recent work indicates that all these solutions are used in concert to simplify the demands on the genome and assemble neural circuitry.

Here, we review the evidence in support of these wiring rules, taken from recent work in the mouse retina. These studies outline a model in which specific wiring develops through a series of stages that include the directed axonal and dendritic growth, the formation of neuropil layers, the positioning of such layers, and the matching of co-laminar synaptic partners. Each section below focuses on one of these stages, the molecular mechanisms that guide each step and, when possible, parallels to layered circuitry in other brain regions and species. Next, we synthesize these recent findings into a series of open questions to help focus future inquiry, and, finally, we conclude by highlighting new optical methods that could be used to gain insight into this fundamental process.

THE RETINA

The mouse retina has recently emerged as an attractive model for circuit development (Fuerst et al., 2009; Sanes and Zipursky, 2010; Matsuoka et al., 2011b; Wei et al., 2011; Lefebvre et al., 2012; Sun et al., 2013; Duan et al., 2014; Krishnaswamy et al., 2015). The retina is a thin sheet of neural tissue located at the back of the eye, which can be accessed with ease but is a part of the central nervous system (CNS) and contains many of the anatomical, cellular, and molecular features of circuits in the brain. The retina is composed of six principal cell types, arranged in three nuclear layers: Photoreceptors (PR) reside in the outer nuclear layer, interneurons called horizontal, amacrine and bipolar cells (HZs, ACs, and BCs) and Müller glia reside in the inner nuclear layer (INL), and retinal ganglion cells (RGCs) reside in the ganglion cell layer (GCL; **Figure 1A**). The outer, inner, and GCLs are separated by two specialized neuropils: an outer plexiform layer (OPL) containing synapses between PR, HZs and BCs, and an inner plexiform layer (IPL) containing synapses among RGCs, BCs and ACs (Masland, 2001, 2012; Sanes and Zipursky, 2010).

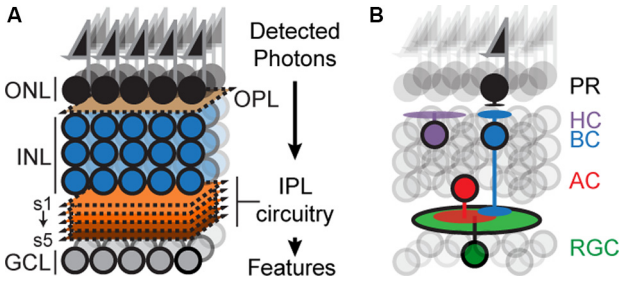

FIGURE 1 | Schematic of retinal organization. **(A)** Outer and inner nuclear layers (ONL, INL), as well as ganglion cell layer (GCL), are separated by two neuropil layers called an outer plexiform layer (OPL) and an inner plexiform layer (IPL). The IPL can be subdivided into at least five sublayers or sublaminae (s1–s5). **(B)** Schematic showing the position of the principal cell types concerning overall retinal structure: photoreceptors (PR), bipolar (BCs), horizontal (HC), amacrine (AC), and retinal ganglion cells (RGC). Feature selectivity on RGCs arises from connections with a subset of BC and AC types.

Decades of studies show that RGCs, ACs, and BCs can be divided into subtypes, each possessing characteristic anatomy, visual response, and molecular expression profile (Gollisch and Meister, 2010; Masland, 2012; Sanes and Masland, 2015). Many of the ∼30 RGC, ∼130 AC and ∼13 BC types can be marked with type-specific antibodies and a full list of such markers is within sight due to an increasingly complete molecular taxonomy of the retina (Wässle et al., 2009; Macosko et al., 2015; Shekhar et al., 2016; Rheaume et al., 2018; Peng et al., 2019; Tran et al., 2019). Furthermore, many marker genes have been targeted by transgenic approaches to create an increasingly complete encyclopedia of cell-type-specific mouse lines housed at commercial repositories. Together, these discoveries make the retina among the few regions of the CNS where neural circuits can be perturbed, analyzed, and dissected with ease.

Retinal circuitry endows each RGC type with a unique preference for features in the visual scene such as edges, color, motion, and so on (Gollisch and Meister, 2010; Jadzinsky and Baccus, 2013; Sanes and Masland, 2015). The plan of such circuits is well understood (**Figure 1B**). Each circuit begins with a photoreceptor that detects photons and each ends with an RGC that sends visual information to the brain (Gollisch and Meister, 2010; Sanes and Zipursky, 2010; Masland, 2012; Sanes and Masland, 2015). Photoreceptor signals are relayed to the IPL *via* BCs which form glutamatergic synapses on RGCs and ACs; ACs form glycinergic or GABAergic synapses on RGCs, BCs, and/or other ACs depending on the cell type. Preferences for visual features arise because each RGC type receives input from a specific subset of BC and AC types, but how such subsets become wired is not completely understood.

IPL FORMATION

Connections among RGCs, BCs, and ACs are organized in the IPL. The dendrites and axons of each RGC, BC, and AC type grow into just one or perhaps two of the ∼5 IPL sublayers. Each of these classes is born sequentially: RGCs are born first

(E8–E17), alongside ACs (E8–P5), followed by BCs (E17–P6), and Müeller glia (E14–P8; Young, 1985; Voinescu et al., 2009).

Birth, migration, and targeting occur sequentially for each retinal neuron, which means that synaptic partners appear asynchronously in target lamina. The direction-selective circuit in the retina offers a good illustration of this phenomenon: It is composed of connections among direction-selective ganglion cells (DSGCs), two populations of cholinergic starburst amacrine cells (SACs), and at least four subtypes of bipolar cells (Helmstaedter et al., 2013; Ding et al., 2016). Their interconnections are contained within IPL sublaminae 2 and 4, but each cell invades sublamina 2 and 4 at different times. SACs arrive by P1 (Stacy and Wong, 2003; Lefebvre et al., 2015; Ray et al., 2018), DSGCs by P5 (Kim et al., 2010; Ray et al., 2018), and BCs at P7–10 (Lefebvre et al., 2012; Duan et al., 2014). Specific wiring, therefore, does not depend on the synchronous appearance of these partners within the IPL. Instead, the sublaminae are used as meeting points; each neuron is endowed with information about the sublamina position, grows into these areas, and waits until its eventual synaptic partner arrives. Cell-type-specific ablation in zebrafish retinae further emphasize the widespread use of this strategy; loss of RGCs, ACs, Müeller glia, or combinations of these types delays the layer-specific growth of the spared neurons but does not prevent it (Kay et al., 2004; Randlett et al., 2013). It is an efficient strategy because it means that developmental mechanisms do not need to coordinate the birth, migration, and ingrowth of eventual partners to ensure their synapses. Rather, each cell is programmed with the laminar position of its eventual partner. How do these sublamina form?

Repulsive Molecular Cues Help Define the IPL

The absence of somata in the IPL is among the most striking features of the retinal organization (**Figure 1A**). They are absent at the onset of IPL development, suggesting that somata and neurites are actively repelled from one another. Recent work shows that this separation is driven, in part, by members of the Semaphorin family.

Semaphorins (Semas) and their Plexin receptors (Plex) belong to a highly conserved protein family with important roles in dendritic and axon growth, including axon guidance, polarization, and repulsion (Huber et al., 2003). Sema-Plex interactions take on two forms: in one case, secreted Semas interact directly with Plex receptors on developing neurites, in the other, membrane-bound Semas interact with Plex receptors and its co-receptor, neuropilin. In both cases, activated Plex receptors cause growth cone collapse and repel Plex-expressing neurites from Sema expressing substrates (Huber et al., 2003). The retina expresses several Sema and Plex isoforms (Matsuoka et al., 2013; Zhang et al., 2017) and two pairs of these, Sema5A and 5B, and their receptors PlexA1 and A3, play an essential role in defining the IPL.

Sema5A and 5B mRNA is expressed broadly by neurons in the INL during retinal synaptogenesis (P3–P14) and disappears from these cells by P21. Their receptors, PlexA1 and A3, adopt a complementary expression pattern and broadly label axons and dendrites in the IPL. In the absence of Sema5A, Sema5B, PlexA1, or PlexA3, axons, and dendrites are unconfined to the IPL, often growing into the INL where they form ectopic IPL-like structures or growing through the INL to invade the outer nuclear layer (Matsuoka et al., 2011a). These ectopic projections are not the result of mistargeted IPL projections, rather these projections result from new processes that emanate from INL neurons. Thus, Sema-Plex signaling prevents these inappropriate processes from forming, thereby reinforcing a pre-existing attraction to the IPL. Little is known about the identity of such attractive cues, but the atypical cadherin FAT3 could be a potential candidate. Loss of FAT3 causes ACs to extend processes within the INL like they do in Sema/Plex mutants (Deans et al., 2011). The presence of such neurites might reflect an inability of Sema/Plex signaling to repel large numbers of mistargeted neurites or reflect an absence of Plex receptors on FAT3 ACs. Determining how attractive FAT3 signals coordinate with repulsive Sema/Plex signals requires the identity of FAT3-expressing neurons and the identity of the FAT3 ligand; both are currently unknown. Taken together, a balance of attractive and repulsive cues appears to separate dendrites and axons from somas to create the IPL.

Interestingly, the ectopic IPL structures formed in Sema/Plex mutants can recruit processes to form sublamina, even though they are located in the INL. These results suggest that sublaminar assembly and IPL formation are guided by independent molecular mechanisms.

Attractive Cues Bind Growing Neurites Together to Create Sublamina

A recent study sheds new light on such sublaminar assembly mechanisms by analyzing the way SACs establish their layers in the developing mouse retina (Ray et al., 2018). One population of SACs resides in the INL and extends processes into sublamina 2. The other resides in the GCL and extends processes into sublamina 4. Each forms these sublayers at P0-P1, well before their BC and RGC synaptic partners arrive (Stacy and Wong, 2003; Sun et al., 2013; Ray et al., 2018).

By carefully analyzing the morphology of newly migrated INL SACs, Ray et al. (2018) observed that neighboring SACs contact each other, forming an initial plexus before they extend neurites into the IPL. Such contacts require a transmembrane protein called Megf10, whose loss ablates the inter-SAC contacts and, surprisingly, disrupts SAC lamination in sublamina 2 and 4; a similar disruption of SAC lamination was caused by ablating SACs earlier in development. Specifically, these manipulations cause SAC dendrites to diffuse out of their sublamina, disrupting the fine structure of these layers and creating ectopic SAC layers in adjacent sublamina (Ray et al., 2018). Exactly how the initial plexus ensures the proper formation of SAC laminae is unclear. However, its appearance coincides with a switch from a multipolar, migratory SAC morphology to one where SAC dendrites are oriented towards the IPL. Thus, inter-SAC contacts, sensed by Megf10, at this stage may act as a checkpoint that ensures SAC dendrite growth only when their cell bodies are positioned beside the IPL. Interestingly, the ectopic layers

formed in Megf10 mutants can recruit the processes of SAC synaptic partners. For example, both direction-selective RGCs (DSGC) and BC projections colocalize with aberrant SAC projections in Megf10 nulls just as they would in controls, suggesting that partner recruitment is regulated independently of Megf10-dependent layer formation. The errors, however, are too severe to preserve DSGC function and result in a loss of their direction-selective responses. Thus, Megf10-based signals are critical for SACs to form an early pair of laminae, which serve as a substrate for their eventual synaptic partners.

Whether each retinal type possesses its own Megf10-like mechanism to establish sublamina or whether this mechanism is unique to SACs is not clear. In the case of the latter scenario, the pair of SAC laminae might act as reference points that later-born neurons could use to position their arbors. The observation that ectopic SAC laminae can recruit the processes of later-arriving neurons favors this possibility.

SUBLAMINA SELECTION

The sublaminar location of RGC or AC dendrites is a major determinant of their function. For example, RGCs become responsive to light onset (ON) because they synapse with BCs located in the inner half of the IPL; RGCs responding to light offset (OFF) synapse with BCs in the outer half (**Figure 1B**; Masland, 2012). ON or OFF BC/RGC pairs must, therefore, select a common sublamina in which to meet and synapse. How does such sublaminar selection occur? Recent work on Cadherin (Cdh) superfamily members in neurons of the retinal direction-selective circuit indicate that Cdhs play a crucial role in this process.

Cdhs Target Neurons to Appropriate Layers

With a few exceptions, Cdhs are single-pass transmembrane proteins named for a characteristic calcium-dependent binding motif in their ectodomains and an intracellular domain that transmits binding events to the cell's interior (Takeichi, 1988). Typically, a Cdh isoform on one cell will preferentially bind to the same isoform located on another cell. Such homophilic adhesion is an attractive property because it could be used to force Cdh-matched neurons to synapse specifically (Hatta et al., 1987; Suzuki et al., 1991; Inoue et al., 1998; Miskevich et al., 1998). Early studies lent support to this idea and showed that $Cdh6^+$ or $Cdh8^+$ cortical areas receive projections from $Cdh6^+$ or $Cdh8^+$ thalamic inputs, respectively (Suzuki et al., 1997). A similar matching was observed between $Cdh9^+$ mossy fibers and their $Cdh9^+$ CA3 targets in the hippocampus. Loss of Cdh9 in either mossy fibers or CA3 neurons selectively reduces their synaptic connectivity (Williams et al., 2011), suggesting that Cdh9 wires these populations together. Thus, Cdhs are expressed in complementary subsets of pre- and postsynaptic neurons and are important for these subsets to synapse with one another.

Recent work in the mouse retina extends this idea further and shows that two types of BCs, called BC2 and BC5, express specific Cdhs to find IPL sublamina containing their synaptic targets (Duan et al., 2014). BC2s express Cdh8 and grows into sublamina 2, BC5s express Cdh9 and grows into sublamina 4. Overexpression of Cdh8 in BC5 forces its growth into sublamina 2 instead of 4, the opposite was true when Cdh9 was expressed in BC2s, forcing these cells to grow into sublamina 4 instead of 2. Such misexpression experiments were able to redirect BC arbors regardless of whether the endogenous Cdh was present and could even redirect a Cdh-AC to the corresponding sublamina. Thus, Cdh8 and 9 impart layer position information for developing BCs. Interestingly, BC2s in Cdh8 nulls and BC5s in Cdh9 nulls distributed themselves randomly to both sublamina 2 and 4, suggesting that Cdh8 and 9 force BCs to choose between two equally attractive sublaminar locations.

Sublamina 2 and 4 contain the dendrites of DSGCs and SACs. DSGCs integrate OFF and ON BC excitation with SAC inhibition to detect the motion direction of an edge in the visual field; four ON-OFF DSGC subtypes exist, one for each cardinal direction (ventral, dorsal, temporal, nasal). Given this and given that BC2s are OFF-BCs and BC5s are ON-BCs, the authors next asked how Cdh loss impacts DSGC function.

To address this, the authors devised an optogenetic approach in which they recorded from fluorescently labeled DSGCs while delivering two-photon excitation to hundreds of individual Channelrhodopsin-2 (ChR2) expressing BC2s or BC5s (Duan et al., 2014; Krishnaswamy et al., 2015). In controls, ∼50% of BC2s or BC5s whose axons overlapped DSGC dendritic arbors evoked inward glutamatergic currents. Loss of Cdh8 reduced this convergence from BC2s to fewer than 10%; loss of Cdh9 produced an equivalent loss of convergence from BC5s. Such deficits severely disrupt DSGC function—OFF or ON DSGC responses are effectively ablated by the loss of Cdh8 or 9, respectively. Oddly, these deficits occur even though Cdh-null BC2s and BC5s randomly distribute their axons to either sublamina 2 or 4, where the dendritic arbors of DSGCs reside. One reason for the increased severity of the functional deficit is that Cdh loss in these BCs prevents them from initiating synapse formation, possibly because they cannot adhere tightly to their DSGC targets. Testing this idea would require the identity of the Cdh8 and 9 ligands within sublamina 2 and 4. However, such ligands cannot be Cdh8 or Cdh9 themselves because these proteins are exclusively expressed by BC2 and BC5 respectively (Duan et al., 2014).

A follow-up study would identify a surprising set of culprits: a pair of isoforms closely related to Cdh9, called Cdh6 and 10, expressed selectively by SACs and a subpopulation of DSGCs selective for ventral motion (vDSGCs). All three of these Cdhs can bind heterophilically and, given their expression pattern, the authors asked whether their interactions bind the processes of BCs, DSGCs, and SACs together (Duan et al., 2018). A single and double knockout analysis produced no observable functional or anatomical deficit, which, together with expression studies, confirmed their suspicion that loss of one isoform could be compensated by another. Triple knockouts would be required but breeding such mice is impractical since Cdh6, 9, and 10 genes are arranged in tandem on chromosome 15. Using CRISPR-based genome editing to generate triple mutants (Basu et al., 2017; Duan et al., 2018), the authors discovered

a surprising consequence of Cdh6/9/10 loss: the dendrites of vDSGCs diffused away from sublamina 2 and 4, but SACs dendrites were unaffected and laminated normally. Could SACs be using Cdhs to scaffold DSGC and BC projections instead of using them to grow into sublamina 2 and 4? To test this idea, the authors ablated SACs before IPL assembly and observed vDSGCs targeting deficits that phenocopied those seen in triple mutants (Duan et al., 2018). Without Cdh6, 9, and 10, vDSGCs are unable to find and synapse with SAC dendrites, rendering these vDSGC neurons unable to detect ventral motion.

Interestingly, sequencing studies revealed the expression of nine other Cdhs in cells of the direction-selective circuit, including Cdh7 in nasal motion selective DSGCs (nDSGCs) and its binding partner Cdh18 in SACs. Disrupting Cdh7 in nDSGCs with RNA interference led to synaptic targeting deficits that mimicked the phenotype seen in vDSGCs following Cdh6/9/10 deletion. Misexpression of Cdh18 in interneurons redirected arbors to Cdh7-positive DSGCs, indicating that Cdh7 binds to Cdh18 (Duan et al., 2018). Importantly, neither Cdh7 nor 18 perturbation nor the loss of Cdh6/9/10 alters SAC layering, further supporting the idea that SACs express Cdhs to scaffold projections from later-born neurons. Taken together, these results suggest that Cdh expression among DSGCs, BCs, and SACs directs these cells to a common pair of layers and creates direction-selective circuitry.

The scaffold strategy has the advantage of robustness; neurons that enter a layer using a Cdh can use the same Cdh to recruit later-laminating neurons. How the appropriate spatiotemporal combination of Cdh isoforms is regulated in targeting and scaffolding cells is unclear, but likely involves type-specific transcriptional regulation. Relating Cdh-expression patterns to transcription factor expression in single-cell sequencing atlases offer a way to uncover such factors.

Semaphorins Repel Neurons From Inappropriate Layers

Adhesive mechanisms ensure contact between eventual partners, which recruits synapse formation machinery, and eventually leads to functional properties in circuits. However, what prevents inappropriate synapses that could disrupt function? For example, if OFF-RGCs received erroneous ON BC inputs, their responses to dark objects would be reduced or ablated. Controlling which neurons synapse after initial contact may be difficult because such sites are rapidly stabilized by transsynaptic interactions scaffolded by nascent pre- and postsynaptic organizers. Indeed, such powerful interactions can lead to remarkably normal-looking synapses even if they are between neurons with mismatched neurotransmitter and neurotransmitter receptor, or between a neuron and itself (Bekkers and Stevens, 1991; Sanes and Yamagata, 2009; Hassan and Hiesinger, 2015; Krishnaswamy, 2016). An alternate strategy is to avoid initial contact altogether by physically segregating inappropriately matched neurons.

Recent studies provide support for this view and show that segregation of ON and OFF neurons depends in part on repulsive Semaphorin signaling. Sema6a labels the dendrites of ON types, whereas its receptors, PlexA4 and PlexA2, are expressed on subsets of OFF types. Loss of Sema6A or PlexA4 causes AC and RGC processes that normally reside in OFF layers to reside in the ON layers instead. For example, loss of PlexA4 leads sublamina 1-preferring melanopsin positive RGCs and tyrosine-hydroxylase positive ACs to grow into sublamina 5 (Matsuoka et al., 2011a). A similar abnormality is seen in the absence of Sema6a, suggesting that Sema6a-PlexA4 binding restricts melanopsin positive RGC and tyrosine-hydroxylase positive AC projections to sublamina 1. Interestingly, these abnormal, sublamina 5-located RGC and AC projections still colocalize with one another, suggesting that these neurons still synapse despite their ectopic location. In another example, OFF SACs in PlexA2 mutants form aberrant projections to sublayers normally reserved for ON SACs; this mistargeting impairs direction selectivity because OFF motion signals are inappropriately combined with ON motion signals (Sun et al., 2013).

TARGET SELECTION

Laminae simplify wiring complexity because they place eventual partners close by and inappropriate ones far apart (Sanes and Yamagata, 2009; Baier, 2013). A potential drawback of this arrangement is that late-born neurons must find their targets within layers that are increasingly crowded. How do they do this? An initial hypothesis proposed that all neurons within a lamina connect, with the number of type-specific synapses scaling in proportion to contact frequency. However, several connectomic efforts indicate that there is no correlation between how widely two neurons contact each other and how often they synapse (Briggman et al., 2011; Helmstaedter et al., 2013; Kasthuri et al., 2015). Instead, such studies indicate that neurons synapse on target cells whose membranes are within microns of the membranes of several non-target cells. How does such selectivity arise?

Immunoglobulin Superfamily Members Enrich Connections Among Synaptic Partners

An increasingly likely scenario is that eventual partners can recognize each other at a micrometer scale because they express matching recognition molecules from the immunoglobulin superfamily (Ig). There are ∼500 Igs in mice, whose names refer to their extracellular domains, which have similarities to the antigen-combining site of antibodies (Shapiro et al., 2007; Katidou et al., 2008; Baier, 2013). Igs typically interact homophilically, but heterophilic interactions among some isoforms have been described. They are expressed in complex combinatorial patterns in the retinae of several species and are of interest because of their recently uncovered roles in wiring co-laminar neurons.

In the fly retina, a multilayered IPL-analog called the medulla organizes indirect input from PR across several sublaminae to create circuits selective for features such as motion direction (Sanes and Zipursky, 2010). Indirect input cells, called laminar neurons grow into specific medullary layers and synapse with specific interneurons or projection neuron types. These

type-specific connections are not exclusive; laminar neurons form large numbers of synapses with their targets, but synapse at low levels with nearby cells. Thus, specificity reflects enriched connectivity between laminar and medullary cell types. An Ig family of defective probosci's proteins (Dprs) and their receptors from the Dip family are essential for this enrichment (Tan et al., 2015; Xu et al., 2018). Laminar neurons expressing a Dpr isoform form numerous synapses with medullary targets that express cognate Dips. Loss of a Dpr reduces selective synapses between the laminar neuron and its Dip-matched medullary partner with minimal effect on layer selection or gross morphology (Xu et al., 2019). Consistent with this, Dpr misexpression in neurons that overlap a Dip-matched target promotes synapses between the pair but cannot promote synapses with non-overlapping neurons (Courgeon and Desplan, 2019; Menon et al., 2019; Xu et al., 2019). Thus, Ig interactions in flies bias connectivity between physically proximate neurons in favor of appropriate pairings.

New work indicates a similar role for Igs in vertebrates. A recent study shows that the Ig member Sidekick 2 (Sdk2) enriches connections among co-laminar ACs and RGCs in the mouse retina. The two Sdks in mice were named for the related Sdk gene in Drosophila (Nguyen et al., 1997; Astigarraga et al., 2018). They are large (∼250 kD) single-pass transmembrane proteins with six immunoglobulin domains, thirteen fibronectin repeats, and a cytoplasmic domain containing a PDZ binding motif. The PDZ anchors Sdks to nascent synapses where they have been shown to interact with the Magi family of scaffold proteins (Yamagata and Sanes, 2010). Sdks bind homophilically across cell-cell junctions *via* their Ig domains (Yamagata and Sanes, 2010; Krishnaswamy et al., 2015), raising the possibility that Sdk expression in co-laminar AC and RGC subsets could enrich their connectivity.

To test this idea, Krishnaswamy et al. (2015) probed Sdk expression in the mouse retina and found that Sdk2 labels an RGC called W3B and an AC called VG3. Both neurons overlap extensively in the same sublamina, each forming small-diameter, highly branched dendritic arbors. W3B-RGCs are thought to be object motion detectors and fire action potentials if motion in its narrow receptive field center differs from a motion in its millimeter-sized surround. VG3-ACs are named for their expression of the non-classical vesicular glutamate transporter, VGlut3, and were a previously uncharacterized AC type (Grimes et al., 2011). The anatomical overlap between these two neurons and their shared expression of Sdk2 led Krishnaswamy et al. (2015) to ask whether VG3 and W3B synapse selectively with one another.

Using optogenetic mapping, the authors recorded from individual W3B-RGCs while stimulating hundreds of presynaptic VG3-ACs located at various distances from the patched cell. Stimulation of VG3-ACs evokes excitatory synaptic currents on W3B-RGCs that result from direct glutamatergic synapses. Comparing evoked current amplitude vs. inter somatic spacing for each VG3-W3B pair revealed an inverse relationship–the strongest responses were produced by the closest VG3-ACs, with the strength of these responses decreasing to no different than baseline at spacings greater than 100 μm. This threshold distance corresponds to the maximal spacing a VG3-AC and W3B-RGC can be positioned and still be in contact. On the other hand, every VG3-AC located within 100 μm of a W3B-RGC was functionally connected. This enriched connectivity pattern is specific to W3B-RGCs and VG3-ACs, although they have substantially weaker, spatially disordered connections with nearby cells. Importantly, none of these equally proximate alternatives express Sdk2, which led the authors to study the consequences of Sdk2 loss. Repeating the mapping experiment in Sdk2 knockout mice revealed pronounced deficits in connectivity–fewer than 10% of VG3-ACs synapse with W3B-RGCs in the absence of Sdk2, and what few were connected have amplitudes reduced to ∼20% of that found in controls. This connectivity loss was restricted to VG3-ACs and W3B-RGCs and arose without major changes in the layering of these two cells. Rescuing Sdk2 expression in VG3 could not rescue VG3-W3B connectivity, indicating that Sdk2 homophilic interactions enrich VG3-W3B connectivity. Moreover, loss of VG3-AC connections in Sdk2 knockouts caused severe loss of excitatory drive to W3B-RGCs, impairing their ability to sense object motion. Taken together, these results indicate that Sdk2 biases connections among proximate partners. Intriguingly, a close relative of Sdk2, Sidekick 1, labels an interneuron-RGC pair that overlaps with W3B and VG3, suggesting that Sdk isoform choice may wire two functionally distinct circuits despite physical entanglement (Krishnaswamy et al., 2015; Yamagata and Sanes, 2018).

Earlier work in chicks suggested that Igs like Sdks direct laminar targeting, rather than synaptic bias (Yamagata et al., 2002; Krishnaswamy et al., 2015). Species-specific differences could explain this discrepancy and have been observed for close relatives of Sdks. For example, Down syndrome cell adhesion molecules (DSCAMs) direct laminar targeting in chicks (Yamagata and Sanes, 2008) but serve dendritic self-avoidance and cell survival functions in mice (Fuerst et al., 2008, 2009, 2012). Another possibility reflects experimental differences; in chicks, Sdk2 expression was reduced in isolated neurons in control retinae, which may have amplified their morphological deficits due to competition between the perturbed and wildtype neurons (Yamagata and Sanes, 2008). A final possibility suggested by a recent study in mouse retinae is that Igs can alter laminar morphology depending on when they are expressed. For example, early Sdk2 misexpression in Sdk1ACs causes their morphology to resemble VG3 and W3B (Yamagata and Sanes, 2018). Whether this is because Sdks regulate dendritic morphology, as has been shown for related Contactins (Peng et al., 2017), or because morphological changes result from increased Sdk1AC-W3B and/or Sdk1AC-VG3 synapses is not clear. More work will be needed to decide whether Igs bias connectivity because of when they are expressed, because of their intrinsic properties, or both. Whatever the mechanism, a growing number of studies strongly point to Igs as conserved neural wiring genes that direct local synapse formation.

AN ADHESIVE CODE?

Much more work is needed to understand the basis of wiring specificity, but the following tentative conclusions

would fit the evidence reviewed so far. First, specificity comprises at least three steps: layer formation, layer targeting, and intralaminar targeting. Second, neurons find appropriate layers even if their eventual targets have not arrived. Third, layer formation is orchestrated by diverse adhesive and repulsive molecular cues. Fourth, layer targeting is dominated by members of the Cdh and Sema/Plex families. Fifth, target selection is dominated by members of the Ig family (**Figures 2A,B**).

These conclusions outline a model in which the expression of a given Sema, Cdh, and Ig defines a neuron's wiring pattern in the same way an address directs an envelope to a specific state/province, city, and mailbox (**Figures 2A,B**).

This model drastically reduces the number of wiring cues. For example, a Cdh that directs retinal neurons to an ON sublamina could be reused for an OFF sublamina, so long as the OFF-projecting cells are repelled from ON layers using Sema/Plex members. As another example, a single Sdk isoform could be used to connect several pairs so long as each pair expresses a different Cdh/Sema combination to target different lamina. The hierarchical nature of circuit assembly in the retina, paired with the diversity-generating process of combinatorics dramatically simplifies the genetic needs for wiring.

GENETICALLY ENCODED OPTICAL TOOLS TO GAIN INSIGHT

Anatomical Connectivity Mapping

Connections from subsets of interneuron types on a single RGC type create circuits, each attuned to a unique aspect of the visual scene. Current models predict that wiring patterns specific to each circuit arise because the component neurons make wiring decisions guided by recognition molecules. A satisfying understanding of this process requires that we test the ability of this model to predict connectivity patterns across all retinal circuits. However, such mature connectivity patterns for most retinal circuits are unknown. Straightforward, high-throughput methods to map connectivity are needed to cross this hurdle.

In principle, labeling a single RGC and its presynaptic partners followed by immunostaining with cell-type-specific markers offers a route to progress. Rabies-based transsynaptic tracing offers a way to achieve such labeling (**Figure 3A**). Initial attempts with this approach were hard to interpret because the virus would "hop" across synapses so rapidly that it was difficult to distinguish mono- vs. polysynaptically connected cells (Wickersham and Feinberg, 2012). The solution was to employ two viruses, mutated rabies incapable of transsynaptic infection that encodes a reporter, and an adeno-associated virus bearing cre-dependent rabies glycoprotein (rG), which permits transsynaptic transfer (Wickersham et al., 2007a). Injecting these two viruses into the medial terminal nucleus of mice retrogradely infects ON-DSGCs (Dhande et al., 2013) and ON-OFF DSGCs (Yonehara et al., 2011) and labels their monosynaptically connected interneuron inputs, such as SACs. A further refinement uses the two viruses above, but pseudotypes the rabies virus with avian capsid proteins, which restricts infection to neurons that bear avian rabies receptors, called TVA receptors (Wickersham et al., 2007b). Infecting medial terminal nucleus with viruses bearing TVA and rG, followed by injection of g-deleted rabies into the eye allowed for even more precise labeling of ON-DSGC inputs, revealing their connections with Type 5 BCs (Yonehara et al., 2013). Current viral reagents encode cre-dependent TVA and rG within a single virus which is used along with g-deleted rabies viruses. However, this approach still labels several cre-expressing starter neurons which in turn labels so many presynaptic neurons that it can overwhelm measurements of convergence on individual starters. This is a particularly troublesome feature for the retina since each

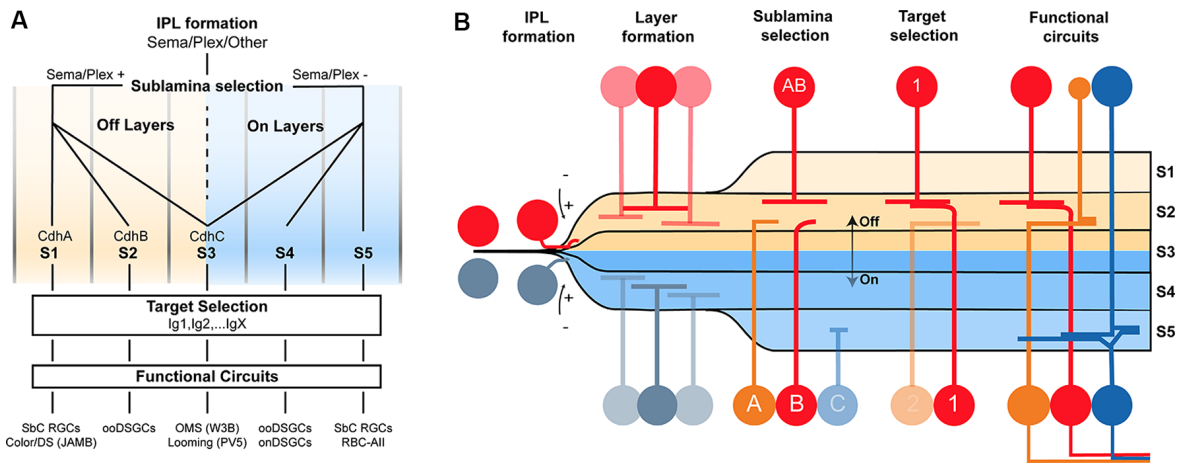

FIGURE 2 | Potential model of the circuit assembly. A wiring model (A) and developmental stages (B) followed by developing retinal neurons to form functional neural circuits. **(A)** Speculative decision tree model that summarizes the studies reviewed in this text. The diagram has been populated with recognition molecule candidates with known roles at each stage. **(B)** Cartoon of circuit assembly in the mouse retina illustrating the stages of migration, IPL formation, layer formation, sublamina selection, and target selection which ultimately result in mature neural circuitry.

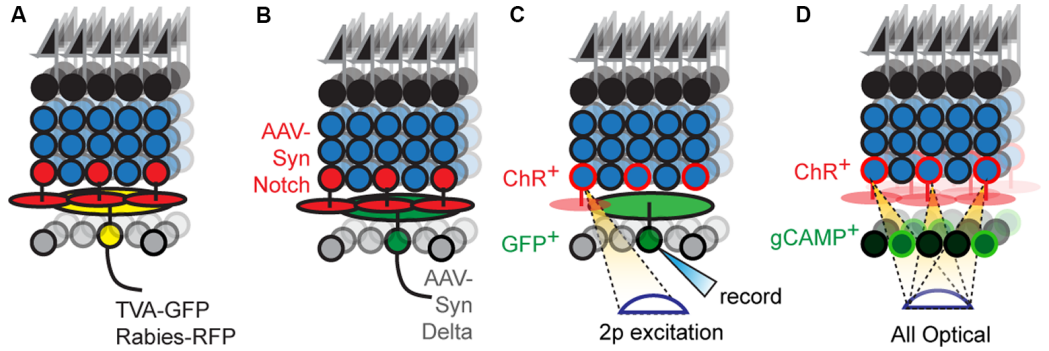

FIGURE 3 | New optical tools to map retinal connectivity. **(A)** Retrograde infection with the rabies virus and cre-dependent TVA/rG allows tracing of monosynaptic connections from defined starter cells. **(B)** Putative synthetic delta constructs delivered retrogradely to RGCs alongside retinal infection with synthetic notch reveals connected interneuron types. **(C)** Two-photon excitation of ChR2$^+$ interneurons while recording individual RGCs allows maps of convergence. **(D)** All-optical physiological methods permit divergence maps from defined interneuron types to be measured.

circuit repeats itself across the retinal surface with a substantial lateral overlap in the wiring. Delivering TVA/rG to a single starter circumvents this issue at the cost of a loss in throughput (Schubert et al., 2018).

Another widely used strategy involves the cell-type-specific expression of wheat germ agglutinin (WGA) fused to GFP or Cre-recombinase. However, transfer with these genetically encoded tracers is not limited to monosynaptic inputs which dilute the WGA signal in directly connected neurons as the WGA diffuses through the network. Moreover, the transfer can be non-synaptic and can be biased to some synapses over others, resulting in erroneous wiring diagrams (Wickersham and Feinberg, 2012).

Newer strategies employ proteins that bind transsynaptically to label the synapses of connected neurons (**Figure 3B**). A good example is a GRASP, which reconstitutes GFP across synaptic partners (GRASP). Briefly, a membrane-bound, incomplete piece of GFP is expressed presynaptically while the missing piece of GFP is fused to a postsynaptically localized membrane protein (Feinberg et al., 2008). If the two neurons synapse, their membranes are close enough to unite the pieces and GFP fluorescently labels the synapse. This approach is widely used in invertebrates to label synapses, in part, because the well-studied neuronal morphologies in these systems allow one to translate the punctate signal into type-specific wiring diagrams. A few versions have been optimized for mice (Kim et al., 2011; Luo et al., 2018) and used in the retina (Yamagata and Sanes, 2012), but the wiring complexity in these systems makes it hard to assign synaptic labeling to specific pre- and postsynaptic neurons. For this reason, soma-filling labels that result from transsynaptic interactions have been devised, but at present are only available in invertebrate models (Jagadish et al., 2014; Talay et al., 2017). A recent study has used synthetic reporters based on the Notch-Delta signaling pathway (synNotch) in vertebrates (Morsut et al., 2016); in this pathway, Notch intracellular domain is cleaved following Notch-Delta binding and activates gene transcription. Synthetic versions replace Notch intracellular domains with Cre while replacing Notch and Delta ectodomains with GFP and GFP-nanobodies, respectively. The proximity produced by synaptic contact results in nanobody-GFP binding, which frees the cre-containing intracellular domain to activate reporter gene expression. Potential is the concern that normally unconnected neurons expressing either GRASP or artificial Notch reporters might erroneously synapse because these tools might act as adhesion proteins. Current reports using GRASP have carefully controlled for this possibility for the circuit under study, and at least in these cases, the likelihood of such artifactual synapses is low. Less is known about the behavior of Notch-based reporters which have used in culture (Morsut et al., 2016). A more comprehensive strategy to validate these methods could be to compare resulting wiring diagrams with those obtained using electron microscopy (EM) based connectomic methods. Such correspondence would be powerful, and with the advent of new EM compatible genetically encoded reporters, the labor cost of this approach is significantly reduced (Joesch et al., 2016).

Viral and genetically encoded tracers offer powerful avenues for labeling connected neurons. Their major drawback is sensitivity–presynaptic neurons that form a single synapse with a target are labeled just as brightly as those synapsing many times with the same target. This is a worrisome limitation given that specificity mechanisms may simply enrich connections between appropriate partners rather than preventing connections among inappropriate ones. Thus, an approach that measures connectivity strength would be ideal. One way to add this information to tracer-labeled circuits could be to process them for array tomography, which combines the ultra-thin sections employed in EM with the histological approaches common to light microscopic assays. Such EM-prepared sections can be stained with multiple rounds of antibodies that label synaptic proteins which results in an "array" of staining that identifies synapses between traced neurons. This approach has limitations–significant time is needed to process, image, and reconstruct tissue, which places practical limits on the number of samples one can acquire. An alternate track is to

relate anatomically traced neurons to the strength of their functional connections.

Functional Connectivity Mapping

A straightforward way to link physical and functional connectivity is to record synaptic transmission in one neuron while stimulating another and label each cell with different intracellular dyes (**Figure 3C**). Incorporating type-specific cre lines into this scheme permits connectivity analysis of specific interneuron-RGC pairs that include their spatial relationship.

This approach has proved invaluable to the study of retinal direction-selective circuits. Briefly, there are four types of DSGCs; each responds to stimuli moving in one of four cardinal directions (ventral, dorsal, nasal, and temporal). Their preference is established by SACs who inhibit DSGC responses to stimuli moving opposite the preferred direction, called the null direction; for example, dorsal motion responses are inhibited on DSGCs selective for ventral motion. Paired recording methods were essential to learning that these inputs were strongest on the null side of DSGC dendrites and that such strength develops over the first postnatal week (Wei et al., 2011). Optogenetic tools accelerate and simplify these studies, allowing activation of interneurons expressing channelrhodopsins (ChRs) in arbitrary patterns while recording from individual RGC types, allowing one to rapidly assess the strength and geometry of interneuron-RGC connections. The relative ease of this experiment, for example, allowed Yonehara et al. (2011) to rapidly measure the asymmetric GABAergic SAC input and symmetric cholinergic SAC input on dozens of individual DSGCs (Yonehara et al., 2011).

As a further refinement of this optogenetic strategy, Krishnaswamy et al. (2015) excited ChR^+ interneurons with automated two-photon excitation, resolving interneuron-RGC connectivity maps at the level of individual pairs (Duan et al., 2014, 2018; Krishnaswamy et al., 2015). Across three studies, these authors comprehensively mapped the convergence between seven interneurons and four RGCs types and found several unique connectivity patterns, which could then be targeted by developmental approaches. For example, mapping BC2-DSGC and BC5-DSGC connectivity revealed that only about 50% of the BCs situated above the DSGC dendritic arbor were connected (Duan et al., 2014, 2018). Why this occurs is not clear but could be related to the array-like organization of BC axon terminals and the sparseness of DSGC dendritic arbors. Stimulating the terminals of $ChR2^+$ BCs rather than their somas, using the same approach, could allow a direct test of this idea. In another study, two-photon mapping interneurons and RGCs that co-stratify in sublamina 3 revealed that only a few of these neurons exhibit strong connections; VG3-ACs and W3B RGCs connect whenever their dendrites overlap, whereas connectivity is absent between Nex-Cre labeled ACs and W3B-RGCs despite comparable anatomical overlap (Krishnaswamy et al., 2015).

One drawback of this approach is speed; two-photon mapping measures the strength and geometry of an interneuron's connections to a single RGC with exquisite detail, but analysis of this interneuron's connections to other nearby RGCs requires a separate experiment. This separation can be costly because of the significant time investment needed to generate mice that label a single AC type with ChR2 and single RGC type with GFP. This is an important consideration in light of data showing that Cdhs coordinate the growth of many RGCs to a common layer and bring them within proximity of several common interneuron partners. Determining whether this proximity causes such RGCs to share interneuron inputs would ideally require an approach that maps several interneuron-RGC pairs in parallel.

All-optical connectivity mapping approaches are a possible route for parallelization; in this scheme, $ChR2^+$ interneurons are individually excited while simultaneously imaging the responses of all RGCs (**Figure 3D**). Briefly, a spatial light modulator is used to sculpt two-photon laser emission into holograms that are aimed at an arbitrary number of interneuron somas, while simultaneous two-photon scanning images responses from RGCs that express calcium indicators. The <2 μm axial resolution of this approach ensures that there is no crosstalk between stimulating and recording planes. Such all-optical methods have already been applied to cortical circuits with great success (Packer et al., 2015; Marshel et al., 2019).

Given the graded, non-spiking membrane properties of most interneurons, the application of this method to retinal circuitry is likely to be successful. Indeed, a preprint describing this approach in retina indicates that one can stimulate hundreds of rod BCs while measuring responses in a field of RGCs expressing genetically encoded calcium indicators (Spampinato et al., 2019).

This functional mapping offers a powerful way to define connectivity strength among synaptically coupled neurons. But combining these methods with the viral or genetic tracers described above may allow for even faster, higher-detail connectivity diagrams. For example, labeling the interneurons connected to an RGC with rabies viruses bearing ChRs could allow one to optogenetically map their connectivity onto the starter RGC as well as nearby non-starter RGCs. Comparisons across such maps could reveal systematically stronger connectivity strengths to the starter RGC relative to non-starter RGCs, directly testing the notion that specificity enriches synapses between partners rather than ensuring exclusive synapses between partners. A further improvement to this scheme would follow functional mapping with array tomographic or EM-based connectomic approaches to relate pair connection strength to synapse number, or synaptic molecular profile. A combination of functional, anatomical, and ultrastructural approaches is needed for a complete picture.

CONCLUSION

A major goal of developmental neuroscience is to unearth the rules and blueprints used to wire the brain. Recent efforts to understand how the well-defined circuits of the mouse retina assemble are shedding new light on this issue. These studies outline a wiring model in which connectivity develops through a series of stages; a neuron's route through these stages is governed by the expression of specific recognition molecules, which direct them to grow in a specific direction, to a specific layer, and

synapse with a specific target. New advances in neurophotonics offer a way to accelerate our understanding of this process and develop a comprehensive model that relates recognition molecule expression to wiring patterns. By gaining these valuable insights in the retina and improving our circuit tracing toolkit, we ready ourselves to translate these advances to understand circuit assembly in the brain where genetically programmed wiring patterns are modified by neural activity.

AUTHOR CONTRIBUTIONS

AR, P-LR, and AK planned and wrote the manuscript.

FUNDING

This work was supported by funding from both the Canada Research Chairs program and the Alfred P. Sloan Foundation to AK, a CIHR Banting fellowship, and HBHL fellowship to P-LR, and an HBHL fellowship and CONACYT fellowship to AR.

ACKNOWLEDGMENTS

We thank E. Cooper for thoughtful comments on the manuscript.

REFERENCES

Astigarraga, S., Douthit, J., Tarnogorska, D., Creamer, M. S., Mano, O., Clark, D. A., et al (2018). *Drosophila* sidekick is required in developing photoreceptors to enable visual motion detection. *Development* 145:dev158246. doi: 10.1242/dev.158246

Baier, H. (2013). Synaptic laminae in the visual system: molecular mechanisms forming layers of perception. *Annu. Rev. Cell Dev. Biol.* 29, 385–416. doi: 10.1146/annurev-cellbio-101011-155748

Basu, R., Duan, X., Taylor, M. R., Martin, E. A., Muralidhar, S., Wang, Y., et al (2017). Heterophilic type II cadherins are required for high-magnitude synaptic potentiation in the hippocampus. *Neuron* 96, 160.e8–176.e8. doi: 10.1016/j.neuron.2017.09.009

Bekkers, J. M., and Stevens, C. F. (1991). Excitatory and inhibitory autaptic currents in isolated hippocampal neurons maintained in cell culture. *Proc. Natl. Acad. Sci. U S A.* 88, 7834–7838. doi: 10.1073/pnas.88.17.7834

Briggman, K. L., Helmstaedter, M., and Denk, W. (2011). Wiring specificity in the direction-selectivity circuit of the retina. *Nature* 471, 183–188. doi: 10.1038/nature09818

Courgeon, M., and Desplan, C. (2019). Coordination between stochastic and deterministic specification in the *Drosophila* visual system. *Science* 366. doi: 10.1126/science.aay6727

Deans, M. R., Krol, A., Abraira, V. E., Copley, C. O., Tucker, A. F., and Goodrich, L. V. (2011). Control of neuronal morphology by the atypical cadherin Fat3. *Neuron* 71, 820–832. doi: 10.1016/j.neuron.2011.06.026

Dhande, O. S., Estevez, M. E., Quattrochi, L. E., El-Danaf, R. N., Nguyen, P. L., Berson, D. M., et al (2013). Genetic dissection of retinal inputs to brainstem nuclei controlling image stabilization. *J. Neurosci.* 33, 17797–17813. doi: 10.1523/jneurosci.2778-13.2013

Ding, H., Smith, R. G., Poleg-Polsky, A., Diamond, J. S., and Briggman, K. L. (2016). Species-specific wiring for direction selectivity in the mammalian retina. *Nature* 535, 105–110. doi: 10.1038/nature18609

Duan, X., Krishnaswamy, A., De la Huerta, I., and Sanes, J. R. (2014). Type II cadherins guide assembly of a direction-selective retinal circuit. *Cell* 158, 793–807. doi: 10.1016/j.cell.2014.06.047

Duan, X., Krishnaswamy, A., Laboulaye, M. A., Liu, J., Peng, Y.-R., Yamagata, M., et al (2018). Cadherin combinations recruit dendrites of distinct retinal neurons to a shared interneuronal scaffold. *Neuron* 99, 1145.e6–1154.e6. doi: 10.1016/j.neuron.2018.08.019

Feinberg, E. H., Vanhoven, M. K., Bendesky, A., Wang, G., Fetter, R. D., Shen, K., et al (2008). GFP reconstitution across synaptic partners (GRASP) defines cell contacts and synapses in living nervous systems. *Neuron* 57, 353–363. doi: 10.1016/j.neuron.2007.11.030

Fuerst, P. G., Bruce, F., Rounds, R. P., Erskine, L., and Burgess, R. W. (2012). Cell autonomy of DSCAM function in retinal development. *Dev. Biol.* 361, 326–337. doi: 10.1016/j.ydbio.2011.10.028

Fuerst, P. G., Bruce, F., Tian, M., Wei, W., Elstrott, J., Feller, M. B., et al (2009). DSCAM and DSCAML1 function in self-avoidance in multiple cell types in the developing mouse retina. *Neuron* 64, 484–497. doi: 10.1016/j.neuron.2009.09.027

Fuerst, P. G., Koizumi, A., Masland, R. H., and Burgess, R. W. (2008). Neurite arborization and mosaic spacing in the mouse retina require DSCAM. *Nature* 451, 470–474. doi: 10.1038/nature06514

Gollisch, T., and Meister, M. (2010). Eye smarter than scientists believed: neural computations in circuits of the retina. *Neuron* 65, 150–164. doi: 10.1016/j.neuron.2009.12.009

Grimes, W. N., Seal, R. P., Oesch, N., Edwards, R. H., and Diamond, J. S. (2011). Genetic targeting and physiological features of VGLUT3+ amacrine cells. *Vis. Neurosci.* 28, 381–392. doi: 10.1017/s0952523811000290

Hassan, B. A., and Hiesinger, P. R. (2015). Beyond molecular codes: simple rules to wire complex brains. *Cell* 163, 285–291. doi: 10.1016/j.cell.2015.09.031

Hatta, K., Takagi, S., Fujisawa, H., and Takeichi, M. (1987). Spatial and temporal expression pattern of N-cadherin cell adhesion molecules correlated with morphogenetic processes of chicken embryos. *Dev. Biol.* 120, 215–227. doi: 10.1016/0012-1606(87)90119-9

Helmstaedter, M., Briggman, K. L., Turaga, S. C., Jain, V., Seung, H. S., and Denk, W. (2013). Connectomic reconstruction of the inner plexiform layer in the mouse retina. *Nature* 500, 168–174. doi: 10.1038/nature12346

Huber, A. B., Kolodkin, A. L., Ginty, D. D., and Cloutier, J.-F. (2003). Signaling at the growth cone: ligand-receptor complexes and the control of axon growth and guidance. *Annu. Rev. Neurosci.* 26, 509–563. doi: 10.1146/annurev.neuro.26.010302.081139

Inoue, T., Tanaka, T., Suzuki, S. C., and Takeichi, M. (1998). Cadherin-6 in the developing mouse brain: expression along restricted connection systems and synaptic localization suggest a potential role in neuronal circuitry. *Dev. Dyn.* 211, 338–351. doi: 10.1002/(SICI)1097-0177(199804)211:4<338::AID-AJA5>3.0.CO;2-I

Jadzinsky, P. D., and Baccus, S. A. (2013). Transformation of visual signals by inhibitory interneurons in retinal circuits. *Annu. Rev. Neurosci.* 36, 403–428. doi: 10.1146/annurev-neuro-062012-170315

Jagadish, S., Barnea, G., Clandinin, T. R., and Axel, R. (2014). Identifying functional connections of the inner photoreceptors in drosophila using tango-trace. *Neuron* 83, 630–644. doi: 10.1016/j.neuron.2014.06.025

Joesch, M., Mankus, D., Yamagata, M., Shahbazi, A., Schalek, R., Suissa-Peleg, A., et al (2016). Reconstruction of genetically identified neurons imaged by serial-section electron microscopy. *Elife* 5:e15015. doi: 10.7554/eLife.15015

Kasthuri, N., Hayworth, K. J., Berger, D. R., Schalek, R. L., Conchello, J. A., Knowles-Barley, S., et al (2015). Saturated reconstruction of a volume of neocortex. *Cell* 162, 648–661. doi: 10.1016/j.cell.2015.06.054

Katidou, M., Vidaki, M., Strigini, M., and Karagogeos, D. (2008). The immunoglobulin superfamily of neuronal cell adhesion molecules: lessons from animal models and correlation with human disease. *Biotechnol. J.* 3, 1564–1580. doi: 10.1002/biot.200800281

Kay, J. N., Roeser, T., Mumm, J. S., Godinho, L., Mrejeru, A., Wong, R. O. L., et al (2004). Transient requirement for ganglion cells during assembly of retinal synaptic layers. *Development* 131, 1331–1342. doi: 10.1242/dev.01040

Kim, I.-J., Zhang, Y., Meister, M., and Sanes, J. R. (2010). Laminar restriction of retinal ganglion cell dendrites and axons: subtype-specific developmental patterns revealed with transgenic markers. *J. Neurosci.* 30, 1452–1462. doi: 10.1523/JNEUROSCI.4779-09.2010

Kim, J., Zhao, T., Petralia, R. S., Yu, Y., Peng, H., Myers, E., et al (2011). mGRASP enables mapping mammalian synaptic connectivity with light microscopy. *Nat. Methods* 9, 96–102. doi: 10.1038/nmeth.1784

Krishnaswamy, A. (2016). Building connections. *Science* 354:558. doi: 10.1126/science.aak9763

Krishnaswamy, A., Yamagata, M., Duan, X., Hong, Y. K., and Sanes, J. R. (2015). Sidekick 2 directs formation of a retinal circuit that detects differential motion. *Nature* 524, 466–470. doi: 10.1038/nature14682

Langley, J. N. (1892). On the origin from the spinal cord of the cervical and upper thoracic sympathetic fibres, with some observations on white and grey rami communications. *Philos. Trans. R. Soc. London B* 183, 85–124. doi: 10.1098/rstb.1892.0002

Lefebvre, J. L., Kostadinov, D., Chen, W. V., Maniatis, T., and Sanes, J. R. (2012). Protocadherins mediate dendritic self-avoidance in the mammalian nervous system. *Nature* 488, 517–521. doi: 10.1038/nature11305

Lefebvre, J. L., Sanes, J. R., and Kay, J. N. (2015). Development of dendritic form and function. *Annu. Rev. Cell Dev. Biol.* 31, 741–777. doi: 10.1146/annurev-cellbio-100913-013020

Luo, L., Callaway, E. M., and Svoboda, K. (2018). Genetic dissection of neural circuits: a decade of progress. *Neuron* 98, 256–281. doi: 10.1016/j.neuron.2018.03.040

Macosko, E. Z., Basu, A., Satija, R., Nemesh, J., Shekhar, K., Goldman, M., et al (2015). Highly parallel genome-wide expression profiling of individual ccells using nanoliter droplets. *Cell* 161, 1202–1214. doi: 10.1016/j.cell.2015.05.002

Marshel, J. H., Kim, Y. S., Machado, T. A., Quirin, S., Benson, B., Kadmon, J., et al (2019). Cortical layer-specific critical dynamics triggering perception. *Science* 365:eaaw5202. doi: 10.1126/science.aaw5202

Masland, R. H. (2001). The fundamental plan of the retina. *Nat. Neurosci.* 4, 877–886. doi: 10.1038/nn0901-877

Masland, R. H. (2012). The neuronal organization of the retina. *Neuron* 76, 266–280. doi: 10.1016/j.neuron.2012.10.002

Matsuoka, R. L., Chivatakarn, O., Badea, T. C., Samuels, I. S., Cahill, H., Katayama, K.-I., et al (2011a). Class 5 transmembrane semaphorins control selective mammalian retinal lamination and function. *Neuron* 71, 460–473. doi: 10.1016/j.neuron.2011.06.009

Matsuoka, R. L., Nguyen-Ba-Charvet, K. T., Parray, A., Badea, T. C., Chedotal, A., and Kolodkin, A. L. (2011b). Transmembrane semaphorin signalling controls laminar stratification in the mammalian retina. *Nature* 470, 259–263. doi: 10.1038/nature09675

Matsuoka, R. L., Sun, L. O., Katayama, K., Yoshida, Y., and Kolodkin, A. L. (2013). Sema6B, sema6c and sema6d expression and function during mammalian retinal development. *PLoS One* 8:e63207. doi: 10.1371/journal.pone.0063207

Menon, K. P., Kulkarni, V., Takemura, S.-Y., Anaya, M., and Zinn, K. (2019). Interactions between dpr11 and DIP-γ control selection of amacrine neurons in drosophila color vision circuits. *Elife* 8:e48935. doi: 10.7554/elife.48935

Miskevich, F., Zhu, Y., Ranscht, B., and Sanes, J. R. (1998). Expression of multiple cadherins and catenins in the chick optic tectum. *Mol. Cell. Neurosci.* 12, 240–255. doi: 10.1006/mcne.1998.0718

Morsut, L., Roybal, K. T., Xiong, X., Gordley, R. M., Coyle, S. M., Thomson, M., et al (2016). Engineering customized cell sensing and response behaviors using synthetic notch receptors. *Cell* 164, 780–791. doi: 10.1016/j.cell.2016.01.012

Nguyen, D. N., Liu, Y., Litsky, M. L., and Reinke, R. (1997). The sidekick gene, a member of the immunoglobulin superfamily, is required for pattern formation in the drosophila eye. *Development* 124, 3303–3312.

Packer, A. M., Russell, L. E., Dalgleish, H. W. P., and Häusser, M. (2015). Simultaneous all-optical manipulation and recording of neural circuit activity with cellular resolution *in vivo*. *Nat. Methods* 12, 140–146. doi: 10.1038/nmeth.3217

Peng, Y. R., Shekhar, K., Yan, W., Herrmann, D., Sappington, A., Bryman, G. S., et al (2019). Molecular classification and comparative taxonomics of foveal and peripheral cells in primate retina. *Cell* 176, 1222.e22–1237.e22. doi: 10.1016/j.cell.2019.01.004

Peng, Y. R., Tran, N. M., Krishnaswamy, A., Kostadinov, D., Martersteck, E. M., and Sanes, J. R. (2017). Satb1 regulates contactin 5 to pattern dendrites of a mammalian retinal ganglion cell. *Neuron* 95, 869.e6–883.e6. doi: 10.1016/j.neuron.2017.07.019

Randlett, O., MacDonald, R. B., Yoshimatsu, T., Almeida, A. D., Suzuki, S. C., Wong, R. O., et al (2013). Cellular Requirements for Building a Retinal Neuropil. *Cell Rep.* 3, 282–290. doi: 10.1016/j.celrep.2013.01.020

Ray, T. A., Roy, S., Kozlowski, C., Wang, J., Cafaro, J., Hulbert, S. W., et al (2018). Formation of retinal direction-selective circuitry initiated by starburst amacrine cell homotypic contact. *Elife* 7:e34241. doi: 10.7554/eLife.34241

Rheaume, B. A., Jereen, A., Bolisetty, M., Sajid, M. S., Yang, Y., Renna, K., et al (2018). Author correction: single cell transcriptome profiling of retinal ganglion cells identifies cellular subtypes. *Nat. Commun.* 9:3203. doi: 10.1038/s41467-018-05792-3

Sanes, J. R., and Masland, R. H. (2015). The types of retinal ganglion cells: current status and implications for neuronal classification. *Annu. Rev. Neurosci.* 38, 221–246. doi: 10.1146/annurev-neuro-071714-034120

Sanes, J. R., and Yamagata, M. (2009). Many paths to synaptic specificity. *Annu. Rev. Cell Dev. Biol.* 25, 161–195. doi: 10.1146/annurev.cellbio.24.110707.175402

Sanes, J. R., and Zipursky, S. L. (2010). Design principles of insect and vertebrate visual systems. *Neuron* 66, 15–36. doi: 10.1016/j.neuron.2010.01.018

Schubert, R., Trenholm, S., Balint, K., Kosche, G., Cowan, C. S., Mohr, M. A., et al (2018). Virus stamping for targeted single-cell infection *in vitro* and *in vivo*. *Nat. Biotechnol.* 36, 81–88. doi: 10.1038/nbt.4034

Shapiro, L., Love, J., and Colman, D. R. (2007). Adhesion molecules in the nervous system: structural insights into function and diversity. *Annu. Rev. Neurosci.* 30, 451–474. doi: 10.1146/annurev.neuro.29.051605.113034

Shekhar, K., Lapan, S. W., Whitney, I. E., Tran, N. M., Macosko, E. Z., Kowalczyk, M., et al (2016). Comprehensive classification of retinal bipolar neurons by single-cell transcriptomics. *Cell* 166, 1308.e30–1323.e30. doi: 10.1016/j.cell.2016.07.054

Spampinato, G. L. B., Ronzitti, E., Zampini, V., Ferrari, U., Trapani, F., Khabou, H., et al (2019). All-optical interrogation of a direction selective retinal circuit by holographic wave front shaping. *Biorxiv* [preprint]. doi: 10.1101/513192

Sperry, R. W. (1943). Visuomotor coordination in the newt (triturus viridescens) after regeneration of the optic nerve. *J. Comp. Neurol.* 79, 33–55. doi: 10.1002/cne.900790104

Stacy, R. C., and Wong, R. O. L. (2003). Developmental relationship between cholinergic amacrine cell processes and ganglion cell dendrites of the mouse retina. *J. Comp. Neurol.* 456, 154–166. doi: 10.1002/cne.10509

Sun, L. O., Jiang, Z., Rivlin-Etzion, M., Hand, R., Brady, C. M., Matsuoka, R. L., et al (2013). On and off retinal circuit assembly by divergent molecular mechanisms. *Science* 342:1241974. doi: 10.1126/science.1241974

Suzuki, S., Sano, K., and Tanihara, H. (1991). Diversity of the cadherin family: evidence for eight new cadherins in nervous tissue. *Cell Regul.* 2, 261–270. doi: 10.1091/mbc.2.4.261

Suzuki, S. C., Inoue, T., Kimura, Y., Tanaka, T., and Takeichi, M. (1997). Neuronal circuits are subdivided by differential expression of type-II classic cadherins in postnatal mouse brains. *Mol. Cell. Neurosci.* 9, 433–447. doi: 10.1006/mcne.1997.0626

Takeichi, M. (1988). The cadherins: cell-cell adhesion molecules controlling animal morphogenesis. *Development* 102, 639–655.

Talay, M., Richman, E. B., Snell, N. J., Hartmann, G. G., Fisher, J. D., Sorkaç, A., et al (2017). Transsynaptic mapping of second-order taste neurons in flies by trans-tango. *Neuron* 96, 783.e4–795.e4. doi: 10.1016/j.neuron.2017.10.011

Tan, L., Zhang, K. X., Pecot, M. Y., Nagarkar-Jaiswal, S., Lee, P.-T., Takemura, S.-Y., et al (2015). Ig superfamily ligand and receptor pairs expressed in synaptic partners in drosophila. *Cell* 163, 1756–1769. doi: 10.1016/j.cell.2015.11.021

Tran, N. M., Shekhar, K., Whitney, I. E., Jacobi, A., Benhar, I., Hong, G., et al (2019). Single-cell profiles of retinal ganglion cells differing in resilience to injury reveal neuroprotective genes. *Neuron* 104, 1039.e12–1055.e12. doi: 10.1016/j.neuron.2019.11.006

Voinescu, P. E., Kay, J. N., and Sanes, J. R. (2009). Birthdays of retinal amacrine cell subtypes are systematically related to their molecular identity and soma position. *J. Comp. Neurol.* 517, 737–750. doi: 10.1002/cne.22200

Wässle, H., Puller, C., Müller, F., and Haverkamp, S. (2009). Cone contacts, mosaics and territories of bipolar cells in the mouse retina. *J. Neurosci.* 29, 106–117. doi: 10.1523/JNEUROSCI.4442-08.2009

Wei, W., Hamby, A. M., Zhou, K., and Feller, M. B. (2011). Development of asymmetric inhibition underlying direction selectivity in the retina. *Nature* 469, 402–406. doi: 10.1038/nature09600

Wickersham, I. R., and Feinberg, E. H. (2012). New technologies for imaging synaptic partners. *Curr. Opin. Neurobiol.* 22, 121–127. doi: 10.1016/j.conb.2011.12.001

Wickersham, I. R., Finke, S., Conzelmann, K.-K., and Callaway, E. M. (2007a). Retrograde neuronal tracing with a deletion-mutant rabies virus. *Nat. Methods* 4, 47–49. doi: 10.1038/nmeth999

Wickersham, I. R., Lyon, D. C., Barnard, R. J. O., Mori, T., Finke, S., Conzelmann, K.-K., et al (2007b). Monosynaptic restriction of transsynaptic tracing from single, genetically targeted neurons. *Neuron* 53, 639–647. doi: 10.1016/j.neuron.2007.01.033

Williams, M. E., Wilke, S. A., Daggett, A., Davis, E., Otto, S., Ravi, D., et al (2011). Cadherin-9 regulates synapse-specific differentiation in the developing hippocampus. *Neuron* 71, 640–655. doi: 10.1016/j.neuron.2011.06.019

Xu, C., Theisen, E., Maloney, R., Peng, J., Santiago, I., Yapp, C., et al (2019). Control of synaptic specificity by establishing a relative preference for synaptic partners. *Neuron* 103, 865.e7–877.e7. doi: 10.1016/j.neuron.2019.06.006

Xu, S., Xiao, Q., Cosmanescu, F., Sergeeva, A. P., Yoo, J., Lin, Y., et al (2018). Interactions between the Ig-superfamily proteins DIP-α and dpr6/10 regulate assembly of neural circuits. *Neuron* 100, 1369.e6–1384.e6. doi: 10.1016/j.neuron.2018.11.001

Yamagata, M., and Sanes, J. R. (2008). Dscam and sidekick proteins direct lamina-specific synaptic connections in vertebrate retina. *Nature* 451, 465–469. doi: 10.1038/nature06469

Yamagata, M., and Sanes, J. R. (2010). Synaptic localization and function of sidekick recognition molecules require MAGI scaffolding proteins. *J. Neurosci.* 30, 3579–3588. doi: 10.1523/jneurosci.6319-09.2010

Yamagata, M., and Sanes, J. R. (2012). Transgenic strategy for identifying synaptic connections in mice by fluorescence complementation (GRASP). *Front. Mol. Neurosci.* 5:18.doi: 10.3389/fnmol.2012.00018

Yamagata, M., and Sanes, J. R. (2018). Expression and roles of the immunoglobulin superfamily recognition molecule sidekick1 in mouse retina. *Front. Mol. Neurosci.* 11:485. doi: 10.3389/fnmol.2018.00485

Yamagata, M., Weiner, J. A., and Sanes, J. R. (2002). Sidekicks: synaptic adhesion molecules that promote lamina-specific connectivity in the retina. *Cell* 110, 649–660. doi: 10.1016/s0092-8674(02)00910-8

Yonehara, K., Balint, K., Noda, M., Nagel, G., Bamberg, E., and Roska, B. (2011). Spatially asymmetric reorganization of inhibition establishes a motion-sensitive circuit. *Nature* 469, 407–410. doi: 10.1038/nature09711

Yonehara, K., Farrow, K., Ghanem, A., Hillier, D., Balint, K., Teixeira, M., et al (2013). The first stage of cardinal direction selectivity is localized to the dendrites of retinal ganglion cells. *Neuron* 79, 1078–1085. doi: 10.1016/j.neuron.2013.08.005

Young, R. W. (1985). Cell differentiation in the retina of the mouse. *Anat. Rec.* 212, 199–205. doi: 10.1002/ar.1092120215

Zhang, C., Kolodkin, A. L., Wong, R. O., and James, R. E. (2017). Establishing wiring specificity in visual system circuits: from the retina to the brain. *Annu. Rev. Neurosci.* 40, 395–424. doi: 10.1146/annurev-neuro-072116-031607

Zipursky, S. L., and Sanes, J. R. (2010). Chemoaffinity revisited: dscams, protocadherins and neural circuit assembly. *Cell* 143, 343–353. doi: 10.1016/j.cell.2010.10.009

Conflict of Interest: The authors declare that the research was conducted in the absence of any commercial or financial relationships that could be construed as a potential conflict of interest.

frontiers in Neural Circuits

ORIGINAL RESEARCH
published: 15 October 2020
doi: 10.3389/fncir.2020.00057

Activity-Dependent Remodeling of Synaptic Protein Organization Revealed by High Throughput Analysis of STED Nanoscopy Images

Theresa Wiesner[1], *Anthony Bilodeau*[1†], *Renaud Bernatchez*[1†], *Andréanne Deschênes*[1], *Bastian Raulier*[1], *Paul De Koninck*[1,2*] *and Flavie Lavoie-Cardinal*[1,3*]

[1] CERVO Brain Research Centre, Québec, QC, Canada, [2] Department of Biochemistry, Microbiology and Bioinformatics, Université Laval, Québec, QC, Canada, [3] Department of Psychiatry and Neuroscience, Université Laval, Québec, QC, Canada

The organization of proteins in the apposed nanodomains of pre- and postsynaptic compartments is thought to play a pivotal role in synaptic strength and plasticity. As such, the alignment between pre- and postsynaptic proteins may regulate, for example, the rate of presynaptic release or the strength of postsynaptic signaling. However, the analysis of these structures has mainly been restricted to subsets of synapses, providing a limited view of the diversity of synaptic protein cluster remodeling during synaptic plasticity. To characterize changes in the organization of synaptic nanodomains during synaptic plasticity over a large population of synapses, we combined STimulated Emission Depletion (STED) nanoscopy with a Python-based statistical object distance analysis (pySODA), in dissociated cultured hippocampal circuits exposed to treatments driving different forms of synaptic plasticity. The nanoscale organization, characterized in terms of coupling properties, of presynaptic (Bassoon, RIM1/2) and postsynaptic (PSD95, Homer1c) scaffold proteins was differently altered in response to plasticity-inducing stimuli. For the Bassoon - PSD95 pair, treatments driving synaptic potentiation caused an increase in their coupling probability, whereas a stimulus driving synaptic depression had an opposite effect. To enrich the characterization of the synaptic cluster remodeling at the population level, we applied unsupervised machine learning approaches to include selected morphological features into a multidimensional analysis. This combined analysis revealed a large diversity of synaptic protein cluster subtypes exhibiting differential activity-dependent remodeling, yet with common features depending on the expected direction of plasticity. The expanded palette of synaptic features revealed by our unbiased approach should provide a basis to further explore the widely diverse molecular mechanisms of synaptic plasticity.

Keywords: super-resolution microscopy, synaptic plasticity, synaptic proteins, quantitative image analysis, synapse organization, unsupervised machine learning

OPEN ACCESS

Edited by:
Jean-Claude Béïque,
University of Ottawa, Canada

Reviewed by:
Thomas A. Blanpied,
University of Maryland, Baltimore, United States
Eric Hosy,
UMR5297 Institut Interdisciplinaire de Neurosciences (IINS), France
Valentin Nägerl,
UMR5297 Institut Interdisciplinaire de Neurosciences (IINS), France

***Correspondence:**
Paul De Koninck
paul.dekoninck@neurosciences.ulaval.ca
Flavie Lavoie-Cardinal
flavie.lavoie-cardinal@cervo.ulaval.ca

† These authors have contributed equally to this work

Received: *15 March 2020*
Accepted: *29 July 2020*
Published: *15 October 2020*

Citation:
Wiesner T, Bilodeau A, Bernatchez R, Deschênes A, Raulier B, De Koninck P and Lavoie-Cardinal F (2020) Activity-Dependent Remodeling of Synaptic Protein Organization Revealed by High Throughput Analysis of STED Nanoscopy Images. Front. Neural Circuits 14:57. doi: 10.3389/fncir.2020.00057

1. INTRODUCTION

Learning and memory at the molecular level is characterized by a remodeling of protein organization at synapses. Neurons can have several thousands of synapses, which contain a dense assembly of a wide diversity of proteins (Micheva et al., 2010). The wealth of the synaptic proteome gives rise to supercomplexes of structural and functional proteins that encode synaptic function through multiple signaling cascades (Frank and Grant, 2017). This allows synapses to respond to a rich variety of stimuli and therefore shape circuit activity (Branco and Staras, 2009). Hence, to understand the molecular mechanisms underlying learning and memory at the circuit level, the heterogeneous synaptic population, beyond the individual synapses, needs to be considered.

Fluorescence labeling combined with optical nanoscopy allows different protein species to be discriminated and their organization to be resolved into subsynaptic nanodomains. Groundbreaking studies using STochastic Optical Reconstruction Microscopy (STORM) on dissociated and slice cultures described the highly organized nano-architecture of synaptic proteins (Dani et al., 2010; Nair et al., 2013; Tang et al., 2016). Further studies have described the nanometric arrangement of several proteins at excitatory and inhibitory synapses, ranging from glutamatergic receptors and scaffold proteins to transsynaptic adhesion proteins, and assessed their activity-dependent re-organization (Nair et al., 2013; Broadhead et al., 2016; Glebov et al., 2016, 2017; Tang et al., 2016; Haas et al., 2018; Hruska et al., 2018; Crosby et al., 2019). However, a particular challenge for quantitative assessment of synaptic remodeling with microscopy is that the changes in synaptic strength are heterogeneously distributed across the neuron and are expressed in diverse forms (Edelmann et al., 2017), such that selection of regions of interest (ROIs) can bias the results. Thus, exploiting an analysis framework that can address synaptic remodeling at the population level and discriminate distinct characteristics of synaptic domains should help to further understand the rules that govern synaptic plasticity.

The identification of pre- and postsynaptic nanodomains or protein clusters is generally performed in manually selected, well-identifiable synapses. This is necessarily influenced by the microscope resolution, labeling quality and specificity, and selected morphological criteria, which can vary across studies. A defining criterion for the identification of a functional synapse has been the presence of pre- and postsynaptic proteins in a close vicinity. Characterization of the organization of pre- and postsynaptic proteins can be performed using several metrics, such as their distance to each other (e.g., Nearest Neighbor Distance), correlation of intensity (Pearson coefficient) and degree of overlap (Manders Overlap coefficient) (Dunn et al., 2011). However, these metrics are sensitive to factors such as signal to noise ratio, labeling density, optical resolution, and signal intensity (Lagache et al., 2018). A further challenge is to determine whether the detected protein clusters are distributed in a spatially organized manner or are randomly distributed to each other (Helmuth et al., 2010; Szoboszlay et al., 2017; Lagache et al., 2018). To address these limitations, distance-based methods that statistically infer spatial association (coupling) between sub-cellular structures have been introduced (Helmuth et al., 2010; Lagache et al., 2013, 2018). Statistical Object Distance Analysis (SODA) was recently developed to analyze automatically and quantitatively the spatial association (coupling) between molecules (or protein clusters) in microscopy images (Lagache et al., 2018). In this approach the distance between protein pairs is measured and the enrichment of protein clusters at a given distance is statistically assessed given the null hypothesis of randomly positioned objects. SODA generates maps of spatially associated (coupled) and randomly positioned clusters (uncoupled), providing quantitative measurements of the association level (coupling index) and of the distance (coupling distance) between two associated objects. This approach allows to compute the probability of finding spatially associated protein cluster pairs at a given distance (coupling probability) (Lagache et al., 2018).

To explore the diversity of activity-dependent remodeling of synaptic proteins at the nanoscale over a large population of synapses, we adapted SODA into Python (pySODA). We used this approach to quantify the coupling properties (probability and distance) of synaptic protein clusters in cultured hippocampal neurons exposed to various stimulation conditions and imaged with STimulated Emission Depletion (STED) microscopy. We applied pySODA to analyse the spatial distribution of different pre- and postsynaptic protein pairs and found them to exhibit variable coupling probabilities and coupling distances. We found that stimuli driving synaptic plasticity caused significant changes in coupling properties for distinct protein pairs. For the protein pair Bassoon and PSD95, both chronic inhibition (leading to synaptic scaling) and an acute stimulus (leading to Long Term Potentiation of synaptic transmission [LTP]) caused an increase in their coupling probability, whereas an acute stimulus leading to Long Term Depression of synaptic transmission (LTD) had an opposite effect. To enrich the characterization of the synaptic cluster remodeling at the population level, we applied unsupervised machine learning approaches to include selected morphological features into a multidimensional analysis. This combined analysis revealed a large diversity of synaptic protein cluster subtypes exhibiting differential activity-dependent changes. Mapping of these changes revealed common features depending on the expected direction of plasticity. Our results provide a new framework to investigate the rich diversity of synaptic remodeling processes from a large population of synapses.

2. MATERIALS AND METHODS

2.1. Cell Culture and Neuronal Stimulations

Dissociated rat hippocampal neurons were prepared as described previously (Nault and De Koninck, 2009). In brief, before dissection of hippocampi, neonatal rats were sacrificed by decapitation, in accordance with procedures approved by the animal care committee of Université Laval. Thereafter, dissociated cells were plated on PDL-Laminin coated glass coverslips (12 mm) in a 24 well plate at a density of 200 cells/mm^2. The growth media consisted of Neurobasal and B27 supplement (50:1) and was supplemented with penicillin/streptomycin (50 U per mL; 50 μg per mL) and

0.5 mM L-GlutaMAX (Invitrogen). Fetal bovine serum (2%; Hyclone) was added at the time of plating. After five days, half of the media was replaced by new media without serum and in which Ara-C (5 μM; Sigma-Aldrich) was added to limit non-neuronal cell proliferation. Thereon the cultures were fed twice a week by replacing half of the growth medium with serum- and Ara-C-free medium.

Acute stimuli to neuronal cultures were performed in HEPES buffered solutions at 37°C at 21-22 DIV. The following solutions were used: high Mg^{2+}/low Ca^{2+} (in mM: NaCl 98, KCl 5, HEPES 10, $CaCl_2$ 0.6, Glucose 10, $MgCl_2$ 5), 0Mg^{2+}/Gly/Bic (in mM: NaCl 104, KCl 5, HEPES 10, $CaCl_2$ 1.2, Glucose 10, $MgCl_2$ 0, Glycine 0.2, Bicuculline 0.01), and Glu/Gly (in mM: NaCl 102, KCl 5, HEPES 10, $CaCl_2$ 1.2, Glucose 10, $MgCl_2$ 1; Glutamate 0.1, Glycine 0.01); Osmolality: 240–250 mOsm/kg, pH: 7.0–7.35. Incubation lasted 10 min for high Mg^{2+}/low Ca^{2+} and 0Mg^{2+}/Gly/Bic treatments and 2 min for Glu/Gly stimulation. After the treatment, the cells were directly transferred in a 4% paraformaldehyde (PFA) solution for fixation (See Fixation and Immunostaining). To induce synaptic scaling TTX (2 μM final concentration, Sigma-Aldrich) was added 48, 24, or 4 h before fixation.

2.2. Fixation and Immunostaining

Cultured hippocampal neurons were fixed at 21-22 DIV for 10 min in freshly prepared 4% PFA solution containing: 4% Sucrose, 100 mM phosphate buffer, 2 mM Na-EGTA. The solution was adjusted to pH 7.4 and used at 37°C. Fixed cells were subsequently washed three times for 5 min with phosphate buffer saline (PBS) supplemented with 100 mM Glycine. Before immunostaining, cells were permeabilized with 0.1% Triton X-100 and blocked with 2% goat serum (GS) for 30 min. Incubation with primary (PAB) and secondary antibody (SAB) was performed in a 0.1% Triton X-100 and 2% GS PBS solution at room temperature (see **Table 1**). PAB were incubated for 2 h followed by 3 washes in PBS. SAB and Oregon Green 488 Phalloidin (Invitrogen (A12379), dilution 1:50) (Baddeley et al., 2011) were incubated for 1 h and finally washed 3 times in PBS. Coverslips were mounted in Mowiol-DABCO for imaging.

2.3. STED Microscopy

STimulated Emission Depletion microscopy (Hell and Wichmann, 1994) was performed on a 4 color Abberior Expert-Line STED system (Abberior Instruments GmbH, Germany), equipped with a 100x 1.4NA oil objective, a motorized stage, and auto-focus unit. Imaging of synaptic proteins labeled with Alexa 594 and STAR 635P was performed with 561 and 640 nm pulsed excitation lasers and a single pulsed 775 nm depletion laser (40 MHz). Fluorescence was detected on two avalanche photodiodes (APD) using a ET685/70 (Chroma, USA) filter for STAR 635P and 615/20 (Semrock, USA) filter for Alexa 594. Phalloidin Oregon Green 488 was excited in confocal mode using a 40 MHz excitation laser at 485 nm and the fluorescence was detected on a third APD with a 525/50 (Semrock, USA) fluorescence filter. Scanning was conducted in a line scan mode with a pixel dwell time of 30μs and pixel size of 15 nm. Line repetitions of 5 and 3 were selected for the STAR 635P and Alexa 594, respectively. Confocal detection pinhole was set around 1 Airy unit. Spectral unmixing was performed using the ImageJ Spectral Unmixing Plugins (Zimmermann et al., 2002; Neher and Neher, 2004; Schindelin et al., 2012). The lateral resolution was approximated by measuring the Full Width at Half Maximum (FWHM) on the fitted line profiles (Lorentzian fit) of 12 isolated protein clusters (STAR 635P : 67.5 nm, SEM 6.7; Alexa 594 nm : 72.6 nm, SEM 8.7).

2.4. SODA Analysis

The Statistical Object Distance Analysis (SODA) algorithm was used to analyze the spatial distribution and relations of synaptic protein clusters in STED images (Lagache et al., 2018). Initially developed as a plugin within the Icy image analysis software (De Chaumont et al., 2012), SODA was adapted as a stand-alone Python analysis routine to improve its integration into other high throughput analysis frameworks. SODA requires binary images of segmented protein clusters for each channel (561 and 640 nm) as well as a mask of the region of interest (ROI) comprising the neuronal processes. To generate the ROI mask, we applied a gaussian blur (standard deviation of 10) on the sum of both STED channels and subsequently thresholded the image using 50% of the mean intensity value. Large fields of view (2,000 μm^2) were acquired and clusters were automatically segmented using wavelet transform decomposition (Olivo-Marin, 2002). The wavelet segmentation parameters (scales 3 and 4) were chosen to discard small low intensity clusters due to non-specific staining and to avoid undesirable separation of clusters. Detected clusters with an area < 5 pixels and a width/height <3 pixels were removed. The weighted centroids of the detected clusters were calculated on the raw STED images and only clusters inside the foreground mask were considered for the SODA analysis.

SODA is based on Ripley's K function (Ripley, 1976) with an additional boundary correction element k (Haase, 1995).

$$\boldsymbol{K(r)} = \frac{\text{Volume of ROI}}{n_1 n_2} \sum_{x,y} 1\left\{d(x,y) \leq r\right\} k(x,y) \qquad (1)$$

where n_i is the number of objects in the channel i. This function is used to count objects that are separated by a distance $d(x, y)$ shorter than a radius r. For SODA, incremental subtractions of the K function for a series of distances r (corresponding to the pixel size of 15 nm in our experiments) are used in order to count objects from different channels that are within specific distance intervals. This creates the vector

$$\boldsymbol{G} = \left[K(r_{i+1}) - K(r_i)\right]_{i=0..N-1} \qquad (2)$$

where N is the number of rings (see **Supplementary Figure 1**). With a large enough amount of objects ($>$100, generally reached in STED imaging of synaptic proteins for a large field of view of 2,000 μm^2), each component G_i of $\boldsymbol{G}$ is normally distributed with mean μ_i and standard deviation σ_i, forming vectors $\boldsymbol{\mu}$ and $\boldsymbol{\sigma}$. The reduced Ripley's vector

$$\boldsymbol{G^0} = \frac{1}{\boldsymbol{\sigma}} \boldsymbol{A}^{-1} \cdot [\boldsymbol{G} - \boldsymbol{\mu}] \qquad (3)$$

TABLE 1 | Primary and secondary antibodies used for STED imaging.

Primary antibodies					
Antibody	**Company**	**Catalogue no.**	**Dilution**	**Epitope**	**Reference**
Mouse anti-PSD95 (6G6-1C9)	Abcam	MA1-045	1 : 500	Purified recombinant rat PSD-95	Ladépêche et al. (2018)
Mouse anti-Bassoon	Enzo	ADI-VAM-PS003	1 : 500	AA 3569 to 3769 from rat Bassoon	Dani et al. (2010); Tang et al. (2016)
Rabbit anti-Bassoon	Synaptic Systems	141003	1 : 500	AA 3569 to 3769 from rat Bassoon	Dani et al. (2010)
Rabbit anti-Homer1c	Synaptic Systems	160023	1 : 500	AA 152 to 354 from human Homer1b/c	Lagache et al. (2018)
Rabbit anti-RIM1/2	Synaptic Systems	140203	1 : 500	AA 1 to 466 from rat Rim2	Dani et al. (2010); Tang et al. (2016)
Rabbit anti-KCC2	Millipore	07-432	1 : 1000	residues 932-1043 of rat KCC2	Doyon et al. (2011)
Secondary Antibodies					
Antibody	**Company**	**Catalogue no.**	**Dilution**		**Reference**
GAM STAR 635P	Abberior	2-0002-007-5	1 : 250		Durand et al. (2018)
GAM Alexa 594	Thermofisher	A11005	1 : 100		Durand et al. (2018)
GAR STAR 635P	Abberior	2-0012-007-5	1 : 250		Durand et al. (2018)
GAR Alexa 594	Thermofisher	A11037	1 : 100		Di Biase et al. (2009)

is used to detect these enriched rings, where $\boldsymbol{A}$ is a matrix that corrects for the overlap between rings. Only elements of $\boldsymbol{G^0}$ that are higher than a universal threshold $T(N) = 2\log(N)$ (Donoho et al., 1997) are deemed significant and are conserved; the other elements are set to 0. The coupling probability $P(x, y)$ for each pair of objects (x, y) in different channels can then be calculated with

$$P(x,y) = \sum_{i=0}^{N-1} 1\left\{r_i < d(x,y) \leq r_{i+1}\right\} \frac{\sigma_i G_i^0 1\left\{G_i^0 > T(N)\right\}}{G_i} \quad (4)$$

where 1{} is the Iverson bracket and equals 1 if the inequality inside the brackets is true and 0 otherwise.

In our pySODA workflow, 16 rings with a width of 15 nm were used, for a maximal distance of 240 nm, which is further than the largest distance described between synaptic elements such as Bassoon and Homer1c (Dani et al., 2010).

2.5. Multidimensional Analysis

Multidimensional analysis was performed on all acquired 2-color images of PSD95 and Bassoon. Analysis was performed independently for chronic (Naive, 48 h TTX) and acute (high Mg^{2+}/low Ca^{2+}, $0Mg^{2+}$/Gly/Bic, Glu/Gly) stimuli. Only coupled clusters were considered. Morphological features were obtained from the detected clusters in the wavelet segmented image consisting in : (1) area, (2) eccentricity, (3) perimeter, (4) major, and (5) minor axis length. These were further combined with the coupling distance and probability that were obtained from the pySODA analysis, resulting in a 7 dimensional feature space. All features were normalized to [0, 1] range using a min-max scaling. A Uniform Manifold Approximation and Projection (UMAP) was used to embed the 7-dimensional feature space onto a 2-dimensional plane (McInnes et al., 2018). UMAP analysis was performed using the provided Python implementation of this dimension reduction technique. We used a number of 25 neighbors to make a compromise between local and broad structure in the input feature space. A minimal distance of 0.05 in the embedded space was used to avoid compressing points together too tightly and allow more sparse local structures.

The embedded feature space was characterized by estimating the density of points using a bivariate kernel density estimation (KDE) of the UMAP for each stimuli. Ten uniformly spaced contour levels were generated for visualization. The local average cluster features (morphological, distance and coupling) was overlaid on the KDE maps to give better insight into each feature's evolution. Hence, it allowed an improved visualization of the remodeling that occurs during stimulation and therefore enabled correlation of feature changes with activity. Local maxima in the KDE map, depicting different subtypes of synapses, were identified and their position was estimated using *peak_local_max* implemented in Scikit-Image (van der Walt et al., 2014). The average features from each local maximum were extracted to create a 7-dimensional vector describing each local maximum, termed synaptic subtype, in the KDE plot.

To group synaptic subtypes with similar features, agglomerative hierarchical grouping (also referred to as hierarchical clustering) was performed using the feature vector corresponding to each local maximum of the KDE plots. The *AgglomerativeClustering* function from Scikit-Learn with euclidean affinity and Ward linkage was used to perform hierarchical grouping (Pedregosa et al., 2011). We calculated the number of groups (synaptic subtypes) that best describe our data based on maximization of the silhouette score, a measure of similarity within a group and dissimilarity between different groups (Rousseeuw, 1987; Zhao et al., 2018).

To investigate the association between the groups identified with hierarchical grouping in the acute and chronic stimulation datasets, we projected all instances (detected protein clusters) of one dataset onto the other dataset and vice versa. We used the Euclidean distance to assign each detected protein cluster to one group. With this approach, we computed the proportion of detected protein clusters of one dataset belonging to each

synaptic subtype in the feature space of the other dataset (see **Figures 8B,C**).

2.6. Statistical Analysis

Statistical analysis on cumulative frequency curves (CF) and histograms (H) was performed using a randomization test with the null hypothesis being that the different conditions (A, B) belong to the same distribution. The absolute difference between mean values of A and B was calculated for each bin of the CF or H ($D_{gt} = |\mu_A - \mu_B|$).

For the randomization test, each value belonging to A and B was randomly reassigned to A' and B', with the sizes of A' and B' being N_A and N_B, respectively. The absolute difference between the mean values of A' and B' was determined ($D_{rand} = |\mu_{A'} - \mu_{B'}|$) and the randomization test was repeated 10,000 times. The obtained distribution was compared with the absolute difference of the mean of A and B (D_{gt}) to verify the null hypothesis.

When the number of groups was greater than two, the F-statistic was sampled from each group using a resampling method. The F-statistic was calculated from each group (A, B, C, etc.) as a ground truth (F_{gt}). Each value of the CF or H was randomly re-assigned to new groups (A', B', C', etc.) where group X' has the same size as group X. The F-statistic from each newly formed group (F_{rand}) was calculated and we repeated this process 10,000 times. We compared F_{rand} with F_{gt} to confirm the null hypothesis that the groups have the same mean distribution. When the null hypothesis was rejected, i.e. at least one group did not have the same mean distribution, we compared each group in a one-to-one manner using the randomization test described above. In all cases, a confidence level of 0.05 was used to reject the null hypothesis (**Supplementary Figures 4, 6, 8, 9, 18, 21**).

To calculate the statistical difference between synaptic subtypes, a Chi-square test was used, followed by a *post-hoc* Chi-square test comparing each synaptic subtype with all other subtypes (**Supplementary Tables 2, 4, 6, 8**).

2.7. Localization Error

The weighted centroid of the synaptic clusters was calculated from the intensity image and the synaptic cluster shape using the *weighted_centroid* attributes of the *regionprops* method implemented in Scikit-Image (van der Walt et al., 2014). Hence, a localization error is arising from the uncertainty of the number of counts in the intensity image. The STED setup uses a single photon counting module (Excelitas Technologies, SPCM-AQRH-13) which has an uncertainty on the number of counts of 0.5%. Therefore, using the general error propagation equation one can calculate the uncertainty of localization of the weighted centroid. The calculated localization error is 3 nm.

3. RESULTS

3.1. Quantitative Assessment of Synaptic Protein Coupling Properties at the Population Level

To examine the nanometric distribution of synaptic proteins, we fixed 21-22 DIV primary cultured rat hippocampal neurons and immunostained them for pre- (Bassoon, RIM1/2) and postsynaptic (Homer1c, PSD95) scaffold proteins. We performed two-color STED microscopy of these protein pairs combined with confocal imaging of the F-actin cytoskeleton (stained with Phalloidin-Oregon Green 488) to highlight proximal dendrites with spines (**Figure 1A**).

To quantify the spatial organization of the protein pairs, we implemented SODA in Python (pySODA). Protein clusters were segmented using wavelet transform, and a foreground mask was generated with a gaussian kernel convolution on the sum of both STED channels (see section Materials and Methods and **Figures 1B,C**). Using the pySODA framework, the coupling properties between synaptic scaffold protein pairs were calculated (Lagache et al., 2018) (**Supplementary Figure 1**). The coupling probability was determined for each cluster from the statistical analysis of the measured distances between neighboring clusters of different channels (see section Materials and Methods and **Supplementary Figure 1**). Coupled clusters were identified when the probability of localizing two synaptic partners at a given distance was greater than the statistical threshold (Lagache et al., 2018) (**Figures 1D,E**, **Supplementary Figure 1**, and section Materials and Methods). For each synaptic cluster, pySODA identified neighboring clusters found within concentric rings spaced 15 nm apart (pixel size of the STED images), providing distance-dependent coupling probabilities (**Supplementary Figure 1** and section Materials and Methods).

We first assessed the performance of pySODA by measuring the coupling probability of presynaptic Bassoon clusters that were concurrently marked with two distinct secondary antibodies labeled with the fluorophores Alexa 594 and STAR 635P, respectively. As expected for antibodies targeting the same protein, a maximal coupling probability of 0.98 was calculated for clusters found within 15 nm (**Supplementary Figures 2A,B**). We next evaluated the coupling probability between the presynaptic protein Bassoon and the membrane receptor KCC2 (reported not to be enriched at synapses in basal conditions) (Doyon et al., 2011). As expected, even though the cluster density of KCC2 is high, the calculated coupling probability for Bassoon - KCC2 was very low (0.05, SEM 0.03) and was only above the statistical threshold for clusters spaced by more than 200 nm (**Supplementary Figures 2C,D**). We also tested whether the increased resolution provided by STED, as compared to confocal microscopy, was necessary for assessing the association between synaptic proteins using the pySODA analysis. We found that the confocal resolution (approximately 235 nm) is not sufficient for such analysis (**Supplementary Figure 3**).

Next, we used pySODA to characterize four different pairs of pre- and postsynaptic scaffold proteins: (1) Bassoon and RIM1/2 (presynaptic), (2) PSD95 and Homer1c (postsynaptic), (3) Bassoon and PSD95 (transsynaptic), and (4) Bassoon and Homer1c (transsynaptic) (**Figures 2A,B**). Both Bassoon - RIM1/2 and PSD95 - Homer1c protein pairs show maximal coupling probability (CP) between 30 and 45 nm (CP Bassoon - RIM1/2: 0.88, SEM 0.01; CP PSD95 - Homer1c: 0.83, SEM 0.01) (**Figure 2C**), consistent with the distances measured between these protein pairs with STORM (Dani et al., 2010). Though a similar distribution of coupling distances was calculated for

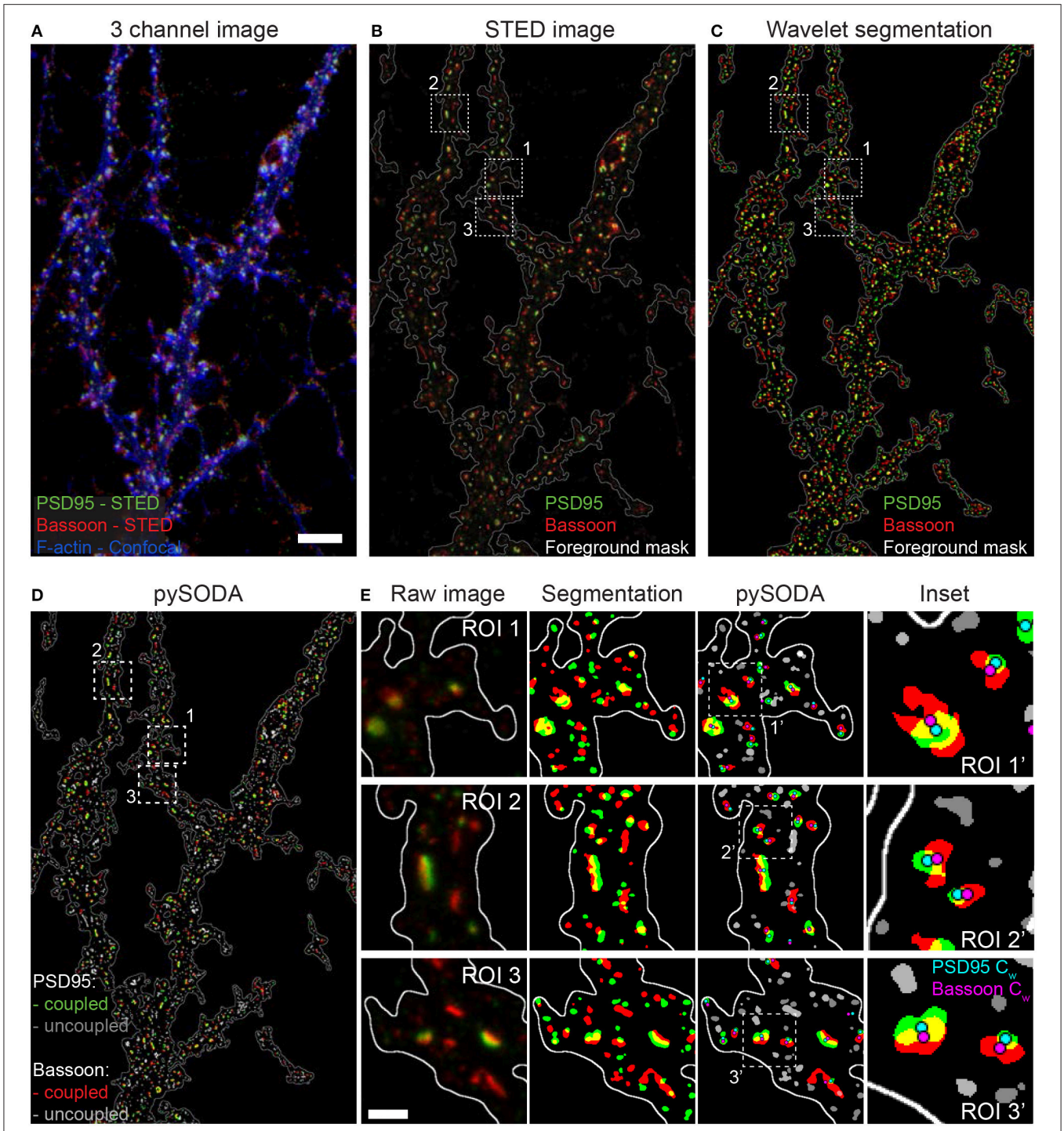

FIGURE 1 | Statistical object distance analysis (SODA) of two-color STED images of the scaffold protein pair PSD95 and Bassoon. **(A)** 3 channel image of a neuron stained with Bassoon-STAR 635P (red), PSD95-Alexa 594 (green) with the corresponding confocal image of Phalloidin-Oregon Green 488 (blue). To better distinguish low intensity clusters combined with the F-actin staining, a log intensity scale was used. **(B)** Raw 2-color STED image (linear intensity scale) showing the region boundaries used for SODA analysis (white contour line). **(C)** Segmented clusters, within the region boundaries, of PSD95 (green) and Bassoon (red) using wavelet transform. **(D)** pySODA analysis of the image shown in **(C)**. Coupled (Bassoon-red, PSD95-green) and uncoupled (Bassoon-light gray, PSD95-dark gray) clusters identified with the pySODA analysis approach. **(E)** Representative regions of interest (ROI) from the image shown in **(D)** (Insets 1-3) showing the raw 2-color STED images *(left)*, the corresponding segmented clusters within the foreground mask *(middle-left)* as well as the coupled and uncoupled clusters identified with pySODA *(middle-right)* and enlarged insets (ROI') from the pySODA map *(right)*. Cyan (PSD95 C_w) and magenta (Bassoon C_w) circles represent the weighted centroids of coupled clusters *(right)*. Scale bars: 5 μm **(A)**, 500 nm **(E)**.

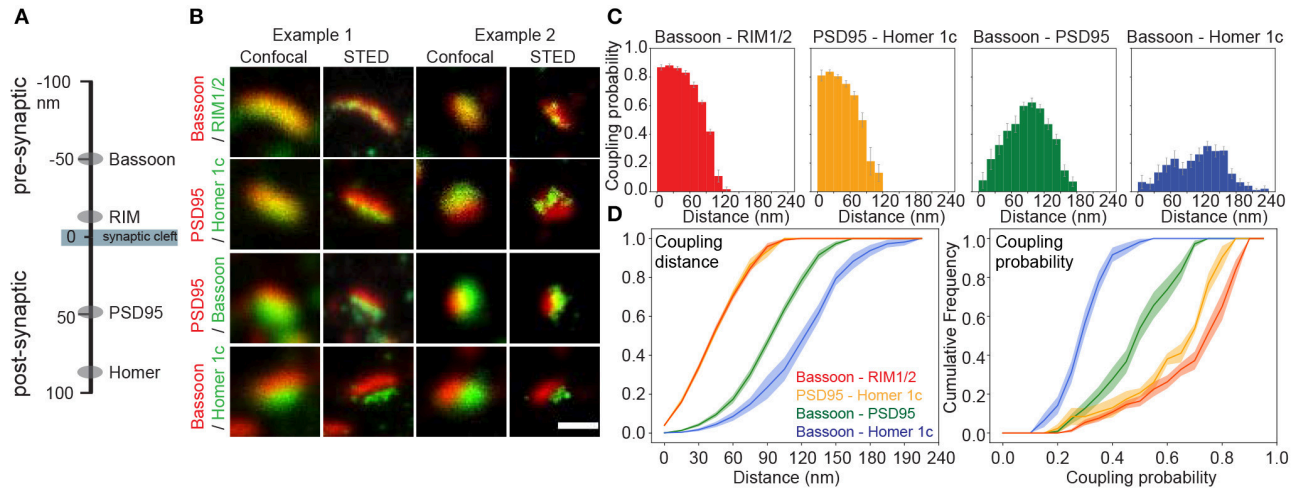

FIGURE 2 | Coupling properties of synaptic scaffold protein pairs at low neuronal activity measured with pySODA. **(A)** Schematic representation of the axial positions of the four synaptic scaffold proteins analyzed in this work. **(B)** Two examples of representative confocal and STED images of synaptic scaffold pairs. **(C)** Coupling probability and distance histograms measured for coupled cluster pairs of Bassoon - RIM1/2 (red, $n = 16$), PSD95 - Homer1c (yellow, $n = 6$), Bassoon - PSD95 (green, $n = 18$), Bassoon - Homer1c (blue, $n = 17$). Each 15 nm bin represents the average coupling probability calculated from the individual images of independent neurons with standard error. **(D)** Cumulative frequency plots of coupling distance *(left)* and coupling probability *(right)* for each synaptic element pair with standard error (shaded area). **(C,D)** n = number of neurons from 2 independent cultures. Statistical difference between scaffold protein pairs was assessed using a randomization test (see section Materials and Methods and **Supplementary Figure 4**). Scale bar 250 nm.

Bassoon - RIM1/2 and PSD95 - Homer1c pairs (**Figure 2D**, left), the distribution of coupling probabilities for Bassoon - RIM1/2 is shifted to higher levels (**Figure 2D**, right and **Supplementary Figure 4A**). This suggests a more organized distribution of Bassoon and RIM1/2 clusters compared to PSD95 and Homer1c.

Since proteins involved in synaptic transmission are thought to be strategically apposed on each side of the cleft (Tang et al., 2016), we examined the coupling properties of two pairs: Bassoon - PSD95 and Bassoon - Homer1c. The highest coupling probability for Bassoon - PSD95 is at a distance of 90–105 nm (CP 0.62, SEM 0.03), while it is between 120 and 135 nm (CP 0.32, SEM 0.03) for Bassoon - Homer1c (**Figure 2C**), in accordance with distances reported for these proteins (Dani et al., 2010). For Bassoon, the coupling probability was significantly higher with PSD95 than with Homer1c (**Figures 2C,D** and **Supplementary Figure 4F**). Indeed >60% of Bassoon - PSD95 couples showed a coupling probability >0.5, while it is only the case for 2% of the Bassoon - Homer1c couples (**Figure 2D**). These results suggest higher spatial organization between Bassoon and PSD95, as compared to Homer1c. The coupling probability of the transsynaptic partners, as compared to that of the pre- or postsynaptic protein pairs, is necessarily reduced by the fact that a certain proportion of the detected synaptic protein clusters are not part of a functional synapse (i.e., not associated with a pre- or postsynaptic counterpart) (**Figure 2C**).

Our pySODA framework confirms previous observations regarding the measured distance between synaptic scaffold elements (Dani et al., 2010), while characterizing the coupling properties of the different protein pairs. We thus aimed to use this unbiased approach to analyze synaptic cluster organization at the population level under conditions affecting synaptic plasticity.

3.2. Activity-Dependent Stimuli Modulate Coupling Properties of Synaptic Protein Pairs

Recent studies have shown that manipulation of synaptic strength in dissociated cultures can re-organize synaptic scaffold proteins at the nanoscale (Fukata et al., 2013; Tang et al., 2016; Hruska et al., 2018). An increase in synaptic strength can be induced in cultured hippocampal neurons using brief applications of an external solution containing no Mg^{2+}, 200 μM glycine and 10 μM bicuculline (0Mg^{2+}/Gly/Bic), which drives strong synaptic NMDA receptor activation (Lu et al., 2001; Arnold et al., 2005). We assessed whether such a stimulation alters the coupling properties of synaptic scaffold proteins, by incubating the neurons for 10 min in 0Mg^{2+}/Gly/Bic or in an activity-reducing solution containing 5 mM Mg^{2+} and 0.6 mM Ca^{2+} (high Mg^{2+}/low Ca^{2+}) prior to fixation (see section Materials and Methods) (Lu et al., 2001; Bayer et al., 2006).

For the Bassoon - RIM1/2 cluster pairs, identified as coupled with pySODA, the mean coupling distance was 59 nm in high Mg^{2+}/low Ca^{2+} and remained unchanged upon a 0Mg^{2+}/Gly/Bic stimulation (61 nm, **Figures 3A,B** and **Supplementary Figure 5**). For both conditions, more than 50% of the coupled Bassoon - RIM1/2 clusters exhibited a coupling probability >0.75, suggesting that the eminent spatial organization of the presynaptic pair is not affected by neuronal activity (**Figures 3C,D**). By

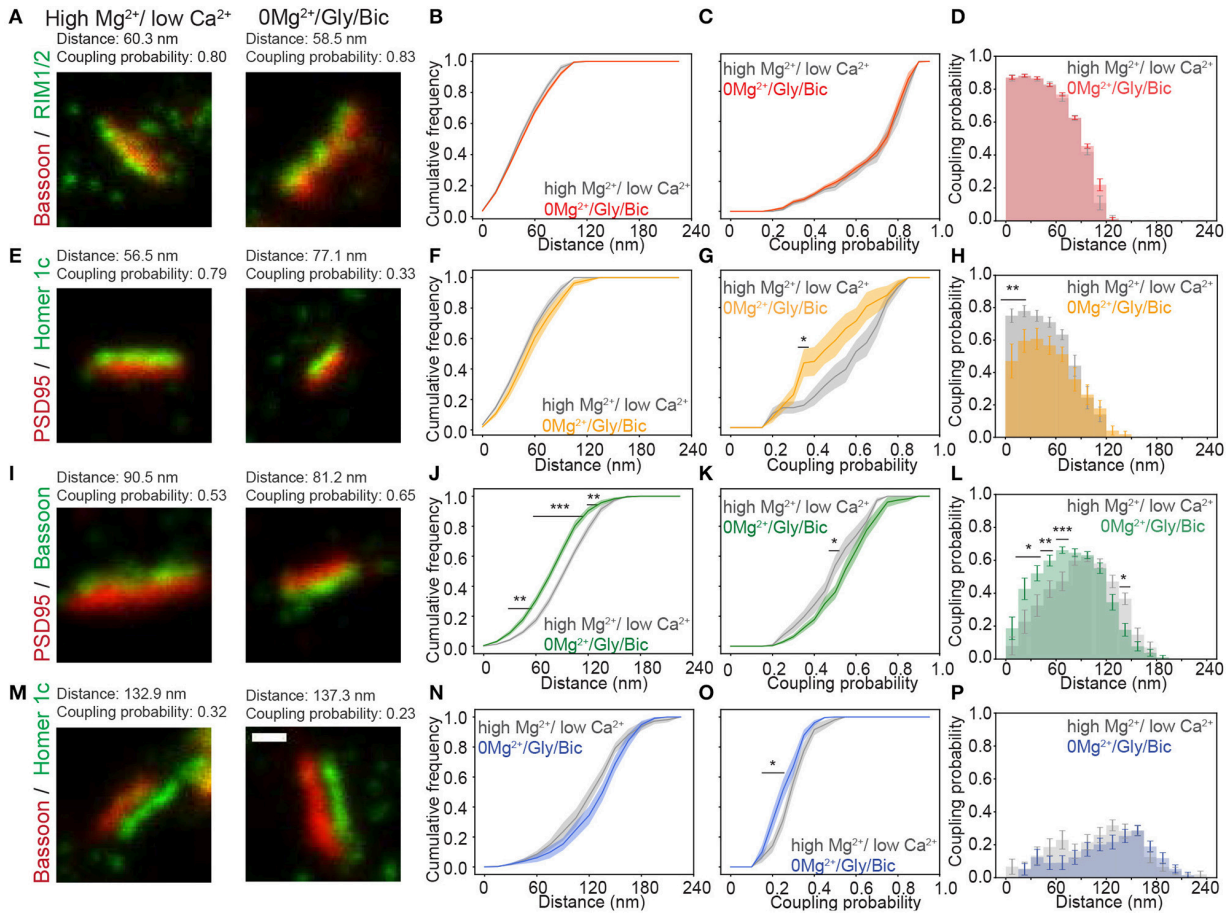

FIGURE 3 | Activity-dependent re-organization of pre- and postsynaptic scaffolding protein pairs measured with the pySODA analysis framework. **(A,E,I,M)** Representative two-color STED images of synaptic protein pairs for the activity reducing high Mg^{2+}/low Ca^{2+} condition *(left)* or synaptic stimulation $0Mg^{2+}$/Gly/Bic *(right)*. Cumulative frequency graphs of the coupling distance **(B,F,J,N)** and of the coupling probability **(C,G,K,O)** measured for coupled protein pairs. **(D,H,L,P)** Histograms of the mean coupling probability per neuron at a given distance. Measurements were performed on two-color STED images of **(A–D)** the presynaptic protein pair Bassoon - RIM1/2 (High Mg^{2+} / low Ca^{2+}(gray): $n = 16$ and $0Mg^{2+}$/Gly/Bic (red): $n = 21$); **(E–H)** the postsynaptic protein pair PSD95 - Homer1c (high Mg^{2+} / low Ca^{2+}(gray): $n = 9$ and $0Mg^{2+}$/Gly/Bic (orange): $n = 12$); **(I–L)** the transsynaptic pair Bassoon - PSD95 (High Mg^{2+}/ low Ca^{2+}(gray): $n = 18$ and $0Mg^{2+}$/Gly/Bic (green): $n = 24$) and **(M–P)** the transsynaptic pair Bassoon - Homer1c (High Mg^{2+}/ low Ca^{2+}(gray): $n = 17$ and $0Mg^{2+}$/Gly/Bic (blue): $n = 17$). Shown are the means (plain lines) with standard error (shaded area). n = number of neurons from 3 independent cultures. Statistical difference was assessed using a randomization test (see section Materials and Methods and **Supplementary Figure 6**). Exact p-values are reported in **Supplementary Figure 6**, with $^{*}p < 0.05$, $^{**}p < 0.01$, and $^{***}p < 0.001$. Scale bar 250 nm.

contrast, there was an activity-dependent increase of the mean coupling distance between PSD95 and Homer1c (**Figures 3E,F** and **Supplementary Figure 5**), which was associated with a reduced coupling probability (statistically significant for clusters separated by less than 30 nm) (**Figures 3G,H** and **Supplementary Figure 6B**). Thus, these two pairs of proteins exhibit different activity-dependent re-organization.

We next assessed whether neuronal activity affects the coupling properties between the transsynaptic protein pairs : (1) Bassoon - PSD95 and (2) Bassoon - Homer1c. For Bassoon and PSD95, increasing neuronal activity yielded a larger population of couples characterized by a smaller coupling distance, combined with an increased coupling probability (**Figures 3I–L**). Indeed, in the $0Mg^{2+}$/Gly/Bic condition, a significantly higher coupling probability was calculated for coupling distances between 15 and 75 nm (**Figure 3L**), while the mean distance between coupled cluster pairs was significantly decreased from 106 to 93 nm (**Supplementary Figures 5, 6C**). By contrast, synaptic stimulation increased the mean coupling distance between Bassoon and Homer1c and decreased their coupling probability (**Figures 3M–P** and **Supplementary Figure 5**). This decrease is consistent with the reduction of the coupling probability measured for the postsynaptic pair Homer1c - PSD95 (**Figure 3G**). These results suggest that the synaptic distributions of Homer1c with respect to other synaptic scaffolding proteins is regulated by activity. Our results thus show that pySODA is sufficiently sensitive to reveal activity-dependent changes in coupling properties between scaffold protein pairs at the population level.

3.3. The Coupling Properties and Morphological Features of Bassoon and PSD95 Are Differently Affected by Long Term Potentiation- or Depression-Inducing Stimuli

In cultured neurons, while the synaptic NMDA receptor stimulation ($0Mg^{2+}$/Gly/Bic) can induce LTP, stimulation of extrasynaptic NMDA receptors can induce LTD (Carroll et al., 1999; Lu et al., 2001). We thus assessed the impact of these LTP- or LTD-inducing stimuli on the coupling properties of the Bassoon - PSD95 pair, by fixing the neuronal cultures immediately after a 10 min $0Mg^{2+}$/Gly/Bic or 2 min Glu/Gly stimulation.

As shown in the previous section, $0Mg^{2+}$/Gly/Bic stimulation compared to the high Mg^{2+}/low Ca^{2+} condition resulted in an increase of the coupling probability and a reduction of the mean coupling distance of Bassoon and PSD95 (**Figures 3J–L** and **Supplementary Figure 7**). In contrast, the Glu/Gly stimulation led to a reduction in both the coupling probability and the mean coupling distance (**Figures 4A,B** and **Supplementary Figures 7,8**). These results suggest that while an LTP-inducing stimulus tends to increase the spatial organization between PSD95 and Bassoon, the LTD-inducing stimulus has an opposite effect toward more randomly distributed cluster pairs (**Figure 4B** and **Supplementary Figure 8**).

Our results thus far described the activity-dependent changes in coupling properties of synaptic scaffold proteins at the population level. Characterizing additional morphological features of synaptic scaffold protein clusters would be beneficial to appreciate the diversity of the remodeling and to understand further synaptic plasticity (Lagache et al., 2018). We thus added quantitative morphological feature measurements of the Bassoon - PSD95 cluster pairs to the coupling properties analysis. Previous studies (Harris et al., 1992; Matsuzaki et al., 2004) have shown a positive correlation between synaptic strength, spine volume and PSD area. We therefore wondered how the observed changes in coupling probability are reflected in the area and eccentricity of the Bassoon and PSD95 clusters, as well as on their spatial distribution in dendritic shafts and spines. We observed opposing effects of the two stimulation paradigms, with the Glu/Gly treatment decreasing significantly the size of both Bassoon and PSD95 couples (**Figures 4C,D** and **Supplementary Figure 9**) and with the $0Mg^{2+}$/Gly/Bic stimulation increasing of the size of PSD95 clusters (**Figure 4D** and **Figure S9**), which was independent from the cluster density (**Supplementary Figure 10**). In accordance with previous reports (Colledge et al., 2003; Chowdhury and Hell, 2019), we also observed a similar trend in the cluster intensity of coupled PSD95 clusters (**Supplementary Figure 11A**). We found a higher proportion of coupled Bassoon and PSD95 clusters within spines compared to the dendritic shafts (**Supplementary Figure 12**).

To enrich the characterization of synaptic features in our analysis, we included for each cluster, in addition to the (i) coupling probability and (ii) coupling distance, the (iii) area, (iv) eccentricity, (v) minor axis length, (vi) major axis length, and (vii) perimeter (see section Materials and Methods). To visualize the impact of the different stimulation protocols on these features, we used the dimension reduction technique Uniform Manifold Approximation and Projection (UMAP), which can be used to visualize a high dimensional dataset in a 2-dimensional space (**Figure 4E**) (McInnes et al., 2018). Local maxima on the Kernel Density Estimate plots (KDE) generated from the scatterplot of the UMAP embedding for each stimulation paradigm were used to identify the major categories of Bassoon and PSD95 clusters (synaptic subtypes) for each stimulation condition (**Figure 4F** and **Supplementary Figure 13**). This yielded a wide range of Bassoon and PSD95 cluster subtypes exhibiting different morphological features and coupling properties (**Supplementary Figures 14, 15**). To identify the synaptic subtypes that are most prominent across the stimulation conditions, we used agglomerative hierarchical grouping (also known as hierarchical clustering) (**Figures 5A,B**, **Supplementary Figures 16, 17**, and section Materials and Methods). This approach allows to group observations in a way that the similarity within a group (in our case synaptic protein pairs belonging to one synaptic subtype) is maximized and that the dissimilarity between groups (synaptic subtypes) is also maximized. We relied on the maximization of the silhouette score (Rousseeuw, 1987), a measure of similarity within groups, to determine the number of synaptic cluster subtypes that best describe the properties of the detected protein clusters at the population level and across stimulation conditions (**Supplementary Figures 16, 17**, and section Materials and Methods). With this approach we identified 12 main groups, which we refer to as synaptic subtypes, for Bassoon and 8 for PSD95 protein clusters (**Figures 5A–D**). We next measured the euclidean distance between each detected protein cluster and the synaptic subtypes in the multidimensional feature space (comprising morphological features and coupling properties). This allowed to assign each detected cluster to one main subtype and to quantify the prevalence of the synaptic subtypes for each stimulation condition (**Figures 5E–H** and **Supplementary Tables 1, 3**).

This analysis revealed that the coupling properties and morphological features of coupled Bassoon - PSD95 pairs are not directly correlated. For example, similar coupling probabilities (e.g., $ST_{Bassoon}$1-4, CP 0.48–0.55) were associated with a large range of mean coupling distances (53–100 nm) and cluster eccentricities (0.41–0.83), (**Supplementary Tables 1, 3**). Indeed, the population of coupled Bassoon and PSD95 clusters can be described by subtypes exhibiting a large diversity of complementary coupling and morphological features (**Figures 5A–D**).

Using this approach we identified three levels of coupling for the detected synaptic subtypes : (1) weak coupling (CP $<$ 0.5), (2) moderate coupling (0.5 $>$ CP $<$ 0.7), and (3) strong coupling (CP $>$ 0.7) (**Figures 5A,B** and **Supplementary Tables 1, 3**). As expected from the pySODA analysis, we observed for both Bassoon and PSD95 clusters a significant increase in the proportion of strongly coupled subtypes following the LTP-inducing stimulus $0Mg^{2+}$/Gly/Bic ($ST_{Bassoon}$9-12, ST_{PSD95}4,7, **Figures 5E,F** and **Supplementary Tables 1–4**). In contrast, the LTD-inducing stimulus significantly increased the prevalence of weakly coupled clusters ($ST_{Bassoon}$3,5-8, ST_{PSD95}2-3, **Figures 5G,H** and **Supplementary Tables 1–4**).

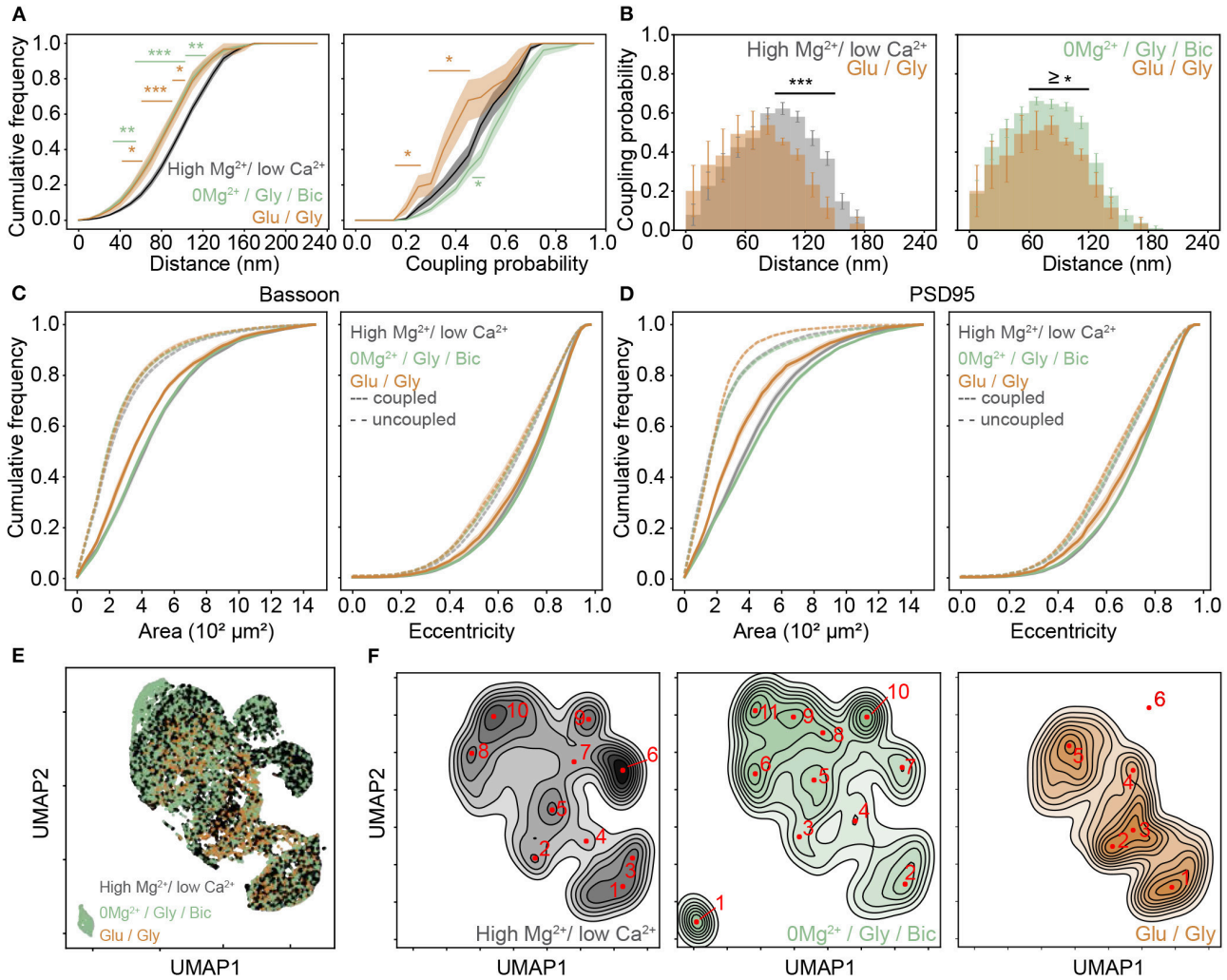

FIGURE 4 | Activity dependent re-organization of Bassoon and PSD95 cluster pairs for different activity promoting stimuli. **(A)** Cumulative frequency curves of the coupling distance *(left)* and probability *(right)* measured for coupled Bassoon and PSD95 clusters in high Mg^{2+}/low Ca^{2+} (black, $n = 18$), $0Mg^{2+}$/Gly/Bic (green, $n = 24$), and Glu/Gly (orange, $n = 7$). n = number of neurons from 2 (Glu/Gly) or 3 (high Mg^{2+}/low Ca^{2+}, $0Mg^{2+}$/Gly/Bic) independent neuronal cultures. **(B)** Histograms of the mean coupling probability per neuron at a given distance in high Mg^{2+}/low Ca^{2+} (gray), Glu/Gly (orange), and $0Mg^{2+}$/Gly/Bic (green). **(C,D)** Cumulative frequency curves of area *(left)* and eccentricity *(right)* of coupled *(solid line)* and uncoupled (dashed line) Bassoon **(C)** and PSD95 **(D)** protein clusters. (**E**) Scatterplot of the UMAP embedding and **(F)** corresponding kernel density estimation (KDE) maps of coupled Bassoon clusters in high Mg^{2+}/low Ca^{2+} (black), $0Mg^{2+}$/Gly/Bic (green), and Glu/Gly (orange). Local maxima identifying synaptic **(A,C,D)** shown are the means (plain and dashed lines) with standard error (shaded area). Statistical difference was accessed using a randomization test (see section Materials and Methods and **Supplementary Figures 8, 9**). Exact p-values are reported in **Supplementary Figures 8, 9** with $^{*}p < 0.05$, $^{**}p < 0.01$, and $^{***}p < 0.001$.

When considering morphological features such as area and eccentricity, the $0Mg^{2+}$/Gly/Bic and Glu/Gly stimulations had an opposite effect on the proportion of small and round subtypes ($ST_{Bassoon}4$, $ST_{PSD95}4$-5) that could not be explained solely by the analysis of their coupling properties (**Figures 5A,B,E,H**). Additionally, we identified for each protein one subtype of small, eccentric and highly coupled clusters ($ST_{Bassoon}12$, $ST_{PSD95}7$) that are solely detected following the LTP paradigm (**Figures 5E,F** and **Supplementary Tables 1, 3**).

This multidimensional analysis of morphological and coupling properties confirms that both stimuli have an opposite effect on the prevalence of certain synaptic subtypes, and it underlines the diversity in the characteristics and activity-dependent remodeling of the cluster subtypes forming functional synapses. The complementary information on the morphological and coupling properties of the cluster subtypes reveals a more complete description of synaptic plasticity.

3.4. Chronic Inhibition of Neuronal Activity Influences the Morphological and Coupling Properties of Bassoon and PSD95

The chronic inhibition of action potentials with the sodium channel blocker Tetrodotoxin (TTX) leads to the strengthening

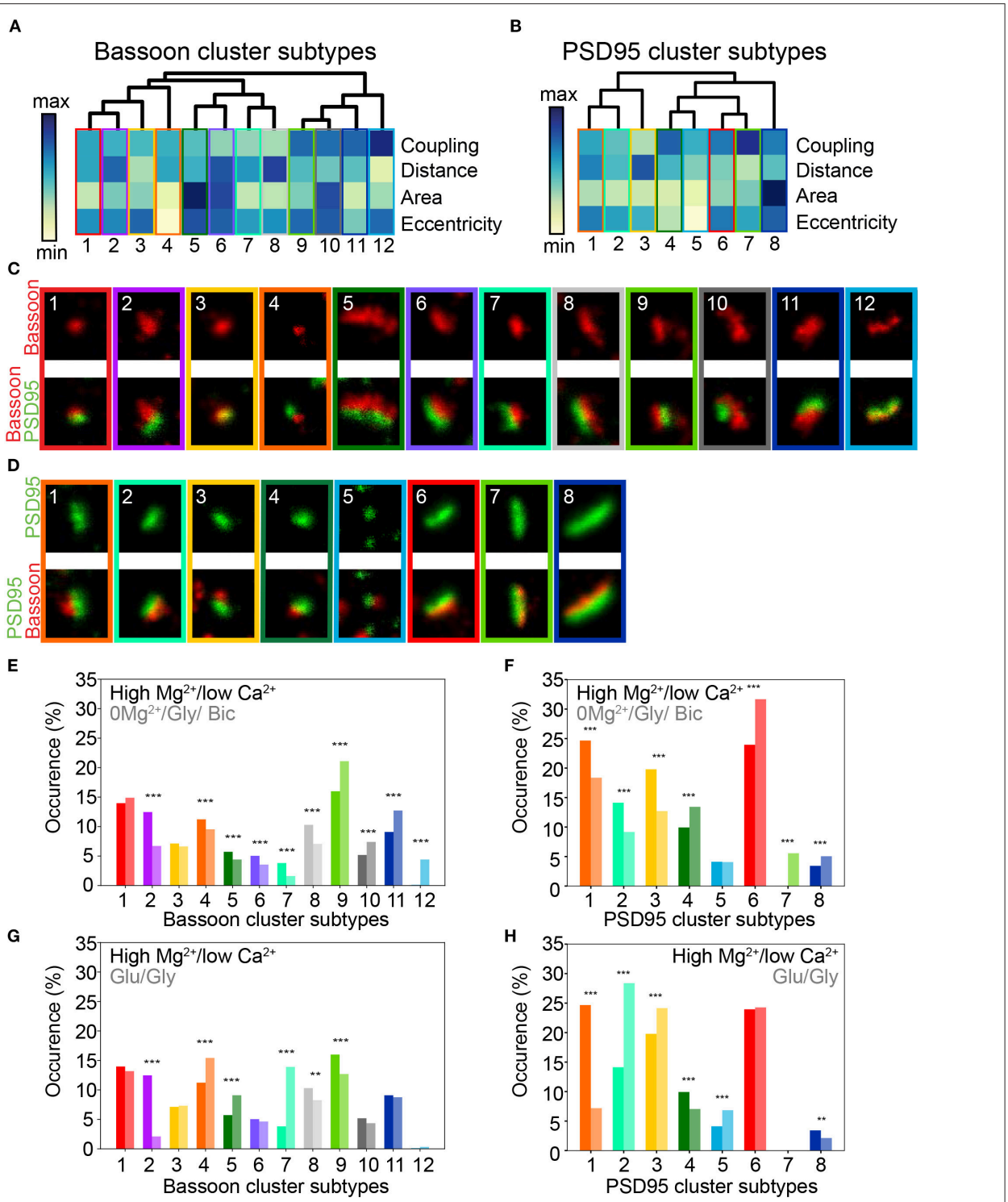

FIGURE 5 | Activity dependent modification of the prevalence of synaptic cluster morphology and organization. **(A,B)** Hierarchical grouping of presynaptic Bassoon **(A)** and postsynaptic PSD95 **(B)** cluster subtypes for 4 selected features (hierarchical grouping including all features are shown in **Supplementary Figures 16, 17**). Synaptic subtypes were identified from the detected local maxima in the KDE plots generated from the scatterplot of the UMAP embedding of all detected Bassoon and PSD95 clusters (**Figure 4**, **Supplementary Figure 13**). Minimum *(yellow)* and maximum *(dark blue)* value of the heatmap for each feature: coupling probability (min: 0, max: 1), distance (min: 0 nm, max: 180 nm), area (min: $0.7 \cdot 10^{-2}$ μm^2, max: $11.8 \cdot 10^{-2}$ μm^2), and eccentricity (min: 0.4, max: 1). **(C,D)** Representative STED images of **(C)** Bassoon and **(D)** PSD95 clusters *(top)* with corresponding two-color STED image *(bottom)*. Proportions of Bassoon **(E,G)** and PSD95 **(F,H)** cluster belonging to each synaptic subtype depending on the neuronal activity state: high Mg^{2+}/low Ca^{2+} vs. 0Mg^{2+}/Gly/Bic **(E,F)**, high Mg^{2+}/low Ca^{2+} vs. Glu/Gly **(G,H)**. Stars represent significant changes in the proportion of synaptic subtypes using Chi-square test. Exact *p*-values are reported in **Supplementary Tables 2, 4** with $*p < 0.05$, $**p < 0.01$, and $***p < 0.001$. Image size: 0.96 μm^2.

of excitatory synapses, referred to as synaptic scaling (Turrigiano et al., 1998), which is mediated by the insertion of postsynaptic glutamate receptors (Watt et al., 2000) and the remodeling of pre- and postsynaptic scaffold proteins (Sun and Turrigiano, 2011; Glebov et al., 2016). We therefore hypothesized that a prolonged TTX treatment in cultured neurons would lead to an increase in Bassoon and PSD95 coupling probability.

We incubated 21-22 DIV neuronal cultures with TTX for 4, 24, and 48 h prior to fixation. The duration of TTX treatment correlated with increased coupling probability between Bassoon and PSD95, but had no effect on the mean coupling distance (**Figures 6A,B** and **Supplementary Figures 18, 19**). The modulation of the coupling probability was also observed when comparing the LTP and LTD conditions to the naive condition (**Supplementary Figure 20**). The TTX treatment led to a significant increase in the size of the coupled PSD95 (**Figures 6C,D** and **Supplementary Figure 21**), the cluster density, number of coupled clusters, and cluster intensity (**Supplementary Figures 11B, 22**).

We applied again the UMAP-based analysis to characterize the diverse features of the Bassoon - PSD95 synaptic clusters, following chronic TTX treatment (**Figures 6E,F** and **Supplementary Figure 23**). Hierarchical grouping identified 9 groups that we refer to as the main synaptic subtypes for each protein (**Figures 7A–D** and **Supplementary Figures 24–27**).

Consistent with the results obtained with pySODA (**Figures 6A,B**), chronic TTX significantly promoted strongly coupled synaptic subtypes ($ST_{Bassoon}$1,6; ST_{PSD95}6,7,9; CP $>$ 0.6), while the prevalence of weakly coupled subtypes was reduced ($ST_{Bassoon}$7-9; ST_{PSD95}1-3; CP $<$ 0.4) (**Figures 7E,F** and **Supplementary Tables 5–8**). Our results also indicate that compared to basal condition, the 48h TTX treatment strongly reduced the proportion of small synaptic subtypes (area $<$ 0.03 μm^2) from 49 to 30% ($ST_{Bassoon}$4,5,8,9) for Bassoon and for PSD95 from 37 to 23% (ST_{PSD95}1,8), (**Figures 7E,F** and **Supplementary Tables 5–8**). Interestingly, while the PSD95 cluster population in this homeostatic plasticity paradigm is best represented by similar percentages (10–20%) of the main synaptic subtypes (**Figure 7F**), a large proportion of Bassoon clusters (38%) belongs to a small, eccentric, and strongly coupled subtype ($ST_{Bassoon}$6, **Figure 7E**).

Thus, the pySODA approach combined with multidimensional analysis of morphological and coupling properties revealed that the organization of functional synapses at the nanoscale is modulated by chronic inhibition of action potentials.

3.5. Mapping of Synaptic Subtypes of PSD95/Bassoon Reveals Common Features Between Different Forms of Plasticity Induction

This diverse array of synaptic subtypes revealed from hierarchical grouping is the product of non-biased approaches which had no pre-conceived notion of what features of synaptic plasticity should emerge following different stimuli. Hence, the number of groups resulting from this data-driven unsupervised grouping approach intrinsically varied with the number of instances supporting the model and the distribution of these instances in the representation space.

In the face of this diversity, we asked whether certain synaptic subtypes emerged across the acute and chronic treatments (**Supplementary Figure 28**). We projected all instances (detected protein clusters) of one dataset (e.g. acute treatment) into the groups (synaptic subtypes) determined from the other dataset (e.g. chronic treatment) and vice versa (**Figure 8A**). We next computed the proportion of the protein clusters of one dataset that were associated to each synaptic subtype of the other dataset (**Figures 8B,C**). This approach shows strong correspondence between some groups, while others are unique to an experimental paradigm (**Figures 8D,E**). For example, for 7 of the 12 groups identified in the acute treatment experiment, more than 75% of their detected Bassoon clusters can be associated with a single group in the chronic treatment experiment (**Figure 8B**, ST_{acute}2, 7-11). A predominant subtype emerges in the chronic inhibition experiment ($ST_{chronic}$6, 32% of all coupled Bassoon clusters), which can be represented by 4 subgroups in the acute stimulation experiment (ST_{acute}1, 9, 11, 12) (**Figures 8B,D**). In addition to the observed similarity in morphological and coupling properties between $ST_{chronic}$6 and ST_{acute}1, 9, 11, 12, we note that all these subgroups are favored by the treatments that typically induce synaptic potentiation (cLTP stimulation and chronic TTX application) (**Figures 5**, **7**, **9**, favored by 0Mg^{2+}/Gly/Bic : yellow, favored by 48 h TTX : blue). A similar association between both experiments is observed for strongly coupled PSD95 clusters for which ST_{acute}4, 6, 7, 8 & $ST_{chronic}$6, 7, 9 are highly correlated (**Supplementary Figure 28**) and are favored by cLTP or chronic TTX stimuli (**Figures 5**, **7**, **9**, favored by 0Mg^{2+}/Gly/BIC : yellow, favored by 48 h TTX : blue). Similarly, a correlation, although less strong, is observed between the subtypes promoted by the LTD paradigm and those decreasing following chronic TTX treatment (**Figure 9**, favored by Glu/Gly : red/orange, decreased by 48 h TTX : violet).

Additionally, the unsupervised machine learning approach identified subtypes that are specific to one stimulation paradigm, generally encompassing a small proportion of the overall detected clusters, and that are not mapped between experiments. This is the case for the Bassoon ST_{acute}12 and PSD95 ST_{acute}7 which describe small, eccentric, and strongly coupled protein clusters and are solely found following a cLTP stimulus (**Figures 5E,F**, **8B,C**). These subtypes would likely have been overlooked by conventional rule-based analysis, as they describe only a small proportion of the data of a single stimulus paradigm.

Thus, the unsupervised grouping approach used to describe synaptic remodeling shows strong correlation between synaptic subtypes of the acute and homeostatic plasticity paradigms. It highlights strong similarities in the effect of cLTP and 48 h TTX treatment on synaptic organization and architecture.

4. DISCUSSION

We implemented a high-throughput analysis framework based on statistical object distance analysis, pySODA, to investigate

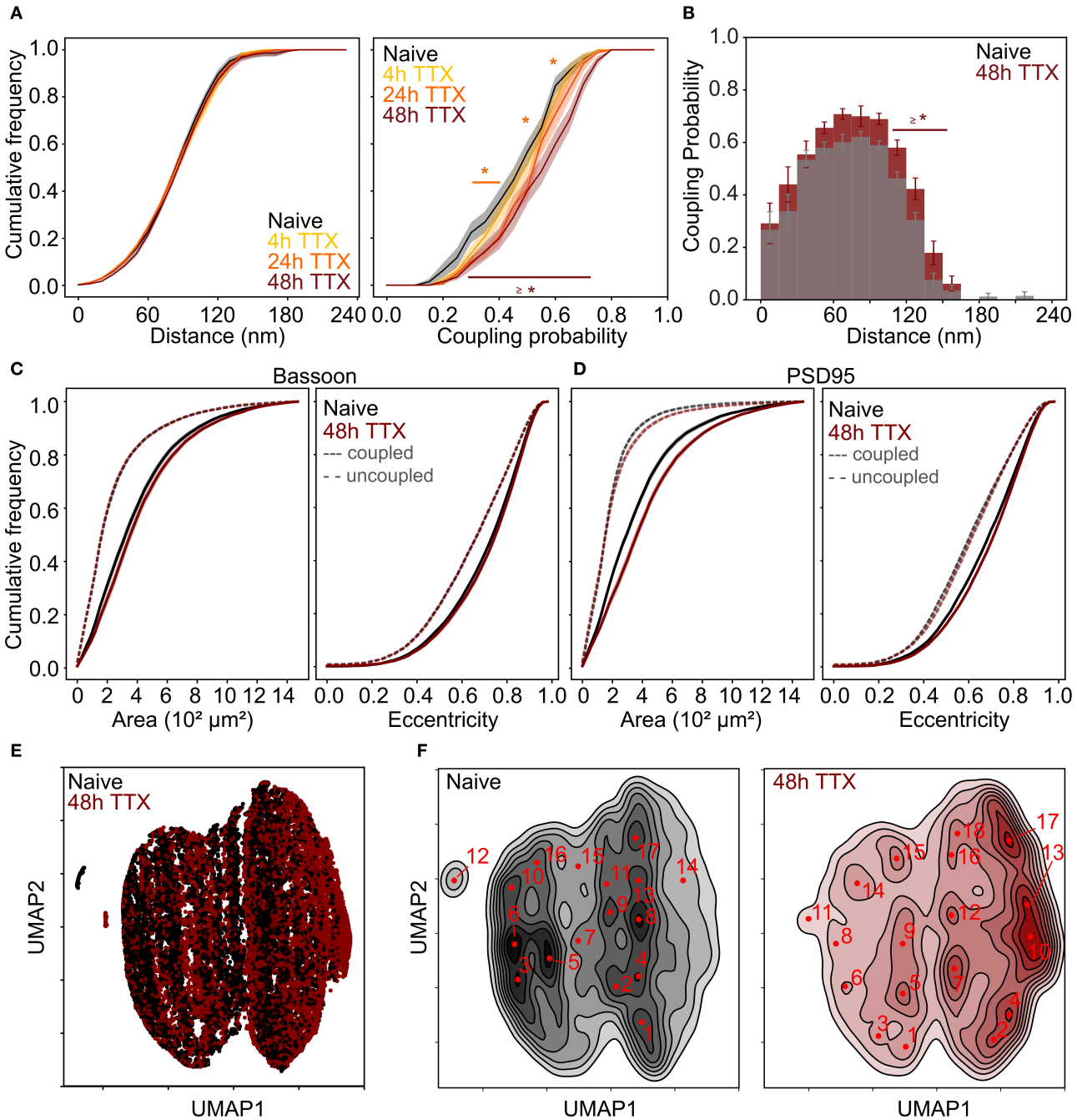

FIGURE 6 | Chronic TTX treatment induced re-organization of the synaptic scaffold protein pair Bassoon - PSD95. **(A)** Cumulative frequency curves of the coupling distance *(left)* and probability *(right)* measured for coupled Bassoon and PSD95 clusters for naive (gray, $n = 35$), 4 h TTX (light orange, $n = 20$), 24 h TTX (dark orange, $n = 23$) and 48 h TTX (red, $n = 33$). **(B)** Histogram of the mean coupling probability per neuron at a given distance for naive (gray) and 48 hours TTX (red). **(C,D)** Cumulative frequency curves of the area *(left)* and eccentricity *(right)* of coupled *(solid line)* and uncoupled *(dashed line)* Bassoon **(C)** and PSD95 **(D)** protein clusters. **(E)** Scatterplot of the UMAP embedding and **(F)** corresponding KDE plots of coupled Bassoon clusters for naive (black) and 48 h TTX (red). Subtypes of synaptic clusters are indicated on the KDE maps (numbers in red) referring to local maxima (see section Materials and Methods). **(A,C,D)** Shown are the means with standard error (shaded area). Statistical difference was assessed using a randomization test (see section Materials and Methods, **Supplementary Figures 18, 21**). n = number of neurons from 2 independent neuronal cultures.

the diversity of synaptic remodeling at the population level and discriminate distinct characteristics of synaptic protein clusters. We chose pySODA to detect pairs of synaptic protein clusters, as this approach was shown to be less dependent on labeling density, optical resolution, and signal intensity. Importantly, it provides an unbiased selection of clusters, ensuring the analysis

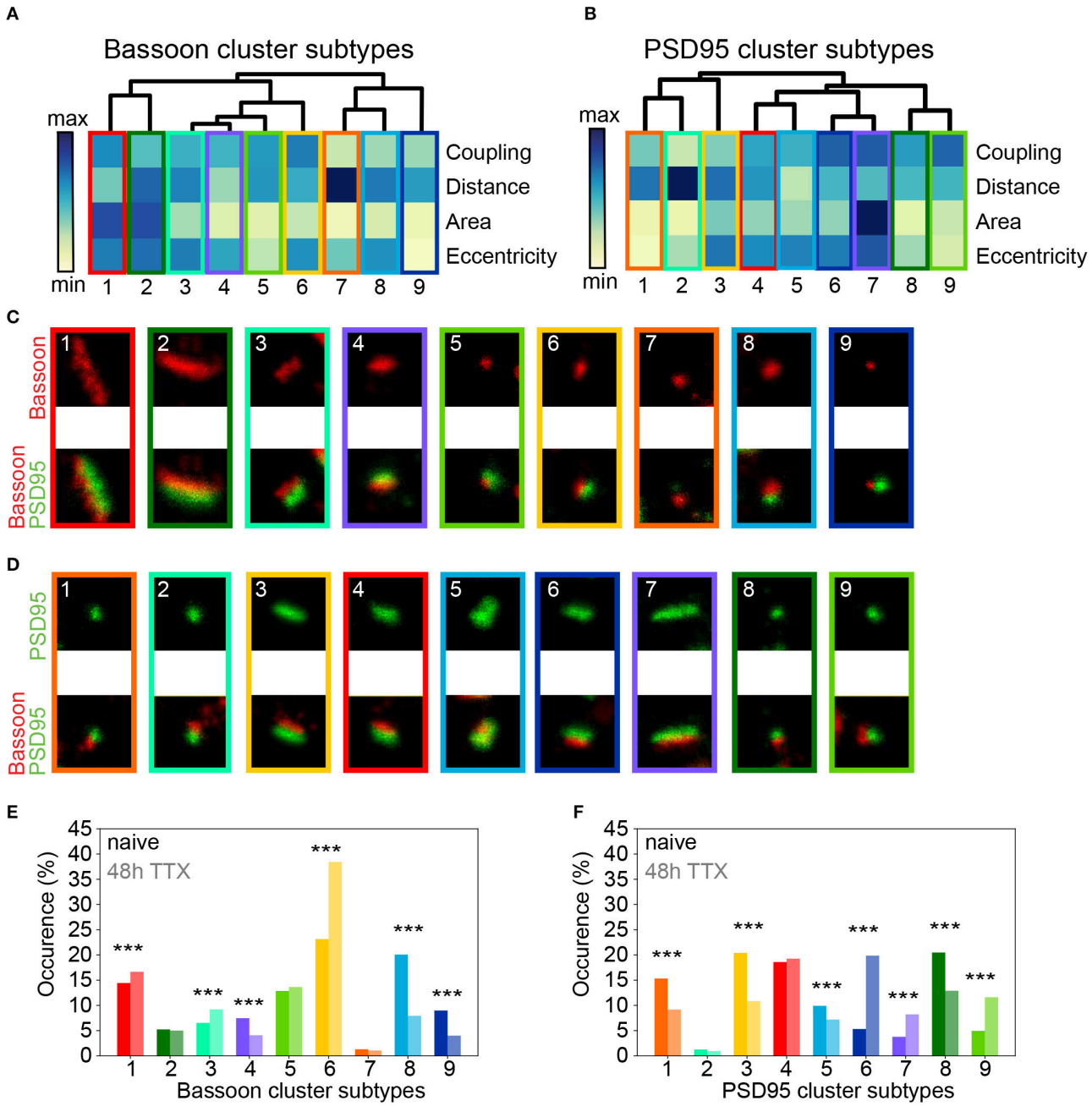

FIGURE 7 | Chronic TTX treatment modifies the prevalence of synaptic cluster morphology and organization. **(A,B)** Hierarchical grouping of presynaptic Bassoon **(A)** or postsynaptic PSD95 **(B)** synaptic subtypes for 4 selected features (hierarchical grouping including all features are shown in **Supplementary Figures 26, 27**). Synaptic subtypes were identified from the detected local maxima in the KDE plots generated from the scatterplot of the UMAP embedding of all detected Bassoon and PSD95 clusters (**Figure 6** and **Supplementary Figure 23**). Minimum *(yellow)* and maximum *(dark blue)* value of the heatmap for each feature: coupling probability (min: 0, max: 1), distance (min: 0 nm, max: 180 nm), area (min: $0.7 \cdot 10^{-2}$ μm^2, max: $11.8 \cdot 10^{-2}$ μm^2), and eccentricity (min: 0.4, max: 1). **(C,D)** Representative STED images of **(C)** Bassoon and **(D)** PSD95 clusters *(top)* with corresponding two-color STED image *(bottom)*. **(E,F)** Proportions of Bassoon **(E)** and PSD95 **(F)** clusters belonging to each synaptic subtype depending on the neuronal activity state: naive vs. 48 h TTX. Stars represent significant activity-dependent changes in the proportion of each synaptic type using a Chi-square test. Exact *p*-values are reported in **Supplementary Tables 6, 8** with $^*p < 0.05$, $^{**}p < 0.01$, and $^{***}p < 0.001$. Image size: 0.96 μm^2.

of nearly all detectable synapses. Our study examined the activity-dependent remodeling of the nanoscale architecture of the active zone and the postsynaptic density by characterizing the interactions between pre- (RIM 1/2, Bassoon) and postsynaptic (PSD95, Homer1c) protein pairs in cultured neuronal circuits. We combined pySODA with unsupervised machine learning approaches to enrich the characterization of activity-dependent changes in synaptic protein organization based on the coupling

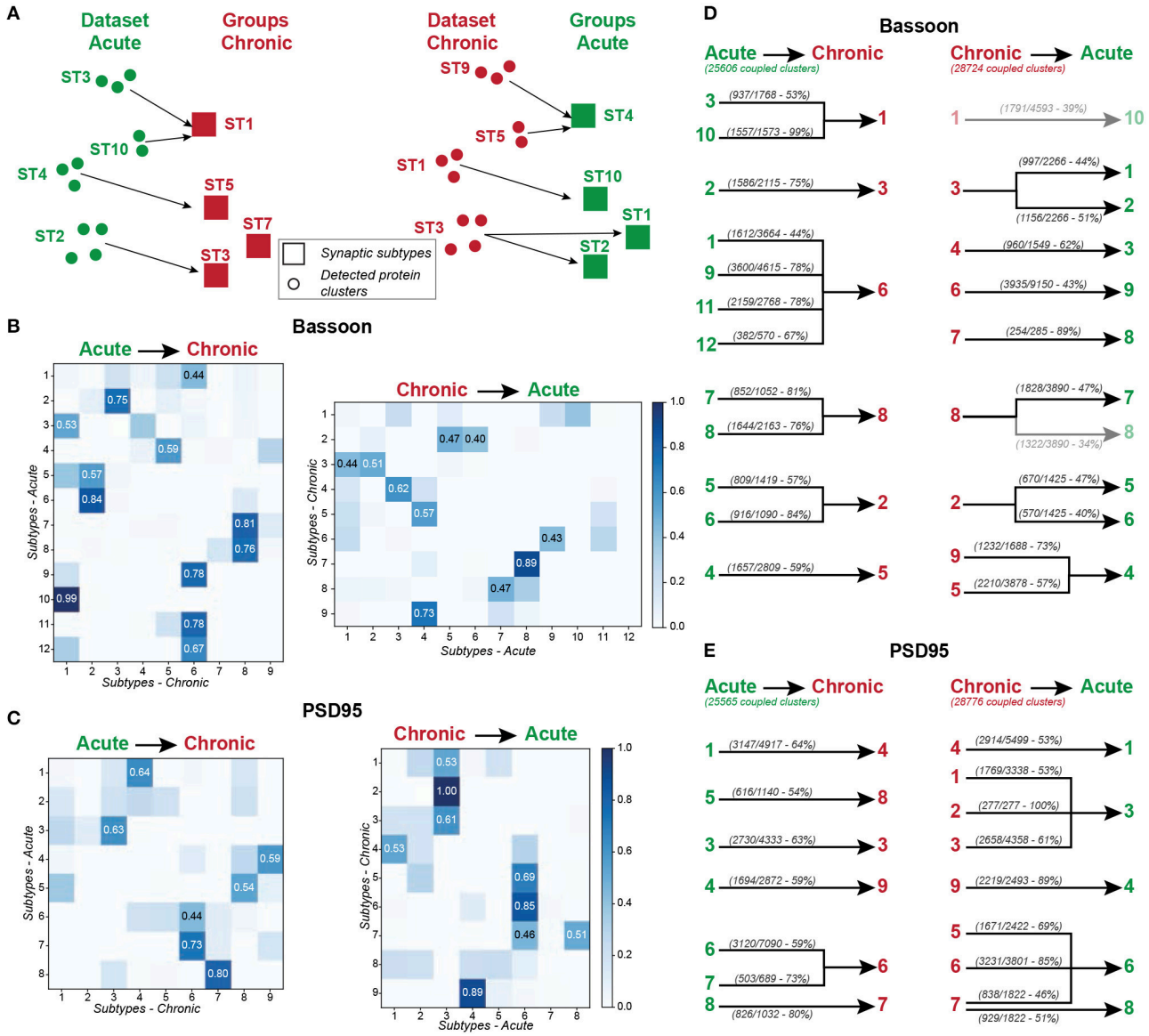

FIGURE 8 | Mapping the synaptic subtypes that emerged from the acute and chronic treatments. **(A)** Schematic representation of the mapping approach. Each detected protein cluster of the acute treatment experiments (Dataset Acute, green circles) is assigned to the most similar (smallest Euclidean distance) synaptic subtype of the chronic treatment experiment (Groups Chronic, red squares) and vice versa. **(B,C)** Results of the mapping analysis, showing the percentage of clusters for Bassooon **(B)** and PSD95 **(C)** from each subtypes of one experiment (y- axis, Acute: left, Chronic: right) that are assigned to each subtype of the other experiment (x-axis, Chronic: left, Acute: right). The most prominent association (proportion above 0.4) between groups are highlighted. **(D,E)** Results of the mapping experiments for Bassoon **(D)** and PSD95 **(E)** showing all projections for which more than 40% of the protein clusters belonging to one synaptic subtype of the acute (left) or chronic (right) treatment experiment where mapped into a specific subtype of the other experiment (Chronic: left, Acute: right). The majority of the synaptic subtypes of one experiment exhibit one major connection (more than 40% of the protein clusters are associated) to one group of the other experiment.

and morphological properties of PSD95 and Bassoon synaptic clusters. This high-throughput analysis of STED images allowed us to examine the synaptic re-organization at the population level (between 12,500 and 25,000 protein clusters depending on the condition) in response to treatments inducing acute or homeostatic plasticity.

We first addressed whether a chemical LTP-inducing stimulus (0Mg^{2+}/Gly/Bic) affects the organization of these scaffold elements within their synaptic compartment (pre- or postsynaptic). We show that Bassoon and RIM1/2 are strongly coupled and that neither their coupling probability nor their mean coupling distance are affected by the LTP-inducing stimulus. Conceivably, the presynaptic pair may still undergo activity-dependent re-organization at a scale that the resolution of this approach cannot detect. For example, Glebov et al. (2017) implemented a FRET-based measurement to show unclustering

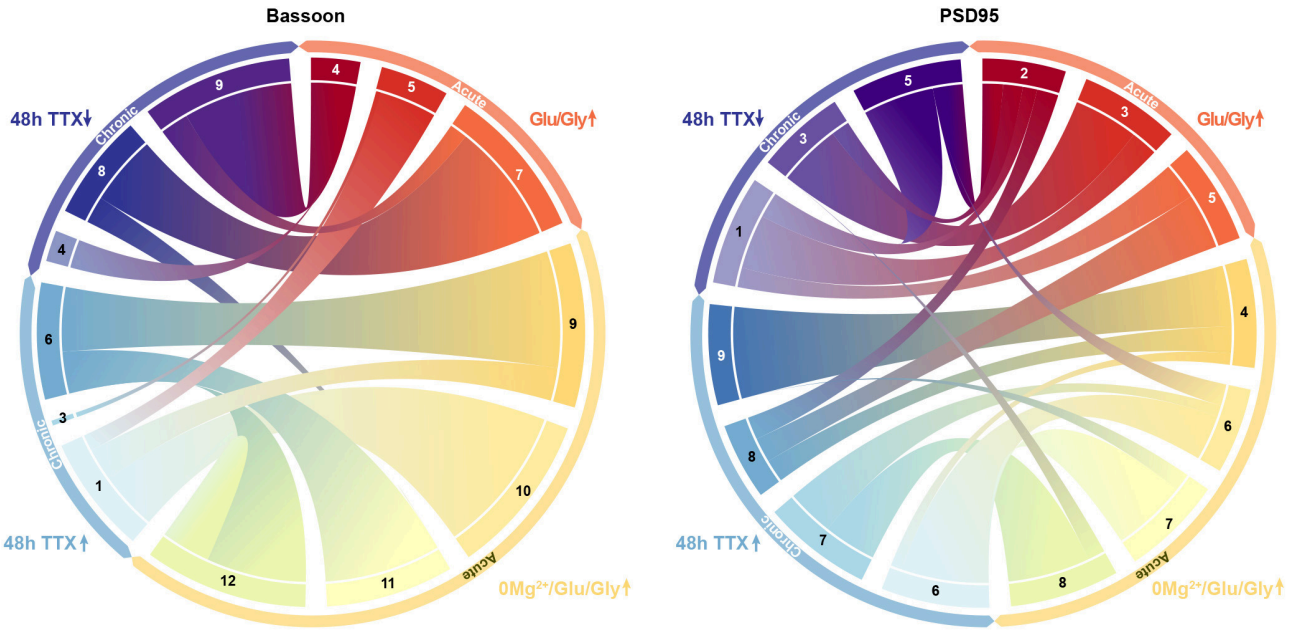

FIGURE 9 | Association between synaptic subtypes depending on their prevalence in acute and chronic treatments. Synaptic subtypes that are increasing following acute treatment of $0Mg^{2+}$/Gly/Bic (yellow) are strongly associated with the ones increasing following a 48 h chronic TTX treatment (blue). Synaptic subtypes increasing following an acute treatment of Glu/Gly (red/orange) are mostly linked with subtypes decreasing following a 48 h chronic TTX treatment (violet) for both Bassoon (left) and PSD95 (right). The magnitude of the links between each synaptic subtype was determined from the results of the mapping experiments shown in **Figures 8B,C**.

of Bassoon upon chronic TTX treatment, an effect that was not detectable with STORM.

In contrast, we show that the same stimulus reduces the coupling probability and increases the mean coupling distance between Homer1c and PSD95. These results indicate that the extent of remodeling between the postsynaptic pair is more pronounced as compared to that of the presynaptic pair. While the relationship between Bassoon and RIM1/2 during synaptic plasticity has not been examined previously, it has been shown that activity inducing stimuli can induce a rapid declustering of Homer1c (Okabe et al., 2001; Kuriu et al., 2006) as well as PSD95 (Steiner et al., 2008; Fukata et al., 2013) at the postsynaptic compartment. Our data on the decreasing coupling properties of PSD95 - Homer1c during synaptic stimulation are thus consistent with these studies.

When looking at the relationship between pre- and post-synaptic partners, we found that the cLTP stimulus has opposite effects on the spatial organization of Homer1c and PSD95 to Bassoon. Indeed the coupling probability of Homer1c - Bassoon decreases (and coupling distance increases), whereas it increases for Bassoon - PSD95 (and coupling distance decreases). A pool of PSD95 was reported to leave the synapse upon synaptic stimulation (Steiner et al., 2008; Doré et al., 2014), while we observed an increase in the coupling probability between PSD95 and Bassoon. We can speculate that a loosely coupled pool of PSD95 leaves the postsynaptic area upon stimulation, and that the remaining pool exhibits an increased degree of coupling. The further activity-dependent reduction in coupling probability of Homer1c to both PSD95 and Bassoon suggests that Homer1c has a weaker association with pre- and postsynaptic scaffolds upon LTP-inducing stimulation. The activity-dependent redistribution of Homer1c has not been clearly established (Okabe et al., 2001; Tao-Cheng et al., 2014; Lagache et al., 2018). It is interesting to note that Homer1c was shown to associate with Shank and GTPase dynamin-3 to form a complex linking the PSD with the clathrin endocytotic zone, which is necessary for endocytosis of AMPA receptors, a process occurring mainly on the periphery of the PSD (Lu et al., 2007). Hence, the activity-dependent uncoupling of Homer1c from the postsynaptic area may regulate AMPA receptors endocytosis supporting synaptic plasticity (Petrini et al., 2009).

Tang et al. (2016) nicely showed, using super-resolution microscopy, that LTP- and LTD-inducing stimuli produce opposite effects on the alignment of transsynaptic nanocolumns in dissociated hippocampal circuits. Using pySODA, we measured an opposite effect of these stimuli on the coupling probability of PSD95 and Bassoon at the population level. The cLTP condition exhibited a larger proportion of highly coupled pairs, as compared to controls, while in the LTD condition, weakly coupled pairs were more prevalent. Thus, these observed changes in the coupling probability could serve as a readout of synaptic re-organization at the population level representing early phases of LTP and LTD. Chronic inhibition of neuronal activity, known to induce synaptic upscaling (Turrigiano et al., 1998), also resulted in increased coupling probability between PSD95 and Bassoon. On the other hand, the TTX treatment did not significantly change the mean coupling distance, contrasting with the effect of the LTP stimulus, which may reflect a different mechanism of potentiation.

Our results are consistent with previous reports of an increase in PSD95 area associated with acute or homeostatic synaptic plasticity (MacGillavry et al., 2013; Tang et al., 2016). They

additionally demonstrate an increase in the organization of pre- and postsynaptic scaffolds as reported by recent studies (Tang et al., 2016; Hruska et al., 2018; Crosby et al., 2019). Furthermore, we observed that highly coupled Bassoon and PSD95 clusters exhibit a wide range of sizes and eccentricities, which may reveal different strategies employed by synapses to express plasticity, that include the modulation of PSD shape (Stewart et al., 2005), increase in spine size (Matsuzaki et al., 2004), *de novo* synapse formation (Kwon and Sabatini, 2011), nanometric re-organization of transsynaptic nanocolumns (Tang et al., 2016) or spine organelle content (Borczyk et al., 2019).

Using the dimensionality reduction technique UMAP combined with hierarchical grouping, we identified a broad range of synaptic subtypes based on their morphological and coupling characteristics. The plasticity-inducing treatments changed the proportions of these subtypes in various ways, yet, remarkably, common subtypes emerged for conditions causing synaptic potentiation as well as for depression. Thus, the two independent methods of analysis presented here, with no prior knowledge of the conditions or pre-determined criteria of synaptic features, converge on common features of synaptic properties encoding synaptic potentiation or depression.

We suggest that the expanded palette of synaptic features revealed by our unbiased approach, focusing on large numbers of synapses, provides a basis to further explore the widely diverse molecular mechanisms of synaptic plasticity. In our study, we exploited dissociated cultured hippocampal neurons, a preparation frequently used to highlight molecular traits of LTP, LTD, or synaptic scaling (Tang et al., 2016; Glebov et al., 2017). This approach does not, however, provide the physiological information obtained from recordings of paired neurons in brain slice. Combining both types of information will be important and will require the ability to monitor a large number of live synapses with combined readouts of synaptic proteins and functional activity. Future studies may profit from our analysis framework to investigate the diversity of the synaptic protein organization across various brain regions (Broadhead et al., 2016), during aging (VanGuilder et al., 2011), or even across species (Ryan and Grant, 2009) to learn more on the diversity of synaptic protein organization supporting learning and memory.

DATA AVAILABILITY STATEMENT

The analysis routine generated for this study can be found online: https://github.com/FLClab/pySODA and https://github.com/FLClab/MultidimSynapticProteins. The dataset generated for this study can be obtained from the corresponding author upon reasonable request.

ETHICS STATEMENT

The animal study was reviewed and approved by the Animal Care Committee of Université Laval.

AUTHOR CONTRIBUTIONS

TW and BR performed STED imaging. TW prepared samples. RB, AB, AD, and TW wrote the analysis routine. TW, AB, AD, RB, and FL-C analyzed the data. TW and FL-C planned the STED experiments. AB, TW, and FL-C designed and implemented the machine learning-based analysis. TW, AB, PDK, and FL-C wrote the manuscript. PDK and FL-C co-supervised the project.

FUNDING

Operating costs and student stipends were funded by grants from the Natural Sciences and Engineering Research Council (NSERC 250127-2012, PDK; NSERC 2019-06704, FL-C), from the CERVO Foundation (FL-C), and from the Canadian Institute of Health Research (CIHR-378058, PDK). AB and TW are supported by Ph.D. scholarships from the Fonds de Recherche du Québec Nature et Technologies (FRQNT) (AB) and FRQNT strategic cluster Unifying AI and Neuroscience Québec (UNIQUE) (TW). FL-C is a Canada Research Chair Tier II. The STED microscope was funded by a grant from the Canadian Foundation for Innovation and the Government of Québec (32786, PDK).

ACKNOWLEDGMENTS

Francine Nault, Charleen Salesse, Laurence Émond, and Audrey Emond for the neuronal cell culture. Gabriel Leclerc for preliminary simulation routines of protein cluster distributions. Gabrielle Laramée for preliminary immunocytochemistry experiments and Annette Schwerdtfeger for careful proofreading.

SUPPLEMENTARY MATERIAL

The Supplementary Material for this article can be found online at: https://www.frontiersin.org/articles/10.3389/fncir.2020.00057/full#supplementary-material

REFERENCES

Arnold, F. J., Hofmann, F., Bengtson, C. P., Wittmann, M., Vanhoutte, P., and Bading, H. (2005). Microelectrode array recordings of cultured hippocampal networks reveal a simple model for transcription and protein synthesis-dependent plasticity. *J. Physiol.* 564, 3–19. doi: 10.1113/jphysiol.2004.077446

Baddeley, D., Crossman, D., Rossberger, S., Cheyne, J. E., Montgomery, J. M., Jayasinghe, I. D., et al. (2011). 4D super-resolution microscopy with conventional fluorophores and single wavelength excitation in optically thick cells and tissues. *PLoS ONE* 6:e20645. doi: 10.1371/journal.pone.0020645

Bayer, K. U., LeBel, É., McDonald, G. L., O'Leary, H., Schulman, H., and De Koninck, P. (2006). Transition from reversible to persistent binding of CaMKII to postsynaptic sites and NR2B. *J. Neurosci.* 26, 1164–1174. doi: 10.1523/JNEUROSCI.3116-05.2006

Borczyk, M., Śliwińska, M. A., Caly, A., Bernas, T., and Radwanska, K. (2019). Neuronal plasticity affects correlation between the size of dendritic spine and its postsynaptic density. *Sci. Rep.* 9, 1–12. doi: 10.1038/s41598-018-38412-7

Branco, T., and Staras, K. (2009). The probability of neurotransmitter release: variability and feedback control at single synapses. *Nat. Rev. Neurosci.* 10, 373–383. doi: 10.1038/nrn2634

Broadhead, M. J., Horrocks, M. H., Zhu, F., Muresan, L., Benavides-Piccione, R., DeFelipe, J., et al. (2016). PSD95 nanoclusters are postsynaptic building blocks in hippocampus circuits. *Sci. Rep.* 6:24626. doi: 10.1038/srep24626

Carroll, R. C., Beattie, E. C., Xia, H., Lüscher, C., Altschuler, Y., Nicoll, R. A., et al. (1999). Dynamin dependent endocytosis of ionotropic glutamate receptors. *Proc. Natl. Acad. Sci. U.S.A.* 96, 14112–14117. doi: 10.1073/pnas.96.24.14112

Chowdhury, D., and Hell, J. W. (2019). Ca2+/calmodulin binding to PSD-95 downregulates its palmitoylation and ampars in long-term depression. *Front. Synapt. Neurosci.* 11:6. doi: 10.3389/fnsyn.2019.00006

Colledge, M., Snyder, E. M., Crozier, R. A., Soderling, J. A., Jin, Y., Langeberg, L. K., et al. (2003). Ubiquitination regulates PSD-95 degradation and AMPA receptor surface expression. *Neuron* 40, 595–607. doi: 10.1016/S0896-6273(03)00687-1

Crosby, K. C., Gookin, S. E., Garcia, J. D., Hahm, K. M., Dell'Acqua, M. L., and Smith, K. R. (2019). Nanoscale subsynaptic domains underlie the organization of the inhibitory synapse. *Cell Rep.* 26, 3284–3297. doi: 10.1016/j.celrep.2019.02.070

Dani, A., Huang, B., Bergan, J., Dulac, C., and Zhuang, X. (2010). Superresolution imaging of chemical synapses in the brain. *Neuron* 68, 843–856. doi: 10.1016/j.neuron.2010.11.021

De Chaumont, F., Dallongeville, S., Chenouard, N., Hervé, N., Pop, S., Provoost, T., et al. (2012). Icy: an open bioimage informatics platform for extended reproducible research. *Nat. Methods* 9:690. doi: 10.1038/nmeth.2075

Di Biase, V., Flucher, B. E., and Obermair, G. J. (2009). Resolving sub-synaptic compartments with double immunofluorescence labeling in hippocampal neurons. *J. Neurosci. Methods* 176, 78–84. doi: 10.1016/j.jneumeth.2008.08.025

Donoho, D. L., Johnstone, I. M., Kerkyacharian, G., and Picard, D. (1997). "Universal near minimaxity of wavelet shrinkage," in *Festschrift for Lucien Le Cam*, eds D. Pollard, E. Torgersen, and G. L. Yang (New York, NY: Springer), 183–218. doi: 10.1007/978-1-4612-1880-7_12

Doré, K., Labrecque, S., Tardif, C., and De Koninck, P. (2014). FRET-FLIM investigation of PSD95-NMDA receptor interaction in dendritic spines; control by calpain, CaMKII and Src family kinase. *PLoS ONE* 9:e112170. doi: 10.1371/journal.pone.0112170

Doyon, N., Prescott, S. A., Castonguay, A., Godin, A. G., Kröger, H., and De Koninck, Y. (2011). Efficacy of synaptic inhibition depends on multiple, dynamically interacting mechanisms implicated in chloride homeostasis. *PLoS Comput. Biol.* 7:e1002149. doi: 10.1371/journal.pcbi.1002149

Dunn, K. W., Kamocka, M. M., and McDonald, J. H. (2011). A practical guide to evaluating colocalization in biological microscopy. *Am. J. Physiol. Cell Physiol.* 300, C723–C742. doi: 10.1152/ajpcell.00462.2010

Durand, A., Wiesner, T., Gardner, M.-A., Robitaille, L.-É., Bilodeau, A., Gagné, C., et al. (2018). A machine learning approach for online automated optimization of super-resolution optical microscopy. *Nat. Commun.* 9, 1–16. doi: 10.1038/s41467-018-07668-y

Edelmann, E., Cepeda-Prado, E., and Leßmann, V. (2017). Coexistence of multiple types of synaptic plasticity in individual hippocampal CA1 pyramidal neurons. *Front. Synapt. Neurosci.* 9:7. doi: 10.3389/fnsyn.2017.00007

Frank, R. A., and Grant, S. G. (2017). Supramolecular organization of NMDA receptors and the postsynaptic density. *Curr. Opin. Neurobiol.* 45, 139–147. doi: 10.1016/j.conb.2017.05.019

Fukata, Y., Dimitrov, A., Boncompain, G., Vielemeyer, O., Perez, F., and Fukata, M. (2013). Local palmitoylation cycles define activity-regulated postsynaptic subdomains. *J. Cell Biol.* 202, 145–161. doi: 10.1083/jcb.201302071

Glebov, O. O., Cox, S., Humphreys, L., and Burrone, J. (2016). Neuronal activity controls transsynaptic geometry. *Sci. Rep.* 6:22703. doi: 10.1038/srep22703

Glebov, O. O., Jackson, R. E., Winterflood, C. M., Owen, D. M., Barker, E. A., Doherty, P., et al. (2017). Nanoscale structural plasticity of the active zone matrix modulates presynaptic function. *Cell Rep.* 18, 2715–2728. doi: 10.1016/j.celrep.2017.02.064

Haas, K. T., Compans, B., Letellier, M., Bartol, T. M., Grillo-Bosch, D., Sejnowski, T. J., et al. (2018). Pre-post synaptic alignment through neuroligin-1 tunes synaptic transmission efficiency. *elife* 7:e31755. doi: 10.7554/eLife.31755

Haase, P. (1995). Spatial pattern analysis in ecology based on Ripley's k-function: Introduction and methods of edge correction. *J. Veget. Sci.* 6, 575–582. doi: 10.2307/3236356

Harris, K. M., Jensen, F. E., and Tsao, B. (1992). Three-dimensional structure of dendritic spines and synapses in rat hippocampus (ca1) at postnatal day 15 and adult ages: implications for the maturation of synaptic physiology and long-term potentiation. *J. Neurosci.* 12, 2685–2705. doi: 10.1523/JNEUROSCI.12-07-02685.1992

Hell, S. W., and Wichmann, J. (1994). Breaking the diffraction resolution limit by stimulated emission: stimulated-emission-depletion fluorescence microscopy. *Opt. Lett.* 19, 780–782. doi: 10.1364/OL.19.000780

Helmuth, J. A., Paul, G., and Sbalzarini, I. F. (2010). Beyond co-localization: inferring spatial interactions between sub-cellular structures from microscopy images. *BMC Bioinformatics* 11:372. doi: 10.1186/1471-2105-11-372

Hruska, M., Henderson, N., Le Marchand, S. J., Jafri, H., and Dalva, M. B. (2018). Synaptic nanomodules underlie the organization and plasticity of spine synapses. *Nat. Neurosci.* 21:671. doi: 10.1038/s41593-018-0138-9

Kuriu, T., Inoue, A., Bito, H., Sobue, K., and Okabe, S. (2006). Differential control of postsynaptic density scaffolds via actin-dependent and-independent mechanisms. *J. Neurosci.* 26, 7693–7706. doi: 10.1523/JNEUROSCI.0522-06.2006

Kwon, H.-B., and Sabatini, B. L. (2011). Glutamate induces de novo growth of functional spines in developing cortex. *Nature* 474, 100–104. doi: 10.1038/nature09986

Ladépêche, L., Planagumà, J., Thakur, S., Suárez, I., Hara, M., Borbely, J. S., et al. (2018). NMDA receptor autoantibodies in autoimmune encephalitis cause a subunit-specific nanoscale redistribution of NMDA receptors. *Cell Rep.* 23, 3759–3768. doi: 10.1016/j.celrep.2018.05.096

Lagache, T., Grassart, A., Dallongeville, S., Faklaris, O., Sauvonnet, N., Dufour, A., et al. (2018). Mapping molecular assemblies with fluorescence microscopy and object-based spatial statistics. *Nat. Commun.* 9:698. doi: 10.1038/s41467-018-03053-x

Lagache, T., Meas-Yedid, V., and Olivo-Marin, J.-C. (2013). "A statistical analysis of spatial colocalization using Ripley's K function," in *2013 IEEE 10th International Symposium on Biomedical Imaging* (San Francisco, CA: IEEE), 896–901. doi: 10.1109/ISBI.2013.6556620

Lu, J., Helton, T. D., Blanpied, T. A., Rácz, B., Newpher, T. M., Weinberg, R. J., et al. (2007). Postsynaptic positioning of endocytic zones and AMPA receptor cycling by physical coupling of dynamin-3 to homer. *Neuron* 55, 874–889. doi: 10.1016/j.neuron.2007.06.041

Lu, W.-Y., Man, H.-Y., Ju, W., Trimble, W. S., MacDonald, J. F., and Wang, Y. T. (2001). Activation of synaptic NMDA receptors induces membrane insertion of new AMPA receptors and LTP in cultured hippocampal neurons. *Neuron* 29, 243–254. doi: 10.1016/S0896-6273(01)00194-5

MacGillavry, H. D., Song, Y., Raghavachari, S., and Blanpied, T. A. (2013). Nanoscale scaffolding domains within the postsynaptic density concentrate synaptic AMPA receptors. *Neuron* 78, 615–622. doi: 10.1016/j.neuron.2013.03.009

Matsuzaki, M., Honkura, N., Ellis-Davies, G. C., and Kasai, H. (2004). Structural basis of long-term potentiation in single dendritic spines. *Nature* 429, 761–766. doi: 10.1038/nature02617

McInnes, L., Healy, J., and Melville, J. (2018). UMAP: uniform manifold approximation and projection for dimension reduction. *arXiv preprint arXiv:1802.03426*. doi: 10.21105/joss.00861

Micheva, K. D., Busse, B., Weiler, N. C., O'Rourke, N., and Smith, S. J. (2010). Single-synapse analysis of a diverse synapse population: proteomic imaging methods and markers. *Neuron* 68, 639–653. doi: 10.1016/j.neuron.2010.09.024

Nair, D., Hosy, E., Petersen, J. D., Constals, A., Giannone, G., Choquet, D., et al. (2013). Super-resolution imaging reveals that AMPA receptors inside synapses are dynamically organized in nanodomains regulated by PSD95. *J. Neurosci.* 33, 13204–13224. doi: 10.1523/JNEUROSCI.2381-12.2013

Nault, F., and De Koninck, P. (2009). "Dissociated hippocampal cultures," in *Protocols for Neural Cell Culture* (New York, NY: Springer), 137–159. doi: 10.1007/978-1-60761-292-6_8

Neher, R., and Neher, E. (2004). Optimizing imaging parameters for the separation of multiple labels in a fluorescence image. *J. Microscopy* 213, 46–62. doi: 10.1111/j.1365-2818.2004.01262.x

Okabe, S., Urushido, T., Konno, D., Okado, H., and Sobue, K. (2001). Rapid redistribution of the postsynaptic density protein PSD-Zip45 (homer 1c) and its differential regulation by NMDA receptors and calcium channels. *J. Neurosci.* 21, 9561–9571. doi: 10.1523/JNEUROSCI.21-24-09561.2001

Olivo-Marin, J.-C. (2002). Extraction of spots in biological images using multiscale products. *Pattern Recogn.* 35, 1989–1996. doi: 10.1016/S0031-3203(01)00127-3

Pedregosa, F., Varoquaux, G., Gramfort, A., Michel, V., Thirion, B., Grisel, O., et al. (2011). Scikit-learn: machine learning in Python. *J. Mach. Learn. Res.* 12, 2825–2830.

Petrini, E. M., Lu, J., Cognet, L., Lounis, B., Ehlers, M. D., and Choquet, D. (2009). Endocytic trafficking and recycling maintain a pool of mobile surface AMPA receptors required for synaptic potentiation. *Neuron* 63, 92–105. doi: 10.1016/j.neuron.2009.05.025

Ripley, B. D. (1976). The second-order analysis of stationary point processes. *J. Appl. Probabil.* 13, 255–266. doi: 10.2307/3212829

Rousseeuw, P. J. (1987). Silhouettes: a graphical aid to the interpretation and validation of cluster analysis. *J. Comput. Appl. Math.* 20, 53–65. doi: 10.1016/0377-0427(87)90125-7

Ryan, T. J., and Grant, S. G. (2009). The origin and evolution of synapses. *Nat. Rev. Neurosci.* 10, 701–712. doi: 10.1038/nrn2717

Schindelin, J., Arganda-Carreras, I., Frise, E., Kaynig, V., Longair, M., Pietzsch, T., et al. (2012). Fiji: an open-source platform for biological-image analysis. *Nat. Methods* 9:676. doi: 10.1038/nmeth.2019

Steiner, P., Higley, M. J., Xu, W., Czervionke, B. L., Malenka, R. C., and Sabatini, B. L. (2008). Destabilization of the postsynaptic density by PSD-95 serine 73 phosphorylation inhibits spine growth and synaptic plasticity. *Neuron* 60, 788–802. doi: 10.1016/j.neuron.2008.10.014

Stewart, M., Medvedev, N., Popov, V., Schoepfer, R., Davies, H., Murphy, K., et al. (2005). Chemically induced long-term potentiation increases the number of perforated and complex postsynaptic densities but does not alter dendritic spine volume in CA1 of adult mouse hippocampal slices. *Eur. J. Neurosci.* 21, 3368–3378. doi: 10.1111/j.1460-9568.2005.04174.x

Sun, Q., and Turrigiano, G. G. (2011). PSD-95 and PSD-93 play critical but distinct roles in synapticscaling up and down. *J. Neurosci.* 31, 6800–6808. doi: 10.1523/JNEUROSCI.5616-10.2011

Szoboszlay, M., Kirizs, T., and Nusser, Z. (2017). Objective quantification of nanoscale protein distributions. *Sci. Rep.* 7, 1–10. doi: 10.1038/s41598-017-15695-w

Tang, A.-H., Chen, H., Li, T. P., Metzbower, S. R., MacGillavry, H. D., and Blanpied, T. A. (2016). A trans-synaptic nanocolumn aligns neurotransmitter release to receptors. *Nature* 536, 210. doi: 10.1038/nature19058

Tao-Cheng, J.-H., Thein, S., Yang, Y., Reese, T. S., and Gallant, P. E. (2014). Homer is concentrated at the postsynaptic density and does not redistribute after acute synaptic stimulation. *Neuroscience* 266, 80–90. doi: 10.1016/j.neuroscience.2014.01.066

Turrigiano, G. G., Leslie, K. R., Desai, N. S., Rutherford, L. C., and Nelson, S. B. (1998). Activity dependent scaling of quantal amplitude in neocortical neurons. *Nature* 391, 892–896. doi: 10.1038/36103

van der Walt, S., Schönberger, J. L., Nunez-Iglesias, J., Boulogne, F., Warner, J. D., Yager, N., et al. (2014). scikit-image: image processing in Python. *PeerJ* 2:e453. doi: 10.7717/peerj.453

VanGuilder, H. D., Farley, J. A., Yan, H., Van Kirk, C. A., Mitschelen, M., Sonntag, W. E., et al. (2011). Hippocampal dysregulation of synaptic plasticity-associated proteins with age-related cognitive decline. *Neurobiol. Dis.* 43, 201–212. doi: 10.1016/j.nbd.2011.03.012

Watt, A. J., van Rossum, M. C., MacLeod, K. M., Nelson, S. B., and Turrigiano, G. G. (2000). Activity coregulates quantal AMPA and NMDA currents at neocortical synapses. *Neuron* 26, 659–670. doi: 10.1016/S0896-6273(00)81202-7

Zhao, S., Sun, J., Shimizu, K., and Kadota, K. (2018). Silhouette scores for arbitrary defined groups in gene expression data and insights into differential expression results. *Biol. Proced. Online* 20:5. doi: 10.1186/s12575-018-0067-8

Zimmermann, T., Rietdorf, J., Girod, A., Georget, V., and Pepperkok, R. (2002). Spectral imaging and linear un-mixing enables improved FRET efficiency with a novel GFP2-YFP FRET pair. *FEBS Lett.* 531, 245–249. doi: 10.1016/S0014-5793(02)03508-1

Conflict of Interest: The authors declare that the research was conducted in the absence of any commercial or financial relationships that could be construed as a potential conflict of interest.

frontiers in Neural Circuits

METHODS
published: 13 May 2021
doi: 10.3389/fncir.2021.541676

Optical Imaging-Based Guidance of Viral Microinjections and Insertion of a Laminar Electrophysiology Probe Into a Predetermined Barrel in Mouse Area S1BF

Victor M. Mocanu[1,2] *and Amir Shmuel*[1,2,3,4]*

[1] McConnell Brain Imaging Centre, Montreal Neurological Institute, McGill University, Montreal, QC, Canada, [2] Department of Neurology and Neurosurgery, McGill University, Montreal, QC, Canada, [3] Department of Physiology, McGill University, Montreal, QC, Canada, [4] Department of Biomedical Engineering, McGill University, Montreal, QC, Canada

Wide-field Optical Imaging of Intrinsic Signals (OI-IS; Grinvald et al., 1986) is a method for imaging functional brain hemodynamic responses, mainly used to image activity from the surface of the cerebral cortex. It localizes small functional modules – such as cortical columns – with great spatial resolution and spatial specificity relative to the site of increases in neuronal activity. OI-IS is capable of imaging responses either through an intact or thinned skull or following a craniotomy. Therefore, it is minimally invasive, which makes it ideal for survival experiments. Here we describe OI-IS-based methods for guiding microinjections of optogenetics viral vectors in proximity to small functional modules (S1 barrels) of the cerebral cortex and for guiding the insertion of electrodes for electrophysiological recording into such modules. We validate our proposed methods by tissue processing of the cerebral barrel field area, revealing the track of the electrode in a predetermined barrel. In addition, we demonstrate the use of optical imaging to visualize the spatial extent of the optogenetics photostimulation, making it possible to estimate one of the two variables that conjointly determine which region of the brain is stimulated. Lastly, we demonstrate the use of OI-IS at high-magnification for imaging the upper recording contacts of a laminar probe, making it possible to estimate the insertion depth of all contacts relative to the surface of the cortex. These methods support the precise positioning of microinjections and recording electrodes, thus overcoming the variability in the spatial position of fine-scale functional modules.

Keywords: functional localization, optical imaging of intrinsic signals, viral microinjection, optogenetics, neurophysiology, laminar probe, cortical columns, barrel field

OPEN ACCESS

Edited by:
Yves De Koninck,
Laval University, Canada

Reviewed by:
Heiko J. Luhmann,
Johannes Gutenberg University
Mainz, Germany
Daniel Llano,
University of Illinois
at Urbana-Champaign, United States

***Correspondence:**
Amir Shmuel
amir.shmuel@mcgill.ca

Received: *10 March 2020*
Accepted: *31 March 2021*
Published: *13 May 2021*

Citation:
Mocanu VM and Shmuel A (2021) Optical Imaging-Based Guidance of Viral Microinjections and Insertion of a Laminar Electrophysiology Probe Into a Predetermined Barrel in Mouse Area S1BF. Front. Neural Circuits 15:541676. doi: 10.3389/fncir.2021.541676

INTRODUCTION

Optogenetics activates light-sensitive ion channels – or pumps – termed opsins at a physiologically relevant, millisecond-scale on/off kinetics (Zhang et al., 2010; Fenno et al., 2011; Yizhar et al., 2011). Depending on whether they allow cations to cross down their gradient or they pump anions or protons across the cell membrane, opsins can activate (Boyden et al., 2005; Zhang et al., 2008;

Gunaydin et al., 2010; Volkov et al., 2017) or inactivate (Zhang et al., 2007; Gradinaru et al., 2008, 2010), respectively, specific populations of neurons. For a wide range of experimental objectives and hypothesis, optogenetics can be combined with readout techniques to measure *in vivo* neural activity, such as extracellular electrophysiology recordings (Gradinaru et al., 2007; Scanziani and Hausser, 2009; Dugué et al., 2012; Yang et al., 2017, 2018), functional imaging techniques such as functional magnetic resonance imaging (fMRI) (Lee et al., 2010) or intrinsic optical imaging (Scott and Murphy, 2012; Chernov et al., 2018), and behavioral observations (Adamantidis et al., 2007; Gradinaru et al., 2007; Han et al., 2017). To study cortical processing at the scale of cortical columns, it is important to optimize the opsin gene introduction into neurons around a predetermined, small cortical module and the readout from such a module.

Selecting the cortical sites for microinjections and for inserting the recording electrodes is commonly done by using stereotaxic coordinates referenced from structural brain atlases (Kirkcaldie et al., 2012; Watson et al., 2012; Knutsen et al., 2016; Yang et al., 2017; Paxinos and Franklin, 2019). This approach has been commonly used and optimized for applying optogenetics in rodents (Cetin et al., 2007). However, atlas-based positioning of microinjections and electrodes provides only an approximation of the true locations of functional modules, as there can be significant inter-individual (between-subject) variation (Jellema et al., 2004; Oberlaender et al., 2012; Knutsen et al., 2016; Paxinos and Watson, 2017). This is especially problematic for small functional modules such as cortical columns with diameters as small as 200 – 300 microns. For example, maps of cortical columns for the same functional feature from the same cortical area in two different individuals may feature two different organizations: a radial pinwheel organization (Bonhoeffer and Grinvald, 1993) or a linear organization (Shmuel and Grinvald, 2000). Therefore, localizing an insertion with high precision with respect to cortical columns cannot be based solely on stereotactic coordinates.

A different method used for guiding the insertion of an electrode prior to recording from a functional module is based on multiple insertions of an electrode to sparsely sample the responses from the region of interest. Previous studies located barrels in the rodent primary somatosensory barrel field (S1BF) by systematically inserting electrodes in a trial-and-error approach while administering a stimulus to characterize the cortical column properties and performing *post hoc* histology to validate the insertion site (Andermann and Moore, 2006; Yang et al., 2017; Laboy-Juárez et al., 2019). However, this method takes a long time to perform, it can damage the cortex before the experiment has even begun, and it gives only a partial view and sparse sampling of a small area of barrels and septa.

The purpose of the method we present here is to enable high-precision targeting of injections and neurophysiological recordings relative to small functional modules in rodents. To this end, we have devised a protocol to guide microinjections and electrode insertions more efficiently and more precisely than the methods described above. Based on stimulus-evoked hemodynamic responses imaged with Optical Imaging of Intrinsic Signals (OI-IS) (Grinvald et al., 1986), the protocol allows guiding the insertions of microinjection pipettes and/or recording electrodes around or into small functional modules.

Optical Imaging of Intrinsic Signal primarily measures the local changes in the content of deoxy-hemoglobin (deoxy-Hb), oxy-Hb, and the total volume of Hb elicited by neural activation (Grinvald et al., 1986; Frostig et al., 1990; Grinvald et al., 1999; Berwick et al., 2008). These changes cause changes in the absorption of light of specific wavelengths shone onto the surface of the cortex. As we will demonstrate, the results can be used for several steps in an optogenetics experiment. They can be used for guiding viral microinjections around a small target area as was previously demonstrated in monkey area V1 (Ruiz et al., 2013), optimizing the photostimulation used for optogenetics as described by Yizhar et al. (2011), and guiding electrophysiology electrode to a functional module as small as a single barrel with a diameter of 200 microns. Regardless of the brain region to investigate, the principle is the same: apply stimuli known to activate the functional module and obtain a spatially mapped stimulus-activated hemodynamic response. The response amplitude needs to be sufficient to create visible spatial contrast between modules that respond preferentially to the specific stimulus and other modules in the area. Throughout the text, we will use the terms 'targeted module,' 'pre-defined module,' or 'targeted barrel' to refer to the small stimulus-activated region around which we aim to perform microinjections or into which we guide the electrode insertion.

Optical Imaging of Intrinsic Signals resolves fine-scale modules showing hemodynamic responses that correlate with neuronal responses (Grinvald et al., 1986; Shmuel and Grinvald, 1996). The imaging can be performed with a low degree of invasiveness – through the intact (in mice) or thinned skull (in mice and rats), which is optimal for survival experiments.

Optical Imaging of Intrinsic Signals-based guidance of electrode insertions to small functional modules was previously introduced in large animals (Grinvald et al., 1986; Shmuel and Grinvald, 1996; Arieli and Grinvald, 2002; Shmuel et al., 2005). In rats, OI-IS can localize individual cortical columns and barrels in area S1 (Drew and Feldman, 2009; Bortel et al., 2019). OI-IS has recently gained ground as a means of localizing cortical targets for optogenetics manipulation and investigation (Ruiz et al., 2013; Chernov et al., 2018; Yang et al., 2018). This targeting functionality using OI-IS resembles previous studies that localized cortical functional columns in non-human primates, with the purpose of recording from them (Ts'o et al., 2001; Shmuel et al., 2005; Chen et al., 2008; Lu et al., 2010; Tanigawa et al., 2010). However, only one article has described the OI-IS as explicitly tailored and designed to guide optogenetics viral microinjections (Yang et al., 2018). Our paper presents detailed methods for OI-IS-based guidance of optogenetics viral microinjections close to – and around a predetermined small functional module and extends the OI-IS-based guidance to the readout/recording from within such a module.

Our current study focuses on the guidance of microinjections of viral vectors around a small functional module in the rodent cortex and – following an incubation period – the guidance of an electrode insertion into a pre-defined module

for electrophysiology recordings. These methods also allow the user to visualize the spatial spread of the optogenetics photostimulation and – at higher magnification – to estimate the cortical depth of the electrode contacts by imaging the upper recording contacts visible outside of the cortex (Sotero et al., 2015). We verify that the method indeed results in the insertion of the electrode into the targeted module by visualizing the insertion site in images of the histology-processed tissue. Overall, the methods we describe allow for precise and consistent functional localization of small cortical structures with a minimal degree of invasiveness as required for optogenetics experiments.

MATERIALS AND METHODS

(1) Pre-surgery Preparation

All procedures were approved by the animal care committees of the Montreal Neurological Institute and McGill University and were carried out in accordance with the guidelines of the Canadian Council on Animal Care. Adult C57BL/6 10–15 weeks old female and male mice were used for all experiments. The choice of mice, and their genotype and phenotype must be made judiciously according to the specific experimental needs.

A list of equipment items and materials commonly used in the experiments we describe is provided in **Table 1**. Before experiments, sterilize surgical instruments using a hot bead sterilizer (Germinator 500, Stoelting, IL, United States) or by autoclaving. Apply aseptic protocols to the surgery and recovery areas.

(1.1) Induce and then systematically maintain an appropriate plane of anesthesia and analgesia for the surgical procedure. We use 'Mouse Cocktail' combination of ketamine 80–100 mg/kg, xylazine 10 mg/kg and acepromazine 2.5–3 mg/kg, injected I.P. to induce a surgical plane of anesthesia, followed by ketamine 80–100 mg/kg and xylazine 10 mg/kg to maintain anesthesia (Flecknell, 2009). For analgesia, we inject an initial one-time bolus of carprofen 5–10 mg/kg subcutaneously (Flecknell, 2009; Ferry et al., 2014). To verify the surgical level of anesthesia, check for the absence of whisking and withdrawal reflex during a hindpaw painful pinch, and the absence of blinking upon eye contact (to be done while also constantly hydrating the cornea with a protective ophthalmic ointment). In addition, monitor the heartbeat, and make sure the respiration is regular with no signs of gasping (Flecknell, 2009; Ferry et al., 2014).

The anesthetics used should maintain neurophysiological activity and neurovascular coupling as much as possible unchanged. For this, a light plane of anesthesia during the recording sessions must be kept constant by systematically monitoring the vital signs and reflexes, as well as the electrophysiology readout (Flecknell, 2009). Any systematic increases in the heart beat or respiration rate must be counteracted by additional low doses of injectable anesthetic. Conversely, if the vital measures decrease and the spontaneous electrophysiological activity is visibly poor, provide the appropriate antagonist (Flecknell, 2009; Ferry et al., 2014).

(1.2) If using a piezoelectric whisker stimulation, tape or cut away all the same-side whiskers that will not be stimulated during the experiment. Use the surgical microscope to identify these whiskers and ensure their cutting.

(1.3) Position the animal in a small-animal stereotaxic frame (David Kopf Instruments, CA, United States) in a manner consistent with the conventions of the reference atlas, and provide free-flowing oxygen via a nose cone (Ferry et al., 2014). During electrophysiology recordings, switch to a mixture of 70% medical air and 30% oxygen. To reduce discomfort, use non-penetrating ear bars, covered with a drop of Xylocaine ointment (Aspen Pharmacare Canada Inc., ON, Canada).

(2) Stereotaxic Surgery and Skull Thinning or Craniotomy

(2.1) Cut the skin longitudinally along the midline with a scalpel and retract it laterally with a clamp. Remove soft tissue and dry off the exposed skull surface using cotton swabs. Administer topical epinephrine 1 mg/mL (Epiclor, McCarthy & Sons Service, AB, Canada) sparingly or sterile isotonic 0.9% NaCl saline in case of muscle or bone bleeding.

(2.2) Flush the surgical site with small amounts of topical lidocaine hydrochloride 2% (Wyeth, NJ, United States). As soon as the bone has been pierced, do not use lidocaine nor epinephrine, as they will modify the animal's physiology and brain state. Instead, use sterile isotonic 0.9% NaCl saline (Baxter Healthcare Corporation, IL, United States) or preferably Hanks' Balanced Salt solution (HBSS) (MilliporeSigma Canada Co., ON, Canada) to thoroughly clean the surgical site. Because bleeding can impact the quality of the OI-IS, any sources of bleeding must be controlled immediately using persistent flushing with HBSS and absorbing the mixture of blood and HBSS with cotton swabs or Sugi cellulose absorbent triangles (Kettenbach GmbH & Co. KG, Germany) without ever touching the actual brain surface or the dura mater.

(2.3) Find on the skull the bregma, the rostrocaudal and mediolateral coordinates for the cortical region of interest (Ferry et al., 2014; Paxinos and Franklin, 2019).

(2.4) Drill the cranium with a fine micro-drill tip (Fine Science Tools, BC, Canada) under the microscope, using low-force long movements. We observed that constantly applying sterile saline or HBSS to the bone before drilling makes it soft and spongy, and smoothens the drilling process.

(2.4.1) For a survival microinjection experiment, thin the bone until it is flexible under gentle pressure. Homogenize and polish the surface with a silicone polisher micro-drill tip. The bone will be made transparent via an HBSS or silicone oil-filled silicone chamber in step 2.5 (Arieli and Grinvald, 2002).

(2.4.2) For an acute electrode insertion, perform a craniotomy by carefully delineating an area of ∼3 millimeter (mm) × 3 mm, and thinning the perimeter of this area until it can be safely pierced. Then gently lift the central piece of bone, while avoiding

TABLE 1 | Materials.

Name of material/Equipment	Company	Catalog number	Comments/Description
0.9% Saline Sodium Chloride Injection Bag	Baxter Healthcare Corporation	288-0006AA	SURGERY. To safely flush tissue other than the brain
Hanks' Balanced Salt solution (HBSS)	MilliporeSigma Canada Co.	55021C	SURGERY. Solution applied topically to the brain during surgery, to keep the brain from drying
Sugi cellulose absorbent triangles	Kettenbach GmbH & Co. KG, Germany	001911	SURGERY. To absorb excess solutions or blood from tissues
Dowsil Silicone sealant	Dow Corning	3140 90ML MIL-A-46146	SURGERY. For a rigid hydrophobic silicone chamber for holding HBSS
Ethilon Sutures 5-0	Ethicon-Johnson & Johnson	661H (nylon monofilament, FS-2, 45 cm strands)	RECOVERY SURGERY. To connect the skin flaps after the recovery surgery
Polysporin Complete ointment	Johnson & Johnson	60245-43775	RECOVERY SURGERY. To avoid infections during post-op recovery period; it contains three antibiotics plus lidocaine hydrochloride
Syringe Priming Kit	Chromatographic Specialties Inc.	HPRMKIT	VIRAL MICROINJECTIONS. Indispensable to load up the virus into the syringe
Syringe 10 μL removable needle	Hamilton	701RN	VIRAL MICROINJECTIONS. To hold the virus
Glass micropipettes tubes	World Precision Instruments Inc.	18100-3 (3IN BOROSIL GL 1.0 MM OD)	VIRAL MICROINJECTIONS. They will need to be pulled into shape
PHD ULTRA™ Syringe Infuse/Withdraw Programmable Micropump	Harvard Apparatus	70-3007	VIRAL MICROINJECTIONS. For pumping the viral solution through the micropipette at an optimal low rate
Master9 Programmable Pulse Stimulator	A.M.P.I.		STIMULATION. For timing the sensory stimuli
Electrical constant current stimulator	World Precision Instruments Inc.	A365	STIMULATION. For generating electrical current sent to the piezoelectric actuator
Piezoelectric actuator	Piezo Systems Inc.	PSI-5A4E, Y-poled, double quick-mount bender	STIMULATION. For whisker stimulation
VDAQ 3001	Optical Imaging Inc.		OPTICAL IMAGING. For data acquisition
Camera lens	Nikon	1987 (60 MM F/2.8 D-AF)	OPTICAL IMAGING. Optimal for wide-field OI-IS
Camera zoom lens	Edmund Optics	VZM1000i	OPTICAL IMAGING. Optimal for imaging at high-magnification
LED 530 nm	Mightex	BLS-LCS-0530-15-22	OPTICAL IMAGING. LED for Optical Imaging
Electrode for acute insertion and recordings	NeuroNexus	A1 × 32-50-177-A32	NEUROPHYSIOLOGY. Electrode characteristics customizable to the experimental needs
Optogenetic virus	Neurophotonics Centre – Molecular Tools Platform – Ulaval	Viral vector selected according to the scientific question	OPTOGENETICS. The viral vector to be injected into the brain
LED 470 or 595 nm	ThorLabs	M470F3, M595F2	OPTOGENETICS. LED for optogenetic photostimulation
Multimode optical fiber	ThorLabs	FPC-1000-37-02SMA	OPTOGENETICS. Multimode Fiber Patchcord with 0.37 NA, 1000 μm core diameter and SMA connectors
DiI Vybrant cell-labeling solution	Life Technologies	V22885	HISTOLOGY. For marking the track of the electrode
Cytochrome C from bovine heart	Sigma Aldrich	C3131-10MG	HISTOLOGY. For cytochrome oxidase staining
DAB (3,3′-Diaminobenzidine tetrahydrochloride)	Sigma Aldrich	D5905	HISTOLOGY. For cytochrome oxidase staining
DAPI (4′,6-Diamidino-2-Phenylindole, Dilactate)	Thermo Fisher Scientific	D3571	HISTOLOGY. For DAPI fluorescence counterstaining

damage to the brain. For electrophysiology recordings, place a stainless steel skull screw in a region of no-interest in the contralateral hemisphere to use as a ground and reference.

(2.5) Around either the thinned or removed part of the bone, lay down in successive layers a thin-walled silicone chamber (Dow Corning, MI, United States). Allow it to harden, then fill it with HBSS. Make sure the silicone does not spill into the

thinned bone nor into the craniotomy, by applying it in several small layers that build upon each other, before it hardens solid.

(3) Stimulation

(3.1) Set up the hardware, as required. Configure the sensory stimulation and OI-IS setups as shown in **Figure 1A**.

(3.1.1) Turn on the stimulation system. In our setup, we use a constant current stimulus isolator (World Precision Instruments, FL, United States) to deliver bipolar impulses to a 0.58 mm-thick rectangular piezoelectric double-quick-mount actuator (Mide Technology – Piezo, MA, United States), which can deflect ± 270 microns. This deflection is amplified by extending the length of the device using a 3D-printed hollow plastic micropipette (Armstrong-James et al., 1992; Welker et al., 1993), although even a 200 micron deflection should be sufficient to elicit cortical responses (Welker et al., 1993). When the stimulus isolator delivers pulses of 400 microamperes, the 3D-printed micropipette will be displaced at a speed of approximately 35 microns per millisecond, optimal for eliciting cortical evoked responses (unpublished observations).

(3.1.2) Turn on the impulse generator. In our setup, we use a Master-9 Programmable Pulse Stimulator [A.M.P.I., Israel] to deliver 245 milliseconds long square-wave pulses at 4 Hz to the piezoelectric actuator.

(3.2) Prepare the somatosensory stimulation: insert each individual whisker inside the micropipette attached to the piezoelectric device, which is deflected with a ramp-hold-return paradigm at a frequency close to the rodent natural whisking range (Mitchinson et al., 2011; Clancy et al., 2015; Knutsen et al., 2016; Laboy-Juárez et al., 2019). The micropipette should ideally reach as close as 2 mm from the face, and deflect only rostro-caudally, a preferred direction for the whisker sensory system (Andermann and Moore, 2006; Jacob et al., 2008; Le Cam et al., 2011; Vilarchao et al., 2018). Ideally, different micropipettes should be moved without touching any of the other micropipettes or intact whiskers.

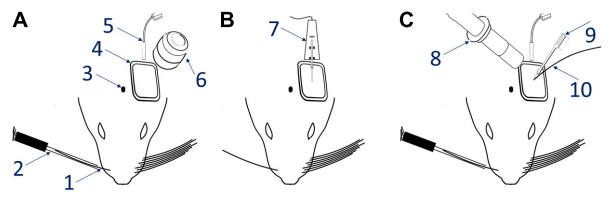

FIGURE 1 | Experimental setup. The left-most panel **(A)** shows the OI-IS recommended setup, before either microinjections or electrophysiology recordings. The middle panel **(B)** shows the optogenetics virus microinjection setup using a micropump directly connected to a mounted 10 microliter syringe. The right-hand panel **(C)** is the setup for acute electrophysiology recordings together with optogenetics photostimulation. 1 – Single whisker contralateral to imaging/recording site, 2 – Piezoelectric device with whisker adapter, 3 – Bregma marking on the skull, 4 – Cortical chamber with silicone chamber, 5 – 530 nm Optical Imaging illumination, 6 – Optical Imaging lens, 7 – Microinjector pump and syringe, 8 – Zoom lens imaging of the insertion site, 9 – Multichannel electrode, 10 – Optogenetics illumination and optic fiber.

(4) Optical Imaging of Intrinsic Signals

(4.1) Optical Imaging of Intrinsic Signals is performed with a monochrome Dalsa DS-21-01M60 camera fitted with a 60 mm AF Micro-Nikkor f/2.8D lens (Nikon Corporation, Japan), linked to a Brain Imager 3001M interface (Optical Imaging Ltd., Israel) and controlled by the VDAQ imaging software (Optical Imaging Ltd., Israel). Throughout all experiments, the camera resolution is 1024 × 1024 and frame rate is 30 Hz, down-sampled to a 10 Hz data frame rate. For electrophysiology insertion recordings, VZM1000i zoom lens with up to 10x-magnification (Edmund Optics, NJ, United States) in order to view and count the electrode's upper contacts that remain above the cortical surface. This makes it possible to monitor the insertion of the probe and estimate the electrode's cortical insertion depth.

(4.2) Turn on the 530 nanometers (nm) LED (Mightex, CA, United States), and position it such that it illuminates the entire ROI uniformly, with the peak of luminosity at the center of the region intended for microinjections (based on atlas coordinates) or insertion of a neurophysiology probe (based on the optical imaging pursued in a previous imaging session, prior to performing the microinjections). Leave it on continuously while adjusting the position of the charge-coupled device camera.

(4.3) Translate and rotate the camera until the entire ROI is within the field of view of the camera. Position the camera above the ROI, so that its optical axis is approximately orthogonal to its cortical surface. Define the imaged region within the field of view.

(4.4) Adjust the LED output to maximize the luminosity values within the area imaged, while avoiding saturation. If there are any light reflections – such as reflections caused by the silicone chamber or the HBSS inside it – keep them outside of the imaged region or try repositioning the illumination light-guide.

(4.5) Before each run, save an image of the pial vessels under green-light illumination, as a reference. The imaged ROI can be saved as a separate image, to be used in step 4.8. The topography of the cortical vessels can then be viewed *in vivo* using a surgical microscope, thus making it possible to guide the insertion of a micropipette or electrode to the small target area. It can also be used for analyzing whether the targeted module shifted for unexpected reasons.

(4.6) Use the OI-IS system to image the response to stimulating each individual whisker of interest. Experimental runs consist of ten stimulation trials (Condition 1) interleaved with ten trials of spontaneous activity (Condition 0). Each stimulation trial consists of 2 s of baseline activity, 6 s of stimulation (in our case, bidirectional whisker piezoelectric deflections), and then 2 s with no stimulus, followed by an inter-trial interval of 7 s. Optical imaging is performed throughout all stimulation and spontaneous activity trials.

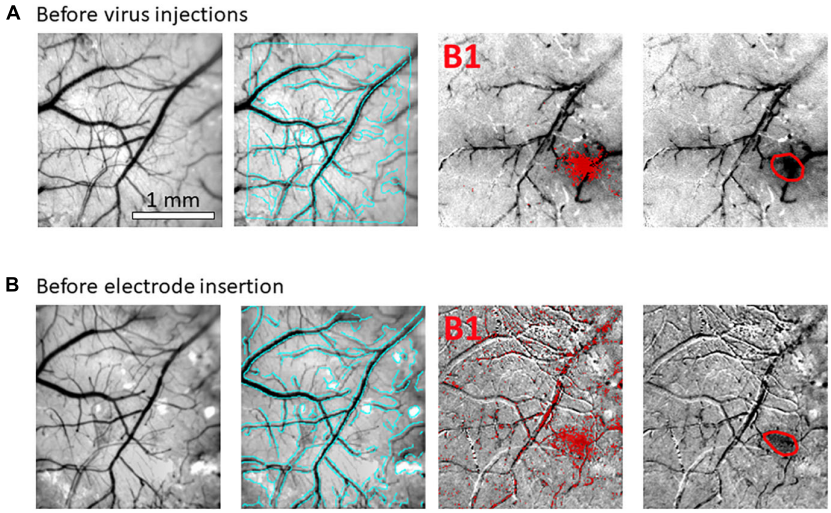

FIGURE 2 | Hemodynamic responses to single-whisker piezoelectric stimulations. **(A)** OI-IS through the thinned skull for guiding microinjections. The 2 left-most panels shows an image of the surface of cortex, taken under green light illumination (peak wavelength of 530 nm) at the beginning of the experiment to obtain the pial vessel topography. The cyan curves are edges of the pial vessels computed before the insertion of the electrode (second panel in **B**) and superimposed on the pial vessels image before the injections, for demonstrating the alignment of the imaged regions and responses. The third panel presents the hemodynamic response to single whisker (whisker B1) stimulation, averaged over 10 trials. Pixels with superimposed red dots showed statistically significant responses. The fourth column shows the perimeter encompassing the responding region, obtained by computing the convex hull around all clusters of connected responding pixels that showed statistically significant response. **(B)** OI-IS following a craniotomy, for guiding the insertion of the recording electrode and the positioning of the optic fiber. All four panels are identical in scope to those presented in **(A)**. The cyan colored curves present the edges of the pial vessels computed (using Canny edge detection) from the green image obtained before electrode insertion.

(4.7) Compute a trial-by-trial single-condition map by dividing the average of images obtained during the response to the whisker (condition 1) of interest by the average of images obtained during the no-stimulus condition (condition 0; **Figures 2**, **3**; Grinvald et al., 1986, 1999). Alternatively, or in addition, compute a trial-by-trial differential response map by dividing the average of images obtained during the response to the whisker of interest by the average of images obtained during the response to stimulating a different whisker (**Figure 4**; Bonhoeffer and Grinvald, 1993; Shmuel and Grinvald, 1996; Grinvald et al., 1999). Both in single condition analysis and differential analysis, we recommend subtracting the frame obtained just before the stimulation begins, to remove slow drifts in cerebral blood volume (CBV) and/or oxygenation.

For each of the trial-by-trial single-condition map and differential maps, the results obtained from the ten trials (10 stimulation blocks) within a run are used for computing the mean and standard deviation (SD), to obtain an averaged stimulus-evoked response or a difference map for the current run.

(4.8) On each of the hemodynamic response images, estimate the activated area using an automated (except for determining the statistical threshold for activation), objective algorithm, and then overlay this result on top of the ROI image from step 4.5 (**Figures 2**, **3**). The algorithm estimates the pixel-wise mean and SD of the relative response over stimulation blocks in one or more runs. We perform pixel-wise statistical testing of the null hypothesis that there is no difference between the mean response in the stimulation condition compared to the no stimulation condition; t-test, $p < 0.01$. This results in a binary map of pixels where the null hypothesis was accepted or rejected. We then mask out pixels located within pial vessels segmented from the OI image taken under illumination wavelength centered at 530 nm. To eliminate spurious response-like results from single pixels, we perform pixel by pixel neighborhood connectivity analysis on the binary map from which blood vessels regions were excluded, and eliminate all responses that form clusters of 7 or less 'connected' pixels. 'A connected pixel' is defined as any pixel adjacent to the currently analyzed pixel by sharing and edge or a corner (eight pixels neighborhood). Lastly, we compute the convex hull of the remaining clustered pixels in the binary image.

(4.9) In case you stimulate whiskers individually in separate runs, repeat steps 3.2, and 4.5 – 4.8 for each whisker. In the end, superimpose a delineation of the responses of all whiskers of interest for a comprehensive overview of all the responses on the reference image of the pial vessels obtained under green light illumination.

(5) Microinjection of Optogenetics Viral Vector

Configure the viral stereotaxic microinjection setup as shown in **Figure 1B**. NOTE: Set up the microinjection apparatus and surgical area in accordance with your local government and

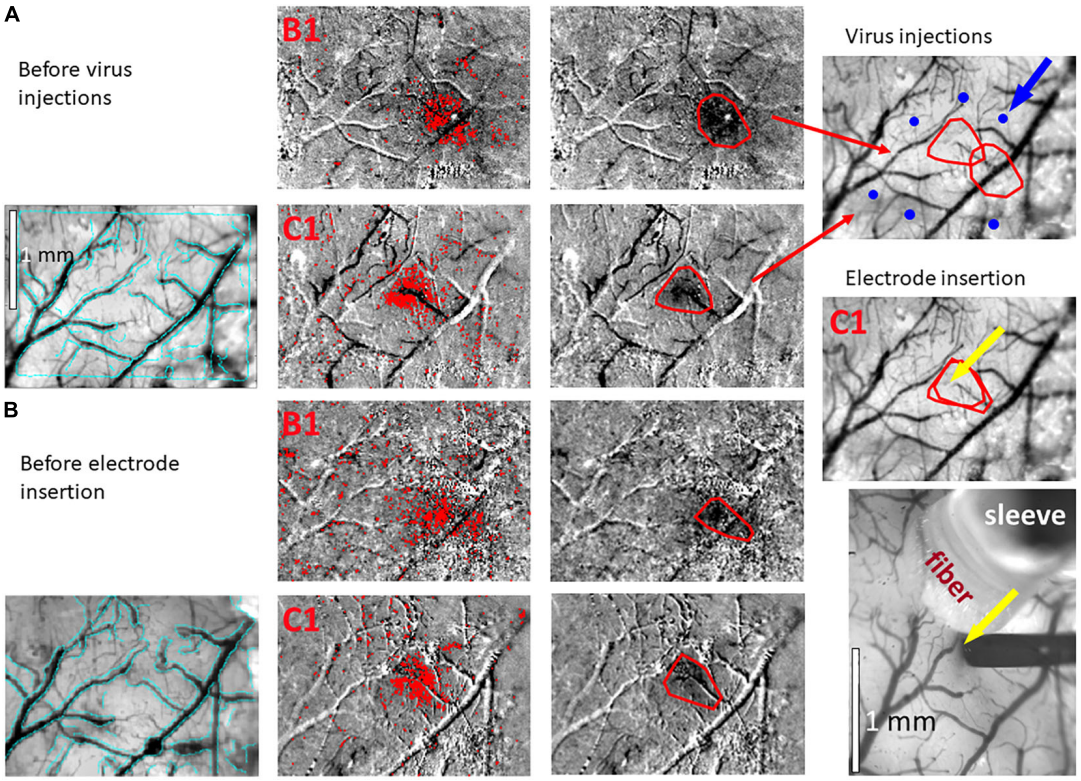

FIGURE 3 | Hemodynamic responses to single-whisker piezoelectric stimulations. **(A)** OI-IS through the thinned skull for guiding microinjections. The left-most panel shows an image of a mouse's right hemisphere. This image was taken under green light illumination (peak wavelength of 530 nm) at the beginning of the experiment to obtain the pial vessel topography. The cyan curves are edges of the pial vessels computed before the insertion of the electrode (left-most panel in **B**) and superimposed on the pial vessels image before the injections, for demonstrating the alignment of the imaged regions and responses. The scale bar represents 1 mm. Each row presents OI-IS steps in their chronological order, for stimulating a single whisker: B1 or C1, respectively. The second column presents images of hemodynamic responses to single whisker stimulation, averaged over ten trials. Pixels with superimposed red dots showed statistically significant responses. The third column shows the perimeter (red curves) encompassing the responding region, obtained by computing the convex hull around all clusters of connected responding pixels. The image in the fourth column overlays the perimeters computed in response to stimulating the B1 and C1 whiskers on top of the green reference image to localize the hemodynamic response with respect to the pial vessels topography. It outlines the overall stimulus-activated region comprising the responses to all the stimulated barrels (red curves), so that microinjections (blue circles; indicated by a blue arrow) can be planned around it, as close as possible to the barrels of interest without damaging these barrels and/or pial blood vessels. **(B)** OI-IS following a craniotomy, for guiding the insertion of the recording electrode and the positioning of the optic fiber. The first three columns are identical in scope to those presented in **(A)**. The cyan colored curves present the edges of the pial vessels computed (using Canny edge detection) from the green image obtained before electrode insertion. The upper image in the right-most column shows in red curves the delineation of the responses stimulating whisker C1 before the injections and before the insertion of the electrode. The yellow arrow points to the position of electrode insertion. The lower image is a high-magnification image of the region where the electrode was inserted. The experimenter selects a site for recording (yellow arrow) in the center of a barrel whose location is estimated by the hemodynamic response, along with the region where photostimulation will be applied. In the bottom-right panel, the electrode is shown after it was inserted at the recording site (yellow arrow). The tip of the optic fiber is placed on top of the cortical surface immediately adjacent to the electrode; the fiber's protective outer sleeve is seen out of focus. The scale bar represents 1 mm.

university regulations, and following previous publications on the subject (Cetin et al., 2007; Lowery and Majewska, 2010; Zhang et al., 2010; Thompson and Towne, 2018; Yang et al., 2018). We use a 10 microliter (μL) 701-RN glass micro-syringe (Hamilton, NV, United States) controlled by a PHD ULTRA programmable microinjection pump (Harvard Apparatus, MA, United States). We use a Syringe Priming Kit (Chromatographic Specialties Inc., ON, Canada) to load up just over 10 microliters of mineral oil (Millipore-Sigma Canada Co., ON, Canada).

To minimize cortical damage, use borosilicate glass micropipettes (World Precision Instruments, FL, United States) pulled to an outer diameter of the tip of 30–100 microns or smaller. If these are not available in your lab, use 36 G or higher G needles (NanoFil, World Precision Instruments, FL, United States). Beveled needles and micropipettes will penetrate the dura easier, whereas blunt ones will expel a more controlled drop of viral solution. Keep in mind that the smaller the tip's inner diameter is, the higher the chance of tissue backflow clogging it. To prevent this, apply a constant slightly positive pressure when moving the micropipette up or down through the cortex.

(5.1) Load up the virus into the glass micropipette at a rate of 50–250 nanoliter (nL) per minute, using a piece of sterile parafilm (Yang et al., 2018) or metal foil, which is non-reactive with the virus. It serves as a shallow non-porous

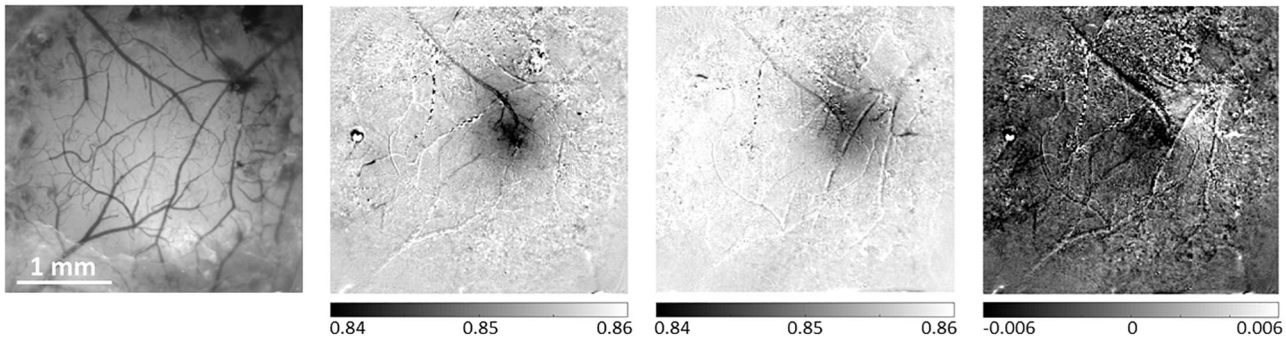

FIGURE 4 | Differential analysis of evoked hemodynamic responses improves spatial contrast and definition of a single barrel activation area. The left-most panel presents a reference image taken under illumination wavelength of 530 nm, showing the pial vessel topography. The second panel shows the hemodynamic response to a single-whisker stimulation of the B1 whisker, calculated as the division of the images acquired during stimulation trials by the images acquired during control/no stimulation trials. The third panel shows a similar result for the Alpha whisker. In the third panel, the differential analysis of these two neighboring whiskers' responses improves the spatial discrimination between the two individual but partially overlapping responses. The grayscale applied to all images represents the same range of relative responses. The scale bar represents 1 mm.

'dish' in which to safely deposit the virus, so that it gets taken up by the micropipette. Do not allow the virus to reach past the glass micropipette and into the syringe. For our optogenetics experiments, we used the virus AAV2/8-CAG-flex-ChR2-tdTomato-WPRE with a titer of 1.5e13 genome copies per ml, as prepared by the Neuro-Photonics Centre's Molecular Tools Platform (Université Laval, QC, Canada).

NOTE: Translation of a floxed or double-floxed inverted open-reading-frame viral genome depends exclusively on the spatially specific presence of the Cre-recombinase in Cre knock-in mice, allowing virtually 100% tropism for the targeted tissue/layer/cells (Cardin et al., 2009; Sohal et al., 2009; Zhang et al., 2010; Fenno et al., 2011).

(5.2) Select sites for viral microinjections in close proximity around the modules of interest while considering the lateral spread of the virus, but strictly avoiding sites close to macroscopic blood vessels. Take note of the stereotaxic location of the selected sites relative to bregma. Importantly, the site selected for microinjection should be projected onto the image of the cortical surface and pial vessels (**Figures 3**, **5**). This will make it possible to guide the insertion of the micropipette to the selected site, while viewing the pial vessels using a surgical microscope.
(5.3) For each site, gently pierce the thinned cranium, creating a small hole with a fine needle or scalpel, while flushing thoroughly with HBSS.
(5.4) Position the glass micropipette above the insertion site, insert and lower it down to the desired cortical depth, while keeping positive pressure in it throughout the insertion to avoid clogging. The cortical depth of the insertion can be estimated relative to the point in which the micropipette first touched the surface of the cortex, based on continuous imaging of the insertion site using the OI system. Wait up to 5 min following the insertion of the micropipette, to allow the brain tissue to settle. Taking images of all micropipette insertions is highly recommended, as it is part of the documentation of the experiment.
(5.5) Inject 100–150 nL of virus solution per site, at a rate of 20–100 nL per minute. Given the original titer, this provides 1.5–2.25e12 total genome copies per microinjection. While the viral spread and infection efficiency are also significant factors in opsin expression, it has been previously reported that at least 1e12 genome copies are sufficient for a cortical transduction volume of 1 mm^3 (Zhang et al., 2010). Note that other researchers have used as low as 6e7 viral particles per injection, with excellent results (Yang et al., 2017).

Wait 10 minutes for the injected solution to diffuse out into the tissue.

(5.6) Retract the glass micropipette up while keeping a positive pressure inside.
(5.7) Repeat steps 5.1–5.5 at other selected insertion sites.
(5.8) After completing all the microinjections for an animal, clean the glass micropipette tip with sterile isotonic saline or HBSS drips. At the end of the microinjection session, drop the micropipette with any remaining virus in a solution of 0.5% sodium hypochlorite for at least 15 min, and then dispose it in a biohazard sharps container. Disinfect the surgical area and tools with a bleach- or peroxide-based solution, not an alcohol-based one.
(5.9) Animal Recovery

(5.9.1) Clean the treated area with sterile isotonic saline or HBSS. Close the skin flaps and suture them together using absorbable sutures of size 5-0 or 6-0 (Ethicon Inc., NJ, United States).

(5.9.2) Apply Polysporin triple antibiotic cream with lidocaine topically (Johnson & Johnson Inc., NJ, United States) onto the sutured flaps. Administer isotonic sterile saline or dextrose solution subcutaneously in the back of the animal, to prevent dehydration.

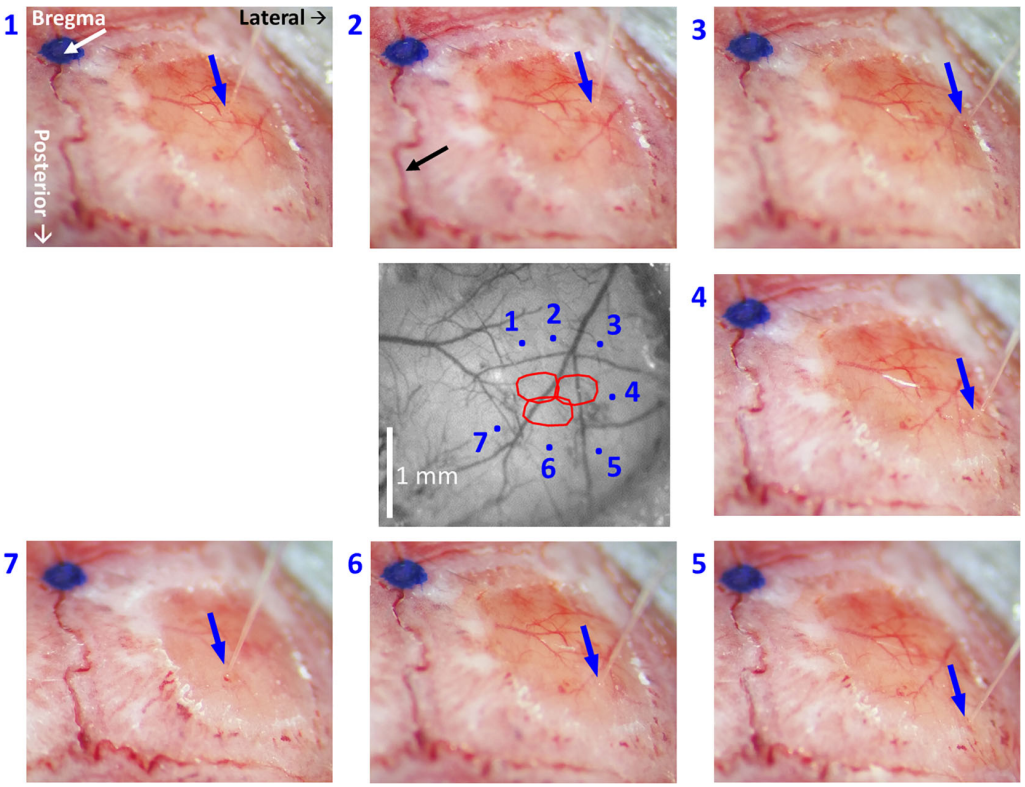

FIGURE 5 | High-resolution images of each individual microinjection location, compared to the corresponding planned site. The image at the center was taken under green light illumination (peak wavelength of 530 nm). It shows the region of interest comprising all the stimulated barrels (red contours, calculated as in **Figure 2**, **3**). Each of the seven images around it was taken after the insertion of the glass micropipette at one of the sites selected for viral micro-injection. The insertion points are indicated by blue arrows. The numbers next to the images of the micropipettes correspond to the microinjection sites displayed in the center image by blue dots. The white arrow in the top-left panel points at a blue dot: this is a fiducial we placed onto the skull to mark the bregma. In the top-middle panel, the black arrow points to the midline suture going posteriorly. The stereotaxic axis directions are marked in the top-left panel. The scale bar represents 1 mm.

(5.9.3) Monitor the animal until it recovers from anesthesia and demonstrates full mobility. If no signs of discomfort are visible, return the animal to its cage.

(5.9.4) Monitor daily and inject an analgesic agent (carprofen 5–10 mg/kg subcutaneous) for 3 days postoperatively.

(6) Electrophysiology Recordings

(6.1) Allow 3–6 weeks (Zhang et al., 2010; Miyashita et al., 2013) for the virus to incubate and express.

(6.2) Repeat steps 1.1–4.9 of the protocol.

(6.3) Select a site(s) for electrophysiology recording. The position is guided by the OI-IS responses obtained in the session that preceded the microinjections. We perform optical imaging in preparation for the neurophysiological recordings too, both for verification and evaluation of the functionality of the modules of interest following the virus microinjections. Strictly avoid electrode insertions close to macroscopic blood vessels. The images of the responses from the two sessions can be spatially registered by aligning the pial vessel images obtained in the two sessions (**Figures 2**, **3**). Similarly to the guidance of the insertions for microinjections, electrode insertions are also guided according to the image of the pial vessels (**Figure 3**, bottom-right panel).

(6.4) Configure the setup for optogenetics photostimulation together with electrophysiology recordings, as shown in **Figure 1C**. If applicable, switch the OI-IS lens to a high-magnification lens, to make it possible to monitor the position of insertion and the depth of the insertion based on imaging the contacts of the probe.

(6.5) Position an acute recording electrode above the selected site, with its recording axis orthogonal to the local surface of the cortex. If using a linear/laminar probe, estimate the angle relative to the cortex from multiple viewpoints, and – if needed – modify the insertion angle for an approximate orthogonal orientation relative to the cortical manifold. For post-experiment localization of the electrode track, gently dip the recording electrode shank a few millimeters in a DiI Vybrant (Life Technologies, CA, United States) cell-labeling solution (An et al., 2012; Laboy-Juárez et al., 2019) prior to inserting it into its final position.

NOTE: Electrophysiological signals sampled at 24,414 Hz are pre-processed by a PZ5 NeuroDigitizer 128-channel preamplifier (Tucker-Davis Technologies, FL, United States), and then

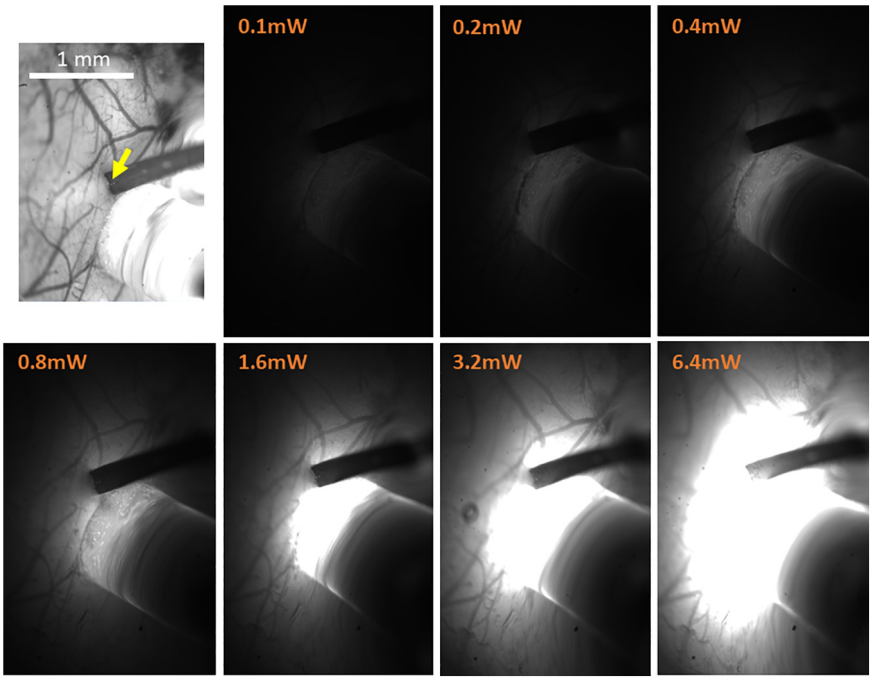

FIGURE 6 | High-resolution imaging of the spatial extent of the optic fiber photostimulation. The top-left panel presents the high-resolution reference image taken under illumination wavelength of 530 nm, just prior to the electrophysiology recordings. It features the pial vessel topography and the electrode insertion site (yellow arrow). The scale bar represents 1 mm. The next seven panels show the optic fiber illumination of the region of interest at the indicated output power of amber light (wavelengths distribution centered on 590 nm; used with eNpHR3.0), taken in otherwise complete darkness and with identical imaging parameters.

processed and recorded using the Synapse Suite software (Tucker-Davis Technologies, FL, United States). For mouse experiments that do not require electrolytic micro-lesions, we use A1 × 32-50-177 probes with a 50 micron thick shaft (NeuroNexus, MI, United States).

(6.6) Place an optic fiber connected to high-powered light-emitting diode immediately next to the electrode. The optic fiber should be positioned approximately 0.5 mm from the dura mater, pointing to the region of cortex where the electrode is inserted, which is expected to be infected by the previously injected virus.

NOTE: Use Dr. Karl Deisseroth's link at: https://web.stanford.edu/group/dlab/cgi-bin/graph/chart.php for a "Brain tissue light transmission calculator" to predicted irradiance values from a given user-defined optic fiber through standard mammalian brain tissue. For example, our experiments used a multimode optic fiber with numerical aperture of 0.37 and 1 mm inner core diameter (Mightex, CA, United States), connected by SMA to a high-power, fiber-coupled, 470 nm LED (ThorLabs Inc., NJ, United States) for exciting the ChR2 opsin. For an LED light power output of 6.4 milliWatt (mW), the irradiance measured at the fiber tip is 2.03 mW/mm^2, as verified before each experiment using a digital handheld power meter (ThorLabs Inc., NJ, United States). Then, the calculated irradiance value at a cortical depth of 100 micron is 1.43 mW/mm^2, and at 1 mm deep, it is 0.1 mW/mm^2.

Choose the optic fiber parameters based on the calculations of brain tissue volume intended to be recruited by photostimulation, as per your experimental needs (Aravanis et al., 2007; Yizhar et al., 2011; Shin et al., 2016). Power outputs of up to 20 mW/mm^2 are safe to use in neurons *in vivo* (Gradinaru et al., 2010; Fenno et al., 2011). Conversely, even sub-mW light intensities are sufficient to elicit optogenetics effects, although the induced voltage changes from the resting membrane potential will be understandably smaller (Madisen et al., 2012; Vazquez et al., 2013; Honjoh et al., 2014).

While monitoring with the high-magnification lens attached to the OI-IS camera, slowly insert the electrode down to the desired cortical depth. This can be estimated by the number of contacts that remain visible above the cortical surface, and by taking into account the geometry of the probe, such as the arrangement of contacts and the distance between them (**Figures 3**, **6**). Wait 5 min for the brain tissue to settle.

(6.7) Record the responses to the planned combinations of sensory stimulations and/or LED optogenetics photostimulation. We use the same experimental paradigm as in steps 3.1.2 and 4.6, except that we turn on the optogenetics photostimulation 2.25 s after the first sensory stimulation, and turn it off 2 s later. Applying the calculations from step 6.6, we use an exponential series of eight LED power outputs, from 0.1 to 12.8 mW, as measured at the tip of the optic fiber. Typically, this encompasses the full range of optogenetics effects, as 0.1 mW elicits negligible effects,

whereas 12.8 mW virtually saturates the system. As a control, photo-stimulation in opsin-negative mice, whether wild-types injected with a Cre-dependent viral vector or mice expressing local Cre recombinase injected with a virus containing no opsin genome, should produce no observable optogenetics effects (Honjoh et al., 2014).

(7) Post-experiment Histology Evaluation

(7.1) At the end of the recording experiment, euthanize and perfuse the animal according to your institutional guidelines, using isotonic saline and 4% paraformaldehyde solution in phosphate buffered saline.

(7.2) Extract and fixate the brain. In order to confirm the location of the electrode, flatten the cortical hemisphere containing the ROI by removing the contralateral hemisphere if not needed (Strominger and Woolsey, 1987), gently scooping out the brainstem and sub-cortical parts, and placing a light flat weight made from a non-reactive material (we use an empty 15 mL glass Erlenmeyer flask), on top of the cortex, which will then be submerged in fixative.

(7.3) When fixation is complete, perform your histology protocol to obtain slices parallel to the cortical surface. Frozen fixed mouse brain blocks are sectioned to obtain 30 micron-thick slices using a cryostat (Leica Biosystems, Germany), although 40 microns is safer for fragile tissues. We use triple fluorescent slices [DiI and the opsins' fluorescent tags, counterstained with 4',6-diamidino-2-phenylindole (DAPI) to visualize cell bodies] in conjunction with interleaved slices stained with cytochrome oxidase to visualize S1BF barrels (Isett et al., 2018; Laboy-Juárez et al., 2019; **Figures 7**, **8**). To verify opsin expression and tropism, a typical protocol involves successive steps in 0.1% Triton X-100 (MilliporeSigma, MA, United States) to permeabilize cell membranes; in normal donkey or horse serum (MilliporeSigma, MA, United States) step to minimize non-specific binding; in the primary antibody usually overnight; finally, in the secondary antibody with fluorescent tags, which comes from a different species than the primary (Dako, 2009; Yang et al., 2018).

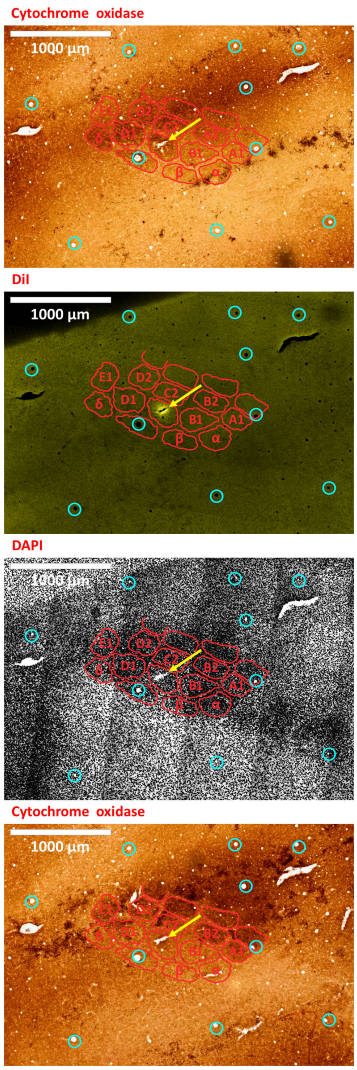

FIGURE 7 | An electrode insertion into a pre-defined barrel is verified by DiI fluorescence co-localized with DAPI and cytochrome oxidase staining of the flattened cortex. Post-experiment histology was performed on the flattened cortex of the mouse's right hemisphere, from which we present three consecutive slices. In all panels, red perimeters delineate the major barrels, as identified by cytochrome oxidase and DAPI, and yellow arrows point to the insertion within the targeted barrel. Penetrating blood vessels (marked with cyan circles) were used to optimize the finescale registration of the three adjacent slices using translation and rotation (see Shmuel et al., 2005). The top-most and bottom-most panels present brightfield images of cytochrome oxidase staining of the first and third slices, respectively, showing the targeted C1 barrel. The second and third panels represent the same second slice imaged using different filters; therefore, corresponding pixels are perfectly co-aligned between them. The second panel shows the electrode insertion site, imaged using a TRITC filter at 580 nm. The recording electrode was coated with DiI prior to insertion; thus, the DiI fluorescence image identifies the insertion site (yellow arrow). Twelve penetrating blood vessels (marked with cyan circles) were used to optimize the registration of consecutive slices using translation and rotation (see Shmuel et al., 2005). The DiI mark of the insertion site in the second panel shows that the insertion was inside the targeted C1 barrel in the top and bottom panels. The third panel shows the DAPI counterstaining of cell bodies' nuclei of the same slice, performed using a DAPI filter (distribution of wavelengths centered on 455 nm). A grayscale filter was applied to the DAPI image in order to improve visualization of the barrel field. The scale bar represents 1 mm.

RESULTS

Our first methodological objective is to inject an optogenetics virus in the mouse barrel field around a single barrel, to infect both this barrel as well as its immediate neighbors, while ensuring that the barrel itself is not damaged (**Figures 3**, **5**). For guiding microinjections which are followed by the recovery of the animal, we propose to perform minimally invasive OI-IS through the thinned skull (**Figures 2A**, **3A**, **4**) and gently break the surface of the skull at the selected injection points.

Following an incubation period of 21–42 days (Zhang et al., 2010; Miyashita et al., 2013), we repeat the OI-IS in order to identify the target barrel and evaluate whether any injection-related damage could hamper its functionality (**Figures 2B**, **3B**). This makes it possible to guide the insertion of an electrode within the barrel and optimize the positioning of

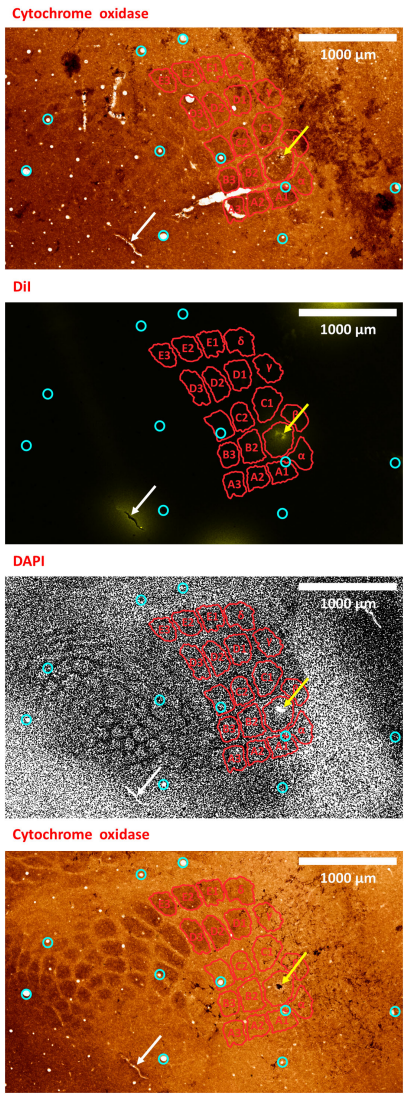

FIGURE 8 | A second example of verifying an electrode insertion into a pre-defined barrel using tissue processing. Post experiment histology was performed on the flattened cortex of the mouse right hemisphere, from which we present three consecutive slices. In all panels, red perimeters delineate the major barrels identified in the second panel, as localized using both cytochrome oxidase and DAPI, yellow arrows point to the insertion within the targeted barrel, and white arrows point to one of the four user-made DiI fiducial markers. The top-most and bottom-most panels present bright-field images of cytochrome oxidase staining of the first and third slices, respectively, showing the targeted B1 barrel. The second and third panels present the second slice imaged using different microscope filters; therefore, every pixel is perfectly co-localized between them. The second panel presents the DiI fluorescence imaging of the second slice. It shows the DiI fiducial markers as well as the recording site, using a TRITC filter with wavelength distribution centered at 580 nm. The third panel shows the DAPI counterstaining of cell bodies' nuclei of this same slice, performed using a filter with wavelength distribution centered at 455 nm. A grayscale filter was applied to the DAPI image in order to improve visualization of the barrel field. Four user-made DiI fiducial markers were used for the initial co-registration of the slices. Ten penetrating blood vessels (cyan circles) were then used to optimize the fine-scale registration of the consecutive slices. The DiI-marked electrode insertion site (yellow arrow) is inside the pre-selected B1 barrel. The scale bar represents 1 mm.

the optic fiber attached to the LED or laser photo-stimulation. For this part of the experiment, we propose to perform a craniotomy, which makes it possible to obtain sharp images of the cortical surface, and to insert the electrode or multi-contact probe safely. In addition to guiding the insertion of the electrode to the pre-determined barrel, the user can use the OI system to estimate the spatial extent of the optogenetics photostimulation, by comparing the image obtained under the fiber-optic illumination to the pial vessels around the optic fiber (**Figure 6**).

In our experiments, the OI-IS hemodynamic responses obtained before the microinjections and following the incubation period were consistent: a single barrel's localizations before and after the incubation period were always overlapping (**Figures 2**, **3**). Thus, imaging post incubation is required for evaluating whether post-injection tissue damage interferes with the response of the module of interest or if the user needs to evaluate plasticity of the organization. Assuming that the virus on its own does not cause plasticity, the guidance of the neurophysiology can be based on the OI-IS results obtained before the microinjections and the topography of the cortical vessels (**Figures 2**, **3**).

The expected outcome of the OI-IS is a well-delineated area of hemodynamic activation, verifying the original shape of – and centered on – the targeted structure. Ideally, two or more small structures such as barrels can thus be delineated and differentiated, with minimal overlap (Pouratian and Toga, 2002; Drew and Feldman, 2009; **Figures 3**, **4**).

To validate our proposed method for OI-IS guided insertion of an electrode into a small cortical functional domain – a predetermined barrel, we performed histology of tissue slices cut tangential to the surface of the flattened brain. Barrels were stained with cytochrome oxidase, and cells were stained with the DAPI nuclear stain.

By default, the microinjection sites should not generate clearly visible long-lasting marks on the cortex. To mark the electrode insertion track, we dipped the electrode in DiI prior to insertion, in order to leave a fluorescent mark on a DAPI stained background, and to compare to the barrel field map obtained with cytochrome oxidase staining (Isett et al., 2018; Laboy-Juárez et al., 2019; **Figures 7**, **8**). All our fluorescence histology slices were imaged at the appropriate filters for the three respective excitation wavelengths of DAPI, DiI and the opsin fluorescent tag. Therefore, each slice outputs three images that are perfectly co-aligned, with each pixel having a one-to-one spatial association in all three images. Thus, after performing alignment between the cytochrome oxidase and DAPI images, the DiI image needs only to be super-imposed on its matching DAPI image. Alignment of penetrating cortical blood vessels (**Figures 7**, **8**) is used to optimize the fine-scale registration of two consecutive histology slices (Malach et al., 1993; Shmuel et al., 2005), even with different staining. **Figures 7**, **8** demonstrate that the insertion was into the center of the pre-determined barrel – validating the method we propose for guiding the microinjections and electrode insertion at high-precision.

DISCUSSION

Our proposed methodology aims to guide viral microinjections of viral vectors around – and electrode insertion into – a pre-defined small functional module. Given the delicate, long-term nature of optogenetics experiments as well as the efforts they require, it is important to have the viral microinjections and electrode insertions precisely in their intended locations.

Optical-Imaging-Based Guidance of Optogenetics Viral Injections and Electrode Insertions

Optical Imaging of Intrinsic Signals is a widely used and easy to implement functional imaging technique with high spatial specificity and resolution (Grinvald et al., 1986). Relatively low-cost hardware is required for implementing OI-IS: a charge-coupled device or CMOS camera with a standard 50 mm – 60 mm lens, and an image acquisition system. The systems to generate the stimuli are required for the main experiment, independent of the OI-IS-based guidance that we propose. There are several facets of an optogenetics experiment that can be improved with this setup. These include the precise guidance of viral microinjections and the recording probe around or into a small functional module, and guiding the positioning of the optic fiber by estimating the region excited by the optogenetics illumination. By switching to a zoom lens, the experimenter can monitor the probe's contacts at high-magnification, making it possible to control the depth of the electrode insertion.

While the current experiments have focused on barrels in mouse area S1BF, OI-IS can be used to localize several distinct cortical areas and modules of interest to deliver optogenetics viruses, photostimulate optogenetically, and record from multiple sites. Given its non-invasive nature, it would also be ideal for reading the long-term chronic-effects of optogenetics stimulation. Finally, OI-IS would be ideal for guiding optogenetics experiments in non-human primates and marmosets.

The main sources of error during OI-IS and their troubleshooting have been discussed in detail in the Results section. When used properly, this technique provides reliable, consistent identification of functional modules on the scale of hundreds of microns, to a degree of precision not attainable by using atlas coordinates and/or by trial-and-error of electrode insertion. We have demonstrated the accuracy of the OI-IS-guided insertions by post-experiment histology of the flattened brain. The DiI-marked electrode track is located inside the targeted barrel of interest, as identified by cytochrome oxidase and by counterstaining techniques such as DAPI. Additional immunohistochemistry options are available, such as using NeuN as the counterstain or using specific markers to identify the user's particular target that would then be co-localized with the DiI from the recording site.

Whereas OI-IS requires craniotomy in large animals, it can be performed through the thinned skull in rodents. However, imaging through the skull blurs the images because of the light scattering caused by the bone. When imaging through the skull, a commonly observed issue is spatially blurred images of the pial vessels and hemodynamic response. The first step is to make sure that the lens is focused on the pial vessels. If the blurring persists, additional thinning of the skull may help. To overcome blurring when targeting small functional modules on the scale of hundreds of microns, imaging the cortex following craniotomy can be pursued (compare rows A and B in each of **Figures 2**, **3**). Resecting the dura mater is required for imaging in large animals. In rodents – especially in mice – resecting the dura mater is not a condition for imaging; however, to obtain sharp images, it is recommended to resect the dura mater in rodents too. Therefore, the user can evaluate the tradeoff between the degrees of invasiveness against the spatial precision required for the guidance.

Another issue that we have commonly observed is that the activated region is larger than the corresponding anatomical structure (**Figure 4**), possibly because the stimulus may activate adjacent regions that are connected to the stimulated barrel (e.g., neighboring barrels) (Berwick et al., 2008; Drew and Feldman, 2009). To overcome this issue, the user can ensure a more balanced stimulus, such as reduced total duration, amplitude and/or frequency of whisker deflection (Berwick et al., 2008). Importantly, a hemodynamic response to stimulating a single module can overlap with neighboring modules. To address this issue, we recommend to image the responses to stimulation of the neighboring modules separately. Then, differential analysis of the different responses can be used to remove the common response and present the spatial contrast, as we as we demonstrate in **Figure 4** (Bonhoeffer and Grinvald, 1993; Shmuel and Grinvald, 1996; Grinvald et al., 1999). Differential analysis eliminates the common response and enhances the visualization of the specific representation of the stimulus/module/barrel of interest (**Figure 4**).

Illuminating at an isosbestic wavelength of 550, 569, or 586 nm measures the total Hb content and, by extension, the CBV (Frostig et al., 1990). Functional imaging studies indicate that CBV responses co-localize faithfully to sites of increases in neural activity (Fukuda et al., 2006; Yao et al., 2017) whereas the patterns of changes in deoxygenated blood are most prominent in draining veins (Hess et al., 2000; Sheth et al., 2003, 2004; Lu et al., 2004; Hillman, 2014; Chaimow et al., 2018). Given the importance of spatial precision in identifying the pre-defined cortical column, we exclusively use green 530 nm illumination for both surface vasculature reference images and OI-IS. While 530 nm illumination shows a clear pattern of the pial vessels, it also provides the best contrast to noise (CNR) ratio. In other words, it gives a clear functional image in a short time frame. This feature is important for using OI-IS for guiding microinjections and insertion of electrodes to small functional modules, because the OI-IS stage has to be short. In addition, green illumination reflects changes in CBV, which show spatial specificity to the site of increased neuronal activity at a level comparable to that obtained by the OI-IS initial deep (Fukuda et al., 2006).

A critical aspect of OI-IS is the need of maintaining appropriate anesthesia, as this may influence both the neuronal and hemodynamic responses (Janssen et al., 2004; Masamoto and Kanno, 2012; Juavinett et al., 2017). It is critical for the quality

of the experiment to avoid anesthetics that interfere with the cortical blood flow or with neurovascular coupling (Masamoto and Kanno, 2012). Isoflurane represents a non-optimal choice, as it depresses evoked responses and is a vasodilator at typical regimes (Iida et al., 1998; Bortel et al., 2020). In our mouse experiments, we use a combination of ketamine and xylazine or dexmedetomidine and isoflurane administered at low-percentage (Bortel et al., 2020).

OI-IS Is Optimal for Guidance of Insertions Around and Into Fine-Scale Cortical Modules

Optical Imaging of Intrinsic Signals relies solely on intrinsic neurovascular elements and does not require adding an extrinsic indicator of neuronal activity (Grinvald et al., 1999). Thus, it requires no additional injections of viruses for the purpose of imaging (Seidemann et al., 2016), which may damage the cortical module of interest.

Membrane-bound dyes such as voltage-sensitive dyes (VSD) used *in vivo* report voltage changes in neurons at an excellent temporal and spatial resolution (Grinvald et al., 1988, 1999; Grinvald and Hildesheim, 2004; Devonshire et al., 2013). The VSD pharmacological and cytotoxic side effects have recently been alleviated to near-negligible levels, using newer generations of blue dyes and lower dye concentrations (Ross et al., 1977; Grinvald et al., 1988; Shoham et al., 1999; Grinvald and Hildesheim, 2004; Lippert et al., 2007; Grandy et al., 2012; Devonshire et al., 2013; Habib et al., 2013; Carter and Shieh, 2015). Compared to *in vivo* VSD imaging, OI-IS is an indirect indicator of neural activity. Nevertheless, while VSD imaging has undeniable advantages for imaging neuronal membrane potentials, OI-IS provides faster functional mapping in space because VSDs require 1–2 h to penetrate cortex and bind to the neurons' membranes (Shoham et al., 1999; Lippert et al., 2007; Grandy et al., 2012; McVea et al., 2012). Obtaining the mapping from OI-IS faster than with VSD is important for OI-based guidance of viral microinjections, because it reduces the time under anesthesia in recovery experiments. Similarly, in acute experiments, OI-IS makes it possible to start the neurophysiological recordings earlier than VSD does, thus reducing effects of accumulated anesthesia during the recordings.

In addition, OI-IS is minimally invasive when performed through a thinned skull, whereas VSD imaging requires craniotomy. Although VSD imaging can be successfully combined with optogenetics (Willadt et al., 2014), it requires a judicious choice of dyes and opsins and a more advanced photostimulation/imaging setup (Vogt et al., 2011; Willadt et al., 2014). We posit that for guiding insertions of microinjection pipettes and/or electrodes into fine-scale functional modules, OI-IS is superior to VSD imaging.

Consideration of Selecting the Viral Vector, Serotype, and Promoter for Applying Optogenetics in Fine-Scale Cortical Modules

For combining OI-IS with optogenetics, it is important to consider the bands of wavelengths for the OI-IS illumination and for exciting the optogenetic opsin. If these distributions overlap considerably, the OI-IS illumination will excite the optogentic opsin, which will, in turn, manipulate the neuronal activity. This is especially important if the OI-IS serves as a readout to quantify the effect of the optogenetic manipulation. However, to prevent undesired effects, it is important to consider the distributions of wavelengths also for using OI-IS to guide the insertion of probes into brains that already carry the optogenetic opsin. Here we imaged relative changes in total hemoglobin using a narrow band of wavelengths centered on 530 nm. The optogenetics opsin we used is ChR2, whose maximum sensitivity is at 466 nm (Nagel et al., 2003; Zhang et al., 2010; Yizhar et al., 2011). At 530 nm, ChR2's sensitivity drops to 21% of the maximum sensitivity.

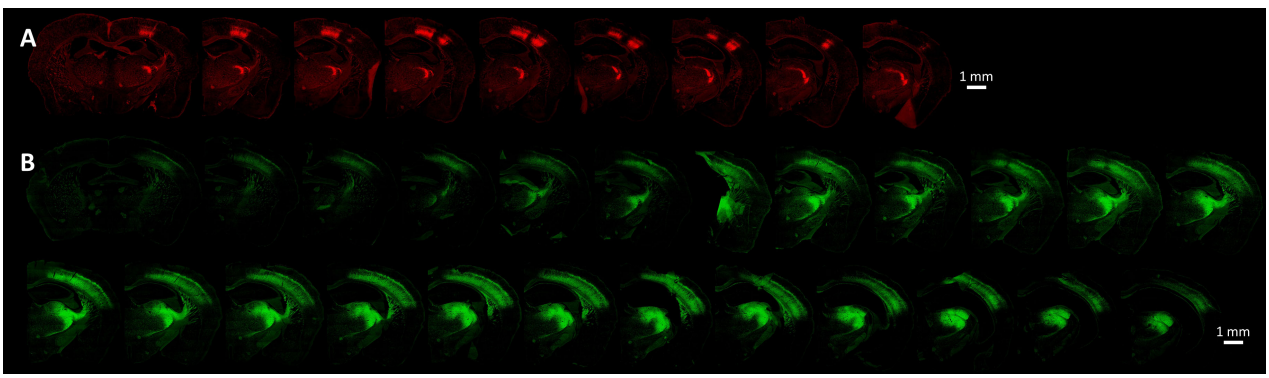

FIGURE 9 | Cortical opsin expression is significantly dependent on viral and microinjection characteristics such as the promoter-serotype combination. **(A)** Presents the opsin expression from the virus AAV2/8-CAG-Flex-ChR2-tdTomato (titer of 1e13 GC/ml). The coronal sections in the bottom panel show the spread of the virus AAV2/5-EF1α-DIO-ChR2-EYFP (titer of 5e12 GC/ml). Both viruses were injected at two locations determined by OI-IS, with each location receiving two injections of 150 nL at a rate of 20 nL per minute. In each of these cases, injections were made at two cortical depths, 700 microns, and 900 microns. The imaged slices were 30 micron-thick. The images were taken at 10x magnification by an Olympus VS120 slide scanner, using the orange (TRITC, 580 nm) and green (FITC, 518 nm) channels, respectively.

Given that the power used for OI-IS illumination is lower than that used for optogenetics, we expect that the effect of the OI-IS illumination on the neuronal activity through excitation of the optogenetics opsin is diminished.

In animal models, opsins are commonly introduced into neurons via viral microinjections (Bernstein and Boyden, 2011; Fenno et al., 2011; Yizhar et al., 2011). Recently, adeno-associated viruses (AAV) have become favored because of their low immunogenicity, good production titer, and expression efficiency, but especially because they can be manipulated in Bio-Safety Level 1 conditions (Zhang et al., 2010; Fenno et al., 2011; Thompson and Towne, 2018; Addgene, 2020). The user can control the degree of specificity of the optogenetics manipulation by using different viral characteristics and microinjection parameters (Gradinaru et al., 2010; Chernov et al., 2018). For example, some viral capsids are taken up into cells faster than others, thus modulating the volume of infection; the promoter can allow expression in an exclusive type of cells or tissue, which is termed tropism; the serotype, viral type, and genome can influence the levels of expression, antero- or retrograde transport, and *trans*-synaptic infection (Cearley and Wolfe, 2006; Cohen et al., 2011; Fenno et al., 2011; Yizhar et al., 2011; Urban and Rossier, 2012; Aschauer et al., 2013; Scheyltjens et al., 2015; Watakabe et al., 2015; Thompson and Towne, 2018; Yizhar and Adamantidis, 2018).

The viral and microinjection characteristics influence directly the opsin expression, but also the experimental approach. The promoter-serotype combination is the most significant intrinsic factor determining the viral infection spread and pattern, although some variations may occur, especially at extreme titers (Nathanson et al., 2009; Yizhar et al., 2011; Aschauer et al., 2013; Scheyltjens et al., 2015). For example, chicken β-actin (CBA), its derivative called CAG, and human cytomegalovirus (CMV) are generally considered strong transcription promoters (Powell et al., 2015), while CaMKIIα 0.4 constructs specifically infect more than 90% excitatory neurons (Yizhar et al., 2011; Scheyltjens et al., 2015). The new hybrid vector AAV-DJ combines elements from eight different serotypes to achieve high transduction efficiency (Grimm et al., 2008; Thompson and Towne, 2018). The cortical spread of various recombinant, hybrid AAV serotypes using either the CMV or the CaMKIIα promoters, shows an increasing serotype efficacy of $2/1 << 2/7 \sim 2/8 \sim 2/9 < 2/5$ (in this terminology, the AAV2 inverted terminal repeat has been cross-packaged in the capsid from the second numbered serotype, Choi et al., 2005), based on mean expression spread from the injection site (Scheyltjens et al., 2015). Other researchers have found serotype 2/8 to spread less than 2/9 (Cearley and Wolfe, 2006; Aschauer et al., 2013; Thompson and Towne, 2018), but since they share axonal transport mechanisms (Castle et al., 2014), a possible explanation would be that the uptake of 2/8 into neurons is faster and thus the virus has less time to spread, possibly due to improved uptake through the plasma membrane. Therefore, if the experiment requires a smaller confined area of opsin expression, then a good option is to inject AAV2/8 with the CMV promoter, as long as the microinjection sites can be positioned less than 1 mm apart from each other and from the center of the cortical module of interest (Scheyltjens et al., 2015). If the region of interest (ROI) is widespread, forcing the microinjection sites to be too numerous or far away from each other, then 2/5 or 2/9 can be used instead (Scheyltjens et al., 2015; Thompson and Towne, 2018). See an empirical comparison of a narrow spreading expression of AAV2/8-CAG versus a far-spreading AAV2/5-EF1α in the top and bottom panels of **Figure 9**, respectively. Since cell tropism and infection efficiency may vary with the location and type of tissue being targeted (Burger et al., 2004), the best practice is to test several viral vectors to compare the resulting opsin expressions empirically.

CONCLUSION

Pursuing optogenetic microinjections or recording neurophysiology from inside a predetermined fine-scale cortical module requires a careful consideration of the experimental parameters, such as viral serotypes and promoter. More importantly, it also requires to precisely map these modules *in vivo*. The OI-IS-based guidance methodology described in this manuscript makes it possible to insert micropipettes for viral microinjection and neurophysiology electrodes quickly and accurately to their pre-determined functional module. It allows sub-millimeter spatial resolution and minimal overlap of activated modules. It also features a low degree of invasiveness; thus, it is safe for use in long-duration protocols such as microinjections of optogenetic viral vectors in a recovery surgery, followed by a period of several weeks allowing opsin expression, then performing the readout and/or behavioral measurements.

DATA AVAILABILITY STATEMENT

The data supporting the conclusions of this article will be made available upon a request sent by email to the corresponding author. See https://www.mcgill.ca/neuro/amir-shmuel-phd.

ETHICS STATEMENT

This animal study was reviewed and approved by the Animal Care Committee of the Montreal Neurological Institute, McGill University.

AUTHOR CONTRIBUTIONS

VMM designed the study, acquired and analyzed the data, and wrote the manuscript. AS initiated and designed the study, oversaw the data acquisition and analysis, wrote part of the code for the OI-IS data analysis, and wrote the manuscript. Both authors contributed to the article and approved the submitted version.

FUNDING

This study was supported by grants from the Canadian Institute of Health Research (Grant MOP-102599) and the Natural Sciences and Engineering Research Council of Canada (RGPIN 2015-05103) awarded to AS, and a Brain Canada Foundation platform support grant (PSG15-3755).

ACKNOWLEDGMENTS

We thank Aleksandra Bortel for the helpful discussions, Alhusain Abdalla for writing the code for aligning images of the pial vessels, and Zeshan Yao for writing part of the code for the OI-IS data analysis. We thank Dr. Marie-Eve Paquet, coordinator of the Neurophotonics Centre – Molecular Tools Platform of Laval University, for her advice on selecting and manufacturing the viruses for our lab. We also thank Melina Jaramillo Garcia, core facility manager at the Molecular and Cellular Microscopy Platform of the Douglas Mental Health University Institute, for scanning the histology slides.

REFERENCES

Adamantidis, A., Zhang, F., Aravanis, A. M., Deisseroth, K., and De Lecea, L. (2007). Neural substrates of awakening probed with optogenetic control of hypocretin neurons. *Nature* 450, 420–424. doi: 10.1038/nature06310

Addgene (2020). "Viral Plasmids and Resources," in *Use this guide to learn more about the different types of viruses that are commonly used in research, and to find plasmids that can be used to engineer viruses for a wide array of research purposes*, (Massachusetts, MA: Addgene).

An, S., Yang, J.-W., Sun, H., Kilb, W., and Luhmann, H. J. (2012). Long-term potentiation in the neonatal rat barrel cortex in vivo. *J. Neurosci.* 32, 9511–9516. doi: 10.1523/jneurosci.1212-12.2012

Andermann, M. L., and Moore, C. I. (2006). A somatotopic map of vibrissa motion direction within a barrel column. *Nat. Neurosci.* 9, 543–551. doi: 10.1038/nn1671

Aravanis, A. M., Wang, L.-P., Zhang, F., Meltzer, L. A., Mogri, M. Z., Schneider, M. B., et al. (2007). An optical neural interface: in vivo control of rodent motor cortex with integrated fiberoptic and optogenetic technology. *J. Neural Engine.* 4, S143–S156.

Arieli, A., and Grinvald, A. (2002). Optical imaging combined with targeted electrical recordings, microstimulation, or tracer injections. *J. Neurosci. Methods* 116, 15–28. doi: 10.1016/s0165-0270(02)00022-5

Armstrong-James, M., Fox, K., and Das-Gupta, A. (1992). Flow of excitation within rat barrel cortex on striking a single vibrissa. *J. Neurophysiol.* 68, 1345–1358. doi: 10.1152/jn.1992.68.4.1345

Aschauer, D. F., Kreuz, S., and Rumpel, S. (2013). Analysis of transduction efficiency, tropism and axonal transport of AAV serotypes 1, 2, 5, 6, 8 and 9 in the mouse brain. *PLoS One* 8:e76310. doi: 10.1371/journal.pone.0076310

Bernstein, J. G., and Boyden, E. S. (2011). Optogenetic tools for analyzing the neural circuits of behavior. *Trends Cognit. Sci.* 15, 592–600. doi: 10.1016/j.tics.2011.10.003

Berwick, J., Johnston, D., Jones, M., Martindale, J., Martin, C., Kennerley, A. J., et al. (2008). Fine detail of neurovascular coupling revealed by spatiotemporal analysis of the hemodynamic response to single whisker stimulation in rat barrel cortex. *J. Neurophys.* 99, 787–798. doi: 10.1152/jn.00658.2007

Bonhoeffer, T., and Grinvald, A. (1993). The layout of iso-orientation domains in area 18 of cat visual cortex: optical imaging reveals a pinwheel-like organization. *J. Neurosci.* 13:4157. doi: 10.1523/jneurosci.13-10-04157.1993

Bortel, A., Pilgram, R., Yao, Z. S., and Shmuel, A. (2020). Dexmedetomidine - Commonly Used in Functional Imaging Studies - Increases Susceptibility to Seizures in Rats But Not in Wild Type Mice. *Front. Neurosci.* 14:832. doi: 10.3389/fnins.2020.00832

Bortel, A., Yao, Z. S., and Shmuel, A. (2019). A rat model of somatosensory-evoked reflex seizures induced by peripheral stimulation. *Epilepsy Res.* 157, 106209. doi: 10.1016/j.eplepsyres.2019.106209

Boyden, E. S., Zhang, F., Bamberg, E., Nagel, G., and Deisseroth, K. (2005). Millisecond-timescale, genetically targeted optical control of neural activity. *Nat. Neurosci.* 8, 1263–1268. doi: 10.1038/nn1525

Burger, C., Gorbatyuk, O. S., Velardo, M. J., Peden, C. S., Williams, P., Zolotukhin, S., et al. (2004). Recombinant AAV viral vectors pseudotyped with viral capsids from serotypes 1, 2, and 5 display differential efficiency and cell tropism after delivery to different regions of the central nervous system. *Mol. Ther.* 10, 302–317. doi: 10.1016/j.ymthe.2004.05.024

Cardin, J. A., Carlen, M., Meletis, K., Knoblich, U., Zhang, F., Deisseroth, K., et al. (2009). Driving fast-spiking cells induces gamma rhythm and controls sensory responses. *Nature* 459, 663–667. doi: 10.1038/nature08002

Carter, M., and Shieh, J. (2015). "Chapter 7 Visualizing Neural Function," in *Guide to Research Techniques in Neuroscience*, 2nd Edn, eds M. Carter and J. Shieh (San Diego: Academic Press), 167–183. doi: 10.1016/b978-0-12-800511-8.00007-1

Castle, M. J., Gershenson, Z. T., Giles, A. R., Holzbaur, E. L., and Wolfe, J. H. (2014). Adeno-associated virus serotypes 1, 8, and 9 share conserved mechanisms for anterograde and retrograde axonal transport. *Hum. Gene Ther.* 25, 705–720. doi: 10.1089/hum.2013.189

Cearley, C. N., and Wolfe, J. H. (2006). Transduction characteristics of adeno-associated virus vectors expressing cap serotypes 7, 8, 9, and Rh10 in the mouse brain. *Mol. Ther.* 13, 528–537. doi: 10.1016/j.ymthe.2005.11.015

Cetin, A., Komai, S., Eliava, M., Seeburg, P. H., and Osten, P. (2007). Stereotaxic gene delivery in the rodent brain. *Nat. Protoc.* 1, 3166–3173. doi: 10.1038/nprot.2006.450

Chaimow, D., Yacoub, E., Uğurbil, K., and Shmuel, A. (2018). Spatial specificity of the functional MRI blood oxygenation response relative to neuronal activity. *NeuroImage* 164, 32–47. doi: 10.1016/j.neuroimage.2017.08.077

Chen, G., Lu, H. D., and Roe, A. W. (2008). A map for horizontal disparity in monkey V2. *Neuron* 58, 442–450. doi: 10.1016/j.neuron.2008.02.032

Chernov, M. M., Friedman, R. M., Chen, G., Stoner, G. R., and Roe, A. W. (2018). Functionally specific optogenetic modulation in primate visual cortex. *Proc. Natl. Acad. Sci.* 115, 10505–10510. doi: 10.1073/pnas.1802018115

Choi, V. W., McCarty, D. M., and Samulski, R. J. (2005). AAV hybrid serotypes: improved vectors for gene delivery. *Curr. Gene Ther.* 5, 299–310. doi: 10.2174/1566523054064968

Clancy, K. B., Schnepel, P., Rao, A. T., and Feldman, D. E. (2015). Structure of a Single Whisker Representation in Layer 2 of Mouse Somatosensory Cortex. *J. Neurosci.* 35:3946. doi: 10.1523/jneurosci.3887-14.2015

Cohen, S., Au, S., and Panté, N. (2011). How viruses access the nucleus. *Biochim. Biophys. Acta Mol. Cell Res.* 1813, 1634–1645. doi: 10.1016/j.bbamcr.2010.12.009

Dako (2009). *Immunohistochemical (IHC) Staining Methods, Updated and Expanded*, 5thEdn Edn. Denmark: Dako.

Devonshire, I. M., Zheng, Y., and Berwick, J. (2013). "Voltage-Sensitive Dye Imaging, Intrinsic Optical Signals," in *Encyclopedia of Computational Neuroscience*, eds D. Jaeger and R. Jung (New York, NY: Springer), 1–4. doi: 10.1007/978-1-4614-7320-6_541-1

Drew, P. J., and Feldman, D. E. (2009). Intrinsic signal imaging of deprivation-induced contraction of whisker representations in rat somatosensory cortex. *Cereb. Cortex* 19, 331–348. doi: 10.1093/cercor/bhn085

Dugué, G. P., Akemann, W., and Knöpfel, T. (2012). "Chapter 1 - A comprehensive concept of optogenetics," in *Progress in Brain Research*, eds T. Knöpfel and E. S. Boyden (Amsterdam: Elsevier), 1–28. doi: 10.1016/b978-0-444-59426-6.00001-x

Fenno, L. E., Yizhar, O., and Deisseroth, K. (2011). The Development and Application of Optogenetics. *Annu. Rev. Neurosci.* 34, 389–412. doi: 10.1146/annurev-neuro-061010-113817

Ferry, B., Gervasoni, D., and Vogt, C. (2014). *Stereotaxic Neurosurgery in Laboratory Rodent*, 1 Edn. Paris: Springer-Verlag.

Flecknell, P. A. (2009). *Laboratory Animal Anaesthesia*, 3 Edn. Cambridge: Academic Press.

Frostig, R. D., Lieke, E. E., Ts'o, D. Y., and Grinvald, A. (1990). Cortical functional architecture and local coupling between neuronal activity and the microcirculation revealed by in vivo high-resolution optical imaging of intrinsic signals. *Proc. Natl. Acad. Sci. U S A.* 87, 6082–6086. doi: 10.1073/pnas.87.16.6082

Fukuda, M., Moon, C.-H., Wang, P., and Kim, S.-G. (2006). Mapping iso-orientation columns by contrast agent-enhanced functional magnetic resonance imaging: reproducibility, specificity, and evaluation by optical imaging of intrinsic signal. *J. Neurosci.* 26, 11821–11832. doi: 10.1523/jneurosci.3098-06.2006

Gradinaru, V., Thompson, K. R., and Deisseroth, K. (2008). eNpHR: a Natronomonas halorhodopsin enhanced for optogenetic applications. *Brain Cell Biol.* 36, 129–139. doi: 10.1007/s11068-008-9027-6

Gradinaru, V., Thompson, K. R., Zhang, F., Mogri, M. Z., Kay, K., Schneider, M. B., et al. (2007). Targeting and Readout Strategies for Fast Optical Neural Control In Vitro and In Vivo. *J. Neurosci.* 27, 14231–14238. doi: 10.1523/jneurosci.3578-07.2007

Gradinaru, V., Zhang, F., Ramakrishnan, C., Mattis, J., Prakash, R., Diester, I., et al. (2010). Molecular and Cellular Approaches for Diversifying and Extending Optogenetics. *Cell* 141, 154–165. doi: 10.1016/j.cell.2010.02.037

Grandy, T. H., Greenfield, S. A., and Devonshire, I. M. (2012). An evaluation of in vivo voltage-sensitive dyes: pharmacological side effects and signal-to-noise ratios after effective removal of brain-pulsation artifacts. *J. Neurophysiol.* 108, 2931–2945. doi: 10.1152/jn.00512.2011

Grimm, D., Lee, J. S., Wang, L., Desai, T., Akache, B., Storm, T. A., et al. (2008). In vitro and in vivo gene therapy vector evolution via multispecies interbreeding and retargeting of adeno-associated viruses. *J. Virol.* 82, 5887–5911. doi: 10.1128/jvi.00254-08

Grinvald, A., and Hildesheim, R. (2004). VSDI: A new era in functional imaging of cortical dynamics. *Nat. Rev. Neurosci.* 5, 874–885. doi: 10.1038/nrn1536

Grinvald, A., Frostig, R. D., Lieke, E., and Hildesheim, R. (1988). Optical imaging of neuronal activity. *Physiol. Rev.* 68, 1285–1366.

Grinvald, A., Lieke, E., Frostig, R. D., Gilbert, C. D., and Wiesel, T. N. (1986). Functional architecture of cortex revealed by optical imaging of intrinsic signals. *Nature* 324, 361–364. doi: 10.1038/324361a0

Grinvald, A., Shoham, D., Shmuel, A., Glaser, D., Vanzetta, I., Shtoyerman, E., et al. (1999). "In-vivo Optical Imaging of Cortical Architecture and Dynamics," in *Modern Techniques in Neuroscience Research*, eds U. Windhorst and H. Johansson (Berlin: Springer), 893–969. doi: 10.1007/978-3-642-58552-4_34

Gunaydin, L. A., Yizhar, O., Berndt, A., Sohal, V. S., Deisseroth, K., and Hegemann, P. (2010). Ultrafast optogenetic control. *Nat. Neurosci.* 13, 387–392. doi: 10.1038/nn.2495

Habib, E. R. M. S., Komuro, R., Yan, P., Hayashi, S., Inaji, M., Momose-Sato, Y., et al. (2013). Evaluation of voltage-sensitive fluorescence dyes for monitoring neuronal activity in the embryonic central nervous system. *J. Membr. Biol.* 246, 679–688. doi: 10.1007/s00232-013-9584-1

Han, W., Tellez, L. A., Rangel, M. J. Jr., Motta, S. C., Zhang, X., Perez, I. O., et al. (2017). Integrated Control of Predatory Hunting by the Central Nucleus of the Amygdala. *Cell* 168, 311.e–324.e.

Hess, A., Stiller, D., Kaulisch, T., Heil, P., and Scheich, H. (2000). New insights into the hemodynamic blood oxygenation level-dependent response through combination of functional magnetic resonance imaging and optical recording in gerbil barrel cortex. *J. Neurosci.* 20, 3328–3338. doi: 10.1523/jneurosci.20-09-03328.2000

Hillman, E. M. C. (2014). Coupling mechanism and significance of the BOLD signal: a status report. *Annu. Rev. Neurosci.* 37, 161–181. doi: 10.1146/annurev-neuro-071013-014111

Honjoh, T., Ji, Z.-G., Yokoyama, Y., Sumiyoshi, A., Shibuya, Y., Matsuzaka, Y., et al. (2014). Optogenetic Patterning of Whisker-Barrel Cortical System in Transgenic Rat Expressing Channelrhodopsin-2. *PLoS One* 9:e93706. doi: 10.1371/journal.pone.0093706

Iida, H., Md, Ohata, H., Md, Iida, M., Md, et al. (1998). Isoflurane and Sevoflurane Induce Vasodilation of Cerebral Vessels via ATP-sensitive K+Channel Activation Anesthesiology. *J. Am. Soc. Anesthesiol.* 89, 954–960. doi: 10.1097/00000542-199810000-00020

Isett, B. R., Feasel, S. H., Lane, M. A., and Feldman, D. E. (2018). Slip-Based Coding of Local Shape and Texture in Mouse S1. *Neuron* 97, 418.e–433.e.

Jacob, V., Le Cam, J., Ego-Stengel, V., and Shulz, D. E. (2008). Emergent properties of tactile scenes selectively activate barrel cortex neurons. *Neuron* 60, 1112–1125. doi: 10.1016/j.neuron.2008.10.017

Janssen, B. J. A., Celle, T. D., Debets, J. J. M., Brouns, A. E., Callahan, M. F., and Smith, T. L. (2004). Effects of anesthetics on systemic hemodynamics in mice. *Am. J. Physiol. Heart Circulat. Physiol.* 287, H1618–H1624.

Jellema, T., Brunia, C. H., and Wadman, W. J. (2004). Sequential activation of microcircuits underlying somatosensory-evoked potentials in rat neocortex. *Neuroscience* 129, 283–295. doi: 10.1016/j.neuroscience.2004.07.046

Juavinett, A. L., Nauhaus, I., Garrett, M. E., Zhuang, J., and Callaway, E. M. (2017). Automated identification of mouse visual areas with intrinsic signal imaging. *Nat. Protoc.* 12, 32–43. doi: 10.1038/nprot.2016.158

Kirkcaldie, M., Watson, C., Paxinos, G., and Franklin, K. (2012). *Straightening out the mouse neocortex*. Adelaide, SA: Australian Neuroscience Society.

Knutsen, P. M., Mateo, C., and Kleinfeld, D. (2016). Precision mapping of the vibrissa representation within murine primary somatosensory cortex. *Philosoph. Transact. R. Soc. B Biol. Sci.* 371:20150351. doi: 10.1098/rstb.2015.0351

Laboy-Juárez, K. J., Langberg, T., Ahn, S., and Feldman, D. E. (2019). Elementary motion sequence detectors in whisker somatosensory cortex. *Nat. Neurosci.* 22, 1438–1449. doi: 10.1038/s41593-019-0448-6

Le Cam, J., Estebanez, L., Jacob, V., and Shulz, D. E. (2011). Spatial structure of multiwhisker receptive fields in the barrel cortex is stimulus dependent. *J. Neurophysiol.* 106, 986–998. doi: 10.1152/jn.00044.2011

Lee, J. H., Durand, R., Gradinaru, V., Zhang, F., Goshen, I., Kim, D.-S., et al. (2010). Global and local fMRI signals driven by neurons defined optogenetically by type and wiring. *Nature* 465, 788–792. doi: 10.1038/nature09108

Lippert, M. T., Takagaki, K., Xu, W., Huang, X., and Wu, J.-Y. (2007). Methods for voltage-sensitive dye imaging of rat cortical activity with high signal-to-noise ratio. *J. Neurophysiol.* 98, 502–512. doi: 10.1152/jn.01169.2006

Lowery, R. L., and Majewska, A. K. (2010). Intracranial injection of adeno-associated viral vectors. *J. Vis. Exp.* 2010:2140.

Lu, H. D., Chen, G., Tanigawa, H., and Roe, A. W. (2010). A motion direction map in macaque V2. *Neuron* 68, 1002–1013. doi: 10.1016/j.neuron.2010.11.020

Lu, H., Patel, S., Luo, F., Li, S. J., Hillard, C. J., Ward, B. D., et al. (2004). Spatial correlations of laminar BOLD and CBV responses to rat whisker stimulation with neuronal activity localized by Fos expression. *Magnet. Resonan. Med.* 52, 1060–1068. doi: 10.1002/mrm.20265

Madisen, L., Mao, T., Koch, H., Zhuo, J. M., Berenyi, A., Fujisawa, S., et al. (2012). A toolbox of Cre-dependent optogenetic transgenic mice for light-induced activation and silencing. *Nat. Neurosci.* 15, 793–802. doi: 10.1038/nn.3078

Malach, R., Amir, Y., Harel, M., and Grinvald, A. (1993). Relationship between intrinsic connections and functional architecture revealed by optical imaging and in vivo targeted biocytin injections in primate striate cortex. *Proc. Natl. Acad. Sci. U S A.* 90, 10469–10473. doi: 10.1073/pnas.90.22.10469

Masamoto, K., and Kanno, I. (2012). Anesthesia and the quantitative evaluation of neurovascular coupling. *J. Cereb. Blood Flow Metab.* 32, 1233–1247. doi: 10.1038/jcbfm.2012.50

McVea, D. A., Mohajerani, M. H., and Murphy, T. H. (2012). Voltage-sensitive dye imaging reveals dynamic spatiotemporal properties of cortical activity after spontaneous muscle twitches in the newborn rat. *J. Neurosci.* 32, 10982–10994. doi: 10.1523/jneurosci.1322-12.2012

Mitchinson, B., Grant, R. A., Arkley, K., Rankov, V., Perkon, I., and Prescott, T. J. (2011). Active vibrissal sensing in rodents and marsupials. *Philos. Trans. R. Soc. Lond. B Biol. Sci.* 366, 3037–3048. doi: 10.1098/rstb.2011.0156

Miyashita, T., Shao, Y. R., Chung, J., Pourzia, O., and Feldman, D. E. (2013). Long-term channelrhodopsin-2 (ChR2) expression can induce abnormal axonal morphology and targeting in cerebral cortex. *Front. Neural Circuits* 7:8. doi: 10.3389/fncir.2013.00008

Nagel, G., Szellas, T., Huhn, W., Kateriya, S., Adeishvili, N., Berthold, P., et al. (2003). Channelrhodopsin-2, a directly light-gated cation-selective membrane channel. *Proc. Natl. Acad. Sci. USA* 100, 13940–13945. doi: 10.1073/pnas.1936192100

Nathanson, J. L., Yanagawa, Y., Obata, K., and Callaway, E. M. (2009). Preferential labeling of inhibitory and excitatory cortical neurons by endogenous tropism of adeno-associated virus and lentivirus vectors. *Neuroscience* 161, 441–450. doi: 10.1016/j.neuroscience.2009.03.032

Oberlaender, M., de Kock, C. P. J., Bruno, R. M., Ramirez, A., Meyer, H. S., Dercksen, V. J., et al. (2012). Cell type-specific three-dimensional structure of

thalamocortical circuits in a column of rat vibrissal cortex. *Cereb. Cortex* 22, 2375–2391. doi: 10.1093/cercor/bhr317

Paxinos, G., and Franklin, K. B. J. (2019). *The Mouse Brain in Stereotaxic Coordinates*, 5 Edn. Cambridge: Academic Press.

Paxinos, G., and Watson, C. (2017). *The Rat Brain in Stereotaxic Coordinates: Compact*, 7th Edn. Cambridge: Academic Press.

Pouratian, N., and Toga, A. (2002). "Optical Imaging Based on Intrinsic Signals," in *Brain Mapping: The Methods*, eds A. W. Toga and J. C. Mazziottapp (Amsterdam: Elsevier), 97–140. doi: 10.1016/b978-012693019-1/50007-1

Powell, S. K., Rivera-Soto, R., and Gray, S. J. (2015). Viral expression cassette elements to enhance transgene target specificity and expression in gene therapy. *Discov. Med.* 19, 49–57.

Ross, W., Salzberg, B., Cohen, L., Grinvald, A., Davila, H., Waggoner, A., et al. (1977). Changes in absorption, fluorescence, dichroism, and birefringence in stained giant axons: Optical measurement of membrane potential. *J. Membr. Biol.* 33, 141–183. doi: 10.1007/bf01869514

Ruiz, O., Lustig, B. R., Nassi, J. J., Cetin, A., Reynolds, J. H., Albright, T. D., et al. (2013). Optogenetics through windows on the brain in the nonhuman primate. *J. Neurophysiol.* 110, 1455–1467. doi: 10.1152/jn.00153.2013

Scanziani, M., and Hausser, M. (2009). Electrophysiology in the age of light. *Nature* 461, 930–939. doi: 10.1038/nature08540

Scheyltjens, I., Laramée, M.-E., Van den Haute, C., Gijsbers, R., Debyser, Z., Baekelandt, V., et al. (2015). Evaluation of the expression pattern of rAAV2/1, 2/5, 2/7, 2/8, and 2/9 serotypes with different promoters in the mouse visual cortex. *J. Comparat. Neurol.* 523, 2019–2042. doi: 10.1002/cne.23819

Scott, N. A., and Murphy, T. H. (2012). Hemodynamic Responses Evoked by Neuronal Stimulation via Channelrhodopsin-2 Can Be Independent of Intracortical Glutamatergic Synaptic Transmission. *PLoS One* 7:e29859. doi: 10.1371/journal.pone.0029859

Seidemann, E., Chen, Y., Bai, Y., Chen, S. C., Mehta, P., Kajs, B. L., et al. (2016). Calcium imaging with genetically encoded indicators in behaving primates. *eLife* 5:e16178.

Sheth, S. A., Nemoto, M., Guiou, M., Walker, M., Pouratian, N., Hageman, N., et al. (2004). Columnar specificity of microvascular oxygenation and volume responses: implications for functional brain mapping. *J. Neurosci.* 24, 634–641. doi: 10.1523/jneurosci.4526-03.2004

Sheth, S., Nemoto, M., Guiou, M., Walker, M., Pouratian, N., and Toga, A. W. (2003). Evaluation of coupling between optical intrinsic signals and neuronal activity in rat somatosensory cortex. *NeuroImage* 19, 884–894. doi: 10.1016/s1053-8119(03)00086-7

Shin, Y., Yoo, M., Kim, H.-S., Nam, S.-K., Kim, H.-I., Lee, S.-K., et al. (2016). Characterization of fiber-optic light delivery and light-induced temperature changes in a rodent brain for precise optogenetic neuromodulation. *Biomed. Opt. Express* 7, 4450–4471. doi: 10.1364/boe.7.004450

Shmuel, A., and Grinvald, A. (1996). Functional organization for direction of motion and its relationship to orientation maps in cat area 18. *J. Neurosci.* 16, 6945–6964. doi: 10.1523/jneurosci.16-21-06945.1996

Shmuel, A., and Grinvald, A. (2000). Coexistence of linear zones and pinwheels within orientation maps in cat visual cortex. *Proc. Natl. Acad. Sci. U S A.* 97, 5568–5573. doi: 10.1073/pnas.97.10.5568

Shmuel, A., Korman, M., Sterkin, A., Harel, M., Ullman, S., Malach, R., et al. (2005). Retinotopic axis specificity and selective clustering of feedback projections from V2 to V1 in the owl monkey. *J. Neurosci.* 25, 2117–2131. doi: 10.1523/jneurosci.4137-04.2005

Shoham, D., Glaser, D. E., Arieli, A., Kenet, T., Wijnbergen, C., Toledo, Y., et al. (1999). Imaging cortical dynamics at high spatial and temporal resolution with novel blue voltage-sensitive dyes. *Neuron* 24, 791–802. doi: 10.1016/s0896-6273(00)81027-2

Sohal, V. S., Zhang, F., Yizhar, O., and Deisseroth, K. (2009). Parvalbumin neurons and gamma rhythms enhance cortical circuit performance. *Nature* 459, 698–702. doi: 10.1038/nature07991

Sotero, R. C., Bortel, A., Naaman, S., Mocanu, V. M., Kropf, P., Villeneuve, M. Y., et al. (2015) Laminar distribution of phase-amplitude coupling of spontaneous current sources and sinks. *Front. Neurosci.* 9:454. doi: 10.3389/fnins.2015.00454

Strominger, R. N., and Woolsey, T. A. (1987). Templates for locating the whisker area in fresh flattened mouse and rat cortex. *J. Neurosci. Methods* 22, 113–118. doi: 10.1016/0165-0270(87)90004-5

Tanigawa, H., Lu, H. D., and Roe, A. W. (2010). Functional organization for color and orientation in macaque V4. *Nat. Neurosci.* 13, 1542–1548. doi: 10.1038/nn.2676

Thompson, K., and Towne, C. (2018). "A Hitchhiker's Guide to the Selection of Viral Vectors for Optogenetic Studies," in *Optogenetics: A Roadmap*, ed. A. Stroh (Berlin: Springer), 1–23. doi: 10.1007/978-1-4939-7417-7_1

Ts'o, D. Y., Roe, A. W., and Gilbert, C. D. (2001). A hierarchy of the functional organization for color, form and disparity in primate visual area V2. *Vis. Res.* 41, 1333–1349. doi: 10.1016/s0042-6989(01)00076-1

Urban, A., and Rossier, J. (2012). Genetic targeting of specific neuronal cell types in the cerebral cortex. *Prog. Brain Res.* 196, 163–192. doi: 10.1016/b978-0-444-59426-6.00009-4

Vazquez, A. L., Fukuda, M., Crowley, J. C., and Kim, S.-G. (2013). Neural and Hemodynamic Responses Elicited by Forelimb- and Photo-stimulation in Channelrhodopsin-2 Mice: Insights into the Hemodynamic Point Spread Function. *Cereb. Cortex* 24, 2908–2919. doi: 10.1093/cercor/bht147

Vilarchao, M. E., Estebanez, L., Shulz, D. E., and Férézou, I. (2018). Supra-barrel Distribution of Directional Tuning for Global Motion in the Mouse Somatosensory Cortex. *Cell Rep.* 22, 3534–3547. doi: 10.1016/j.celrep.2018.03.006

Vogt, K. E., Gerharz, S., Graham, J., and Canepari, M. (2011). High-resolution simultaneous voltage and Ca2+ imaging. *J. Physiol.* 589, 489–494. doi: 10.1113/jphysiol.2010.200220

Volkov, O., Kovalev, K., Polovinkin, V., Borshchevskiy, V., Bamann, C., Astashkin, R., et al. (2017). Structural insights into ion conduction by channelrhodopsin 2. *Science* 358:eaan8862. doi: 10.1126/science.aan8862

Watakabe, A., Ohtsuka, M., Kinoshita, M., Takaji, M., Isa, K., Mizukami, H., et al. (2015). Comparative analyses of adeno-associated viral vector serotypes 1, 2, 5, 8 and 9 in marmoset, mouse and macaque cerebral cortex. *Neurosci. Res.* 93, 144–157. doi: 10.1016/j.neures.2014.09.002

Watson, C., Paxinos, G., and Puelles, L. (2012). *The Mouse Nervous System*. Cambridge: Academic Press.

Welker, E., Armstrong-James, M., Van der Loos, H., and Kraftsik, R. (1993). The Mode of Activation of a Barrel Column: Response Properties of Single Units in the Somatosensory Cortex of the Mouse upon Whisker Deflection. *Eur. J. Neurosci.* 5, 691–712. doi: 10.1111/j.1460-9568.1993.tb00534.x

Willadt, S., Canepari, M., Yan, P., Loew, L. M., and Vogt, K. E. (2014). Combined optogenetics and voltage sensitive dye imaging at single cell resolution. *Front. Cell. Neurosci.* 8:311. doi: 10.3389/fncel.2014.00311

Yang, J. W., Prouvot, P. H., Reyes-Puerta, V., Stuttgen, M. C., Stroh, A., and Luhmann, H. J. (2017). Optogenetic Modulation of a Minor Fraction of Parvalbumin-Positive Interneurons Specifically Affects Spatiotemporal Dynamics of Spontaneous and Sensory-Evoked Activity in Mouse Somatosensory Cortex in Vivo. *Cereb. Cortex* 27, 5784–5803. doi: 10.1093/cercor/bhx261

Yang, J.-W., Prouvot, P.-H., Stroh, A., and Luhmann, H. J. (2018). "Combining Optogenetics with MEA, Depth-Resolved LFPs and Assessing the Scope of Optogenetic Network Modulation," in *Optogenetics: A Roadmap*, ed. A. Stroh (New York, NY: Springer), 133–152. doi: 10.1007/978-1-4939-7417-7_8

Yao, Z.-S., Villeneuve, M., Kropf, P., Shaikh, D., Chaimow, D., and Shmuel, A. (2017). "Mechanisms of Decoding Oriented Grating Stimuli Investigated by Optical Imaging of Cat Area 18," in *23rd annual meeting of the International Organization for Human Brain Mapping*, (Vancouver, BC: OHBM).

Yizhar, O., and Adamantidis, A. (2018). "Cell Type-Specific Targeting Strategies for Optogenetics," in *Optogenetics: A Roadmap*, ed. A. Stroh (Berlin: Springer), 25–42. doi: 10.1007/978-1-4939-7417-7_2

Yizhar, O., Fenno Lief, E., Davidson Thomas, J., Mogri, M., and Deisseroth, K. (2011). Optogenetics in Neural Systems. *Neuron* 71, 9–34. doi: 10.1016/j.neuron.2011.06.004

Zhang, F., Gradinaru, V., Adamantidis, A., Durand, R., Airan, R. D., de Lecea, L., et al. (2010). Optogenetic interrogation of neural circuits: technology for probing mammalian brain structures. *Nat. Protoc.* 5, 439–456. doi: 10.1038/nprot.2009.226

Zhang, F., Prigge, M., Beyriere, F., Tsunoda, S. P., Mattis, J., Yizhar, O., et al. (2008). Red-shifted optogenetic excitation: a tool for fast neural control derived from Volvox carteri. *Nat. Neurosci.* 11, 631–633. doi: 10.1038/nn.2120

Zhang, F., Wang, L.-P., Brauner, M., Liewald, J. F., Kay, K., Watzke, N., et al. (2007). Multimodal fast optical interrogation of neural circuitry. *Nature* 446, 633–639. doi: 10.1038/nature05744

Conflict of Interest: The authors declare that the research was conducted in the absence of any commercial or financial relationships that could be construed as a potential conflict of interest.

Advantages of publishing in Frontiers

OPEN ACCESS
Articles are free to read for greatest visibility and readership

FAST PUBLICATION
Around 90 days from submission to decision

HIGH QUALITY PEER-REVIEW
Rigorous, collaborative, and constructive peer-review

TRANSPARENT PEER-REVIEW
Editors and reviewers acknowledged by name on published articles

Frontiers
Avenue du Tribunal-Fédéral 34
1005 Lausanne | Switzerland

Visit us: www.frontiersin.org
Contact us: frontiersin.org/about/contact

REPRODUCIBILITY OF RESEARCH
Support open data and methods to enhance research reproducibility

DIGITAL PUBLISHING
Articles designed for optimal readership across devices

FOLLOW US
@frontiersin

IMPACT METRICS
Advanced article metrics track visibility across digital media

EXTENSIVE PROMOTION
Marketing and promotion of impactful research

LOOP RESEARCH NETWORK
Our network increases your article's readership